

Monographs in Electrochemistry

Series Editor: F. Scholz

Marek Orlik

Self-Organization in Electrochemical Systems I

General Principles of Self-Organization.
Temporal Instabilities

 Springer

Self-Organization in Electrochemical Systems I

For further volumes:

<http://www.springer.com/series/7386>

Monographs in Electrochemistry

Surprisingly, a large number of important topics in electrochemistry is not covered by up-to-date monographs and series on the market, some topics are even not covered at all. The series Monographs in Electrochemistry fills this gap by publishing indepth monographs written by experienced and distinguished electrochemists, covering both theory and applications. The focus is set on existing as well as emerging methods for researchers, engineers, and practitioners active in the many and often interdisciplinary fields, where electrochemistry plays a key role. These fields will range – among others – from analytical and environmental sciences to sensors, materials sciences and biochemical research.

Information about published and forthcoming volumes is available at <http://www.springer.com/series/7386>

Series Editor: Fritz Scholz, University of Greifswald, Germany

Marek Orlik

Self-Organization in Electrochemical Systems I

General Principles of Self-Organization.
Temporal Instabilities

 Springer

Marek Orlik
University of Warsaw
Faculty of Chemistry
Warsaw
Poland

Some figures were taken from publications of the APS, for these the following applies:
Readers may view, browse, and/or download material for temporary copying purposes only, provided these uses are for noncommercial personal purposes. Except as provided by law, this material may not be further reproduced, distributed, transmitted, modified, adapted, performed, displayed, published, or sold in whole or part, without prior written permission from the American Physical Society.

ISSN 1865-1836 ISSN 1865-1844 (electronic)
ISBN 978-3-642-27672-9 ISBN 978-3-642-27673-6 (eBook)
DOI 10.1007/978-3-642-27673-6
Springer Heidelberg New York Dordrecht London

Library of Congress Control Number: 2012940712

© Springer-Verlag Berlin Heidelberg 2012

This work is subject to copyright. All rights are reserved by the Publisher, whether the whole or part of the material is concerned, specifically the rights of translation, reprinting, reuse of illustrations, recitation, broadcasting, reproduction on microfilms or in any other physical way, and transmission or information storage and retrieval, electronic adaptation, computer software, or by similar or dissimilar methodology now known or hereafter developed. Exempted from this legal reservation are brief excerpts in connection with reviews or scholarly analysis or material supplied specifically for the purpose of being entered and executed on a computer system, for exclusive use by the purchaser of the work. Duplication of this publication or parts thereof is permitted only under the provisions of the Copyright Law of the Publisher's location, in its current version, and permission for use must always be obtained from Springer. Permissions for use may be obtained through RightsLink at the Copyright Clearance Center. Violations are liable to prosecution under the respective Copyright Law.

The use of general descriptive names, registered names, trademarks, service marks, etc. in this publication does not imply, even in the absence of a specific statement, that such names are exempt from the relevant protective laws and regulations and therefore free for general use.

While the advice and information in this book are believed to be true and accurate at the date of publication, neither the authors nor the editors nor the publisher can accept any legal responsibility for any errors or omissions that may be made. The publisher makes no warranty, express or implied, with respect to the material contained herein.

Printed on acid-free paper

Springer is part of Springer Science+Business Media (www.springer.com)

Preface

Self-organization is one of the most important and most general features of nature, being practically omnipresent in our world, viz., in physical and inorganic systems, in organic and living systems, and even in social systems. Already 200 years ago, self-organization phenomena have been observed in electrochemical experiments and much later a vast number of carefully designed electrochemical experiments have been described where self-organization plays a role. Electrochemistry lends itself for such studies in a very special way, as it allows easy control and measurement of the electrode potential and current. Therefore, it is no surprise that the quantitative data of electrochemical experiments have given a very sound basis for mathematical modeling of self-organization. Professor Dr. Marek Orlik is an experienced electrochemist who now specializes in the physical chemistry of self-organization. His profound knowledge of mathematics, physics, and chemistry, together with his clear-cut thinking and his experimental abilities, enables him to present the theoretical background and the experimental details of self-organization in electrochemistry in a very lucid and appealing way. Professor Orlik is a disciple of the Warsaw electrochemical school. He did his Ph.D. with Zbigniew Galus, and worked as postdoc with Gerhard Gritzner (Linz), and he was an *Alexander von Humboldt Fellow* with Karl Doblhofer and Gerhard Ertl in Berlin.

The publishing house Springer and the editor of the series *Monographs in Electrochemistry* regard it as a big fortune that Marek Orlik accepted the invitation to write this monograph because it is the first comprehensive description of that topic, and it is clearly a very seriously needed monograph. When starting to write this monograph, the author quickly realized that the topic cannot be adequately covered in one volume because the mathematical and physical background needs careful and extended explanations. We are thankful to Springer for agreeing to publish this monograph in two volumes, allowing the author to present both the theoretical and the experimental side in detail. Writing such 2-volume monograph is a task which absorbs all energy for several years, and it is not only an intellectual

achievement, but also physically very demanding, especially when considering that the author has all the duties of a professor at a chemistry department of a major university! I am sure that the appreciation of the readers will give Marek Orlik the deserved reward and I hope that the monograph will stimulate further studies of this important branch of physical chemistry.

Greifswald, May 2012

Fritz Scholz
University of Greifswald, Germany

Introduction

The world is a *dynamical system* and this system is generally *nonlinear*. This simple sentence describes the fundamental feature of phenomena described in these books. Although most of them belong to the world of electrochemistry, it is extremely important to note that their dynamics exhibit striking analogies, when compared with other types of dynamical systems, like chemical, physical, and biological ones, and even with some social processes or phenomena occurring in the capital market. Since each of these categories deals with its specific language, the universalities in the dynamic behaviors manifest themselves clearly only at the level of mathematical description, which in turn is based on the behavior of solutions of *nonlinear differential equations*. Therefore, *nonlinear dynamics* is really an interdisciplinary science. Electrochemical processes described in these books are thus only specific examples of more general features of nonlinear dynamic processes.

Many phenomena which we experience in everyday life, not only in the scientific laboratory, are nonlinear in their dynamics, but at the elementary level of education their mathematical description is often linearized, like in the case of diffusion transport or heat conduction processes. The advantage of such simplification is the relative simplicity of the mathematical form of respective equations and of the way in which the solutions of them can be obtained. When the differential equation (or the set of them) is nonlinear, the analytical solution is often unknown and one has to use the computer to solve the problem numerically. That is why the invention and development of digital computers assisted the progress in nonlinear dynamics. In course of computer calculations not only numerical solutions of various problems were obtained, but also completely unexpected phenomena were discovered. A seminal example is the observation made in 1963 by Lorenz, who discovered the unpredictable long-term evolution of the solutions of only three differential equations. This invention led to the idea of *deterministic chaos*, which means complex, aperiodic dynamics generated by entirely deterministic dynamical system, without any assumed stochasticity. One should remember that such unpredictability was treated already at the end of nineteenth century by Poincaré who analyzed *qualitatively* the chaotic dynamics of a three-body system, the problem of

not having explicit solution in terms of Newton's analytical methods. In fact, Poincaré was the pioneer of a modern approach to complex systems in which the emphasis is on the *qualitative type* of dynamics rather than on strict quantitative solutions, frequently not existing.

Deterministic chaos is however an extremely complex example of dynamic phenomena, which manifests itself as aperiodic oscillatory variations of the system's state. But the oscillations can be also periodic, like pulsating of our heart. In chemistry, the best known examples are the periodic variations of the color of the solution in which the Belousov–Zhabotinsky redox reaction is running. In electrochemistry, the oldest examples of analogous phenomena include oscillations of electric current upon anodic electrodisolution of some metals. Periodic dissolution of metals was described as early as in 1828 by Fechner, who reported repetitive bursts of effervescence (gas bubbles evolution) during the dissolution of iron in nitric acid.

One should note an extremely important, common feature of those oscillations: they can set in absolutely spontaneously, i.e., without any external periodic perturbation of the system. Therefore, we consider such behavior a *dynamic self-organization*, i.e., the *spontaneous*, coherent dynamic behavior of the system's components, leading, e.g., to periodic (or more complex) variations of its entire characteristics. Furthermore, under appropriate conditions also the spatial symmetry of the dynamical system can be broken and then various types of spatial or spatiotemporal patterns can also *spontaneously* develop. A famous example of stationary patterns of that type was theoretically predicted by A. Turing in his seminal work published in the year 1952. The experimental confirmation of his ideas happened only in 1990s for chemical systems and at the beginning of twenty-first century for electrochemical processes. Thus, self-organization may occur both in time and in space.

One should emphasize that such self-organization phenomena can occur only beyond the state of equilibrium. This is justified by the second law of thermodynamics which forbids the decrease of entropy of Universe. Since creation of any order, including dynamic self-organization, decreases the entropy, there must occur simultaneously an irreversible, dissipative process, in which the production of entropy at least compensates its decrease. This is the thermodynamic condition. In turn, the important kinetic requirement is that the differential equations defining the dynamical systems must be nonlinear. However, it is still not a sufficient condition for the occurrence of self-organization. Analysis of the origin of such phenomena clearly indicates also the necessity of positive and negative *feedback loops* in the steps composing the entire mechanism of a given process. Therefore, understanding of given manifestation of self-organization requires, among others, identification of appropriate feedback loops. In fact, even the simplest case of temporal oscillatory behavior can be understood as the interplay of such feedback loops: during the operation of the positive feedback, the concentration of given species increases quickly in time until the negative feedback loop takes over the control and leads to a decrease in this concentration, creating the conditions for which positive feedback eventually sets in again, etc. In other words, the oscillatory

behavior requires a presence of a fast positive and a slow negative feedback loops in the system's dynamics.

A typical sequence of events is that even relatively uncomplicated system, described in terms of deterministic evolution equations, may exhibit sudden change to a completely new, qualitatively different behavior upon smooth variations of the control parameter. A (too) simple deterministic approach, assuming the smooth response of the system's behavior upon increasing distance from equilibrium, must be replaced by a far more sophisticated view, accepting the existence of sudden transitions, mathematically called the *bifurcations*. It is like for the tourist who left the flatlands and entered the mountain area—he has to consider the presence of chasms which can suddenly and dramatically change his situation. This is more than just a simple conclusion; this is a new view of the way in which dynamic processes may develop in nature.

Now it is high time to define the place of electrochemistry in the area of such phenomena. Chemical reactions can exhibit linear or non-linear dynamics, but electrochemical processes are always inherently nonlinear. This is clearly evidenced even in the simplest case of electric current dependent exponentially on the voltage applied between the electrodes. Furthermore, compared to chemical systems, in electrochemical practice it is extremely easy to drive the system smoothly away from the equilibrium state, by appropriate increase of the voltage applied or the current density imposed. Thus, two fundamental conditions for dynamic self-organization are met, but of course not in every process the appropriate, destabilizing feedback loops can operate, so not every electrochemical process is automatically a source of self-organization under any conditions. Such additional conditions will be shown in these books, based on both numerous experimental examples and theoretical considerations.

In these books thus various kinds of *temporal*, *spatial*, and *spatiotemporal self-organization* in electrochemical systems are described. In spite of specific features of such systems, like the presence and the structure of the electrode–electrolyte interface, the reader will notice analogies in the bifurcation schemes between electrochemical and chemical systems, i.e., those universalities that are so striking at the level of mathematical description. The reader will also be able to notice the evolution of explanations of such phenomena which took place over recent decades. While early works were usually purely electrochemical, i.e., the authors looked for the source of instabilities only in the properties of the electrode–electrolyte interface, later works reflect increasing interest in a treatment based on the concepts of nonlinear dynamics. In particular, as the source of dynamic instabilities the characteristics of not only the single interface, but of the entire electric circuit could be considered. The books contain numerous examples of both approaches and the reader will be able to choose which of them appears to him/her more convincing. The books' content is organized so that the description of particular electrochemical systems is preceded by an introduction to the basic concepts of nonlinear dynamics, in order to help the reader unfamiliar with this discipline to understand at least the fundamental concepts and methods of stability analysis. Also for this purpose this introductory part utilizes selected chemical processes for illustration

of self-organization and extends their description for basic stability analysis of electrochemical systems. The next chapters include the description of electrochemical dynamical systems, according to the author's personal selection of papers, including also very recent works. Noteworthy, the presentation of the systems is not always limited to their laboratory construction, but indicates, if possible, their relevance to realistic objects and processes, including systems of biological importance, like neurons in living matter. In fact, in order to understand better the conduction of nerve impulse, it is necessary to update earlier knowledge and models of this process for the recently made progress in self-organization in electrochemical, spatially extended systems.

It is the author's hope that these monographs will trigger and increase the interest of electrochemists, and hopefully also of the students and researchers working in other areas of science, in the modern, interdisciplinary and fascinating subject of dynamic self-organization.

Warsaw, May 2012

Marek Orlik

Contents

1	Basic Principles of Nonlinear Dynamics	1
1.1	Concise Vocabulary of Nonlinear Dynamics	1
1.2	Types of Stability	5
1.3	Linear Stability Analysis	8
1.3.1	Stability of One-Dimensional Homogeneous System	8
1.3.2	Stability of Two-Dimensional Homogeneous System	14
1.3.3	The Hopf Bifurcation	25
1.3.4	The Saddle–Node Bifurcation	31
1.3.5	The Cross-Shaped Bifurcation Diagram	33
1.4	Global Bifurcations Leading to Oscillations	34
1.4.1	Saddle–Node Bifurcation of Cycles	35
1.4.2	Saddle–Node Infinite Period (SNIPER) Bifurcation	36
1.4.3	Saddle–Loop (Homoclinic) Bifurcation	37
1.5	Nullcline Representation of Dynamical Systems	38
1.6	Fast and Slow Dynamical Variables	42
1.7	Canard Explosion	50
1.8	The Activator–Inhibitor Systems	52
1.8.1	The Concept of the Activator and the Inhibitor	52
1.8.2	Correlation Between the Nullclines and the Properties of the Jacobian Matrix	54
1.9	The Existence of Closed Trajectories—The Poincaré–Bendixson Theorem	55
1.10	The Stability of the N -Dimensional Dynamical System	57
1.10.1	Linear Stability Analysis of N -Dimensional Dynamical System	57
1.10.2	Complex Periodic Behavior and Routes to Chaos in N -Dimensional Systems	60
1.10.3	Control of Chaos	68
	References	72

2	Stability of Electrochemical Systems	75
2.1	The Role of Negative Differential Resistance in the Stability of Electrochemical Systems	75
2.1.1	The Load Line and the Simplest Electrochemical Circuit	75
2.1.2	Stability of the N-NDR System Under Potentiostatic Control	76
2.1.3	Stability of N-NDR System Under Galvanostatic Control	79
2.1.4	Origins of NDR in Electrochemical Systems	80
2.1.5	Comparison of N-NDR and S-NDR Characteristics	82
2.2	Stability of a Realistic Electrochemical N-NDR System	83
2.2.1	Linear Stability Analysis of 1D Electrochemical System	83
2.2.2	Linear Stability Analysis of 2D Electrochemical System	88
2.2.3	The Advantage of Dimensionless Representation	93
2.2.4	The Electrode Potential as an Autocatalytic Variable in the N-NDR Systems	96
2.2.5	The Electrode Potential as a Negative Feedback Variable in S-NDR Systems	99
2.3	Essential and Non-essential Variables in Electrochemical Instabilities	102
2.4	Frequency of Oscillations in the N-NDR Systems	105
	References	108
3	Application of Impedance Spectroscopy to Electrochemical Instabilities	111
3.1	Outline Concept of Impedance of Electrochemical Systems	111
3.1.1	Basic Definitions	111
3.1.2	Kramers–Kronig Transforms and Electrochemical Instabilities	116
3.2	The Impedance of the Streaming Mercury Electrode	117
3.3	Application of Impedance to the Diagnosis of Stability of Electrochemical Systems	125
3.3.1	Positive and Negative Elements in Impedance Characteristics	125
3.3.2	Diagnosis of Bifurcations from Impedance Spectra	128
3.4	Impedance Characteristics of N-NDR and HN-NDR Systems	133
3.4.1	The Hidden Negative Impedance	133
3.4.2	Mechanisms Underlying the HN-NDR Oscillator	137
3.5	Classification of Electrochemical Oscillators Based on Impedance Characteristics	148
3.6	Instabilities Involving Adsorption on Electrodes	156
3.6.1	The Frumkin Isotherm	156
3.6.2	Model Mechanisms Involving Strong Adsorption	157

3.7	The Advantages of Zero–Pole Representation of Impedance for the Stability Analysis	174
3.8	Application of the Dynamic Electrochemical Impedance Spectroscopy to Electrochemical Instabilities	183
3.9	Impedance Spectroscopy and Electrochemical Pattern Formation	187
	References	190
4	Temporal Instabilities in Cathodic Processes at Liquid and Solid Electrodes	197
4.1	Electroreduction of Peroxodisulfate Ions	197
4.1.1	The N-NDR Region as a Double Layer Effect	197
4.1.2	Bifurcation Analysis	201
4.1.3	Mechanistic Aspects of $S_2O_8^{2-}$ Electroreduction	208
4.1.4	Studies at High Ionic Strength	212
4.2	Electroreduction of Iodate(V) Ions	217
4.2.1	The Role of Additional Current Carrier in the Onset of Instabilities	217
4.2.2	The NDR-Based vs. the Electrochemical Reactions and Diffusion–Convection Approach	225
4.3	The Indium–Thiocyanate Polarographic Oscillator	229
4.3.1	Basic Experimental Characteristics of In(III)–SCN [−] Oscillator	229
4.3.2	Models of the In(III)–SCN [−] Polarographic Oscillator	233
4.4	Oscillations and Bistability in the Nickel(II)–SCN [−] Electroreduction	249
4.4.1	Origin of the N-NDR Region in the Ni(II)–SCN [−] Electroreduction	249
4.4.2	Oscillations at the HMDE	251
4.4.3	Oscillations and Bistability at the Streaming Mercury Electrode	255
4.5	Tristability in the Ni(II)–N ₃ [−] System	276
4.5.1	Two N-NDR Regions as a Source of Tristability	276
4.5.2	The Source of Two N-NDR Regions in the Ni(II)–N ₃ [−] Electroreduction	279
4.5.3	Linear Stability Analysis of the Ni(II)–N ₃ [−] Electroreduction	284
4.5.4	Impedance Studies of the Ni(II)–N ₃ [−] Electroreduction	286
4.6	Oscillations in Polarographic Processes Inhibited by Surfactans	289
4.6.1	The Cu ²⁺ –Tribenzylamine Oscillator	289
4.6.2	The Mathematical Model of the “Inhibitor Oscillator”	292
4.7	Oscillatory Reduction of Hydrogen Peroxide	294
4.7.1	Oscillations on Metal Electrodes	294
4.7.2	Oscillatory Reduction of H ₂ O ₂ on Semiconductor Electrodes	308
	References	321

5	Temporal Instabilities in Anodic Oxidation of Small Molecules/Ions at Solid Electrodes	327
5.1	Oscillations in Anodic Oxidation of Molecular Hydrogen	327
5.1.1	Experimental Results and Oscillation Mechanism	327
5.1.2	Modeling the Galvanostatic Oscillations	335
5.1.3	Experimental Observation and Modeling the Potentiostatic Oscillations	340
5.2	Oscillations in Anodic Oxidation of Carbon Monoxide	345
5.3	Bistability and Oscillations in Anodic Oxidation of $H_2 + CO$ Mixture	354
5.4	Instabilities in the Anodic Oxidation of Formate Ions	357
5.4.1	Experimental Results and Outline Oscillation Mechanism	357
5.4.2	The Model of Oscillations Under Potentiostatic Conditions	363
5.4.3	The Oxidation of Formic Acid as the System of Two Suboscillators	370
5.4.4	Mechanism of Oscillations Under Galvanostatic Conditions	374
5.4.5	Recent Suggestions for the Formic Acid Oxidation Mechanism	375
5.4.6	Temperature Overcompensation Effect in Formic Acid Oxidation	376
5.4.7	Oxidation of Formic Acid as an Analog of the Stimulus–Response of Neuronal Cells	379
5.5	Oscillatory Oxidation of Formaldehyde	382
5.6	Instabilities in the Anodic Oxidation of Alcohols	392
5.6.1	Oscillations in Alcohols Oxidation	392
5.6.2	Multistability and Excitability in Alcohols Oxidation	399
5.7	Oscillatory Oxidation of Sulfur Compounds	408
5.8	Other Oscillatory Oxidation Reactions	414
	References	417
6	Temporal Instabilities in Corrosion Processes	425
6.1	Oscillations in Anodic Dissolution of Metal Electrodes	425
6.1.1	General Characteristics of Passivation/Dissolution Processes	425
6.1.2	The Fe/H_2SO_4 Oscillatory System	434
6.1.3	The Oscillatory Electrodissolution of Copper	454
6.1.4	Oscillatory Dissolution of Nickel in H_2SO_4 Medium	473
6.1.5	Oscillatory Oxidation of Cobalt Electrodes	485
6.1.6	Oscillatory Oxidation of Vanadium Electrodes	489
6.1.7	Oscillatory Dissolution of Other Metals	492
6.2	Application of Metal Electrodissolution Processes in Micromachining	501

6.3 Anodic Oscillatory Dissolution of Semiconductor Electrodes	504
6.3.1 Cadmium-Based Semiconductors	504
6.3.2 Silicon in Fluoride Media	506
References	511
About the Author	521
About the Editor	523
Index	525

Contents for Volume II

1 Theoretical Background of Spatial and Spatiotemporal Patterns in Dynamical Systems	1
1.1 Chemical Reaction–Diffusion Systems	1
1.1.1 Basic Characteristics of Spatiotemporal Instabilities	1
1.1.2 Spatiotemporal Patterns in Excitable Chemical Media	3
1.1.3 Linear Stability Analysis of the Reaction–Diffusion Systems	13
1.1.4 The Turing Bifurcation	25
1.2 Electrochemical Reaction–Migration Systems	32
1.2.1 Spatial Inhomogeneities in Electrochemical Systems	32
1.2.2 Types of Spatial Coupling in Spatially Extended Electrochemical Systems	34
1.2.3 The Interaction of Spatial Couplings with the NDR Systems	47
References	60
2 Experimental and Model Spatiotemporal and Spatial Patterns in Electrochemical Systems	65
2.1 Simple Examples of Dissipative Pattern Formation	65
2.2 Patterns in $S_2O_8^{2-}$ Electroreduction	72
2.3 Patterns in Co Electrodeposition	77
2.4 Spatial Patterns in the Ni/H ₂ SO ₄ Oscillator	84
2.5 Modeling the Spatiotemporal Patterns in Electrodeposition Processes	86
2.5.1 The Two-Dimensional Model for Bistable and Oscillatory Process	86
2.5.2 The Extension to Three-Dimensional Model	88
2.5.3 Modeling the Electrochemical Turbulence	98
2.6 Patterns in H ₂ Oxidation	102
2.7 Patterns in CO Oxidation	108

2.8	Patterns in HCOOH Oxidation	110
2.9	Spatiotemporal Patterns in Sulfide Electrooxidation	122
2.10	Turing Patterns in Electrochemical Systems	123
2.11	Dendritic Patterns in Metal Electrodeposition	128
	2.11.1 Dendritic Deposition on Solid Surfaces	128
	2.11.2 Dendritic Deposition on Liquid/Liquid Interface	138
2.12	Dendritic Patterns in Silicon Electrodisolution	144
	References	147
3	Cooperative Dynamics of Coupled and Forced Oscillators	153
3.1	Coupled Oscillators	153
	3.1.1 Outline Theoretical Aspects of Coupling the Electrochemical Oscillators	153
	3.1.2 Single and Coupled H ₂ O ₂ Oscillators	156
	3.1.3 Coupling in the Oscillatory Oxidation of Formic Acid	162
	3.1.4 Coupled Fe/H ₂ SO ₄ Oscillators	164
	3.1.5 Coupled Co/HCl + CrO ₃ Oscillators	170
	3.1.6 Coupled Ni/H ₂ SO ₄ Oscillators	174
	3.1.7 Coupled Oscillators and <i>IR</i> Compensation	182
	3.1.8 Coupling the S-NDR Oscillators	184
	3.1.9 Coupled Electrochemical Oscillators and Neural Cells	187
	3.1.10 The Pitting Corrosion of Steel as a Cooperative Process	193
3.2	Forced Oscillators	204
	3.2.1 The Perturbed Formaldehyde and Formic Acid Oscillators	204
	3.2.2 The Forced Fe/H ₂ SO ₄ Oscillator	206
	3.2.3 The Laser-Perturbed Fe/H ₂ SO ₄ Oscillator	209
	3.2.4 The Forced Ni/H ₂ SO ₄ Oscillator	212
	References	216
4	Spatial and Spatiotemporal Patterns in Anodized Semiconductors	221
4.1	Spatiotemporal Nature of Silicon Electrooxidation and the Origin of Oscillations	221
	4.1.1 The Model of Two Oxides	221
	4.1.2 The Current-Burst Model	226
	4.1.3 The Outline New Model Involving Ohmic Potential Drops	242
4.2	Self-organization in III–V Semiconductors	243
4.3	Anodization of Ti and the Patterned TiO ₂ Layers	248
	4.3.1 Oscillations of Current During Anodization of Ti	248
	4.3.2 TiO ₂ Nanotubes	249
	4.3.3 TiO ₂ Nanogrooves	251
4.4	Overview of Spatiotemporal Self-organization in Etched Semiconductors	256
	References	260

5 Convection as a Source of Self-Organization in Electrochemical Systems	265
5.1 Convection as a Self-Organized Phenomenon	265
5.1.1 The Navier-Stokes Equation	265
5.1.2 Classical Bénard-Rayleigh Instability	266
5.2 Electrochemical Analogues of the Bénard-Rayleigh Instabilities	271
5.2.1 The Cu CuSO ₄ Cu System	271
5.2.2 Oscillations in Electroformation of Ionic Liquids	276
5.3 Oscillatory Convective Instabilities Leading to Spatiotemporal Patterns	278
5.4 Bénard-Marangoni Instabilities	280
5.4.1 The Marangoni Number	280
5.4.2 Instabilities at the Mercury-Solution Interface	282
5.4.3 Instabilities at the Solid Electrode-Solution Interface	289
5.5 Bistability Caused by Potential-Dependent Convection	300
5.5.1 Experimental Realization	300
5.5.2 Linear Stability Analysis	300
5.6 Self-Induced Convection in the Processes at Hg Electrodes in Nonaqueous Media	307
5.7 The Old and New Versions of the Beating Mercury Heart	309
5.8 Convective Instabilities Caused by Gas Evolution Reactions in Electrode Processes	317
5.8.1 Oscillations in the Electrode Reactions of Anions at Solid Electrodes	317
5.8.2 Convection-Driven Oscillations in Methanol Oxidation	323
5.8.3 Convection-Driven Oscillations and Dendritic Formation During Metal Deposition	326
5.9 The Self-Organized Electrohydrodynamic Convection	332
5.9.1 Principles of the Electrohydrodynamic (EHD) Convection	332
5.9.2 EHD Convection in Liquid Crystals	336
5.9.3 EHD Convection in Colloidal Systems	338
5.9.4 The Low-Voltage EHD Convective Luminescent Patterns	344
5.9.5 Electroconvection in Membrane Systems	365
5.10 Interaction of Spatial Pattern Formation and Forced Convection	366
References	368

6	Liquid Membrane and Other Membrane Oscillators	375
6.1	Dynamics of the Liquid–Liquid Interface and Liquid Membrane Systems	375
6.2	Liquid Membrane Systems as the Model Chemoreceptors	378
6.2.1	Construction and Oscillatory Dynamics of the Liquid Membrane System	378
6.2.2	Electrochemical Model of Taste Sensor	381
6.2.3	Electrochemical Model of Smell Sensor	385
6.3	Recent Developments in Liquid Membrane Oscillators	385
6.4	Outline Characteristics of Solid Membrane Oscillators	396
6.4.1	Biochemical Membrane Oscillators	396
6.4.2	Artificial Solid Membrane Oscillators	399
6.5	Oscillations in Conducting Polymer Systems	404
	References	406
7	Control of Electrochemical Chaos and Unstable Steady-States	411
7.1	Application of Map-Based Control Algorithms	411
7.2	Application of Derivative Control Strategy	413
7.3	Application of Delayed-Feedback Control	419
7.4	Application of Sinusoidal Forcing	423
7.5	Application of Sinusoidal Forcing to Control of Spatio-Temporal Behavior	425
7.6	Noise-Induced Order in Electrochemical Systems	431
7.7	Stabilization of Oscillations in the Systems with Spontaneous Drift	436
	References	438
	About the Author	441
	About the Editor	443
	Index	445

Chapter 1

Basic Principles of Nonlinear Dynamics

1.1 Concise Vocabulary of Nonlinear Dynamics

In this section, we shall briefly explain the most fundamental terms necessary to understand the concepts of nonlinear dynamics. As stated in Introduction, the term “dynamic self-organization” means generally the spontaneous formation of order in the domain of time and/or space, when the system is maintained sufficiently far from equilibrium. There are two reasons for this condition: the thermodynamic and kinetic one. The first one is justified by the second law of thermodynamics: since the creation of any order, including dynamical self-organization phenomena, is associated with the decrease in entropy, there must exist, in the same system, a dissipative process characterized with entropy production at least compensating this decrease. This condition was the basis for the new term, introduced by the Nobel prize winner, I. Prigogine: *dissipative structures* [1]. In fact, all the manifestations of self-organization under nonequilibrium conditions, like the formation of temporal or spatiotemporal patterns, are dissipative structures, i.e., they emerge only as long as the sufficient dissipation of energy occurs. The formation of the dissipative structures is thus a dynamic phenomenon. In order to exhibit self-organization, the kinetic characteristics of this process must however meet also the following additional conditions: (1) the (usually) *nonlinear* dependence between the driving forces and the resulting flows¹; (2) the presence of *feedback loops*, i.e., of autocatalysis and/or autoinhibition in the kinetic mechanism. Mathematically, the dynamical systems are defined in terms of differential equations which can be

¹In spite of nonlinear nature of dynamics of vast majority of processes leading to self-organization, in rare cases it can occur also due to linear nonequilibrium phenomena; an example is the concentration gradient appearing in the multicomponent system in the presence of imposed temperature gradient, due to thermal diffusion which is a process of linear characteristics. In the following, we shall however avoid these rare cases and focus on nonlinear phenomena.

ordinary ones (abbreviated as ODE), if the dynamic variables depend solely on time, or partial ones (PDE) if the variables depend also on the spatial coordinates. In this chapter we shall focus on the ODEs properties, while the systems requiring analysis in terms of PDEs will be described in Chap. 1 of volume II.

Let us now repeat those three fundamental conditions of self-organization: the irreversible course of the process, the (usually) nonlinearity of its dynamic characteristics, and the presence of appropriate feedback loops in its mechanism. Let us assume that the differential equations meeting all these conditions were formulated in terms of appropriate dynamic variables, e.g., the intermediate concentrations, electrode potential, etc. The occurrence of self-organization, e.g., of spontaneous oscillations of these variables depends now on the values of parameters that are included in these equations. We shall call them *control parameters* (this may be, e.g., the flow rate through the reactor for the homogeneous chemical reactions or the applied electrode potential/the imposed electric current for electrochemical processes). It may happen that for some control parameters which we choose initially, the solutions of those equations will be quite trivial, i.e., they will predict the existence of only a single steady state. However, for another set of those parameters the same equations may generate, e.g., spontaneous temporal oscillations of the variables. It is now important to find the critical value of one (or more) parameter at which such *qualitative* (see the Poincaré idea, mentioned in the Introduction) change in the system's behavior occurs. This is the *bifurcation point* (following the Latin word "bifurcus"—*forked*). This topological, essentially mathematical term, refers strictly to the theory of differential equations, as they describe the dynamics of any system.

In fact, mathematical background of self-organization is the *bifurcation theory* and in terms of such an approach those striking universalities in the dynamics of various systems manifest themselves. Completely different, physically or chemically, processes can exhibit the same *types of bifurcations*, i.e., the same *types of qualitative* changes of dynamics upon variation of appropriate control parameters. In the example earlier, the bifurcation involved the *loss of stability* of the steady state and the birth of the *stable oscillatory regime*, instead. Such a change of stability of the states can be an example of the *Hopf bifurcation*, one of the most frequent mechanisms in which the oscillations are born from the trivial, nonoscillatory steady state.

At the bifurcation point the system may be particularly sensitive to the fluctuations. In fact, it is the *amplification* of the small fluctuations to macroscopic scale which manifests itself as the qualitatively new system's behavior. This also means that in the trivial, linear range of the system's behavior the fluctuations are damped, but in a *nonlinear* region, due to the feedback loops, they are quickly (exponentially) enhanced. Furthermore, at the bifurcation point several possibilities for the further system's evolution may be opened and which of them will be chosen, depends on the actual random fluctuation; in this way in the essentially deterministic system, as defined by the respective differential equations, the stochastic element appears.

What is further important, if we now try to go back to the equilibrium state, we should not expect that always all the events observed will repeat in the reverse order at the same critical values of the bifurcation parameter. In some cases, the hysteresis may happen when the system switches to a new state upon increasing the control parameter, and the return to the original state may occur for the decreasing value of the control parameter lower than that observed before. The same may be the case for two different regimes of oscillations, the switch between which depends on the direction of the variation of the bifurcation parameters. Such hysteresis is a manifestation of an important phenomenon, called *bistability*, which means the possibility of existence of the system in one of two stable steady states, for certain range of control parameter. If more than two stable states are involved in the hysteresis loop, we call this phenomenon *multistability*. If two oscillatory regimes are involved in the hysteresis loop, like in the example earlier, this specific case of bistability is called *birhythmicity*. Such hysteresis can be associated with the fact that upon cyclic variation of control parameters the system experiences either the same type of bifurcation or two different types of bifurcations on a way forth and back.

All phenomena of this type are strictly related to the *stability* of the states. When in the initially homogeneous system, a dynamical temporal or spatiotemporal order emerges, it means that the initial state lost its stability and a new behavior acquired it. If one type of self-organized phenomena turns into another one, it also means the exchange of their stability. It is very important to distinguish between the terms “steady state” and “stable state.” The term “steady state” (or *stationary* state) means the state, the characteristics of which do not change as a function of time. In mathematics, the steady state is termed also the *fixed point* or the *equilibrium point*, although the latter term may seem a bit controversial for the chemists, if one considers the nonequilibrium steady state. It is further important to note that the steady state can be *stable* or *unstable*. We shall give here the simplest interpretation of these terms, which will be developed in more detail later. The *stable* steady state is resistant to external or internal perturbations in this way that if they happen, they are eventually damped and the system returns to its original state. The *unstable* steady states will not survive any fluctuation, as the system driven out of it goes then to the closest stable state. This is the reason for which the states which are observable must also be stable, since real systems are always a subject of fluctuations. Unstable steady states are not observable, unless they are stabilized by special procedures, but their existence can be indicated in theoretical models.

One may additionally test the stability of the given state by introducing external fluctuations of increasing amplitude. If the system returns always exactly to the original state, one calls its stability as the *asymptotic* one, as all the fluctuations decay to zero asymptotically as a function of time. If the system characteristics survive in this way even relatively large fluctuations, covering the entire possible range of the dynamic variables considered, it is called “globally stable.” Otherwise, if sufficiently large perturbations cause the switching of the system to another, concurrent stable state, the original one is called only “locally stable.”

It appears useful to introduce one more type of stability. If the system perturbed by relatively small fluctuations leaves the original state, but remains *close* to its characteristics (instead of escape towards a concurrent distant state), it is called

stable in a Lyapunov (or Liapunov) sense. In other words, the Lyapunov stability means that perturbations applied in the vicinity of the steady state cause that the system still remains in the neighborhood of this state, meaning accepting certain tolerance for this deviation. Of course, if this neighborhood shrinks eventually to zero, the (thus more general) Lyapunov stability turns into its special case of asymptotic stability.

The evolution of dynamical systems, defined by respective differential equations, can be very conveniently visualized using the *trajectories* defined in the respective *phase space*. For homogeneous chemical reactions, involving the concentrations of species X and Y as the dynamical variables, the phase space may be defined as the [Y]–[X] coordinate system, or, alternatively through derivatives: [X] – (d[X]/dt) or [Y] – (d[Y]/dt). Of course, the phase space may be generally constructed in N dimensions. In electrochemistry, one of the convenient definitions of the phase space involves the $E - c(0)$ coordinate system, where E is the electrode potential (interfacial potential drop) and $c(0)$ is the concentration of the electroactive species at the reaction site (less precisely called as the “surface concentration” at the electrode).

We shall consider here only the case of solutions of *autonomous differential equations*, which do not contain an explicit dependence on time. In consequence, the phase portraits obtained from the solutions of such equations are also independent of time. Note that the N -dimensional nonautonomous systems can be transformed to autonomous ones by definition of time as an additional dynamical variable: $x_{N+1} = t$ which allows to add the $(N + 1)$ th differential equation, making the new system autonomous [2]:

$$\frac{dx_i}{dt} = f_i(x_1, x_2, \dots, x_N, t); \quad i = 1, \dots, N \quad (1.1)$$

$$\frac{dx_{N+1}}{dt} = 1 \quad (\text{i.e., } x_{N+1} = t) \quad (1.2)$$

Removing of the time dependence is thus done at the cost of adding an extra dimension to the system. One can also say that an N th order *time-dependent* equation can be considered a special case of $(N + 1)$ -dimensional system.

In the phase space of the autonomous system, the single steady state is represented by a point. If this state is stable, trajectories from the surroundings lead to this point, otherwise leave it and develop into the phase space. It is thus natural to call the single *stable steady state* the *point attractor*, while the (asymptotically) unstable steady state is named a *point repeller*, respectively. There can be more than one steady state (point) in the phase space. It may happen that each of them is stable, but it is only a *local stability*, as there is always a concurrent attractor in the phase space. In such a case we say that every such stable steady state has its own *basin of attraction* in the phase space. This means the existence of respective ranges of values of dynamical variables, for which the trajectories still tend to the given steady state.

The oscillations of the damped amplitude are represented in the phase space by the snail-like trajectory, tending asymptotically to the final point—stable steady state which is the point attractor. This type of trajectory is called also the *stable focus*, indicating that focus may be also unstable, and then the trajectory starts in the point *repeller* (or *source*) and develops to its vicinity. Oscillations of the constant amplitude are represented in a phase space by a closed curve. This trajectory may be either stable or unstable depending on its response to perturbations. Similarly as for the point attractors one can distinguish between “asymptotically stable” or “asymptotically unstable” trajectories—*limit cycles*, stable or unstable, respectively. Also, trajectories of cyclic shapes may be stable in the Lyapunov sense.

A particularly complex phase trajectory corresponds to the chaotic oscillations. If this is not really a stochastic disorder, but only complex order of great sensitivity to initial conditions and further fluctuations, the chaos is called “deterministic” and the respective complicated phase trajectory is named *strange attractor*. The above terms will be now discussed in more detail.

1.2 Types of Stability

The simplest schematic illustration of stability and instability of single steady states (fixed points), mentioned in the previous section, is given by Fig. 1.1, which shows the evolution of the ball placed initially either in the valley or at the top of the idealized, smooth mountain. The first of these states, corresponding to the minimum potential energy in the gravitational field, is stable, while the second one, corresponding to maximum potential energy, is unstable with respect to any fluctuation.

For the purposes of the analysis of dynamical systems, it is however necessary to treat the definitions of stability more strictly and in more detail, according to [2].

1. *Attracting* properties of the state (of an attractor) manifest themselves in this way that every perturbation of this state is eventually (i.e., for $t \rightarrow \infty$) damped. In more strict notation, if x is a dynamical variable (or, more generally, a vector of variables) with a steady-state value x_{ss} , its attracting character means meeting the condition $\lim_{t \rightarrow \infty} x(t) = x_{ss}$ for various initial values $x(0)$ (see Fig. 1.2). Note that reaching the steady state must occur only when $t \rightarrow \infty$, so it may happen that for $0 < t < \infty$ the trajectory temporarily escapes for quite a long distance from the steady state, but eventually it must reach it [2].
2. If this attractive property concerns with all phase trajectories in the phase space, we say that the steady state considered is *globally attractive*, otherwise it is only *locally attractive*. In the latter case, this part of the phase space which includes trajectories tending asymptotically to the given steady state is called its *basin of attraction*.

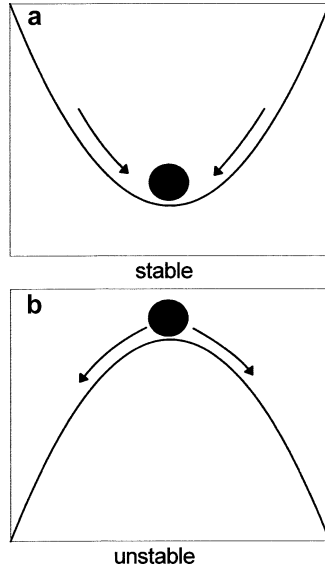


Fig. 1.1 Stable (a) and unstable (b) steady states of the model ball. Stability means that perturbations of the position (and thus of potential energy) of the ball are damped; the state of minimum potential energy is an *attractor* for other states. The instability means that perturbations are amplified, the perturbed ball inevitably leaves (to the *left* or to the *right*) the steady state of maximum potential energy which then appears to be a *repeller* (named also a *source*)

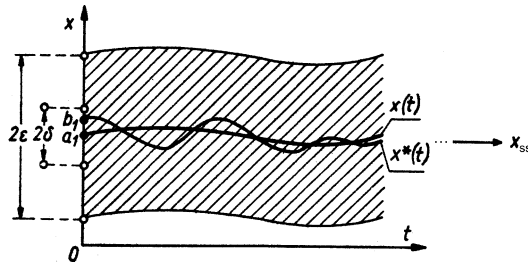


Fig. 1.2 Geometric interpretation of an asymptotically stable solution x of a single differential equation, leading asymptotically to the same point attractor x_{ss} for different initial conditions a_1 and b_1 . Any trajectory that starts within a distance of $\pm\delta$ of x_{ss} converges eventually to x_{ss} [3]

3. Lyapunov stability—if upon the perturbation the system state moves to its neighborhood in the phase space and remains there for *all time*, not only for time tending to infinity. In other words, for every initial condition $x(0)$ and for *every* time $t \geq 0$, the trajectories do not diverge over distance $\varepsilon > 0$, i.e., $\|x(t) - x_{ss}\| < \varepsilon$ (Fig. 1.3). Note that compared to above-mentioned stability this behavior occurs for both $t \rightarrow \infty$ and $t \rightarrow -\infty$.

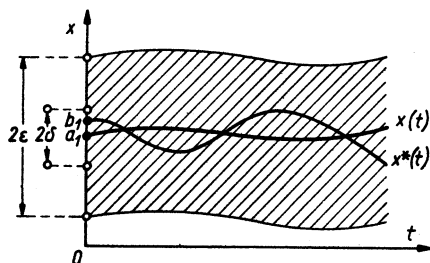


Fig. 1.3 The principle of Lyapunov stability for the one-dimensional system in $x - t$ coordinates: there is such a $\delta > 0$ that if the trajectory starts within a distance of $\pm\delta$ from steady-state value x_{ss} , it remains within 2ϵ for all positive times [3]

Noteworthy, the attractive properties and Lyapunov stability may occur simultaneously or not. One can consider the following cases:

- (a) If the fixed point is Lyapunov stable, but not attracting, it is called **neutrally stable**. Theoretically such type of stability could be ascribed to, e.g., mechanical systems without friction (without dissipation of energy and thus without tending of the system towards equilibrium). In other words, this is a feature of systems conserving the energy. The neutral stability feature is also characteristic of both the steady state and the oscillations in the classical Lotka–Volterra model.
 - (b) If the fixed point is both Lyapunov stable and attractive, the perturbations simply decay as function of time tending to infinity; the steady state is then called *asymptotically stable* (sometimes only attractive properties are identified as asymptotical stability, but the present definition is more strict). In practice, the system driven away from the steady state comes back to this state asymptotically with the perturbation decaying as a function of time; the classical Lotka model, exhibiting damped oscillations, is a good example.
 - (c) It is also possible that the fixed point is attracting, but not Lyapunov stable: the trajectories may begin in close vicinity to the fixed point, but before returning to it they go to distant area of the phase space.
4. **Instability**—this generally means that the fixed point is neither attractive nor Lyapunov stable, and we can call it the *repeller* (or *source*). In this case, all perturbations are exponentially enhanced and the system's state evolves through the phase space to the competing stable state (if it exists). Quite formally one can say that the unstable steady state is reached when $t \rightarrow -\infty$. As an example of such a transformation of an attractor into a repeller, upon changing the control (bifurcation) parameter, may serve the characteristics of the classical Brusselator model in which the single steady state loses its original asymptotic stability and the stable limit cycle evolves around it in the phase space.

1.3 Linear Stability Analysis

Let us pose a fundamental question for the stability analysis: is it possible to learn which type of stability does represent the given system of differential equations, for given parameters? In particular, is it possible to obtain this *qualitative* information without getting solutions of these equations which can be even nonexistent in the explicit, analytical form?

In the case of nonlinear equations, which are here of our particular interest, in a general case it is difficult to get full information on possible *types* of solutions. The problem can be solved unambiguously only for the *linear* systems. However, also for nonlinear systems it is possible to obtain at least fragmentary, but often quite valuable information on the stability of the solutions. The method to do that is called *linear stability analysis*. The basis for the application of this approach to nonlinear systems is the *Lyapunov theorem* which says that the course (type) of the phase trajectories in the close neighborhood of the given steady state is the same for the nonlinear equations and for the equations, obtained by their linearization. Mathematically it is done by the expansion of the nonlinear expressions in the Taylor series around the given steady state of the stability under consideration, with quadratic and higher terms neglected. The neighborhood of the steady state must then be small enough to satisfy such linearization. In spite of this simplification, linear stability analysis is a very powerful approach which yields valuable information on bifurcations occurring in the system analyzed.

The principles of the linear stability analysis will be first given for the simplest case when only one dynamical variable is involved and the system's evolution occurs only in time, i.e., the breaking of spatial symmetry is here not considered (for the latter case, see Chap. 1, volume II). The best realistic example of such system is the chemical reaction running in the flow reactor with intensive, by assumption perfect mixing.

1.3.1 Stability of One-Dimensional Homogeneous System

Let x be a single dynamical variable identical with, e.g., concentration of species X or with the electrode potential E . The dynamics of the system is described by the kinetic equation, the right-hand side of which is in general a nonlinear function of the variable x and parameters a, b, c, \dots which may be the factors dependent on the rate constants of (electro)chemical reactions, transport coefficients, etc.:

$$\frac{dx}{dt} = F(x, a, b, c, \dots) \quad (1.3)$$

The aim of the linear stability analysis is to find out, without getting an explicit solution $x(t)$, the stability of all possible steady states (fixed points), as their number may be greater than one. Every steady state is defined by the condition $dx/dt = 0$. For example, in the case of the Schlögl model of bistability [4], $F(x)$ is a polynomial of the third degree, so up to three different steady states are possible.

In our analysis we shall limit our considerations to one exemplary steady state x_{ss} , for which the algebraic equation is met:

$$F(x_{ss}, a, b, c \dots) = 0 \quad (1.4)$$

For convenience, in further derivations we define a new variable γ which measures the distance of the actual value of $x(t)$ from the steady-state value x_{ss} :

$$\gamma = x - x_{ss} \quad (1.5)$$

Since x_{ss} is a constant, $d\gamma/dt = dx/dt$ and Eq. (1.3) may be transformed to an equivalent form:

$$\frac{d\gamma}{dt} = F(\gamma, a, b, c \dots) \quad (1.6)$$

the right-hand side of which is now expanded in the Taylor series around x_{ss} :

$$\frac{d\gamma}{dt} = F(\gamma_{ss}, a, b, c \dots) + \left[\frac{dF}{d\gamma} \right]_{ss} \gamma + \frac{1}{2} \left[\frac{d^2F}{d\gamma^2} \right]_{ss} \gamma^2 + \dots \quad (1.7)$$

Since $F(\gamma_{ss}, a, b, c \dots)$ is equal to zero by definition of a steady state (1.4), and the quadratic (and higher order nonlinear) terms in the expansion have to be omitted as a condition for linearization, the equation for the *linear stability analysis* takes a final form:

$$\frac{d\gamma}{dt} = \left[\frac{dF}{d\gamma} \right]_{ss} \gamma \equiv \lambda \cdot \gamma \quad (1.8)$$

with $\lambda = [dF/d\gamma]_{ss}$ being a slope of the dependence of the rate of the process (F) on the variable x , calculated *in the vicinity of a given steady state* x_{ss} . The differential equation (1.8) shows in fact that, upon linearization, the initial nonzero perturbation of the steady state [$\gamma(0)$] evolves further exponentially on time:

$$\gamma(t) = \gamma(0) \exp[\lambda \cdot t] \quad (1.9)$$

One can consider the following three cases of this evolution:

1. If $\lambda < 0$, the perturbation decays exponentially as a function of time, so the steady state is asymptotically stable.

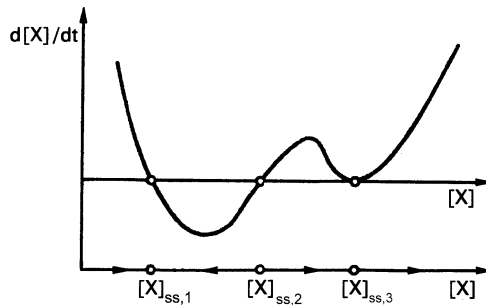


Fig. 1.4 The exemplary course of the $F([X])$ function (1.3) showing three steady states. The stability of these states is given by the direction of *arrows* indicating the temporal evolution of $[X]$ variable in the vicinity of every steady state: stable $[X]_{ss,1}$, unstable $[X]_{ss,2}$, half-stable $[X]_{ss,3}$. After [5]

2. If $\lambda > 0$, the steady state is unstable, since the perturbation exponentially increases.
3. The case $\lambda = 0$ requires more detailed discussion. Apparently, it might suggest the Lyapunov stability, as the perturbation remains constant at the initial value $\gamma(0)$ but this would be completely true only for originally linear (and not linearized nonlinear) system. However, since Eq. (1.8) was derived through the linearization of the original nonlinear dependence (1.3), the *limitations* of the linear stability analysis become now obvious. In this case the real dynamics of perturbations is determined by the *omitted nonlinear* terms of the Taylor expansion which thus cannot be neglected any more.

It is very instructive to compare Eq. (1.3) with its (exemplary) graphical interpretation, for the case when three steady states are possible, and all three cases of stability are considered [5]. One should emphasize again that the plot in Fig. 1.4 is based on the original, nonlinear form of the right-hand side of Eq. (1.3), so it conveys full nonlinear, not simplified information on the system's dynamics which will now be confronted with the results of linear stability analysis.

Let us identify the dynamical variable x with the concentration of species X : $x \equiv [X]$. The steady state $x_{ss,1} \equiv [X]_{ss,1}$ is asymptotically stable, since the slope $\lambda = dF/dx$ (equal to $dF/d\gamma$), *around this steady state*, is negative. The physical sense of this purely mathematical conclusion is better understandable if we analyze the way in which our dynamical systems react with respect to perturbations of $x_{ss,1}$. For $x < x_{ss,1}$, the dx/dt is positive, so the local increase in x results in restoration of the steady-state value $x_{ss,1}$. If another local perturbation makes x higher than the steady-state value: $x > x_{ss,1}$, the resulting negative production of x ($dx/dt < 0$) also restores $x_{ss,1}$. So, irrespectively of the direction of perturbations, they are damped and the steady state $x_{ss,1}$ is asymptotically stable, indeed. Analogy with the ball returning always to the valley in Fig. 1.1 is clear. The steady state characterizing with $x_{ss,1}$ is thus an attractor and the range of x , for which its attractive properties remain, defines the corresponding basin of attraction.

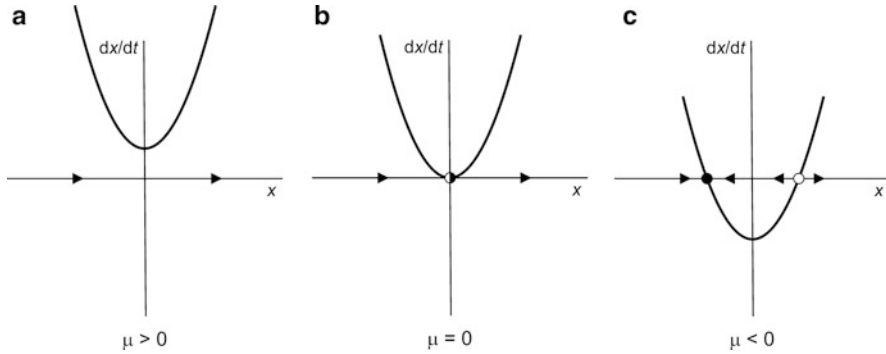


Fig. 1.5 The creation/annihilation of the pair of stable and unstable steady states through the saddle–node bifurcation in the one-dimensional dynamical system (1.10) (after [2])

Quite analogous line of thought leads to the conclusion that the $x_{ss,2}$ steady state must be unstable. The positive slope λ corresponds to the situation that the x values perturbed to values lower than $x_{ss,2}$ decrease further, while for $x > x_{ss,2}$ a further increase of x occurs.

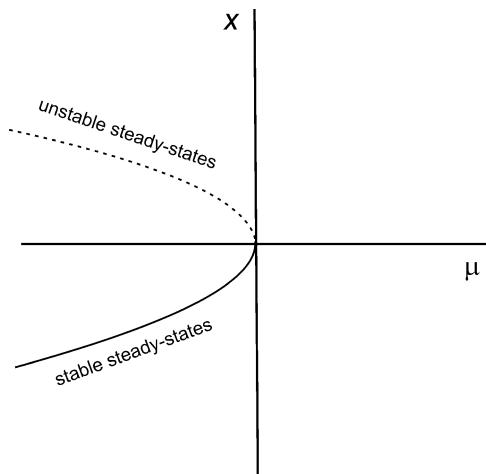
The stability of the third steady state $x_{ss,3}$ cannot be diagnosed from the linear analysis and this is the above-mentioned case ($\lambda = 0$), in which omitted nonlinear terms of the Taylor expansion have now to be taken into account. The plot in Fig. 1.4 reveals now that if perturbation causes $x < x_{ss,3}$, the $dx/dt > 0$, so the system's dynamics restores the steady-state value. However, if another perturbation causes that the steady-state value is exceeded: $x > x_{ss,3}$, the dx/dt is also positive, so x now continues to move away from the steady-state value. As a consequence, taking into account the local nonlinear characteristics of the system's dynamics, we come to the conclusion that the $x_{ss,3}$ steady state is *half-stable* (effectively unstable, since it is difficult to expect only negative fluctuations in a real system), contrary to the linear analysis that would predict the local Lyapunov stability for $x_{ss,3}$.

1.3.1.1 Saddle–Node Bifurcations in One-Dimensional System

Figure 1.4 corresponds to the exemplary dynamical system characterized with certain values of control parameters. If those parameters are changed, the presented curve can move and/or change its shape, indicating that the stability of a given state may change and even the steady states may appear or disappear. This means the respective bifurcations. Let us consider the model, described with the differential equation in which $F(x)$ defines the parabolic dependence of the system's dynamics on the actual value of x [2]:

$$\frac{dx}{dt} = \mu + x^2 \quad (1.10)$$

Fig. 1.6 Bifurcation diagram for the saddle–node (fold, blue sky) bifurcation



The *bifurcation parameter* μ determines the position of the parabola on the ordinate axis of the dx/dt vs. x dependence. As long as $\mu > 0$, no steady states (fixed points) exist since $dx/dt = 0$ cannot be attained for any μ (Fig. 1.5a). For $\mu = 0$ (Fig. 1.5b), a half-stable steady state (cf. the properties of $x_{ss,3}$ in Fig. 1.4) appears which upon further decrease in μ splits into two steady states: one called a *stable node*, and the other one—a *saddle* which is always an unstable state (Fig. 1.5c). The names of these steady states are not obvious in this one-dimensional case, since they come from analogous analysis for the two-dimensional system (see next section). Since the vector fields change *qualitatively* for $\mu = 0$, to this value we ascribe the occurrence of a *saddle–node bifurcation*, also called a *fold bifurcation*, a *turning point bifurcation*, or even a *blue sky bifurcation* (meaning that a pair of the steady states appears as “out of the clear blue sky”) [2].

The term “fold bifurcation” becomes clear in view of the *bifurcation diagram* constructed in the x – μ coordinate system, usually oriented as shown in Fig. 1.6.

This diagram shows in an alternative way the sequence of events upon continuous decrease in parameter μ . Starting from positive values, where no any steady states exist (“clear blue sky”), at $\mu = 0$ “from nowhere” two coexisting steady states are born—the stable one (a stable node) and the unstable one (a saddle). Upon further decrease in the control parameter, the stable node (solid line) and the saddle (dotted line) become more and more separated, and the nodes are globally attracting as the only attractors in the phase space.

However, if we add a second fold, sharing with the first one the medium unstable steady states, the typical characteristics of bistable regime are formed (see Fig. 1.7). This bistable region is thus limited by two saddle–node bifurcations occurring at both edges of the fold (this is the so-called degenerate case of the saddle–node bifurcations). The middle set of unstable steady states separates the basins of attraction for the upper and the lower sets of the stable steady states. Such connection of two folds guarantees that there are always steady states in the phase space

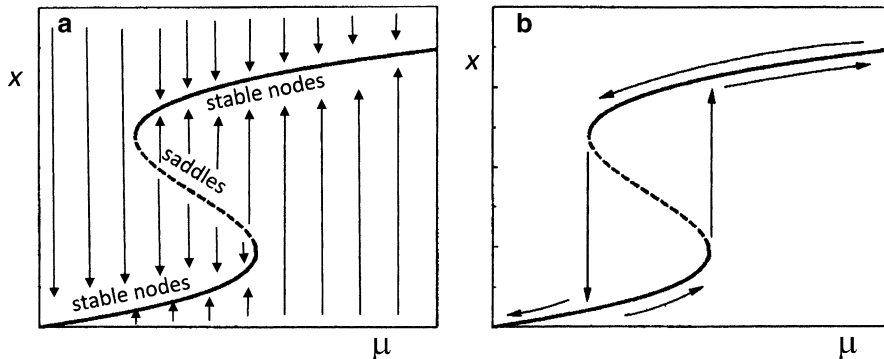


Fig. 1.7 (a) The bifurcation diagram for the degenerate case of the saddle–node bifurcation, corresponding to the bistable behavior; (b) the associated hysteresis observed upon cyclic change of the control parameter

considered: either a single one (meaning monostability) or two stable and one unstable (meaning bistability). As only stable states can be directly observed, the bistable system exhibits hysteresis in its behavior upon cycling changes of the control parameter (Fig. 1.7b).

For one-dimensional continuous systems (i.e., defined by differential equations), one can expect only the stable or unstable steady states, but no oscillations. The latter ones are possible only if dynamical system involves minimum two variables. In turn, in the two-dimensional case only simple periodic oscillations in homogeneous systems are possible. The reproduction of more complex oscillatory regimes, including, e.g., the alternating low- and high-amplitude courses, called the *mixed-mode oscillations* (MMO) and of course *chaotic* oscillations, requires at least three dynamical variables.

As an important comment to latter conclusion one should note that oscillations are possible for one-dimensional systems, but defined by *delay-differential equations* of a general form $dN/dt = f[N(t), N(t - \tau)]$ where parameter τ is a *delay*. Such definition of dynamical systems, introduced by Mackey and Glass [6] means that the rate of change of quantity N depends not only on its actual value (at time t), but also on its value at certain past time τ which effects thus manifests itself with this delay. Such delay models are quite popular in description of, e.g., population dynamics affected by a delay due to, e.g., pregnancy period. For appropriate range of control parameters, the single *delay-differential equation* can generate not only stable steady state, but also oscillations, i.e., stable limit cycle. In case of oscillations, even chaotic dynamics is then possible. From the mathematical point of view, this complexity occurs due to the fact that the state of delay-differential equation is infinite-dimensional, since at time t_0 this state is given by a function $x(t_0 - s)$, for s in the range from 0 to τ . For one-dimensional, nondelay differential equation this state is defined by a single value $x(t_0)$ [7]. The case of delay equations is not considered here in more detail, so more information the reader can find, among others, in [8, 9]. Furthermore, oscillations can occur in

difference equations, i.e., discrete *maps* which correspond to the case when the assumptions of continuity and coexistence of populations are not true. Also such maps can include delays which appropriately complicate the bifurcation scenario [9, 10]. Although such discrete models are less useful for the description of real chemical or electrochemical systems, their dynamics exhibit certain universalities observed also in real processes (cf. Feigenbaum scenario). We shall devote some attention to such maps in further part of this book (cf. Sect. 1.9.2), but now we stay with continuous systems and extend our considerations to two dimensions.

1.3.2 Stability of Two-Dimensional Homogeneous System

For more than one dynamical variable, the diagnosis of stability of the steady states is based also on the parameter λ , which definition and interpretation is however more complicated, compared to one-dimensional case. Let us consider the model system of two autonomous differential equations:

$$\frac{dx}{dt} = f(x, y) \quad (1.11)$$

$$\frac{dy}{dt} = g(x, y) \quad (1.12)$$

As above, the stability analysis is applied to the steady states (fixed points) determined by simultaneous meeting of two conditions: $dx/dt = dy/dt = 0$. Let us denote the parameters of the i th steady state as $(x_{ss, i}, y_{ss, i})$. We shall choose one of these states, denote its parameters as (x_{ss}, y_{ss}) , and investigate its properties using linear stability analysis, according to the following procedure.

Both functions $f(x, y)$ and $g(x, y)$ are expanded in the Taylor series, with only linear terms left:

$$\frac{dx}{dt} = \left(\frac{\partial f}{\partial x} \right)_{ss} (x - x_{ss}) + \left(\frac{\partial f}{\partial y} \right)_{ss} (y - y_{ss}) \quad (1.13)$$

$$\frac{dy}{dt} = \left(\frac{\partial g}{\partial x} \right)_{ss} (x - x_{ss}) + \left(\frac{\partial g}{\partial y} \right)_{ss} (y - y_{ss}) \quad (1.14)$$

In terms of new variables measuring the distance of the actual state (x, y) from the steady-state characteristics (x_{ss}, y_{ss}) :

$$\delta = x - x_{ss} \quad (1.15)$$

$$\gamma = y - y_{ss} \quad (1.16)$$

Equations (1.13) and (1.14) can be expressed in the equivalent forms:

$$\frac{d\delta}{dt} = a \cdot \delta + b \cdot \gamma \quad (1.17)$$

$$\frac{d\gamma}{dt} = c \cdot \delta + d \cdot \gamma \quad (1.18)$$

The respective partial derivatives form a Jacobian matrix \mathbf{J} :

$$\mathbf{J} = \begin{bmatrix} \left(\frac{\partial f}{\partial x}\right)_{ss} & \left(\frac{\partial f}{\partial y}\right)_{ss} \\ \left(\frac{\partial g}{\partial x}\right)_{ss} & \left(\frac{\partial g}{\partial y}\right)_{ss} \end{bmatrix} \equiv \begin{bmatrix} a & b \\ c & d \end{bmatrix} \quad (1.19)$$

If the determinant $\text{Det}(\mathbf{J}) \neq 0$, the only solution of Eqs. (1.17) and (1.18) for $d\delta/dt = d\gamma/dt = 0$ is the steady-state $(0, 0)$. The properties of that matrix are further of crucial importance for diagnosis of stability of this steady state. This diagnosis is based on the sign of the trace $[\text{Tr}(\mathbf{J})]$ and of the determinant $[\text{Det}(\mathbf{J})]$ of the matrix and allows to determine the shape of trajectories in the phase space, i.e., to classify the type of the steady state (fixed point) *without obtaining the explicit solutions of the differential equations*.

In order to diagnose the stability of the steady state considered we substitute the *trial* solutions to Eqs. (1.17) and (1.18):

$$\delta = A \exp(\lambda t) \quad (1.20)$$

$$\gamma = B \exp(\lambda t) \quad (1.21)$$

and obtain the system of algebraic equations:

$$A(a - \lambda) + Bb = 0 \quad (1.22)$$

$$Ac + B(d - \lambda) = 0 \quad (1.23)$$

The trivial solution $A = B = 0$ is meaningless, so we look for the solution with coefficients A and B having nonzero values. This is the case only if the determinant of the matrix (1.24) is equal to zero [3]:

$$\text{Det} \begin{bmatrix} a - \lambda & b \\ c & d - \lambda \end{bmatrix} = 0 \quad (1.24)$$

The condition (1.24) is equivalent to the trinomial square, called *characteristic* (or *eigenvalue*) *equation*:

$$\lambda^2 - \text{Tr}(\mathbf{J}) \cdot \lambda + \text{Det}(\mathbf{J}) = 0 \quad (1.25)$$

with the trace and $\text{Tr}(\mathbf{J})$ and $\text{Det}(\mathbf{J})$ of the Jacobian matrix (1.19) defined as, respectively:

$$\text{Tr}(\mathbf{J}) = a + d \quad (1.26)$$

$$\text{Det}(\mathbf{J}) = ad - bc \quad (1.27)$$

Equation (1.25) has generally two solutions:

$$\lambda_{1,2} = \frac{\text{Tr}(\mathbf{J}) \pm \sqrt{[\text{Tr}(\mathbf{J})]^2 - 4 \cdot \text{Det}(\mathbf{J})}}{2} \quad (1.28)$$

which are called the *characteristic values* (or *eigenvalues*). This terminology will be explained later. These two values $\lambda_{1,2}$ are of course the solutions of equation system (1.17, 1.18), but in fact there is an infinity of solutions (due to infinite number of initial conditions) of a general form:

$$\delta = C_1 \exp(\lambda_1 t) + C_2 \exp(\lambda_2 t) \quad (1.29)$$

$$\gamma = C_3 \exp(\lambda_1 t) + C_4 \exp(\lambda_2 t) \quad (1.30)$$

where coefficients $C_1 \dots C_4$ depend on those initial conditions. Alternatively, by invoking definitions (1.15, 1.16), one can express these solutions in terms of evolution of original variables $x(t)$, $y(t)$, with respect to the stationary values x_{ss} , y_{ss} :

$$x = x_{ss} + C_1 \exp(\lambda_1 t) + C_2 \exp(\lambda_2 t) \quad (1.31)$$

$$y = y_{ss} + C_3 \exp(\lambda_1 t) + C_4 \exp(\lambda_2 t) \quad (1.32)$$

The latter expressions describe thus the trajectories $x(t)$ and $y(t)$ around the steady state (x_{ss}, y_{ss}) , starting from initial conditions (x_0, y_0) .

The general thinking leading to diagnosis of stability of given state is essentially analogous to that for one-dimensional system: if both roots λ_1 and λ_2 are negative real numbers, all perturbations are exponentially damped and the considered steady state is stable. If though only one of these roots is positive, the respective perturbations grow exponentially, giving rise to the instability of the steady state.

However, in the two-dimensional case, there are more variants of the dynamic evolution of the system's state, than in one-dimensional case: e.g., the oscillatory ones, which were previously absent and now are possible based on the following mathematical reasoning. Note that if in Eq. (1.28), $[\text{Tr}(\mathbf{J})]^2 - 4 \cdot \text{Det}(\mathbf{J}) < 0$, then λ_1 and λ_2 are a pair of complex conjugated numbers:

$$\lambda_{1,2} = p \pm i\omega \quad (1.33)$$

where:

$$p = \operatorname{Re}(\lambda) = \frac{\operatorname{Tr}(\mathbf{J})}{2} \quad (1.34)$$

$$\omega = \operatorname{Im}(\lambda) = \frac{\sqrt{4\operatorname{Det}(\mathbf{J}) - [\operatorname{Tr}(\mathbf{J})]^2}}{2} \quad (1.35)$$

and $i = \sqrt{-1}$. Based on the Euler's formula $e^{i\omega} = \cos(\omega) + i\sin(\omega)$, one can present solutions (1.31, 1.32) in an equivalent periodic form:

$$x = x_{\text{ss}} + C_1' \exp[pt] \cos[\omega t + \phi_1] \quad (1.36)$$

$$y = y_{\text{ss}} + C_2' \exp[pt] \cos[\omega t + \phi_2] \quad (1.37)$$

where ϕ_1 and ϕ_2 are arbitrary phase angles.

In terms of this representation of the evolution of $x(t)$ and $y(t)$ trajectories, the exponential terms are responsible for the general decay ($p < 0$) or amplification ($p > 0$) of the perturbations, while cosine term determines that this happens in an oscillatory manner, with ω meaning the angular frequency of these oscillations. In other words, depending on a sign of $p = \operatorname{Re}(\lambda)$, one obtains oscillatory damping or growth of perturbations.

A special case occurs when $\operatorname{Re}(\lambda) = 0$, since then λ is a purely imaginary number, so the oscillations neither decay nor grow, having thus a constant amplitude and frequency ω . The steady state surrounded by such closed phase trajectory is called the *center* which is only Lyapunov stable, but not asymptotically stable (i.e., perturbations do not exponentially decay, but also do not diverge to infinite size). In terms of Eq. (1.34), this case clearly occurs when the trace of the Jacobian matrix is equal to zero.

Note that in analogous case for the one-dimensional system (then only real $\lambda = 0$) it was necessary to consider nonlinear terms of the Taylor expansion to diagnose properly the stability of the steady state, for which, in terms of linear approximations, perturbations neither grew nor decayed. A similar situation will occur now—the existence of a center in a linearized system will mean, for the original **nonlinear** system, a transition to a closed, asymptotically stable trajectory, called *stable limit cycle* which means stable oscillations in nonlinear systems. The transition to this limit cycle from the point attractor which occurs through the center is called the *Hopf bifurcation* and is undoubtedly the most typical way in which oscillations are born in many dynamical systems. This case will be therefore discussed later in more detail (Sect. 1.3.3).

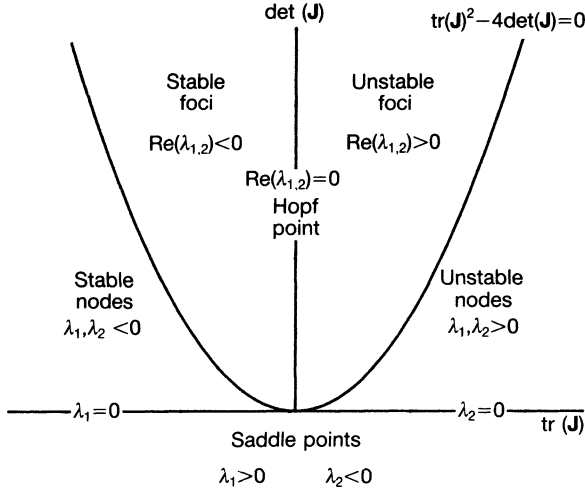


Fig. 1.8 Variation in local stability and character of stationary-state solutions with the values of the trace and determinant of the corresponding Jacobian matrix (see also Table 1.1). Reproduced from [11] by permission of Oxford University Press, Inc.

For the readers who will perform the linear stability analysis for practical conclusions, the most important point is to correlate the properties of the Jacobian matrix for the given steady-state with the dynamical behavior of the system in the close vicinity of this state. Only local surroundings can be considered in this analysis, since otherwise, for the nonlinear system, the linearization of the problem would not be valid. Therefore, we can call this analysis a classification of *local* stability, similarly as it could have been done for one-dimensional systems. However, in the case of two-dimensional systems this classification means also *qualitative* conclusion about the detailed way in which this state is being attained or left. In other words, we can diagnose the local shape of phase trajectories, which are most conveniently constructed in the x - y phase space. Figure 1.8 shows all possible trajectories for the linearized system depending on the relation between the trace $\text{Tr}(\mathbf{J})$ and the determinant $\text{Det}(\mathbf{J})$ of the Jacobian matrix (1.19). Note that the vertical line, corresponding to $\text{Tr}(\mathbf{J}) = 0$ and $\text{Det}(\mathbf{J}) > 0$, is a set of centers which was here indicated as a set of *Hopf (bifurcation)* points, according to the above remark that centers in linear systems correspond to this way of the birth of oscillations in nonlinear systems. For future diagnosis of bifurcations, one should also note another important case of $\text{Det}(\mathbf{J}) = 0$, corresponding to the change of sign of the determinant of Jacobian matrix (irrespective of the sign of trace); this situation usually corresponds to the *saddle-node bifurcation* in two-dimensional systems.

The shape of particular trajectories is shown in Fig. 1.9. Note that the “spiral,” called also a “focus” can be associated either with stable or unstable steady states depending on the direction of development of such trajectory in time. Similarly, stability or instability can be associated with the *nodes*, and the difference is that the corresponding steady state is attained or left in a monotonic (nonoscillatory) manner. In contrast, *saddle* point (see also Fig. 1.10) is always unstable.

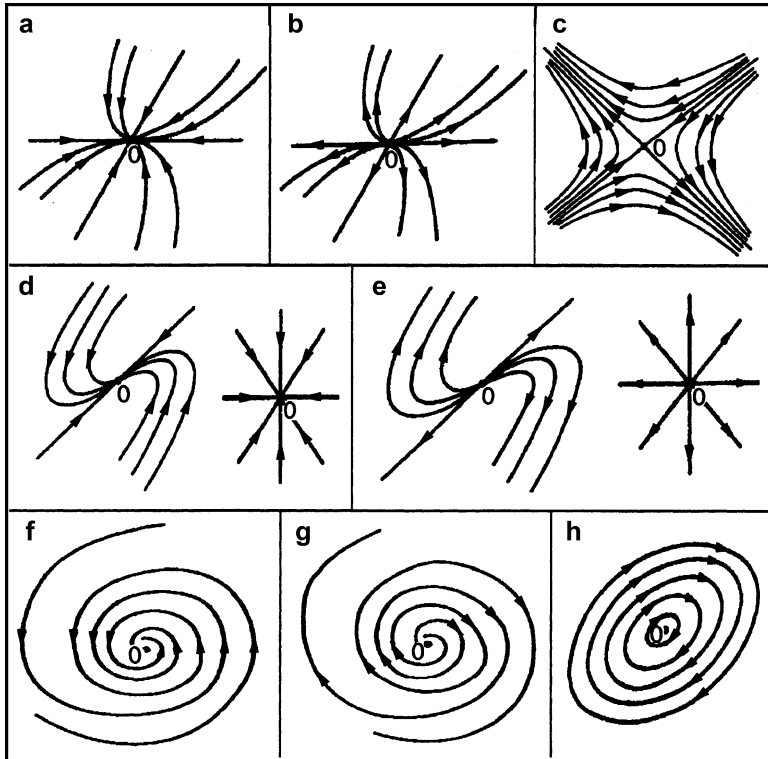


Fig. 1.9 Graphical illustration of various possible phase trajectories associated with the steady state of system of two linear ordinary differential equations: (a) stable node, (b) unstable node, (c) saddle, (d) stable degenerated nodes, (e) unstable degenerated nodes, (f) stable spiral (focus), (g) unstable spiral (focus), (h) center. After [3]

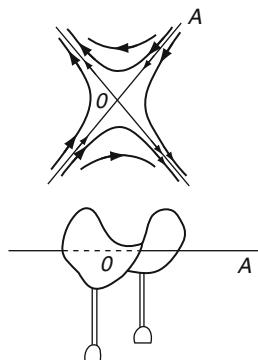


Fig. 1.10 The phase trajectories of the saddle point (*top*), with illustration justifying its nomenclature (*bottom*). Reproduced from [12] with permission from John Wiley and Sons, Inc. © 1986

Table 1.1 Classification of local stability and character in terms of Jacobian matrix and its eigenvalues

Tr(J)	Det(J)	$[\text{Tr}(\mathbf{J})]^2 - 4\text{Det}(\mathbf{J})$	$\lambda_{1,2}$	Character and stability
–	+	+	Real, both –ve	Stable node (monotonic approach)
–	+	–	Complex real parts, –ve	Stable focus (damped oscillatory approach)
0	+	–	Imaginary (real parts = 0)	Hopf bifurcation point or center
+	+	–	Complex real parts +ve	Unstable focus (oscillatory divergence)
+	+	+	Real, both +ve	Unstable node (monotonic divergence)
±	0	+	One zero, one –ve, or one +ve	Saddle–node bifurcation point
±	–	+	Real, one –ve, one +ve	Saddle point (unstable)
0	0	0	Both zero	Double-zero eigenvalue bifurcation point

Reproduced from [11] by permission of Oxford University Press, Inc.

It is further useful to correlate the shape of these trajectories with the λ_1 and λ_2 roots derived from the following equivalent form of Eq. (1.25) [2]:

$$(\lambda - \lambda_1)(\lambda - \lambda_2) = \lambda^2 - \lambda(\lambda_1 + \lambda_2) + \lambda_1\lambda_2 = 0 \quad (1.38)$$

which leads to the alternative expressions for the trace and the determinant of the Jacobi matrix:

$$\text{Tr}(\mathbf{J}) = \lambda_1 + \lambda_2 \quad (1.39)$$

$$\text{Det}(\mathbf{J}) = \lambda_1\lambda_2 \quad (1.40)$$

Obviously, as long as $\text{Tr}(\mathbf{J}) < 0$ and $\text{Det}(\mathbf{J}) > 0$, the system is stable, since in this case both roots have to have the same sign, which must also be negative. It is further clear that the trace is negative if both roots λ , controlling the time evolution of perturbations, are negative, or if only one of them, e.g., λ_1 , is negative, with $|\lambda_1| > \lambda_2$. The first case corresponds to the stable nodes or spirals, if $\text{Det}(\mathbf{J}) > 0$, the second one—to the saddles, if $\text{Det}(\mathbf{J}) < 0$. Condition $\text{Det}(\mathbf{J}) < 0$ generally corresponds to the saddle points, since this means λ_1 and λ_2 of opposite signs. Then the trace may be either positive or negative, in dependence on that whether $|\lambda_1| > \lambda_2$ or $|\lambda_1| < \lambda_2$. Analysis of expression for $\lambda_{1,2}$ (1.28) proves that if $\text{Det}(\mathbf{J}) < 0$, then both these roots are real numbers, so the steady state is reached/left in nonoscillatory manner. The detailed dependences between the value of eigenvalues λ_1 and λ_2 and the type of local stability of steady states are given in Table 1.1 [11].

We shall illustrate the above theoretical considerations with the stability analysis of an exemplary linear (i.e., already linearized nonlinear) system, defined by the following equations:

$$\frac{dx}{dt} = 3x + 5y \quad (1.41)$$

$$\frac{dy}{dt} = -2x - 8y \quad (1.42)$$

The steady state (fixed point) of this dynamical system is $(x_{ss}, y_{ss}) = (0,0)$. Our aim is to study the type of this state, according to principles of linear stability analysis. For that purpose we have to consider the properties of Jacobian matrix:

$$\mathbf{J} = \begin{bmatrix} 3 & 5 \\ -2 & -8 \end{bmatrix} \quad (1.43)$$

Since its determinant is negative, $\text{Det}(\mathbf{J}) = -14$, we immediately come to the conclusion that the $(0,0)$ steady state is the saddle, irrespective of the trace which is here $\text{Tr}(\mathbf{J}) = -5$. The corresponding eigenvalues are $\lambda_1 = 2$, $\lambda_2 = -7$, which quantitatively describe the variation of perturbed variables x and y in time. In practice one usually computes numerically the phase portrait which reveals the course of the phase trajectories, tending both to the steady state and in the opposite direction (see Fig. 1.11a, prepared under Mathematica[®] v.7).

1.3.2.1 Vector Representation of Phase Trajectories

Based on the above example, it is instructive to show the correlation between the phase portrait and the computed values of eigenvalues. For this purpose we shall explicitly indicate the position of *straight line* trajectories (Fig. 1.11b), corresponding to $\Delta y(t)/\Delta x(t) = \text{const}$ at any time t .

Intuitively, for these trajectories to be linear, the exponential evolution of $x(t)$ should be ruled by the same exponential term as that of $y(t)$, involving only a single value of λ for given trajectory, i.e., $x(t) = A\exp(\lambda t)$ and $y(t) = B\exp(\lambda t)$, so that $\Delta y(t)/\Delta x(t) = B/A = \text{const}$. This exponential motion of the system's state along these trajectories either veers towards the fixed point $(0,0)$ (see the line corresponding to $\lambda_2 = -7$) or veers away from it (for $\lambda_1 = 2$), when time tends to infinity. In the former case, the trajectory is a *stable manifold*, i.e., a set of initial conditions (x_0, y_0) such that $\lim_{t \rightarrow \infty} [x(t), y(t)] = (x_{ss}, y_{ss})$. In the latter case, the trajectory corresponds to *unstable manifold*, meaning the set of initial conditions (x_0, y_0) such that $\lim_{t \rightarrow -\infty} [x(t), y(t)] = (x_{ss}, y_{ss})$. The trajectories placed between these lines exhibit apparently paradoxical feature: for $t \rightarrow \infty$ asymptotically reached there is unstable manifold is, while the stable manifold would be approached for

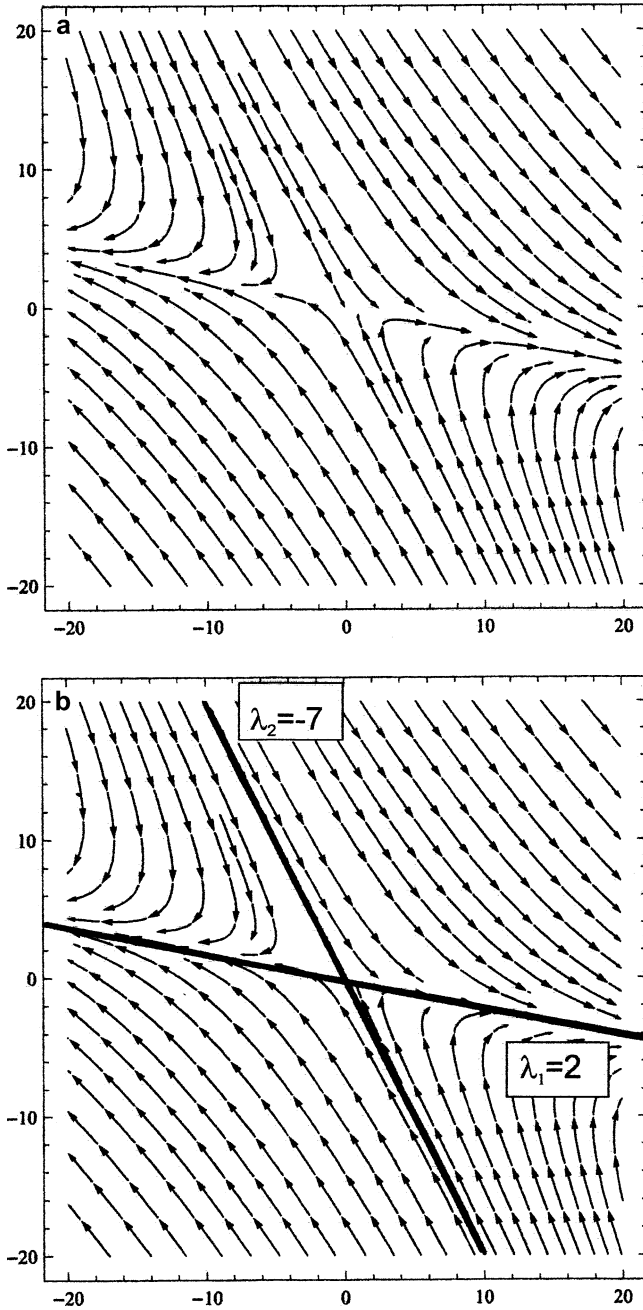


Fig. 1.11 (a) Trajectories of the linear dynamical system (1.41, 1.42) in the x (abscissa)– y (ordinate) coordinates, indicating the steady state $(0, 0)$ of saddle type; (b) phase portrait from (a) with indicated two straight-line trajectories, determined by eigenvalues $\lambda_1 = 2$ and $\lambda_2 = -7$, respectively

$t \rightarrow -\infty$. So, both straight-line manifolds determine the direction of trajectories for $t \pm \infty$. The position of these straight line manifolds in the Cartesian coordinate system $[x, y]$ is determined by the direction of certain *fixed* vectors, which we denote here as $\mathbf{v}_1 = [v_{1,x}, v_{1,y}]$ and $\mathbf{v}_2 = [v_{2,x}, v_{2,y}]$, respectively. Although in typical practical application of the stability analysis usually we do not need to determine these vectors, it is useful to realize (at least once in life) how this determination can be done [2].

The exponential evolution (decay or growth) of the system's state $[x(t), y(t)]$ along every of these straight lines is generally described in the following way:

$$\begin{bmatrix} x \\ y \end{bmatrix} = \exp(\lambda t) \begin{bmatrix} v_x \\ v_y \end{bmatrix} \quad (1.44)$$

We substitute this equation into the system of linear (or linearized) differential equations (analogous to Eqs. (1.13, 1.14), for the (0,0) steady state):

$$\begin{bmatrix} \frac{dx}{dt} \\ \frac{dy}{dt} \end{bmatrix} = \mathbf{J} \begin{bmatrix} x \\ y \end{bmatrix} \quad (1.45)$$

and after comparison with the time derivative of (1.44) we obtain a dependence showing that \mathbf{v} is the *eigenvector* of Jacobian matrix \mathbf{J} , with the eigenvalue λ :

$$\mathbf{J} \begin{bmatrix} v_x \\ v_y \end{bmatrix} = \lambda \begin{bmatrix} v_x \\ v_y \end{bmatrix} \quad (1.46)$$

Now it becomes clear why λ_1 and λ_2 were called the *eigenvalues*. Alternatively, one can write:

$$\begin{bmatrix} a - \lambda & b \\ c & d - \lambda \end{bmatrix} \begin{bmatrix} v_x \\ v_y \end{bmatrix} = \mathbf{0} \quad (1.47)$$

Based on the known every value of λ we can now compute v_x and v_y as the solutions of this system of equations. Since there are two different eigenvalues $\lambda_{1,2}$, the corresponding two different eigenvectors \mathbf{v}_1 and \mathbf{v}_2 are found which determine the positions of the straight-line trajectories in the (x, y) phase space. In other words, every value of λ determines the corresponding manifold. For Eqs. (1.41) and (1.42), we obtain the following nontrivial solutions:

for $\lambda_1 = 2$:

$$\mathbf{v}_1 = \begin{bmatrix} \frac{5}{9} \\ -\frac{1}{9} \end{bmatrix} \text{ (or any scalar multiple of it)} \quad (1.48)$$

for $\lambda_2 = -7$:

$$\mathbf{v}_2 = \begin{bmatrix} 1 \\ -2 \end{bmatrix} \text{ (or any scalar multiple of it)} \quad (1.49)$$

In terms of these values, the general solution of the system (1.41, 1.42) is given by the explicit formulas:

$$x(t) = C'_1 \left(\frac{5}{9} \right) \exp(2t) + C'_2 \exp(-7t) \quad (1.50)$$

$$y(t) = -C'_1 \left(\frac{1}{9} \right) \exp(2t) - 2C'_2 \exp(-7t) \quad (1.51)$$

For the *exemplary* initial condition $(x_0, y_0) = (1, 2)$, the corresponding constants are $C'_1 = 4$ and $C'_2 = -11/9$. In turn, if the initial state belongs exactly either to unstable or stable manifold, one of the constants C'_1 or C'_2 must be zero, since the system's evolution is then entirely controlled by eigenvalue either λ_1 or λ_2 . For example, if $(x_0, y_0) = (5, -1)$ lies on the unstable manifold with $\lambda_1 = 2$ then $C'_1 = 9$ and $C'_2 = 0$, i.e., the system veers away from the initial state according to $x(t) = 5 \exp(2t)$ and $y(t) = -\exp(2t)$. In turn, for $(x_0, y_0) = (2, -4)$ lying on the stable manifold with $\lambda_2 = -7$, $C'_1 = 0$, and $C'_2 = 2$, this time the system tends to the fixed point $(0,0)$ according to the equations $x(t) = 2\exp(-7t)$ and $y(t) = -4\exp(-7t)$.

This analysis is of course valid not only for the saddle point which was here used as an example. Also other types of fixed points and associated trajectories can be found in this way. If eigenvalues become complex numbers: $\lambda_{1,2} = p \pm i\omega$, the evolution equations remain valid with that generalization that the coefficients C'_1 and C'_2 must also be complex numbers. In a particular case of equal eigenvalues $\lambda_1 = \lambda_2 = \lambda$ one obtains special trajectories, named either as *star nodes* (if there are two independent eigenvectors corresponding to single value of λ) or named *degenerate nodes* (if there is only one eigenvector) [2] (cf. Fig. 1.9).

1.3.2.2 Two First Order ODEs vs. a Single Second-Order ODE

At the end of this section, we shall briefly confront the reliability of the description of the physicochemical system with the mathematical equivalence between the system of two ODEs of the first order:

$$\frac{dx}{dt} = ax + by \quad (1.52)$$

$$\frac{dy}{dt} = cx + dy \quad (1.53)$$

and a single, second-order differential equation [7]:

$$\frac{d^2x}{dt^2} - (a + d) \frac{dx}{dt} + (ad - bc)x = 0 \quad (1.54)$$

In order to perform this transformation one first calculates d^2x/dt^2 from Eq. (1.52), in the obtained expression substitutes the dy/dt derivative with Eq. (1.53) and finally substitutes the resulting term by with the expression derived from Eq. (1.52).

Now, assuming the trial solution of (1.54) in an exponential form: $x = Ce^{\lambda t}$ one calculates its first and second derivatives and substitutes them to (1.54), obtaining the equation:

$$\exp(\lambda t)[\lambda^2 - \lambda(a + d) + (ad - bc)] = 0 \quad (1.55)$$

which is true for any finite λ and t , if:

$$\lambda^2 - \lambda(a + d) + (ad - bc) = 0 \quad (1.56)$$

or, equivalently, in terms of Jacobian matrix \mathbf{J} (1.19):

$$\lambda^2 - \text{Tr}(\mathbf{J})\lambda + \text{Det}(\mathbf{J}) = 0 \quad (1.57)$$

Thus, one obtains exactly the same form of solutions for λ_1 and λ_2 , as earlier, and the dynamics of x as a function in time is described as:

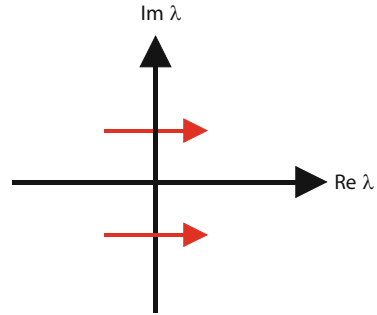
$$x(t) = C_1 \exp[\lambda_1 t] + C_2 \exp[\lambda_2 t] \quad (1.58)$$

In spite of this mathematical equivalence, for the chemical systems, the representation of the system's dynamics in terms of two explicitly defined variables may be more useful and illustrative than reduction of the problem to a single variable. The single variable is sufficient to describe, e.g., the motion of pendulum, but if various chemical species are involved in the reaction, then it is more natural to describe the dynamics of each of them with a separate first-order ODE. Concluding, not always the mathematical equivalence of equations means realistic treatment of a given (electro)chemical problem.

1.3.3 The Hopf Bifurcation

Typical linear stability analysis of the two-dimensional dynamical system aims to find the conditions for the *Hopf* and the *saddle-node* bifurcations. According to analysis described in previous section, as long as the properties of the Jacobian matrix for the analyzed steady state are the following: $\text{Tr}(\mathbf{J}) < 0$ and $\text{Det}(\mathbf{J}) > 0$, this state system is stable, but when the trace and/or the determinant change their

Fig. 1.12 The scheme of Hopf bifurcation in the two-dimensional system, indicating the change of sign of real parts of eigenvalues λ_1 and λ_2 , with nonzero imaginary parts, guaranteeing the oscillations



signs, respective bifurcations take place. If the bifurcation involves only a close neighborhood of a fixed point, is called a *local* bifurcation. If the representation of the bifurcations requires considerations of larger regions of the phase space, such bifurcations will be called *global* (they will be described later in this chapter).

The **Hopf bifurcation**, which can be diagnosed from the linear stability analysis, is a *local* bifurcation. As said earlier, this bifurcation will indicate the possibility of oscillations arising through the loss of stability of the single steady state for the dynamical system that is *at least* two-dimensional. According to Fig. 1.8, the occurrence of such bifurcation in nonlinear system is detected in the linearized system as the condition of the formation of the center, i.e., when the trace of Jacobian matrix \mathbf{J} changes its sign from the negative to the positive one, with the determinant having positive sign. Thus, the condition for the Hopf bifurcation is:

$$\text{Tr}(\mathbf{J}) = 0 \quad \text{with} \quad \text{Det}(\mathbf{J}) > 0 \quad (1.59)$$

In terms of eigenvalues λ_1 and λ_2 (1.28) which then change the signs of their real part, one can illustrate this bifurcation with the scheme shown in Fig. 1.12.

For the linear system these conditions mean only the loss of stability of the steady state, for which, after this bifurcation, the trajectories evolve in a spiral way “into the unknown.” For *nonlinear systems* this trip will, however, end with the closed trajectory—*limit cycle*. This is the essential content of the *Hopf theorem* which justifies the application of linear stability analysis to the diagnosis of oscillatory cycles in nonlinear systems.

One should note that criterion (1.59) shows only the possibility of the Hopf bifurcation, but will not indicate whether it is *supercritical* or *subcritical*. In order to distinguish between these two cases, a deeper analysis of the oscillations characteristics as a function of varying bifurcation parameter is necessary.

1.3.3.1 Supercritical Hopf Bifurcation

Let us consider a model two-dimensional system involving the dynamic variables r and θ which may be placed in the Cartesian (x, y) coordinates: then θ is the angle between the radius r and the x axis, with: $x = r \cos\theta$ and $y = r \sin\theta$ [2].

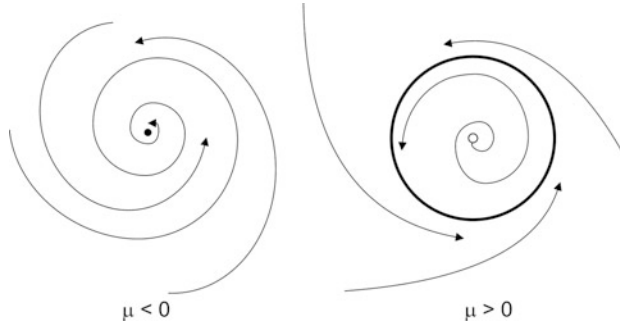


Fig. 1.13 The phase portraits of dynamical system (1.60, 1.61) before (for $\mu < 0$) and after (for $\mu > 0$) the point of supercritical Hopf bifurcation

$$\frac{dr}{dt} = \mu r - r^3 \quad (1.60)$$

$$\frac{d\theta}{dt} = \omega + br^2 \quad (1.61)$$

For this equations' system, the linear stability analysis indicates the occurrence of Hopf bifurcation for the critical value of the bifurcation parameter $\mu_c = 0$. For $\mu < 0$, the single stable steady state is the only attractor (stable focus) in the phase space, while for $\mu > 0$ the only attractor is the *stable limit cycle*, surrounding (the now unstable) central steady state (Fig. 1.13).

The Hopf bifurcation, occurring in the model system (1.60, 1.61) is *supercritical*. For this type of bifurcation, at the critical value of the bifurcation parameter μ_c , the size (radius) of the limit cycle, or the amplitude of oscillations, grows *continuously from zero* at this point, and proportionally to the $\sqrt{(\mu - \mu_c)}$ factor, as long as μ remains close to the critical value. Thus, in practice, in order to confirm the supercritical nature of the Hopf bifurcation, one verifies that the plot of the oscillation amplitude is, near the bifurcation point, a linear function of the $\sqrt{(\mu - \mu_c)}$, with zero intercept.

The frequency of the limit cycle oscillations is approximately equal to $\omega = \text{Im}(\lambda)$ (or the period of oscillations approximately equals to $2\pi/\text{Im}(\lambda)$), where λ is the eigenvalue of the characteristic equation. In fact, inspection of Eq. (1.61) shows that the angular frequency $d\theta/dt$ tends to ω , when the limit cycle radius r tends to zero. It is here also noteworthy to invoke Eq. (1.35) from which it follows that *at the point of a Hopf bifurcation* [i.e., when $\text{Tr}(\mathbf{J}) = 0$], the frequency of the oscillations is generally equal to $\omega_0 = \text{Im}(\lambda) = [\text{Det}(\mathbf{J})]^{1/2}$.

With μ being more and more distant from μ_c toward positive values, these dependences become more approximate, with the phase trajectories becoming more complicated, losing its initial circular shape, and this is a general phenomenon for the nonlinear systems. The reader interested in another example of this type of

bifurcation and the shape of trajectories is advised to analyze the classical Brusselator model (see e.g., [12]).

In order to complete the characteristics of the supercritical Hopf bifurcation one should note that upon decreasing bifurcation parameter the oscillations decay at exactly the same value of the bifurcation parameter ($\mu_c = 0$), i.e., *no hysteresis* in the system's dynamics upon cyclic variation of μ would be observed.

1.3.3.2 Subcritical Hopf Bifurcation

The manifestation of the subcritical Hopf bifurcation is markedly different from the supercritical case. The system which experiences this type of bifurcation does not start to oscillate with the amplitude rising gradually from zero at the critical point, but the oscillations set in with at once remarkable amplitude. In terms of the phase space representation, it means that when at the bifurcation point the steady state loses its stability, the system jumps to the limit cycle of nonzero radius. Sometimes such a type of bifurcation is called a “hard transition,” compared to the “soft” supercritical case and this terminology can be generalized also for other bifurcations.

The model system for the subcritical Hopf bifurcation is [2]:

$$\frac{dr}{dt} = \mu r + r^3 - r^5 \quad (1.62)$$

$$\frac{d\theta}{dt} = \omega + br^2 \quad (1.63)$$

When increasing the bifurcation parameter μ from negative towards positive values (this direction is now important), the onset of high-amplitude oscillations is again observed at a critical value $\mu_c = 0$. What exactly happens upon variation of μ from the negative to positive values is shown on the respective phase portraits (Fig. 1.14). The phase representation is evidently more complex than in supercritical case.

For $\mu < 0$ there are two attractors, both only locally stable, i.e., having their own basins of attraction: the central point and the outer limit cycle, separated with the unstable limit cycle, i.e., repeller (dashed middle circle). Thus, in dependence on the initial conditions, corresponding to one or another basin of attraction, the system may exhibit either damped oscillations to the steady state or sustained (stable) oscillations. In other words, the system is then bistable, involving in this case the coexistence of the steady state and the oscillatory state for certain range of (negative) values of the bifurcation parameter μ .

Let us assume that our system is initially in the single steady state (central point) before the bifurcation. With increasing μ up to a critical value of $\mu_c = 0$, the radius of the unstable limit cycle shrinks to zero, engulfing more and more of this point attractor and eventually making it a repeller. The only attractor is then the stable

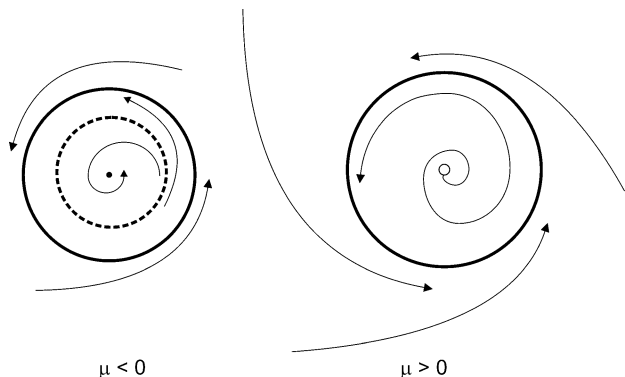
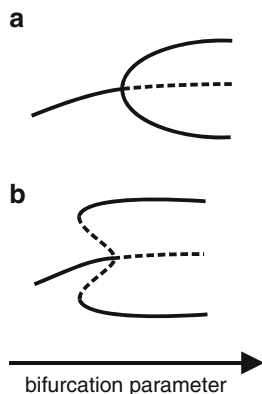


Fig. 1.14 The phase portraits of dynamical system (1.62, 1.63) before (for $\mu < 0$) and after (for $\mu > 0$) the point of subcritical Hopf bifurcation, observed upon increasing value of bifurcation parameter μ . After [2]

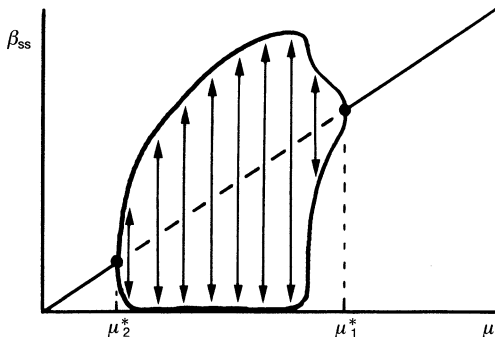
Fig. 1.15 Typical bifurcation diagrams of a supercritical (a) and a subcritical (b) Hopf bifurcation. For the oscillatory regimes, the distance between the upper and lower branches indicates the amplitude of oscillations



limit cycle, to which the system jumps, i.e., the system attains the oscillatory regime of at once large amplitude. Also after this bifurcation, i.e., for $\mu > 0$ there exists only this single attractor, so the system continues to oscillate.

The dynamic behavior of the system is thus indeed more complex than in the case of the supercritical Hopf bifurcation, but it is not the end of complication. The next important feature is that if we want to bring system from the actual large amplitude oscillations back to the situation corresponding to $\mu < 0$, we shall observe the *hysteresis*: oscillations will decay not at $\mu = 0$, but only at $\mu = -1/4$, and through another type bifurcation which is called the *saddle-node bifurcation of cycles* (one of the *global* bifurcations, discussed later in this chapter). For comparison of the supercritical and subcritical Hopf bifurcation, it is very instructive to inspect their alternative schematic diagrams shown in Fig. 1.15.

Fig. 1.16 Schematic representation of the onset, growth, and death of oscillations in the isothermal autocatalytic model reaction system, showing emergence of the stable limit cycle at μ_1^* and its disappearance at μ_2^* . Reproduced from [11] by permission of Oxford University Press, Inc.



In the subcritical case, clearly visible is the hysteresis upon variation of parameter μ . Also the destructive role of the middle unstable limit cycle (dashed arc) for either attractors is indicated—its collision with either the central point attractor or with the external stable limit cycles either destroys its stability (in the former case) or causes mutual annihilation of cycles (in the latter case).

Thus, the practical detection of the subcritical Hopf bifurcation involves both the sudden onset of large amplitude of oscillations and hysteresis in also abrupt decay of oscillations when the variation of the bifurcation parameter is reversed.

1.3.3.3 The Degenerate Case of Two Hopf Bifurcations

According to the principles of the linear stability analysis, the diagnosis of the Hopf bifurcation requires the condition $\text{Tr}(\mathbf{J}) = 0$, with $\text{Det}(\mathbf{J}) > 0$. In this section, we shall discuss a particular case showing the necessity of careful interpretation of this condition. Let us first consider a system, for which upon tuning the system's parameter in search of the oscillations through the supercritical Hopf bifurcation, the sequence of the onset (from zero amplitude), stepwise growth of the amplitude, and decay of oscillations back to zero amplitude are observed (Fig. 1.16).

For each of these two bifurcations, the above discussed condition $\text{Tr}(\mathbf{J}) = 0$ must be met, i.e., for the neighboring values of the control parameter μ , the trace of \mathbf{J} must be positive (when trajectories tend to limit cycle) and negative (when trajectories converge to the point attractor), respectively. In other words, at the critical (bifurcation) points μ_1^* and μ_2^* shown in Fig. 1.16, the derivatives at μ_1^* and at μ_2^* : $d\text{Tr}(\mathbf{J})/d\mu \neq 0$. There is however possible a particular situation, when for the critical value of μ , not only $\text{Tr}(\mathbf{J}) = 0$, but also $d\text{Tr}(\mathbf{J})/d\mu = 0$. Thus, the real part of the eigenvalues $\text{Re}(\lambda)$ does not change a sign at this point, so does not become positive, as required for the oscillatory region. The Hopf bifurcation is then named to be “degenerate.” This degeneration usually means that at this point two Hopf bifurcations merge and cancel each other out, so the oscillations cannot emerge. This case shows that it is necessary to check whether the trace (hence also real parts of eigenvalues) attains positive values and not only zero value [11].

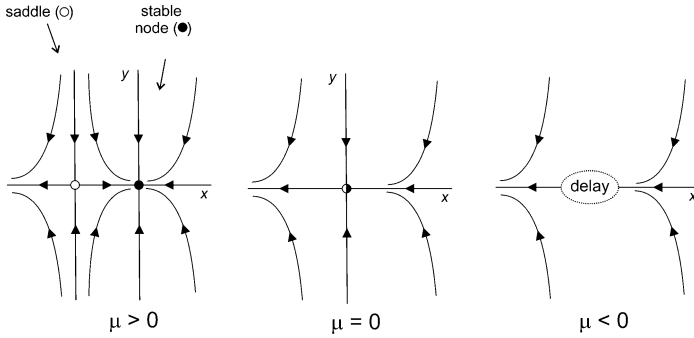


Fig. 1.17 Typical scenario of saddle–node bifurcation in two-dimensional system, involving mutual annihilation of the stable node and a saddle, with an appearance of a region in the phase space in which the run on phase trajectories is delayed. Based on [2]

1.3.4 The Saddle–Node Bifurcation

This bifurcation is often related to the phenomenon of **bistability** which for many systems is closely related to the oscillatory behavior. According to linear stability analysis, in two-dimensional system the saddle–node bifurcation occurs when:

$$\text{Det}(\mathbf{J}) = 0 \tag{1.64}$$

since then (cf. Fig. 1.8) a node [stable or unstable, depending on the sign of $\text{Tr}(\mathbf{J})$] transforms to a saddle point (or vice versa). Of great practical importance is that this condition involves frequently (thus, not always! [11]) the coming together and mutual destruction of two different steady states and we shall deal further with this typical case. This is illustrated by bifurcation scenario in the following model system [2]:

$$\frac{dx}{dt} = \mu - x^2 \tag{1.65}$$

$$\frac{dy}{dt} = -y \tag{1.66}$$

For $\mu > 0$, there are two steady states possible: a stable node at $(x_{ss}, y_{ss}) = (\sqrt{\mu}, 0)$ and a saddle at $(x_{ss}, y_{ss}) = (-\sqrt{\mu}, 0)$. The determinant of the Jacobian matrix of the linearized system (1.65, 1.66) is equal to $\text{Det}(\mathbf{J}) = 2x_{ss}$, thus the condition of the saddle–node bifurcation is met for $\mu = 0$. Figure 1.17 illustrates what happens upon decreasing parameter μ from positive, through the critical zero value, up to negative values.

As parameter μ decreases, the saddle (o) and the node (•) approach each other and eventually collide at the bifurcation point. One can say that at this point the

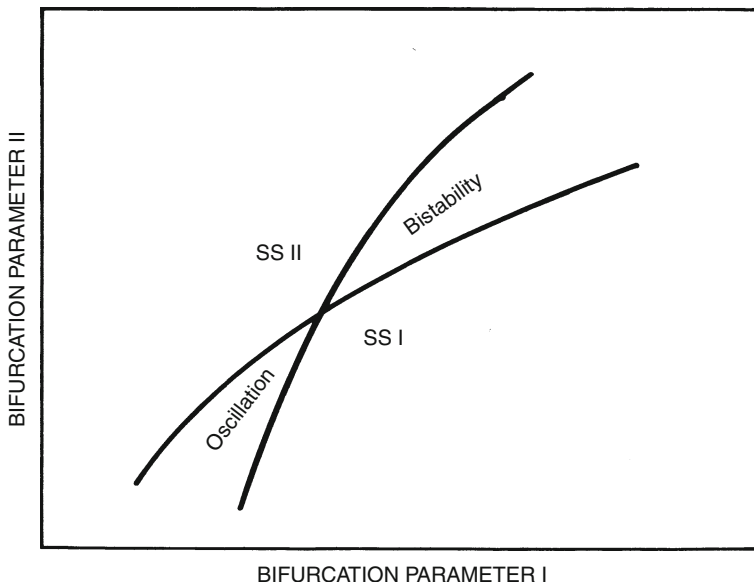


Fig. 1.18 A schematic diagram of the “cross-shaped” bifurcation borders separating areas where monostability, bistability, or oscillations appear in a CSTR experiment as experimental variables (bifurcation parameters) such as flow rate, k_0 , or the concentrations of reactants in the feedstreams are varied. Such a relationship is expected whenever a chemical reaction oscillates by a switching mechanism. Reprinted with permission from [14]. Copyright 1999 American Chemical Society

characteristics of the saddle become identical with those of the node. After the bifurcation these states do not exist anymore, so they annihilated each other. There, however, remains in the system’s dynamics a trace of this annihilation, shown in Fig. 1.17, as the region in which the motion on the phase trajectories is delayed. In his impressive handbook of nonlinear dynamics, Strogatz [2] uses the vivid terms of “ghost” or the “bottleneck region” which sucks all trajectories in and delays them before allowing passage out to the other side. In other words, although steady states already annihilated each other, the system still “remembers” that they existed.

The correlation of this scheme with the folded representation of states in the bistable region was shown in Fig. 1.7. The upper and lower branches of the fold are the sets of stable nodes, while the middle unstable branch consists of saddle points. Every edge of the fold is the place in which a pair of saddle and node is born or disappears, respectively. Of course, in order to confirm such a diagram of steady states, the stability analysis should be performed for each of steady states present for the given value of the bifurcation parameter. For monostable regions, only one stable steady state will be found and this will be a stable node (for this state (1) $\text{Tr}(\mathbf{J})$ should be negative, guaranteeing the asymptotic stability and (2) $\text{Tr}^2(\mathbf{J}) - 4\text{Det}(\mathbf{J})$ should be positive, ensuring that these stable states are the nodes). For the bistable region, three such states will exist: one saddle and two nodes and upon variation of the bifurcation parameter in one direction a saddle and one of the nodes will be involved in the annihilating saddle–node bifurcation, while the stability of the other node will not be affected, and it remains then the only attractor in the phase space.

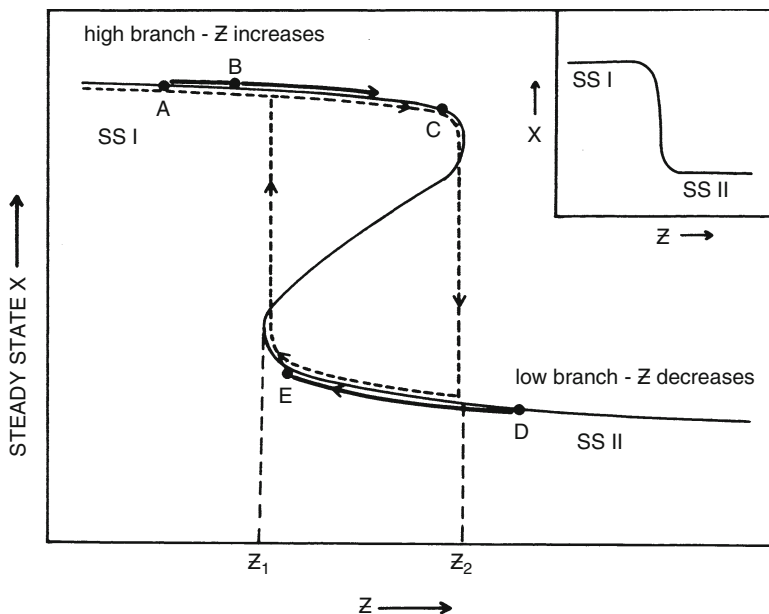


Fig. 1.19 Principle of the occurrence of oscillations related to the bistability region. Schematic plot of steady state X vs. Z calculated from equations corresponding to OREGONATOR model of the Belousov–Zhabotinsky reaction (see Sect. 1.6) under conditions of a flow stirred reactor, for appropriate set of parameters. The curve is folded so that the system may be monostable, bistable, or oscillatory, depending on the exact parameter values. The *bold lines* show evolution to steady states while the *dotted line* show an oscillatory trajectory. The inset shows the same plot using parameters for which the curve is not folded and only one steady state is possible. SSI is a high X steady state and SSII is a low steady state. Reprinted with permission from [14]. Copyright 1999 American Chemical Society

1.3.5 The Cross-Shaped Bifurcation Diagram

Based on the criteria of the Hopf and saddle–node bifurcations one can easily construct the stability diagram for the given system. For quite many oscillators, both chemical and electrochemical ones, it has a characteristic cross-shaped form which is schematically depicted in Fig. 1.18 [13, 14].

This shape reveals a close correspondence between oscillations and bistability that may be observed for the same system, depending on the control parameters. In fact, the occurrence of the oscillations means that in this case the system switches between the upper and lower branches of steady states due to spontaneously occurring cyclic variation of, e.g., the concentration of a species that acts as a bifurcation parameter (Fig. 1.19) [14]. Theoretical description of such correlation and conditions for its occurrence is known as the Boissonade–De Kepper model [13, 15].

The bifurcation diagram like that presented in Fig. 1.18 is usually both determined experimentally and constructed theoretically, in terms of respective models.

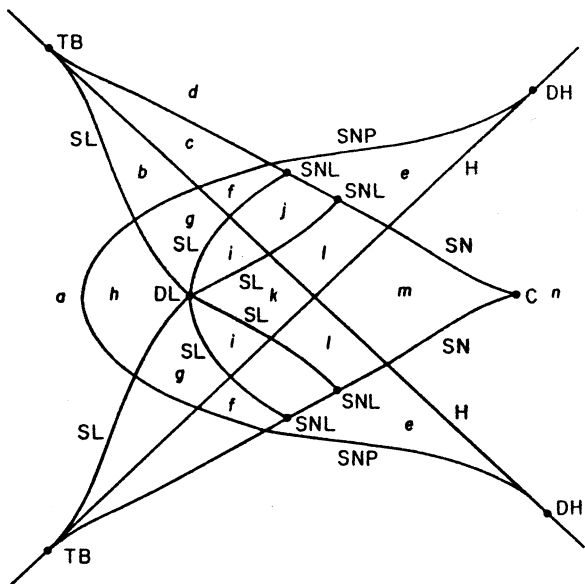


Fig. 1.20 Corrected tableau for Boissonade–De Kepper cross-shaped diagram model. *Lower case letters* correspond to phase portraits on Fig. 3.3 in original reference [14]. Labels: *C* cusp, *DH* degenerate Hopf bifurcation, *DL* double saddle–loop bifurcation, *H* Hopf bifurcation, *SL* saddle–loop bifurcation, *SN* saddle–node bifurcation, *SNL* saddle–node loop bifurcation, *SNP* saddle–node for periodic orbits, *TB* Takens–Bogdanov bifurcation. Reprinted from [16], Copyright 1986, with permission from Elsevier

The similarity of both diagrams is one of the methods of verification of the validity of the model assumed for the description of a real system. One can only remember that only stable steady states are experimentally observable (if no special stabilization procedures are involved), so theoretical model may unravel additional, unobservable states and their bifurcations. Following the Boissonade and De Kepper seminal works [13, 15], Guckenheimer [16] showed an extended and improved mathematical (bifurcation) structure of the cross-shaped diagram for the model chemical reactors. Some of these bifurcations will be described in the next section and their concise description is also given in the original Guckenheimer paper.

1.4 Global Bifurcations Leading to Oscillations

In the previous sections, we learned about a Hopf bifurcation that is undoubtedly the most popular route to the oscillations, but not the only one. At least three other bifurcations that lead to the oscillatory behavior in the two-dimensional system can be diagnosed. Their common feature is that they, contrary to the local nature of a Hopf bifurcation, are *global*, i.e., not only the close vicinity of the steady state, but larger region of the phase space is engaged in this instability. Such bifurcations are indicated in the Guckenheimer scheme (Fig. 1.20).

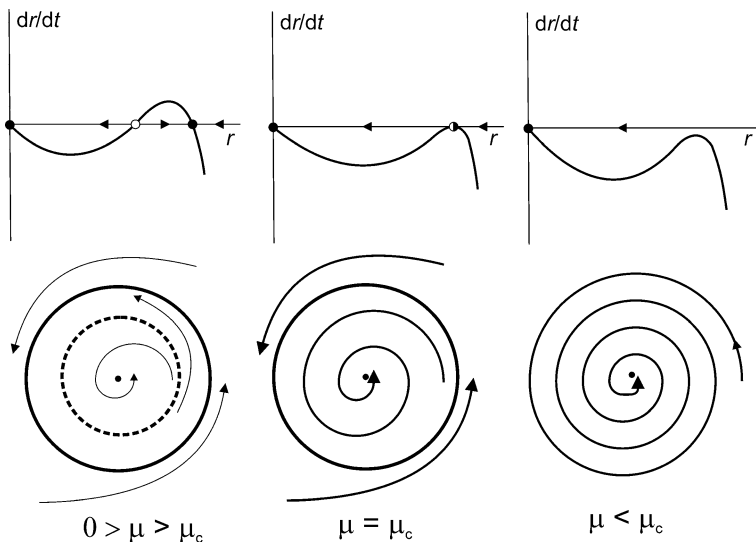


Fig. 1.21 The scheme of the saddle–node bifurcation of limit cycles. Based on [2]

1.4.1 Saddle–Node Bifurcation of Cycles

This type of global bifurcations was implicitly mentioned (but not explicitly named) in Sect. 1.3.3 as occurring in the system in its return trip after the subcritical Hopf bifurcation. The oscillations then decayed with a hysteresis at a new critical point, just via the *saddle–node bifurcation of cycles*.

In a way the essential nature of this bifurcation is a generalization of scheme of the saddle–node bifurcation involving the fixed points (cf. Fig. 1.17): then, one stable node and the (always unstable) saddle annihilated each other at the bifurcation point. If we replace fixed points with two limit cycles: one stable and one unstable, we obtain the bifurcation discussed in this section. Its scheme is illustrated in Fig. 1.21.

If we start from the system’s dynamics after a subcritical Hopf bifurcation and go back with the bifurcation parameter, we first enter the region in which the actually observed limit cycle is not the only attractor, since there is also a central point attractor separated by the unstable limit cycle (see Figs. 1.14 and 1.15). The left picture in Fig. 1.14 is the same as the most left one in Fig. 1.21. Again we can say that this region is bistable. When μ decreases, exactly at $\mu = \mu_c$ in Fig. 1.21 both cycles coalesce, yielding the *half-stable* cycle, from outside of which the states are attracted to, but from inside they tend to the central point attractor. This is the situation when sustained, large-amplitude oscillations, born earlier through the subcritical Hopf bifurcation, now decay. At $\mu < \mu_c$ only the single point attractor survives. Noteworthy, as follows from the schematic Fig. 1.21, the stability of this central point attractor remained intact during the discussed bifurcation.

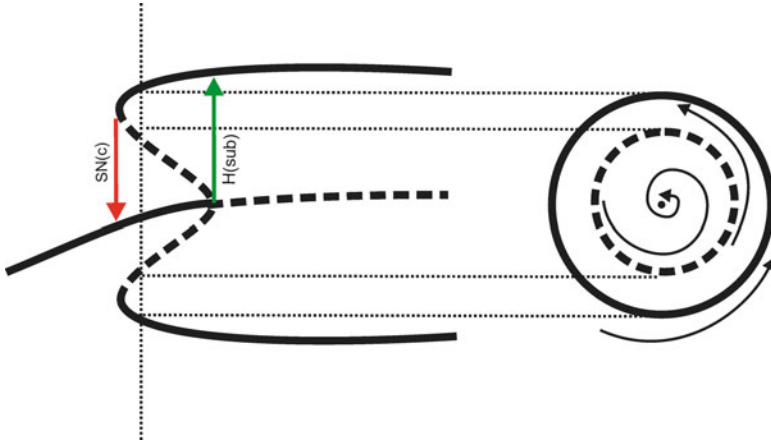


Fig. 1.22 The relationship between the local subcritical Hopf bifurcation [H(sub)] and the global saddle–node bifurcation of the unstable and stable limit cycles [SN(c)]

It can be useful to compare the occurrence of the global saddle–node bifurcation of cycles and of local subcritical Hopf bifurcation, separated by hysteresis region, in terms of the equivalent diagram shown in Fig. 1.22.

This diagram clearly shows how “aggressive” the middle, unstable limit cycle is for his locally stable dynamical partners: the central point attractor and the external limit cycle. When the unstable limit cycle, by changing its radius, collides with one or the other attractor, either the stability of the central attractor decays at the Hopf point or both cycles annihilate each other at the saddle–node point, when only the (now globally stable) point attractor remains. Such bifurcation schemes were found, among others, in the OREGONATOR model of the Belousov–Zhabotinsky process [14] (see Sect. 1.6).

1.4.2 Saddle–Node Infinite Period (SNIPER) Bifurcation

This another example of global bifurcation is called also shortly the Infinite Period bifurcation. It is however better to use the full name, or the abbreviation SNIPER, as it is not the only infinite period bifurcation possible in nonlinear systems. The SNIPER bifurcation occurs in the model system [2]:

$$\frac{dr}{dt} = r(1 - r^2) \quad (1.67)$$

$$\frac{d\theta}{dt} = \mu - \sin \theta \quad (1.68)$$

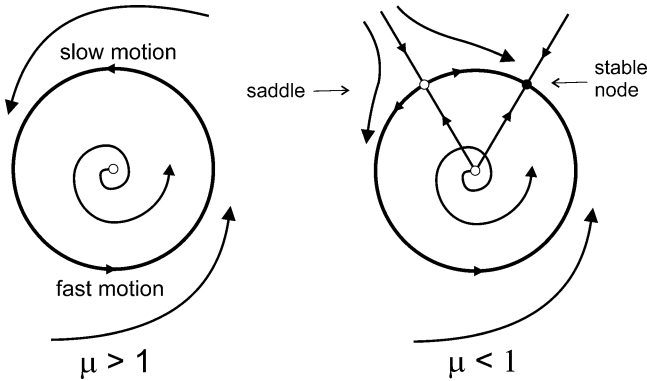


Fig. 1.23 The dynamics of the model system (1.67, 1.68) before and after the SNIPER bifurcation. Based on [2]

for the critical value of bifurcation parameter $\mu_c = 1$. Figure 1.23 shows the difference in the system's dynamics before and after this bifurcation.

For $\mu > 1$ there exists a stable limit cycle, but the system moves along this trajectory with varying velocity—it slows down in a region, which is particularly important for the bifurcation scheme. When the bifurcation parameter decreases from the initial values of $\mu > 1$, the motion becomes slower and slower, and at the point of bifurcation $\mu_c = 1$ the velocity drops to zero for $\theta = \pi/2$ (since then $d\theta/dt = 1 - \sin(\pi/2) = 0$). It means that upon decreasing μ , the period of the oscillations lengthens and at $\mu_c = 1$ becomes *infinitely large*, so the oscillations effectively cease—this is a source of the main part of the name of this bifurcation. Quantitatively, the period of the oscillations increases like $(\mu - \mu_c)^{-1/2}$. After the bifurcation, for $\mu < 1$ the pair of two steady states is born: one stable node and one saddle—and this explains the rest of the name of this bifurcation. Obviously, there is now only a single attractor in the phase space. One should note that unchanged radii of the cycles in Fig. 1.23 indicate that the amplitude of decaying oscillations remains constant. The above features of the SNIPER bifurcation suggest that its existence in real experimental systems or in numerical calculations can be supposed if, upon variation of the bifurcation parameter, the oscillations decay through lengthening of their period, with almost constant amplitude. On the other hand, the dynamical system with SNIPER bifurcation can find potential applications as a device with a tunable period of oscillations, for which purpose the Hopf bifurcation is not suitable.

1.4.3 Saddle–Loop (Homoclinic) Bifurcation

This is another type of the infinite period bifurcation of a global nature, alternative name of which is *homoclinic bifurcation*, as it involves the so-called *homoclinic*

orbit in the phase space. Such homoclinic (“from the same bed”) trajectory has this specific feature that it starts and ends at the same fixed point. The model system in which this type of bifurcation occurs is [2]:

$$\frac{dx}{dt} = y \quad (1.69)$$

$$\frac{dy}{dt} = \mu y + x - x^2 + xy \quad (1.70)$$

Numerical computations showed that the respective bifurcation occurs at $\mu_c \approx -0.8645$. Figure 1.24 shows the variation of the system’s dynamics associated with this type of bifurcation.

This scheme shows that this global bifurcation requires that in the phase space there are present the stable limit cycle and the saddle point. Picture (a) corresponds to sustained oscillations, occurring due to this stable limit cycle, which is slightly deformed, but still separated enough from the saddle point. Upon approaching the bifurcation point, the period of the oscillations lengthens. Picture (b) corresponds to dynamics very close to the saddle–loop bifurcation point which is schematically shown in the right column: the sufficiently deformed limit cycle touches the saddle point and as a consequence the homoclinic orbit is formed. By definition, the homoclinic orbit is a trajectory that connects a saddle fixed point with itself. Beyond the bifurcation point (picture c) the periodic loop is completely destroyed, i.e., the period of oscillations grows to infinity.

1.5 Nullcline Representation of Dynamical Systems

In this section, we shall describe a particularly convenient way to represent the dynamics around the steady states of the two-dimensional system, defined with general equations (1.11) and (1.12). This problem is particularly important if the equations are nonlinear, since then it is frequently impossible to obtain their solutions analytically. Of course, one can always perform numerical integration of Eqs. (1.11) and (1.12). For this purpose, one should first determine the characteristics of the steady state(s), (x_{ss}, y_{ss}) from the conditions: $f(x, y) = 0$ and $g(x, y) = 0$ met simultaneously. Having these steady states determined we further generate numerically the discrete sequences of $[x(\Delta t), y(\Delta t)], [x(2\Delta t), y(2\Delta t)], \dots, [x(n\Delta t), y(n\Delta t)]$, starting in each series from different initial values (x_0, y_0) , corresponding to various distances from the steady-state values. Obtained phase trajectories consist of discrete sets of points $[x(t), y(t)]$ which we plot in the y – x coordinate system. If such calculations were made for sufficiently large number of different initial values of x and y , covering a wide region of phase space with reasonable density, one can reconstruct the reliable phase portrait of the system (1.11, 1.12).

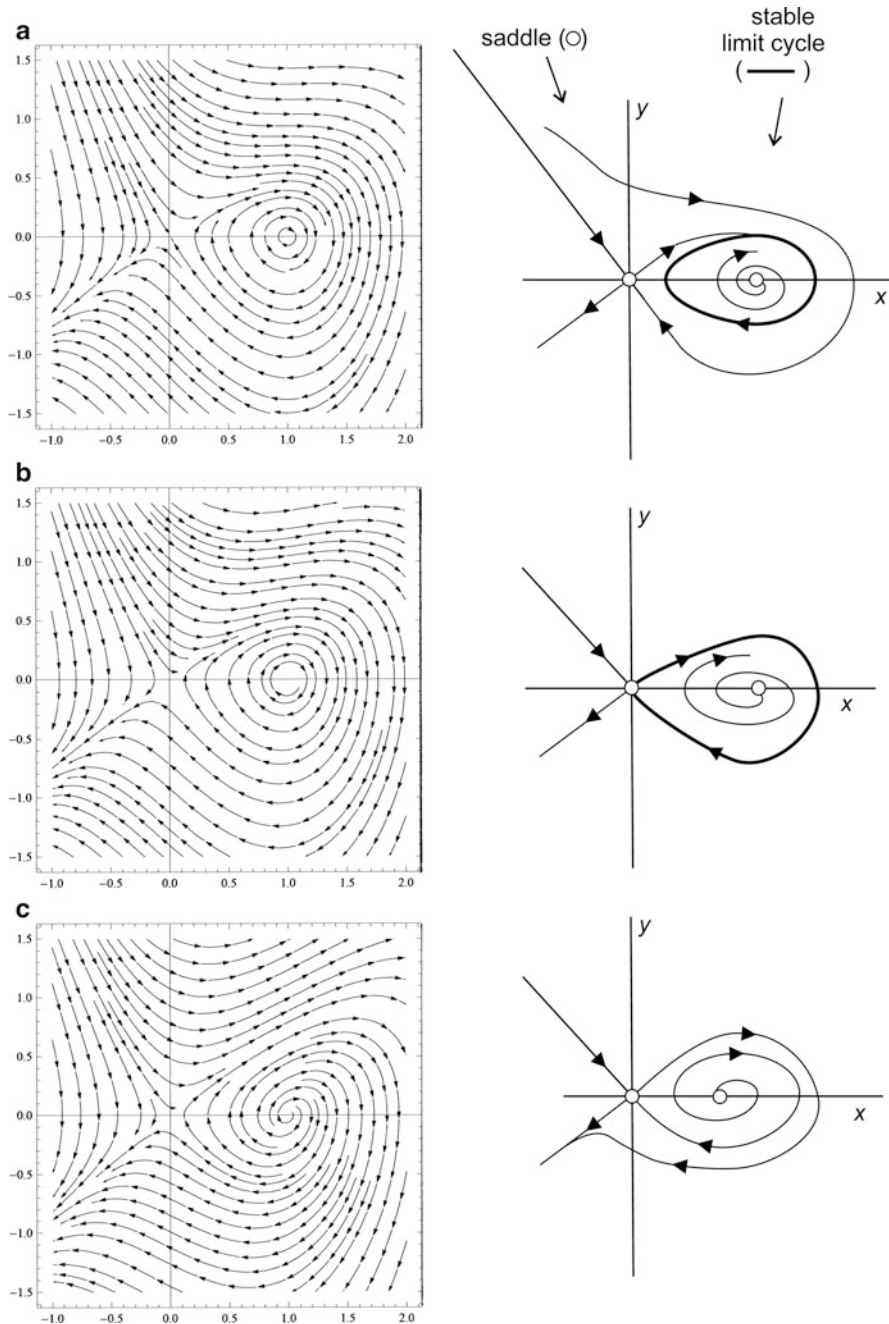
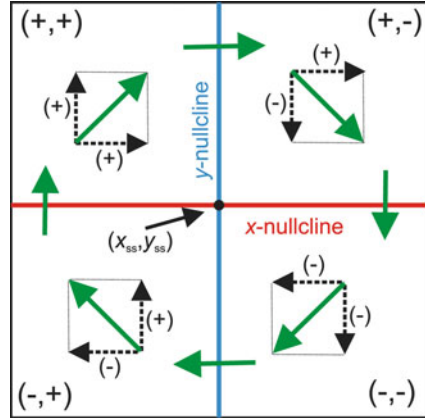


Fig. 1.24 Phase portraits of the dynamical system (1.69), (1.70) in which homoclinic bifurcation occurs upon variation of the control parameter: (a) $\mu = -1 < \mu_c$; (b) $\mu = -0.8645 \approx \mu_c$ and (c) $\mu = -0.5 > \mu_c$. Phase portraits in left column are generated by Mathematica[®] v. 7, while in right column the corresponding schematic trajectories show the essence of homoclinic bifurcation

Fig. 1.25 Principle of correlation between the signs of dx/dt and dy/dt derivatives beyond the nullclines and the direction of arrows indicating the local flows around the intersection of x -nullcline and y -nullcline, determining the steady-state parameters (x_{ss}, y_{ss}) . According to definition of nullclines, at the x -nullcline $dx/dt = 0$ (motion is vertical only) and at y -nullcline $dy/dt = 0$ (motion is horizontal only)



We shall here describe in more detail an alternative and very informative approach that does not need numerical integration of Eqs. (1.11) and (1.12). This very convenient way to inspect the trajectories around the steady states involves *nullclines*. These are defined as curves $y = f_1(x)$ and $y = f_2(x)$ obtained from the right-hand sides of Eqs. (1.11) and (1.12), i.e., after applying the $dx/dt = 0$ and $dy/dt = 0$ condition separately to each respective equation. The nullclines derived from applying the $dx/dt = 0$ and $dy/dt = 0$ conditions are called the x -nullcline and y -nullcline, respectively. For example, if $dx/dt = y - x^2$ and $dy/dt = x - y$, the x -nullcline is defined with $y = x^2$ and the y -nullcline with $y = x$. In conventional Cartesian coordination system (x - y phase space), the x -nullcline shows where the flow is vertical (due to variations of y only), and the y -isocline indicates the points for which the flow is purely horizontal, i.e., parallel to the x axis. Beyond the nullclines the dx/dt and dy/dt derivatives are both nonzero, with the *signs* crucial for the determination of local dynamics. Furthermore, the intersection of both nullclines means mutual meeting of the $dx/dt = 0$ and $dy/dt = 0$ conditions, i.e., determines the position of the steady state in the phase space. Of course, if more than one steady state is possible, nullclines intersect in appropriate number of points. To summarize, the nullclines partition the xy plane around the steady state into four regions of *various signs* of dx/dt and dy/dt , composed of the following variants: $(+, +)$, $(+, -)$, $(-, +)$, $(-, -)$. Equivalently, one can represent the local direction of flows of x and y with the appropriately oriented arrows (see Fig. 1.25).

It is undoubtedly useful to become familiar with the representation of the system's dynamics in terms of nullclines, as it is quite a popular approach in nonlinear dynamics. As an example we shall now apply the nullclines approach to the dynamical system corresponding to the classical Lotka model of damped oscillations:

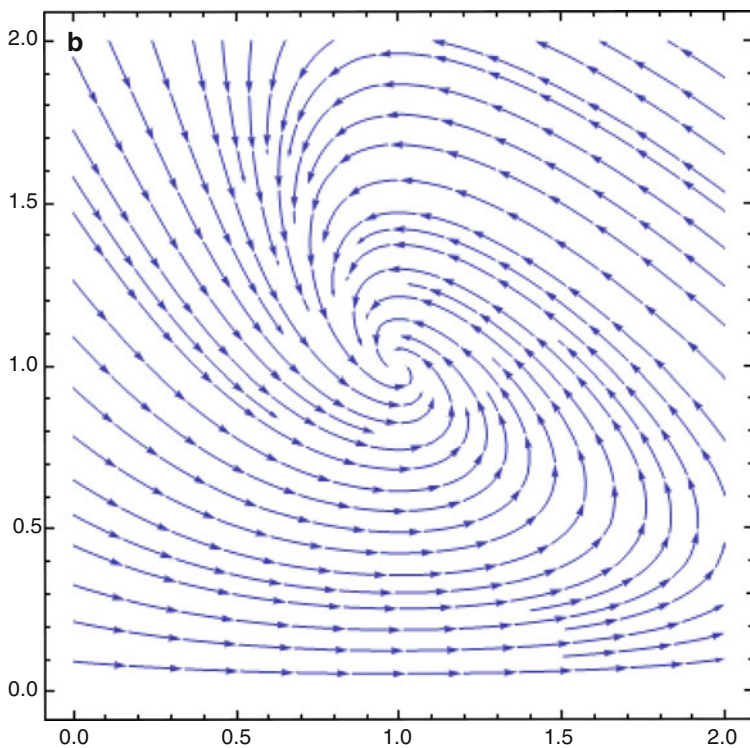
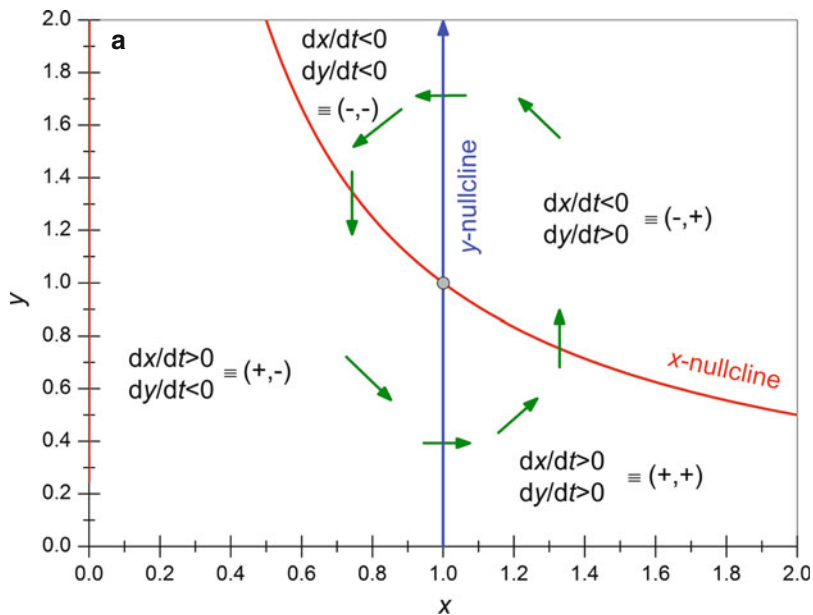


Fig. 1.26 (a) Nullclines of the dynamical system (1.71, 1.72), the Lotka model for $a = b = c = 1$; (b) the corresponding phase portrait with a $(1, 1)$ stable focus, generated by Mathematica[®] v.7

$$\frac{dx}{dt} = a - bxy \quad (1.71)$$

$$\frac{dy}{dt} = bxy - cy \quad (1.72)$$

where x and y can be identified with the concentrations of oscillating intermediate chemical species and parameters a – c depend on the rate constants of particular reaction steps and the constant concentration of a reactant. Based on linear stability analysis one obtains the condition for damped oscillations (steady state of stable focus type): $ab < 4c^2$, so we can choose here, e.g.: $a = b = c = 1$. The steady state of the system (1.71), (1.72) is then $(x_{ss}, y_{ss}) = (1, 1)$ and the corresponding nullclines are defined with equations:

$$x \text{ - nullcline : } y = \frac{a}{bx} = \frac{1}{x} \quad (1.73)$$

$$y \text{ - nullcline : } x = \frac{c}{b} = 1 \quad (1.74)$$

Figure 1.26a shows the course of the nullclines intersecting at the steady state as well as the signs of derivatives dx/dt and dy/dt determining the direction of the flows in each of four parts of the x – y space created by those nullclines. For comparison, Fig. 1.26b shows the corresponding phase portrait generated by Mathematica® v.7.

Applications of nullclines will be described in further sections of this chapter.

1.6 Fast and Slow Dynamical Variables

The conclusion from the previous sections is that the continuous dynamical system may exhibit oscillatory instabilities if it is defined by at least two ordinary differential equations (at this step we do not yet discuss the role of spatial coordinates). If the oscillations occur under given conditions, as a result of respective bifurcation, it is further important to analyze the shape and the period of oscillations, since this can reveal important quantitative characteristics of the system's dynamics. Many real systems, including the electrochemical ones, exhibit oscillations which are not sinusoidal, but often consist of relatively slow and fast changes of the system's state. Such oscillations are called "relaxation" ones, meaning that the system's behavior reflects sudden release of a kind of "tension" accumulated during the slow course. For a two-dimensional system such relaxation behavior means that the *time scales* of the two dynamical variables x , y are *markedly different*, and therefore we can identify in this case the *fast* (e.g., x) and the *slow* (then y) variable.

It is useful to demonstrate this problem first in terms of the simple model, like the well-established van der Pol equation, used mainly in physical sciences.

This single, second-order differential equation may be written in an equivalent, more convenient form of two ordinary differential equations of the first order [7]:

$$\frac{dx}{dt} = \frac{1}{\varepsilon} \left(y - \frac{x^3}{3} + x \right) \quad (1.75)$$

$$\frac{dy}{dt} = -\varepsilon x \quad (1.76)$$

where $\varepsilon > 0$ is a parameter of crucial importance for the indication of the fast and the slow variables, since it quantitatively describes the difference in their *time scales*. In fact, we shall see later (Chap. 2) in the description of model electrochemical systems that the differential equations will be often transformed to dimensionless forms, allowing for the convenient definition of parameter analogous to ε .

An inspection of Eqs. (1.75) and (1.76) immediately shows that if ε is close to 1, the dynamics of $x(t)$ and $y(t)$ are comparable, or—in other words—the time scales of the variation of x and y are similar. However, upon decreasing ε these time scales become more and more separated. This is clearly shown by the results of numerical integration of Eqs. (1.75) and (1.76), for various parameters, shown in the caption of Fig. 1.27. For sufficiently small parameter, like, e.g., for the case of $\varepsilon = 0.01$ shown in this figure, the x variable evidently becomes a fast variable (compared to y), the dynamics of which corresponds then to typical relaxation oscillations.

It is instructive to correlate the shape of these oscillations and phase trajectories with the nullclines (Fig. 1.28), the course of which is independent of ε :

$$x \text{ - nullcline : } y = \frac{x^3}{3} - x \quad (1.77)$$

$$y \text{ - nullcline : } x = 0 \quad (1.78)$$

The only steady state, indicated by the intersection of these nullclines is $(x_{ss}, y_{ss}) = (0, 0)$ and is unstable. It is surrounded by a limit cycle of a smooth or angular shape, depending on parameter ε , so the slopes of arrows indicating the directions of motion will adapt to this shape, respectively.

Of our particular interest is now the case of small ε , when the oscillations attain strongly relaxation shape. The corresponding superposition of the nullclines and the limit cycle is shown in Fig. 1.29. This is a very important and representative picture which shows the close course of the slow trajectory and the x -nullcline, interrupted by fast switches of x between the two branches of this nullcline (with y remaining then practically constant).

Now let us trace in more detail the dynamics of the fast and slow change of x variable. For that purpose we shall use a generalized form of a two-dimensional dynamical system with different time scales of both variables:

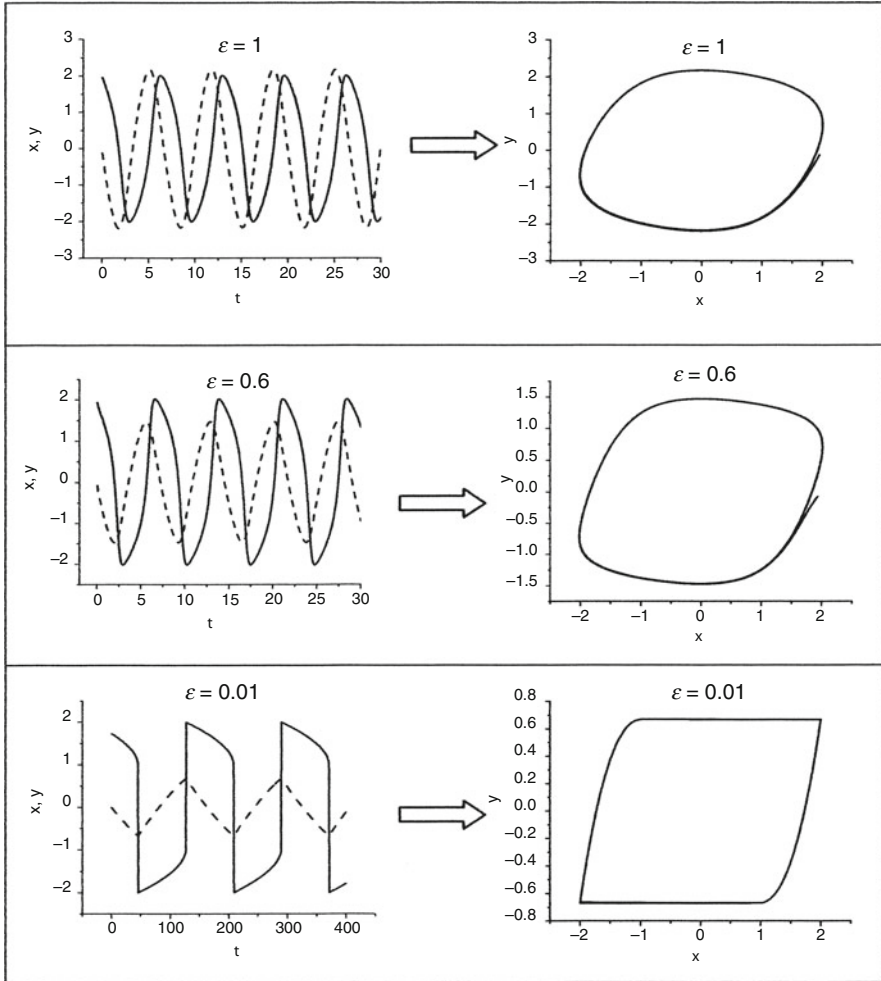


Fig. 1.27 Oscillatory solutions x (solid line) and y (dashed line) of the van der Pol equations (1.75, 1.76) (left column) and corresponding phase portraits (right column), for the parameter values (from top to bottom): $\epsilon = 1$, $\epsilon = 0.6$, $\epsilon = 0.01$

$$\frac{dx}{dt} = \frac{1}{\epsilon}P(x, y) \tag{1.79}$$

$$\frac{dy}{dt} = \epsilon Q(x, y) \tag{1.80}$$

In terms of these equations, the relation between the simultaneous changes of y and x variables is given by:

Fig. 1.28 Nullclines of the van der Pol equations (1.75) and (1.76)

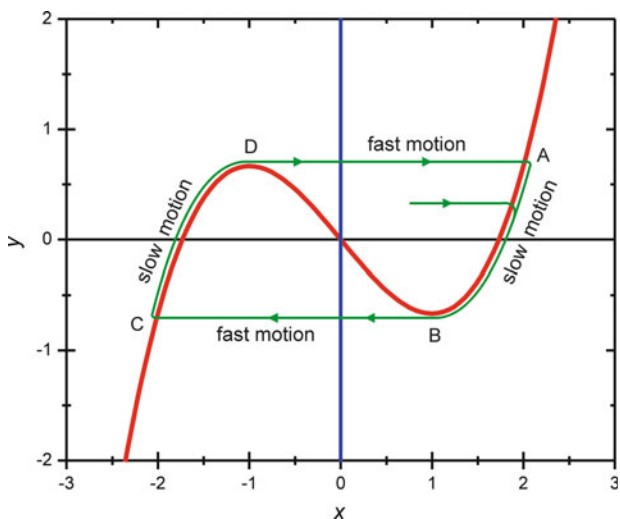
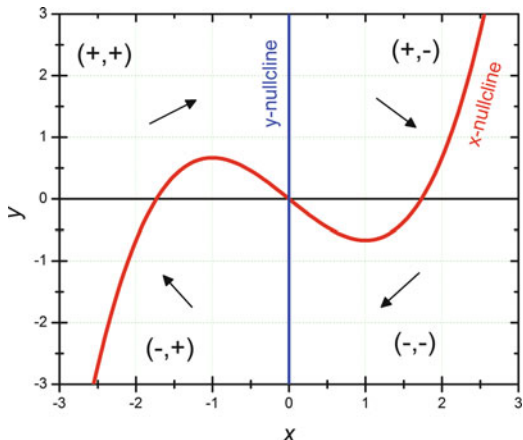


Fig. 1.29 Superposition of nullclines of the van der Pol oscillator from Fig. 1.28 and of the limit cycle for relaxation oscillations (small ϵ)

$$\frac{dy}{dx} = \epsilon^2 \frac{Q(x, y)}{P(x, y)} \tag{1.81}$$

For the state lying exactly on the x -nullcline [i.e., when $P(x, y) = 0$], the $dx = 0$ and the dy/dx ratio tends to infinity. On the other hand, if the initial state is *not* close to the x -nullcline, and especially if $\epsilon \ll 1$, the dy/dx ratio is very small, meaning that dx is much larger than dy , so the move of the system's state is almost horizontal, like in Fig. 1.29. One can say that $|dx/dt|$ is then of the order of $1/\epsilon$ [we use also the notation $O(1/\epsilon)$], while $|dy/dt|$ is $O(\epsilon)$. The direction of motion along the x -direction,

i.e., towards the x -nullcline is diagnosed from Fig. 1.28, when the signs of dx/dt and dy/dt for all four sections of the phase space were indicated. Now, when the system's state approaches the x -nullcline, the motion along x -direction (according to the definition of this nullcline) slows down, with values of $|dx/dt|$ and $|dy/dt|$ being now comparable, both $O(\varepsilon)$. When x -nullcline is reached, $dx/dt = 0$, so the only motion possible is now along y -coordinate. Based on Fig. 1.28 one concludes that in this section $dy/dt < 0$, so the system crosses the x -nullcline vertically, going a bit down. Since in this way the x -nullcline was crossed, the dx/dt changed sign to negative, with $|dx/dt|$ becoming however a small value due to close position to x -nullcline. Thus, x decreases relatively slowly, with $|dx/dt|$ and $|dy/dt|$ being again comparable. Note that due to decrease in x , the system remains close to the x -nullcline until point B is reached. Then the continued decrease in x makes the system's state more and more apart from the x -nullcline: it cannot go up, since y can only decrease in this section. At this point, due to increasing $P(x, y)$ the motion of x is again strongly accelerated, compared to y , so the system moves quickly to point C, when it slows down and slowly covers the path C–D, according to the same reasoning as above for the initial stages of the trip. Finally, at point D the fast trip to point A occurs, the oscillatory cycle is closed and further repeats along the ABCD path.

Analogously to the above model considerations based on van der Pol equation, in real chemical and electrochemical systems one can find dynamical variables of significantly separated time scales. In homogeneous chemical kinetics [17], it becomes then useful, if possible, to write the full system of kinetic equations:

$$\frac{dx_i}{dt} = F_i(x_1, x_2, \dots, x_n); \quad i = 1, 2, \dots, n \quad (1.82)$$

in the sequence arranged according to decreasing powers of the small parameter ε ($\varepsilon \ll 1$):

$$\varepsilon^2 \frac{dx_i}{dt} = F_i(x_1, x_2, \dots, x_n); \quad i = 1, 2, \dots, l \quad (1.83)$$

$$\varepsilon \frac{dx_j}{dt} = F_j(x_1, x_2, \dots, x_n); \quad j = l + 1, \dots, l + m \quad (1.84)$$

$$\frac{dx_k}{dt} = F_k(x_1, x_2, \dots, x_n); \quad k = l + m + 1, \dots, n \quad (1.85)$$

or, equivalently in the form:

$$\frac{dx_i}{dt} = \frac{1}{T_1} F_i \quad (1.86)$$

$$\frac{dx_j}{dt} = \frac{1}{T_2} F_j \quad (1.87)$$

$$\frac{dx_k}{dt} = \frac{1}{T_3} F_k \quad (1.88)$$

where $T_1 = \varepsilon^2$, $T_2 = \varepsilon$, $T_3 = 1$.

If we wish to analyze exactly the dynamics of all variables both in short and long time scales, the integration of all equations is of course necessary. However, if we are interested in the time courses of the order of $T_2 = \varepsilon$, then the processes described by Eq. (1.86) are relatively fast, whereas processes of the dynamics defined by Eq. (1.88) are relatively slow. In other words, during time T_2 all the concentrations x_k can be considered practically constant, e.g., equal to initial ones. As a consequence, the system of n differential equations is reduced for Eq. (1.88), i.e., its order decreases for $[n - (l + m)]$.

Next, due to $T_1 \ll T_2$, before x_j values undergo significant changes, all x_i concentrations [Eq. (1.86)] will attain their final (steady-state) concentrations, which can be inserted as constant values in Eq.(1.87). Thus, finally only m differential equations (1.87), characterized with similar time scale of the concentration dynamics, survive the reduction process. This can seriously simplify numerical calculations and also reduce eventual problems with their numerical stability, possible for the systems of many differential equations.

Based on analogous considerations, also complicated mechanisms of oscillatory chemical reactions, like, e.g., of the Belousov–Zhabotinsky process, could have been simplified to the “core” reaction scheme responsible for the generation of the oscillations. One of the most famous mechanisms of that type is the OREGONATOR (“OREGON oscillATOR”) [18], being a simplified, model version of the FKN mechanism, named so after its authors: Field et al. [19, 20]:

Process A:



Process B:



Process C:



where $A = \text{BrO}_3^-$ and $B = \text{bromomalonic acid}$ are the reactants of the BZ-type process, $P = \text{HOBr}$ is the final product in this model, while the key (oscillating) intermediates are $X = \text{HBrO}_2$, $Y = \text{Br}^-$, and $Z = \text{Ce(IV)}$. The factor f is a stoichiometric coefficient, which in the model can vary between 0.5 and 2.5, having a strong effect on the system's stability and thus possible bifurcation scenario. The oscillatory course involves two steady-state concentrations of HBrO_2 : one defined by reactions of group A which require Y concentrations above certain critical value, and the other one defined by reactions (B) which predominate when $[Y]$ drops below this critical value. The oscillations occur in this way that when Y species, consumed in reactions of group (A) drop below the critical value, the system switches to reactions (B) which produces species Z that, in turn, through a relatively slow Process C, i.e., with certain delay, regenerates Y to a supercritical level and then Processes A temporarily take over the control on the system's characteristics. The reader particularly interested in chemical oscillations should consult also, e.g., the monographs [11, 21, 22]. Also, the concise characteristics of OREGONATOR, including animation of its phase portrait can be found on the Internet Scholarpedia.org page [23].

The original kinetic equations corresponding to mechanism (1.89)–(1.93) can be transformed to the form involving dimensionless variables, indicating simultaneously the different time scales for each of the three dynamical variables (x, y, z):

$$\varepsilon \frac{dx}{d\tau} = qy - xy + x(1 - x) \quad (1.94)$$

$$\varepsilon' \frac{dy}{d\tau} = -qy - xy + fz \quad (1.95)$$

$$\frac{dz}{d\tau} = x - z \quad (1.96)$$

with $\varepsilon' \ll \varepsilon \ll 1$; typically: $\varepsilon' = 4 \times 10^{-4}$, $\varepsilon = 4 \times 10^{-2}$ and $q = 7.6 \times 10^{-5}$. In view of a very low value of ε' , y appears to be the fastest variable. So, when slower variables tend to their steady-state values, y -variable should already attain the corresponding steady-state value. Or, in other words, the value of y adjusts immediately to the given actual values of x and z variables. Thus, it is reasonable to consider only the dynamics of x and z , while for given (x, z) the condition $dy/d\tau = 0$ should be practically met. Hence the actual steady state y_{ss} concentration is [24]:

$$y_{\text{ss}} = \frac{fz}{q + x} \quad (1.97)$$

After inserting this expression in Eqs. (1.95) and (1.96) one obtains the description of the OREGONATOR dynamics, reduced to two dynamical variables:

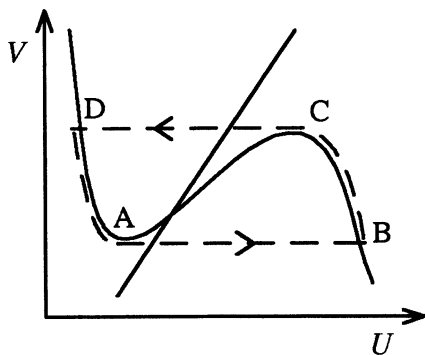


Fig. 1.30 Nullclines of two-variable model of the Belousov–Zhabotinsky reaction (1.98) and (1.99). Reprinted from [25] with kind permission from Springer Science+Business Media. Coordinates: $U \equiv x, V \equiv z$ (in order to avoid confusion with spatial coordinates when analyzing later the spatiotemporal patterns)

$$\varepsilon \frac{dx}{d\tau} = x(1-x) + \frac{f(q-x)z}{q+x} \tag{1.98}$$

$$\frac{dz}{d\tau} = x - z \tag{1.99}$$

Since $\varepsilon \ll 1$, one can expect that solution of this equation system will exhibit relaxation oscillations which should be represented in the phase space by the trajectory of the features similar to those for the van der Pol equation (Fig. 1.29). The nullclines of system (1.98) and (1.99) are defined as:

$$x \text{ - nullcline : } z = - \frac{-qx + (1-q)x^2 - x^3}{f(q-x)} \tag{1.100}$$

$$z \text{ - nullcline : } z = x \tag{1.101}$$

Figure 1.30 shows schematically the course of these nullclines for such parameters q and f that they intersect at the point being the unstable steady state around which the limit cycle ABCD develops [25]. Note the replacement of the symbols of variables: $x \rightarrow U, z \rightarrow V$, in order to avoid the confusion with later description of spatiotemporal patterns when x becomes a symbol of a spatial coordinate.

Depending on q and f parameters, also other nullcline characteristics are possible in this model:

1. The intersection of nullclines occurs only within the AD section, corresponding to the single stable steady state of relatively low x value (monostability).

2. The intersection of nullclines occurs only within the BC section, corresponding to the stable steady state of relatively high x value (monostability).
3. Nullclines intersect in three points; the steady states lying within the AD and BC sections are stable, while the middle state belonging to AC section is unstable; these characteristics correspond to bistability.

Regarding case (1), particularly interesting is the system's response when the single stable steady state is perturbed to the right so much that the U value crosses the middle AC section of the U -nullcline. Then the sign of dU/dt changes from negative to positive one and the perturbation of U is no longer damped, but grows towards the right branch of the U -nullcline and makes further an extensive trip in the phase space, until it returns to the original stable steady state. In other words, the system enters (here only once) the high-amplitude limit cycle. Such a dynamical feature of the system that *only large enough* perturbation of the steady state causes the single oscillation, instead of its trivial fast damping, is called *excitability*. This phenomenon plays an important role in the explanation of the origin of travelling fronts in dynamical systems (see also Sect. 1.1.2, volume II), both model and real ones: e.g., the response of neurons to external stimulus exhibits excitable characteristics.

1.7 Canard Explosion

Following the section about fast and slow variables in dynamical systems, we shall briefly discuss the related subject of *canard explosion* [26]. The classical canard phenomenon means the very fast transition from small amplitude oscillations (small amplitude limit cycle) to a large amplitude relaxation oscillations (large amplitude relaxation limit cycle) upon such a small variation of a control parameter that it can even be difficult to confirm experimentally a precise canard mechanism in real chemical systems (taking also into account the presence of natural, inherent system's noise). The name of this phenomenon refers to the appearance of a canard, so simply a lie, in a newspaper. Canards were first discovered and analyzed by Benoît et al. [27] during the studies of, among others, the van der Pol oscillator. Thus, the prototypical example of the canard explosion is given by the van der Pol oscillator with external forcing, expressed by the parameter a :

$$\varepsilon \frac{dx}{dt} = z - \frac{x^3}{3} + x \quad (1.102)$$

$$\frac{dz}{dt} = a - x \quad (1.103)$$

For $\varepsilon \ll 1$, i.e., for the case of fast (x) and slow (z) variables, considered above, the sequence of events leading to canard explosion is schematically shown in Fig. 1.31.

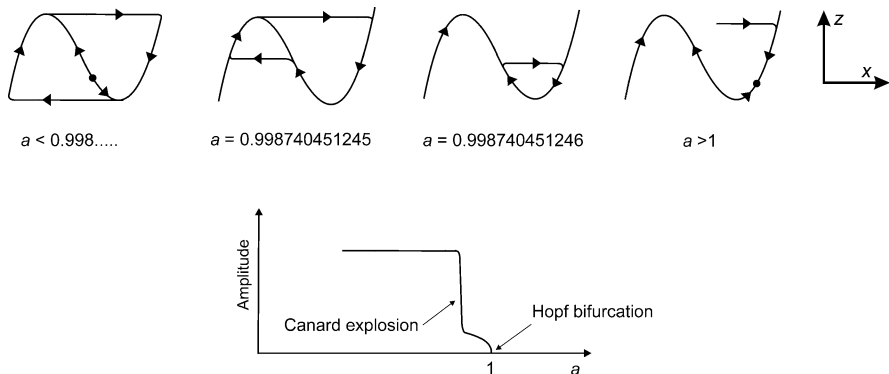


Fig. 1.31 Canard explosion of the van der Pol oscillator (for $\varepsilon = 0.01$) within an exponentially small neighborhood of $a = 0.998740451245$ where the transition from relaxation oscillations to small amplitude limit cycles happens via canard cycles. The small amplitude limit cycles then terminate at $a = 1$ via a Hopf bifurcation. Based on [26]

In chemical literature such *canard explosion* is classified as “hard transition,” because large amplitude change occurs practically immediately. Due to difficulties in experimental diagnosis, the supercritical Hopf bifurcation followed soon by the canard explosion can be easily mistaken with the subcritical Hopf bifurcation. Furthermore, according to Peng et al. [28] the canard explosion should be considered a *false bifurcation*, since it causes *only quantitative*, not qualitative changes in the system’s dynamics. That is why canard explosion is not a true, but a “lie” regarding the bifurcation.

The existence of canard explosion was discovered in the two-variable OREGONATOR by Brøns and Bar-Eli [29], and discussed for the two-variable OREGONATOR and AUTOCALATOR [28]. It was also applied to the analysis of diffusion-induced instabilities of phase waves in one spatial dimension for a two-variable model of the BZ reaction [30], indicating that this reaction–diffusion system may provide a means of differentiating between a subcritical Hopf bifurcation and a supercritical Hopf bifurcation with a closely associated canard explosion, when appropriate relations hold between the diffusion coefficients. Furthermore, the canard explosion was found by Xie et al. [31] in the Hodgkin–Huxley model of the initiation and propagation of action potential in neurons and in the model of the platinum-catalyzed oxidation of carbon monoxide [32]. Epstein et al. [33] have used the canard phenomenon to the localization of oscillations in the BZ reaction with globally coupled oscillators (localization means in this context the occurrence of spatial domains of large amplitude oscillation on a background of small amplitude oscillation in a reaction–diffusion system). These studies were later extended for the theoretical study of a discrete system of relaxation oscillators globally coupled via inhibition [34].

Noteworthy is also the possible relation of the canard phenomena with the important class of oscillations that are composed of small and large amplitude

(relaxation) oscillations, and are therefore called MMO (Mixed Mode Oscillations). It is thus not surprising that discovery of canards was followed by the suggestion that they could be involved in the mechanism of formation of MMOs [26]. This mechanism would be alternative to other routes to such dynamics, e.g., proposing the formation of MMO through the break-up/loss of stability of a homoclinic orbit in the three-variable autonomous van der Pol–Duffing model [35], suggesting the break-up of an invariant torus [36] or considering a congruence of a saddle–node bifurcation and Hopf bifurcation [37].

1.8 The Activator–Inhibitor Systems

1.8.1 The Concept of the Activator and the Inhibitor

In the discussion of the mechanisms underlying the formation of temporal, spatio-temporal, and spatial patterns, in both homogeneous and heterogeneous dissipative systems, it is sometimes useful to invoke the concept of an *activator–inhibitor system* [8]. Let us consider the model chemical system in which X species produces Y species, with various feedback loops involved in this process. The dynamics of $[X] \equiv x$ and $[Y] \equiv y$ are described in terms of general equations (1.11) and (1.12). Let us invoke again the principles of linear stability analysis, in which the Jacobian matrix \mathbf{J} is calculated, in the notation explicitly illustrating the effect of x or y on the temporal dynamics: $\dot{x} \equiv dx/dt$ and $\dot{y} \equiv dy/dt$ around the steady state (ss):

$$\mathbf{J} = \begin{bmatrix} a_{11} & a_{12} \\ a_{21} & a_{22} \end{bmatrix} = \begin{bmatrix} \left[\frac{\partial f}{\partial x} \right]_{\text{ss}} & \left[\frac{\partial f}{\partial y} \right]_{\text{ss}} \\ \left[\frac{\partial g}{\partial x} \right]_{\text{ss}} & \left[\frac{\partial g}{\partial y} \right]_{\text{ss}} \end{bmatrix} \equiv \begin{bmatrix} \left[\frac{\partial \dot{x}}{\partial x} \right]_{\text{ss}} & \left[\frac{\partial \dot{x}}{\partial y} \right]_{\text{ss}} \\ \left[\frac{\partial \dot{y}}{\partial x} \right]_{\text{ss}} & \left[\frac{\partial \dot{y}}{\partial y} \right]_{\text{ss}} \end{bmatrix} \quad (1.104)$$

In terms of this notation, the definitions of activators and inhibitors are related to the particular cases of the feedbacks in the following way:

1. x (or y) is a *self-activator*, i.e., an *autocatalytic* variable, if an increase in x (or y) results in an increase in dx/dt (or dy/dt); mathematically this means that, respectively:

$$a_{11} = \left[\frac{\partial f}{\partial x} \right]_{\text{ss}} > 0 \quad (1.105)$$

or

$$a_{22} = \left[\frac{\partial g}{\partial y} \right]_{\text{ss}} > 0 \quad (1.106)$$

2. x (or y) is a *self-inhibitor*, if an increase in x (or y) causes a decrease in dx/dt (or dy/dt); mathematically:

$$a_{11} = \left[\frac{\partial f}{\partial x} \right]_{ss} < 0 \quad (1.107)$$

or

$$a_{22} = \left[\frac{\partial g}{\partial y} \right]_{ss} < 0 \quad (1.108)$$

3. x *activates* (or *inhibits*) y if an increase in x causes an increase (or decrease) in dy/dt , i.e

$$x \text{ activates } y : a_{21} = \left[\frac{\partial g}{\partial x} \right]_{ss} > 0 \quad (1.109)$$

$$x \text{ inhibits } y : a_{21} = \left[\frac{\partial g}{\partial x} \right]_{ss} < 0 \quad (1.110)$$

4. x is an *activator* (or *inhibitor*) if it activates (or inhibits) *both itself and* y :

$$\text{Activation through } x : a_{11} = \left[\frac{\partial f}{\partial x} \right]_{ss} > 0 \text{ and } a_{21} = \left[\frac{\partial g}{\partial x} \right]_{ss} > 0 \quad (1.111)$$

$$\text{Inhibition through } x : a_{11} = \left[\frac{\partial f}{\partial x} \right]_{ss} < 0 \text{ and } a_{21} = \left[\frac{\partial g}{\partial x} \right]_{ss} < 0 \quad (1.112)$$

In terms of the above-given definitions, the Jacobian matrix with the elements characterized with the following signs:

$$\mathbf{J} = \begin{bmatrix} + & - \\ + & - \end{bmatrix} \quad (1.113)$$

corresponds to the so-called **pure activator–inhibitor system** (or simply an activator–inhibitor system), with x being an activator and y , the inhibitor. The corresponding scheme of feedback loops is shown in Fig. 1.32 [8].

In turn, the Jacobian matrix of the form:

$$\mathbf{J} = \begin{bmatrix} + & + \\ - & - \end{bmatrix} \quad (1.114)$$

corresponds to the **cross-activator–inhibitor** system, shown schematically in Fig. 1.33 [8].

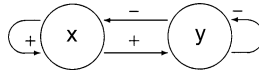


Fig. 1.32 The (pure) activator–inhibitor system: x activates both itself and y ; y inhibits both itself and x . Reproduced from [8] with kind permission from Springer Science+Business Media B.V.

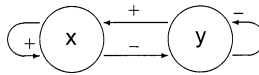


Fig. 1.33 The cross-activator–inhibitor system: x activates itself but inhibits y ; y inhibits itself but activates x . Reproduced from [8] with kind permission from Springer Science+Business Media B.V.

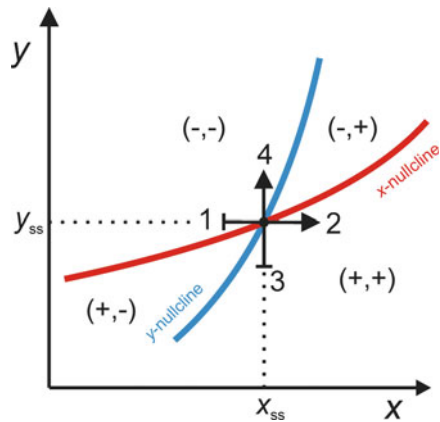


Fig. 1.34 Principle of determination of the signs of the elements of Jacobian matrix for the steady state from the course of the x - and y -nullclines

Both types of the activator–inhibitor system play an important role in the interpretation of the oscillatory dynamics, including the formation of the Turing patterns (see Sects. 1.1.3 and 1.1.4, volume II). In the OREGONATOR model (1.89)–(1.93) one can identify an activator and an inhibitor, since it contains both an autocatalytic step and a (delayed) negative feedback loop. The activator species is X and the inhibitor species is Z . The inhibition process (negative feedback loop) occurs via the sequence: Step (1.91) \rightarrow Step (1.93) \rightarrow Step (1.90) which inhibits autocatalytic production of X in Step (1.91) [23].

1.8.2 Correlation Between the Nullclines and the Properties of the Jacobian Matrix

Since for the detection of the activator and the inhibitor it is sufficient to know only the signs of particular elements of the Jacobian matrix of the given steady state, it is useful to note that these signs can be easily diagnosed from the course of nullclines around this state. Let us consider again schematic, exemplary course of nullclines (Fig. 1.34).

Then, one can realize that the small increment $\Delta x > 0$, realized from point (1) to point (2), is associated with the increase of both dx/dt and dy/dt , since the corresponding pair of signs of dx/dt and dy/dt changes from $(-, -)$ to $(+, +)$. Hence $a_{11} \equiv [(d/dx)(dx/dt)]_{ss} > 0$ and $a_{21} \equiv [(d/dx)(dy/dt)]_{ss} > 0$. Analogously, for the small increase Δy , realized from point (3) to point (4), the signs change from $(+, +)$ to $(-, -)$, i.e., $a_{12} \equiv [(d/dy)(dx/dt)]_{ss} < 0$ and $a_{22} \equiv [(d/dy)(dy/dt)]_{ss} < 0$. So, the distribution of signs is the same as in matrix (1.113), corresponding to the pure activator–inhibitor system.

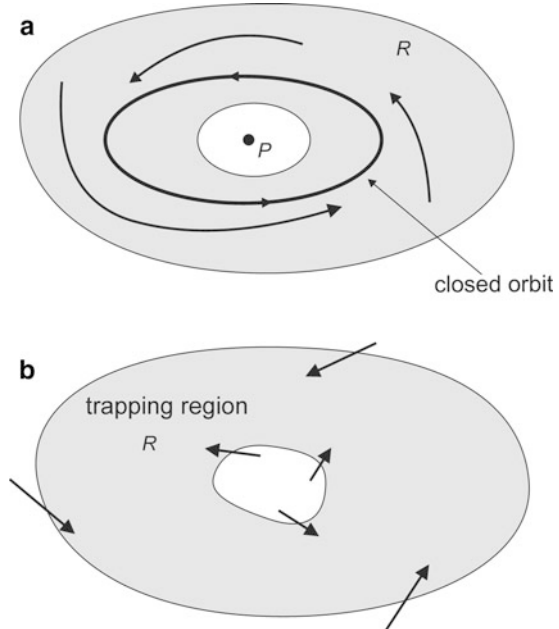
1.9 The Existence of Closed Trajectories—The Poincaré–Bendixson Theorem

Remaining still with the two-dimensional dynamical system, one can pose an important problem of the theoretical conditions for existence and features of cyclic (closed) trajectories in the phase space. For that purpose it is first useful to invoke the *existence and uniqueness theorem* for the solutions of (generally N differential equations) which says, that such solutions *exist* and are *unique* if continuous functions $\mathbf{f}(\mathbf{x})$ (in the general vector notation of the dynamical system $d\mathbf{x}/dt = \mathbf{f}(\mathbf{x})$) are *continuously differentiable*, i.e., if all partial derivatives $\partial f_i / \partial x_j$ ($i, j = 1, \dots, N$) of functions \mathbf{f} are continuous [2].

A particularly important consequence of the existence and uniqueness theorem is that *different trajectories never intersect*. If such situation occurred, the system could start its evolution from the crossing point along two trajectories at once, which case is forbidden, since it would violate the condition for uniqueness. Keeping in mind the existence and uniqueness theorem one can particularly easily predict the following situation in the two-dimensional system. Let us imagine that there is a closed orbit on the phase plane. Then *any* trajectory starting inside this orbit remains imprisoned there forever, otherwise it would eventually cross the orbit, which event is just forbidden.

This conclusion implies the next one. If this imprisoned trajectory cannot leave the region surrounded by an external closed orbit, what can *eventually* happen to it? If there is (are) a fixed point(s) there, it (one of them) can be attained by this trajectory, finishing the system's evolution. However, if there are no any fixed points, the answer is given by the *Poincaré–Bendixson theorem*, but only for a two-dimensional case (i.e., planar vector field): if a trajectory is confined to a closed bounded region, in which there are no fixed points (steady states), then the trajectory either already is, or must eventually approach the *closed orbit*, i.e., limit cycle in a nonlinear system. In other words, in such a case the system's behavior must end with the sustained oscillations. These oscillations have to be simple periodic, since a simple closed trajectory means just that. Thus, the Poincaré–Bendixson theorem excludes, in the two-dimensional system, more complex trajectories, including chaotic courses. For the systems with more than two dimensions, when complex

Fig. 1.35 Principle of application of the Poincaré–Bendixson theorem to the diagnosis of cyclic trajectory. (a) Construction of the ring-shaped region R of the phase plane, which does not contain fixed point P ; (b) construction of the “trapping region” inside which there must exist a closed orbit in the absence of fixed points. Based on [2]



and chaotic oscillations can be generated, the Poincaré–Bendixson theorem is not applicable. One can summarize the Poincaré–Bendixson theorem also in this way that in the phase space of the two-dimensional system of nonlinear differential equations there may exist only single fixed points or closed orbits (cycles).

Practical application of the Poincaré–Bendixson theorem for the diagnosis of existence of limit cycle on the phase plane is, however, not always simple. The region of the phase plane, investigated for the presence of closed orbits, has to be constructed in this way that it must not contain any fixed points. Thus, if the cyclic trajectory would surround the fixed point, it is necessary to construct the ring-shaped R domain, so that the fixed points do not fall in this region (Fig. 1.35a).

Now, if it is possible to find in practice such a “trapping region” R which does not contain any fixed points, and all trajectories from its internal and external surroundings enter the area of R (Fig. 1.35b), we prove the existence of a closed orbit inside R . The application of the Poincaré–Bendixson theorem to the diagnosis of limit cycle was described [2] for the CIMA (i.e., chlorine dioxide–iodine–malonic acid) homogeneous oscillator [38].

1.10 The Stability of the N -Dimensional Dynamical System

1.10.1 Linear Stability Analysis of N -Dimensional Dynamical System

The linear stability analysis described in Sect. 1.3 for one-dimensional and two-dimensional systems may be generalized for the N -dimensions (i.e., N dynamical variables) [11]. The diagnosis of stability of a given steady state is in principle the same as above: it is determined by the sum of N exponential terms of the form $\exp(\lambda_i t)$:

$$x_i = C_{i1} \exp(\lambda_1 t) + C_{i2} \exp(\lambda_2 t) + C_{i3} \exp(\lambda_3 t) \quad (1.115)$$

with $i = 1, \dots, N$, and eigenvalues λ_i (real or complex numbers), determined based on the Jacobian $N \times N$ matrix (1.116):

$$\mathbf{J} = \begin{bmatrix} a_{11} & a_{12} & \dots & a_{1n} \\ a_{21} & a_{22} & \dots & \\ \dots & \dots & \dots & \dots \\ a_{n1} & a_{n2} & \dots & a_{nn} \end{bmatrix} \quad (1.116)$$

In particular, the direct diagnosis of stability is based on the signs of the eigenvalues λ_i . If all eigenvalues λ_i are negative real numbers or have negative real parts of complex numbers, all perturbations will asymptotically decrease to zero as a function of time, so the steady state considered is asymptotically stable.

Let us consider the case when one of the eigenvalues is a real negative number, while the other ones are either also negative real numbers or complex numbers with negative real parts. If, upon variation of a control parameter, any of the real eigenvalues changes its sign to a positive one, while for all other $(N - 1)$ eigenvalues their real parts remain negative, a **saddle-node bifurcation** in N -dimensional system occurs, leading to the (always unstable) saddle point in the phase space. This eigenvalue which first changed the sign is called a *principal* one.

In turn, if upon changing the control parameter, the real parts of a *complex conjugated pair of eigenvalues* (called then the *principal pair*) are passing through zero from negative to positive values (making then both eigenvalues purely imaginary), a **Hopf bifurcation** in N -dimensional system occurs; again, for all other $(N - 2)$ eigenvalues their real parts should remain negative. One should note that eventual further changes of signs of these other eigenvalues do not change the principal property of the system, since the system already moves away from the unstable steady state [11].

We shall consider in more detail the three-dimensional autonomous system [11]:

$$\frac{dx_1}{dt} = f_1(x_1, x_2, x_3) \quad (1.117)$$

$$\frac{dx_2}{dt} = f_2(x_1, x_2, x_3) \quad (1.118)$$

$$\frac{dx_3}{dt} = f_3(x_1, x_2, x_3) \quad (1.119)$$

with the corresponding 3×3 Jacobian matrix:

$$\mathbf{J} = \begin{bmatrix} a_{11} & a_{12} & a_{13} \\ a_{21} & a_{22} & a_{23} \\ a_{31} & a_{32} & a_{33} \end{bmatrix} \quad (1.120)$$

where $a_{ij} = (\partial f_i / \partial x_j)_{ss}$.

The matrix form of the characteristic equation:

$$\text{Det} \begin{bmatrix} a_{11} - \lambda & a_{12} & a_{13} \\ a_{21} & a_{22} - \lambda & a_{23} \\ a_{31} & a_{32} & a_{33} - \lambda \end{bmatrix} = 0 \quad (1.121)$$

is equivalent to the cubic equation:

$$\lambda^3 + b\lambda^2 + c\lambda + d = 0 \quad (1.122)$$

with real coefficients b , c [sum of minors of (1.120)] and d defined as²:

$$b = -\text{Tr}(\mathbf{J}) = -(a_{11} + a_{22} + a_{33}) \quad (1.123)$$

$$\begin{aligned} c &= \text{Det} \begin{bmatrix} a_{11} & a_{12} \\ a_{21} & a_{22} \end{bmatrix} + \text{Det} \begin{bmatrix} a_{22} & a_{23} \\ a_{32} & a_{33} \end{bmatrix} + \text{Det} \begin{bmatrix} a_{11} & a_{13} \\ a_{31} & a_{33} \end{bmatrix} \\ &= a_{11}a_{22} + a_{11}a_{33} + a_{22}a_{33} - a_{12}a_{21} - a_{13}a_{31} - a_{23}a_{32} \end{aligned} \quad (1.124)$$

$$\begin{aligned} d &= -\text{Det}(\mathbf{J}) \\ &= -(a_{11}a_{22}a_{33} + a_{21}a_{13}a_{32} + a_{31}a_{12}a_{23} - a_{11}a_{23}a_{32} - a_{22}a_{31}a_{13} \\ &\quad - a_{33}a_{12}a_{21}) \end{aligned} \quad (1.125)$$

Generally, the solutions of Eq. (1.122) include either three real roots or one real and two complex conjugate roots λ_i .

As indicated earlier, for the *Hopf bifurcation* to occur in three-dimensional system, the real part of the principal pair of eigenvalues must pass through zero,

²In practice it is possible that some of the a_{ij} elements of Jacobian matrix are equal to zero, so expressions (1.124) and (1.125) undergo appropriate simplification [11].

with the third eigenvalue real and negative, which means that Eq. (1.122) must be factorizable in the form [11]:

$$(\lambda^2 + \omega_0^2)(\lambda + a) = 0 \quad \text{with } a > 0 \quad (1.126)$$

since then the eigenvalues meet the above conditions:

$$\lambda_{1,2} = \pm i\omega_0 \quad (1.127)$$

and

$$\lambda_3 = -a \quad (1.128)$$

Comparison of Eq. (1.122) and Eqs. (1.127) and (1.128) allows to derive the criteria for a Hopf bifurcation in three-dimensional system, involving a zero discriminant ($bc - d$) of Eq. (1.122):

$$bc - d = 0 \quad \text{with } b > 0 \quad (1.129)$$

with the dependences defining the frequency of oscillations at a Hopf point:

$$a\omega_0^2 = d \quad \omega_0 = c^{1/2} \quad (1.130)$$

Note that since $b = -\text{Tr}(\mathbf{J})$, the trace of Jacobian matrix must be *negative* at the Hopf bifurcation point, not zero, as in two-dimensional case. Furthermore, since d must be positive, the determinant $\text{Det}(\mathbf{J})$ has to be also *negative*. Finally, coefficient c must be positive. Thus, the conditions for a Hopf bifurcation in the three-dimensional system are:

$$\text{Det}(\mathbf{J}) - c \times \text{Tr}(\mathbf{J}) = 0 \quad \text{with: } \text{Tr}(\mathbf{J}) < 0, \text{Det}(\mathbf{J}) < 0, c > 0 \quad (1.131)$$

For further discussion of these conditions, see Ref. [11].

We have discussed in detail the conditions for a Hopf bifurcation. Systematic classification of types of fixed points in three-dimensional system, done based on linear stability analysis, can be conveniently performed based on the signs of two discriminants of characteristic polynomial (1.121) [39]:

$$\delta = bc - d \quad (1.132)$$

$$\Delta = -b^2c^2 + 4b^3d + 4c^3 - 18bcd + 27d^2 \quad (1.133)$$

and possible cases are given in Table 1.2

The pictorial representations of those trajectories are depicted in Table 1.3.

Table 1.2 Types of fixed points in three-dimensional phase space and conditions for the occurrence, referred to characteristic Eq. (1.122)

Parameter range	Δ	Type of fixed point in three-dimensional phase space	Roots of characteristic polynomials (1.118)	Case no.
$\delta > 0, d > 0, c > 0$	$\Delta < 0$	Stable node	$\text{Im } \lambda_i = 0$ $\lambda_i < 0, i = 1, 2, 3$	A-1
	$\Delta > 0$	Stable focus	$\text{Re } \lambda_{1,2} < 0$ $\lambda_3 < 0$	A-2
$\delta < 0, d < 0, c > 0$	$\Delta < 0$	Unstable node	$\text{Im } \lambda_i = 0$ $\lambda_i > 0, i = 1, 2, 3$	B-1
	$\Delta > 0$	Unstable focus	$\text{Re } \lambda_{1,2} > 0$ $\lambda_3 > 0$	B-2
$\delta > 0, d < 0, c \leq 0$ or $d < 0, c > 0$	$\Delta < 0$	Saddle node	$\text{Im } \lambda_i = 0$ $\lambda_{1,2} < 0, \lambda_3 > 0$	C-1
	$\Delta > 0$	Saddle focus	$\text{Re } \lambda_{1,2} < 0$ $\lambda_3 > 0$	C-2
$\delta < 0, d > 0; c \leq 0$ or $d > 0, c > 0$	$\Delta < 0$	Saddle node	$\text{Im } \lambda_i = 0$ $\lambda_{1,2} > 0, \lambda_3 < 0$	D-1
	$\Delta > 0$	Saddle focus	$\text{Re } \lambda_{1,2} > 0$ $\lambda_3 < 0$	D-2

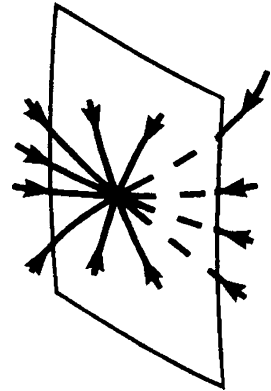
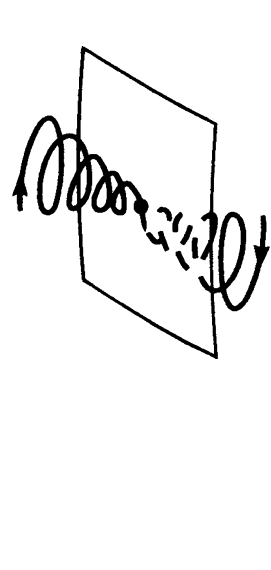
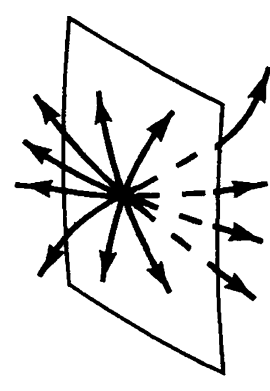
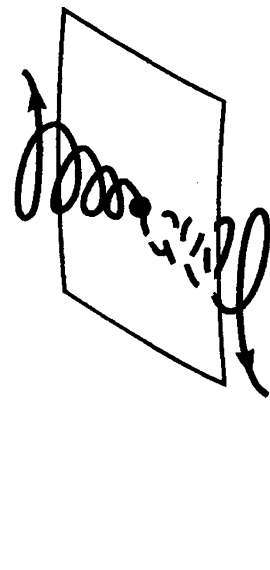
Reproduced from [39] with kind permission of Verlag Harri Deutsch

1.10.2 Complex Periodic Behavior and Routes to Chaos in N-Dimensional Systems

With increasing dimension of the dynamical system the complexity of possible behaviors increases. For example, upon variation of the bifurcation parameter of the N -dimensional system the trivial birth of the stable limit cycle from the stable steady state can be followed by the period-doubling sequence or transition to quasi-periodicity [11]. The latter transitions are the bifurcations of the oscillatory solutions, so in order to predict them, one has to analyze the *local stability of the limit cycle*, in a way in principle analogous to that applied for the single steady state. The practical difference is that such analysis usually must be performed by numerical computations, since nonlinear differential equations do not offer analytical solutions for the limit cycles.

Already for three-dimensional systems quite complex dynamics can be observed. This includes, for example, so-called MMO that are composed of large (L) amplitude peaks followed by a series of small (S) amplitude spikes, with the notation $L^m S^n$ showing the number of corresponding peaks in a periodically repeating sequence. If such periodic MMO's patterns are observed, often it is sufficient to tune a bifurcation parameter to observe transition to aperiodic, i.e., chaotic behavior. Such regime can be interpreted as a motion involving aperiodic succession of unstable stages removing the trajectory from the fixed point, followed by a reinjection back to the vicinity of the fixed point (in this context cf. the saddle focus type of the fixed point, discussed in the previous section, which combines in a single

Table 1.3 Pictorial representation of three-dimensional phase portraits from Table 1.3. Reproduced in part from [39] with kind permission of Verlag Harri Deutsch

Type of fixed point (case no.)	1 ($\Delta < 0$)	2 ($\Delta > 0$)
A-1/2 stable node/stable focus		
B-1/2 unstable node/unstable focus		

(continued)

Table 1.3 (continued)

Type of fixed point (case no.)	1 ($\Delta < 0$)	2 ($\Delta > 0$)
C-1/2 saddle node/saddle focus		
D-1/2 saddle node/saddle focus		

dynamics a stabilizing trend coexisting with a destabilizing one [40]). For a nonlinear system, such a scenario is related to the concept of *homoclinic orbits* (see Sect. 1.4.3). Shil'nikov [41] in his works showed how the homoclinic orbits can form and undergo destruction, leading to complicated phase trajectory called *strange attractor*. Such strange attractors are the phase portraits of *deterministic chaos* which term means aperiodic oscillations, of a course determined by nonstochastic equations, but with complexity making the system's dynamics practically unpredictable on the long run. In particular, the term "strange" means particularly high, not observed for the "usual" attractor of the periodic motion, sensitivity of the course of the trajectories to initial conditions which makes it impossible to obtain reproducible chaotic courses in real systems, always subject to stochastic noise.

One should emphasize here again that deterministic chaos requires at least three-dimensional dynamical system. Historically, such chaos was first observed in numerical calculations performed by Lorenz [42]. With intention to understand the difficulties in the forecasting of weather, Lorenz constructed a set of three ODEs simplifying the convective motions in the atmosphere. For certain parameters, this purely deterministic system generated aperiodic oscillations, very sensitive to input data, so the predicted model "weather" depended strongly on the day of calculations when new, updated information about atmospheric conditions was introduced. In the chaotic courses of the Lorenz model, the homoclinic trajectories were found during later analyses [40]. Another famous model, related more to chemical kinetics than the Lorenz system, and also involving homoclinic trajectories, was introduced by Rössler [43]:

$$\frac{dx}{dt} = -(y + z) \quad (1.134)$$

$$\frac{dy}{dt} = x + ay \quad (1.135)$$

$$\frac{dz}{dt} = b + z(x - c) \quad (1.136)$$

The fixed point of Eqs. (1.134)–(1.136) is $(x_{ss}, y_{ss}, z_{ss}) = (0, 0, 0)$. Linear stability analysis around this point leads to the characteristic equation [40]:

$$\lambda^3 + (c - a)\lambda^2 + (1 + b - ac)\lambda + c - ab = 0 \quad (1.137)$$

For $a = 0.38$, $b = 0.30$, and $c = 4.82$, the dynamical system (1.134)–(1.136) exhibits the homoclinic orbit (see Fig. 1.36a). In turn, for $a = 0.32$, $b = 0.30$, and $c = 4.50$, the chaotic trajectory is generated (Fig. 1.36b).

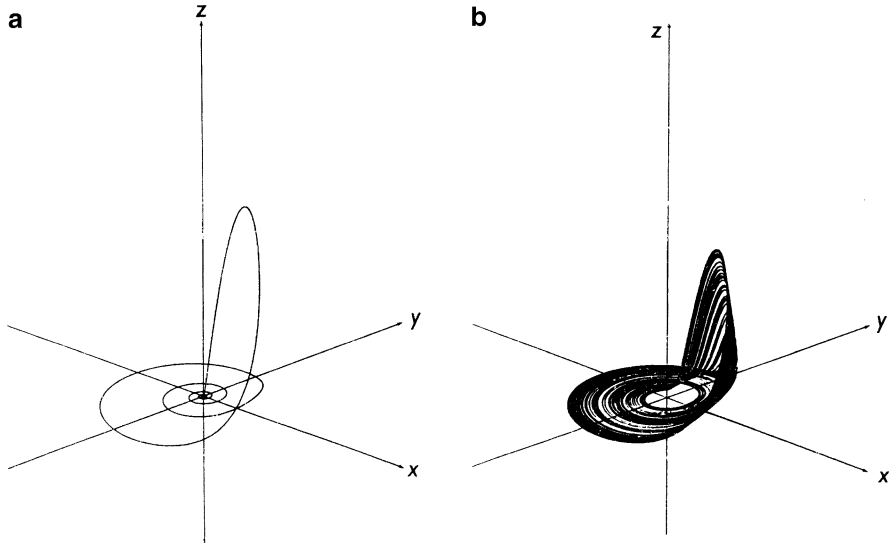


Fig. 1.36 (a) Homoclinic orbit associated with the fixed point $(0,0,0)$ of Rössler model (1.136)–(1.138), for parameter values: $a = 0.38$, $b = 0.30$, $c = 4.82$; (b) Chaotic attractor obtained from numerical integration of Rössler model for $a = 0.32$, $b = 0.30$, $c = 4.50$. The trajectories are injected on the same side of the unstable fixed point, a situation referred to as *spiral chaos*. Reproduced from [40] with kind permission of Cambridge University Press

Routes to Chaos

The Shil'nikov (homoclinic) chaos is a specific case of deterministic aperiodicity. Analysis of chaotic regime in various systems allowed to indicate the following main routes to chaotic behavior, which are best recognized:

1. *Scenario of Ruelle, Takens, and Newhouse*, involving successive Hopf bifurcations, leading from a stable steady state (point attractor) through a stable limit cycle (sustained oscillations) and a two-dimensional torus (quasi-periodic oscillations), characterized by two incommensurable characteristic frequencies of motion to a strange attractor (Fig. 1.37). Even three successive Hopf bifurcations can be sufficient to cause chaotic regime. Note that if the characteristic frequencies are a rational number, the quasi-periodicity reduces to a frequency-locking phenomenon [44].
2. *The Feigenbaum scenario*, involving successive period-doubling bifurcations which eventually form a cascade of intriguing universal quantitative characteristics (Feigenbaum constants) derived from the analysis of the famous logistic map:

$$x_{n+1} = ax_n(1 - x_n) \quad (1.138)$$

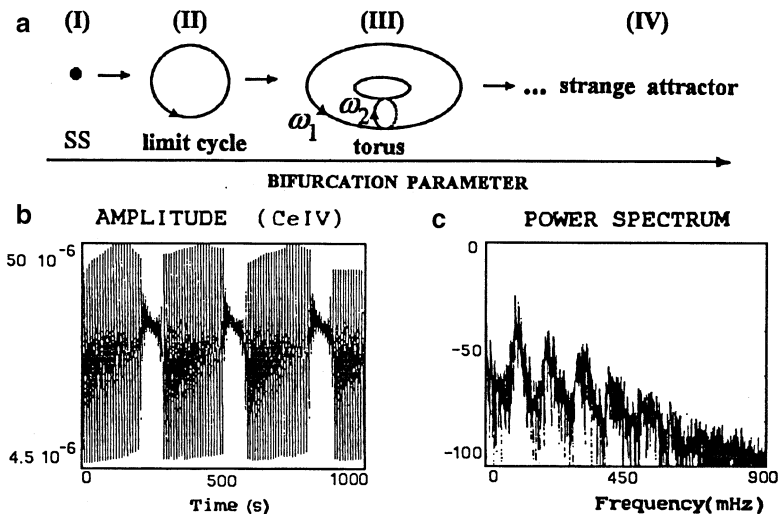


Fig. 1.37 (a) A schematic picture of the route to chaos (strange attractor) through quasiperiodicity (torus) (after [42]); (b, c) experimental time series (b) and corresponding power spectrum (c) of a chaotic regime involving two characteristic frequencies for the Belousov–Zhabotinsky process. Reprinted with permission from [45]. Copyright 1987 American Institute of Physics

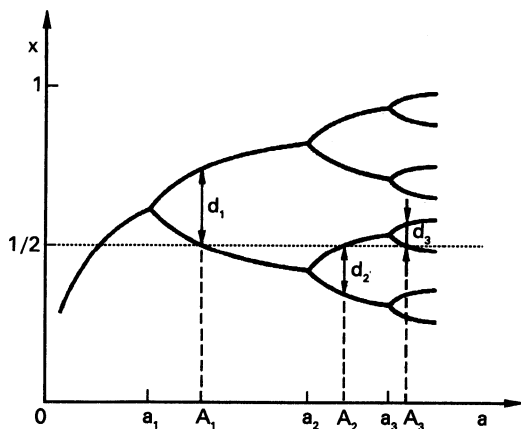


Fig. 1.38 The scheme of period doubling bifurcations in the Feigenbaum scenario, indicating the symbols used in the scaling laws (1.139, 1.140). Reproduced with permission from [44], Copyright Wiley-VCH Verlag GmbH & Co. KGaA

with a being a bifurcation parameter [46, 47]. The period-doubling routes to chaos in various systems satisfy the scaling relations predicted by the Feigenbaum constants δ and α with δ asymptotically converging to the value 4.6692016... and α asymptotically converging to 2.50290787... [48–50]. The quantity δ is defined through the successive values of parameter a , at which bifurcations occur:

$$\lim_{n \rightarrow \infty} \frac{a_n - a_{n-1}}{a_{n+1} - a_n} = \lim_{n \rightarrow \infty} \frac{A_n - A_{n-1}}{A_{n+1} - A_n} = \delta \quad (1.139)$$

and thus allows to predict the parameter values for each of these bifurcations. In turn, another quantity α allows to predict the size of the system's response with each bifurcation:

$$\lim_{n \rightarrow \infty} \frac{d_n}{d_{n+1}} = -\alpha \quad (1.140)$$

with d_n meaning the distance between $x = 1/2$ and the closest point of the period- 2^n cycle. The particular role of $x = 1/2$ comes from the fact that the highest stability (i.e., the strongest attractive effect on the neighboring points) is exhibited by those cycles, for which one of the fixed points is equal just to $1/2$. These cycles are called *supercycles*. The meaning of the above symbols is also explained in Fig. 1.38. The bifurcation diagrams illustrating such route to chaos in different model and real systems are shown in Fig. 1.39. One should note the regions of “order inside chaos”—the period-3 windows emerging in chaotic areas of the diagram. In addition to those well-established characteristics of the Feigenbaum scenario, one should note that recently Showalter, Parmananda et al. [55] have described how the Fibonacci sequence appears within the Feigenbaum scaling of the period-doubling cascade to chaos. An important consequence of this discovery is that the ratio of successive Fibonacci numbers converges to the golden mean ϕ in every period-doubling sequence and therefore the convergence to ϕ , the most irrational number, occurs in concert with the onset of deterministic chaos. The authors emphasize that the Fibonacci sequence will be found in all dynamical systems exhibiting period-doubling route to chaos, as it is directly linked to the Feigenbaum scaling constant α (Fig. 1.40, Table 1.4).

3. *Scenario of Pomeau and Manneville*, involving successive occasional bursts of noise (*intermittencies*) in periodic behavior which upon change in bifurcation parameter occur more and more often, leading eventually to completely chaotic behavior. The intermittences are divided into three types: I, II, and III, but apparently only types I and III were observed in real experiments (Fig. 1.41).

Crises

There are also possible several other scenarios involving chaos, e.g., the route through the *crises*, i.e., sudden qualitative change in chaotic dynamics which occur due to collisions between a chaotic attractor and, e.g., coexisting unstable fixed points or periodic orbits. Of various possible detailed scenarios of such events (cf. e.g., [58–60]) we shall choose here as an example the *interior crisis*, named also an *explosion*, which is a kind of global bifurcation which manifests itself as the

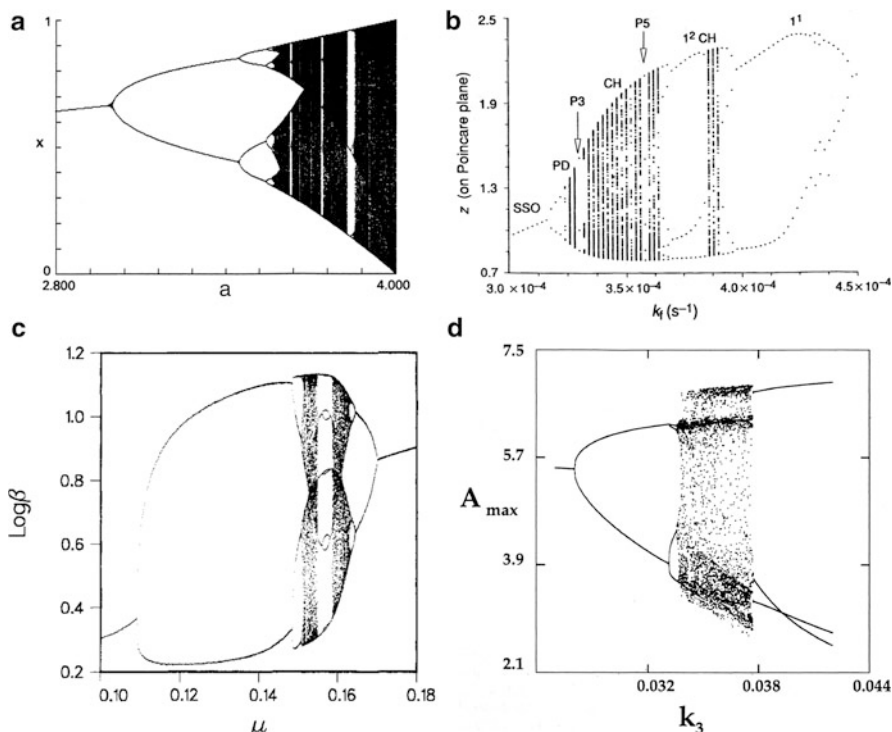


Fig. 1.39 A comparison of bifurcation diagrams exhibiting a route to chaos through a period-doubling cascade (and reverse bifurcations leading to order) for different model systems [51]: (a) logistic map, (b) Györgyi and Field model of the BZ reaction; notations: *SSO* small amplitude sinusoidal oscillations, *PD* sequence of period-doubling bifurcations, *P3* period-3 oscillations, *P5* period-5 oscillations, *CH* a chaotic regime, I^n a cycle consisting of one large amplitude and n small-amplitude oscillations. Reprinted by permission from Macmillan Publishers Ltd: [52], Copyright 1992, (c) AUTOCALATOR model. Reprinted with permission from [53]. Copyright 1990 American Chemical Society, (d) Olsen model of enzyme peroxidase-oxidase oscillator. Reprinted with permission from [54] Copyright 1993 American Chemical Society

sudden qualitative change in the chaotic attractor size and shape. This kind of crisis is caused by the tangent collision of strange attractor with an unstable periodic orbit that is contained within the *interior* of the basin of attraction of this attractor, so the new attractor contains a locus of the former attractor [58, 61]. In more detail, one can describe such a crisis as an event in which a small-amplitude chaotic attractor becomes tangent to the separatrix associated with a saddle-type fixed point (or orbit). When the chaotic attractors reach the other side of the separatrix, this will lead to a large excursion (i.e., large amplitude oscillation). As a result of reinjection, the system goes back onto the chaotic attractor, until it reaches the other side of separatrix again and another large excursion occurs [62]. Noteworthy, crises of various types can induce intermittencies in the system's dynamics.

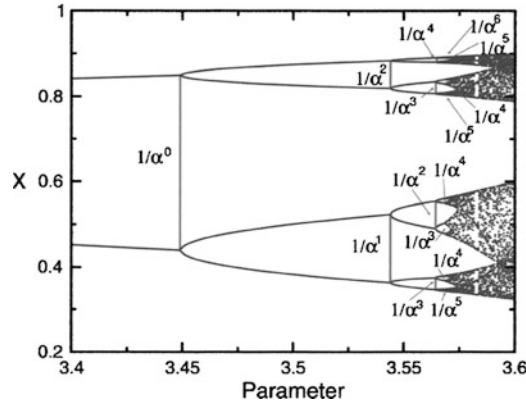


Fig. 1.40 Typical period-doubling bifurcation diagram for the logistic map, in which, after the normalization of width of the period-2 branch to unity ($1/\alpha^0$), the widths of the branches corresponding to higher periods are written as inverse powers of α . Reprinted from [55], Copyright 2006 with permission from Elsevier

Table 1.4 Development of the Fibonacci series in the period-doubling cascade—distribution of powers of $1/\alpha$ in successive period-doubling bifurcations

	P2 ($n = 0$)	P4 ($n = 1$)	P8 ($n = 2$)	P16 ($n = 3$)	P32 ($n = 4$)	P64 ($n = 5$)	F.N.
$1/\alpha^0$	1						1
$1/\alpha^1$		1					1
$1/\alpha^2$		1	1				2
$1/\alpha^3$			2	1			3
$1/\alpha^4$			1	3	1		5
$1/\alpha^5$				3	4	1	... 8
$1/\alpha^6$				1	6	5	... 13
$1/\alpha^7$					4	10	... 21
$1/\alpha^8$					1	10	... 34

Reprinted from [55], Copyright 2006 with permission from Elsevier

1.10.3 Control of Chaos

The concept of deterministic chaos has been one of the most intriguing ideas in nonlinear dynamics since the 1970s of the twentieth century. For last two decades of particular importance there became also the problem of the *control of chaos*, meaning in particular selection and stabilization of the desired single closed trajectory of the strange attractor. One of the most efficient algorithms of control of chaos is the OGY-algorithm (named after its inventors: Ott, Grebogi and Yorke) [63].

In order to present the principle of this algorithm, it is useful to introduce first a convenient way of presentation of periodic and chaotic trajectories in terms of the so-called *Poincaré sections*. Their construction is shown in Fig. 1.42.

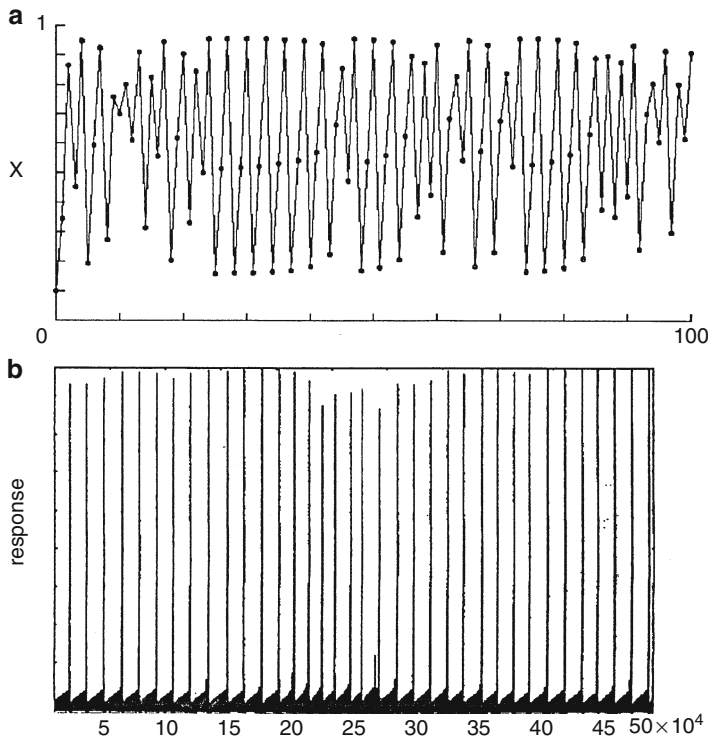


Fig. 1.41 Intermittent route to chaos in: (a) logistic map for $a = 3.826$ [44] and (b) real process—Belousov–Zhabotinsky reaction [56, 57]. (b) Reproduced from [57], Copyright 1983, with permission from Elsevier

If the phase trajectory is intersected with the plane and every transition of trajectory going *in one direction* through this plane is reported, then the period-1 motion is represented by a single point in this Poincaré section, the period- n motion—by n such points, while deterministic chaos is represented by a rich set of points, forming an appropriate pattern. Let us denote the x -coordinate of n th point of the section as x_n . Then, one can plot the dependence between the next (x_{n+1}) and actual (x_n) values and in this way obtain a *one-dimensional map*. Having defined such type of maps, we shall briefly describe the *map-based* control of chaos.

Let us consider the small vicinity of typical one-dimensional map and draw the straight line (1) of unit slope (Fig. 1.43a). The intersection of the two lines, denoted as x^* , is a very important point—it corresponds to equality between the actual and the next values of x belonging to this map: $x_{n+1} = x_n$. If this situation could be maintained for the sequence of events, this would mean the stabilization of the respective cycle. But in order to achieve that, one has to introduce a specially designed *feedback* which continuously modifies the system’s characteristics through the change of the control parameter p , and in this way maintains the value of x at least very close to x^* . In practice, it can be done by appropriate

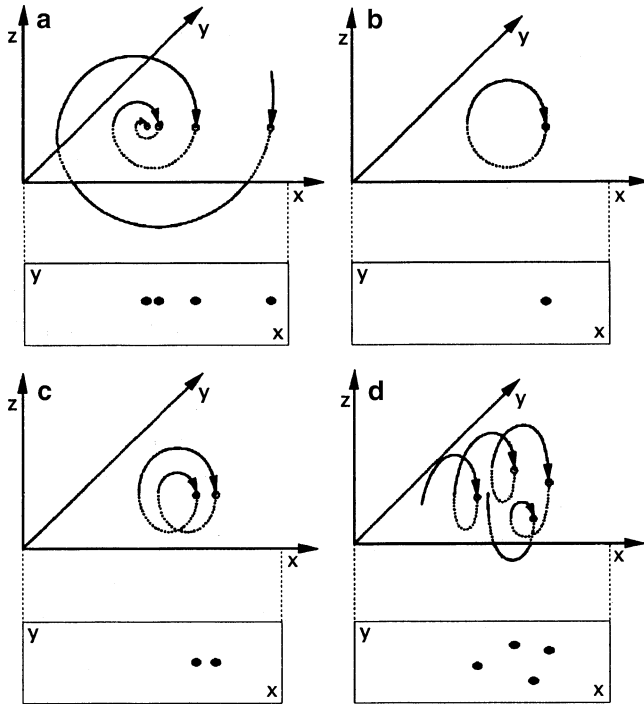


Fig. 1.42 Principle of the construction of Poincaré sections, illustrated for: (a) damped oscillations (stable focus), (b) period-1 oscillation, (c) period-2 oscillation, and (d) chaotic oscillation (based on [44, 64])

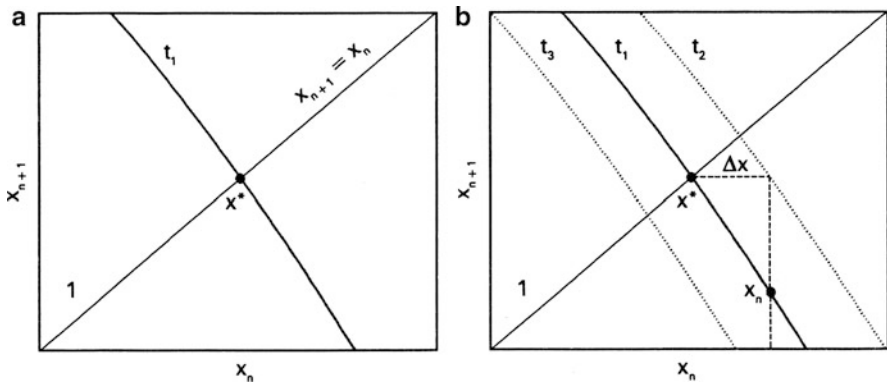


Fig. 1.43 (a) Fragment of the one-dimensional map for chaotic system; (b) the principle of the map-based algorithm of control of chaos, involving appropriate feedback ([64], based on [65])

variation of the flow rate of reactants through the reactor or by the variation of the electrode potential. The idea of such control of chaos is schematically depicted in Fig. 1.43b. Let us assume that the actual value of x variable is equal to x_n , which is

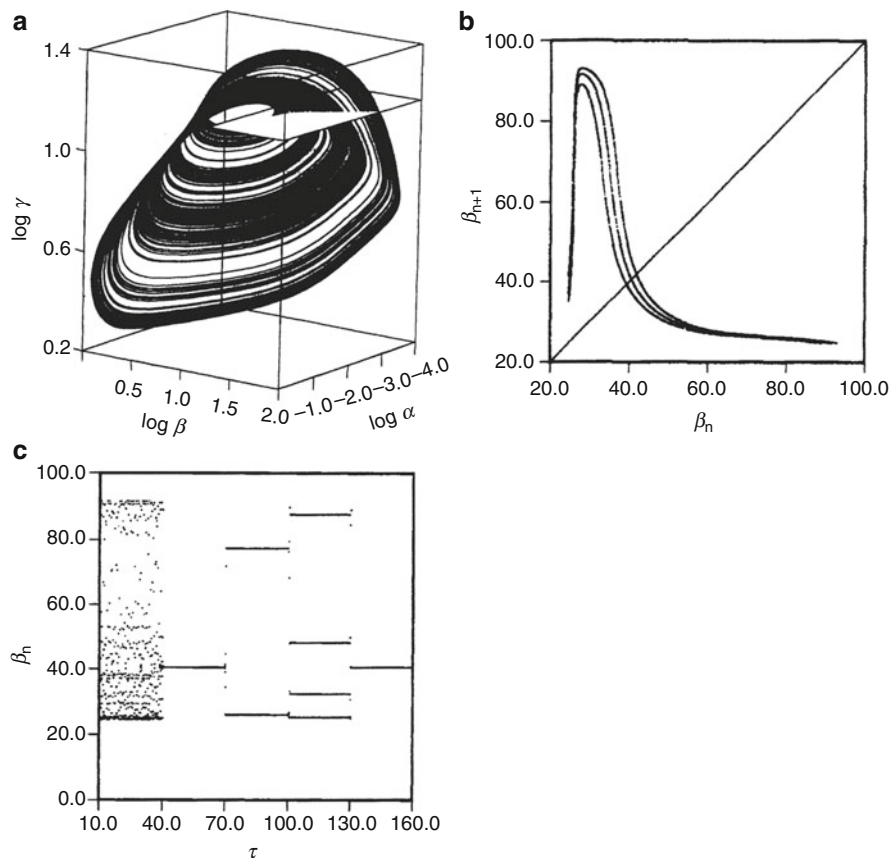


Fig. 1.44 Control of chaos in the AUTOCALATOR model. (a) phase portrait (chaotic attractor) with the Poincaré section indicated, (b) one-dimensional return map constructed from this Poincaré section, (c) values of variable β on Poincaré section shown in (a) vs. time, indicating successive stabilizations of period-1, period-2, period-4, and period-1 unstable limit cycles as controlling begins and changes accordingly. See [65] for details. Reprinted with permission from [65] Copyright 1991 American Chemical Society

different from x^* in terms of the original map (denoted as t_1). Therefore, in order to obtain $x_{n+1} = x^*$, one has to *move* the map to new position denoted as t_2 , i.e., horizontally, for the appropriate Δx value. This move, if realized through the appropriate, small enough perturbation of the control parameter p , can be expressed by a linearized dependence:

$$\frac{\Delta x}{\Delta p} = g \approx \text{const} \quad (1.141)$$

Hence the desired, actual control parameter perturbation can be determined as:

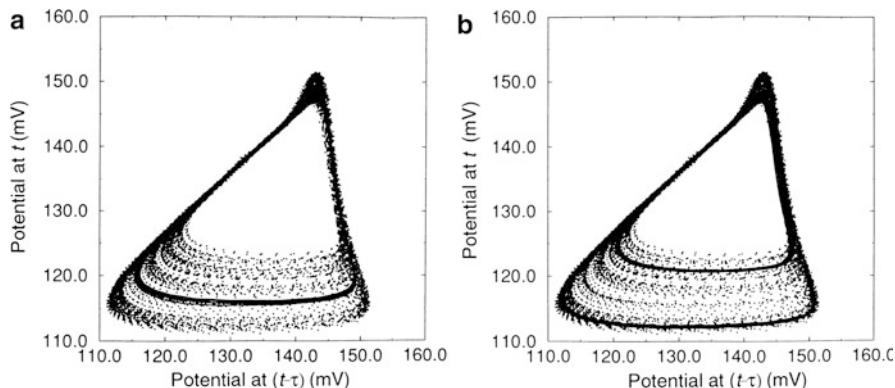


Fig. 1.45 Control of chaos in BZ reaction: stabilized period-1 (a) and period-2 (b) cycles embedded in strange attractor of the BZ reaction. See [67] for details. Reprinted by permission from Macmillan Publishers Ltd.: [67], Copyright 1993

$$\Delta p = \frac{\Delta x}{g} = \frac{x_n - x^*}{g} \quad (1.142)$$

The magnitude of this perturbation has to be calculated every time when the trajectory that should be stabilized intersects the Poincaré section in the vicinity of x^* value. The striking feature of this map-based control of chaos is its conceptual simplicity. For the case of chemical dynamical systems, this algorithm was successfully applied by Showalter et al. [65, 66] to stabilize various period- n orbits in the three-variable AUTOCALATOR model (Fig. 1.44) and to experimental control of chaos in the Belousov–Zhabotinsky process (Fig. 1.45) [67]. Examples of control of chaos in electrochemical systems are described in Chap. 7 of volume II.

References

1. Nicolis G, Prigogine I (1977) Self-organization in nonequilibrium systems. Wiley-Interscience, From dissipative structures to order through fluctuations
2. Strogatz SH (1994) Nonlinear dynamics and chaos. Perseus, Massachusetts
3. Żakowski W, Leksiański W (1995) Mathematics, vol IV. WNT, Warsaw
4. Ebeling W, Feistel R (1982) Physik der Selbstorganisation und Evolution. Akademie-Vlg, Berlin
5. Ebeling W (1976) Strukturbildung bei irreversiblen Prozessen. Teubner, Leipzig
6. Mackey MC, Glass L (1977) Oscillation and chaos in physiological control systems. Science 197:287–289
7. Kaplan D, Glass L (1995) Understanding nonlinear dynamics. Springer, New York
8. Britton NF (2003) Essential mathematical biology. Springer, London, p 220
9. Murray JD (2002) Mathematical biology I: an introduction. Springer, New York
10. Buchner T, Żebrowski JJ (2000) Logistic map with a delayed feedback: stability of a discrete time-delay control of chaos. Phys Rev E 63:016210-0–016210-7

11. Gray P, Scott SK (1990) *Chemical oscillations and instabilities. Non-linear chemical kinetics.* Clarendon, Oxford
12. Babloyantz A (1986) *Molecules, dynamics and life. An introduction to self-organization of matter.* Wiley-Interscience, New York
13. Boissonade J, De Kepper P (1980) Transitions from bistability to limit cycle oscillations. Theoretical analysis and experimental evidence in an open chemical system. *J Phys Chem* 84:501–506
14. Field RJ, Schneider FW (1989) Oscillating chemical reactions and nonlinear dynamics. *J Chem Educ* 66:195–204
15. De Kepper P, Boissonade J (1981) Theoretical and experimental analysis of phase diagrams and related dynamic properties in the Belousov-Zhabotinskii system. *J Chem Phys* 75:189–195
16. Guckenheimer J (1986) Multiple bifurcation problems for chemical reactors. *Physica D* 20:1–20
17. Czernawski DS, Romanowski JM, Stiepanowa NW (1979) *Mathematical modeling in biophysics.* PWN, Warsaw (in Polish)
18. Field RJ, Noyes RM (1974) Oscillations in chemical systems IV. Limit cycle behavior in a model of a real chemical reaction. *J Chem Phys* 60:1877–1884
19. Noyes RM, Field RJ, Körös E (1972) Oscillations in chemical systems I. Detailed mechanism in a system showing temporal oscillation. *J Am Chem Soc* 94:1394–1395
20. Field RJ, Körös E, Noyes RM (1972) Oscillations in chemical systems II. Thorough analysis of temporal oscillation in the bromated-cerium-malonic acid system. *J Am Chem Soc* 94:8649–8664
21. Field RJ, Burger M (eds) (1985) *Oscillations and travelling waves in chemical systems.* Wiley, New York
22. Epstein IR, Pojman JA (1998) *An introduction to nonlinear chemical dynamics. Oscillations, waves, patterns, and chaos.* Oxford University Press, Oxford, New York
23. Field RJ (2007) Oregonator. *Scholarpedia* 2(5):1386
24. Tyson JJ, Fife PC (1980) Target patterns in a realistic model of the Belousov-Zhabotinskii reaction. *J Chem Phys* 73:2224–2237
25. Schneider FW, Münster AF (1996) *Nichtlineare Dynamik in der Chemie.* Spektrum Akademischer Verlag, Heidelberg
26. Wechselberger M (2007) Canards. *Scholarpedia* 2(4):1356
27. Benoît E, Callot JF, Diener F, Diener M (1981) Chasse au canard. *Collectanea Mathematica* 31–32:37–119
28. Peng B, Gáspár V, Showalter K (1991) False bifurcations in chemical systems: canards. *Phil Trans R Soc Lond A* 337:275–289
29. Brøns M, Bar-Eli K (1991) Canard explosion and excitation in a model of the Belousov-Zhabotinsky reaction. *J Phys Chem* 95:8706–8713
30. Buchholtz F, Dolnik M, Epstein IR (1995) Diffusion-induced instabilities near a canard. *J Phys Chem* 99:15093–15101
31. Xie Y, Chen L, Kang YM, Aihara K (2008) Controlling the onset of Hopf bifurcation in the Hodgkin-Huxley model. *Phys Rev E* 77:061921-1–061921-13
32. Moehlis J (2001) Canards in a surface oxidation reaction. *J Nonlin Sci* 12:319–345
33. Rotstein HR, Kopell N, Zhabotinsky AM, Epstein IR (2003) Canard phenomenon and localization of oscillations in the Belousov-Zhabotinsky reaction with global feedback. *J Chem Phys* 119:8824–8832
34. Rotstein HR, Kopell N, Zhabotinsky AM, Epstein IR (2003) A canard mechanism for localization in systems of globally coupled oscillators. *SIAM J Appl Math* 63:1998–2019
35. Koper MTM (1995) Bifurcations of mixed-mode oscillations in a three-variable autonomous Van der Pol-Duffing model with a cross-shaped phase diagram. *Physica D* 80:72–94
36. Larter R, Steinmetz CG (1991) Chaos via mixed-mode oscillations. *Phil Trans R Soc Lond A* 337:291–209

37. Larter R, Steinmetz CG, Aguda BD (1988) Fast-slow variable analysis of the transition to the mixed-mode oscillations and chaos in the peroxidase reaction. *J Chem Phys* 89:6506–6514
38. Lengyel I, Rábai G, Epstein IR (1990) Experimental and modeling study of oscillations in the chlorine dioxide-iodine-malonic acid reaction. *J Am Chem Soc* 112:9104–9110
39. Bronstein IN, Semendjajev KA, Musiol G, Mühlig H (2001) *Taschenbuch der Mathematik*. Verlag Harri Deutsch, Thun/Frankfurt am Main
40. Nicolis G (1995) *Introduction to nonlinear science*. Cambridge University Press, New York
41. Shil'nikov LP (1965) A case of the existence of a denumerable set of periodic motions. *Sov Math Dokl* 6:163–166
42. Lorenz EN (1963) Deterministic nonperiodic flow. *J Atmos Sci* 20:130–141
43. Rössler OE (1976) Chaotic behavior in simple reaction systems. *Z Naturforsch* 31A:259–264
44. Schuster HG (1988) *Deterministic chaos. An Introduction*. VCH Verlagsgesellschaft, Weinheim
45. Argoul F, Arnéodo A, Richetti P, Roux JC (1987) From quasiperiodicity to chaos in the Belousov-Zhabotinsky reaction I. Experiment. *J Chem Phys* 86:3325–3338
46. May RM (1976) Simple mathematical models with very complicated dynamics. *Nature* 261:459–467
47. May RM (1980) Nonlinear phenomena in ecology and epidemiology. *Ann New York Acad Sci* 357:267–281
48. Feigenbaum MJ (1979) The universal metric properties of nonlinear transformation. *J Stat Phys* 21:669–706
49. Feigenbaum MJ (1980) The metric universal properties of period doubling bifurcations and the spectrum of a route to turbulence. *Ann New York Acad Sci* 357:330–336
50. Feigenbaum MJ (1983) Universal behavior in nonlinear systems. *Physica* 7D 16: 39
51. Orlik M (1995) Chemical deterministic chaos. *Polish J Chem* 69:1349–1386
52. Györgyi L, Field RJ (1992) A three-variable model of deterministic chaos in the Belousov-Zhabotinsky reaction. *Nature* 355:808–810
53. Peng B, Scott SK, Showalter K (1990) Period-doubling and chaos in a three-variable autocatalator. *J Phys Chem* 94:5243–5246
54. Steinmetz CG, Geest T, Larter R (1993) Universality in the peroxidase-oxidase reaction: period doublings, chaos, period-three, and unstable limit cycles. *J Phys Chem* 97:5649–5653
55. Linage G, Montoya F, Sarmiento A, Showalter K, Parmananda P (2006) Fibonacci order in the period doubling cascade to chaos. *Phys Lett A* 359:638–639
56. Serra R, Andretta M, Compiani M, Zanarini G (1986) *Introduction to the physics of complex systems*. Pergamon, Oxford
57. Roux JC (1983) Experimental studies of bifurcations leading to chaos in the Belousov-Zhabotinsky reaction. *Physica D* 7:57–68
58. Grebogi C, Ott E, Yorke JA (1983) Crises: sudden changes in chaotic attractors and chaotic transients. *Physica D* 7:181–200
59. Grebogi C, Ott E, Romeiras F, Yorke JA (1987) Critical exponents for crisis induced intermittency. *Phys Rev A* 36:5365–5380
60. Ott E (2002) *Chaos in dynamical systems*, 2nd edn. Cambridge University Press, Cambridge
61. Ott E (2006) Crises. *Scholarpedia* 1(10):1700
62. Koper MTM (1996) Oscillations and complex dynamical bifurcations in electrochemical systems. In: Prigogine I, Rice SA (eds) *Adv. Chem. Phys.*, vol XCII. Wiley, New York, pp. 161–298
63. Ott E, Grebogi C, Yorke JA (1990) Controlling chaos. *Phys Rev Lett* 64:1196–1199
64. Orlik M (1996) *Oscillating reactions. Order and chaos*. WNT, Warsaw (in Polish)
65. Peng B, Petrov V, Showalter K (1991) Controlling chemical chaos. *J Phys Chem* 95:4957–4959
66. Petrov V, Peng B, Showalter K (1992) A map-based algorithm for controlling low-dimensional chaos. *J Chem Phys* 96:7506–7513
67. Petrov V, Gáspár V, Masere J, Showalter K (1993) Controlling chaos in the Belousov-Zhabotinsky reaction. *Nature* 361:240–243

Chapter 2

Stability of Electrochemical Systems

2.1 The Role of Negative Differential Resistance in the Stability of Electrochemical Systems

2.1.1 *The Load Line and the Simplest Electrochemical Circuit*

The subject of the present analysis is the stability of the entire electric circuit in which the electrochemical cell is only one of the components. We shall look for such characteristics (I – E dependence) of the electrode process that gives rise to instability of the whole circuit which, in general, consists of the *power source* and of a *load*. This way of analysis was described already in 1958 by Gerischer [1], who also invoked the ideas of Franck.

We shall consider first a simple electrochemical cell consisting of two electrodes: the polarizable working electrode and an ideally non-polarizable reference electrode. All the resistances exhibited by this system will be summarized to a single value of an equivalent resistance R_s , connected in series with the cell. We apply sufficiently high external voltage which will compensate the own electromotive force of the cell and polarize the working electrode to the value at which the faradaic current flows at the working electrode and, in consequence, electric current flows through the entire circuit. In order to simplify thinking, we can represent this situation in terms of the equivalent circuit shown in Fig. 2.1, which consists of resistor R_s (linear element) and the electrolytic cell (nonlinear element), symbolized by a box with cross. The nonlinear current–potential dependence of the electrode process in this cell is denoted further as with $I_2(E)$.

It is obvious that in the steady-state both currents are equal: $I_1 = I_2$, so there is no increasing accumulation of the electric charge at the working electrode–solution interface, i.e., $dE/dt = 0$. Beyond the steady-state, the electrode potential E changes according to the dependence:

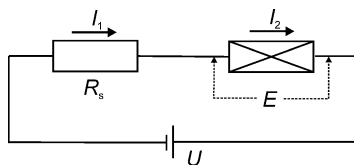


Fig. 2.1 Simplified equivalent circuit of the electrochemical system consisting of electrolytic cell and power source, with all resistances summarized into an equivalent ohmic resistance R_s

$$\frac{dE}{dt} \propto (I_1 - I_2) \quad (2.1)$$

Irrespective of that, whether the system is actually in steady-state or not, current I_1 is given by:

$$I_1 = \frac{U - E}{R_s} = \frac{U}{R_s} - \frac{E}{R_s} \quad (2.2)$$

where E means the potential drop at the working electrode/solution interface (interfacial potential drop). The dependence [Eq. (2.2)] is known as the equation of the *load line*, representing the response of a linear circuit connected to the nonlinear device. It is thus a straight line in the I - E coordinates, with the intercept U/R_s and the slope $-1/R_s$. In terms of such representation it is clear that the steady-state(s) of the circuit from Fig. 2.1 (E_{ss} , I_{ss}) is (are) determined by the intersection(s) of a load line with the $I_2(E)$ characteristics of the electrode process: i.e., when $I_1(E_{ss}) = I_2(E_{ss})$. The analysis of stability/instability of these steady-states, crucial for diagnosis of possible dynamic regimes under different conditions, is described in the next sections.

2.1.2 Stability of the N-NDR System Under Potentiostatic Control

Let us assume that external voltage U is constant, which means here the *potentiostatic conditions* applied to the whole circuit. Note that here this term has a different sense than in classical electrochemistry, where the term “potentiostatic” usually means constant working electrode potential E , due to minimization (compensation) of the serial resistance, and thus of the ohmic drops. From the point of view of possible dynamic instabilities these two cases are fundamentally different. In order to distinguish between them, the case of $E = \text{const}$ will be called throughout the whole book as the “truly potentiostatic condition,” according to typical convention accepted in the literature about electrochemical instabilities.

Coming back to our potentiostatic conditions $U = \text{const}$, we notice that, according to Eq. (2.2), any change in I_1 (e.g., due to fluctuation) will cause the appropriate change in E , the higher the greater the serial resistance: $dE = -R_s(dI_1)$. The response of the electrode potential E on this perturbation (its evolution in time)

will indicate whether the perturbed steady-state is stable or not. This depends on the kinetic characteristics $I_2(E)$ of the electrode process. Based on Eq. (2.1), the stability of the steady-state is given by the sign of the derivative $d(dE/dt)/dE$ which is proportional to the difference in the slopes of $dI_1(E)/dE$ and $dI_2(E)/dE$:

$$\frac{d}{dE} \left(\frac{dE}{dt} \right) \propto \left(\frac{dI_1}{dE} - \frac{dI_2}{dE} \right) \quad (2.3)$$

This means that the direction of the temporal variation of the electrode potential depends on the relation between the charging and discharging of the electrode.

The considered electrochemical system is *unstable* with respect to perturbation dE , if:

$$\frac{d}{dE} \left(\frac{dE}{dt} \right) > 0 \quad (2.4)$$

In view of Eq. (2.2), the slope dI_1/dE is always negative:

$$\frac{dI_1}{dE} = -\frac{1}{R_s} \quad (2.5)$$

so, in view of Eq. (2.3), the instability condition (2.4) requires that:

$$\frac{dI_2}{dE} < -\frac{1}{R_s} \quad (2.6)$$

Since serial resistance R_s cannot be negative (it is a simple linear element), the slope dI_2/dE must be *negative*. This derivation leads us to the first important instability condition: simple electrochemical system, characterized with one dynamical variable—the electrode potential E , will be unstable provided that there is a region of a *negative differential resistance* (NDR) in its current–potential characteristics. The second condition is that the serial resistance must be sufficiently high, as the condition (2.6) is equivalent to:

$$R_s > -\frac{dE}{dI_2} \equiv -\text{NDR} \quad (2.7)$$

It is instructive to compare this condition of instability with its graphical illustration, constructed in terms of realistic $I_2(E)$ dependence (Fig. 2.2). The N-shaped I_2 – E curve (meaning the N-NDR type of characteristics), which is recorded under *truly potentiostatic* conditions, is typical of, e.g., electrodes which undergo passivation in the vicinity of the Flade potential, giving thus rise to the region of the negative dI_2/dE slope. The I_2 – E dependence is intersected by two

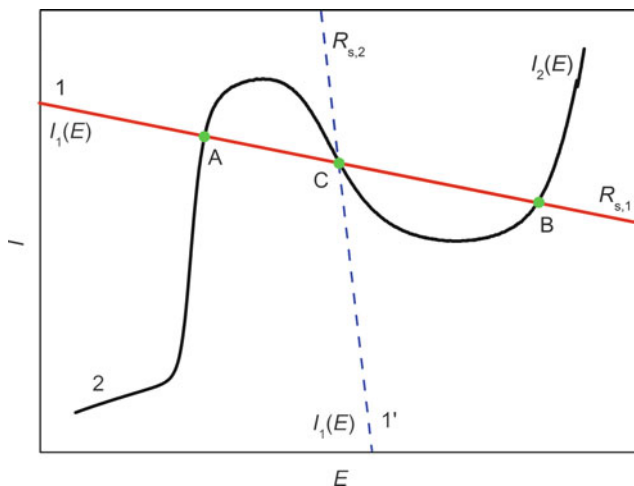


Fig. 2.2 Graphical illustration of the principle of determination of stability of the steady-states for the electrode process characterized with the N-shaped negative differential (N-NDR) region (*curve 2*), for the load lines corresponding to serial resistance: $R_{s,1}$ (*line 1*) and $R_{s,2}$ (*line 1'*), with $R_{s,1} > R_{s,2}$. For $R_{s,1}$ three intersections with *curve 2* determine three steady-states: two stable ones (**A** and **B**) and the unstable middle one (**C**). For $R_{s,2}$ only one steady-state **C** exists which is stable due to appropriate relation between the local slopes of $I_1(E)$ and $I_2(E)$ dependences (after [1])

exemplary linear load lines, of different slopes, corresponding to two serial resistances $R_{s,1}$ and $R_{s,2}$, with $R_{s,1} > R_{s,2}$.

Let us summarize the main conclusions that can be drawn from this picture.

1. If serial resistance R_s is zero, then the load lines **1** and **1'** with finite slopes and intercepts are not existing. The electrode potential E is then equal to external voltage U and the *entire* N-shaped, steady-state dependence I_2-E can be experimentally recorded, point by point, under then *truly potentiostatic* conditions. In other words, all the states composing the I_2-E dependence are *stable* under truly potentiostatic conditions, otherwise they would not be directly detectable. Furthermore, to every value of E , only a single value of steady-state current corresponds. Mathematically, the I_2-E dependence is *single-valued*.
2. When non-zero (positive) serial resistance R_s is inserted in the circuit from Fig. 2.1, the electrode potential E and external voltage U become different in the presence of current. Load line appears on this diagram, with the intercept equal to U/R_s and the slope equal to $-1/R_s$. The number and stability of steady-states possible for given (U, R_s) parameters is now indicated by the intersections of load line I_1-E with the I_2-E characteristics of the electrochemical system.
3. If serial resistance is sufficiently low ($R_{s,2}$), there is only one intersection (**C**) of these two characteristics, for given external voltage U there is only one steady-state possible, which is *stable* against perturbations, in spite of lying on the NDR branch of the system's characteristics. The system is thus monostable.

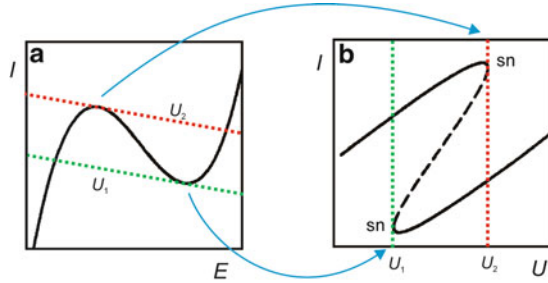


Fig. 2.3 Schematic relation between (a) the relative position of the load line and I - E characteristics of the N-NDR type and (b) the bistable characteristics observed on the I - U dependence, for appropriate fixed resistance R_s , with $U = E + IR_s$. Upon increasing voltage U , the system enters the bistable region at U_1 where the first saddle-node bifurcation (sn) occurs and becomes again monostable at $U = U_2$, when the second saddle-node bifurcation takes place. In terms of (a), and Eq. (2.2), increasing voltage U means vertical motion up of the load line

4. If serial resistance is so high that the condition (2.7) is met, for the corresponding (U, R_s) parameters three steady-states (A, B, C) are possible, of which external ones (A, B) are stable, while the middle one (C)—the only one lying on the NDR branch, is now unstable. This case corresponds of course to bistability, i.e., for given U the system can exist either in state A or B, belonging to the upper (A) and lower (B) branch of the folded diagram of states (cf. Fig. 1.7). Furthermore, in view of general principles of nonlinear dynamics one concludes that this transition between the monostable and bistable behaviors is associated with the saddle-node bifurcations, occurring twice when the condition: $R_s = -dE/dI_2$ is met: once when the system enters the bistable region and second time when it leaves it upon continuous variation of external voltage U .
5. One can generalize the above conclusion in this way that all steady-states, belonging to the N-NDR region of the truly potentiostatic I_2 - E dependence can become unstable under potentiostatic ($U = \text{const}$) conditions, provided sufficiently high resistance R_s is present in the circuit. This resistance cannot be, however, too high (for given voltage U) since then the load line may not penetrate the NDR region and the system returns to monostable behavior. In consequence, typical bifurcation diagrams of such systems contain the region of bistability defined between certain lower and upper limits of serial resistance, for given U (see below, Fig. 2.8).

2.1.3 Stability of N-NDR System Under Galvanostatic Control

Let us stay with the steady-state I_2 - E characteristics shown in Fig. 2.2 and change the operation mode to the *galvanostatic* one. In practice we shall connect the galvanostat, with external resistance R_s being then not necessary. Note, however, that galvanostatic mode does not mean the absence of serial resistance: the switching from potentiostatic to galvanostatic mode can be interpreted as

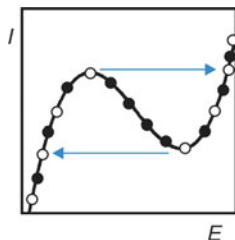


Fig. 2.4 The dependence of the stability of the steady-states belonging to the negative differential resistance (NDR) region of the N-shaped I - E characteristics, on the operation mode: in the potentiostatic mode (*filled circle*) the entire curve I - E is directly recordable for negligible (vanishing) serial resistance R_s , while in the galvanostatic mode (*open circle*) these states are unstable and thus directly inaccessible. For $R_s = 0$ the N-NDR system is thus monostable under potentiostatic conditions and bistable under galvanostatic conditions

the insertion of the (theoretically) infinitely high serial resistance R_s , to which (theoretically) infinitely high voltage U is applied, with U/R_s ratio defining the imposed current. Then, even if the resistance of the electrochemical cell r (with $r \ll R_s$) varies as a function of, e.g., changing electrode potential, the current which flows through the circuit remains practically the same: $U/(R_s + r) \approx U/R_s = I$. This aspect of galvanostatic control will be very important for further description (including impedance characteristics) of electrochemical instabilities observed under such conditions.

Under galvanostatic conditions one observes an important difference in the system's response, i.e., the electrode potential E , upon varying imposed current. Upon cyclic variation of this current a sudden horizontal potential jump occurs which omits the region of negative resistance, with hysteresis indicating bistability (Fig. 2.4). This means that the states belonging to the N-NDR region, which were stable (directly observable) under *truly* potentiostatic conditions, are *unstable* under galvanostatic conditions. In other words, only potentiostatic control, in the absence of ohmic drops, allows to track the entire I - E dependence. Figure 2.4 shows this difference schematically.

Concluding, due to the presence of NDR region, the I - E dependences are different, depending on the choice of the control variable, a case which is not common in classical electrochemistry, when processes meeting the Butler–Volmer kinetics are usually considered and the choice of the control variable is free.

2.1.4 Origins of NDR in Electrochemical Systems

The NDR of the *faradaic process*, meaning the negative slope of the dE/dI_f dependence, can be caused by various factors. When, for simplicity, the electron transfer is assumed to occur only in one direction (irreversible reduction or oxidation), the faradaic current is generally described with the dependence:

$$I_f = nFAk(E)c(0) \quad (2.8)$$

where F is the Faraday constant, A is the electrode surface area, k is the potential-dependent, heterogeneous rate constant of the electron transfer, and $c(0) \equiv c(x=0)$ means the concentration of the reducible species Ox or oxidizable species Red at the reaction site within the electric double layer at the interface (often, but not precisely termed the “surface concentration”). One should remember that according to the present convention, the cathodic currents are negative, so the minus sign should be added to Eq. (2.8) in such a case. The following derivation is strictly (algebraically) valid for anodic processes.

In terms of expression (2.8), the charge-transfer resistance R_{ct} is defined as:

$$R_{ct}^{-1} = \frac{dI_f}{dE} = nF \frac{d}{dE} [Ak(E)c(0)] \quad (2.9)$$

Formally, and also in conjunction with experimental studies, one can name three principal sources of the NDR region (negative R_{ct}) [2]:

- i. A negative dA/dE slope, caused by a decrease of the available electrode surface with increasing polarization. Typical examples of such situation include passivation of a metal surface with a *perfectly insulating* oxide layer or potential-dependent, increasing adsorption of *ideal inhibitor*.
- ii. A negative $dk(E)/dE$ slope, caused by: (a) the potential-dependent adsorption of a non-ideal inhibitor which causes certain decrease in the rate constant of the electron transfer, but, opposite to case (i), does not completely hinder it; (b) the potential-dependent desorption of a catalyst, like, e.g., of SCN^- ions specifically adsorbed on Hg surface and in this state enhancing the rate of polarographic In(III) electroreduction (cf. Chap. 4).
- iii. A negative $dc(0)/dE$ slope, caused by the electrostatic effect of the double layer, which is usually termed the *Frumkin effect* in the electrochemical literature [3, 4]. The source of this effect is that the electric potential at the reaction site (often denoted as ϕ_2) is different from the electric potential in the bulk, and this difference is particularly strongly pronounced at low ionic strength of the electrolyte solutions. Then the concentration of the reactant particles of charge ze at the reaction site is modified by a Boltzmann factor: $\exp(-zF\phi_2/RT)$. In the case of anions undergoing reduction at negatively charged electrode, or cations undergoing oxidation at positively charged surface it may happen that $dc(0)/dE$ becomes negative in certain range of potentials, giving thus rise to NDR region (the static double layer effect). Also, the effective driving force for the electrode process is not the entire interfacial potential drop E , but $E - \phi_2$ (dynamic double layer effect). Both effects are expressed, in the simplest way, in terms of the so-called *Frumkin correction* of the rate constant (see Sect. 4.1).

The fact that the above derivations are valid for Eq. (2.8), the exact form of which corresponds to anodic processes, for which the sign of the current is positive, requires further comment. Analogous criteria can be derived for cathodic process,

with only minus sign ascribed to the current in formula (2.8). Note that for the cathodic process, the NDR means formally *positive* dk_f/dE slope, since the rate constant k_f decreases with increasing negative electrode potential. One should remember this algebraic nuance when considering condition (ii) above: the signs of dI_f/dE are always negative in the NDR region, unambiguously defining the NDR irrespective of the direction of the process, while the sign of dk/dE is negative for anodic process, and positive for the cathodic one. In fact, the current can be positive or negative, depending on the direction of electron flow, while the rate constant cannot be negative.

A more detailed analysis of each type of the above collected sources of NDR regions will be given in the following chapters, devoted to description of particular electrochemical dynamical systems.

2.1.5 Comparison of N-NDR and S-NDR Characteristics

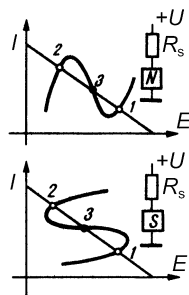
The presence of the NDR is evidently one of the most important sources of instabilities in electrochemical systems and in close analogy to purely electronic circuits. As far as only such simple behavior, like bistability, is concerned, the electrochemical cell with the N-NDR characteristics can be replaced by the respective electronic element of analogous characteristics, e.g., by tunnel diode.

The N-shaped NDR characteristics were found for majority of electrochemical systems exhibiting dynamical instabilities. But there exist also such processes which exhibit another type of NDR, namely S-NDR characteristics, where the shape of $I-E$ dependence resembles the shape of letter S. Systems with S-NDR region have also different dynamical features, compared to N-NDR systems, and therefore they will require separate analysis. There are also electronic elements of such S-NDR type, so the analogies with electrochemical cells remain. One can easily see the fundamental differences between the N-NDR and S-NDR systems by direct comparison of the $I-E$ dependences for the corresponding two circuits, shown in Fig. 2.5 [5].

One notices immediately that for the S-NDR systems, bistability can be observed under potentiostatic control also without any serial resistance (we remove the load line), while under galvanostatic conditions the entire $I-E$ dependence can be tracked, thus quite opposite to N-NDR systems (cf. Fig. 2.4). Furthermore, the effect of increasing serial resistance is also reversed: under potentiostatic conditions, in the presence of serial resistance, bistability persists only until the S-fold is so deformed (stretched along U axis) that the system becomes eventually monostable, or, in other words, the $I-U$ dependence becomes single-valued.

The above analysis introduces only basic ideas of instability of electrochemical systems by indication of the role of NDR of the N-NDR and S-NDR types, in analogy to stability of simple electronic circuits. As far as only bistability is concerned, this analysis can be considered acceptable, but when oscillations are to be explained, the equivalent circuit from Fig. 2.1 appears to be severely oversimplified. First of all it does not include any explicit capacitive element,

Fig. 2.5 Comparison of the I - E dependences for two bistable systems, consisting of the serial connection of linear resistor R_s and the nonlinear element of the N-NDR type (*top*) or of the S-NDR type (*bottom*) (after [5], reproduced with permission)



related to the double layer properties which would determine the time scale of the dynamical system's evolution (although the charging of the electrode was mentioned above). Also, the simple electronic NDR element is not able to reproduce the role of transport of electroactive species between the solution bulk and the electrode surface where the electron transfer occurs. Therefore, the above introductory stability analysis is now followed by a treatment of electrochemical systems in terms of a more reliable equivalent electric circuit.

2.2 Stability of a Realistic Electrochemical N-NDR System

Analogously to Chap. 1, we shall apply the linear stability analysis to electrochemical systems, first for one-dimensional, and then for two-dimensional one. In this section we shall analyze only temporal instabilities, assuming thus the homogeneous state of the working electrode surface, while the spatiotemporal and spatial instabilities will be described in Sect. 1.2 of volume II.

2.2.1 Linear Stability Analysis of 1D Electrochemical System

As indicated in Fig. 2.4, the stability of the states in the NDR region depends on that whether the electrochemical experiment is performed under potentiostatic or galvanostatic conditions. Therefore, the stability analysis should be applied separately to each of these modes of operation.

2.2.1.1 Potentiostatic Control

The electrochemical system, the stability of which is now to be analyzed, is represented by the equivalent circuit, containing an electrolytic cell, composed of the parallel connection of the double layer capacitance C_d and the impedance of the faradaic process; in the case of dc measurement, considered now, it is often termed

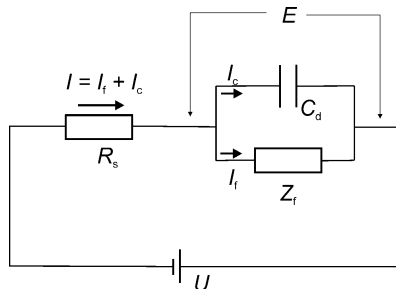


Fig. 2.6 Typical equivalent circuit of the electrochemical system in which external voltage U is applied between the working and reference electrodes through the serial resistor R_s . The interfacial potential drop at the working electrode/solution interface is different from external voltage for the value of ohmic drops: $E = U - (I_f + I_c)R_s$, with I_c and I_f meaning the capacitive and faradaic currents, respectively

“zero-frequency impedance” (Fig. 2.6). As the serial resistance R_s we shall understand the sum of all contributions: the solution resistance, electrode resistance, cables resistance, and the eventual intentionally inserted external ohmic resistance.

The following derivations correspond to *potentiostatic conditions*, meaning $U = \text{const}$. When the electrochemical circuit from Fig. 2.6 attains steady-state, the working electrode potential E is constant and the steady-state current, consisting then of only the faradaic contribution at the electrode–solution interface, is flowing through it. One of typical methods of attaining such situation is the use of the disk electrode rotating with constant speed and thus ensuring the steady-state thickness of the diffusion layer under such convective diffusion conditions. Our aim is to derive the criteria of (in)stability of such a steady-state when it is subjected to perturbations small enough to justify the linearization of the problem.

The fundamental equation for such analysis, which we invoke many times also in further parts of this book, is the expression for charge conservation:

$$\frac{U - E}{R_s} = I = I_f(E) + I_c(E) = I_f(E) + C_d A \frac{dE}{dt} \quad (2.10)$$

rearranged to the form most suitable for considerations of stability:

$$f(E) \equiv \frac{dE}{dt} = \frac{U - E}{C_d A R_s} - \frac{I_f(E)}{C_d A} \quad (2.11)$$

where A is a surface area of the electrode and C_d is the differential double layer capacity for the working electrode/solution interface, expressed per unit area of the electrode surface. Although C_d is generally dependent on the electrode potential E , it will be here, for the sake of mathematical simplicity, assumed to be a constant (average) value.

The condition for the steady-state:

$$\left(\frac{dE}{dt}\right)_{ss} = 0 \quad (2.12)$$

implies that the capacitive current is zero and then the faradaic current attains the steady-state, non-zero value:

$$I_{f,ss} = \frac{U - E_{ss}}{R_s} \quad (2.13)$$

According to the principles of linear stability analysis, the right-hand-side of Eq. (2.11) is expanded into the Taylor series around the steady-state potential, with non-linear terms neglected:

$$\frac{dE}{dt} = f(E) \approx \left(\frac{df}{dE}\right)_{ss} (E - E_{ss}) = \frac{-1}{C_{dA}} \left[\frac{1}{R_s} + \left(\frac{dI_f}{dE}\right)_{ss} \right] (E - E_{ss}) \quad (2.14)$$

By introducing the convenient new variable δ measuring the extent of perturbation of the steady-state:

$$\delta = E - E_{ss} \quad (2.15)$$

one transforms Eq. (2.14) to a form analogous to that used before [cf. Eq. (1.8)] in the analogous abstract mathematical analysis:

$$\frac{d\delta}{dt} = \lambda \cdot \delta \quad (2.16)$$

with λ defined as:

$$\lambda = \frac{-1}{C_{dA}} \left[\frac{1}{R_s} + \left(\frac{dI_f}{dE}\right)_{ss} \right] \quad (2.17)$$

Obviously the steady-state of the electrochemical system is asymptotically stable, if $\lambda < 0$ which condition is met for every trivial electrode process, of kinetics described by Butler–Volmer dependence. Instability, corresponding to $\lambda > 0$, may occur only if:

$$\left(\frac{dE}{dI_f}\right)_{ss} < 0 \quad (2.18)$$

and with serial resistance meeting the condition:

$$R_s > - \left(\frac{dE}{dI_f} \right)_{ss} \quad (2.19)$$

The reader will notice clear analogies with derivations made already in Sect. 2.1.2. The negative slope $(dE/dI_f)_{ss} < 0$ means the NDR of the faradaic process in its steady-state. Note that in the instability condition (2.19) the double layer capacitance C_d is not existing, as for one-dimensional system, when oscillations cannot occur, this parameter does not decide the system's dynamics in the steady-state, it only determines the time scale of transient approaching the stable steady-state (or of leaving the unstable steady-state). At the critical point, when the tuned serial resistance meets the condition:

$$R_s = - \left(\frac{dE}{dI_f} \right)_{ss} \quad (2.20)$$

the 1D variant of the saddle-node bifurcation occurs, i.e., the pair of stable and unstable steady-states is born from “nowhere” (see Sect. 1.3.1). For the I - E characteristics with the N-NDR region (Figs. 2.2 and 2.3), when the steady-state dependence of I on E is unique (single-valued) under true potentiostatic conditions, inserting the ohmic resistance higher than this critical value means the transition from the monostable to bistable behavior, meaning the appearance of hysteresis in the system's behavior, measured as steady-state I_f , versus the cyclically changing external voltage U (Fig. 2.4). This scheme also shows that saddle-node bifurcations occur in pairs, forming thus a so-called degenerate case, in which there is always at least one steady-state possible.

2.2.1.2 Galvanostatic Control

It is useful to compare immediately the above derivations with those for the galvanostatic control of the electrochemical system. Physically it means that at any moment, even if both faradaic and capacitive currents are flowing, their sum must be equal to the externally imposed total current I :

$$I = I_f(E) + I_c(E) = I_f(E) + C_d A \frac{dE}{dt} \quad (2.21)$$

Furthermore, in view of equivalent circuit shown in Fig. 2.6, the term $(U - E)/R_s$ in Eq. (2.10) must be replaced with this fixed current:

$$\frac{U - E}{R_s} \rightarrow I = \text{const} \quad (2.22)$$

In consequence, the equation for the temporal dynamics of the electrode potential takes now the form:

$$f(E) \equiv \frac{dE}{dt} = \frac{I}{C_d A} - \frac{I_f(E)}{C_d A} = \frac{1}{C_d A} [I - I_f(E)] \quad (2.23)$$

meaning that the variation of the electrode potential E is due solely to the capacitive current I_c , which is the difference between the fixed total current I and the potential-dependent faradaic current I_f . This is of course a mathematical illustration of the obvious characteristics of the galvanostatic experiments in which, if at the actual electrode potential, the electrode process does not support the current equal to externally imposed one, the accumulation of charge at the working electrode causes its charging to more positive (or negative) potentials, in search of additional possibility for the transfer of electrons across the interface.

Note also that Eq. (2.23) does not include explicitly the value of serial resistance R_s , but one should note that a (theoretically infinite) resistance is a feature of a galvanostat—see above. The fact that the working electrode potential is a dynamic variable that may vary as a function of time, while the total current is not, is an important feature of the galvanostatic circuit, which dynamic characteristics are essentially different from the potentiostatic case, when both E and I can vary. This is one more illustration of the fact that for NDR systems the galvanostatic response cannot be considered equivalent to the potentiostatic ($U = \text{const}$) response; this conclusion has important consequences for the types and conditions of occurrence of dynamic instabilities observed in both types of the systems.

The linear stability analysis leads now to the following Taylor series, limited to linear terms:

$$\frac{dE}{dt} \approx \left(\frac{df}{dE} \right)_{ss} (E - E_{ss}) = \frac{-1}{C_d A} \left(\frac{dI_f}{dE} \right)_{ss} (E - E_{ss}) \quad (2.24)$$

or, equivalently, in the form of Eq. (2.16), where λ is now defined as:

$$\lambda = \frac{-1}{C_d A} \left(\frac{dI_f}{dE} \right)_{ss} \quad (2.25)$$

In Eq. (2.25), the differential charge-transfer resistance $(dE/dI_f)_{ss}$ is calculated at a given electrode potential E , for a steady-state I_f - E characteristics. Obviously, as long as the slope of these characteristics is positive, the electrochemical system is stable ($\lambda < 0$), but if the electrode potential enters the region of any (i.e., not related this time to any serial resistance) NDR, the system becomes unstable. In view of a typical I - E characteristics this means that for the galvanostatic operation of the electrochemical circuit, the condition:

$$\left(\frac{dE}{dI_f} \right)_{ss} < 0 \quad (2.26)$$

means that the monostable dynamics of the 1D electrochemical system changed to bistable, with the *galvanostatic saddle-node bifurcation* occurring for $(dE/dI_f)_{ss} = 0$. This condition is concordant with the transition between the monostable and bistable behaviors shown in Fig. 2.4 for galvanostatic conditions, in the absence of any extra serial resistance.

To conclude, electrochemical systems characterized with the negative resistance of the N-NDR type exhibit bistability under both potentiostatic ($U = \text{const}$) and galvanostatic ($I = 0$) conditions, with that difference that in the former case the onset of this behavior requires sufficiently large serial ohmic resistance.

In both these one-dimensional cases the electrode potential E was the only dynamical variable considered. In the bistable regime, where three different steady-states can be realized, every steady-state potential is associated with the corresponding current, and with the respective, obviously also steady-state surface concentration(s) of the electroactive species, $c(0)$. Those concentrations adjust thus instantaneously to the given electrode potential, so the $dc(0)/dt$ dynamics is not important for the global dynamics of the system. However, if upon (then relatively fast) change of the electrode potential the change of $c(0)$ appears to be relatively slow, the system may destabilize in a way giving rise to the oscillations of current under potentiostatic conditions. Therefore, it is useful to consider now the stability of an electrochemical system, involving two dynamical variables.

2.2.2 Linear Stability Analysis of 2D Electrochemical System

2.2.2.1 Potentiostatic Control

Two variables involved in the dynamics of electrochemical systems are: the working electrode potential (interfacial potential drop) E and the surface concentration of the reducible or oxidizable species $c(0)$. Since this time we expect the oscillations of both potential and current, and thus the periodical variation of surface concentration in time, we shall introduce the time variable to equation for the faradaic current [Eq. (2.8)]. For simplicity we shall also keep the assumption that the electroreduction or electrooxidation process is practically irreversible within the potential region, when the N-NDR region develops. In further representative derivations we shall invoke this time the cathodic process of Ox electroreduction to Red species, thus the relevant faradaic current is negative:

$$I_f(t) = -nFAk_f c_{\text{Ox}}(0, t) \quad (2.27)$$

where k_f is the potential-dependent rate constant of the electroreduction process of a general scheme:



and $c_{\text{Ox}}(0, t)$ means the concentration of Ox at the reaction site ($x = 0$), at time t .

Now it is necessary to introduce equations defining the 2D electrochemical system. The first of these equations is, in principle, identical with Eq. (2.11), with the difference that the time-dependent surface concentration variable appears in it, due to substitution of expression (2.27) for the faradaic current $I_f(E)$.

$$f(E, t) \equiv \frac{dE}{dt} = \frac{U - E}{C_d A R_s} - \frac{I_f(E)}{C_d A} = \frac{U - E}{C_d A R_s} + \frac{n F k_f(E) c_{\text{ox}}(0, t)}{C_d} \quad (2.29)$$

The equation describing the temporal dynamics of c_{ox} , requires separate derivation. The actual value of $c_{\text{ox}}(0, t)$ is a result of a competition between the consumption of the Ox species at the electrode surface and the diffusion inflow of Ox from the solution bulk to this site. The precise description of the diffusion transport, in terms of the Fick's laws, involves the calculation of the full concentration profile $c(x, t)$ in the solution, where coordinate x is normal to the electrode surface, and a strict approach to this problem requires partial differential equations (PDEs). In classical electrochemistry, including digital simulation of electrode processes [6–8], such an approach is obligatory, if the reliable values of kinetic parameters of electrode process are to be determined. However, in nonlinear dynamics we are interested more in *qualitative types* of possible dynamic behaviors, than in exact values of all system's parameters (which however cannot become unreliable). It is thus possible to make a mathematically useful compromise which results in a presentation of the dynamics of the surface concentration in terms of ordinary differential equation (ODE). In conjunction with Eq. (2.29), this significantly simplifies the stability analysis for the electrochemical systems that are considered spatially homogeneous along the coordinate parallel to the electrode surface. This approach, suggested by Koper and Sluyters [9], is based on the linear approximation of the concentration profile, leading to the definition of the (effective) thickness δ of the Nernst diffusion layer [4]. The time derivative of the surface concentration $c_{\text{ox}}(0, t)$ was derived there according to principle illustrated by Fig. 2.7.

The triangular shaded area in Fig. 2.7 equals to the difference between the amount of Ox species that diffuses toward the electrode and the amount that undergoes electroreduction at the reaction site close to the electrode surface:

$$\begin{aligned} \frac{1}{2} [c_{\text{ox}}(0, t + dt) - c_{\text{ox}}(0, t)] \delta &\equiv \frac{1}{2} dc_{\text{ox}}(0, t) \delta \\ &= D_{\text{ox}} \left[\frac{c_{\text{ox}}^0 - c_{\text{ox}}(0, t)}{\delta} \right] dt - k_f c_{\text{ox}}(0, t) dt \end{aligned} \quad (2.30)$$

By appropriate rearrangement of this equation, one obtains the expression for the $dc_{\text{ox}}(0, t)/dt$ dynamics:

$$g(E, t) \equiv \frac{dc_{\text{ox}}(0, t)}{dt} = \frac{2D_{\text{ox}}}{\delta^2} [c_{\text{ox}}^0 - c_{\text{ox}}(0, t)] - \frac{2k_f c_{\text{ox}}(0, t)}{\delta} \quad (2.31)$$

Thus, finally, the dynamics of the 2D N-NDR system under potentiostatic conditions is defined by Eqs. (2.29) and (2.31).

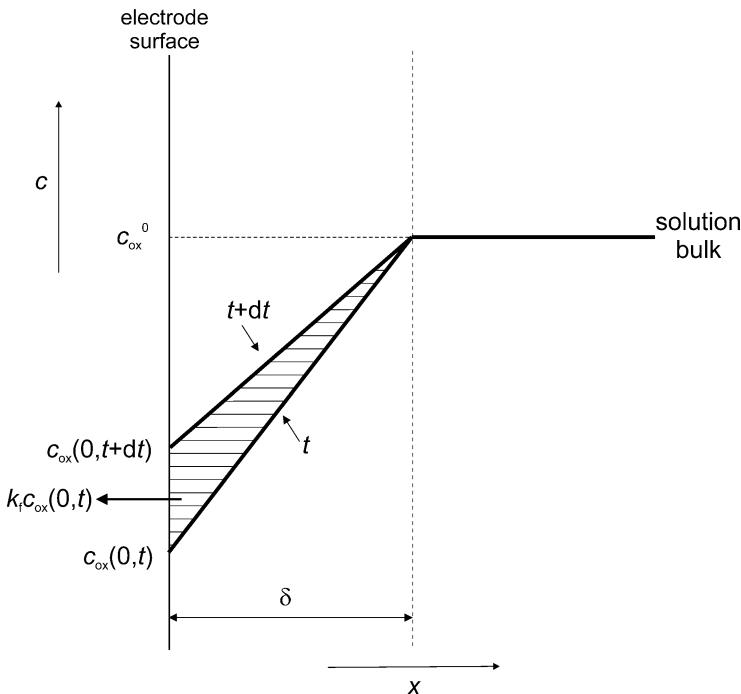


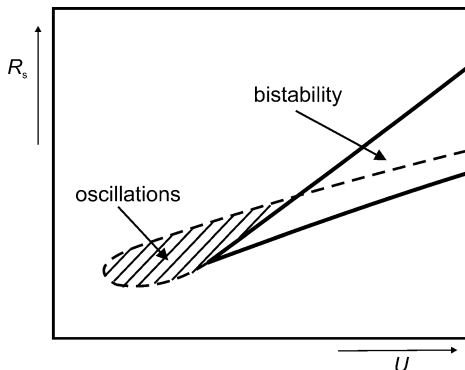
Fig. 2.7 Principle of derivation of the equation (2.31) for the $dc_{ox}(0, t)/dt$ dynamics: the change in the concentration profile near the electrode in the time interval dt , assuming at all times a linear concentration gradient with fixed diffusion layer thickness δ . Based on [9]

Before performing the stability analysis of the dynamical system (2.29, 2.31) it is useful to note that the right-hand-side of Eq. (2.31) is composed of two terms, the first (the “transport” one) is proportional to $(1/\delta^2)$, while the second (the “kinetic” one) one is proportional to $(1/\delta)$. Thus, upon decreasing the Nernst layer thickness (e.g., by increasing the rotation rate of the disk electrode) one increases the relative role of the transport of the fresh portions of Ox from the bulk, compared to the rate of the Ox to Red transformation at the interface [10].

The Jacobian matrix \mathbf{J} of Eqs. (2.29) and (2.31) has a form (in which, for simplification of the notation, $c_s \equiv c_{ox}(0, t)$):

$$\begin{aligned}
 \mathbf{J} &= \begin{bmatrix} \left(\frac{\partial f}{\partial E}\right)_{ss} & \left(\frac{\partial f}{\partial c_s}\right)_{ss} \\ \left(\frac{\partial g}{\partial E}\right)_{ss} & \left(\frac{\partial g}{\partial c_s}\right)_{ss} \end{bmatrix} = \begin{bmatrix} -\frac{1}{C_d A} \left[\frac{1}{R_s} + \left(\frac{\partial I_f}{\partial E}\right)_{ss} \right] & \frac{n F k_f(E_{ss})}{C_d} \\ \frac{2}{n F A \delta} \left(\frac{\partial I_f}{\partial E}\right)_{ss} & -2 \left[\frac{D_{ox}}{\delta^2} + \frac{k_f(E_{ss})}{\delta} \right] \end{bmatrix} \\
 &= \begin{bmatrix} -\frac{1}{C_d A} \left[\frac{1}{R_s} - n F A c_{s,ss} \left(\frac{dk_f}{dE}\right)_{ss} \right] & \frac{n F k_f(E_{ss})}{C_d} \\ -\frac{2 c_{s,ss}}{\delta} \left(\frac{dk_f}{dE}\right)_{ss} & -2 \left[\frac{D_{ox}}{\delta^2} + \frac{k_f(E_{ss})}{\delta} \right] \end{bmatrix}
 \end{aligned}
 \tag{2.32}$$

Fig. 2.8 Two-parameter skeleton bifurcation diagram of the N-NDR oscillator in the U/R_s parameter plane. *Solid*: location of saddle-node bifurcations; *dashed line*: location of Hopf bifurcation. After [10]



with the differential charge-transfer resistance given by $(\partial I_f / \partial E)_{ss}^{-1}$. The bifurcations are diagnosed based on the trace and the determinant (cf. Sect. 1.3.2), given by expressions:

$$\text{Tr}(\mathbf{J}) = -\frac{1}{C_d A} \left[\frac{1}{R_s} + \left(\frac{\partial I_f}{\partial E} \right)_{ss} \right] - \frac{2}{\delta} \left[\frac{D_{ox}}{\delta} + k_f(E_{ss}) \right] \quad (2.33)$$

$$\begin{aligned} \text{Det}(\mathbf{J}) &= \left\{ \frac{1}{C_d A} \left[\frac{1}{R_s} + \left(\frac{\partial I_f}{\partial E} \right)_{ss} \right] \right\} \times \left\{ \frac{2}{\delta} \left[\frac{D_{ox}}{\delta} + k_f(E_{ss}) \right] \right\} - \frac{2k_f(E_{ss})}{C_d A \delta} \left(\frac{\partial I_f}{\partial E} \right)_{ss} \\ &= \frac{2}{C_d A \delta^2} \left[\frac{D_{ox}}{R_s} + \frac{k_f(E_{ss})\delta}{R_s} + D_{ox} \left(\frac{\partial I_f}{\partial E} \right)_{ss} \right] \end{aligned} \quad (2.34)$$

As long as $\text{Tr}(\mathbf{J}) < 0$ and $\text{Det}(\mathbf{J}) > 0$, the system is stable. Equations (2.33) and (2.34) prove that if the I_f - E curve has a positive slope $(\partial I_f / \partial E)_{ss} > 0$, the trace will always be negative, and the determinant always positive. So, the NDR of the faradaic process, obviously just like for 1D system, is required to destabilize the system. Then, if $\text{Det}(\mathbf{J}) = 0$, the saddle-node bifurcation occurs and further in the bistable regime $\text{Det}(\mathbf{J}) < 0$. Furthermore, for $\text{Tr}(\mathbf{J}) = 0$ (provided that $\text{Det}(\mathbf{J}) > 0$) the nonlinear system experiences the onset of oscillations via the Hopf bifurcation, and further in the oscillatory regime $\text{Tr}(\mathbf{J}) > 0$ (cf. Fig. 1.8).

Typical cross-shaped bifurcation diagram for the simple electrochemical system with the single N-NDR region in its I - E characteristics, constructed based on the above criteria, is shown in Fig. 2.8.

2.2.2.2 Galvanostatic Control

The imposed constant current I is at any moment equal to the sum of the faradaic and (if any) capacitive currents, which individually can vary:

$$I = I_f + I_c = -nFAk_f c_{\text{ox}}(0, t) + C_d A \frac{dE}{dt} = \text{const} \quad (2.35)$$

According to reasoning developed for the 1D system, one derives an analogous equation for the electrode potential dynamics under such condition:

$$f(E, t) \equiv \frac{dE}{dt} = \frac{I}{C_d A} - \frac{I_f}{C_d A} = \frac{I}{C_d A} + \frac{nFk_f(E)c_{\text{ox}}(0, t)}{C_d} \quad (2.36)$$

The equation for the $c_{\text{ox}}(0, t)$ dynamics remains the same as for the potentiostatic system (2.31). The present dynamical system is thus defined with Eqs. (2.31) and (2.36). Its Jacobian matrix has a form:

$$\begin{aligned} \mathbf{J} &= \begin{bmatrix} \left(\frac{\partial f}{\partial E}\right)_{\text{ss}} & \left(\frac{\partial f}{\partial c_s}\right)_{\text{ss}} \\ \left(\frac{\partial g}{\partial E}\right)_{\text{ss}} & \left(\frac{\partial g}{\partial c_s}\right)_{\text{ss}} \end{bmatrix} = \begin{bmatrix} -\frac{1}{C_d A} \left(\frac{\partial I_f}{\partial E}\right)_{\text{ss}} & \frac{nFk_f(E_{\text{ss}})}{C_d} \\ \frac{2}{nFA\delta} \left(\frac{\partial I_f}{\partial E}\right)_{\text{ss}} & -2 \left[\frac{D_{\text{ox}}}{\delta^2} + \frac{k_f(E_{\text{ss}})}{\delta} \right] \end{bmatrix} \\ &= \begin{bmatrix} \frac{nFc_{s,\text{ss}}}{C_d} \left[\left(\frac{dk_f}{dE}\right)_{\text{ss}} \right] & \frac{nFk_f(E_{\text{ss}})}{C_d} \\ -\frac{2c_{s,\text{ss}}}{\delta} \left(\frac{dk_f}{dE}\right)_{\text{ss}} & -2 \left[\frac{D_{\text{ox}}}{\delta^2} + \frac{k_f(E_{\text{ss}})}{\delta} \right] \end{bmatrix} \end{aligned} \quad (2.37)$$

with the trace and the determinant, respectively:

$$\text{Tr}(\mathbf{J}) = -\frac{1}{C_d A} \left(\frac{\partial I_f}{\partial E}\right)_{\text{ss}} - 2 \left[\frac{D_{\text{ox}}}{\delta^2} + \frac{k_f(E_{\text{ss}})}{\delta} \right] \quad (2.38)$$

$$\begin{aligned} \text{Det}(\mathbf{J}) &= \left[\frac{1}{C_d A} \left(\frac{\partial I_f}{\partial E}\right)_{\text{ss}} \right] \times 2 \left[\frac{D_{\text{ox}}}{\delta^2} + \frac{k_f(E_{\text{ss}})}{\delta} \right] - \left[\frac{nFk_f(E_{\text{ss}})}{C_d} \right] \times \left[\frac{2}{nFA\delta} \left(\frac{\partial I_f}{\partial E}\right)_{\text{ss}} \right] \\ &= \frac{2D_{\text{ox}}}{C_d A \delta^2} \left(\frac{\partial I_f}{\partial E}\right)_{\text{ss}} \end{aligned} \quad (2.39)$$

The condition for the saddle node bifurcation, $\text{Det}(\mathbf{J}) = 0$ is now met for the $(\partial I_f / \partial E)_{\text{ss}} = 0$, i.e., for the extremum of the $I_f(E)$ (or $k_f(E)$) dependence(s), i.e., for the points at which a transition from the positive to the negative slope of the I - E characteristics takes place. This is clearly illustrated in Fig. 2.4, where the horizontal jumps between the one and other branch of stable steady-states occur at such two points. For $\text{Det}(\mathbf{J}) < 0$, i.e., for the region of negative resistance, $(\partial I_f / \partial E)_{\text{ss}} < 0$, the saddle points emerge, composing, together with the stable states, the bistable fold of states.

In turn, the condition for the Hopf bifurcation would require $\text{Tr}(\mathbf{J}) = 0$ with $\text{Det}(\mathbf{J}) > 0$ but inspection of Eqs. (2.38) and (2.39) clearly shows that these conditions *cannot* be met simultaneously: the zero trace would occur only for the negative

slope of the I – E curve, but then $\text{Det}(\mathbf{J})$ would be also negative. A very important conclusion of this analysis is that for the 2D dynamical system with the electrode process having the N-NDR region, under galvanostatic conditions one can observe bistability, but oscillations of the electrode potential are *not* possible.

To summarize the analyses of the 2D case, the N-NDR system, that can be either bistable or oscillatory under potentiostatic conditions, depending on the external voltage and serial resistance, can only be bistable under galvanostatic conditions [11]. Since, however, galvanostatic oscillations are observed experimentally for some systems, it is clear that the mechanisms of such processes would have to be appropriately complicated, compared to Eq. (2.28). Such processes have to exhibit a region of a negative resistance, hidden under dc conditions by another process. Such HN-NDR oscillators will be described in Chap. 3.

2.2.3 The Advantage of Dimensionless Representation

In Sect. 1.6 it was shown that using dimensionless variables allowed to describe the dynamical system, defined by the van der Pol equations, in a way conveniently showing the difference in the time scale of particular variables by a single parameter ε . Upon decreasing ε , the oscillations were changing from sinusoidal to typical relaxation ones (Fig. 1.27). Analogous procedure will now be applied, as an example, to Eqs. (2.29) and (2.31), defining the N-NDR system under potentiostatic conditions. The following definitions of new dimensionless variables are introduced:

1. Dimensionless concentration (through normalization to the bulk value):

$$c = \frac{c_{\text{ox}}(0, t)}{c_{\text{ox}}^0} \quad (2.40)$$

2. Dimensionless electrode potential:

$$e = \frac{nF}{RT} E \quad (2.41)$$

3. Dimensionless external voltage:

$$u = \frac{nF}{RT} U \quad (2.42)$$

4. Dimensionless time:

$$\tau = \frac{2D_{\text{ox}}}{\delta^2} t \quad (2.43)$$

5. Dimensionless heterogeneous rate constant of electroreduction:

$$k = \frac{\delta}{D_{\text{ox}}} k_f \quad (2.44)$$

Using these definitions, one transforms Eqs. (2.29) and (2.31) into their dimensionless forms:

$$\varepsilon \frac{de}{d\tau} = \frac{u - e}{\rho} + kc \quad (2.45)$$

$$\frac{dc}{d\tau} = -kc + 1 - c \quad (2.46)$$

which contains two dimensionless parameters ρ and ε . Quantity ρ , defined as:

$$\rho = \frac{c_{\text{ox}}^0 D_{\text{ox}} n^2 F^2 R_s A}{RT \delta} \quad (2.47)$$

is proportional to serial resistance and thus can be considered a “dimensionless serial resistance”; it is also a measure of a maximum contribution to the ohmic potential drops from the limiting, steady-state faradaic current which is given by:

$$I_{\text{lim}} = \frac{nFAD_{\text{ox}}c_{\text{ox}}^0}{\delta} \quad (2.48)$$

In turn, the ε parameter, defined as:

$$\varepsilon = \frac{2C_d RT}{c_{\text{ox}}^0 n^2 F^2 \delta} \quad (2.49)$$

expresses, analogously to the example with the van der Pol equation, the time scale of the electrode potential dynamics, compared to the dynamics of the surface concentration of the reacting species. For the conventional electrodes and other typical experimental parameters ε is usually of the order of 10^{-4} to 10^{-5} , so the electrode potential can be qualified as a relatively *fast variable*. This means that upon perturbation of the steady-state, the electrode potential response is faster than that of the surface concentration being then a relatively slow variable [10].

The significance of parameter ε for the description of the dynamics of electrochemical systems is further revealed in the linear stability analysis [10]. The Jacobian matrix of Eqs. (2.45) and (2.46) has a form:

$$\mathbf{J} = \begin{bmatrix} \frac{1}{\varepsilon} \left[c_{ss} \left(\frac{dk}{de} \right)_{ss} - \frac{1}{\rho} \right] & \frac{k(e_{ss})}{\varepsilon} \\ -c_{ss} \left(\frac{dk}{de} \right)_{ss} & -k(e_{ss}) - 1 \end{bmatrix} \quad (2.50)$$

with the trace and the determinant, respectively:

$$\text{Tr}(\mathbf{J}) = \frac{1}{\varepsilon} \left[c_{ss} \left(\frac{dk}{de} \right)_{ss} - \frac{1}{\rho} \right] - k(e_{ss}) - 1 \quad (2.51)$$

$$\begin{aligned} \text{Det}(\mathbf{J}) &= -\frac{1}{\varepsilon} \left[c_{ss} \left(\frac{dk}{de} \right)_{ss} - \frac{1}{\rho} \right] \times [k(e_{ss}) + 1] + \frac{k(e_{ss})}{\varepsilon} \times c_{ss} \left(\frac{dk}{de} \right)_{ss} \\ &= \frac{1}{\varepsilon} \left[-c_{ss} \left(\frac{dk}{de} \right)_{ss} + \frac{1}{\rho} [k(e_{ss}) + 1] \right] \end{aligned} \quad (2.52)$$

Again, the onset of instability of the steady-state through the saddle-node bifurcation requires the condition $\text{Det}(\mathbf{J}) = 0$ which can be met only if $(dk/de)_{ss}$ is positive (for the cathodic process considered), i.e., within the region of the *negative* differential resistance dI_f/dE (N-NDR). Saddle points will persist further for $\text{Det}(\mathbf{J}) < 0$, i.e., when the dimensionless serial resistance is sufficiently large:

$$\rho \geq \frac{[k(e_{ss}) + 1]}{c_{ss}} \left(\frac{de}{dk} \right)_{ss} \quad (2.53)$$

From mathematical form of Eq. (2.52) it follows also that the parameter ε does not affect the onset of bistability. However, its significance manifests itself in the oscillatory regime that requires $\text{Tr}(\mathbf{J}) = 0$, meaning again the NDR region (positive dk/de slope for the cathodic process). The oscillations set in and persist if:

$$\left(\frac{dk}{de} \right)_{ss} \geq \frac{1}{c_{ss}} \left[\frac{1}{\rho} + [k(e_{ss}) + 1] \varepsilon \right] \quad (2.54)$$

which condition requires that ε is not too large. On the other hand, serial resistance included in parameter ρ cannot also be too high, in order to meet the second condition for the Hopf bifurcation, $\text{Det}(\mathbf{J}) > 0$, i.e.:

$$\rho < \frac{[k(e_{ss}) + 1]}{c_{ss}} \left(\frac{de}{dk} \right)_{ss} \quad (2.55)$$

otherwise $\text{Det}(\mathbf{J})$ will become negative and the oscillatory instability will be replaced by bistability.

Let us try to understand the physical sense of this conclusion [10]. If ε is small, as for the relatively slowly rotating disk electrode (high Nernst layer thickness δ), the surface concentration of the reactant responds relatively slowly to the perturbation of the electrode potential. This means that the diffusion of the reactant from the bulk replenishes the surface concentration slower than it is transformed to Red species through the electron transfer at the interface. The consumption and the inflow of the reactant to the reaction site are not balanced and this is the situation which may give rise to the oscillations of the surface concentration. On the contrary, when the disk electrode rotates much faster, the thickness of the Nernst diffusion layer δ is decreased, current increases, so both ρ (ohmic drops) and ε become appropriately large. This means that the rate of the transport increases and surface concentration of a reactant becomes a faster variable than before, relative to the electrode potential. This concentration is thus more forced by the transport rate, approaching in the limit the bulk concentration of reactant. One can expect that the oscillations of the electrode potential (and of the total current) will be continuously losing the relaxation shape, like in the van der Pol model. Finally the oscillations will cease completely, since the only instability which may be observed in such a case will be bistability in the electrochemical model (2.45, 2.46).

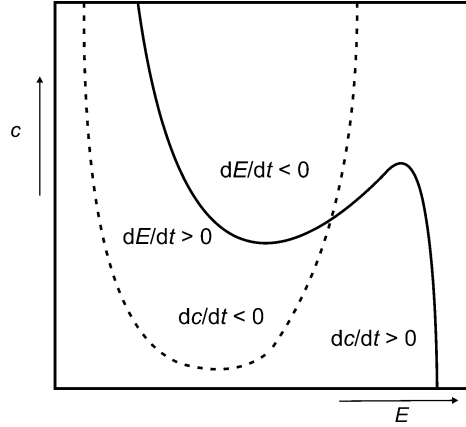
2.2.4 The Electrode Potential as an Autocatalytic Variable in the N-NDR Systems

The content of this section indicates an important dynamic characteristics of the electrode potential in the N-NDR-type systems which is related to the concept of the activator and the inhibitor (Sect. 1.8), represented by appropriate signs of the elements of the Jacobian matrix. In order to apply this idea to the present N-NDR system, the Jacobian matrix (2.50) will be rewritten with the indication of the definition of particular derivatives, in which $\dot{e} \equiv de/dt$ and $\dot{c} \equiv dc/dt$:

$$\mathbf{J} = \begin{bmatrix} \left(\frac{\partial \dot{e}}{\partial e}\right)_{ss} & \left(\frac{\partial \dot{e}}{\partial c}\right)_{ss} \\ \left(\frac{\partial \dot{c}}{\partial e}\right)_{ss} & \left(\frac{\partial \dot{c}}{\partial c}\right)_{ss} \end{bmatrix} = \begin{bmatrix} \frac{1}{\varepsilon} \left[c_{ss} \left(\frac{dk}{de}\right)_{ss} - \frac{1}{\rho} \right] & \frac{k(e_{ss})}{\varepsilon} \\ -c_{ss} \left(\frac{dk}{de}\right)_{ss} & -k(e_{ss}) - 1 \end{bmatrix} \quad (2.56)$$

Of course, the same procedure can be performed for the anodic process, with the faradaic current then always positive: $I_f = nFAk_b(E)c_{\text{red}}(0, t)$, where k_b is the potential-dependent heterogeneous rate constant of the oxidation process. The change of the sign of the current, together with the change of the sign of the dk_b/dE derivative (now negative in the NDR region), leads then to the dimensionless equations:

Fig. 2.9 Typical course of E -nullcline (solid line) and c -nullcline (dashed line) of the electrochemical system (2.57, 2.58) for control parameters ensuring the unstable steady-state lying within the N-NDR region. After [12]



$$\varepsilon \frac{de}{d\tau} = \frac{u - e}{\rho} - kc \tag{2.57}$$

$$\frac{dc}{d\tau} = -kc + 1 - c \tag{2.58}$$

and the corresponding Jacobian matrix:

$$\mathbf{J} = \begin{bmatrix} \left(\frac{\partial \dot{e}}{\partial e}\right)_{ss} & \left(\frac{\partial \dot{e}}{\partial c}\right)_{ss} \\ \left(\frac{\partial \dot{c}}{\partial e}\right)_{ss} & \left(\frac{\partial \dot{c}}{\partial c}\right)_{ss} \end{bmatrix} = \begin{bmatrix} -\frac{1}{\varepsilon} \left[c_{ss} \left(\frac{dk}{de}\right)_{ss} + \frac{1}{\rho} \right] & -\frac{k(e_{ss})}{\varepsilon} \\ -c_{ss} \left(\frac{dk}{de}\right)_{ss} & -k(e_{ss}) - 1 \end{bmatrix} \tag{2.59}$$

The signs of the elements of these matrices can be determined from the course of the e and c nullclines in the vicinity of their intersection, corresponding to the steady-state, in a way explained schematically in Fig. 1.34. Essential conclusions drawn from such procedure are of course the same for both cathodic and anodic processes, but opposite signs of current are the causes for opposite signs of some elements of these matrices. We shall consider in more detail, as an example, only the anodic process, for which the mathematical form of the expression corresponds directly to the intuitive relation: more positive potential means increasing driving force and more positive current means increasing rate of the electrochemical process. For the system (2.57, 2.58), a typical course of nullclines, intersecting in the unstable steady-state lying within the N-NDR region, is shown in Fig. 2.9.

From the signs of derivatives in this plot one obtains the following signs of the elements of matrix (2.59) which should be compared with analogous case (1.113), named before the “pure activator–inhibitor system”¹:

$$\mathbf{J} = \begin{bmatrix} + & - \\ + & - \end{bmatrix} \quad (2.60)$$

In fact, the dimensionless electrode potential e is a *self-activator*, since $\partial\dot{e}/\partial e > 0$, i.e., an enhancement of e causes its further increase. This is why the electrode potential in the N-NDR systems is the *autocatalytic variable* or *positive feedback variable*. Furthermore, the concentration of chemical species is a self-inhibitor, or *negative feedback variable*, since $\partial\dot{c}/\partial c < 0$. Based on previous conclusions about the different time scales of variables e and c for the oscillatory regime one can further specify that the electrode potential is a *fast autocatalytic variable*, while the concentration of chemical species is a *slow self-inhibiting variable*.

Physically, the autocatalytic nature of electrode potential is explained in the following way, taking again the anodic process as an example [12]. Within the NDR region, if the electrode potential is *increased* for the value de , the current decreases for di . As a consequence, the ohmic potential drops also for $R_s di$, and the electrode potential increases further for that value. This causes further decrease of the current and thus the increase of the electrode potential e . Thus, the increase of the electrode potential is a self-enhancing process. Analogously, the negative perturbation $-de$ will result in self-enhancing decrease of the electrode potential. These alternating processes of self-enhanced increase and decrease in e occur during its oscillatory variations. One should emphasize the role of NDR in this positive feedback, since none of the electrochemical reaction steps is autocatalytic in this sense which we know from the classical homogeneous chemical kinetics.

Furthermore, $\partial\dot{c}/\partial e > 0$ means that the increasing electrode potential enhances the surface concentration of the reactant, i.e., the electrode potential is an *activator* for the surface concentration of the oxidized species. In fact, in the NDR region, when the electrode potential increases, the rate of the electrode process decreases and then the transport of the reactant from the bulk can more efficiently replenish the diffusion layer. On the contrary, $\partial\dot{e}/\partial c < 0$, so the chemical species act as an *inhibitor* for the electrode potential. Again, in the NDR region, if the surface concentration of the reactant increases, the faradaic current appropriately increases, and so the ohmic potential drop. This in turn means that the absolute value of the electrode potential decreases ($E = U - IR_s$) which causes further increase of current and ohmic drops.

To summarize the above interpretation, a single oscillation related to the N-NDR region is considered a result of the positive feedback involving fast variable: electrode potential, which increases until the slow chemical, negative feedback variable takes control over the system’s dynamics. One should note that the electrode potential

¹ For the irreversible cathodic process the elements a_{11} and a_{22} would have the same signs, while a_{21} and a_{12} will have opposite signs, since the dc_{ox}/dE and dk_f/dE derivatives have the signs opposite to those of dc_{red}/dE and dk_b/dE derivatives in anodic process.

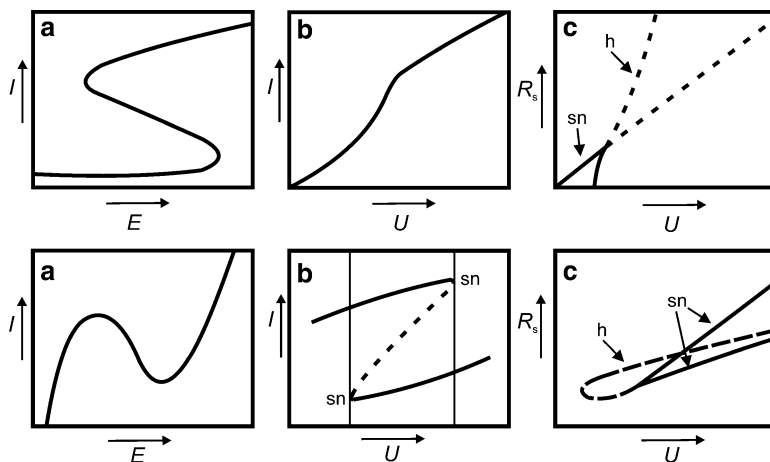


Fig. 2.10 Comparison of I - E , I - U dependences and bifurcation diagrams for the S-shaped (*top*) and N-shaped (*bottom*) NDR characteristics of the electrode processes. *Top*: (a) S-shaped current–potential curve (I - E), meaning the S-NDR characteristics of the electrode process for zero (vanishing) serial resistance R_s , (b) The characteristics from (a), deformed by appropriately high serial resistance R_s so that bistability vanishes on the I - U dependence. (c) Typical bifurcation diagram corresponding to the S-NDR system, indicating the region of bistability (limited by the saddle-node, sn, bifurcation points) and the region of oscillations inside the lines of the Hopf (h) bifurcations. The dependence on the sequence of these dynamical behaviors upon increasing R_s is reversed, compared to N-NDR systems. *Bottom*: analogous plots for the N-NDR (a) system, indicating bistability occurring only at non-zero resistances R_s (b, c). After [12]

remains the autocatalytic variable also for the HN-NDR systems, where the N-NDR region is partly or entirely hidden by another process. This will be no longer true for the systems with the S-shaped NDR regions (S-NDR), for which the chemical species becomes an activator, while the electrode potential takes a role of an inhibitor (negative feedback variable). This case is analyzed in the next section.

2.2.5 The Electrode Potential as a Negative Feedback Variable in S-NDR Systems

Figure 2.10a (top row) shows schematically typical I - E dependence corresponding to the S-shaped region of the negative differential resistance (S-NDR characteristics) which is *multivalued* for zero (or, alternatively speaking, vanishing) serial resistance R_s . As indicated earlier in this chapter, the systems with such characteristics exhibit bistability even under true potentiostatic conditions. It is of course fundamentally different from the N-NDR systems which for zero resistance are bistable only under galvanostatic conditions. Furthermore, the role of ohmic drops is in the case of S-NDR systems reversed, compared to N-NDR systems, as Fig. 2.10b (top row) illustrates. Upon increasing serial resistance R_s , the multivalued S-NDR dependence

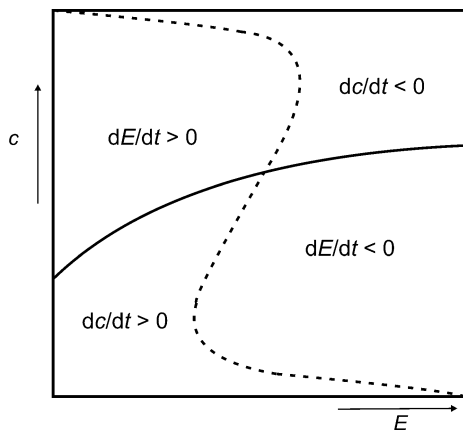


Fig. 2.11 E -nullcline (solid line) and c -nullcline (dashed line) for an S-NDR system. After [12]

deforms and expands along the external voltage U axis, eventually transforming to single-valued I - E dependence, when bistability is not existing any more. In consequence, the bifurcation diagram shown in Fig. 2.10c indicates this reversed effect of R_s ; the Hopf bifurcation leading to oscillations appears only at sufficiently high resistances. Thus, the bifurcation diagrams for the N-NDR and S-NDR systems can be considered complementary. For comparison, analogous characteristics for the N-NDR systems are collected in bottom row of Fig. 2.10 [12].

The shape of the I - E dependence from Fig. 2.10a can correspond, e.g., to the case when the electrode process is inhibited by adsorbed neutral molecules which exhibit sufficiently high attractive intermolecular interactions in the adsorption layer. Formally, this case is often described in terms of the Frumkin isotherm with appropriately large interaction parameter. Experimentally one observes then the hysteresis in the I - E response upon cyclic variations of electrode potential, since the current reflects the actual electrode coverage of an inhibitor: the current is high when the electrode coverage is low and vice versa.

Below we shall present only the basic dynamic properties of the S-NDR systems which will be deepened in Sect. 1.2.4 of volume II devoted to Turing patterns in electrochemical systems. Theoretical analysis performed by Krischer et al. [12, 13], allowed to illustrate the dynamics of S-NDR systems in terms of the nullclines drawn in Fig. 2.11. The reader interested in mathematical construction of the model is advised to consult Refs. [12, 14] and outline considerations included in Sect. 1.2 of volume II. Let us assume that E is an electrode potential, while c means the electrode coverage with an inhibitor, the adsorption of which is an S-shaped function of the electrode potential.

The crucial conclusions (which could also be drawn from the signs of the corresponding Jacobian matrix at the steady-state) come from the analysis of the vicinity of the intersections of both nullclines. For given E , upon adsorbate coverage c increasing around the steady-state, the derivative dc/dt changes its sign from the negative to positive value, so $[\partial/\partial c(dc/dt)]_{ss} > 0$ (a_{22} element of Jacobian matrix

is positive), i.e., the chemical species is now the activator (or more precisely—the self-activator), and the perturbations in c are amplified. On the other hand, if for given c , around the steady-state E increases, dE/dt changes its sign from positive to negative, so $[\partial/\partial E(dE/dt)]_{ss} < 0$ ($a_{11} < 0$) and the electrode potential is now an *inhibitor* (self-inhibitor), i.e., it is the negative feedback variable: its perturbations are damped, opposite to the N-NDR systems.

It is further instructive to establish the physical sense of the autocatalysis in the variable c : the attractive lateral interactions in the adsorption layer cause the self-acceleration of its build-up above certain critical coverage, and also self-accelerated damage of this layer below certain critical coverage, both separated for the region of hysteresis. In turn, with respect to electrode potential E , under potentiostatic conditions ($U = \text{const}$), with ohmic drops IR_s present, we figure out that if, at constant electrode coverage c , the electrode potential E increases, this causes the larger faradaic current, but this means also an increase in ohmic drops, so the increase in the electrode potential E is counteracted. Thus, also in terms of this analysis an electrode potential is a self-inhibitor.

The signs of the remaining two mixed derivatives in the Jacobian matrix are the following. When the electrode potential increases above the steady-state value, for $c = \text{const}$, the derivative dc/dt becomes negative, i.e., $[\partial/\partial E(dc/dt)]_{ss} < 0$, so the potential E “consumes” c (reflecting the desorption of the inhibitor molecules with increasing interfacial potential drop, i.e., at high electric charges of the electrode surface). Finally, if c increases, for $E = \text{const}$, the sign of the derivative $\partial/\partial c[dE/dt]$ is positive, so the electrode coverage is an activator for E ; physically, the increase in c lowers the faradaic current and thus the ohmic drops, hence the effective electrode potential then increases. Concluding, the signs of the elements of the Jacobian matrix for the S-NDR system considered are distributed in the following way [12], corresponding again to the activator–inhibitor system in which now the chemical variable is an activator and the electrode potential is an inhibitor:

$$\mathbf{J} = \begin{bmatrix} - & + \\ - & + \end{bmatrix} \quad (2.61)$$

Concerning the attractive interactions in the adsorption layer of an inhibitor as a possible cause for the S-NDR characteristics, one should note that in this case the dependence of the electrode coverage on the electrode potential can become both S-shaped and Z-shaped, at the potential regions of adsorption and desorption of an inhibitor, respectively (cf. Fig. 1.23 in Vol. II). Another example of the electrochemical system with the S-shaped dependence of current on electrode potential is the Zn electrodeposition, where the origin of such characteristics was ascribed to the chemical autocatalytic step [15].

At this step of analysis of stability of electrochemical systems it is useful to note that by identifying quantities, engaged in fast or slow, positive or negative feedback loops, one also discovers the variables *essential* for the oscillations. The important problem of distinguishing between the variables essential and non-essential for dynamical instabilities in electrochemical systems is outlined in the next section.

2.3 Essential and Non-essential Variables in Electrochemical Instabilities

In relation to the problem of essential dynamical variables, Kiss et al. [16] have elaborated the experimental strategy for characterization of such variables in electrochemical oscillatory systems. The essential species create destabilizing (fast autocatalytic or self-inhibitory) and stabilizing (slow inhibitory) feedback loops, as identified by the stoichiometric network analysis [17]. In electrochemical systems, the electrode potential is an essential variable for the N-NDR systems (an activator) and for the S-NDR systems (an inhibitor). Another essential variable can be a surface concentration of the electroactive species.

The experimental strategy proposed in [16] involved the “differential controller”, allowing for the fine-tuning of the time scale, over which the concentration of chemical species or the value of other dynamical variables can vary. If the oscillations are suppressed by changing the time scale of a given variable, its essential role for such instabilities becomes confirmed. In an unperturbed electrochemical system, the time scale of the variation of the electrode potential can be changed by variation of the capacitance of the electrode.

The idea of differential controller, taken from engineering practice [18], is the following. According to previous considerations (Sect. 1.6), the n -dimensional dynamical system can be defined in terms of a set of ODEs:

$$\varepsilon_k \frac{dx_k}{dt} = f_k(x_1, x_2, \dots, x_n); \quad k = 1, \dots, n \quad (2.62)$$

in which ε_k defines the time scale for the variation of the k -th variable. Then, introducing a differential controller with the feedback strength α_k means the following extension of the above ODE:

$$\varepsilon_k \frac{dx_k}{dt} = f_k(x_1, x_2, \dots, x_n) + \alpha_k \frac{dx_k}{dt} \quad (2.63)$$

or, equivalently:

$$(\varepsilon_k - \alpha_k) \frac{dx_k}{dt} = f_k(x_1, x_2, \dots, x_n) \quad (2.64)$$

The latter equation means that, compared to Eq. (2.62), the time scale of variable x_k can be modified by varying α_k , keeping ε_k constant. In other words, the time scale of x_k variable is now defined by $\varepsilon_k' = \varepsilon_k - \alpha_k$. The parameters of the steady-states are the same, since they remain determined by the same condition: $f(x_1, x_2, \dots, x_n) = 0$, only their stability may change. Application of this strategy to an electrochemical system will be described for the prototypical case of the NDR system,

defined by the charge conservation principle [Eq. (2.10)], expressed here in the equivalent form:

$$C_d \frac{dE}{dt} = -j_f(c, \theta, E, \dots) + \frac{U - E}{AR_s} \quad (2.65)$$

where the faradaic current density j_f is generally dependent on the concentration c , electrode coverage θ , and electrode potential E .

In order to achieve the appropriate differential control of the electrode potential E , the external voltage U treated as the control parameter was varied around the value U_0 according to the following dependence:

$$U = U_0 + \gamma \frac{dU}{dt} - \gamma R_s \frac{di}{dt} = U_0 + \gamma \frac{dU}{dt} - \gamma R_s \frac{d}{dt} \left(\frac{U - E}{R_s} \right) = U_0 + \gamma \frac{dE}{dt} \quad (2.66)$$

where γ is the control gain. Substitution of U in Eq. (2.65) with Eq. (2.66) leads to the following dependence:

$$\left(C_d - \frac{\gamma}{AR_s} \right) \frac{dE}{dt} = -j_f(c, \theta, E, \dots) + \frac{U - E}{AR_s} \quad (2.67)$$

where the term in bracket: $-\gamma/(AR_s) = C_d^*$ acts as a specific pseudo-capacitance. Then, $C_d + C_d^*$ plays the same role as the new time scale $\varepsilon_k' = \varepsilon_k - \alpha_k$ in Eq. (2.64).

The procedure designed according to this philosophy was tested for the three well-known electrochemical oscillators: (1) the electrodisolution of Cu in H_3PO_4 solution, (2) the electrodisolution of Ni in H_2SO_4 solution, and (3) the electrodeposition of Zn in acidic electrolyte, both by simulation based on theoretical models and in experimental studies. Since Cu/ H_3PO_4 and Ni/ H_2SO_4 systems are described in Chap. 6, here we use Zn electrodeposition, characterized with S-shaped NDR region, as an example demonstrating the successful application of the above differential control. In the simulations, the model of Lee and Jorné [19], extended for the implementation of IR_s drops through the electrolyte and a serial external resistance, was used. The existence of oscillations required sufficiently high C_d values (of the order of 1 F cm^{-2}) and then, upon decreasing cathodic overpotential, the oscillations were born through a supercritical Hopf bifurcation and ceased via a saddle-node bifurcation of cycles (following a subcritical Hopf bifurcation). All these features of the model are collected in Fig. 2.12.

In the experiment, current oscillations during Zn electrodeposition were induced by using the differential control algorithm such that pseudo-capacitance of the order of few Farads was generated, in good concordance with the simulations (Fig. 2.13). For the original, non-driven system the electrode potential is too a fast variable, to ensure the oscillations. One should slow down this variable to induce the instability.

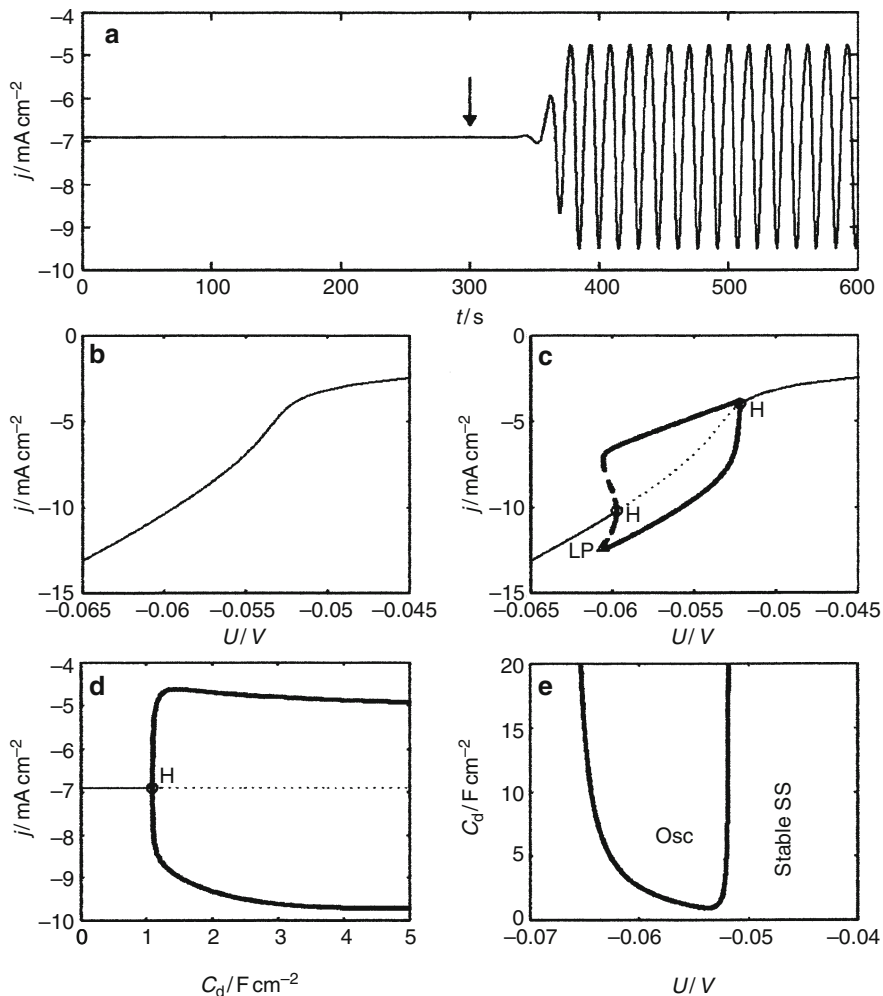


Fig. 2.12 Simulations: effect of changing the time scale associated with the electrode potential on current oscillations in Zn electrodeposition (S-NDR system). (a) Inducing oscillations at $U = -55$ mV by increasing the value of C_d from $2.5 \mu\text{F cm}^{-2}$ to 2.5F cm^{-2} at $t = 300$ s (shown by an arrow). (b) Bifurcation diagram at $C_d = 2.5 \mu\text{F cm}^{-2}$ as a function of U . (c) Bifurcation diagram at $C_d = 2.5 \text{F cm}^{-2}$ as a function of U . LP: saddle-node bifurcation of a periodic orbit. (d) Bifurcation diagram at $U = -55$ mV as a function of C_d . (e) Two-parameter bifurcation diagram showing the locus of Hopf bifurcations. Reprinted with permission from [16]. Copyright 2005 American Chemical Society

Of course, if applying the differential controller on particular variable did not affect the oscillations, this variable would be termed the *non-essential* one. The same way of diagnosis could be applied for the controller that would affect the time scale of the variation of surface concentration of the species, or the electrode coverage, for another experimental system.

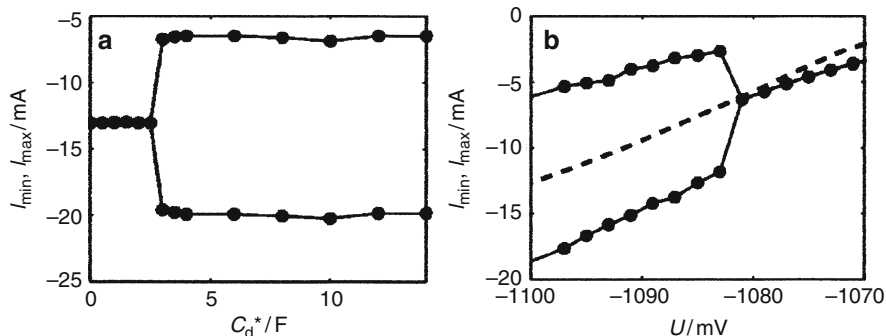


Fig. 2.13 Experiments: effect of changing the time scale associated with the electrode potential on current oscillations in Zn electrodeposition (S-NDR system). (a) One-parameter bifurcation diagram at $U_0 = -1,100$ mV and $R_s = 9.7 \Omega$ showing the minima and maxima of current oscillations as a function of the pseudo-capacitance C_d^* . (b) One-parameter bifurcation diagrams at $R_s = 9.7 \Omega$ with respect to the circuit potential (external voltage) U : dashed line, $C_d^* = 0$ F, solid line, $C_d^* = 20.0$ F. Reprinted with permission from [16]. Copyright 2005 American Chemical Society

The application of the above diagnostic procedure to the classification of the electrochemical oscillators is described in Sect. 3.5.

2.4 Frequency of Oscillations in the N-NDR Systems

In Sect. 1.3.3 the abstract model of the supercritical Hopf bifurcation [Eqs. (1.60) and (1.61)] allowed to find the frequency of oscillations in the vicinity of the point of that bifurcation. The problem of frequency of the oscillations is important for the timing processes in biological systems, in particular with respect to the *temperature compensation* effect, meaning the mechanism which ensures the functioning of physiological clocks independently of environmental temperature changes, i.e., opposite to Arrhenius-type, exponential rise on rate constants with temperature. The relevant studies were published both for chemical [20–22] and electrochemical [23–25] oscillators (see also Sect. 5.4).

Recently, Kiss et al. [26] have derived an approximate formula for the frequency of oscillations in electrochemical systems, close to the supercritical Hopf bifurcation point. Both N-NDR and HN-NDR type systems were considered. For the N-NDR case, the typical skeleton model of Koper and Sluyters (2.29, 2.31) [9] was used for theoretical considerations. The oscillation frequency at the point of supercritical Hopf bifurcation, where $\text{Tr}(\mathbf{J}) = 0$ and $\text{Det}(\mathbf{J}) > 0$, is generally equal to square root of the determinant of the corresponding Jacobian matrix [27] (cf. Sect. 1.3.3):

$$\omega^* = \sqrt{\text{Det}(\mathbf{J})} \quad (2.68)$$

In the case of the model electrochemical process considered here one substitutes for $\text{Det}(\mathbf{J})$ the expression (2.34). A particularly convenient equivalent expression is obtained after combination of expressions for $\text{Det}(\mathbf{J})$ and $\text{Tr}(\mathbf{J})$ [Eqs. (2.33) and (2.34)]:

$$\text{Det}(\mathbf{J}) = \frac{2k(E_{ss})}{\delta C_d R_s A} - \frac{4k(E_{ss})}{\delta^3} - \frac{4D_o^2}{\delta^4} \quad (2.69)$$

where k is the potential-dependent heterogeneous rate constant of the electron transfer at the working electrode–solution interface. If one recognizes that particular terms in Eq. (2.69) reflect three major important time scales, the frequency ω^* may be expressed as a combination of frequencies corresponding to inverse time scales of the chemical, electrical, and diffusional processes, ω_c , ω_e and ω_D :

$$\omega^* = \sqrt{\frac{2k(E_{ss})}{\delta C_d R_s A} - \frac{4k(E_{ss})D_o}{\delta^3} - \frac{4D_o^2}{\delta^4}} = \sqrt{\omega_c \omega_e - \omega_D(\omega_c + \omega_D)} \quad (2.70)$$

where:

$$\omega_c = \frac{2}{\delta} k(E_{ss}) \quad (2.71)$$

$$\omega_e = \frac{1}{C_d R_s A} \quad (2.72)$$

$$\omega_D = \frac{2D}{\delta^2} \quad (2.73)$$

Since for the N-NDR systems the electrode potential is a fast variable (cf. Sect. 2.2.4), this means that $\omega_e \gg \omega_c, \omega_D$ and the dependence [Eq. (2.70)] can be simplified to the following form:

$$\omega^* \approx \sqrt{\omega_c \omega_e} = \sqrt{\frac{2k(E_{ss})}{\delta C_d R_s A}} \quad (2.74)$$

which predicts the frequency of the electrochemical oscillations as the geometric mean of the inverse electrical and chemical time scales. For strict interpretation one should note that in these final dependences the frequency ω is expressed in Hz (usually denoted rather by f), and not in rad s^{-1} [26]. Numerical calculations performed for the three-variable, dimensionless Koper–Gaspard model [28], used here to simulate the copper electrodisolution in phosphoric acid, confirmed the validity of the above derivations and simplifications. Similar results were obtained for experimental studies of the potentiostatic, oscillatory electrodisolution of Cu in phosphoric acid, at least in majority of the range of serial resistance studied.

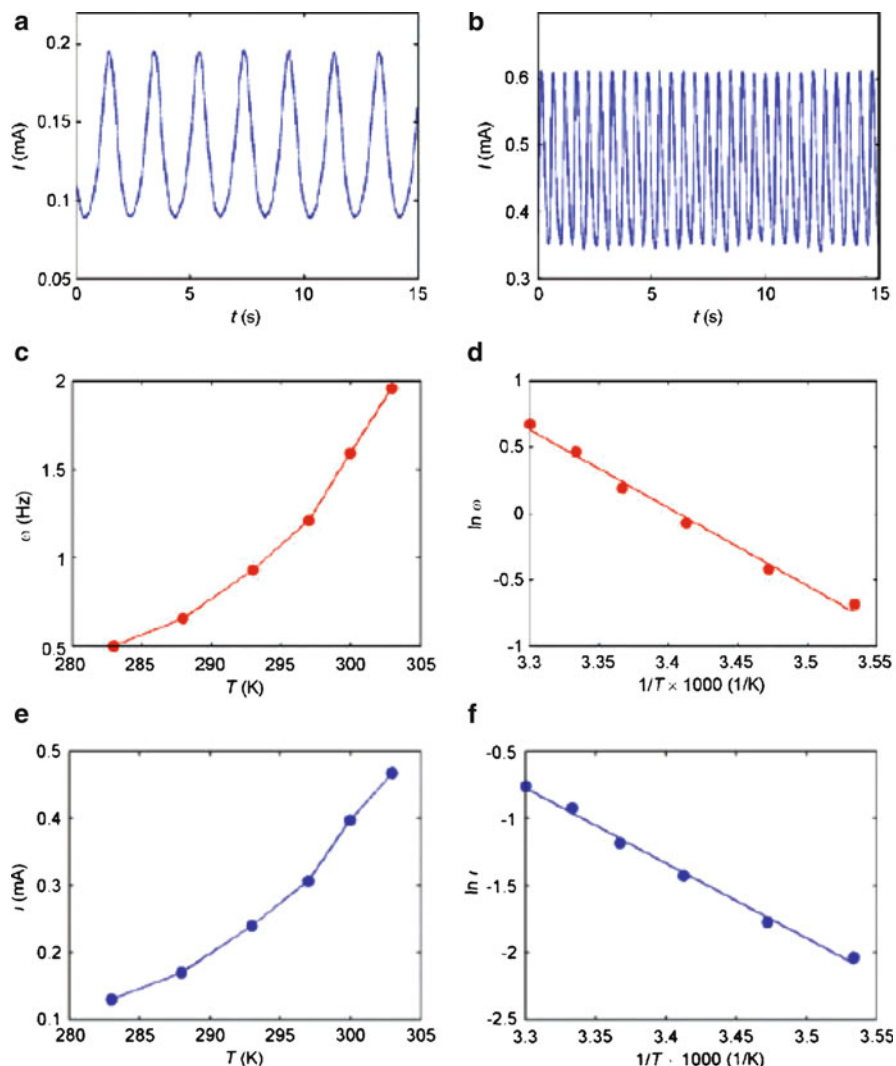


Fig. 2.14 Experiments: frequency dependence on temperature in an HN-NDR system of nickel dissolution. (a) Time series of current oscillations at $T = 10\text{ }^\circ\text{C}$, $R_s = 600\ \Omega$, $U = 1075\text{ mV}$, $\omega = 0.505\text{ Hz}$. (b) Time series of current oscillations at $T = 30\text{ }^\circ\text{C}$, $R_s = 600\ \Omega$, $U = 1,210\text{ mV}$, $\omega = 1.960\text{ Hz}$. (c) The dependence of frequency of current oscillation (at the onset of oscillations) on temperature, $R_s = 600\ \Omega$. (d) Arrhenius plot of frequency of current oscillations vs. temperature, $E_{\text{act}} = 49\text{ kJ mol}^{-1}$. (e) The dependence of mean current (at the onset of oscillations) on temperature, $R_s = 600\ \Omega$. (f) Arrhenius plot of mean current vs. temperature, $E_{\text{act}} = 46\text{ kJ mol}^{-1}$ [26]. Reproduced by permission of the PCCP Owner Societies

Analogous analysis was performed for the appropriate skeleton model of the HN-NDR oscillator and theoretical predictions on the oscillations were successfully verified through comparison with the experimental characteristics of Ni

electrooxidation in aqueous sulfuric acid medium. For details of this approach and the discussion of the above-given result the reader is advised to consult the original reference [26].

Concerning the effect of temperature on the oscillation frequency, which could be interpreted in terms of Eq. (2.70), one should note that the double layer capacitances and the Nernst diffusion layer thickness are relatively weakly dependent on temperature, compared to variations of the rate constant of the electron-transfer process, for which the Arrhenius-type kinetic law should hold. This prediction was quantitatively confirmed by the experimental studies of the effect of temperature on the oscillatory electrodisolution of Ni in H₂SO₄ medium (see Fig. 2.14). The apparent Arrhenius activation energy determined from frequency variations (46 kJ mol⁻¹) was very close to the activation energy 49 kJ mol⁻¹ calculated from the mean oscillating current (approximately equal to the mean current at the Hopf bifurcation point).

In conclusion, the Arrhenius-type dependence of oscillation frequency on temperature is a direct consequence of the $\omega \propto (k(E)/R_s)^{1/2}$ relationship. It should be noted that in spite of complexity of real oscillatory systems, all the above derived dependences are quite simple. This is because close to the bifurcation point the mathematical structure of the oscillatory system's dynamics is greatly simplified. This is the manifestation of the so-called *Principle of critical simplification* (PCS) which was also applied in the interpretation of temperature effects in the oscillatory catalytic oxidation of CO [29]. Finally, one can also suggest that the dependence [Eq. (2.70)] can be applied in an opposite way—as the source of approximate values of rate constants, determined from the oscillation frequency measurements at different resistances. It can be a useful approach, since within the oscillatory (instability) region, classical electrochemical methods are not able to provide direct kinetic parameters. Of course, they have then a physical sense of rather apparent (effective) rate constants of the usually multistep reaction mechanism [26]. The problem of frequency of HN-NDR oscillator is developed further in recent work by Kiss et al [30].

References

1. Gerischer H (1958) Passivität der Metalle. *Angew Chem* 10:285–298
2. Koper MTM, Sluyters JH (1993) On the mathematical unification of a class of electrochemical oscillators and their design procedures. *J Electroanal Chem* 352:51–64
3. Frumkin AN (1933) Wasserstoffüberspannung und Struktur der Doppelschicht. *Z physik Chem* 164A:121–133
4. Bard AJ, Faulkner L (2001) *Electrochemical methods. Fundamentals and applications*. Wiley, New York, pp 571–572
5. Śledziewski R (1978) *Electronics for the physics students*. PWN, Warsaw (in Polish), p 170
6. Feldberg SW (1969) Digital simulation: a general method for solving electrochemical diffusion-kinetic problems. In: Bard AJ, Rubinstein I (eds) *Electroanalytical chemistry*, vol 3. Dekker, New York, pp 199–296

7. Speiser B (1996) Numerical simulation of electroanalytical experiments: recent advances in methodology. In: Bard AJ, Rubinstein I (eds) *Electroanalytical chemistry*, vol 19. Dekker, New York, pp 1–108
8. Britz D (2005) *Digital simulation in electrochemistry*, 3rd edn. Springer, Berlin
9. Koper MTM, Sluyters JH (1991) Electrochemical oscillators: their description through a mathematical model. *J Electroanal Chem* 303:73–94
10. Krischer K (1999) Principles of temporal and spatial pattern formation in electrochemical systems. In: Conway BE et al (eds) *Modern aspects of electrochemistry*, vol 32. Kluwer, New York
11. Koper MTM (1992) The theory of electrochemical instabilities. *Electrochim Acta* 37:1771–1778
12. Krischer K (2001) Spontaneous formation of spatiotemporal patterns at the electrode/electrolyte interface. *J Electroanal Chem* 501:1–21
13. Krischer K, Mazouz N, Flätgen G (2000) Pattern formation in globally coupled electrochemical systems with an S-shaped current–potential curve. *J Phys Chem B* 104:7545–7553
14. Mazouz N, Krischer K (2000) A theoretical study on Turing patterns in electrochemical systems. *J Phys Chem* 104:6081–6090
15. Epelboin I, Ksouri M, Lejay E, Wiart R (1975) A study of the elementary steps of electron-transfer during the electrocrystallization of zinc. *Electrochim Acta* 20:603–605
16. Kiss IZ, Kazsu Z, Gáspár V (2005) Experimental strategy for characterization of essential dynamical variables in oscillatory systems: effect of double-layer capacitance on the stability of electrochemical oscillators. *J Phys Chem A* 109:9521–9527
17. Clarke BL (1980) Stability of complex reaction networks. *Adv Chem Phys* 42:1–213
18. Stephanopoulos G (1984) *Chemical process control: an introduction to theory and practice*. Prentice Hall, Englewood Cliffs, NJ
19. Lee MG, Jorné J (1992) On the kinetic mechanism of zinc electrodeposition in the region of negative polarization resistance. *J Electrochem Soc* 139:2841–2844
20. Burger M, Körös E (1980) Conditions for the onset of chemical oscillation. *J Phys Chem* 84:496–500
21. Ruoff E (1992) Introducing temperature-compensation in any reaction kinetic oscillator model. *J Interdiscip Cycle Res* 23:92–99
22. Ruoff P, Loros JJ, Dunlap JC (2005) The relationship between FRQ-protein stability and temperature compensation in the *Neurospora* circadian clock. *Proc Natl Acad Sci USA* 102:17681–17686
23. Nagao R, Epstein IR, Gonzalez ER, Varela H (2008) Temperature (over)compensation in an oscillatory surface reaction. *J Phys Chem A* 112:4617–4624
24. Carbonio EA, Nagao R, Gonzalez ER, Varela H (2009) Temperature effects on the oscillatory electro-oxidation of methanol on platinum. *Phys Chem Chem Phys* 11:665–670
25. Zhang JX, Datta R (2002) Sustained potential oscillations in proton exchange membrane fuel cells with PtRu as anode catalyst. *J Electrochem Soc* 149:A1423–A1431
26. Kiss IZ, Pelster LN, Wickramasinghe M, Yablonsky GS (2009) Frequency of negative differential resistance electrochemical oscillators: theory and experiments. *Phys Chem Chem Phys* 11:5720–5728
27. Strogatz SH (1994) *Nonlinear dynamics and chaos*. Perseus, Reading, MA
28. Koper MTM, Gaspard P (1992) The modeling of mixed-mode and chaotic oscillations in electrochemical systems. *J Chem Phys* 96:7797–7813
29. Yablonsky GS, Mareels IMY, Lazman M (2003) The principle of critical simplification in chemical kinetics. *Chem Eng Sci* 58:4833–4842
30. Kiss IZ, Sitta E, Varela H (2012) On the limit of frequency of electrochemical oscillators and its relationship to kinetic parameters. *J Phys Chem C* 116:9561–9567

Chapter 3

Application of Impedance Spectroscopy to Electrochemical Instabilities

3.1 Outline Concept of Impedance of Electrochemical Systems

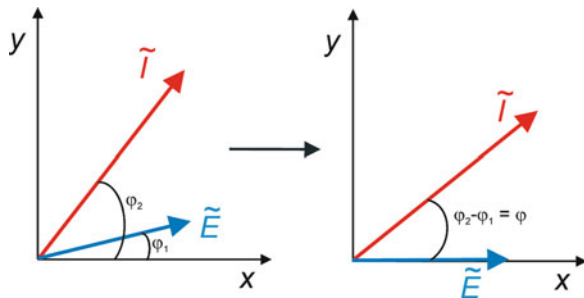
3.1.1 Basic Definitions

Electrochemical impedance spectroscopy (EIS), a well-established technique in classical electrochemistry [1], can also be very useful for the analysis of stability of electrochemical systems, including diagnosis of selected bifurcations. Impedance spectra of such dynamical systems allow also classify electrochemical oscillators into respective types. In fact, due to linearization involved in the concept of impedance, this way of the stability analysis of electric (electrochemical) circuits is a specific variant of linear stability analysis described in Sect. 1.3.

In this section a short presentation of the principle of impedance measurements is described, in order to make the reader familiar with the notation used further in this chapter. The basis for this summary will be typical (Randles-type) equivalent circuit from Fig. 2.6, in which Z_f will henceforth mean generally the ac impedance, measured for ac frequency f [Hz] (or angular frequency $\omega = 2\pi f$ [rad s⁻¹]). The idea of such equivalent circuits, coming from the seminal work of Randles [2], was concordant with the experimental equipment used in early times of impedance measurements. It involved the ac bridge, in which one branch contained the experimental system, the impedance characteristics of which had to be balanced, in the other branch, by the impedance of the electric (equivalent) circuit, possibly closely reflecting the properties of the experimental one.

Typically the electrochemical cell is first brought into steady-state, or at least quasi-steady-state (E_{ss} , I_{ss}) which is further perturbed with the externally applied small amplitude, sinusoidal ac voltage (typically) or ac current. As a consequence, the electrode potential E and the current I will oscillate around their steady-state values with the same frequency ω , but in general case exhibiting (frequency dependent) phase difference. In general notation one can denote the phase shifts for both the electrode potential and the current as φ_1 and φ_2 , respectively, and then:

Fig. 3.1 Representation of phasors \tilde{E} and \tilde{I} on the complex plane plot, with the phase difference $\varphi_2 - \varphi_1$ between them (based on [3])



$$E = E_{ss} + \Delta E_{\max} \exp[j(\omega t + \varphi_1)] = E_{ss} + \Delta E_{\max} \exp(j\varphi_1) \exp(j\omega t) \quad (3.1)$$

$$I = I_{ss} + \Delta I_{\max} \exp[j(\omega t + \varphi_2)] = I_{ss} + \Delta I_{\max} \exp(j\varphi_2) \exp[j(\omega t)] \quad (3.2)$$

where $j = \sqrt{-1}$. The geometrical interpretation of these relationships, in terms of the coordinate system, consisting of real axis x and imaginary axis y , involves the phasors of the potential \tilde{E} and of current \tilde{I} , respectively [3]:

$$\tilde{E} = \Delta E_{\max} \exp(j\varphi_1) \quad (3.3)$$

$$\tilde{I} = \Delta I_{\max} \exp(j\varphi_2) \quad (3.4)$$

while the term $\exp[j(\omega t)]$ describes the rotation of these vectors with angular frequency ω . Dependences (3.1)–(3.4) describe thus vectors of the length ΔE_{\max} and ΔI_{\max} , which rotate with the same rate ω and a constant phase difference $\varphi_2 - \varphi_1$. If phase shift φ_1 is assumed as the reference value, then the above formulas simplify by involving explicitly only phase difference $\varphi = \varphi_2 - \varphi_1$ between the current and the potential responses (see Fig. 3.1).

It is here useful to invoke the concept of a *transfer function* that is a mathematical representation of the relation between the input and output of a linear, time-invariant system. Simply speaking, transfer function transfers one signal into another. Thus, when the current is the stimulus and the potential is the response signal, this is the impedance which is the transfer function. In other words, impedance is the direct information obtained from the ac experiment under galvanostatic conditions. In turn, the transfer function for the potentiostatic experiment is admittance Y (which mean generalized conductivity), i.e., when the potential is the stimulus and the current is the response signal.

The impedance Z is defined as the ratio of phasors:

$$Z = \frac{\tilde{E}}{\tilde{I}} = \frac{\Delta E_{\max}}{\Delta I_{\max}} \exp[-j(\varphi_2 - \varphi_1)] = \frac{\Delta E_{\max}}{\Delta I_{\max}} \exp(-j\varphi) = |Z| \exp(-j\varphi) \quad (3.5)$$

where $\varphi = \varphi_2 - \varphi_1$. In view of Euler's formula: $\exp(j\varphi) = \cos(\varphi) + j\sin(\varphi)$, expression (3.5) is equivalent to $Z = |Z|\cos(\varphi) - j|Z|\sin(\varphi) = Z' - jZ''$. One should note that in many cases the definition of impedance is taken as

$$Z = |Z| \cos(\varphi) + j|Z| \sin(\varphi) = Z' + jZ'' \quad (3.6)$$

and we shall use this notation onwards, keeping in mind that the change of convention reverses the sign of the imaginary part of impedance (cf. e.g., [23]). In terms of Eq. (3.6), one separates the total impedance Z into the real part $Z' \equiv \text{Re}(Z) = |Z| \cos(\varphi)$ and the imaginary part $Z'' \equiv \text{Im}(Z) = |Z| \sin(\varphi)$, with $\varphi = \arctan(Z''/Z')$. Of course, the term “imaginary” refers only to the mathematical notation of the complex number, because both components of impedance are measurable. The impedance spectrum is often constructed in a coordinate system $Z'-Z''$, called a complex plane (known also as Nyquist, or complex plane plot). In classical electrochemistry, when the imaginary impedance is often related to the capacitive contribution and therefore attains negative values ($Z'' = -1/\omega C$), it is plotted on the imaginary axis as positive $-Z''$ values. Then, if Z' is only positive [i.e., the system does *not* exhibit the negative differential resistance (NDR)], the typical Nyquist diagram is located in the first quadrant of the Z' vs. ($-Z''$) complex plane. It is thus clear that the systems of our interest, with NDR, will exhibit qualitatively different spectra, which will penetrate also other quadrants of the Z' vs. ($-Z''$) complex plane.

In terms of Eq. (3.5), the admittance Y is defined as

$$Y = \frac{1}{|Z|} \exp(j\varphi) \quad (3.7)$$

So the vector of admittance has a magnitude $1/|Z|$ and the phase shift the same as for $|Z|$, but with the opposite sign. In terms of the complex notation, the real and imaginary components of admittances can be explicitly calculated from the respective components of the impedance:

$$Y' = \frac{Z'}{(Z')^2 + (Z'')^2} \quad (3.8)$$

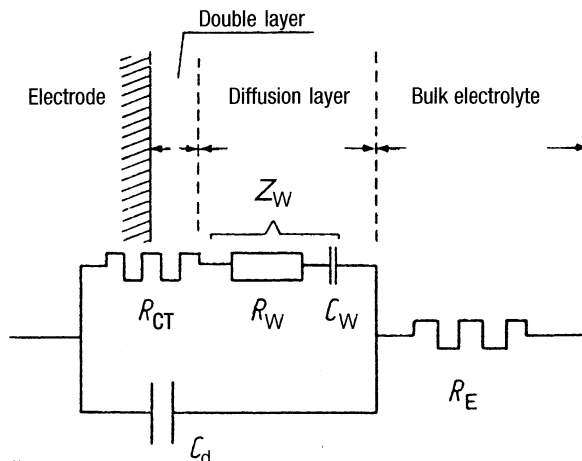
$$Y'' = \frac{Z''}{(Z')^2 + (Z'')^2} \quad (3.9)$$

Admittance Y is also useful if the equivalent circuit includes *parallel* connection of impedances Z_1, Z_2 , etc., as the total admittance of the parallel components is simply a sum of their individual admittances.

Modern electrochemical equipment allows to determine both admittance and impedance from the same measurement, but, as will be shown below in the discussion of the Kramers–Kronig transformation, in the analysis of nonlinear electric circuits one has to make an appropriate choice between the admittance and impedance data.

The interfacial impedance Z consists of contributions from the double layer capacitance and the faradaic impedance Z_f . In turn, the faradaic impedance consists of the (purely real) charge-transfer resistance R_{ct} (closely related to the rate constant of the electron-transfer at the interface) and of the (complex) Warburg impedance Z_W ,

Fig. 3.2 Equivalent ac circuit for a half-cell. R_{ct} is the electron-transfer resistance, $Z_w = R_w + 1/j\omega C_w$ is the Warburg impedance, R_E is the electrolyte resistance and C_d is the double layer capacitance [4]. Copyright Wiley-VCH Verlag GmbH & Co. KGaA. Reproduced with permission



expressing the limited rate of the reactant transport (e.g., diffusion) toward the electrode–solution interface. For the Ox + ne → Red process the charge-transfer (or activation) resistance R_{ct} is defined as

$$R_{ct}^{-1} = \left(\frac{\partial I_f}{\partial E} \right)_{c_{ox}(0), c_{red}(0)} = nFA \left[c_{red}(0) \frac{dk_b}{dE} - c_{ox}(0) \frac{dk_f}{dE} \right] \quad (3.10)$$

where $c_{ox}(0)$ and $c_{red}(0)$ mean the steady-state (time-independent) “surface” concentrations of Ox and Red species, which undergo reduction with the rate constant $k_f(E)$ and oxidation with the rate constant $k_b(E)$, respectively. Figure 3.2 illustrates the physical sense of the above quantities, for the case when the serial resistance R_s of the circuit is here due to the electrolyte resistance R_E .

For the case of highly irreversible electrode process, when the limitation from the mass-transfer rate do not manifest themselves (which is the case also for high reagents concentration), the Nyquist plot for the wide range of ω attains a shape of a semicircle. This shape is justified by the following reasoning, in view of the circuit shown in Fig. 3.2. For infinite ω , the double layer capacitance has zero impedance, so the cell impedance is entirely reduced to the real electrolyte resistance R_E . On the contrary, when $\omega \rightarrow 0$, the impedance of the double layer increases to infinity, so the current can flow only through the serial connection of $R_E + R_{ct} + Z_w$, constituting then the entirely real (in this irreversible case) cell impedance. For the region of intermediate frequencies ω , the current flows through both R_{ct} and double layer capacitance, the latter one exhibiting then finite imaginary impedance which passes through a maximum for $\omega = (R_{ct}C_d)^{-1}$.

When the electrode process is fast or the concentration of electroactive species is finite, the limitations from the mass-transport rate also manifest themselves. The presence of the mass-transport impedance Z_{mt} (called the Warburg impedance Z_w in the case of diffusion) comes from the variation of the concentration profiles in the diffusion layer adjacent to the electrode. The periodically changing electrode

potential induces the oscillations of the surface concentrations of Ox and Red around the steady-state values. If the electrode process is fast and reversible, then these concentration changes are relatively significant and propagate into the diffusion layer, with the amplitude decaying as a function of the distance from the electrode surface. Just this concentration polarization is a source of the Warburg impedance which is generally a complex function, i.e., the periodic variations of concentrations can exhibit phase shift with respect to the periodic variation of imposed ac perturbation. The extent of the propagation of the perturbation of the diffusion layer depends also on the frequency ω of the applied ac voltage: with increasing ω the propagation of [Ox] and [Red] perturbations into the bulk of the solution becomes more and more limited. The concentration polarization is then less advanced, and thus the Warburg impedance in the limit $\omega \rightarrow \infty$ becomes insignificant, compared to the charge-transfer resistance R_{ct} . On the contrary, when ω attains low values, the Warburg impedance can become so high that it can take over the dependence of the total impedance on the ac frequency ω . The particular expression for the Warburg impedance, and thus the shape of the Nyquist plot, depends on particular characteristics of a given system, i.e., whether the diffusion can penetrate the solution infinitely (so-called semi-infinite diffusion) or only to certain limit, as in the case of the thin-layer electrolytic systems or for convective diffusion, when the rate of convection determines the steady-state diffusion layer thickness.

The examples of unstable dynamical systems, described in this book, include processes studied at the rotating solid disk or at the streaming liquid (mercury) electrodes, where the thickness of the diffusion layer attains a constant value, dependent on the rotation rate of the disk, or on the velocity of flowing mercury stream, respectively. Furthermore, for the systems exhibiting NDR, the expressions for the impedance of electrode processes obeying the simple Butler–Volmer exponential dependence (cf. e.g., [3, 5]) are not applicable. More general, even if somewhat abstract, relationships between the rate constants of the electron transfer (k_f or k_b) and the electrode potential, implementing the NDR region, have to be invoked. Without invoking now particular mathematical expressions for $k_f(E)$ and $k_b(E)$ one can derive the following general expression for the Warburg impedance:

$$Z_W = \frac{R_{ct}}{\sqrt{j\omega}} \left[\frac{k_f}{\sqrt{D_{ox}}} \tanh \sqrt{\frac{j\omega}{D_{ox}}} \delta + \frac{k_b}{\sqrt{D_{red}}} \tanh \sqrt{\frac{j\omega}{D_{red}}} \delta \right] \quad (3.11)$$

where D_{ox} and D_{red} are respective diffusion coefficients and δ is the thickness of the Nernst diffusion layer. Relationship (3.11) is meaningful for stability considerations because it indicates that the positive or negative (in the case of NDR region) sign of charge-transfer resistance R_{ct} determines the same sign of Z_W . In other words, it is the illustration of a remarkable conclusion formulated already by de Levie et al. [6, 7] (see also Sect. 3.3.2): if the charge-transfer resistance R_{ct} is negative in certain region of potentials, then the Warburg impedance also becomes negative. This means introducing negative capacitance into the equivalent circuit [8]. Of course, if in Eq. (3.11) one assumes the Butler–Volmer dependences for

$k_f(E)$ and $k_b(E)$ relationships, this expression reduces to the typical definition of Warburg impedance for the simple electrode process.

3.1.2 *Kramers–Kronig Transforms and Electrochemical Instabilities*

Prior to the numerical analysis, experimentally obtained impedance data should be verified, whether they meet the following conditions:

1. Linearity—requiring small enough amplitude of ac perturbations
2. Causality—meaning that the obtained response is entirely determined by the applied perturbation
3. Stability—understood as asymptotic stability, i.e., the return of the system to the initial steady-state state when the perturbation is removed
4. Finiteness—meaning that both real and imaginary components of the impedance or admittance must be finite-valued over the entire range $0 < \omega < \infty$; in particular, the impedance must tend to a constant real value for $\omega \rightarrow 0$ and $\omega \rightarrow \infty$, and also the impedance function must be continuous [3, 9]

Whether all these conditions are met for a given system can be verified using the application of Kramers–Kronig transform [10, 11]. Kramers and Kronig first have noticed that if the given system meets the above conditions, there exist strict relationships between the real Z' and imaginary Z'' components of the total impedance, or between the module of impedance vector $|Z|$ and the phase angle. In other words, one can measure, e.g., only Z' , while the imaginary component Z'' can be calculated based on this transform. This has further important consequences, since if the calculated values of Z'' (or Z') overlap with experimentally measured values of Z'' (or Z'), then one can judge that impedance data are reliable, i.e., they meet all the above-given four conditions. The mathematical expressions for the Kramers–Kronig transforms are given by [10–12]

$$Z''(\omega) = Z''(\infty) + \frac{2}{\pi} \int_0^{\infty} \frac{xZ'(x) - \omega Z''(\omega)}{x^2 - \omega^2} dx \quad (3.12)$$

$$Z'(\omega) = Z'(0) + \frac{2\omega}{\pi} \int_0^{\infty} \frac{\frac{\omega}{x} Z''(x) - Z''(\omega)}{x^2 - \omega^2} dx \quad (3.13)$$

$$Z''(\omega) = -\frac{2\omega}{\pi} \int_0^{\infty} \frac{Z'(x) - Z'(\omega)}{x^2 - \omega^2} dx \quad (3.14)$$

$$\varphi(\omega) = \frac{2\omega}{\pi} \int_0^{\infty} \frac{\log|Z(x)|}{x^2 - \omega^2} dx \quad (3.15)$$

$$R_p = Z'(0) - Z'(\infty) = \frac{2}{\pi} \int_0^{\infty} \frac{Z''(x)}{x} dx \quad (3.16)$$

Concerning dependence (3.16), let us note that the difference $Z'(0) - Z'(\infty)$ can be identified with the zero-frequency differential resistance dE/dI (polarization resistance R_p) of the faradaic process; in fact, it is the zero-frequency total impedance decreased for serial (electrolyte) resistance $R_s = Z'(\infty)$. The $Z'(0) - Z'(\infty)$ resistance can thus be determined either directly from the real components of the impedance at extreme ac frequencies or from only its imaginary component [12]. The valuable commercial software for the analysis of impedance data usually contains built-in procedures for the Kramers–Kronig (KK) transform.

At this point one has to realize an important problem with the application of the Kramers–Kronig (KK) transform to the analysis of impedance data for the nonlinear electric circuits. As indicated by Sadkowski et al. [13], Tyagai and Kolbasov in their work published in Soviet journal *Elektrokhimiya* in 1972 (vol. 8, p. 59) have suggested that KK transform might appear inapplicable to unstable systems, including the oscillatory ones. This problem caused a long-year discussion, including the work by Gabrielli et al. [14], whether the impedance data for the systems with a NDR can at all be validated in terms of the KK transformation. For concise review of various proposals, cf. paper by Sadkowski et al. [13]. In this and also in more recent work by Sadkowski [15] the principal conclusion was formulated: if the parameters of ac measurements of such systems, performed under potentiostatic conditions, approach the region in which, under galvanostatic conditions, the Hopf bifurcation would occur, the Kramers–Kronig transform can be successfully applied, if not the impedance, but the *admittance* data are taken to such analysis. This is because the impedance data correspond directly to the galvanostatic mode of operation (the impedance is then the transfer function), for which the system is unstable due to the Hopf bifurcation occurring under these conditions. As a consequence of this instability, the impedance data are not suitable for the KK analysis.

3.2 The Impedance of the Streaming Mercury Electrode

In the previous section it was mentioned that if the process occurs at the mercury electrode, the true-steady state can be achieved under conditions of the streaming version of such electrode. While the impedance characteristics of the rotating solid disk electrodes have been extensively described in several works (cf. e.g., [3] and references cited therein), for the streaming mercury electrode only introductory studies were published by Ijzermans et al. [16–18]. The subject has been only recently undertaken by Jurczakowski and Orlik [19], in relation to impedance studies of in the $\text{Ni(II)}\text{-SCN}^-$ [20] and $\text{Ni(II)}\text{-N}_3^-$ [21] electroreduction at such electrodes. The detailed construction and application of the streaming electrode to

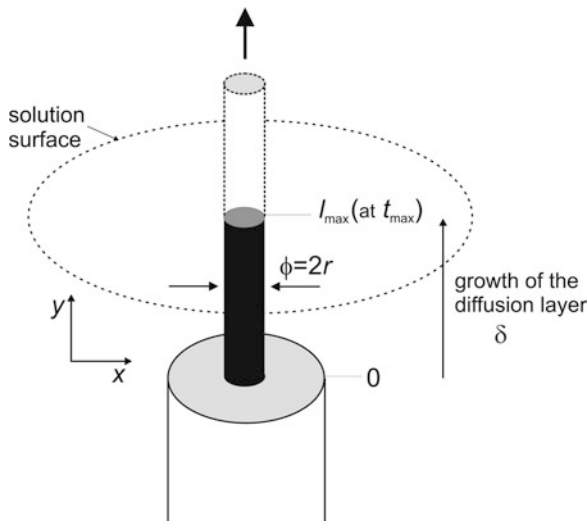


Fig. 3.3 The schematic picture of the geometry of the idealized streaming electrode directed upward toward the solution surface. The mercury stream of a diameter $\phi = 2r$ leaves the orifice of the glass capillary at $y = 0$ and flows along the y direction with the velocity $v = m/\pi r^2 \rho_{\text{Hg}}$, where m is the capillary flow and the density of mercury $\rho_{\text{Hg}} = 13.6 \text{ g cm}^{-3}$. In the absence of the electroactive species (the case studied in this paper) only the capacitive current flows which charges the entire electrode surface $A = 2\pi r l_{\text{max}}$ to the imposed potential E . In the presence of the electroactive species the electrolysis time of the solution (and the corresponding thickness of the diffusion layer) would rise from zero (at $y = 0$) to t_{max} at the geometrical maximum length ($y = l_{\text{max}}$) of the mercury stream. Reprinted from [19], Copyright 2004, with permission from Elsevier

study electrochemical instabilities in these processes is described in Chap. 4, while here only its unique impedance characteristics will be described. The idealized geometry of such an electrode is sketched in Fig. 3.3.

The unique impedance response of the streaming electrode is clearly visible on the Nyquist diagram for the pure solution of the *electrochemically inert* (in the studied potential region) electrolyte, as, e.g., 0.1 M NaF, the ions of which do not adsorb specifically on the mercury surface (Fig. 3.4).

Evidently, although the semicircular Nyquist plot looks like the one of the slow faradaic process, such interpretation is not possible due to the lack of any electroactive species in the studied sample. The source for such an “apparent faradaic” impedance response of the streaming electrode must be a capacitive current. More precisely, this is that part of a total capacitive current which flows permanently even at steady-state potential, since new portions of mercury appearing at the orifice of glass capillary (cf. Fig. 3.3) have to be charged to this imposed potential. Under dc conditions, the steady-state capacitive current is described, according to Delahay [22] with the following dependence:

$$I_{c,1} = I_{c,ss}(E) = 2\pi r K(E) \times (E - E_{\text{pzc}})v \quad (3.17)$$

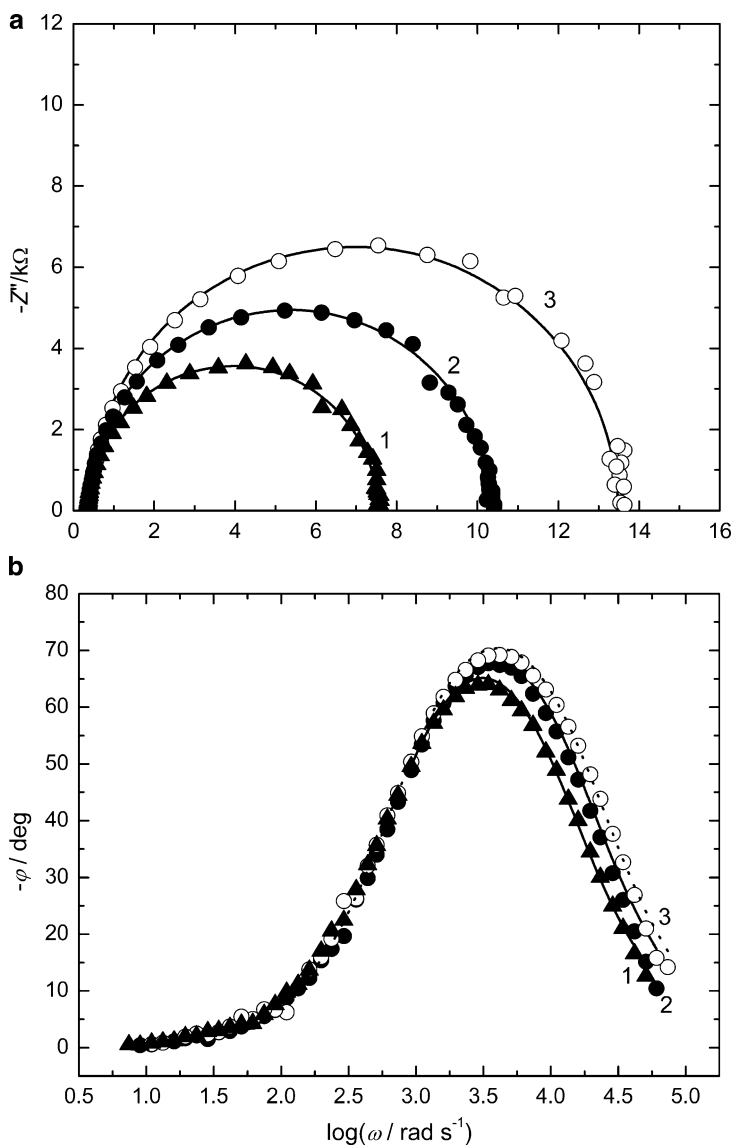


Fig. 3.4 Exemplary experimental (a) Nyquist and (b) phase angle Bode plots determined for 0.1 mol dm^{-3} NaF at the streaming mercury electrode, for different potentials: (1, *filled triangle*) 0 V, (2, *filled circle*) -0.4 V , (3, *open circle*) -0.9 V applied vs. SCE as the reference electrode. The corresponding *continuous lines* (1, 2, 3) were obtained from fitting, to these points, of the resistances R_s , R_d and the *double layer* capacitance C_d^* of the equivalent circuit from Fig. 3.5. Parameters of the streaming electrode: $r = 4.75 \times 10^{-3} \text{ cm}$, $l_{\text{max}} = 1.8 \text{ mm}$, $m = 195 \text{ mg s}^{-1}$ (see also Fig. 3.3 for the explanation of symbols). Reprinted from [19], Copyright 2004, with permission from Elsevier

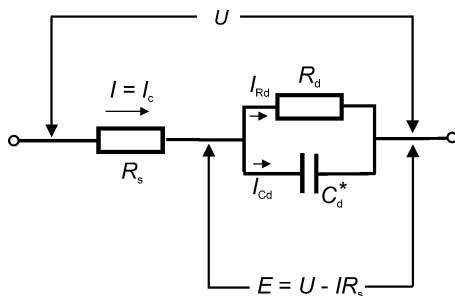


Fig. 3.5 The equivalent circuit for the impedance representation of the flow of the ac capacitive current I_c at the streaming mercury electrode, in the absence of the faradaic process; U —external voltage, R_s —uncompensated ohmic resistance of the solution, C_d^* and R_d —capacity and virtual ohmic resistance associated with the charging of the *double layer* (see text for further explanation). The total capacitive current I_c is divided into the component I_{Rd} that flows through element R_d even at the steady-state potential E_{ss} , and the component I_{Cd} that flows only when the steady-state is perturbed. C_d^* means the actual *double layer* capacitance of the streaming electrode having the surface area A , i.e., $C_d^* \text{ [F]} = C_d \times A$. Reprinted from [19], Copyright 2004, with permission from Elsevier

In Eq. (3.17) $K(E)$ is the *integral* double layer capacitance, expressing the charging of the electrode surface from the potential of zero charge E_{pzc} to the given potential E :

$$K(E) = \frac{1}{E - E_{pzc}} \int_{E_{pzc}}^E C_d(E) dE \quad (3.18)$$

with C_d meaning the differential double layer capacitance (per unit area) at a given potential. The second component of the total capacitive current is the current associated with the perturbation of the electrode potential:

$$I_{c,2} = AC_d \frac{dE}{dt} \quad (3.19)$$

For the formal description of the permanent flow of the capacitive current [Eq. (3.30)], there was introduced the concept of the virtual ohmic resistance R_d which in the equivalent circuit is parallel to the capacitor of the differential double layer capacitance C_d [19]. In Chap. 4 this idea is described for dc conditions of the electrochemical experiment (cf. Fig. 4.47). For ac conditions, discussed here, the relevant equivalent circuit is appropriately simplified, since the virtual cell of the electromotive force E_{pzc} is not necessary (the constant E_{pzc} term vanishes during the differentiation leading to the impedance). If only the inert electrolyte is present in the sample, the flow of only capacitive current can be represented by the circuit shown in Fig. 3.5.

Under ac conditions, the virtual resistor R_d is actually defined in terms of the differential C_d (not the integral K), double layer capacitance, since this resistance is now related to small potential perturbations around the steady-state potential. The expression for R_d is then [19]:

$$R_d^{-1} = \left(\frac{dI_c}{dE} \right)_E = 2\pi r v \frac{d[K(E) \times (E - E_{pzc})]}{dE} = 2\pi r v C_d(E) \quad (3.20)$$

Based on typical, exemplary characteristics of the streaming Hg electrode: $r = 4.75 \times 10^{-3}$ cm, $v = 2.023$ m s $^{-1}$ and double layer capacity in contact with 0.1 M NaF: $C_d = 21.1$ $\mu\text{F cm}^{-2}$ (at $E = -0.4$ V) one calculates the corresponding value of R_d as equal to 7813 Ω .

Using definition of virtual resistance R_d and equivalent circuit from Fig. 3.5, one derives the expression for the complex impedance at given potential E :

$$Z = R_s + \left[\frac{1}{R_d} + \frac{1}{X_c} \right]^{-1} = R_s + [2\pi r C_d v + j2\pi r l_{\max} \omega C_d]^{-1} \quad (3.21)$$

where $X_c = (j\omega C_d)^{-1}$ is the capacitive reactance of the double layer. Equation (3.21) leads further to the explicit expressions for the real (Z') and imaginary (Z'') parts of the total impedance of the circuit from Fig. 3.5:

$$Z' = R_s + \frac{R_d}{1 + 4\pi^2 r^2 l_{\max}^2 \omega^2 C_d^2 R_d^2} = R_s + \frac{v}{2\pi r C_d (v^2 + \omega^2 l_{\max}^2)} \quad (3.22)$$

$$Z'' = \frac{-j2\pi r l_{\max} \omega C_d R_d^2}{1 + 4\pi^2 r^2 l_{\max}^2 \omega^2 C_d^2 R_d^2} = \frac{-j\omega l_{\max}}{2\pi r C_d (v^2 + \omega^2 l_{\max}^2)} \quad (3.23)$$

which also allow to determine the phase angles φ between Z' and Z'' vectors. Theoretical Nyquist and Bode plots, calculated based on these dependences, reveal essentially the same shapes as the corresponding plots of experimental data. Certain quantitative differences were reported for the Nyquist plot, while quite a good concordance was found for the Bode plot (Fig. 3.6). These discrepancies may originate from, larger than theoretical, effective length, and thus also effective surface area of the streaming electrode, since the directed upward mercury streams drags certain portion of the solution above its geometrical surface. Anyway, the semicircular shape of the theoretical Nyquist plot and the dependence of the radius of this semicircle on the electrode potential, caused by the potential dependence of the double layer capacitance, confirms the concept of the purely capacitive origin of the experimental dependences. Analogous shapes of the Nyquist and Bode plots were found for the pure NaClO $_4$ and NaSCN solutions [19].

Based on Eqs. (3.22, 3.23) one can calculate also the following parameters of the Nyquist semicircle in the complex plane:

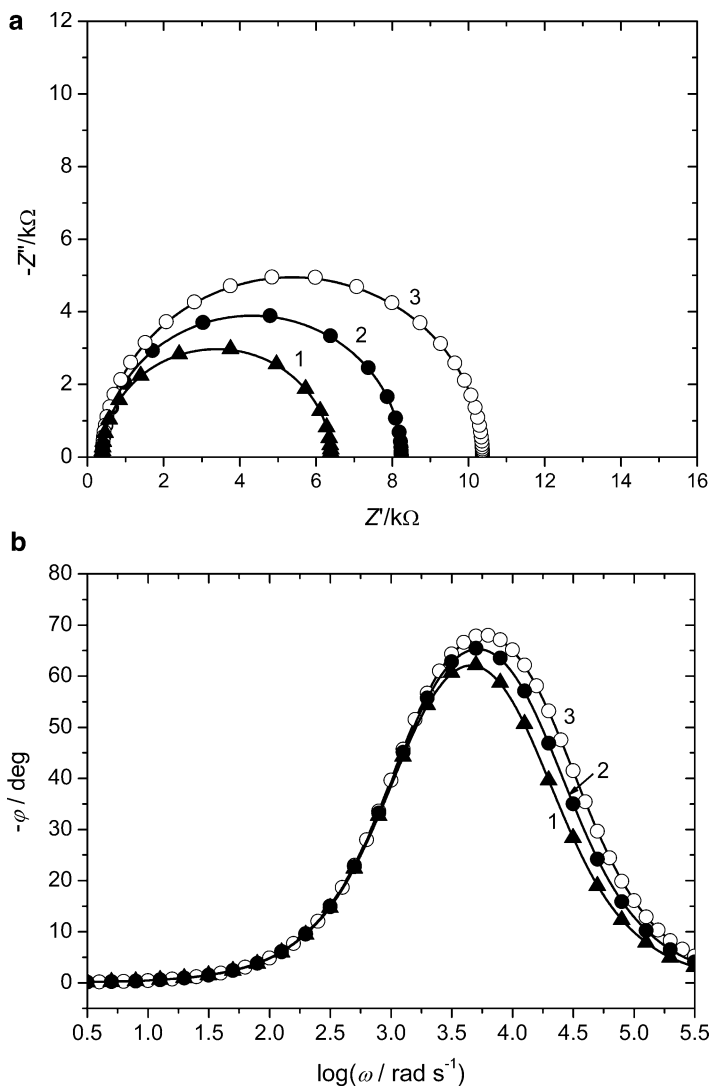
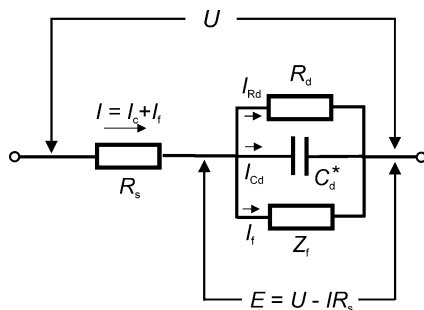


Fig. 3.6 Theoretical (a) Nyquist and (b) phase angle Bode plots for the *capacitive* current at the streaming electrode, in the absence of the faradaic process, constructed from Eq. (3.22, 3.23) for the parameters of the electrode from Fig. 3.3, average solution resistance $R_s = 389 \Omega$ and *double layer* capacitances for 0.1 mol dm^{-3} NaF at different potentials (*filled triangle*, curve 1) $E = 0 \text{ V}$; $C_d = 27.6 \mu\text{F cm}^{-2}$; (*filled circle*, curve 2) $E = -0.4 \text{ V}$; $C_d = 21.1 \mu\text{F cm}^{-2}$ (*open circle*, curve 3) $E = -0.9 \text{ V}$; $C_d = 16.6 \mu\text{F cm}^{-2}$ (cf. experimental diagrams in Fig. 3.4). Reprinted from [19], Copyright 2004, with permission from Elsevier

- The radius of the semicircle, equal to $R_d/2 = 1/(4\pi r C_d \nu)$ which is also the maximum possible imaginary part of impedance;
- The angular frequency ω^* , at which a maximum of Z'' occurs, equal to:

Fig. 3.7 The equivalent circuit from Fig. 3.5, extended for the complex faradaic impedance Z_f associated with the charge-transfer process of the electroactive species at the streaming mercury electrode. Reprinted from [19], Copyright 2004, with permission from Elsevier



$$\omega^* = \frac{1}{R_d C_d A} = \frac{1}{t_{\max}} \quad (3.24)$$

i.e., to the reciprocal value of $t_{\max} = l_{\max}/v$, being a maximum electrolysis time of the solution attained at the maximum length l_{\max} of the streaming electrode (cf. Fig. 3.3); A is the electrode surface area. For example, if $l_{\max} = 1.8$ mm and $v = 2.023$ m s⁻¹, as for Fig. 3.4, then $\omega^* \approx 1124$ rad s⁻¹.

If the faradaic process also occurs at the streaming electrode, the corresponding equivalent circuit has a general construction shown in Fig. 3.7, and, accordingly, the total impedance is given by

$$Z = R_s + (Z_f^{-1} + X_c^{-1} + R_d^{-1})^{-1} \quad (3.25)$$

The mathematical form of the expressions for the Warburg impedance, for both Ox and Red species, is essentially identical with that for the rotating disk electrode [Eq. (3.11)]. Only the thickness of the stationary diffusion layer and surface concentrations of reagents, which were then considered constant along the electrode surface, have now to be replaced with their mean values, averaged along the electrode stream length. In terms of the expression for the instantaneous thickness of the Nernst diffusion layer: $\delta = \sqrt{\pi D_{\text{Ox}} t}$, its mean thickness is given by

$$\bar{\delta} = \left(\frac{1}{t_{\max}} \right) \int_0^{t_{\max}} \delta(t) dt = \left[\frac{(\pi D_{\text{Ox}})^{1/2}}{t_{\max}} \right] \int_0^{t_{\max}} t^{1/2} dt = \left(\frac{2}{3} \right) (\pi D_{\text{Ox}} t_{\max})^{1/2} \quad (3.26)$$

Let us consider the electrode process of a general scheme: $\text{Ox} + ne \rightarrow \text{Red}$. The instantaneous surface concentrations of reagents, at given time t , in the potentiostatic experiment starting from Ox species of bulk concentration c_{Ox}^0 , are given by [23]

$$c_{\text{Ox}}(0, t) = c_{\text{Ox}}^0 \left\{ 1 - \frac{k_f}{\chi \sqrt{D_{\text{Ox}}}} [1 - \exp(\chi^2 t) \text{erfc}(\chi \sqrt{t})] \right\} \quad (3.27)$$

$$c_{\text{red}}(0, t) = \frac{c_{\text{ox}}^0 k_f}{\chi \sqrt{D_{\text{red}}}} [1 - \exp(\chi^2 t) \text{erfc}(\chi \sqrt{t})] \quad (3.28)$$

in which parameter χ expresses the ratio between the electron-transfer kinetics and the rate of diffusion:

$$\chi = \frac{k_f(E)}{D_{\text{ox}}^{1/2}} + \frac{k_b(E)}{D_{\text{red}}^{1/2}} \quad (3.29)$$

Accordingly, the average surface Ox and Red concentrations are given by the following formulas:

$$\begin{aligned} \bar{c}_{\text{ox}}(0) &= \frac{1}{t_{\text{max}}} \int_0^{t_{\text{max}}} c_{\text{ox}}(0, t) dt = c_{\text{ox}}^0 \left(1 - \frac{k_f}{\chi \sqrt{D_{\text{ox}}}} \right) \\ &+ \frac{c_{\text{ox}}^0 k_f}{t_{\text{max}} \chi \sqrt{D_{\text{ox}}}} \left[\frac{2}{\chi} \sqrt{\frac{t_{\text{max}}}{\pi}} + \frac{\exp(\chi^2 t_{\text{max}}) \text{erfc}(\chi \sqrt{t_{\text{max}}}) - 1}{\chi^2} \right] \end{aligned} \quad (3.30)$$

$$\begin{aligned} \bar{c}_{\text{red}}(0) &= \frac{1}{t_{\text{max}}} \int_0^{t_{\text{max}}} c_{\text{red}}(0, t) dt = \frac{c_{\text{ox}}^0 k_f}{\chi \sqrt{D_{\text{red}}}} \\ &- \frac{c_{\text{ox}}^0 k_f}{t_{\text{max}} \chi \sqrt{D_{\text{red}}}} \left[\frac{2}{\chi} \sqrt{\frac{t_{\text{max}}}{\pi}} + \frac{\exp(\chi^2 t_{\text{max}}) \text{erfc}(\chi \sqrt{t_{\text{max}}}) - 1}{\chi^2} \right] \end{aligned} \quad (3.31)$$

These concentrations are used for the calculation of the corresponding charge-transfer resistance [Eq. (3.10)]:

$$R_{\text{ct}}^{-1} = \left(\frac{\partial I_f}{\partial E} \right)_{\bar{c}_{\text{ox}}(0), \bar{c}_{\text{red}}(0)} = -nFA \left[\frac{dk_f}{dE} \bar{c}_{\text{ox}}(0) - \frac{dk_b}{dE} \bar{c}_{\text{red}}(0) \right] \quad (3.32)$$

Finally, the total impedance [Eq. (3.25)] is given by the formula:

$$\begin{aligned} Z &= R_s \\ &+ \left\{ [R_{\text{ct}} + G_{\text{ox}} + G_{\text{red}} + j(H_{\text{ox}} + H_{\text{red}})]^{-1} + \left(\frac{1}{j\omega AC_d} \right)^{-1} + 2\pi r C_d v \right\}^{-1} \end{aligned} \quad (3.33)$$

in which G and H quantities denote the real and imaginary components, respectively, for the Ox and Red species:

$$G_{(\text{ox, red})} = \frac{\frac{R_{\text{ct}}k_{(\text{f, b})}}{\sqrt{\omega D_{(\text{ox, red})}} \left[\sinh\left(\sqrt{\frac{2\omega}{D_{(\text{ox, red})}}\bar{\delta}}\right) + \sin\left(\sqrt{\frac{2\omega}{D_{(\text{ox, red})}}\bar{\delta}}\right) \right]}{\sqrt{2} \left[\cosh\left(\sqrt{\frac{2\omega}{D_{(\text{ox, red})}}\bar{\delta}}\right) + \cos\left(\sqrt{\frac{2\omega}{D_{(\text{ox, red})}}\bar{\delta}}\right) \right]} \quad (3.34)$$

$$H_{(\text{ox, red})} = \frac{\frac{R_{\text{ct}}k_{(\text{f, b})}}{\sqrt{\omega D_{(\text{ox, red})}} \left[\sin\left(\sqrt{\frac{2\omega}{D_{(\text{ox, red})}}\bar{\delta}}\right) - \sinh\left(\sqrt{\frac{2\omega}{D_{(\text{ox, red})}}\bar{\delta}}\right) \right]}{\sqrt{2} \left[\cosh\left(\sqrt{\frac{2\omega}{D_{(\text{ox, red})}}\bar{\delta}}\right) + \cos\left(\sqrt{\frac{2\omega}{D_{(\text{ox, red})}}\bar{\delta}}\right) \right]} \quad (3.35)$$

composing the expression for the Warburg impedance for the Ox and Red species:

$$Z_{\text{W}(\text{ox, red})} = G_{(\text{ox, red})} + jH_{(\text{ox, red})} \quad (3.36)$$

The expression for the Warburg impedance is equivalent to Eq. (3.11), obtained by invoking the equalities: $\sqrt{j} = (1+j)/\sqrt{2}$ and $(\sqrt{j})^{-1} = (1-j)/\sqrt{2}$.

Of course, by removing $R_{\text{d}}^{-1} = 2\pi r C_{\text{d}} \nu$ from Eq. (3.33) and by replacing the average values of $c_{\text{ox}}(0)$, $c_{\text{red}}(0)$ and $\bar{\delta}$ back by their single values, corresponding to the surface of the (idealized) rotating disk electrode, one obtains expression for the impedance of the process at the rotating disk electrode.

To conclude this section, streaming liquid (mercury) electrode has unique impedance characteristics which is caused by a permanent flow of the capacitive current at the steady-state potential. Thus, for the electrochemically inert electrolyte, the Nyquist plot of impedance data has a semicircular shape which, for all types of the non-streaming electrodes, would indicate the slow faradaic process. More details of the above concept and the comparison of experiment and theory can be found in the original references [19, 20].

3.3 Application of Impedance to the Diagnosis of Stability of Electrochemical Systems

3.3.1 Positive and Negative Elements in Impedance Characteristics

As an introduction to impedance studies of unstable electrochemical systems it is useful to review basic concepts of oscillatory electronic circuits containing positive and negative elements. Figure 3.8 compares responses of such elements upon small ac perturbation, i.e., under linear assumption of impedance response [24].

The corresponding impedance in the $Z''-Z'$ coordination system is plotted in Fig. 3.9 (note that Z'' -axis is oriented in direction opposite to convention usually applied in electrochemistry).

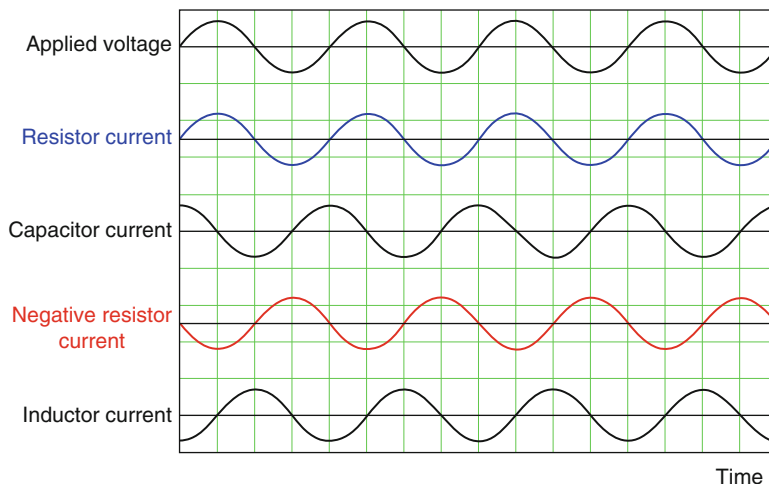


Fig. 3.8 Voltage and current waveforms for linear response of respective circuit elements (after [24])

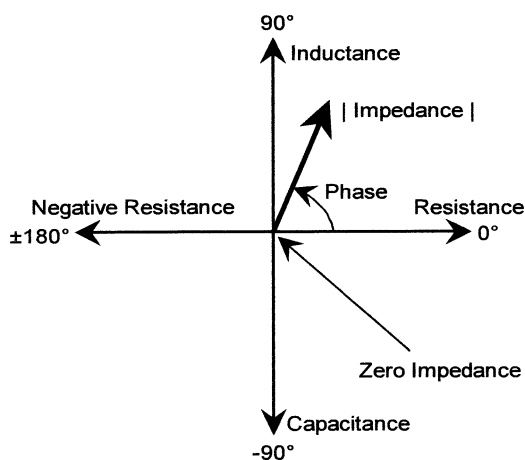


Fig. 3.9 Polar impedance at a specific frequency (reproduced from [24])

It is also instructive to divide this impedance diagrams into halves, depending on the range of phase angle. In this way positive (passive) and negative (active) elements can be ascribed to particular halves (Fig. 3.10).

One of the most important features of those diagrams which determines the classification of unstable electrochemical systems, described in Sect. 3.5, is that the variation of the phase angle between -90° and $+90^\circ$ (through zero) is typical of passive circuit elements (positive resistance, capacitance and inductance), while the

Fig. 3.10 Half planes of polar impedance (reproduced from [24])

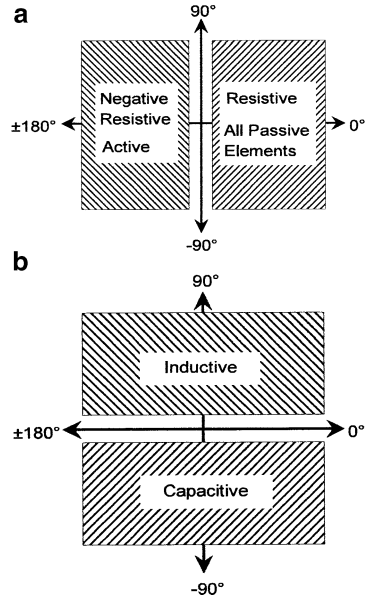
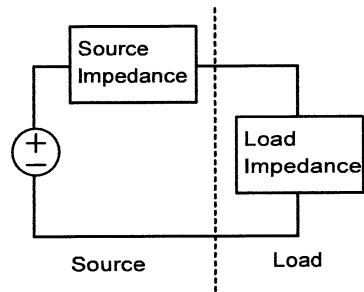


Fig. 3.11 Simplified view of source and load (reproduced from [24])

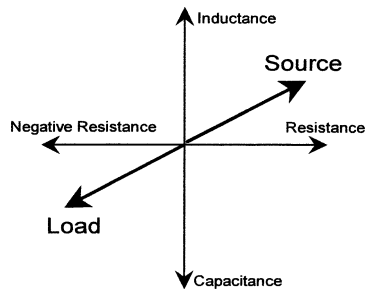


phase angle belonging to the range -90° to 90° (through -180°) are specific of active elements (negative resistance, capacitance and inductance). Negative and positive elements of the same type and the same modulus of impedance are characterized with the phase angle different for 180° . This also means that, e.g., negative inductor is, in terms of impedance response at a single frequency, indistinguishable from a positive capacitor, but behaves like a capacitor whose impedance increases with increasing frequency [24].

Let us now present the circuit as composed of source and load, each having its own impedance (Fig. 3.11). The load uses power and the source impedance heats up the source.

Now, if at given frequency the combined impedance of the load and the source equals zero even a very little source voltage applied at this frequency will cause a very large oscillating current. This will happen if the modulus of the source

Fig. 3.12 Polar plot of oscillation criteria (reproduced from [24])



impedance is equal to that of load impedance, and the phase angles differ for 180° , which case requires both positive and negative elements (Fig. 3.12)

This situation of zero total impedance for non-zero ac frequency of the power source can be often considered a nuisance in electronic practice, as the circuit with negative resistance loses then its desired stability, but for our purposes will be of fundamental significance, because we are interested in just such phenomena.

3.3.2 *Diagnosis of Bifurcations from Impedance Spectra*

3.3.2.1 Principles and Limitations of the Method

The analysis of stability of electrochemical system, understood as the property of the entire electric circuit is in many aspects analogous to the methodology of analysis of stability of the electronic circuits, with the fundamental contribution to this area made, among others, by Nyquist [25] and Bode [26]. In turn, application of the impedance-based stability criteria to electrochemical oscillators was developed, in the pioneers' works, by de Levie et al. [6, 7, 27], with respect to the In(III)–SCN⁻ polarographic oscillator, a typical N-NDR system (see Chap. 4). For the oscillatory systems involving passivation/depasivation of solid electrodes, significant original contribution to the impedance characteristics of such NDR systems was made by Lorenz et al. [28] and Keddah et al. [29–31] (see also classical review of electrochemical oscillators by Wojtowicz [8]). More recently, significant further contribution to this field was made by Koper and Sluyters [32–35]. These works prove that EIS is a powerful tool for diagnosis of stability of electrochemical systems. The methodology of such diagnosis, being a simplified version of the Nyquist criteria for the stability of electric circuit, is described below.

The presence of bifurcations (instabilities) in the dynamics of electrochemical systems is a source of specific problems in the impedance studies. Koper [32] has formulated the general difficulties concerning such measurements. The impedance studies should be performed for the stable steady-state characteristics of an electrochemical system. Let us assume that at the bifurcation point the steady-state, so far stable, loses its stability and the system switches to another attractor (concurrent steady-state or limit cycle). The impedance measurement on this side of the bifurcation point is thus not possible. Moreover, the situation is not much better

just before this bifurcation. Although *theoretically* the stable steady-state is still existing, the measurement is *practically* impossible due to (typical for bifurcation) critical slow-down of the system's dynamics. Thus, the impedance analysis of the potentially unstable system should rather be limited to the conditions where the steady-state is yet stable and the interpretation of the spectra should predict the conditions for respective bifurcations.

As the NDR in the circuit characteristics and the presence of appropriate positive serial resistance are important for large class of electrochemical oscillators, the elementary question is: How do the NDR and this serial resistance manifest themselves in the impedance spectrum, e.g., on a Nyquist diagram? Obviously, for any system, increasing ohmic (positive) serial resistance will cause the shift of the entire Nyquist diagram along the direction of positive Z' -axis. The answer to the former question is more sophisticated. We expect that the NDR of the charge-transfer process, observed under dc conditions, will cause that for $\omega \rightarrow 0$, the Nyquist diagram will penetrate the second quarter of the $Z' - Z''$ space, i.e., the region corresponding to real negative impedance. As indicated above, the sign of the charge-transfer resistance, R_{ct} , determines also the sign of the associated mass-transfer (Warburg) impedance [cf. Eq. (3.11)]. According to de Levie [27], who followed a more general idea of Bode: "if we postulate ideal negative elements, it follows immediately that negative elements of other types are also available" [8]. In other words, since the negative charge-transfer impedance implies also the negative Warburg impedance, and since the Warburg impedance is composed of resistance and capacitance, the negative Z_W value implies the occurrence of a negative (diffusion) capacitance, contrary to usual positive double layer capacitance. Thus, within the potential region corresponding to electrochemical instabilities, the equivalent circuit (for the non-streaming electrode) consists of the NDR element, associated with the charge-transfer process characteristics, the differential double layer capacitance at a given potential (C_d) and the negative Warburg impedance. The positive capacitance C_d and the negative capacitance of the Warburg impedance can be understood as two reservoirs, between which during the oscillations the energy is periodically exchanged.

The principle of diagnosis of bifurcation from the course of impedance spectra corresponds to theoretical linear stability analysis. This is because the definition of impedance is based on the linearization of the I vs. E ac response around the steady-state which requires appropriately small amplitude of ac perturbations (usually ≤ 8 mV). One can say that EIS is a variant of linear stability analysis applied to electrochemical systems and is therefore able to detect only local bifurcations, like the Hopf and saddle-node ones (cf. Chap. 1). Nevertheless, as will be shown below, EIS measurements (i.e., studies made in frequency domain ω) can supply more information about the existence of such bifurcations than the dc measurements (i.e., studies in time domain).

Let us remember that at the bifurcation point the perturbations neither decay nor grow, so the initial magnitude of perturbation remains constant [34]. This is true for both Hopf and saddle-node bifurcations. In the case of 2D nonlinear system, the Hopf bifurcation occurs for such parameters, for which the linear stability analysis

predicts the occurrence of the steady-state called center, i.e., the Lyapunov-stable steady-state surrounded by elliptic trajectories of a radii determined by the initial value of perturbation imposed on that steady-state and by the phase shift φ . Mathematically, the non-zero perturbations of dynamical variables x, y oscillate then with constant amplitude as a function of time, proportionally to $\sin(\omega_H t)$ and $\sin(\omega_H t + \varphi)$, with the characteristic frequency ω_H corresponding exactly to the bifurcation point. In the point of saddle-node bifurcation the perturbation remains constant as a function of time, what one can describe quite formally as the also sinusoidal variation with time, but with zero frequency. The diagnosis of both types of bifurcation by impedance spectroscopy will now be described separately for potentiostatic and galvanostatic conditions.

3.3.2.2 Potentiostatic Conditions

The general principle of application of EIS to stability analysis of electrochemical systems refers to the phenomenon of *resonance* between the own dynamic characteristics of the electric circuit and the characteristics of the sinusoidal ac, small-amplitude perturbation. When the resonance is reached, the impedance of the electric circuit against the externally applied perturbation drops to zero and perturbing signal is amplified without any phase shift [34]. In particular, if the ac perturbing voltage has a *non-zero* frequency ω_H , equal to the own frequency of the circuit at the Hopf bifurcation, then the total impedance should be equal to zero: $Z = 0$ (i.e., $Z' = 0$ and $Z'' = 0$). In turn, if the condition of resonance is reached for zero frequency: $\omega = 0$ (in experimental practice, this means a rather limiting situation for $\omega \rightarrow 0$), the saddle-node bifurcation is diagnosed from impedance data. Of course, the case $\omega = 0$ is identical with dc condition of the electrochemical experiment, so the saddle-node bifurcation requires the NDR, explicitly visible on the steady-state dc $I-E$ dependence, which NDR is also required for the oscillations.

Thus, the conditions for the respective bifurcations in the potentiostatic ($U = \text{const}$) experiment are [34, 35]:

A Hopf bifurcation:

$$Z(\omega) = 0 \quad \text{for } \omega = \omega_H \neq 0 \quad (3.37)$$

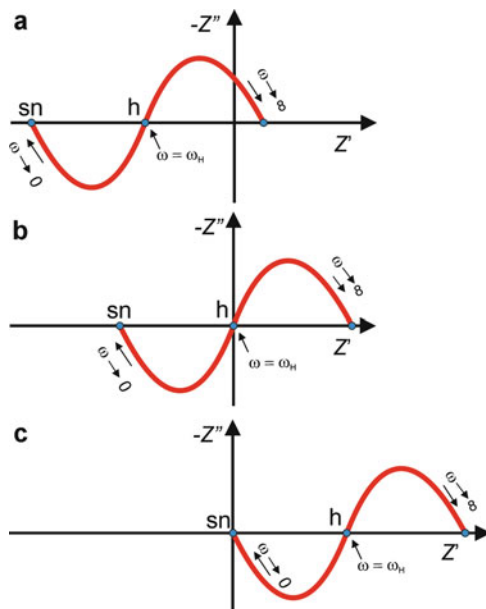
A saddle-node bifurcation:

$$Z(\omega) = 0 \quad \text{for } \omega = 0 \quad (3.38)$$

These criteria mean that the Nyquist diagram should cross the origin ($Z' = 0$, $Z'' = 0$) of the complex plane for either Eq. (3.37) or Eq. (3.38) condition for ac frequency. Figure 3.13 illustrates *schematically* these cases for increasing serial resistances R_s .

Note, however, that situations (b) and (c) are rather theoretical since, from *practical* point of view, the occurrence of the respective bifurcations would mean destabilization of the steady-state, so the measurements of impedance would then

Fig. 3.13 Theoretical schematic illustration of the role of increasing serial resistance R_s on the impedance spectra of the N-NDR system: (a) spectrum for low R_s , insufficient for both Hopf (h) and saddle-node (sn) bifurcations; (b) spectrum for R_s high enough to cause a Hopf bifurcation; (c) spectrum for even higher R_s , corresponding to the saddle-node bifurcation



appear impossible, as indicated above. In order to solve this problem, we perform impedance measurement only for the serial ohmic resistance so small (e.g., being only the solution resistance or compensated by the potentiostat) that it is *not yet* sufficient to destabilize the system, i.e., we get the spectrum like those from Fig. 3.13a. The experimental example of such a spectrum is shown in Fig. 3.14a. From the shape of this spectrum we further determine the serial resistance which *would cause* the shift corresponding to the zero total impedance (i.e., the cases analogous to those shown in Fig. 3.13b or c). For the spectrum in Fig. 3.14a, the condition of resonance can be achieved for $R_s = 4.2 \text{ k}\Omega$, and then $Z = 0$ for non-zero ac frequency (this means the Hopf bifurcation which would occur at $R_s = 4.2 \text{ k}\Omega$). Reasonable extrapolation of this diagram to $\omega \rightarrow 0$ indicates that for $R_s = \text{ca. } 13 \text{ k}\Omega$ the saddle-node bifurcation should be observed, i.e., the system will then enter the bistable regime.

As this impedance spectrum was recorded for the imposed steady-state potential E , in the absence of sufficient ohmic drops that would destabilize the system, one now has to calculate the external voltage U at which, in the presence of such ohmic drops IR_s , the system will exhibit respective bifurcation: $U = E + IR_s$. This means that one has to record also the dc steady-state I - E dependence for the same sample, in order to find the steady-state current I corresponding to potential E for which the impedance spectrum was recorded. In this way one point of the stability diagram in the (U, R_s) phase space is determined. Repeating this procedure for impedance spectra recorded for various potentials E allows one to construct the bifurcation diagram in the appropriate range of U and R_s as control parameters. Figure 3.14b shows results of such a procedure for the In(III)-SCN^- polarographic oscillator. Note that one point of the Hopf bifurcation is placed beyond the “head of the fish,”

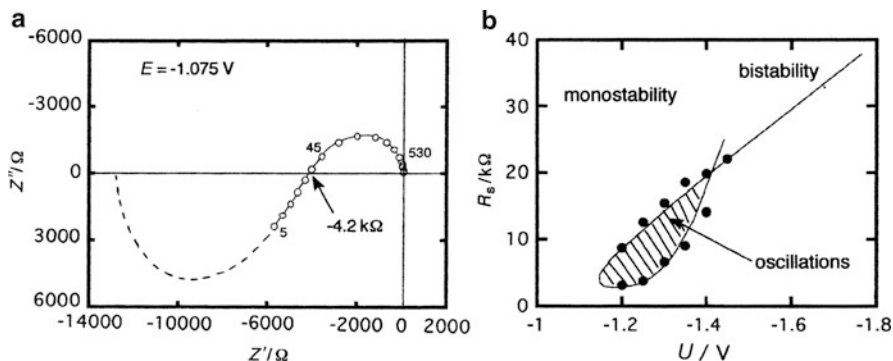


Fig. 3.14 (a) Impedance diagram for a 9 mM In^{3+} solution in 5.0 M NaSCN at $E = -1.075$ V at the HMDE. This particular steady-state exhibits a Hopf bifurcation for $R_s = 4.2$ k Ω and a corresponding applied potential $U = E + IR_s = -1.15$ V vs. SCE, with $I = -17.8$ μA the steady-state current. Indicated frequencies in Hz. (b) Line of Hopf bifurcations determined by the impedance method as explained under (a). Dots represent the onset of oscillations as observed by insertion of an external resistor. Hatched area shows the parameter region where sustained oscillations are observed. Reference electrode: SCE. Reproduced from [34] by permission of The Royal Society of Chemistry

which means that the points of this bifurcation exist also inside the “fish tail,” where however only bistability is observed under dc conditions.

The last sentence is a good premise to discuss the problem, whether impedance measurements supply exactly the same information on the possible bifurcations as the dc measurements. If both methods were strictly equivalent, one could freely choose either one or another for that purpose. However, it is not a case. Both dc and ac methods have their specific advantages and limitations. As mentioned above, the source of limitation of impedance method is that it is based on the linearized system’s response, so it can yield limited information about the local bifurcations. On the contrary, direct dc measurements can detect the results of also global bifurcations, including those which lead to, e.g., mixed-mode oscillations and chaos. But the virtue of the impedance diagnosis is that it can detect also those Hopf bifurcations that do not manifest themselves explicitly in the dc measurements. The diagram in Fig. 3.14b is the representative example of such situation which should be compared with the better developed, theoretically calculated fish-like, cross-shaped stability diagram for the N-NDR system, like that shown in Fig. 2.8. This theoretical diagram reveals the Hopf bifurcation lines also inside the bistability (fish-tail) region, but only hysteresis (bistability), and not the oscillations are there directly observed under dc conditions. The lack of the oscillations is caused by the subcritical character of the Hopf bifurcation in this region, i.e., due to this bifurcation only the *unstable* limit cycle is born, and the only attractors in the phase space are the stable nodes responsible for the bistable behavior [34]. All Hopf bifurcations, irrespective of their supercritical or subcritical nature, are, however, indicated by the experimental impedance spectrum.

3.3.2.3 Galvanostatic Conditions

The idea of resonance between the oscillatory characteristics of the electrochemical circuit and external ac source, used above for diagnosis of a Hopf and saddle-node bifurcations under potentiostatic conditions, can be applied also to the galvanostatic mode of the electrochemical experiment, when the electrode potential E can exhibit oscillations or bistability. At this moment it is again useful to realize that the galvanostat can be considered a potentiostat, to the output of which a very large (infinite) resistance R_s , in series with the electrochemical cell, was connected and very large (infinite) voltage U was applied, with the ratio $U/R_s = I$ ratio defining the imposed current. Since this serial resistance is so large, any change of the resistance (impedance) of the electrochemical cell, caused by the course of electrochemical process, is relatively so low that $R_s + \text{Re}(Z_f) \approx R_s$ and the imposed current remains practically constant. This also means that in the galvanostatic mode, contrary to the potentiostatic one, we cannot adjust R_s from zero to any desirable value, since R_s is already present and is always very high. As a consequence, the condition of resonance requires compensation of very high positive resistance with equally high real negative impedance of the electrochemical cell: $Z' \rightarrow -\infty$, which means equivalently zero real faradaic admittance $Y' = 0$.

Thus, the conditions for the respective bifurcations for the galvanostatic ($I = \text{const}$) experiment are [34, 35]:

A Hopf bifurcation:

$$Y(\omega) = 0 \quad \text{for } \omega = \omega_H \neq 0 \quad (3.39)$$

A saddle-node bifurcation:

$$Y(\omega) = 0 \quad \text{for } \omega = 0 \quad (3.40)$$

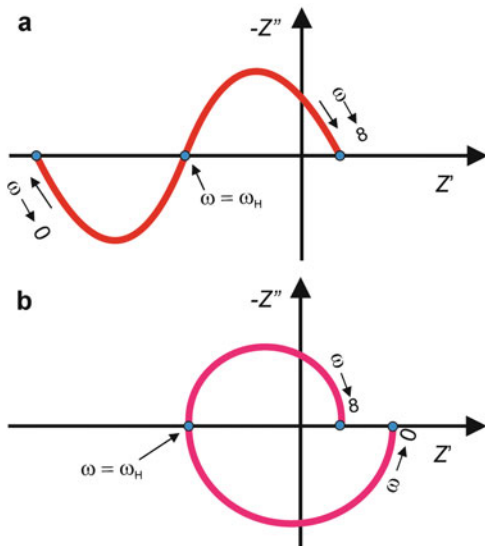
Although under galvanostatic conditions, the insertion of additional serial resistance is not necessary for these bifurcations to occur, the presence of such resistance would be required again under potentiostatic conditions, when the ohmic drops have to be coupled with the NDR. Thus, one concludes that electrochemical systems that exhibit potential oscillations under galvanostatic conditions, should also exhibit current oscillations under potentiostatic conditions, provided that in the latter case appropriate serial resistance is present in the circuit.

3.4 Impedance Characteristics of N-NDR and HN-NDR Systems

3.4.1 *The Hidden Negative Impedance*

Following criteria (3.47)–(3.50) for the local bifurcations, it is instructive to compare typical impedance spectra of the systems that can exhibit oscillations

Fig. 3.15 Schematic shape of the Nyquist diagrams for the systems with (a) explicit (observable at $\omega = 0$) NDR region and (b) hidden NDR region (observable only at intermediate $0 < \omega < \infty$ frequencies), typical of HN-NDR systems



under potentiostatic and galvanostatic conditions, respectively. Figure 3.11 shows schematically typical Nyquist spectra for the processes that will exhibit oscillations and bistability under potentiostatic and galvanostatic conditions, respectively.

Let us consider first the case from Fig. 3.15a, identical with that in Fig. 3.13a, and corresponding to experimental spectrum in Fig. 3.14a. In order to understand why this spectrum guarantees that the galvanostatic oscillations are *not* possible, let us analyze the sequence of bifurcations that will occur under potentiostatic control, upon increasing serial resistance R_s from low value (as corresponding to the picture) to the appropriately large values. The entire spectrum shifts then to the right and when R_s compensates the negative real impedance Z' and $Z'' = 0$ at $\omega = \omega_H$, the total impedance of the circuit becomes zero for the first time during the increase in R_s . Then the Hopf bifurcation, i.e., the onset of oscillations, takes place. Upon further increase of R_s the system still exhibit oscillations, until the compensation of the negative real impedance for $\omega = 0$ takes place again. The system undergoes then the saddle-node bifurcation and the appearing stable node takes control over the system's dynamics, i.e., the oscillations cease to exist. Upon further increase in R_s no other bifurcations occur, so the system does not return to the oscillatory regime.

For comparison, let us now consider the galvanostatic regime, remembering again that it means measurement involving the potentiostat with very large serial resistance already present. In terms of Fig. 3.15a it means that for such a high (theoretically infinite) resistance we are always far beyond the second, saddle-node bifurcation, when no oscillations exist. Therefore the system characterized with the

spectrum from Fig. 3.15a, i.e., with explicit NDR in the dc I - E characteristics, can exhibit only bistability under galvanostatic conditions.

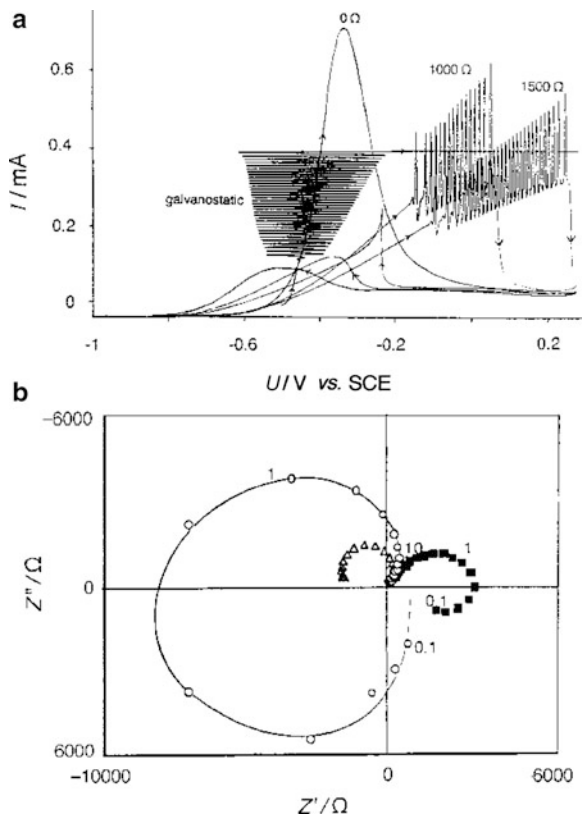
Thus, it becomes obvious that the system in which the electrode potential oscillates under galvanostatic conditions must be characterized with qualitatively different impedance spectrum, excluding the above sequence of the Hopf bifurcation followed by any saddle-node bifurcation upon increasing R_s . In order to avoid such saddle-node bifurcation, for low (tending to zero) ac frequencies the spectrum must return to positive real impedance, as in Fig. 3.15b.

Since $\omega = 0$ means de facto dc conditions, the corresponding limiting positive real resistance is equivalent to the positive slope of the steady-state dc I - E characteristics. But it also means that although the negative resistance is present in the system's characteristics, it does *not* manifest itself explicitly on dc I - E dependence, at the potential E for which the spectrum in Fig. 3.15b was collected. This negative impedance can only be revealed in impedance measurements for the non-zero, intermediate values of ω and therefore remains "hidden" under dc conditions. The oscillatory systems of this type, mentioned already in Chap. 2, belong to the so-called hidden N-NDR or HN-NDR type, the idea of which was introduced by Koper and Sluyters [33]. Obviously, the negative impedance can remain hidden if at least two processes overlap: one, *relatively fast*, with the NDR characteristics and the other one, *relatively slow*, with the positive slope. The slow process manifests itself in the spectrum only at low frequencies, while the faster process characterized with the negative impedance reveals itself for intermediate frequencies. The spectrum from Fig. 3.15b, transformed to the admittance coordination system, should intersect the real axis close to the origin of the complex plane, at its negative side, in concordance with condition (3.39) predicting a Hopf bifurcation for $Y(\omega) = 0$, in an ideal, limiting case.

Typical examples of the galvanostatic oscillators include electrocatalytic oxidation of small organic molecules (methanol, formaldehyde, formic acid) at transition metal electrodes (for more detailed description, cf Chap. 5). Following Koper [34], we shall invoke here the mechanism for the formic acid oxidation at Pt, elaborated by Strasser et al. [36], and compare it with the impedance spectrum of this process occurring at Rh electrode [37, 38] (Fig. 3.16).

Figure 3.16a shows the results of dc experiments: for zero serial resistance (i.e., for only the solution resistance, insufficient for the destabilization of the system) the potentiodynamic experiment yields steady-state I - E dependence with the distinct region of the NDR. This suggests that oscillations should occur for sufficiently high external resistance and in fact, in the presence of, e.g., 1,000 Ω or 1,500 Ω , the oscillations of the anodic current appear during the anodic potential scan, with the I - U dependence appropriately extended along the U -axis. Let us remember that the simple (not hidden) N-NDR system should not exhibit oscillations under galvanostatic conditions. However, under galvanostatic conditions the oscillations of the electrode potential set in without any external resistor inserted, and moreover—these oscillations occur largely around the dc I - E branch with positive slope. According to the above developed theory, these dc measurements should now be compared with the impedance spectra, recorded under potentiostatic conditions at

Fig. 3.16 (a) Voltammogram of 0.1 M HCHO in 0.1 M NaOH on a rhodium RDE for a 0, 1,000 and 1,500 Ω external resistance (internal cell resistance ca 95 Ω). Scan rate 10 mV s^{-1} , 3,000 rev min^{-1} . Amperogram taken at 0.01 mA s^{-1} . (b) Impedance diagrams taken at -0.50 V (filled square), -0.45 V (open circle), -0.35 V (open triangle). Indicated frequencies in Hz. Reference electrode: SCE. Reproduced from [34] by permission of the Royal Society of Chemistry



three different potentials (Fig. 3.16b). The semicircle constructed of points (Δ), for $E = -0.35$ V, confirms the existence of the NDR region under dc conditions and a possibility of a Hopf bifurcation, since the plot tends to intersect the Z' -axis, at a negative value, for non-zero frequency. In turn, the amplitude of potential oscillations under galvanostatic conditions includes the potential $E = -0.45$ V, for which the impedance spectrum is constructed from points (o) and which corresponds to the positive slope of the dc $I-E$ dependence. The shape of this spectrum, concordant with the schematic one in Fig. 3.15b, indicates the HN-NDR nature of the galvanostatic oscillator considered. For low ac frequencies ($\omega \rightarrow 0$) the Nyquist plot tends to the positive real impedance which corresponds to the positive slope of the steady-state dc $I-E$ curve from Fig. 3.16a. When the ac frequency increases, the plot enters the third and the second quarter of the Nyquist diagram, indicating thus the presence of the negative real and imaginary impedance which was hidden for lower frequencies, and thus obviously also for dc curve. In particular, for zero imaginary impedance, the real negative impedance is rather high and can be compensated with the high resistance of the galvanostatic circuit, yielding oscillations.

Note one more important dynamic event that Fig. 3.16a also shows: the bifurcation scenario according to which the galvanostatic oscillations *decay* when the maximum potential of the oscillations amplitude just “touches” the NDR branch on the dc curve (analogous “death” of oscillations was reported, e.g., for the Ni/H₂SO₄ system, described in Chap. 6). The oscillations cease in this case due to the destructive collision of the stable limit cycle with the saddle point (under galvanostatic conditions the NDR branch is a collection of saddle-points, cf. Fig. 2.4). This means the homoclinic (saddle-loop) bifurcation (cf. Fig. 1.24). This homoclinic scenario is quite typical of HN-NDR oscillators and does not occur for the “potentiostatic” oscillators with the explicit NDR region.

3.4.2 Mechanisms Underlying the HN-NDR Oscillator

Above it was said that HN-NDR system is composed of at least two overlapping processes: the *fast* one with the negative impedance and the *slow* one, with the positive *I–E* slope. It is instructive to analyze this situation in more detail based on two model mechanisms.

3.4.2.1 Model Mechanism 1

Let us first consider Fig. 3.17 which shows schematically the dc *I–E* course for the fast process (dashed line) exhibiting the negative impedance. This course overlaps partly with the characteristics of another, slow process (solid line), that is the potential-dependent adsorption of an inhibitor which suppresses the current of the first process in certain potential range (θ is the electrode coverage of an inhibitor). Only when the desorption of an inhibitor begins, the current of the first process can rise until it decreases due to entering the NDR region at the electrode largely free of an inhibitor.

The destabilization of the system’s state can be intuitively imagined in the following way [40]. Let us assume that the steady-state electrode potential lies on the N-NDR branch of the *I–E* dependence of the anodic electrode process, and for that potential the steady-state value of the electrode coverage of the inhibitor lies between 0 and 1. This steady-state is now perturbed through the fluctuation of the electrode potential to a higher value, for which the current is lower. Since the electrode coverage responds, by assumption, much slower, initially it does not play any significant role, so the electrode potential autocatalytically increases and current decreases further, as typically for the N-NDR region, in the presence of ohmic drops. Eventually, with a certain delay the desorption of an inhibitor will manifest itself which will cause the increase of current, thus counteracting a further increase of the electrode potential. In this way the negative feedback loop takes control over the system dynamics. Such interplay of the positive and negative feedback loops generally gives rise to the oscillations.

This source of instabilities will now be expressed in terms of appropriate model equations [39], in which symbol *E* is identical with ϕ_{dl} symbol used in the caption to

Fig. 3.17 (a) Example of a combination of electrode process current density $nFk(\phi_{\text{dl}})$ (dashed curve) in the absence of an inhibiting species and an equilibrium coverage of an inhibitor $\theta(\phi_{\text{dl}})$ that admits a Hopf bifurcation (solid curve). **(b)** Stationary polarization curve. The dashed line indicates where the stationary state becomes unstable under galvanostatic conditions. The horizontal bars display the amplitudes of the oscillations. sn: saddle node bifurcation; sl: saddle-loop bifurcation; h: Hopf bifurcation; $\phi_{\text{dl}} \equiv E$ [39, 40]. Reproduced from [39] with kind permission from Springer Science + Business Media B.V.

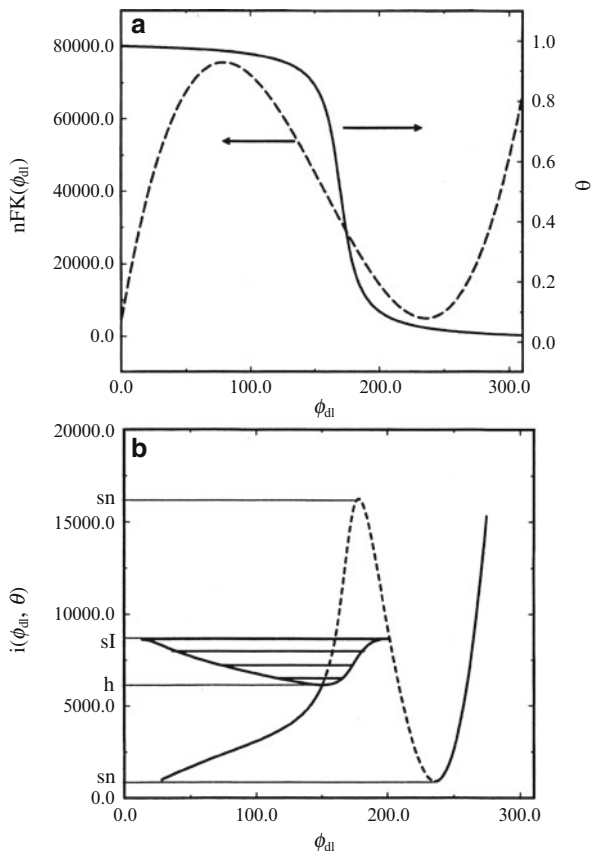


Fig. 3.17 (as in original reference).¹ The (anodic) faradaic current of the electrode process can flow only on this part of the electrode surface that is not covered by the inhibitor:

$$I_f = nFAk_b(E) \times (1 - \theta) \quad (3.41)$$

where rate constant k_b is expressed in $\text{mol m}^{-2} \text{s}^{-1}$. Accordingly, the temporal dynamics of E are described with the following dependence:

$$C_d A \frac{dE}{dt} = \frac{U - E}{R_s} - nFAk_b(E) \times (1 - \theta) \quad (3.42)$$

In the NDR region of the electrode process, the electrode coverage with an inhibitor (θ) decreases with increasing potential E and the desorption of the

¹note that for working electrode potential expressed vs. the reference electrode potential: $E = \phi_{\text{dl}} - \phi_{\text{dl}}(\text{RE})$, $dE/dt = d\phi_{\text{dl}}/dt$ since $\phi_{\text{dl}}(\text{RE}) = \text{const}$.

inhibitor must be slow, compared to the rate of the electrode process. This means appropriate value of the rate constant of the surface (adsorption) process k_{ads} [s^{-1}] in the equation for the dynamics of the electrode coverage:

$$\frac{d\theta}{dt} = k_{\text{ads}}[\theta_{\text{eq}}(E) - \theta] \quad (3.43)$$

where $\theta_{\text{eq}}(E)$ means the equilibrium value of θ at a given potential E . As said above, the crucial quantitative point is that $\theta_{\text{eq}}(E)$ is not immediately reached, but the system tends to this equilibrium value with the relatively low rate controlled by the value of k_{ads} .

It is further useful to perform the stability analysis of the above model in terms of appropriate dimensionless variables [39], defined as

$$e = \frac{nFE}{RT} \quad (3.44)$$

$$u = \frac{nFU}{RT} \quad (3.45)$$

$$\tau = k_{\text{ads}}t \quad (3.46)$$

since this allows to introduce dimensionless quantities, one of which (ε) expresses the difference in time scales of e and θ dynamics (cf. Sects. 1.6 and 2.2.3):

$$\varepsilon = \frac{C_d RT k_{\text{ads}}}{n^2 F^2 k_0} \quad (3.47)$$

$$\rho = \frac{An^2 F^2 R_s k_0}{RT} \quad (3.48)$$

where, in turn, the potential-dependent rate constant of the anodic electrode process $k_b(E)$ was expressed as the product of the dimensionless part $k(E)$ and the part k_0 in which the dimension of k_b was incorporated: $k_b(E) = k_0 k(E)$. Note that the dynamical system (3.42, 3.43) can be analyzed for both potentiostatic and galvanostatic conditions, with $\rho \rightarrow \infty$ in the latter case. The HN-NDR dynamical system is then defined as

$$\varepsilon \frac{de}{d\tau} = -k(e) \times (1 - \theta) + \frac{u - e}{\rho} \quad (3.49)$$

$$\frac{d\theta}{d\tau} = \theta_{\text{eq}}(e) - \theta \quad (3.50)$$

According to the principles of linear stability analysis (Sect. 1.3), the diagnosis of oscillations requires calculations of the elements of Jacobian matrix \mathbf{J} for the steady-state ($e_{\text{ss}}, \theta_{\text{ss}}$):

$$\begin{bmatrix} -\frac{1}{\varepsilon}(1 - \theta_{ss}) \left(\frac{dk}{de} \right)_{ss} - \frac{1}{\varepsilon\rho} & \frac{1}{\varepsilon} k(e_{ss}) \\ \left(\frac{d\theta}{de} \right)_{ss} & -1 \end{bmatrix} \quad (3.51)$$

The Hopf bifurcation occurs if $\text{Tr}(\mathbf{J}) = 0$ and $\text{Det}(\mathbf{J}) > 0$, whose conditions are equivalent to, respectively:

$$-\left[\frac{dk(e)}{de} \right]_{ss} = \left(\varepsilon + \frac{1}{\rho} \right) \left(\frac{1}{1 - \theta_{ss}} \right) \quad (3.52)$$

and

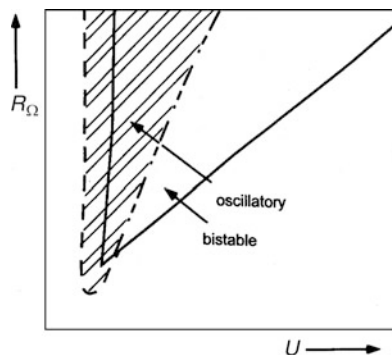
$$\left[\frac{dk(e)}{de} \right]_{ss} (1 - \theta_{ss}) + \frac{1}{\rho} > \left(\frac{d\theta}{de} \right)_{ss} k(e_{ss}) \quad (3.53)$$

Condition (3.52) is met only if the NDR region is present in the I - E characteristics of the electrode process ($dk/de < 0$), so the genesis of a Hopf bifurcation is essentially the same as for the typical N-NDR oscillator. Furthermore, according to Fig. 3.17, the electrode coverage of the inhibitor decreases with increasing positive potential: i.e., $(d\theta/de)_{ss} < 0$, so the condition (3.53) can be met, depending only on other parameter values. In particular, when $\rho \rightarrow \infty$, i.e., in the galvanostatic limit, the negative value of $(d\theta/de)_{ss}$ is obligatory for the Hopf bifurcation to occur. Now one should analyze the role of parameter ε in Eq. (3.52). After a Hopf bifurcation at the condition (3.52), oscillations persist if $\text{Tr}(\mathbf{J}) > 0$, i.e., if:

$$-\left[\frac{dk(e)}{de} \right]_{ss} > \left(\varepsilon + \frac{1}{\rho} \right) \left(\frac{1}{1 - \theta_{ss}} \right) \quad (3.54)$$

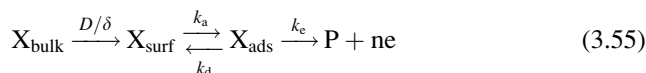
and hence it is clear that parameter ε has to be sufficiently small. In view of Eq. (3.49) this means that the electrode potential is a relatively fast variable (as also for the N-NDR systems), compared to the electrode coverage θ . In other words, the adjustment of the electrode coverage of an inhibitor to an equilibrium value at a given potential should occur on a slower time scale, compared to the change in the electrode potential e . This is of course the illustration of the discussed above principles of the HN-NDR oscillator, for which the NDR region characterizes the faster process. Also, conditions (3.52) and (3.54) show that oscillatory instabilities will persist for infinitely large values of resistance ρ which means galvanostatic conditions. Note that for the N-NDR systems the oscillations existed only between the lower and upper threshold values of serial resistance. Figure 3.18 shows the typical bifurcation diagram of the HN-NDR system which is useful to compare with typical diagram for the N-NDR system, shown in Fig. 2.8.

Fig. 3.18 Skeleton bifurcation diagram in the U/R_Ω parameter plane (with $R_\Omega \equiv R_s$) of an HN-NDR system of the “reaction-inhibition” class [such as model Eqs. (3.49, 3.50)]. The *solid, dashed and dotted-dashed lines* denote the location of saddle-node, Hopf and saddle-loop bifurcations, respectively. Reproduced with permission from [40]. Copyright Wiley-VCH Verlag GmbH & Co. KGaA



3.4.2.2 Model Mechanism 2

The present mechanism was suggested by Koper and Sluyters [33], and since it was later discussed by other authors, it is worth of detailed presentation here. Instead of introducing the potential-dependent adsorption of the inhibitor, it is assumed that the electron-transfer reaction occurs exclusively from the adsorbed state of the reactant, with both the electron-transfer rate and the electrode coverage θ dependent on the electrode potential:



where D means the diffusion coefficient, δ —the thickness of the Nernst diffusion layer, k_a and k_d —the rate constants of the adsorption and desorption of X , respectively. The X species arrives by diffusion at the surface of the electrode when it undergoes adsorption, followed by irreversible oxidation to the product that is not adsorbed and thus diffuses away from the electrode surface. Thus, in other words, this mechanism postulates an exclusively electrocatalytic electrode process of X . In the most general version, where ohmic potential drops occur in the electric circuit and therefore the temporal dynamics of the electrode potential change (dE/dt) is considered, the following three ordinary differential equations can be derived [33]:

$$C_d \frac{dE}{dt} = \frac{U - E}{AR_s} - nFk_e(E, \Gamma_X)\Gamma_X \quad (3.56)$$

$$\frac{dc_0}{dt} = \frac{2}{\delta} \left[-k_a(E, \Gamma_X)c_0 \left(1 - \frac{\Gamma_X}{\Gamma_{\text{max}}} \right) + k_d(E, \Gamma_X)\Gamma_X + \frac{D}{\delta} (c_{\text{bulk}} - c_0) \right] \quad (3.57)$$

$$\frac{d\Gamma_X}{dt} = k_a(E, \Gamma_X)c_0 \left(1 - \frac{\Gamma_X}{\Gamma_{\text{max}}} \right) - k_d(E, \Gamma_X)\Gamma_X - k_e(E, \Gamma_X)\Gamma_X \quad (3.58)$$

In these equations, C_d is the differential double layer capacitance per unit area (for simplification, assumed to be potential-independent), A —the electrode surface area, Γ_X and Γ_{\max} —the actual and maximum surface concentrations of adsorbed species X, c_{bulk} —the bulk concentration of X, c_0 —the concentration of X *in the solution* just outside the double layer; the adsorption process establishes thus directly between the amount Γ_X on the surface and the amount of X in the solution in which the concentration equals to c_0 . As usual, U means the externally applied voltage, which is different from the interfacial potential drop E due to ohmic drops, caused by the serial resistance R_s . This system of equations can undergo appropriate modifications, depending on particular assumed conditions. For example, for the galvanostatic operation, the first term on the right-hand-side of Eq. (3.56) will be replaced by the imposed constant current density (cf. Sect. 2.2.2). In turn, in the absence of ohmic drops, i.e., when $R_s = 0$, $U = E$ and entire Eq. (3.56) is left out from consideration. Using following substitutions:

$$u = c_0/c_{\text{bulk}} \quad (3.59)$$

$$\theta = \Gamma_X/\Gamma_{\max} \quad (3.60)$$

$$\tau = 2Dt/\delta^2 \quad (3.61)$$

it is convenient to transform Eqs. (3.66)–(3.68) into the forms:

$$\varepsilon \frac{dE}{d\tau} = \frac{U - E}{r} - k_e(E, \theta)\theta \quad (3.62)$$

$$\frac{du}{d\tau} = -k_a(E, \theta)u(1 - \theta) + k_d(E, \theta)\theta + 1 - u \quad (3.63)$$

$$\beta \frac{d\theta}{d\tau} = k_a(E, \theta)u(1 - \theta) - k_d(E, \theta)\theta - k_e(E, \theta)\theta \quad (3.64)$$

in which

$$\varepsilon = \frac{2C_d}{\delta nF c_{\text{bulk}}} \quad (3.65)$$

$$\beta = \frac{2 \Gamma_{\max}}{\delta c_{\text{bulk}}} \quad (3.66)$$

$$r = \frac{Dc_{\text{bulk}}nFAR_s}{\delta} \quad (3.67)$$

$$\varepsilon' = \frac{\varepsilon}{\beta} \quad (3.68)$$

and some original quantities changed their definitions:

$$\frac{k_a \delta}{D} \rightarrow k_a \quad (3.69)$$

$$k_d \frac{\Gamma_{\max} \delta}{c_{\text{bulk}} D} \rightarrow k_d \quad (3.70)$$

$$k_e \frac{\Gamma_{\max} \delta}{c_{\text{bulk}} D} \rightarrow k_e \quad (3.71)$$

For typical values of the model parameters, the time scales of the potential and electrode coverage dynamics differ for one order of magnitude, according to the following values: $\varepsilon \approx 10^{-3} \text{ V}^{-1}$, $\beta \approx 10^{-2}$, and thus their ratio $\varepsilon' \approx 10^{-1}$. This model mechanism was used to discuss the possible bifurcations under true potentiostatic ($E = \text{const}$), potentiostatic control with ohmic drops ($U = \text{const}$) and galvanostatic control ($I = \text{const}$). We shall briefly discuss here the latter case.

First the general definition of dynamical system (3.62)–(3.64) will be reduced to two ODEs, describing the dynamics of the electrode potential E and of the electrode coverage θ . Thus, the variations of surface concentration of the species in the solution are assumed negligible due to sufficiently fast mass transport, so the concentration is everywhere equal to the bulk value. Assuming the galvanostatic control, one obtains the following system of ODEs:

$$\varepsilon' \frac{dE}{d\tau} = J - k_e(E)\theta \quad (3.72)$$

$$\frac{d\theta}{d\tau} = k_a(1 - \theta) - k_d\theta - k_e(E)\theta \quad (3.73)$$

where J is the imposed, constant current density. By performing linear stability analysis in a way analogous to that described in Sect. 2.2.2, one concludes that the galvanostatic Hopf bifurcation is *not* possible for this system, because it is impossible to meet simultaneously the conditions of zero trace and positive value of the determinant of the respective Jacobian matrix:

$$\text{Tr}(\mathbf{J}) = 0 \quad \text{if} \quad \frac{dk_e(E)}{dE} = -\varepsilon' \frac{k_a + k_d + k_e(E)}{\theta} \quad (\text{always} < 0) \quad (3.74)$$

$$\text{Det}(\mathbf{J}) > 0 \quad \text{if} \quad \frac{k_a(k_a + k_d)}{k_a + k_d + k_e(E)} \frac{dk_e(E)}{dE} > 0 \quad (3.75)$$

which would require the slope $dk_e(E)/dE$ being simultaneously negative and positive. In order to obtain galvanostatic oscillations of the electrode potential, Koper and Sluyters [33] have modified the above model by looking for the physical

situation that would keep the condition for zero trace but would allow the determinant to become positive for the same parameters. This was done by invoking the dependence of the rate constant of adsorption on the electrode potential (i.e., by introducing the $k_a(E)$ relationship), with the desorption process neglected for simplicity ($k_d = 0$). In other words, the extended version of the model involves two potential-dependent processes, with only one being the charge-transfer step. The relevant ODEs take then the following form:

$$\varepsilon' \frac{dE}{d\tau} = J - k_e(E)\theta \quad (3.76)$$

$$\frac{d\theta}{d\tau} = k_a(E)(1 - \theta) - k_e(E)\theta \quad (3.77)$$

From the condition $dE/d\tau = d\theta/d\tau = 0$ one finds the parameters of the steady-states for this model:

$$\theta_{ss} = \frac{k_a}{k_a + k_e} \quad (3.78)$$

$$k_e(E_{ss}) = \frac{J_{ss}}{\theta_{ss}} \quad (3.79)$$

$$J_{ss} = \frac{k_a(E_{ss})k_e(E_{ss})}{k_a(E_{ss}) + k_e(E_{ss})} \quad (3.80)$$

and the trace and the determinant of the Jacobian matrix are given by

$$\text{Tr}(\mathbf{J}) = \frac{1}{\varepsilon'} \frac{dk_e(E)}{dE} \frac{k_a(E)}{k_a(E) + k_e(E)} + k_a(E) + k_e(E) \quad (3.81)$$

$$\text{Det}(\mathbf{J}) = \frac{1}{\varepsilon'} \left[\left\{ k_a^2(E) \frac{dk_e(E)}{dE} + k_e^2(E) \frac{dk_a(E)}{dE} \right\} \times \{k_a(E) + k_e(E)\}^{-1} \right] \quad (3.82)$$

Hence one derives the conditions of a Hopf bifurcation:

$$\frac{dk_e(E)}{dE} = -\varepsilon' \frac{[k_a(E) + k_e(E)]^2}{k_a(E)} \equiv k_e'(E)^{\text{crit}} \quad (3.83)$$

with

$$k_e^2(E)k_a'(E) > -k_a^2(E)k_e'(E)^{\text{crit}} \quad (3.84)$$

where the prime denotes differentiation with respect to E . These dependences are equivalent to the following conclusions of quite a general importance for the

prediction of galvanostatic oscillations: the charge-transfer step should exhibit the negative slope ($dk_e(E)/dE < 0$), the potential dependence of the adsorption rate constant on the electrode potential should exhibit a positive slope $dk_a(E)/dE > 0$ and, *last not least*, **the rate constant for the electron transfer is higher than the rate constant of adsorption**. Thus, of two potential-dependent processes, the (destabilizing) electron-transfer process has to be faster than the stabilizing (adsorption) process, which does not involve electron-transfer. This conclusion in fact explains again the formation of hidden negative impedance, being a source of galvanostatic oscillations on the $J-E$ branch of the positive slope under dc conditions. In fact, one can confirm that in terms of the model discussed, the dJ/dE slope is positive at the critical point of a Hopf bifurcation:

$$\left(\frac{dJ_{ss}}{dE}\right)_{\text{crit}} = \frac{k_a^2 k_e^{\text{crit}} + k_e^2 k_a'}{(k_a + k_e)^2} \quad (3.85)$$

The following exemplary relationships were chosen for the dependences of the charge-transfer and adsorption rate constants on the electrode potential:

$$k_e(E) = \frac{k_{e1}^0 \exp(\alpha f E)}{1 + k_d \exp[b_2 f (E - E_d)]} + k_{e2}^0 \exp(\alpha f E) \quad (3.86)$$

$$k_a(E) = \frac{1}{\{1/k_a^0 \exp[b_1 f (E - E_a)]\} + (1/k_m)} \quad (3.87)$$

The bifurcation structure of the model discussed is collected in Fig. 3.19, for the parameter values specified in the caption.

In turn, Fig. 3.20a presents the nullclines of Eqs. (3.76) and (3.77), for a particular set of parameters, whereas parts (b) and (c) show courses of the electrode potential for two sets of parameters. Note that parts (a) and (b) were constructed for the same parameters. Regarding the attractors, the cross-sections of nullclines in Fig. 3.20a indicate one stable steady-state and one stable limit cycle which are both only locally stable, i.e., in order to reach one of them, one has to choose the initial state closely enough to the desired attractor (i.e., to start from the respective basin of attraction). Therefore part b includes two $E(t)$ courses, differing with initial values and therefore tending asymptotically either to a stable steady-state (upper curve) or to a stable limit cycle (lower, oscillatory course).

Finally, Fig. 3.21 shows the schematic comparison of the dc $I-E$ curve of the HN-NDR system with the impedance spectra corresponding to appropriate potentials.

One can reconstruct these impedance spectra, based on the expressions for the real and imaginary parts of the total impedance, derived by Koper and Sluyters [33]:

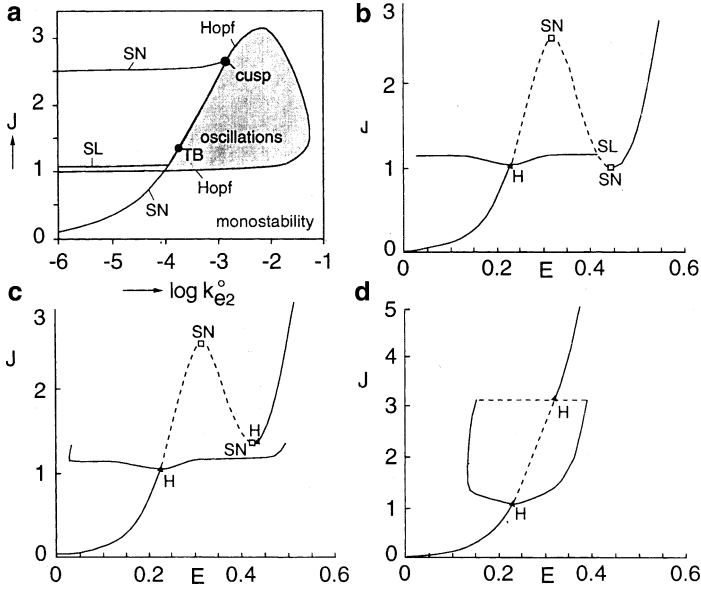


Fig. 3.19 Illustration of the solution behavior of Eqs. (3.76) and (3.77). (a) Bifurcation map showing the different regions of monostability, bistability, oscillations and bistability of steady-state and oscillations in the $J - k_{e2}^0$ plane; (b) section of (a) at $k_{e2}^0 = 0.001$; (c) section of (a) at $k_{e2}^0 = 0.01$; (d) section of (a) at $k_{e2}^0 = 0.01$. H Hopf bifurcation, SN saddle-node bifurcation, TB Takens-Bogdanov bifurcation (merging of H and SN). SL saddle-loop (homoclinic) bifurcation. Other parameter values are: $k_e^0 = 1$, $\alpha = 0.5$, $f = 38.7$, $k_d = 250$, $b_2 = 1$, $k_a^0 = 0.015$, $b_1 = 0.5$, $k_m = 10$, $\varepsilon' = 0.25$, $E_a = 0$ and $E_d = 0.35$. Reprinted from [33], Copyright 1994, with permission from Elsevier

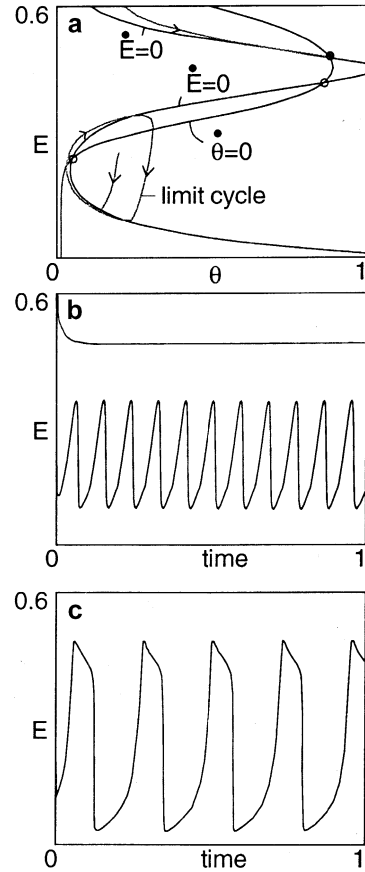
$$Z'(\omega) = \frac{Y_F'}{Y_F'^2 + (\varepsilon'\omega - Y_F'')^2} \quad (3.88)$$

$$Z''(\omega) = \frac{\varepsilon'\omega - Y_F''}{Y_F'^2 + (\varepsilon'\omega - Y_F'')^2} \quad (3.89)$$

where the real and imaginary parts of the faradaic admittance are given by

$$Y_F'(\omega) = \frac{k_a k_e'}{k_a + k_e} + k_e \frac{k_e k_a' - k_a k_e'}{(k_a + k_e)^2 + \omega^2} \quad (3.90)$$

Fig. 3.20 (a) Phase plane representation of the solution behavior of Eqs. (3.76) and (3.77) for $k_{e2}^0 = 0.0001$ and $J = 1.136$. The thin lines are the E and θ nullclines, i.e., $dE/dt = 0$ and $d\theta/dt = 0$; the thicker lines are the trajectories from two different initial conditions, one ending on a stable steady-state (nullcline intersection) and the other settling on a limit cycle (closed curve) (filled circle stable steady-state; open circle unstable steady-state). (b) Potential–time transients for the same parameter values and initial conditions as in (a). (c) Potential oscillations for $k_{e2}^0 = 0.0002$ and $J = 1.2$. Other parameter values as in Fig. 3.19. Reprinted from [33], Copyright 1994, with permission from Elsevier



$$Y_F''(\omega) = \omega \frac{k_e k_a' - k_a k_e'}{(k_e + k_a) [(k_e + k_a)^2 + \omega^2]^2} \tag{3.91}$$

and the primed symbols k' mean the derivatives dk/dE of the respective rate constant.

Finally, Fig. 3.22 summarizes all typical dc and ac characteristics of HN-NDR systems.

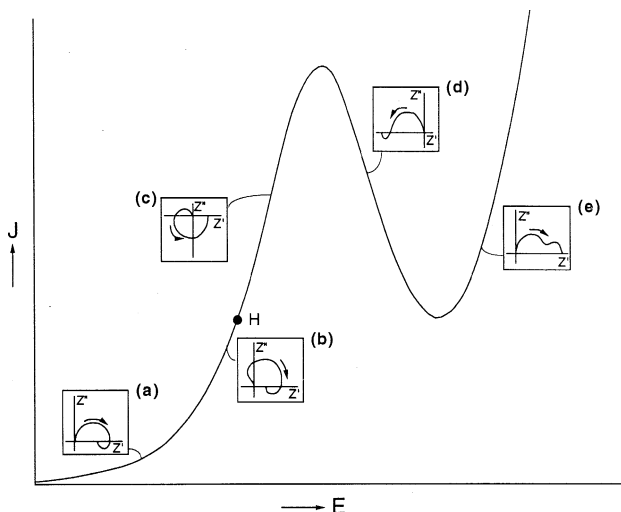


Fig. 3.21 The five qualitatively different impedance plots obtained at different parts of the J - E curve (parameter values as in Fig. 3.19b). The arrows indicate the direction of decreasing frequency and H indicates the current value for which a Hopf bifurcation is observed under galvanostatic conditions. The negative impedance at high frequencies in diagrams (b) and (c) should be noted. Reprinted from [33], Copyright 1994, with permission from Elsevier

3.5 Classification of Electrochemical Oscillators Based on Impedance Characteristics

Quite a large number of presently known electrochemical oscillators implied several attempts to categorize them into respective groups. In search of possible generalizations of that problem, Eiswirth et al. [41] have proposed its relation to the classification of chemical oscillators. Here we shall focus on the electrochemical systems only. Based on the characteristics of unstable electrochemical systems, presented in so far in this chapter and in Chap. 2, it is possible to propose a useful impedance-based classification. Just like mathematical linear stability analysis allows to find the qualitative type of the phase trajectories of the system of linear (ized) differential equations without obtaining their explicit solutions, the impedance spectroscopy, being the electrochemical variant of linear stability analysis, allows one to categorize electrochemical oscillators without *studying the detailed mechanism of the given process*, but looking only at the shape of the impedance spectrum. In other words, based on the impedance spectrum one can predict which bifurcations, under which particular conditions are possible for the system of a given impedance characteristics. Pioneer work in this area was published in 1996 by Koper [32] who divided electrochemical into four groups (classes): Class I—truly potentiostatic ($E = \text{const}$) oscillators, Class II—potentiostatic ($U = \text{const}$) oscillator, Class III—galvanostatic oscillators. Later, Strasser et al. [42] have included also S-NDR type oscillators, extending thus the classification systems to four classes

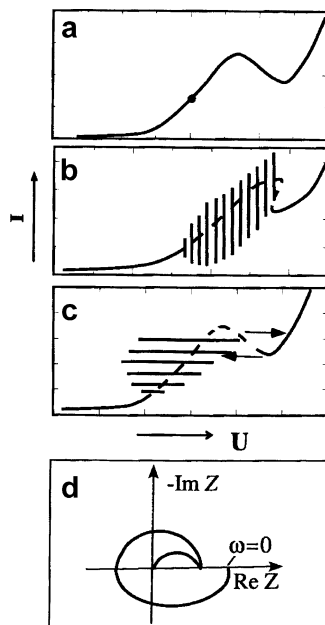


Fig. 3.22 (a–c) Characteristic I – U curves of HN-NDR systems: (a) under potential control for zero (vanishing) ohmic series resistance, R_{Ω} ; (b) under potential control for intermediate values of R_{Ω} and (c) under current control. (d) Typical impedance spectrum of an HN-NDR system in the complex impedance plane at the point indicated in (a). Reproduced with permission from [40]. Copyright Wiley-VCH Verlag GmbH & Co. KGaA

which are briefly characterized below. This classification indicated also the non-essential and essential (for the oscillations) dynamic variables (cf. Sect. 2.3).

Class I. Strictly potentiostatic oscillators, for which thus the **electrode potential** E is a **non-essential** dynamic variable, and which are purely chemical oscillators involving at least one electrochemical step, allowing to reveal the chemical oscillations by means of the electrochemical element. The existence of the NDR region is thus not necessary for the oscillations, as well as non-zero serial resistance. However, if such resistance is present, the oscillating current causes, through the ohmic drops, also the oscillatory variation of the electrode potential and the electrochemical process can affect the concentration of the involved species, interacting in this way with the chemical oscillatory process. The model approach can involve classical Brusselator as a source of chemical oscillations, with one of the reaction steps assumed to be the electrode process. The reader interested in more detailed characteristics of the kinetic and impedance representation of such model process is advised to consult the original reference [42]. Rather rare experimental examples of Class I oscillators include the Belousov–Zhabotinsky-type process. In this case, e.g., the oscillatory variation of the catalyst $[\text{Ce(IV)}]/[\text{Ce(III)}]$ ratio and the recovery of Br^- ions was achieved by the electrochemical process of bromate anions, occurring in the absence of oxidized organic species, in

contact with hydrogen electrode (hydrogen/platinum/oxyhalogen system [43]). It is also possible that to this class belongs the electrodisolution of iron in nitric acid, with the source of instability being presumably an autocatalytic reduction of nitric acid [44, 45]. Finally, the recently described oscillatory oxidation of CO on platinum electrodes occurs for such high solution conductivity, that this system is considered a potential candidate for truly potentiostatic oscillator (see Sect. 5.2).

Class II. Oscillators with the S-shaped NDR. Similarly as for Class I, concentrations of chemical species are dynamic variables involved, but now the **electrode potential** appears to be an *essential system variable*. The electrode potential supplies the *slow, negative feedback* (a condition difficult to meet in practice, cf. section 2.3 for possible solution). Typical model examples of such Class II oscillators include potential-dependent, fast phase transitions of the adsorbate with strong lateral attractive interactions of particles (the case which can be described in terms of the Frumkin isotherm). Clearly, it cannot be the case of truly potentiostatic oscillator of Class I. Potentiostatic experiments, in the absence of ohmic drops, will only reveal the bistable behavior. Oscillations will occur in the presence of sufficiently large ohmic potential drops, when the externally applied voltage differs from the interfacial potential drop of the working electrode. Furthermore, under galvanostatic conditions, either the full S-shape will be revealed or the potential oscillations set in, in dependence of the system's dynamics. Experimental example of the system that exhibits S-shaped polarization curve (but not oscillatory instability) is presumably the electrocrystallization of zinc in the Leclanché cell [46]. Figure 3.23 shows schematically the theoretically possible behaviors for S-NDR systems, including also more complex case and the impedance diagram measured under galvanostatic conditions.

Class III—N-NDR oscillators. Evidently the most numerous class of electrochemical oscillators in which the explicit N-shaped NDR region in the I - E characteristics is crucial for the onset of oscillations. The electrode potential E is an *essential variable*, more strictly, an autocatalytic (positive feedback) variable. Purely chemical instabilities can be completely absent. Various sources of the formation of the N-NDR region were listed in Chap. 2. The system of such characteristics, for given externally applied voltage U , exhibit current oscillations in the presence of appropriate ohmic potential drops, caused by the serial resistance R_s , but under galvanostatic conditions only bistability is observed, since then the NDR region is a collection of unstable (saddle-type), and thus directly inaccessible steady-states (cf. Fig. 2.4). Typical examples of such systems include, e.g., polarographic $\text{In(III)}-\text{SCN}^-$ oscillator (see Chap. 4). Due to ohmic drops, the oscillations of the current are associated with the simultaneous oscillations of the electrode potential $E = U - IR_s$. The bifurcation diagram constructed in the $U - R_s$ space is characteristically cross-shaped (cf. e.g., Fig. 2.8). The impedance Nyquist spectrum for vanishing serial resistance, as discussed above (Figs. 3.13 and 3.14) intersects the real impedance axis on a negative side for $\omega_H > 0$, indicating the Hopf bifurcation and when $\omega \rightarrow 0$, the negative zero real impedance is again reached, indicating the saddle-node bifurcation. The simplest prototype model of the N-NDR oscillator can be defined as [33]

$$\frac{dE}{dt} = g(\theta) - f(\theta, E) \quad (3.92)$$

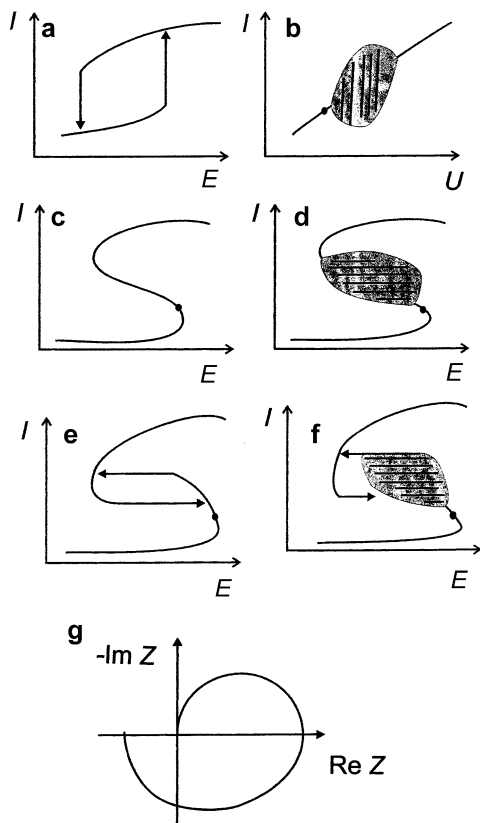


Fig. 3.23 Current/potential characteristics as well as characteristic impedance behavior for Class II (Kodera-type) oscillators. (a) Potentiostatic I - E behavior with IR compensation (strictly potentiostatic case), (b) potentiostatic I - U behavior for sufficiently large values of the uncompensated ohmic resistance; (c) and (d) galvanostatic I - E behavior in the case of a simple S -shaped polarization curve for a subcritical and supercritical value of time scale parameter ε of the electrode potential, respectively, (e) and (f) galvanostatic I - E behavior in the case of a complex S -shaped polarization curve for a subcritical and supercritical value of time scale parameter ε of the electrode potential, respectively, (g) characteristic impedance diagram of Class II oscillators as obtained at the points of the current/potential curves indicated by the black solid circles. Reprinted from [42], Copyright 1999, with permission from Elsevier

$$\frac{d\theta}{dt} = \frac{U - E}{R_s} - f(\theta, E) \quad (3.93)$$

where $f(\theta, E)$ is a “current-function,” i.e., the Butler–Volmer expression modified so that it exhibits the N-NDR region, and $g(\theta)$ describes the (relatively) slow dynamics of the species that is formed or transported by the potential-independent process (remark important also for comparison with class IV, see below).

Class IV—HN-NDR (galvanostatic) oscillators. In terms of this classification, Class IV exhibits partly similar characteristics as Class III, in that sense, that the electrode potential remains the fast autocatalytic variable. However, systems of Class

IV exhibit oscillations under galvanostatic conditions (without ohmic drop) and under potentiostatic conditions (with sufficiently large ohmic drop). These systems are characterized with the hidden negative impedance (HN-NDR type), which manifests itself as the negative impedance for a range of non-zero ac frequencies, with the positive zero frequency impedance (corresponding to the positive slope of the dc I - E curve). For such impedance characteristics to occur, two coupled, potential-dependent processes have to be present: a relatively fast process giving rise to negative impedance and a slower process of a positive impedance which dominates the steady-state dc I - E characteristics. The presence of sufficient external resistance is not necessary for the galvanostatic oscillations, but is required for the onset of potentiostatic ($U = \text{const}$) oscillations of the current for this class of unstable systems (see Fig. 3.22). The bifurcation diagram for HN-NDR oscillators, remarkably different from that for N-NDR systems, was shown in Fig. 3.18. Besides the reversed role of increasing serial resistance which does not suppress oscillations, the bifurcation diagram for the Class IV oscillators always involves the homoclinic bifurcation, corresponding to decay of the oscillations due to collision of the limit cycle with the (galvanostatically unstable) saddle points from the NDR branch (Fig. 3.18).

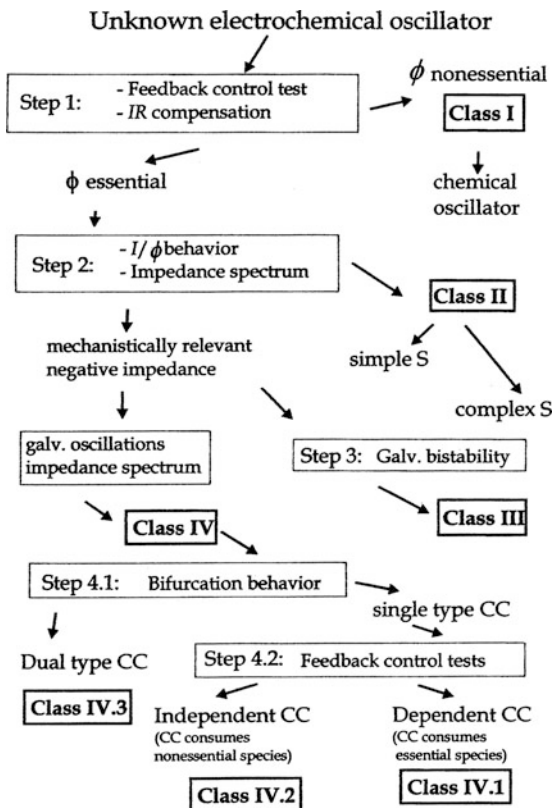
Furthermore, Strasser et al. [42] have suggested to divide further Class IV oscillators into the following subcategories:

Class IV.1. Potential-dependent source of inhibitor (so far, only theoretical case)

Class IV.2. The H_2 /formic acid group, meaning the oxidation of H_2 in the presence of electrosorbing metal cations and anions, the oxidation of formic acid on Pt, of formaldehyde on Rh, the dissolution of nickel in the transpassive region. This subcategory typically involves an independent current carrier, i.e., the species engaged in a faradaic process consuming non-essential species only. Model calculations showed that this faradaic current can be potential-dependent (Butler-Volmer relation) or even potential-independent (i.e., in a plateau region). At the model level, description of dynamical systems of this type requires three variables: electrode potential E , an essential “fast” chemical species and an essential “slow” chemical species, producing the negative feedback. The dynamics of the slow species may completely cover up the N-shaped potential profile of the fast subsystem.

Class IV.3. This category, named the “ IO_3^- group,” includes the systems which are born from typical NDR system by adding an appropriate *independent current carrier* exhibiting usual Butler-Volmer kinetic characteristics. In this case the independent current carrier does *not* consume slow chemical variable. Instead, this additional current providing reaction may proceed on free (not blocked) surface sites. This additional current overlaps with the N-NDR region, hiding it under dc conditions and in this way transforming the N-NDR into HN-NDR oscillator. Examples of such oscillators include, among others, the electrocatalytic galvanostatic reduction of IO_3^- on Ag, the model of which was elaborated by Strasser et al. [47] (see Chap. 4). These authors suggested further that $\text{Fe}(\text{CN})_6^{3-}$ reduction or the $\text{Fe}(\text{CN})_6^{4-}$ oxidation on Pt might occur due to analogous mechanism, contrary to original view of other authors, Li et al. [48, 49] who postulated the significant role of convection caused by evolving gaseous hydrogen or oxygen, respectively (see also Chap. 5, volume II). In more detail, it became a matter of

Fig. 3.24 Overview of an operational method for the experimental classification of an unknown electrochemical oscillator (CC = current carrier). See original reference [42] for details. Reprinted from [42], Copyright 1999, with permission from Elsevier



controversy whether the hydrogen or oxygen evolution at extreme negative or positive potentials played only a role of an independent current carrier or was a source of convective motion, causing the replenishment of the diffusion layer with the essential electroactive species.

Based on the above categorization, Strasser et al. [42] have suggested further a systematic experimental strategy for the classification of electrochemical oscillators, illustrated in Fig. 3.24.

Obviously, the above classification does not include all types of electrochemical dynamical systems—it does not cover the spatiotemporal and spatial pattern formation, as well as it omits instabilities caused by electrochemically generated convection (see Chap. 5, volume II). But even with respect to temporal instabilities, this categorization of electrochemical oscillators became later subject of discussions and several modifications or extensions were proposed, when new types of such systems were discovered. Some of these suggestions will be given later in this book, in the discussion of selected experimental oscillatory systems. Here we shall mention that Kiss et al. [50] have suggested the application of the method of changing the time scale associated with dynamical variables (see Sect. 2.3) to the classification of

oscillating electrochemical systems, complementary to that suggested by Strasser et al. The basis for Kiss's et al. idea is the fact that recursive feedback controller can be applied to add (positive or negative) pseudocapacitance to the inherent double layer capacitance of the electrochemical system. For the N-NDR and HN-NDR type systems, when the electrode potential plays the role of a fast activator species, the added pseudocapacitance destroys the oscillations through the Hopf bifurcation. On the contrary, for the S-NDR systems, when the electrode potential is a slow inhibitor, the onset of current oscillations requires sufficiently high pseudocapacitances. This shows a striking, qualitative difference in the fundamental kinetic features of those two types of electrochemical oscillators. In view of that, it is interesting to note also the possibility of generation of chemically generated pseudocapacitance which can arise at an electrode when the extent of faradaically admitted charge depends (quasi) linearly on the applied voltage, as in the case of conducting polymers and RuO_2 [51]. For galvanostatic oscillations during formic acid oxidation, Inzelt and Kertész [52] have reported effects of changing the capacitance of an electrode by polyaniline film. However, the variations of this pseudocapacitance did not exceed a few mF cm^{-2} , so might be insufficient to change significantly enough the time scale of a given variable. On the contrary, the differential control by Kiss et al. can cause effects of the order of even a few F cm^{-2} . An analogous approach is potentially applicable to CSTR systems, where the inlet concentrations of chemicals could be changed proportional to the concurrently determined time derivative of concentrations [50]. In this way also chemical species essential for the oscillations could be explicitly detected.

Finally, as a complement of the above classification of the oscillators, let us pose a seemingly strange question: Does the existence of the N-NDR region always guarantee the oscillatory behavior, depending only a serial resistance R_s ? In order to consider this problem, we shall invoke again the model by Koper and Sluyters [33], simplified to two dynamical variables, but adapted now to potentiostatic ($U = \text{const}$) conditions. The adsorption and desorption rate constants will first be assumed *independent* of the electrode potential. After dividing both Equations by the β factor, which operation allows to express the difference of the time scales in terms of only one parameter ε' , one obtains

$$\varepsilon' \frac{dE}{d\tau} = \frac{U - E}{r} - k_e(E)\theta \quad (3.94)$$

$$\frac{d\theta}{d\tau} = k_a(1 - \theta) - k_d\theta - k_e(E)\theta \quad (3.95)$$

Linear stability analysis of the steady-state of this system indicates the possibility of both saddle-node bifurcation (bistability) and a Hopf bifurcation (oscillations). For the latter case, based on the condition for zero trace and positive determinant of the Jacobian matrix one derives the following condition for a Hopf bifurcation in this system:

$$\frac{dk_e(E)}{dE} = -\frac{k_a + k_d + k_e(E)}{rk_a} - \varepsilon' \frac{[k_a + k_d + k_e(E)]^2}{k_a} \quad (3.96)$$

provided that

$$\frac{k_e(E)}{r} - \varepsilon'[k_a + k_d + k_e(E)](k_a + k_d) > 0 \quad (3.97)$$

These conditions summarize that what we already know from the analysis of simpler models (see Chap. 2): (1) oscillations set in provided the serial resistance r is sufficiently large and (2) the ε' parameter is sufficiently small, meaning that the dynamics of the electrode potential should be sufficiently fast (the oscillations becoming increasingly relaxation like for decreasing ε'). The bifurcation diagram of this system is also typical of other systems, exhibiting the N-shaped NDR (N-NDR) region (cf. Fig. 2.8).

Now let us go back to the question posed at the beginning of this section: Does the N-NDR region always give rise to oscillations, if the above conditions are met? Following Koper and Sluyters [33] we shall prove that it is not always the case. For that purpose let us introduce to the model (3.94, 3.95) the second surface species, of coverage θ_p , which poisons the electrode surface. The surface equilibrium of this poison establishes quickly, so it is dependent only on the potential E and the coverage θ of the electroactive species, i.e., $\theta_p = f(E, \theta)$. In other words, the poison competes with the electroactive species for the free adsorption sites at the electrode surface. If so, at any moment the number of sites still available for electroactive species is decreased from $(1 - \theta)$ to $[(1 - \theta) - \theta_p]$ which factor affects its adsorption rate:

$$\varepsilon' \frac{dE}{d\tau} = \frac{U - E}{r} - k_e(E)\theta \quad (3.98)$$

$$\frac{d\theta}{d\tau} = k_a[1 - \theta - \theta_p(E, \theta)] - k_d\theta - k_e(E)\theta \quad (3.99)$$

Fundamental conclusions are drawn from the trace and the determinant of the Jacobian matrix of this system:

$$\text{Tr}(J) = - \left\{ \frac{1}{\varepsilon'} \left[\frac{1}{r} + \theta \frac{dk_e(E)}{dE} \right] + k_e(E) + k_d + k_a \left(1 + \frac{\partial\theta_p}{\partial\theta} \right) \right\} \quad (3.100)$$

$$\text{Det}(J) = \frac{1}{\varepsilon'} \left\{ \left[\frac{1}{r} + \theta \frac{dk_e(E)}{dE} \right] \left[k_d + k_a \left(1 + \frac{\partial\theta_p}{\partial\theta} \right) \right] + \frac{k_e(E)}{r} - k_e(E)k_a \frac{\partial\theta_p}{\partial E} \right\} \quad (3.101)$$

Let us consider first the occurrence of bistability, requiring $\text{Det}(\mathbf{J}) = 0$ which case can happen only for *either* appropriate negative slope $dk_e(E)/dE$ or appropriate positive slope $\partial\theta_p/\partial E$. The former case is well known from the simpler models,

while the latter conclusion means that even if there is no NDR of the charge-transfer step, the I - E curve can exhibit negative slope, giving rise to the saddle-node bifurcation, if the poisoning of the electrode increases with increasing potential.

Turning now to a Hopf bifurcation, one concludes that the condition $\text{Tr}(\mathbf{J}) = 0$ can be met only if $dk_c(E)/dE$ is negative, since the last term in the trace must be positive, due to $-1 < \partial\theta_p/\partial\theta < 0$ (because the particles of the electroactive species and the poison compete, by assumption, for the same site at the electrode surface). Thus, if only the competitive adsorption of the poison, without affecting the $k_c(E)$ dependence, causes the negative slope of the I - E curve, the oscillations will *not* set in. The oscillations will appear, however, if the poison causes the decrease of $k_c(E)$ with increasing potential. Passivation of the electrode surface is a good example, provided that the electrode process occurs through an adsorbed intermediate, as in the model.

3.6 Instabilities Involving Adsorption on Electrodes

3.6.1 The Frumkin Isotherm

It is evident that electrode processes involving adsorption state of reagents are numerous. Note that also the electrocatalytic model suggested by Koper and Sluyters [33] involved adsorbed reactant. In particular, the formation of adsorption layer associated with strong attractive lateral interactions of particles can be a source of various kinds of instabilities, caused by the formation of an S-NDR region (cf. Sect. 2.2.5). A series of theoretical papers was devoted to this problem which is thus worth of brief presentation here.

The role of adsorption in destabilization of electrochemical systems will be discussed in terms of the well-established Frumkin isotherm:

$$\frac{\theta}{1-\theta} = K \left(\frac{c_0}{c^0} \right) \exp(-g\theta) \quad (3.102)$$

with c_0 and c^0 meaning the actual and standard concentration of the adsorbate in the solution, while the parameter g describes lateral, inter-particle interactions in the adsorption layer. From the thermodynamic point of view, the non-zero interaction parameter means the dependence of the free Gibbs energy of adsorption on the coverage:

$$\Delta G_{\text{ads}} = \Delta G_{\text{ads}}^0 + gRT\theta \quad (3.103)$$

In notation (3.103), attractive lateral interactions are described by negative value of parameter g , with its critical value $g_{\text{crit}} = -4$, below which the Frumkin isotherm becomes S-shaped. Note that in the literature also exist notations with the reversed signs of g [i.e., with minus sign in Eq. (3.103)], so then the hysteresis between the upper and lower branches of the isotherm is observed for g higher than $+4$.

From the kinetic point of view, the non-zero interaction parameter means that the activation energy for desorption is increased by an amount $rgRT\theta$, and the activation energy for adsorption is decreased by an amount $(1-r)gRT\theta$, where r is the symmetry factor of the activation barrier, lying between 0 and 1. Accordingly, the rate constant for adsorption and desorption are given by the following relationships, respectively:

$$k_a = k_a^0 \exp[-(1-r)g\theta] \quad (3.104)$$

$$k_d = k_d^0 \exp(rg\theta) \quad (3.105)$$

If the adsorption and desorption are single-step processes, then according to the first postulate of formal chemical kinetics, the equilibrium constant K can be expressed as the $K = k_a^0/k_d^0$ ratio. Then, by taking equal rates of adsorption and desorption: $k_a(1-\theta)(c_0/c^0) = k_d\theta$, one derives the isotherm Eq. (3.102) on the kinetic basis. In the following considerations the symbol of the standard concentration $c^0 = 1 \text{ M}$ will be omitted for simplification of mathematical notation.

In the case of strong attractive interactions, expressed by overcritical (-4) value of interaction parameter g , the variation of the bulk concentration or the electrode potential causes the sudden phase transitions of adsorbed species. Nikitas et al. [53–56] have devoted several theoretical papers to this case, called a “polarization catastrophe,” in analogy to the abrupt phase transitions considered in Thom [57–61] catastrophe theory. Also Laviron [62] has analyzed theoretically the ac polarographic and impedance response of strongly adsorbed electroactive species obeying the Frumkin isotherm which undergoes quasi-reversible electron-transfer.

From the point of view of nonlinear dynamics, since the sudden phase transition occurs at the borders of the bistable region, it is associated with saddle-node bifurcation. Not particularly problematic for dc conditions, the situation becomes more complicated for impedance measurements, since close to these bifurcation parameters the condition of linearity, fundamental for impedance, cannot be satisfied, as Armstrong [63], who discussed the results of Wandlowski and de Levie [64], has pointed out. Inspired by this discussion, Berthier et al. have analyzed theoretically the case of adsorption phenomena obeying the Frumkin isotherm which, for the overcritical value of the parameter of the lateral interaction of adsorbed particles, attains the S-shaped course. Their analysis of the effects of saddle-node bifurcations on impedance response is briefly presented in the following section.

3.6.2 Model Mechanisms Involving Strong Adsorption

3.6.2.1 The Simplest Electrosorption Mechanism

In [65, 66] the following electrosorption mechanism involving an anion A^- and its surface-active oxidation product engaged in the reversible electrode process was assumed:



where “s” means the adsorption site. Since this is the only reaction path assumed, the faradaic current is related to the temporal variation of the electrode coverage (θ) of species A which interfacial concentration in the solution is taken as constant and equal to standard concentration 1 M. Then the dimensionless current Ψ , involving the mathematical form of the Frumkin isotherm, is expressed as

$$\Psi = \frac{d\theta}{d\tau} = (1 - \theta) \exp(\alpha_o \xi) \exp[-\alpha_o g(\theta - \frac{1}{2})] - \theta \exp[\alpha_r g(\theta - \frac{1}{2})] \exp[-\alpha_r \xi] \quad (3.107)$$

where $\xi = (F/RT)(E - E^0)$, α_o and α_r are the oxidation (anodic) and reduction (cathodic) transfer coefficient, respectively (the sum is equal to unity for the one-electron process: $\alpha_o + \alpha_r = 1$), g is the lateral interaction parameter in the Frumkin isotherm, and other symbols have their usual meaning. If the steady-state ($d\theta/d\tau = 0$) is achieved from Eq. (3.107) one derives the potential-dependent surface coverage θ described by the Frumkin isotherm:

$$\frac{\theta}{1 - \theta} \exp[g(\theta - \frac{1}{2})] = \exp(\xi) \quad (3.108)$$

In the case considered here the interaction parameter $g = -6$, i.e., lower than the critical value -4 , so the isotherm is S-shaped, as illustrated by Fig. 3.25a for the electrode coverage determined by the externally imposed, varying electrode potential E .

This picture visualizes the saddle-node bifurcations that occur at points denoted by D_1 and D_2 in Fig. 3.25a. The corresponding coverages θ_{D1} and θ_{D2} are given by the roots of the second degree equation:

$$\theta^2 - \theta - \frac{1}{g} = 0 \quad (3.109)$$

i.e.,

$$\theta_{D1,2} = \frac{1 \pm \left(1 + \frac{4}{g}\right)^{1/2}}{2} \quad (3.110)$$

The dimensionless potentials, at which the switching between the upper and lower branches of the stable steady-states occurs, are given by the equations:

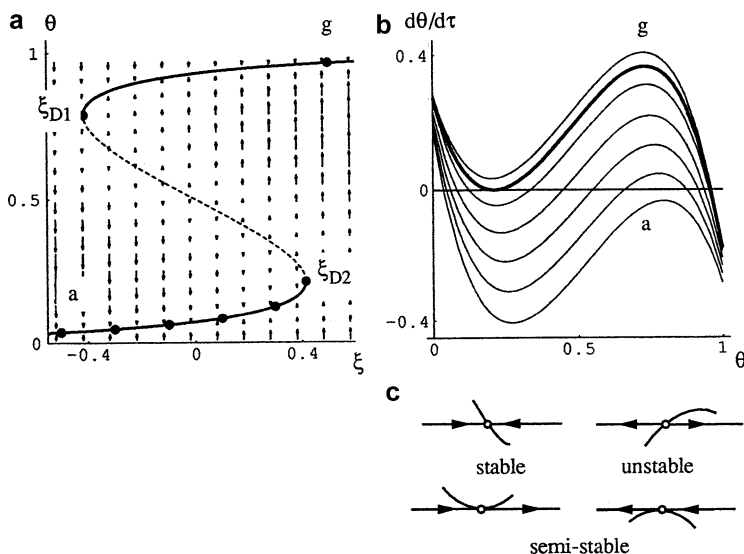


Fig. 3.25 (a) Frumkin isotherm (*solid lines*: stable steady-states; *dashed lines*: unstable steady-states; *bold lines*: dynamic θ vs. ξ curves) and (b, c) vector field, $d\theta/d\tau$ vs. θ phase plane calculated for $a \rightarrow g$ steady-state electrode potential. Parameter $g = -6$. Reprinted from [66], Copyright 1998, with permission from Elsevier

$$\xi_{D1,2} = \pm \left(\left\{ \frac{[g(4+g)]^{1/2}}{2} \right\} - \log \frac{[1 + (1 + \frac{4}{g})^{1/2}]}{[1 - (1 + \frac{4}{g})^{1/2}]} \right) \quad (3.111)$$

Based on this dependence, for $g = -6$ one calculates the corresponding potentials which are: $\xi_{D1} = -0.415$ and $\xi_{D2} = 0.415$.

If the linearity condition is met, the faradaic impedance can be calculated from the linear terms of the Taylor series expansion of Eq. (3.107), as corresponding to the equivalent circuit consisting of the serial connection of the charge-transfer resistance R_{ct} and the adsorption capacitance C_{ads} :

$$Z_f^* = R_{ct}^* + \frac{1}{j \Omega C_{ads}^*} \quad (3.112)$$

where the dimensionless quantities are defined as: $\Omega = \omega/k^0$, $f = F/RT$, $Z_f^* = fF\Gamma k^0 Z_f$, $R_{ct}^* = fF\Gamma k^0 R_{ct}$ and $C_{ads}^* = C_{ads}/(fF\Gamma)$; k^0 —standard kinetic rate constant, Γ —the number of electroadsorption sites per unit of electrode area. If the nonlinearity condition is not met, the impedance has to be computed as the numerical solution of the appropriately modified equation (3.107), in which the periodic perturbation of the steady-state potential was described as a sinusoidal dependence $\xi = \xi_i + d\xi \sin(\Omega t)$.

$$\Psi = \frac{d\theta}{d\tau} = (1 - \theta)\exp[\alpha_o(\xi_i + d\xi\sin \Omega t)]\exp\left[-\alpha_o g\left(\theta - \frac{1}{2}\right)\right] - \theta\exp\left[\alpha_r g\left(\theta - \frac{1}{2}\right)\right]\exp[-\alpha_r(\xi_i + d\xi\sin \Omega t)] \quad (3.113)$$

Using these dependences, the effects of the potential modulation amplitude and frequency on the impedance response were theoretically analyzed. Intuitively, one can understand that if, for given steady-state potential, the ac amplitude ($d\xi$) is so high that reaches the edge of the fold of the Frumkin isotherm, the current (and thus the impedance) response should undergo significant change. Systematic analysis of those effects involved the role of varying potential amplitude, and ac frequency Ω . These results can be summarized as follows.

Influence of ac Amplitude

For relatively *low* ac frequency $\Omega = 10^{-1}$, if the initial steady-state $\xi_i < 0$ lies on the lower isotherm branch and the ac amplitude is sufficiently small to keep the system at this branch, the response is almost linear, i.e., temporal oscillations of θ are nearly sinusoidal. With increasing amplitude, the nonlinearity of the variations of θ becomes more significant, and when the ac amplitude allows to pass the saddle-node bifurcation point, the variations of θ cover both lower and upper branches of the adsorption isotherm, in the form of high amplitude relaxation oscillations.

For the same low ac frequency Ω and the initial steady-state lying also on a lower branch, but closer to the bifurcation point, for small amplitude of the potential variation the response is of course similar to that described above, but exhibits more nonlinearity. For intermediate (overcritical) amplitudes, when the bifurcation point is crossed, the impedance spectrum looks, however, completely differently, since the system switches to the upper branch of the isotherm and, due to hysteresis in the bistable region, is now not able to return to the lower branch. In consequence, after the first perturbation the system's response includes only the small variations of θ in the upper branch. Finally, when the amplitude of the oscillations becomes so high, that the entire bistable region of the isotherm is spanned, both branches are involved in the oscillatory cycle and the power spectrum becomes appropriately complex.

Influence of Ac Frequency

Let us consider again the steady-state $\xi_i < 0$ belonging to the lower branch of the adsorption isotherm, i.e., far from the bifurcation point. Then, if the amplitude of the potential modulation is so low that the varying potential never attains the bifurcation value, the impedance diagram always characterizes the lower states, irrespective of ac frequency. However, if the amplitude allows to reach the bifurcation point, the response significantly depends on the ac frequency, since the system

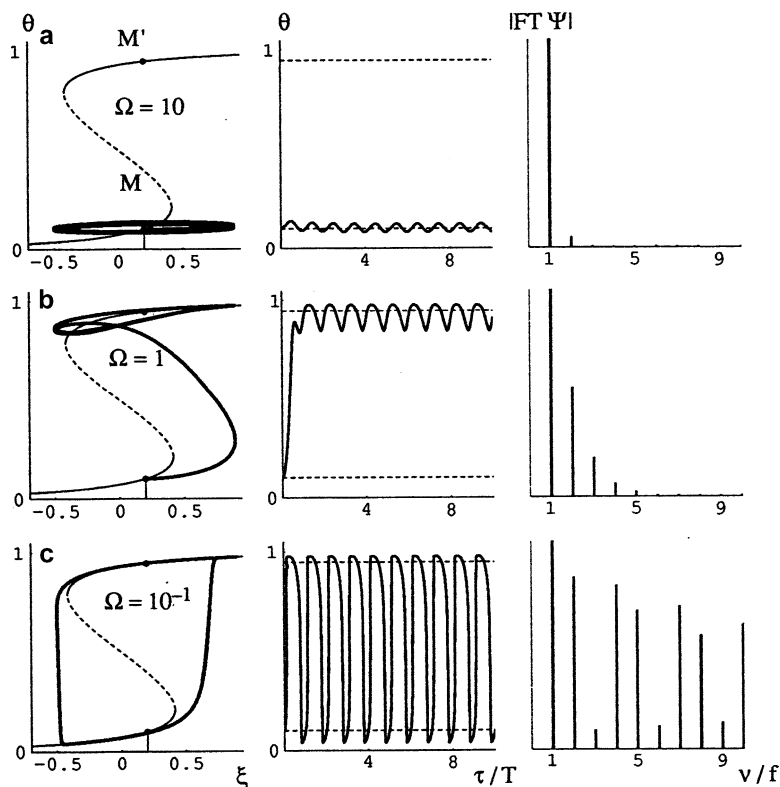


Fig. 3.26 Influence of the potential modulation frequency: θ vs. ξ trajectory (bold lines), variation with dimensionless time and power spectrum of the dimensionless current density Ψ calculated for $\xi_i = 0.2$, $d\xi = 0.7$, $\Omega = 10$ (a), 1 (b), 10^{-1} (c). Reprinted from [66], Copyright 1998, with permission from Elsevier

has, or has not enough time to respond with its electrode coverage. Thus, for sufficiently high ω , the system's response is practically limited to the lower branch of the states, while for sufficiently low values—it visualizes the variations of θ over the entire bistable region.

Figure 3.26 illustrates the case when the initial steady-state is closer to the bifurcation point, with the amplitude of potential perturbation spanning the bistability area (see caption for parameter values). The system's response is then strongly dependent on the ac frequency, covering three cases: (1) when Ω is sufficiently high, the system remains in the area of a lower branch of the isotherm (Fig. 3.26a), (2) for intermediate values of Ω , after the initial perturbation, the system switches permanently to the upper branch and remains there (Fig. 3.26b), (3) for appropriately low Ω , the system's response includes the switching between the lower and upper branches of the isotherm (Fig. 3.26c).

In terms of the above analysis it becomes understandable that the impedance spectra recorded for such conditions that saddle-node bifurcations occur, should

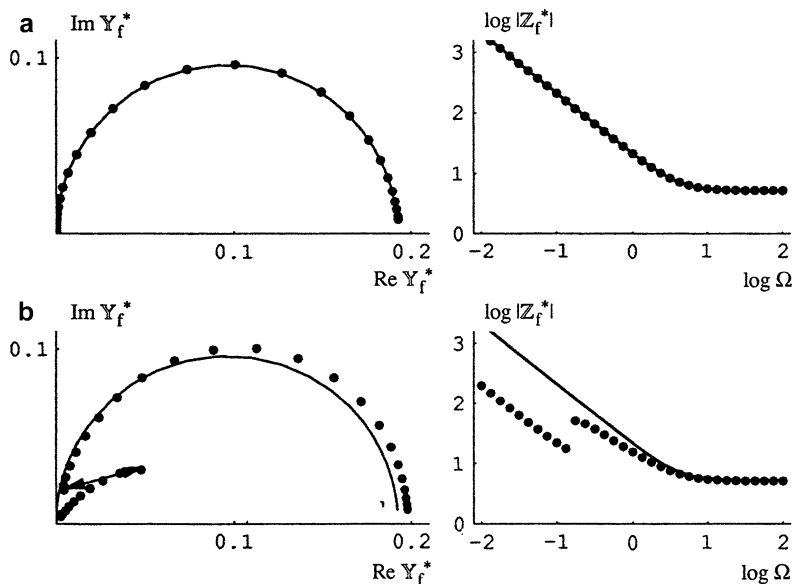


Fig. 3.27 Simulated immittance diagrams: nonlinear immittance diagrams (*dots*) and linear immittance diagrams (*solid lines*) calculated for $\xi_i = -0.45$, $d\xi = 0.2$ (a), 0.95 (b) using the Nyquist representation for the admittance diagrams and the Bode plot (modulus) for the impedance diagrams. The frequency sweep direction is indicated by the *arrows*. Reproduced from [66], Copyright 1998, with permission from Elsevier

exhibit discontinuities, i.e., sudden jumps in the system's response when the ac frequency is varied. Let us consider a few cases of such phenomena.

First, let us assume again that the initial steady-state is $\xi_i < 0$ and far from the bifurcation point. In a trivial case, when the ac amplitude is small enough, the impedance response reflects the characteristics of this steady-state, being practically the linear response of the system toward ac perturbations, the same one, *irrespective of the direction* of frequency changes (Fig. 3.27a).

In the second, more intriguing case, the ac amplitude is chosen so large, that the bifurcation point is reached. Then, when the impedance measurement is performed so that the ac frequency decreases, starting from relatively high values, the impedance spectrum switches from the response corresponding to the initial steady-state to the response illustrating oscillations around the two isotherm branches. Note-worthy, also in this case the same Nyquist diagrams are obtained for the increasing and decreasing ac frequency (Fig. 3.27b).

Next, when the steady-state potential $\xi_i > 0$ is close to the bifurcation point, there are more possible shapes of impedance diagram, depending on whether the ac amplitude reaches the bifurcation value. Again, if ac amplitude is sufficiently small, a single spectrum is obtained, as in Fig. 3.28a, which shows two spectra, depending on that whether the initial steady-state belonged to the lower (M) or upper (M') branch of the adsorption isotherm. When the ac amplitude is slightly higher, so that

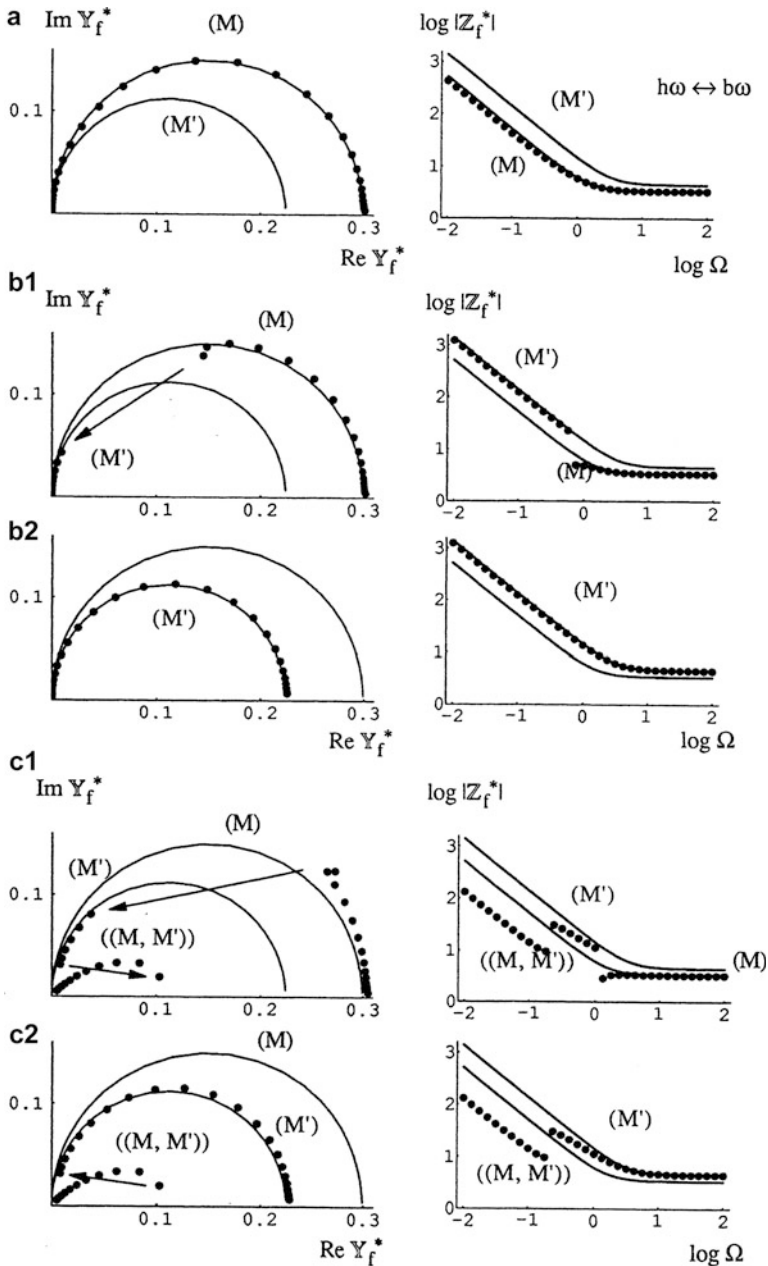


Fig. 3.28 Simulated immittance diagrams: nonlinear immittance diagrams (*dots*) and linear immittance diagrams (*solid lines*) calculated for $\zeta_i = 0.2$, $d\zeta_i = 0.2$ (a), 0.4 (b), 0.7 (c) using the Nyquist representation for the admittance diagrams and the Bode plot (modulus) for the impedance diagrams. The frequency sweep direction is indicated by the *arrows*. Reprinted from [66], Copyright 1998, with permission from Elsevier

one of the bifurcation point is crossed, the impedance spectrum *depends on the frequency sweep direction*. Upon *decreasing* frequency, one obtains two discontinuous parts, the high-frequency part corresponding to the starting lower branch of the isotherm, and the low-frequency part—to its upper branch (Fig. 3.28b1). On the other hand, upon *increasing* frequency, the switch between the branches of the isotherm occurs already for the first measurement frequency and one obtains a single, continuous spectrum, characterizing the steady-state belonging to the upper branch of the isotherm (Fig. 3.28b2).

Finally, ac potential amplitude can be so high that starting from the initial steady-state value, the potential crosses both bifurcation points. Upon *decreasing* the ac frequency, one obtains the impedance spectrum consisting of *three* discontinuous parts (Fig. 3.28c1). The high-frequency (HF) part corresponds to lower branch of the isotherm (when the initial steady-state was chosen, cf. Fig. 3.26a). The intermediate-frequency part corresponds to the system's behavior at the upper branch of the isotherm (cf. Fig. 3.28b). Finally, the low-frequency (LF) part corresponds to the large-amplitude switching of the system's state between the upper and the lower branches of the isotherm (cf. Fig. 3.28c). In turn, when frequency sweep is reversed: LF \rightarrow HF, one obtains a different, *two*-part nonlinear impedance diagram, corresponding to the switching from the large-amplitude, relaxation oscillations of the system's state at low frequencies to the small amplitude, harmonic oscillations of the system's state on the upper branch of the isotherm (Fig. 3.28c2).

In order to complete the description of the above transitions, let us note that the system could switch between the lower and the upper branches of the adsorption isotherm at certain critical angular frequency ω (or its dimensionless value Ω) which therefore can be actually considered the bifurcation parameter for the electric circuit. Detailed theoretical studies of the mechanism associated with this switching indicated also the presence of a kind of saddle-node bifurcation that is called the *tangent bifurcation*² and thus is also related to the creation/annihilation of three steady-states [67]. In order to illustrate this transition and understand the bifurcation name, it is convenient to interpret the respective system's evolution in terms of the Poincaré (or first return) maps (see Chap. 1). These maps reveal that between situations described by parts (c) and (d) a straight line of a unit slope becomes *tangent* to the Poincaré map at a critical point (Fig. 3.29) when the pair of stable and unstable fixed points comes together and disappears. Following this bifurcation, for even lower frequencies, the trajectory tends toward the upper part of the isotherm, whatever the value of the initial coverage ratio. In view of Fig. 3.29 this tangent bifurcation is a second one, since the first one occurs at a bit higher frequency $\Omega_{\text{bif}} = 0.77246$, below which the switching between the isotherm branches occurs, but provided that initial coverage value θ_i is greater than fixed point θ_{f1} indicated in Fig. 3.29a.

²Tangent bifurcation is described also in Section 6.1.3.3.

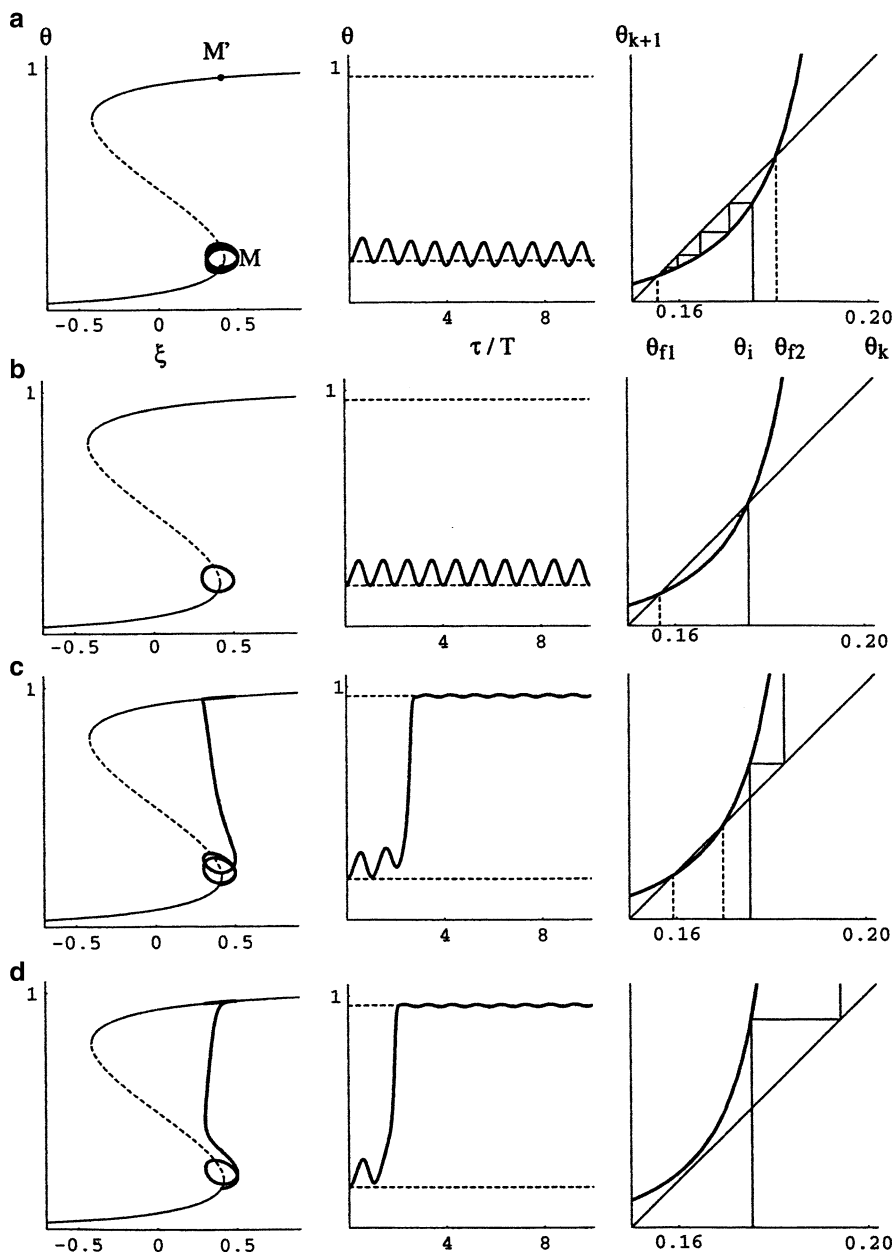


Fig. 3.29 Simulation of impedance measurements near the bifurcation frequency. First return maps plotted for $\xi_i = 0.4$; $d\xi = 0.1$; $\Omega = 0.8$ (a), $\Omega = \Omega_{\text{bif}} = 0.77246$ (b), $\Omega = 0.75$ (c) and $\Omega = 0.73$ (d). The third fixed point ($\theta_k \approx 1$) is not shown. Reprinted from [67], Copyright 1999, with permission from Elsevier

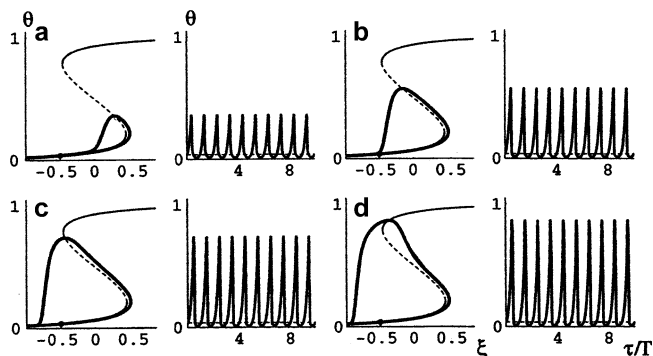


Fig. 3.30 Transition between low-amplitude harmonic oscillations and high-amplitude relaxation oscillations. $\xi_1 = -0.45$, $\Omega = 0.1$, $d\xi = 0.9164$ (a), 0.9168 (b), 0.916803 (c), 0.91681 (d). Reprinted from [67], Copyright 1999, with permission from Elsevier

The transition from the harmonic oscillations to large-amplitude relaxation oscillations was studied as a function of increasing ac perturbation amplitude. Figure 3.30 shows that this transition was characterized with steep but *continuous* increase of the oscillation amplitude, which resembles the so-called canard explosion (see also Sects. 1.6 and 4.1), i.e., not a true, but only an apparent bifurcation. Thus, sometimes it is necessary to distinguish between the terms “bifurcations” and “transitions.”

Finally, one should report another important feature of the presented model—the critical slowdown of the system’s dynamics which is due to the tangent bifurcation [67]. In practice it means that when the impedance measurement frequency approaches the tangent bifurcation frequency, the transient conditions become very long and thus require appropriate delay before impedance data are collected. Figure 3.31 shows this effect in terms of the model considered above.

3.6.2.2 The Volmer–Heyrovský Mechanism

Among other applications of impedance to the stability analysis of electrochemical systems, one should note theoretical paper by Berthier et al. [68] who described the multisteady I – E curves for the Volmer–Heyrovsky mechanism, which in classical electrochemistry has been used to explain the evolution of hydrogen [69] and chlorine [70], including the hydrogen evolution associated with iron electrodeposition [71]. For the oxidation reaction this mechanism consists of the following steps:



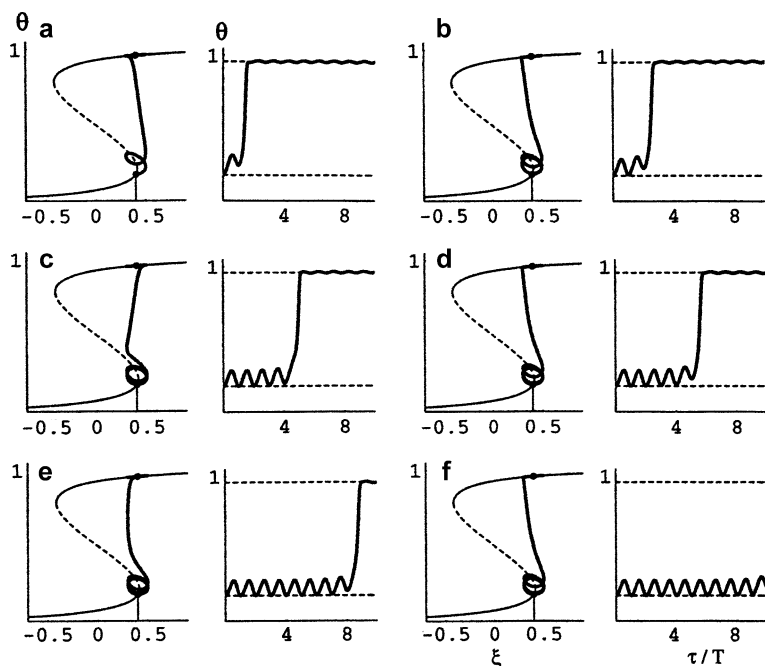


Fig. 3.31 Critical slow down near the bifurcation angular frequency: $\xi_i = 0.4$; $d\xi = 0.1$, $\Omega = 0.7$ (a); 0.75 (b); 0.77 (c); 0.771 (d); 0.7725 (e); 0.7726 (f). Reprinted from [67], Copyright 1999, with permission from Elsevier

The analysis was performed for the assumed irreversibility of both charge-transfer steps and the adsorption of surface active species was described in terms of the Frumkin isotherm, with strong, lateral attractive interactions between adsorbed particles, expressed with the overcritical ($g = -5$) interaction parameter. The faradaic impedance diagrams were calculated and the system's stability was analyzed in terms of zeros and poles (see next section). Also linear sweep voltammograms for the above mechanism were calculated, which showed the hysteresis in the I - E dependence upon cyclic variation of E , in a manner similar to the experimental characteristics of the pitting corrosion of metals, in the presence of depassivating species. The reader interested in particular detailed results of this analysis is advised to consult an original reference [68].

3.6.2.3 Two-Step Electrode Mechanism with Adsorbed Intermediate

Electrocatalytic mechanisms with the adsorption of the intermediate obeying the Frumkin isotherm with the strong lateral interactions, can potentially offer quite complicated dependences between the steady-state electrode coverage θ and the electrode potential. Such a case was analyzed by Sadkowsky [72, 73] for the two-step electrochemical mechanism:



which summarize into the overall reaction:



where $n = n_1 + n_2$

From the studies of the role of variation of different parameters of the model, we shall choose the case of varying lateral interaction parameter g , increasing from zero (as for the Langmuir isotherm) toward eight, i.e., crossing the critical value of 4, above which the hysteresis in the Frumkin response is observed (note that, contrary to earlier dependences, in this case the parameter g was defined so that its positive value means *attractive* interactions). Figure 3.32 shows that θ - ε (with ε meaning the dimensionless potential) dependences transform then from rather trivial shapes to the “mushroom” ones, exhibiting double hysteresis (for $g > 4$), finally splitting (at $g = 6$) into the “isolas.” One should note that isotherms of such complex shapes can contribute to the formation of surface patterns on the electrodes (cf. Chap. 1, volume II).

3.6.2.4 The Electrocatalytic Koper–Sluyters Model

The original, most general electrocatalytic Koper–Sluyters model was defined by Eqs. (3.56)–(3.58). It will be now analyzed for the case of strong attractive interactions of adsorbed particles, for a true potentiostatic case, i.e., at a given fixed potential E . Accordingly, Eq. (3.56) vanishes. One can further extend this model by introducing the linear change of the imposed electric potential, and observe the occurrence of appropriate bifurcations at respective critical potentials.

The potential-independent kinetics of adsorption and desorption is involved in the model, with the rate constants defined by Eqs. (3.104) and (3.105), respectively. Note, however, that below, compared to Eq. (3.102): (1) the coefficient g of lateral interactions in the adsorbed layer is replaced by symbol γ and (2) this coefficient is positive for attractive interactions. The symmetry factor for the activation barrier of the adsorption/desorption processes is equal to 0.5 (symmetrical barrier).

It is further assumed that the rate constant for the charge-transfer step, k_e , does not depend on θ , so $k_e(E, \theta)$ will reduce to $k_e(E)$. The only dynamic variables are thus: the surface concentration u of a reactant in the solution and the electrode coverage with this adsorbed species:

$$f(u, \theta) = \frac{du}{d\tau} = -k_a^0 \exp(0.5\gamma\theta)u(1 - \theta) + k_d^0 \exp(-0.5\gamma\theta)\theta + 1 - u \quad (3.119)$$

$$g(u, \theta) = \beta \frac{d\theta}{d\tau} = k_a^0 \exp(0.5\gamma\theta)u(1 - \theta) - k_d^0 \exp(-0.5\gamma\theta)\theta - k_e(E)\theta \quad (3.120)$$

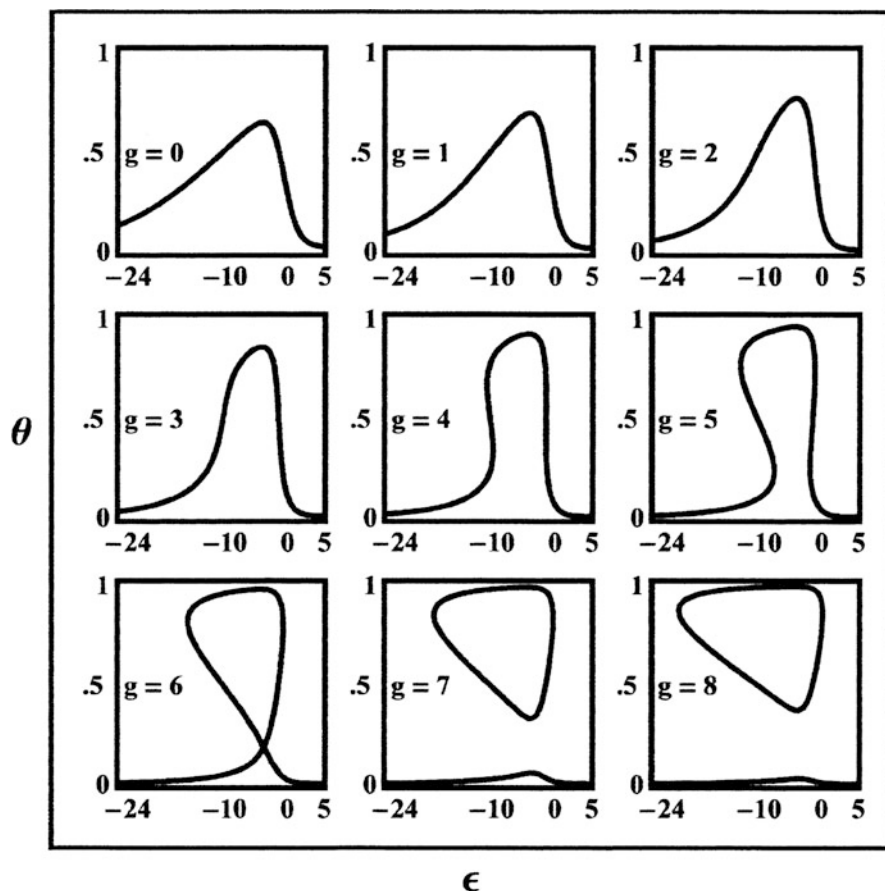


Fig. 3.32 Steady-state θ vs. ϵ relations for various values of the interaction parameter g (heterogeneity factor) shown in plots' panes. Other parameters: standard electron-transfer rate constants $k_1 = 1$, $k_2 = 10$, numbers of electrons exchanged $n_1 = n_2 = 1$, transfer coefficients $\alpha_1 = 0.37922$, $\alpha_2 = 0.5$, dimensionless formal potentials of [Eqs. (3.116) (3.117)]: $\epsilon_1 = 1$, $\epsilon_2 = -1$. Value of $\alpha_1 = 0.37922$ represents the transition from "mushroom" to "isola" shape of the steady-state isotherm for $g = 6$ (in this case positive g corresponds to attractive lateral interactions in the adsorption layer). Reprinted from [73], Copyright 2004, with permission from Elsevier

From the condition $du/d\tau = d\theta/d\tau = 0$ one determines the parameters of the steady-state (u_{ss} , θ_{ss}) and their stability can be found from the properties of the respective Jacobian matrix:

$$\mathbf{J} = \begin{bmatrix} \left(\frac{\partial f}{\partial u}\right)_{ss} & \left(\frac{\partial f}{\partial \theta}\right)_{ss} \\ \beta^{-1} \left(\frac{\partial g}{\partial u}\right)_{ss} & \beta^{-1} \left(\frac{\partial g}{\partial \theta}\right)_{ss} \end{bmatrix} \quad (3.121)$$

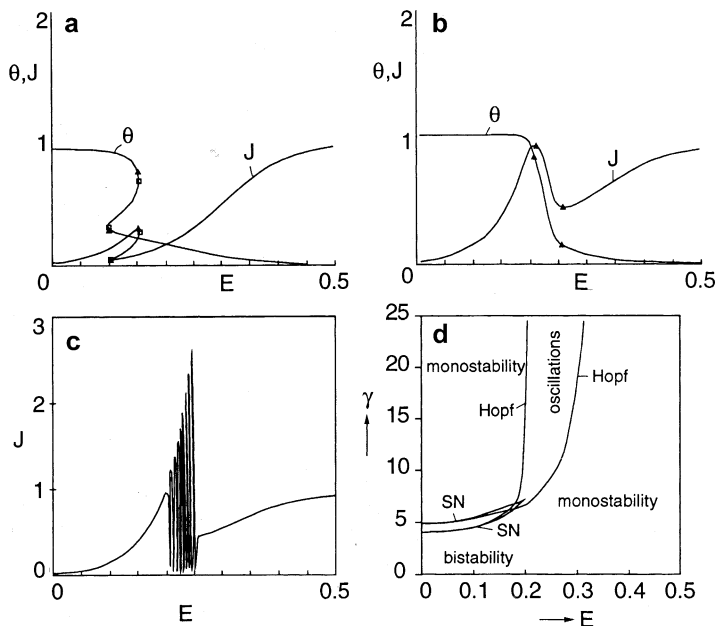


Fig. 3.33 Illustration of the solution behavior of [Eqs. (3.119)–(3.120)]; (a) steady-state solutions of θ and current density J for $\gamma = 5$; (b) as in (a) but for $\gamma = 8$; (c) potential sweep at 0.016 mV s^{-1} for $\gamma = 8$, showing the regions of spontaneous oscillations; (d) bifurcation map showing the different regions of monostability, bistability and oscillations in the γ - E plane. Triangles and squares in (a) and (b) indicate Hopf and saddle-node bifurcations, respectively. Other parameter values are $k_a = 10$, $k_d = 100$, $\beta = 0.01$, $k_e^0 = 0.02$, and $f = 38.7$. Reprinted from [33], Copyright 1994, with permission from Elsevier

The saddle-node bifurcation ($\text{Det}(\mathbf{J}) = 0$) occurs if:

$$uk_a^0 \exp(0.5\gamma\theta)[1 - 0.5\gamma(1 - \theta)] + k_d^0 \exp(-0.5\gamma\theta)[1 - 0.5\gamma\theta] + k_e + k_e k_a^0 \exp(0.5\gamma\theta)(1 - \theta) = 0 \quad (3.122)$$

and a Hopf bifurcation ($\text{Tr}(\mathbf{J}) = 0$) takes place if:

$$uk_a^0 \exp(0.5\gamma\theta)[1 - 0.5\gamma(1 - \theta)] + k_d^0 \exp(-0.5\gamma\theta)[1 - 0.5\gamma\theta] + k_e = -\beta[1 + k_a^0(1 - \theta) \exp(0.5\gamma\theta)] = 0 \quad (3.123)$$

provided that $\text{Det}(\mathbf{J}) > 0$. Analysis of this condition shows that oscillations are possible, as of course one should expect, only for positive values of parameter γ , i.e., for attractive lateral interactions in the adsorption layer. Figure 3.33 shows exemplary θ - E and J - E dependences for the bistable and oscillatory regimes, including the bifurcation diagram, showing the borderlines of these regimes in the E - γ coordinate system.

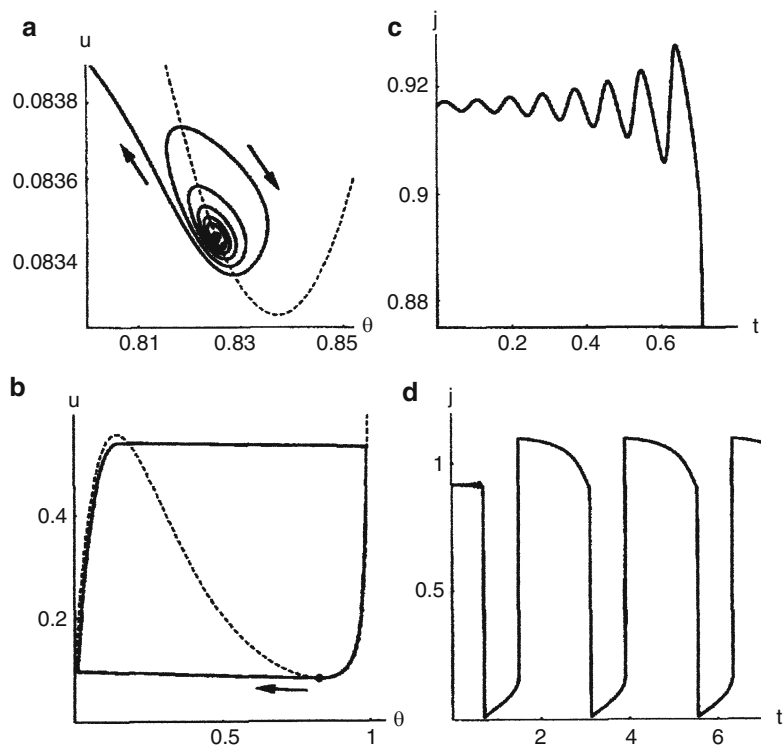


Fig. 3.34 (a, b) Phase plane portraits and (c, d) changes of current J with time. $E_s = 0.2076$; harmonic oscillations for short times (*upper row*) and relaxation oscillations for long times (*lower row*). $\delta\theta = \delta u = 10^{-5}$. Dashed curve: slow manifold. Reprinted from [74], Copyright 1997, with permission from Elsevier

This variant of the Koper–Sluyters electrocatalytic mechanism was later analyzed also by Berthier et al. with respect to the Hopf bifurcations. In the work [74] they have shown that, depending on the increasing distance between the actual electrode potential and the potential corresponding to the Hopf bifurcation ($\delta E = E_s - E_{HB1}$), two different types of behavior can be observed: (1) when the potential exceeds only slightly the bifurcation value (e.g., $E_s = 0.2075673$, $\delta E = E_s - E_{HB1} = 3 \times 10^{-6}$), the limit cycle is born via the supercritical Hopf bifurcation and (2) when the potential is only slightly higher than the previous value (e.g., $E_s = 0.2076$), the oscillations are initially sinusoidal, with the amplitude quickly increasing and at certain time there is a fast transition from small harmonic oscillations to large amplitude, stable relaxation oscillations (Fig. 3.34).

Such sequence of events, as the authors indicate [74] resembles the “canard explosion” (mentioned also above and in Sects. 1.6 and 4.1) and considered only *apparent* bifurcation. Finally, when the electrode potential is even higher, only the relaxation oscillations are observed, which set in as high-amplitude ones

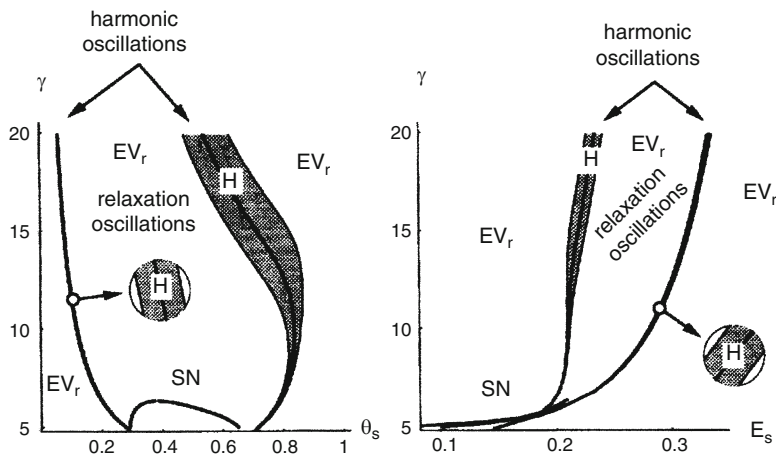


Fig. 3.35 Bifurcation map showing the different regions of oscillations in the γ, θ and γ, E planes. EV_r : real eigenvalues, shaded area: complex eigenvalues. H Hopf bifurcation, SN saddle-node bifurcation. Reproduced from [74], Copyright 1997, with permission from Elsevier

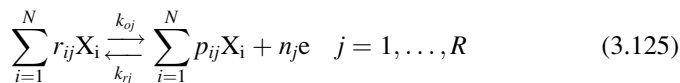
immediately. These behaviors are collected in the respective bifurcation diagrams, shown in Fig. 3.35.

In addition to the analysis under true potentiostatic conditions, there was also considered a case of linear sweep voltammetry, when the dynamics of the imposed potential variations interacts with the inherent dynamics of the electrochemical systems (with ohmic potential drops also neglected). The general phenomenon of delay in occurrence of the Hopf bifurcation, i.e., in this case the delay in the value of the electrode potential where oscillations set in, was reported, in accordance with theoretical earlier reports by Erneux et al. [75, 76] and more recent experimental studies, by Koper and Abuda, of Ni dissolution in aqueous H_2SO_4 medium [77]. Also, in view of the above characteristics of the model system considered it is intuitively understandable that transient harmonic oscillations could be observed only for sufficiently slow scan rates, while for faster scans only the onset of relaxation oscillations was reported.

Later, Berthier et al. [78, 79] have reanalyzed the conditions for the Hopf bifurcation in the Koper and Sluyters model. This approach involved their own derivation of the impedance response which led them to the conclusion that the negative faradaic impedance ($Z_f(s) < 0$, where $s = j\omega$), so important for diagnosis of the electrochemical system's stability, does not necessarily mean the negative charge-transfer resistance (R_{ct}), contrary to earlier suggestions, also described in the present work. The key relationship is expressing the faradaic impedance, $Z_f(s)$, as the product of R_{ct} and the function $F(s)$:

$$Z_f(s) = R_{ct} \times F(s) \quad (3.124)$$

In terms of such a definition, quite formally, the negative impedance requires only different signs of R_{ct} and $F(s)$. Berthier et al. [79] claim that the charge-transfer resistance R_{ct} in the Koper and Sluyters model is always positive even when the steady-state point corresponds to a Hopf bifurcation, so the negative impedance Z_f must be caused by the negative sign of $F(s)$. In a generalized case of a multistep electrode process, consisting of R steps:



the rate of each step is expressed as

$$v_j(t) = k_{oj} \prod_{i=1}^N X_i(t)^{r_{ij}} - k_{rj} \prod_{i=1}^N X_i(t)^{p_{ij}} \quad j = 1, \dots, R \quad (3.126)$$

and, accordingly, the total faradaic current density is given by

$$j_f(t) = F \sum_{j=1}^R n_j v_j(t) \quad (3.127)$$

The perturbation of the current density, $\Delta j_f(t)$, resulting from the perturbation of the input potential, $\Delta E(t)$, is given by

$$\Delta j_f(t) = j_f(t) - j_f = \left(\frac{\partial j_f}{\partial E} \right) \Delta E(t) + \sum_{i=1}^N \left(\frac{\partial j_f}{\partial X_i} \right) \Delta X_i(t) \quad (3.128)$$

and after applying the Laplace transformation (where $s = j\omega$):

$$\Delta j_f(s) = \left(\frac{\partial j_f}{\partial E} \right) \Delta E(s) + \sum_{i=1}^N \left(\frac{\partial j_f}{\partial X_i} \right) \Delta X_i(s) \quad (3.129)$$

Accordingly, the complex faradaic impedance $Z_f(s)$ is defined as

$$Z_f(s) = \frac{\Delta E(s)}{\Delta j_f(s)} = R_{ct} + \sum_{i=1}^N Z_{X_i}(s) \quad (3.130)$$

where the charge-transfer resistance:

$$\begin{aligned} R_{ct} &= \left(\frac{\partial j_f}{\partial E} \right)^{-1} = \left[F \sum_{j=1}^R \left(n_j \frac{\partial v_j}{\partial E} \right) \right]^{-1} \\ &= F \left\{ \sum_{j=1}^R n_j \left[\left(\frac{\partial k_{oj}}{\partial E} \right) \prod_{i=1}^N X_i(t)^{r_{ij}} - \left(\frac{\partial k_{rj}}{\partial E} \right) \prod_{i=1}^N X_i(t)^{p_{ij}} \right] \right\}^{-1} \end{aligned} \quad (3.131)$$

and

$$Z_{X_i}(s) = -\frac{(\partial j_f / \partial X_i)}{(\partial j_f / \partial E)} \times \frac{\Delta X_i(s)}{\Delta j_f(s)} = -R_{ct} \left(\frac{\partial j_f}{\partial X} \right) \times \frac{\Delta X_i(s)}{\Delta j_f(s)} \quad (3.132)$$

The function $F(s)$ in the product (3.124) is thus defined by

$$F(s) = 1 - \sum_{i=1}^N \left(\frac{\partial j_f}{\partial X_i} \times \frac{\Delta X_i(s)}{\Delta j_f(s)} \right) \quad (3.133)$$

In fact, the contribution from Berthier et al. expresses the reservation against, otherwise quite popular for its mathematical usefulness, but physically unclear decrease of the rate constant of the charge-transfer process with increasing potential, i.e., against the classical Butler–Volmer model. The general conclusion is that in view of the above analysis, the presence of a Hopf bifurcation is not always related to a negative sign of the charge-transfer resistance R_{ct} [79].

3.7 The Advantages of Zero–Pole Representation of Impedance for the Stability Analysis

For a more general treatment of the stability of electric circuits it is convenient to define the impedance in a complex frequency domain, as the ratio of the Laplace transforms of the perturbations $\Delta E(t)$ and $\Delta I(t)$:

$$Z(s) = \frac{\Delta E(s)}{\Delta I(s)} \quad (3.134)$$

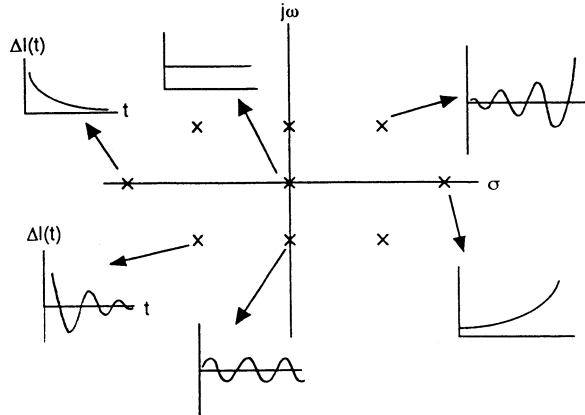
where

$$\Delta E(s) = \int_0^{\infty} \Delta E(t) \exp(-st) dt \quad (3.135)$$

$$\Delta I(s) = \int_0^{\infty} \Delta I(t) \exp(-st) dt \quad (3.136)$$

and $s = \sigma + j\omega$. The perturbation $\Delta E(t)$ and $\Delta I(t)$ are not necessarily a periodic (sine) function, but can be also a step function (or of any other Laplace transformable form). This approach appears particularly useful, when it is not possible to find a unique relevant equivalent circuit or the numerical fitting of the values of parameters of actual circuit appears to be unsuccessful. It is then convenient to represent the impedance of the circuit in terms of *zeros* (i.e., the complex angular

Fig. 3.36 The various transient solutions of $\Delta I(t)$ in Laplace's plane. Reprinted from [35] with permission of John Wiley & Sons, Inc. Copyright 1996



frequencies, for which the total impedance is zero) and *poles* (i.e., the complex angular frequencies for which impedance is infinite, or equivalently the admittance is zero).³ In their important analysis, Naito et al. [80], continuing Koper's intuitive, graphical diagnosis of bifurcations from impedance data, have performed analytical derivations showing that the complex impedance $Z(s)$, expressed as a function of a complex variable $s = \sigma + j\omega$, can be represented as the ratio of characteristic polynomials of the Jacobian matrices of linearized system under potentiostatic control and under galvanostatic control. It was thus shown that the zeros of the impedance are equal to the eigenvalues of the Jacobian matrix of the system under potentiostatic control, while the poles of the impedance are equal to the eigenvalues of the Jacobian matrix for the galvanostatic control. Those zeros or poles of the impedance function $Z(s)$ correspond thus to the solutions of the (linearized) differential equations governing the potentials and the current in the circuit, which are expressed in terms of the exponential form $\exp(st) = \exp[(\sigma \pm j\omega)t]$. Analogies with the predictions of the mathematical linear stability analysis are evident: the electric circuit will exhibit sustained oscillations, initially of frequency ω , when $\sigma \geq 0$ and $\omega > 0$ (see also, de Levie [27]). Figure 3.36 illustrates schematically, how the current response, following the perturbation of the potential of the linearized electric circuit, depends on σ and $j\omega$ components of s . Of course, e.g., zero of impedance $Z(s)$ means that the resonance of the circuit characteristics with the externally applied ac perturbation occurred, and in this way we come back to the same principle of bifurcation diagnosis from impedance spectra, as given in Sect. 3.3.2.

The advantage of expressing impedance in terms of zeros and poles for stability analysis was more recently recommended by Sadkowski et al. in several papers [13, 15, 81, 82] which will be briefly summarized below. In such representation, the

³ A *pole* of the complex function $f(z)$ is the point c meeting the condition that $f(z)$ approaches infinity, when z approaches c ; complex *zero* of $f(z)$ means the point at which $f(z) = 0$.

impedance is expressed as the ratio of two polynomials of the n th order, where the minimum value of n corresponds to the minimum number of capacitances C_i (hence also of the time constants $R_i C_i$) in the equivalent circuit and can be increased for enhancement of the goodness of fit.⁴ Equivalent representation of these polynomials are possible:

$$\begin{aligned} Z(s) &= Z(\infty) \frac{s^n + a_{n-1}s^{n-1} + \dots + a_1s + a_0}{s^n + b_{n-1}s^{n-1} + \dots + b_1s + b_0} \\ &= Z(\infty) \frac{(s - z_1)(s - z_2) \times \dots (s - z_n)}{(s - p_1)(s - p_2) \times \dots (s - p_n)} \end{aligned} \quad (3.137)$$

where $Z(\infty) \equiv R_s$, while z_i are zeros, and p_i the poles of the impedance, in the units of angular frequency (rad s^{-1}). An important advantage is that in terms of Eq. (3.137) one can represent the impedance response of the circuit generated not only with a periodic (ac) perturbation, but also the response generated by the pulse (potential or current) response.

In order to illustrate the application of the poles and zeros representation to the diagnosis of system's stability, let us refer to exemplary experimental data of Cu electrodisolution in $\text{CuSO}_4 + \text{H}_2\text{SO}_4$ medium, reported by Sadkowski [81, 82]. The impedance spectrum shown in Fig. 3.37, obtained for Cu electrode before anodic pre-polarization, is typical for the hidden real negative resistance, manifesting itself for the range of intermediate frequencies, with the zero-frequency impedance (dc slope) remaining positive [82]. In turn, Fig. 3.38 shows the spectrum after anodic pre-polarization in which negative real impedance does not manifest itself.

At this place it is useful to become familiar with the following notation for both types of the electrochemical systems. For the "trivial" systems (like type II), i.e., with only positive resistance (and positive capacitances and inductances), guaranteeing unconditional stability, the phase angle is confined to the $(-90^\circ, 90^\circ)$ range, and this is a definition for the so-called *minimum-phase* (mp) systems. In other words, their impedance spectra must be confined to the right-half of the $-Z''$ vs. Z' coordinate system. For the systems, like system I above, the phase angle exceeds the range of $(-90^\circ, 90^\circ)$ and such systems are therefore classified as *non-minimum phase* (nmp) ones (see Fig. 3.39). Since the phase angle can then attain any value, the impedance spectrum of such system can penetrate all quadrants of the $-Z''$ vs. Z' coordinate system.

The polynomial function for $Z(s)$ was fitted to both impedance spectra from Figs. 3.37 and 3.38, and the resulting zeros and poles are collected in Table 3.1.

In the absence of the additional (R_{ad}) ohmic resistance (rows I and II), when the serial resistance R_s means only the inherent resistance of the electrolytic cell, all

⁴The orders of the polynomials in the numerator (n) and in the denominator (m) meet the conditions: $m = n$, for typical case of dc conducting electrodes or $m = n + 1$ for "blocking electrodes" of capacitive character [15]. Here we always assume case: $n = m$.

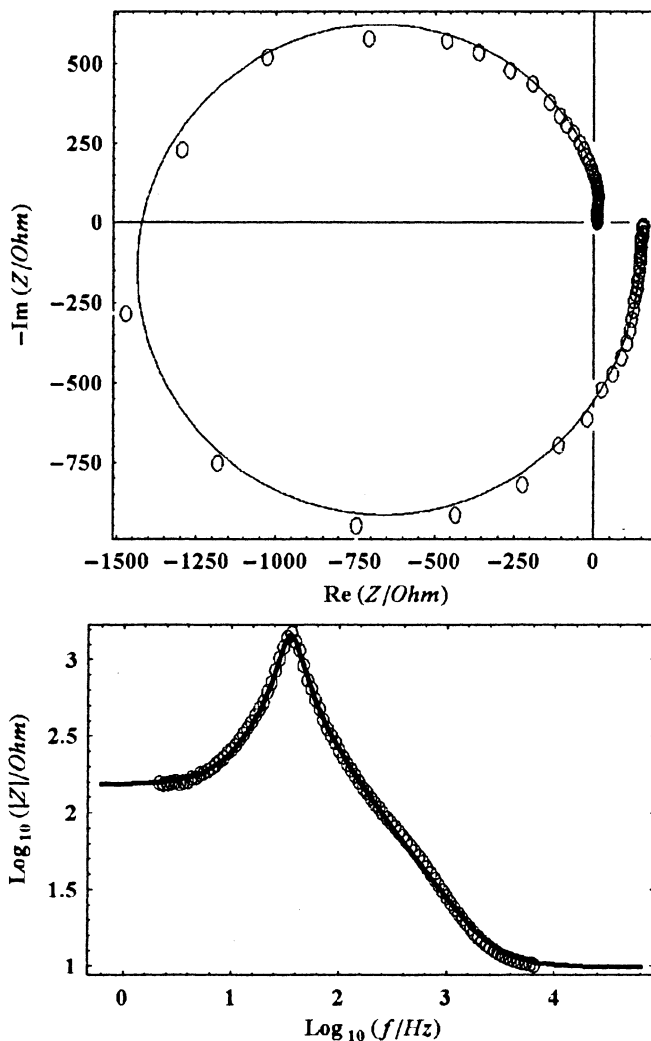


Fig. 3.37 Cu electrodisolution in $\text{CuSO}_4 + \text{H}_2\text{SO}_4$ medium, type I system. Impedance plots at $E = 400$ mV before anodic pre-polarization. *Circles*—experimental data; *solid line*—fitted $Z(s)$ function recalculated to zero pole representation according to Eq. (3.137) with parameters for set I in Table 3.1. Data showing NDR. *Top*: complex impedance coordinates: $-\text{Im}(Z)$ vs. $\text{Re}(Z)$; *bottom*: Bode amplitude coordinates: $\log(|Z|/\text{Ohm})$ vs. $\log(f/\text{Hz})$. Reprinted with permission from [82]

zeros are real and negative, so the system is stable under potentiostatic conditions, with all perturbations of the steady-state decaying exponentially. For system II it should be obvious a priori, since no real negative resistance was detected. If the serial resistance of system I is increased to ca. $2,010 \Omega$, then two zeros become complex numbers, with the real positive parts indicating the instability, and with the non-zero imaginary parts, indicating that this instability is of the oscillatory nature,

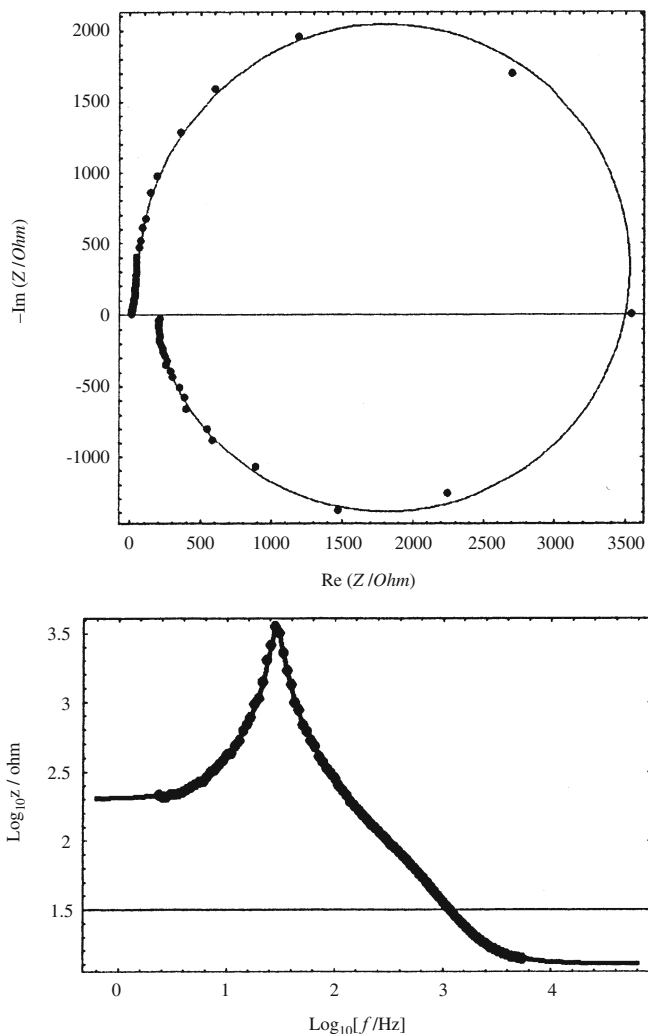


Fig. 3.38 Cu electrodisolution in $\text{CuSO}_4 + \text{H}_2\text{SO}_4$ medium, type II system. Impedance plots at $E = 400$ mV after anodic pre-polarization. Dots—experimental data, solid line—fitted function with parameters for set II in Table 3.1. Data showing only positive differential resistances. Top: Complex impedance coordinates: $-\text{Im}(Z)$ vs. $\text{Re}(Z)$. Bottom: Bode amplitude coordinates: $\log(|Z|/\text{Ohm})$ vs. $\log(f/\text{Hz})$. Reprinted with permission from [82]

under potentiostatic conditions (in the sense of constant external voltage U). On the other hand, for rows I and $I + R_{\text{ad}}$, complex poles with real positive and non-zero imaginary part indicate oscillatory instability under galvanostatic conditions, as it could be expected for the system with a hidden negative resistance. Note that upon addition of extra serial resistance, the poles of system I remained unchanged, so the

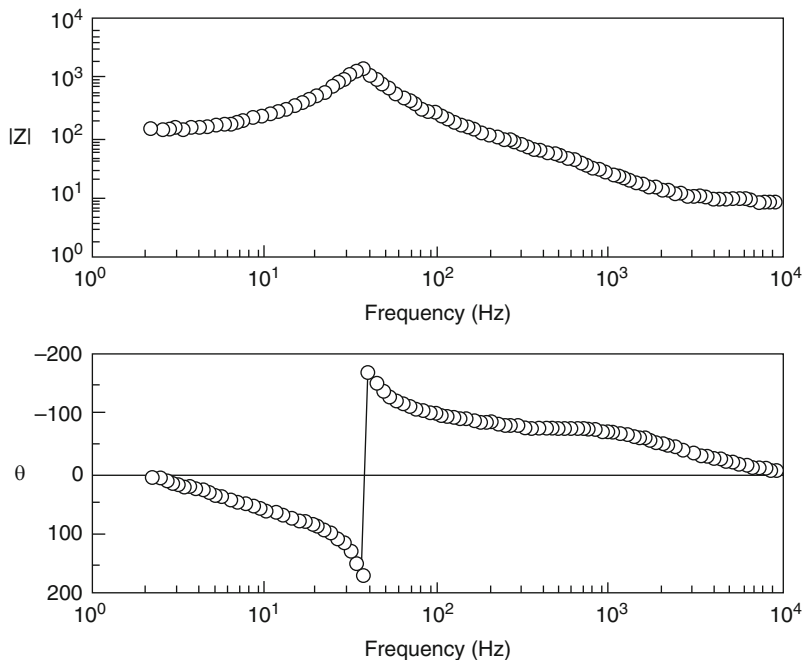


Fig. 3.39 Bode plots $|Z|$ ohm and phase angle (theta, argument) for the type I system, illustrated by impedance spectrum in Fig. 3.37. Reproduced from [13] by permission of The Electrochemical Society

oscillatory instability under galvanostatic conditions remained intact due to this change in the systems characteristics.

If the above analysis of the system's stability seems to be a bit implicit, more convincing can be a direct presentation of the current (or potential) course as a function of time, occurring upon applying the potential step E_{step} or current step I_{step} , for the impedance parameters collected in Table 3.1:

$$I(t) = L^{-1} \left(\frac{E_{\text{step}}}{sZ(s)} \right) \quad (3.138)$$

$$E(t) = L^{-1} \left(\frac{I_{\text{step}}Z(s)}{s} \right) \quad (3.139)$$

where L^{-1} means the inverse Laplace transformation (from the complex frequency domain to time domain), $I_{\text{step}} = 10^{-5}$ A, $E_{\text{step}} = 1$ V. Results of such calculations are shown in Fig. 3.40.

The above results for Cu–CuSO₄, H₂SO₄ system were used for practical verification of the suggestion [13, 83] that for the systems of type under study

Table 3.1 Zero-pole representation according to Eq. (3.137) of the electrochemical impedance data shown in Fig. 3.37 (set I) and in Fig. 3.38 (set II)

Dataset/ parameter	R_s/Ω	z_1	z_2	z_3	p_1	p_2	p_3
I	9.8	-2645	-193	-8.77	-225.4	$7.92 - 34.8j$	$7.92 + 34.8j$
II	12.8	-2618	-182	-6.98	-255.1	$-3.47 - 28.5j$	$-3.47 + 28.5j$
I + R_{ad}	2009.8	-227.4	$2.26 + 36.7j$	$2.26 - 36.7j$	-225.4	$7.92 - 34.8j$	$7.92 + 34.8j$

Dataset I + R_{ad} is for dataset I with resistance $R_{ad} = 2,000 \Omega$ added in series. Dimensions of z_i and p_i : rad s^{-1} [82]

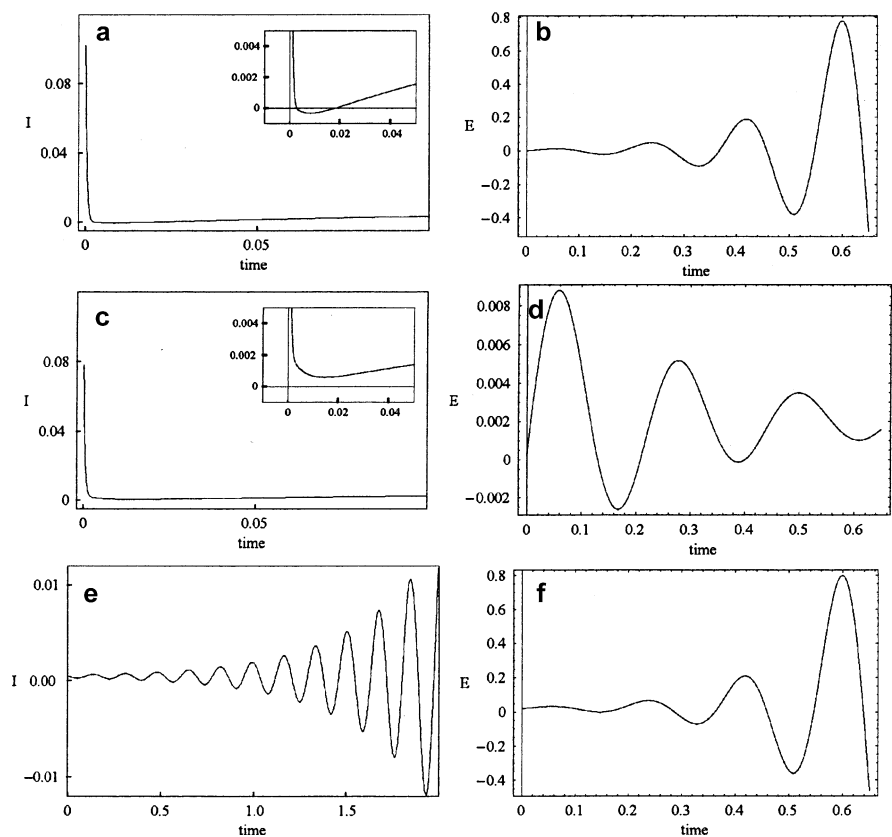


Fig. 3.40 Potential-step ($\Delta E = 1 \text{ V}$) current responses (a, c, e) and current-step ($\Delta I = 10^{-5} \text{ A}$) potential responses (b, d, f) calculated for impedances in zero-pole representation as in Eq. (3.137). (a, b)—dataset I in Table 3.1; (c, d)—dataset II in Table 3.1. (e, f)—dataset I with additional resistance $R_{ad} = 2,000 \Omega$ added in series. Reprinted with permission from [82]

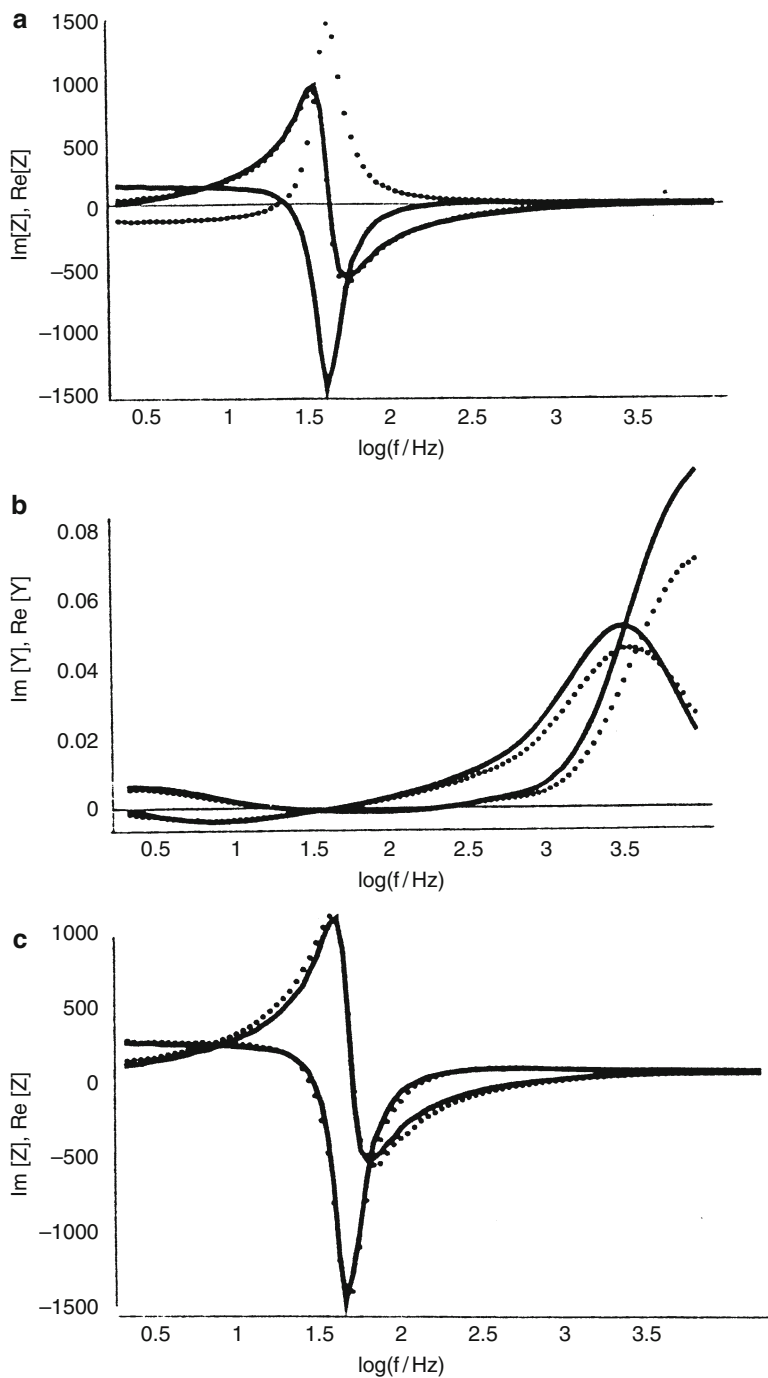


Fig. 3.41 (Thin solid lines) raw and (dots) KK-transformed immittance data for the electrode at $E = 400$ mV without previous exposure to higher potentials. Raw data as in Fig. 3.37. (a) Data KK-transformed as impedance compared with raw data in impedance form: $\text{Re}(Z)$ plots with

(nmp-type), i.e., stable under potentiostatic conditions, but exhibiting instability under galvanostatic conditions, not the impedance, but the admittance data should be involved in the Kramers–Kronig transformation, if this transformation is to be used for their validation. Figure 3.41 is an illustration of that verification.

Finally, according to Sadkowsky [15], the stability analysis in terms of zeros and poles of impedance can be developed into certain generalized classification of electrochemical dynamic systems which can be compared with the one proposed earlier by Strasser et al. and summarized in Sect. 3.5. The systems stable under potential (voltage) control were taken into account, for which the impedance spectra were calculated in terms of the second order polynomials:

$$Z(s) = Z(\infty) \frac{s^2 + a_1s + a_0}{s^2 + b_1s + b_0} = Z(\infty) \frac{(s - z_1)(s - z_2)}{(s - p_1)(s - p_2)} \quad (3.140)$$

The following cases have been proposed:

Case 1. All zeros and poles of impedance negative, meaning unconditional stability of the mp-type system.

Case 2. Positive higher frequency pole, negative lower frequency pole, and two zeros, meaning the nmp-type system with explicit NDR region for $\omega \rightarrow 0$, stable under potentiostatic conditions, but unstable under galvanostatic conditions.

Case 3. Positive lower frequency pole, negative higher frequency pole and all zeros, meaning the nmp system, stable under potentiostatic conditions, unstable under galvanostatic conditions (of the impedance characteristics typical of active–passive transition in some passivating systems)

Case 4. Two poles positive, all zeros negative, meaning the system of nmp type with the hidden negative resistance, i.e., recorded only for intermediate range of frequencies; the system stable under potentiostatic and unstable under galvanostatic conditions.

In accordance with the previously mentioned applicability of the K–K transformation, one should add that for case 1 (unconditionally stable mp system) for the validation of impedance data either the impedance or admittance data could be successfully taken. For cases 2, 3 and 4 (i.e., various nmp-type systems) the K–K transformation was successful only if applied to admittance data.

The reader interested in more advanced treatment of stability of electric circuits in electrochemistry is advised to consult the work of Koper [35], the pioneer work of de Levie [27], and references cited there.

Fig. 3.41 (continued) single maximum (*dots*, KK transformed) or single minimum (*solid line*, raw data): Im(Z) plots switching from + to -. **(b)** KK transformed as admittance compared with raw admittance data: Re(Y) monotonically rising plots at high frequency; Im(Y) peaked plots. **(c)** KK transformed as admittance and recalculated to (*dots*) impedance to compare with (*solid line*) raw impedance data. Note clear deviation of raw and KK-transformed as impedance data in **(a)** (as expected for the non-minimum phase system), but quite good agreement of raw and admittance KK-transformed data in **(c)**. Reproduced from [13] by permission of The Electrochemical Society

3.8 Application of the Dynamic Electrochemical Impedance Spectroscopy to Electrochemical Instabilities

Typical methodology of EIS usually involves, as a strong requirement, perturbation of the stable steady-state, so direct impedance studies of the system being in the oscillatory regime seem to be not possible. An eventual attempt to make such measurements would have to shorten considerably the duration of the sampling time, in order to measure the instantaneous impedance. However, this seems to remain in conflict with the requirements of low-frequency conditions, in the typical experimental approach which is the Frequency Response Analysis (FRA). Therefore it is noteworthy to describe several methodologies of the analysis of the oscillating response that have been recently proposed by Darowicki et al. (for introduction, see, e.g., [84]). The theoretical background of the principles of this analysis is not limited to electrochemical systems, and can be applied to any non-stationary response (EEG, electrocardiogram, or the Belousov–Zhabotinsky process).

Historically, the reduction of measurement time to a few seconds could be attained by application of the Fast Fourier Transform (FFT), as suggested by Popkirov et al. [85, 86], but the requirement of attaining the steady-state prior to the ac perturbation is maintained. Hazi et al. [87] have suggested to use frequency compositions as the perturbation signals with various frequency components applied one by other, while Park et al. [88, 89] have proposed to apply the potential step as the perturbation signal followed by dedicated postprocessing. Barsoukov et al. [90] have suggested to apply the current pulse or interrupt, followed by the processing of the response in terms of Laplace transform. In turn, Ragoisha and Bondarenko [91] have proposed to use the stream of wavelets in a limited frequency range. Recently, Sacci and Harrington have described the hardware and software for the relevant technique, named *dynamic electrochemical impedance spectroscopy* (DEIS) [92].

The variant of DEIS technique briefly described here [93–95] combines the pseudowhite noise and short time Fourier transform (STFT) analysis to obtain impedance spectra of potentiodynamic electrochemical processes. Accordingly, the perturbation signal is a package of a sinusoidal voltage signals:

$$\mathbf{U} = U_0 \begin{bmatrix} \exp[-j(\omega_1 t + \varphi_1)] \\ \exp[-j(\omega_2 t + \varphi_2)] \\ \exp[-j(\omega_n t + \varphi_n)] \end{bmatrix} \quad (3.141)$$

with the amplitude U_0 equal for all components, but the frequencies ω_i and phase angles φ_i chosen randomly, with ω_i meeting the condition that the investigated process undergoes relaxation in the frequency range considered. The resulting current response can be represented in the form

$$\mathbf{I} = \begin{bmatrix} I_1 \exp[-j(\omega_1 t + \varphi_1 + \phi_1)] \\ I_2 \exp[-j(\omega_2 t + \varphi_2 + \phi_2)] \\ I_n \exp[-j(\omega_n t + \varphi_n + \phi_n)] \end{bmatrix} \quad (3.142)$$

indicating that the amplitudes of the individual components of the current, as well as the phase angles are not identical, as dependent on the investigated process. Generally, the decomposition of these current components and their comparison with the components of the voltage signal allows one to calculate the impedance. However, if the electrode process is not stationary (e.g., in a simplest case if it is driven by a potential linearly changing in time), the decomposition of the current response package by means of the regular Fourier transformation leads to an averaged result. The decomposition closer to an instantaneous response requires thus another approach—the short time Fourier transform. Without going into mathematical details which can be found in the literature [96] we shall briefly say here that this variant of Fourier transformation involves the analysis of the non-stationary signal, at time t of its development, in the Gaussian window $s(\tau)$:

$$s(\tau) = \exp\left[-\frac{\lambda}{2}(\tau - t)^2\right] \quad (3.143)$$

where λ is an appropriate parameter and τ denotes time. The choice of the appropriate Gaussian window for given signal is a separate problem. The STFT approach involves cutting off a signal portion at time t by this window (determined by value of λ) and performing for this portion the regular Fourier transformation. The width of the window is defined as: $\langle t - \sigma(t), t + \sigma(t) \rangle$, with σ meaning the standard deviation of the Gaussian peak in the domain of time:

$$\lambda = \frac{1}{2\sigma^2(t)} \quad (3.144)$$

In other words, within the (narrow enough) Gaussian window the signal is assumed to be stationary and thus appropriate for the regular Fourier analysis. The next window is placed at $t + \sigma(t)$. Repeating this procedure for subsequent windows on the time axis produces the dependence of not only the frequency, but also of the amplitude as a function of time. The successful application of the STFT approach to the impedance analysis of the non-stationary electroreduction of Cd(II) was later described by Darowicki and Ślepski for the dropping mercury electrode [95] and the hanging mercury electrode [97]. DEIS method was also applied to the studies of the cracking of the passive layer on the stainless steel surface [98].

In practice, application of the above procedure reveals several limitations, so for the analysis of the non-stationary electrochemical oscillations a more sophisticated approach, involving the joint time–frequency distribution—the Wigner–Ville distribution (WVD), was later developed by the same group [99]. One of the advantages of applying the WVD is the absence of the analyzing window (replaced by the autocorrelation function of the signal) and the higher time–frequency resolution, compared to the SFFT approach. However, there are also some disadvantages of the WVD approach, like, e.g., generation of artificial cross-terms, which makes the signal analysis rather difficult. Additional procedures

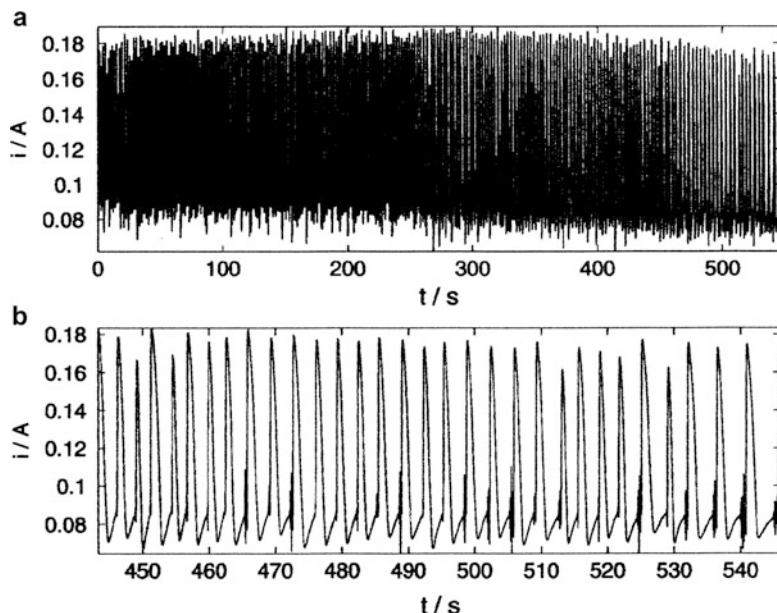


Fig. 3.42 Exemplary records of current oscillations accompanying the anodic dissolution of copper in the 0.3 M NaCl + 0.5 M H₂SO₄ solution: full record (a) and enlarged record in time window 445–545s (b). Anodic polarization 380 mV vs. Hg/Hg₂Cl₂ reference electrode. Sampling frequency 30 Hz. Reprinted from [99], Copyright 2003, with permission from Elsevier

involve application of various filtering kernels (e.g., Choi–Williams distribution). Figure 3.42 shows the experimentally obtained oscillatory course of the dissolution of Cu electrode in NaCl + H₂SO₄ medium, while Figs. 3.43 and 3.44 compare the results of the analysis of those oscillations in terms of the STFT approach and Choi–Williams distribution, respectively.

More recently Darowicki and Ślepski [100] have developed a method, in which the perturbation is caused by the non-stationary “chirp-type” voltage signal of a frequency depending exponentially on time (see Fig. 3.45).

The STFT was again applied to the voltage perturbation and current response, which analysis allowed the determination of impedance spectrum from the following relation (for the given window determined by γ function):

$$\begin{aligned}
 Z(j\omega) &= \left\{ \frac{\text{STFT}\{u(\tau)\}}{\text{STFT}\{i(\tau)\}} \right\}_{\gamma} = \left\{ \frac{\text{STFT}\{u(\tau)\} \text{STFT}^*\{i(\tau)\}}{\text{STFT}\{i(\tau)\} \text{STFT}^*\{i(\tau)\}} \right\}_{\gamma} \\
 &= Z_{\gamma}'(\omega) + jZ_{\gamma}''(\omega)
 \end{aligned}
 \tag{3.145}$$

where $Z(j\omega)$ is the impedance value, $\text{STFT}\{u(\tau)\}$ is the STFT transform of voltage perturbation signal, $\text{STFT}\{i(\tau)\}$ is the STFT transform of the current response

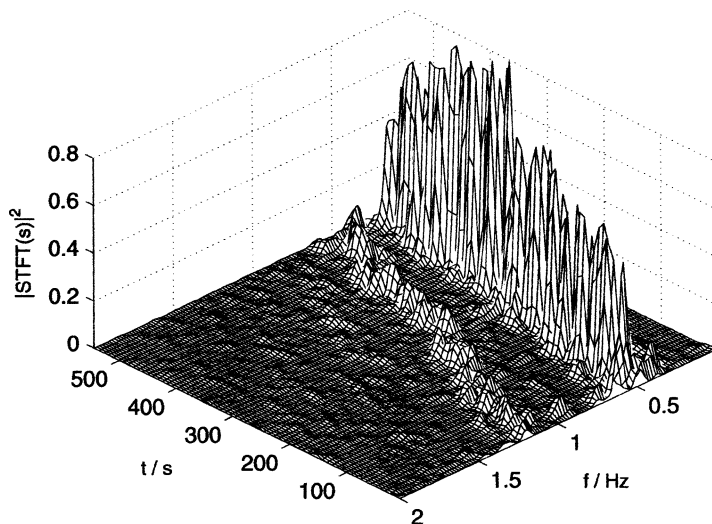


Fig. 3.43 Normalized STFT spectrogram of the signal presented in Fig. 3.42. Hanning window of length 128 samples applied. Reprinted from [99], Copyright 2003, with permission from Elsevier

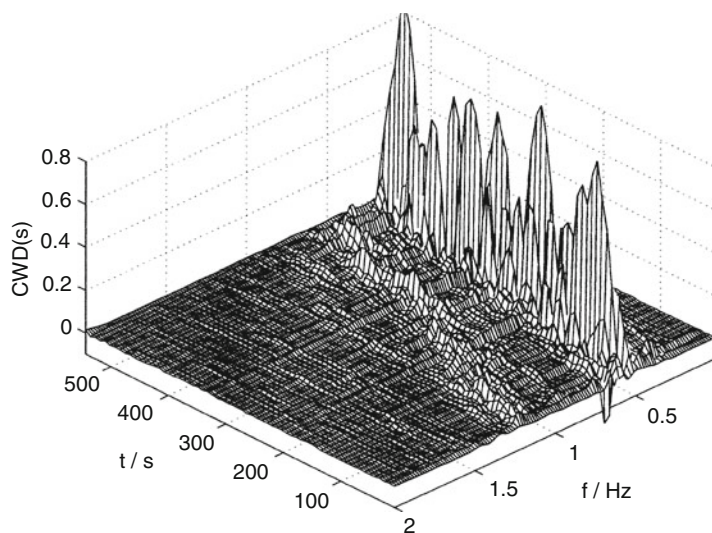


Fig. 3.44 Choi-Williams distribution of the signal presented in Fig. 3.42. Kernel width parameter $\alpha = 1$. Reprinted from [99], Copyright 2003, with permission from Elsevier

signal, $\text{STFT}\{i(\tau)\}$ is the coupled transform of current response signal. The method was later optimized by the same researchers [101]. All techniques of this kind form a basis for future analysis of non-stationary oscillatory signals, including the determination of time-dependent impedance spectra.

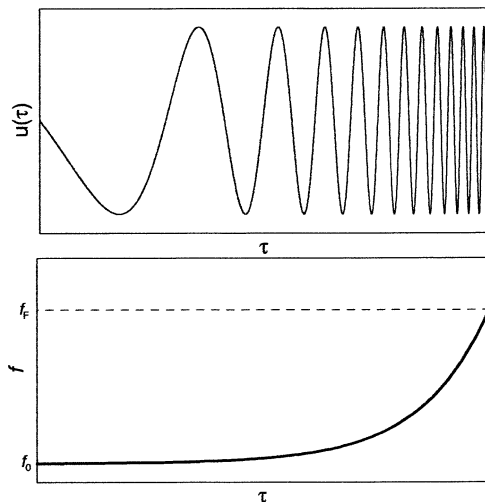


Fig. 3.45 Example of “chirp” signal of exponential characteristic. Reprinted from [100], Copyright 2004, with permission from Elsevier

3.9 Impedance Spectroscopy and Electrochemical Pattern Formation

In the previous sections, analysis of electrochemical instabilities did not take into account the effect of pattern formation on the shape of impedance spectra. The ac response was then interpreted in terms of ideally homogeneous electrode surfaces. In fact, only very recently Bonnefont, Krischer et al. [102] have outlined the application of EIS to studies of pattern formation in electrochemical systems. The model calculations refer to real experimental system: CO bulk electrooxidation on Pt electrodes which exhibits an S-shaped current–potential characteristics (S-NDR region) (see Chap. 2). Under galvanostatic control, due to interaction of an S-NDR characteristics with the global coupling induced by galvanostatic conditions, self-organized stationary patterns emerge on the Pt surface (cf. Sect. 2.7, volume II). These patterns consist of two stationary domains with low and high CO coverages, corresponding to high and low electrochemical reaction rates, respectively (the electrode areas with high reaction rate will be further called “active” ones) (Fig. 3.46).

Using the model for the CO electrooxidation, elaborated earlier by Koper et al. for the homogeneous electrode surface [103] and extended now for the inhomogeneous case, Bonnefont et al. [102] have calculated the respective impedance spectra under conditions of current modulation. Their comparison for the homogeneous and patterned states is shown in Fig. 3.47.

The spectrum for the homogeneous case covers a relatively wide range of frequencies of the modulated current, while the plot for the heterogeneous (spatially

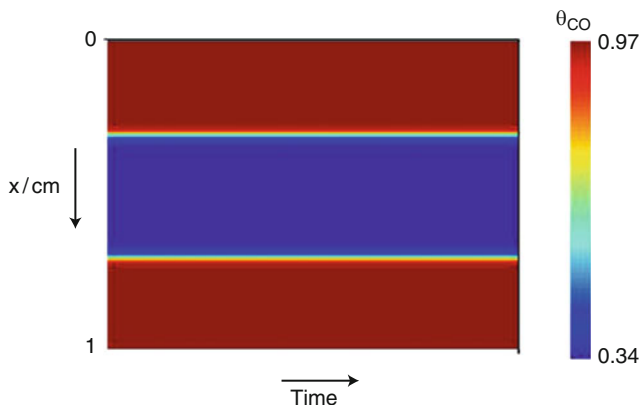


Fig. 3.46 Position–time plot of the CO coverage for $I_0 = 2.0$ mA simulated with the spatially extended model of CO electrooxidation. Reprinted from [102], Copyright 2009, with permission from Elsevier

extended) model is limited to very low frequencies. The comparison of both spectra shows that the zero frequency negative impedance is observed *only* in a homogeneous case. Upon increasing ac frequency, at $f \approx 1.4$ Hz, the impedance curve in Fig. 3.47a intersects the imaginary axis and further course, typical of inductive-capacitive loop, indicates only positive values of real part of impedance. The disappearance of the NDR at 1.4 Hz means that at this frequency at least one process involved in the autocatalytic feedback loop is drastically affected, i.e., it does not have sufficient time to take place. In turn, and it was a surprising result, for the spatially extended case (Fig. 3.47b), the negative real impedance was not observed for the frequencies, for which the homogeneous model exhibited a negative impedance real part. Instead, the impedance modulus $|Z(\omega)|$ tended to zero at very low frequencies.

In order to explain this discrepancy in impedance spectra, the model spatiotemporal evolution of CO coverage, like that shown in Fig. 3.48 was examined.

This figure, corresponding to a very low frequency $f \approx 0.03$ Hz shows that synchronously with the applied current the relative sizes of the CO domains are modulated, the size of the active domain following linearly the applied current modulation, at *nearly constant* electrode potential (<1 mV amplitude). Hence, one concludes that the impedance response at such low frequency is essentially through a change of the relative areas of the CO domains and, consequently, the modulus of the interfacial impedance tends to zero at very low frequencies, with no negative real part of the impedance observed in the simulated impedance spectra. This conclusion is concordant with experimental observation that the electrode potential is nearly independent of the applied current when stationary CO patterns form on the electrode surface [104]. A closer inspection of data from Fig. 3.48 shows a slight modulation of θ_{CO} which is approximately in anti-phase with the electrode potential and $\pi/2$ -phase shifted with respect to the imposed current (or the active size modulation).

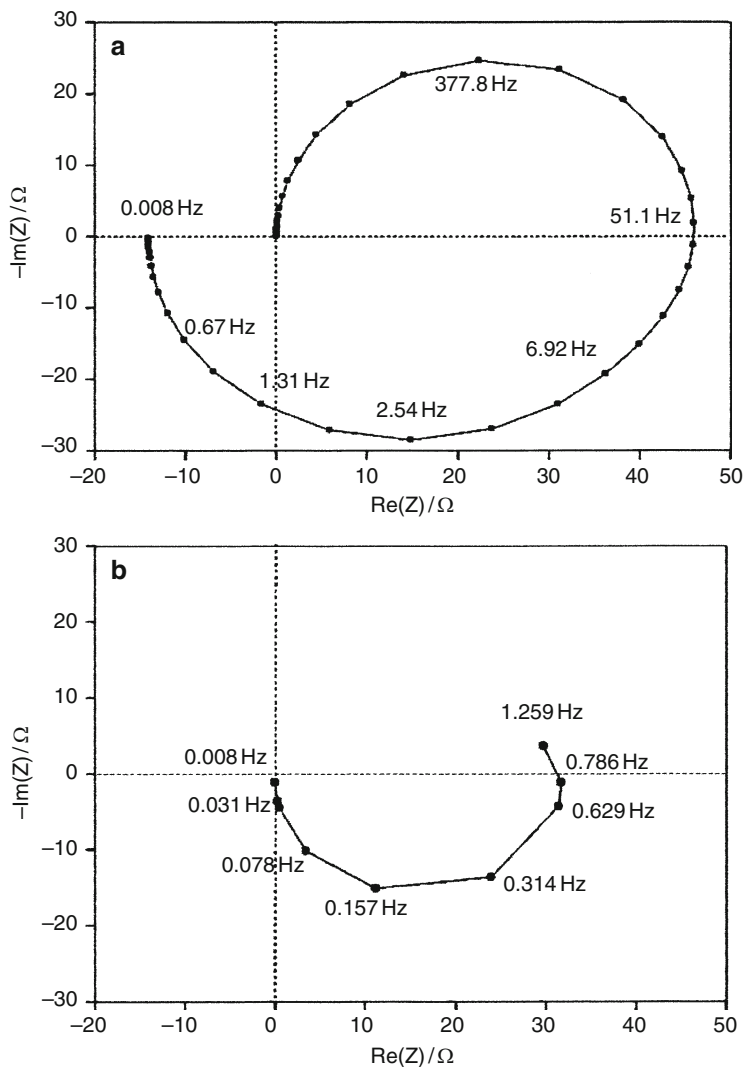
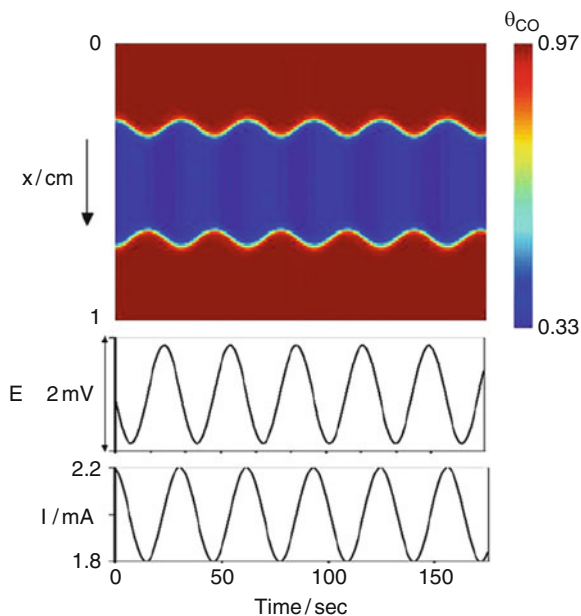


Fig. 3.47 Nyquist diagrams representing the interface impedance calculated with the homogeneous model (a) and with the spatially extended model (b) of CO electrooxidation, for $f = 0.0078, 0.025, 0.031, 0.078, 0.157, 0.314, 0.629, 0.786$ and 1.259 Hz at an applied current value of $I_0 = 2.0$ mA. Reprinted from [102], Copyright 2009, with permission from Elsevier

For intermediate modulation frequencies ($0.03 \text{ Hz} < f < 1.4 \text{ Hz}$), the current affects domain size expansion and contraction, leading to an increase of the electrode potential response amplitude and the dependence of the phase shift on this frequency, causing an increase in modulus of the interface impedance. The phase shift between electrode potential and imposed current becomes lower than $\pi/2$, giving rise to an “inductive loop” in the Nyquist plot.

Fig. 3.48 Position–time plot of the CO coverage for galvanostatic CO electrooxidation under current modulation and corresponding potential and current. Modulation amplitude $I_1 = 0.2$ mA. Modulation frequency, $f = 0.031$ Hz; stationary current, $I_0 = 2.0$ mA. Reprinted from [102], Copyright 2009, with permission from Elsevier



Finally, for frequencies higher than 1.4 Hz, the current modulation period becomes shorter than the characteristic time of the slowest process involved in the positive feedback (autocatalytic) process. In the spectrum for the homogeneous case the real part of impedance becomes then positive, while for heterogeneous case the detailed interpretation of the course of the impedance spectrum is more complex and requires further studies [102].

Concluding, the work described here is a valuable introductory contribution to the impedance studies of electrochemical spatiotemporal patterns (including Turing structures) which, in terms of the respective model, shows how the dynamics of pattern formation may affect the impedance spectrum. One may expect further development of the application of EIS to the analysis of electrochemical temporal and spatiotemporal dissipative patterns in the near future. The reader interested in mechanistic details of the model of CO electrooxidation used for the modeling of impedance spectra is advised to consult the work discussed [102]. Spatial and spatio-temporal patterns in electrochemical systems are treated in detail in Volume II.

References

1. Barsoukov E, Macdonald JR (eds) (2005) Impedance spectroscopy. Theory, experiment, and applications. Wiley, Hoboken, NJ, p 149
2. Randles JEB (1947) Kinetics of rapid electrode reactions. *Discuss Faraday Soc* 1:11–19
3. Lasia A (1999) Electrochemical impedance spectroscopy and its applications. In: Conway BE, Bockris JOM, White RE (eds) *Modern aspects in electrochemistry*, vol 32. Kluwer, New York, NY, pp 143–248

4. Hamann CH, Hamnett A, Vielstich W (2007) *Electrochemistry*, 2nd edn. Wiley-VCH, Weinheim, p 283
5. Orazem ME, Tribollet B (2008) *Electrochemical impedance spectroscopy*. Wiley, New York, NY
6. de Levie R, Husovsky AA (1969) On the negative faradaic admittance in the region of the polarographic minimum of In(III) in aqueous NaSCN solution. *J Electroanal Chem* 22:29–48
7. de Levie R, Pospíšil L (1969) On the coupling of interfacial and diffusional impedances, and on the equivalent circuit of an electrochemical cell. *J Electroanal Chem* 22:277–290
8. Wojtowicz J (1973) Oscillatory behavior in electrochemical systems. In: J O'M Bockris, Conway BE, White RE (eds) *Modern aspects of electrochemistry*, vol 8. Plenum, New York, NY, pp 47–120
9. Bogusz W, Krok F (1995) *Solid electrolytes. Electric properties and methods of their measurements*. WNT, Warsaw (in Polish)
10. Macdonald DD, Urquidi-Macdonald M (1985) Application of Kramers–Kronig transforms in the analysis of electrochemical systems. I. Polarization resistance. *J Electrochem Soc* 132:2316–2319
11. Urquidi-MacDonald M, Real S, Macdonald DD (1986) Application of Kramers–Kronig transforms in the analysis of electrochemical impedance data. Transformations in the complex plane. *J Electrochem Soc* 133:2018–2024
12. Macdonald JR (ed) (1987) *Impedance spectroscopy. Emphasizing solid materials and systems*. Wiley, New York, NY
13. Sadkowski A, Dolata M, Diard JP (2004) Kramers–Kronig transforms as validation of electrochemical impedance data near discontinuity. *J Electrochem Soc* 151:E20–E31
14. Gabrielli C, Keddam M, Takenouti H (1993) In: Scully JR, Silverman DC, Kendig MW (eds) *Electrochemical impedance: analysis and interpretation*. ASTM, Philadelphia, PA, p 140
15. Sadkowski A (2005) Unusual electrochemical impedance spectra with negative resistance and their validation by Kramers–Kronig transformation. *Solid State Ionics* 176:1987–1996
16. Ijzermans AB, Sluyters-Rehbach M, Sluyters JH (1965) On the impedance of galvanic cells. XII. The impedance and admittance of streaming mercury electrodes; theoretical considerations. *Rec Trav Chim* 84:729–739
17. Ijzermans AB, Sluyters-Rehbach M, Sluyters JH (1965) On the impedance of galvanic cells. XIII. Characteristics of streaming mercury electrodes. *Rec Trav Chim* 84:740–750
18. Ijzermans AB, Sluyters-Rehbach M, Sluyters JH (1965) On the impedance of galvanic cells. XIV. The impedance and admittance of streaming mercury electrodes; experimental verification. *Rec Trav Chim* 84:751–763
19. Jurczakowski R, Orlik M (2004) The apparent faradaic response in the impedance characteristics of the capacitive current at a streaming mercury electrode. *J Electroanal Chem* 562:205–215
20. Jurczakowski R, Orlik M (2007) Experimental and theoretical impedance studies of oscillations and bistability in the Ni(II)-SCN^- electroreduction at the streaming mercury electrode. *J Electroanal Chem* 605:41–52
21. Orlik M, Jurczakowski R (2008) The kinetic parameters of the electrocatalytic reduction of the coordinated azide anions found from comparison of dc and ac measurements for the tristable Ni(II)-N_3^- system. *J Electroanal Chem* 614:139–148
22. Delahay P (1965) Electrode kinetics at open circuit at the streaming mercury electrode: I. Theory. *J Electroanal Chem* 10:1–7
23. Bard AJ, Faulkner L (2001) *Electrochemical methods. Fundamentals and applications*. Wiley, New York, NY, pp 368–416
24. Burns S. Distributed power. What causes these systems to oscillate? Venable Technical Paper #19, © Venable Industries; www.venable.biz/tp-19.pdf; downloaded, 25 April 2011
25. Nyquist H (1932) Regeneration theory. *Bell Sys Tech* 11:126–147
26. Bode HW (1945) *Network analysis and feedback amplifier design*. Van Nostrand, New York, NY

27. De Levie R (1970) On the electrochemical oscillator. *J Electroanal Chem* 25:257–273
28. Schweickert H, Lorenz WJ, Friedburg H (1980) Impedance measurements of the anodic iron dissolution. *J Electrochem Soc* 127:1693–1701
29. Keddama M, Mattos OR, Takenouti H (1981) Reaction model for iron dissolution studied by electrode impedance. *J Electrochem Soc* 128:257–266
30. Keddama M, Mattos OR, Takenouti H (1981) Reaction model for iron dissolution studied by electrode impedance. *J Electrochem Soc* 128:266–274
31. Keddama M, Lizee JF, Pallotta C, Takenouti H (1984) Electrochemical behavior of passive iron in acid medium. *J Electrochem Soc* 131:2016–2024
32. Koper MTM (1996) Stability study and categorization of electrochemical oscillators by impedance spectroscopy. *J Electroanal Chem* 409:175–182
33. Koper MTM, Sluyters JH (1994) Instabilities and oscillations in simple models of electrocatalytic surface reactions. *J Electroanal Chem* 371:149–159
34. Koper MTM (1998) Non-linear phenomena in electrochemical systems. *J Chem Soc Faraday Trans* 94:1369–1378
35. Koper MTM (1996) Oscillations and complex dynamical bifurcations in electrochemical systems. In: Prigogine I, Rice SA (eds) *Adv Chem Phys* XCII:161–298
36. Strasser P, Eiswirth M, Ertl G (1997) Oscillatory instabilities during formic acid oxidation on Pt(100), Pt(110) and Pt(111) under potentiostatic control. II. Model calculations. *J Chem Phys* 107:991–1003
37. Hachkar M, Beden B, Lamy C (1990) Oscillating electrocatalytic systems: part I. Survey of systems involving the oxidation of organics and detailed electrochemical investigation of formaldehyde oxidation on rhodium electrodes. *J Electroanal Chem* 287:81–98
38. Koper MTM, Hachkar M, Beden B (1996) Investigation of the oscillatory electro-oxidation of formaldehyde on Pt and Rh electrodes by cyclic voltammetry, impedance and the electrochemical quartz crystal microbalance. *J Chem Soc Faraday Trans* 92:3975–3982
39. Krischer K (1999) Principles of temporal and spatial pattern formation in electrochemical systems. In: Conway BE et al (ed) *Modern aspects of electrochemistry*, vol 32. Kluwer, New York, NY
40. Krischer K (2003) Nonlinear dynamics in electrochemical systems. In: Alkire RC, Kolb DM (eds) *Advances in electrochemical science and engineering*, vol 8. Wiley-VCH, Weinheim
41. Eiswirth M, Freund A, Ross J (1991) Mechanistic classification of chemical oscillators and the role of species. In: Prigogine I, Rice SA (eds) *Adv Chem Phys* 80:127–199. Wiley, New York
42. Strasser P, Eiswirth M, Koper MTM (1999) Mechanistic classification of electrochemical oscillators—an operational experimental strategy. *J Electroanal Chem* 478:50–66
43. Orbán M, Epstein IR (1981) Oscillations and bistability in hydrogen-platinum-oxyhalogen systems. *J Am Chem Soc* 103:3723–3727
44. Gabrielli C, Keddama M, Stupnišek-Lisac E, Takenouti H (1976) Etude du comportement anodique de l'interface feracide nitrique a l'aide d'une regulation a resistance negative. *Electrochim Acta* 21:757–766
45. Epelboin I, Gabrielli C, Keddama M (1984) In: Bockris JO'M, Conway BE, Yeager E, White RE (eds) *Comprehensive treatise of electrochemistry*, vol 4. Plenum, New York, NY (1981, Chapter 3)
46. Epelboin I, Ksouri M, Lejay E, Wiart R (1975) A study of the elementary steps of electron-transfer during the electrocrystallization of zinc. *Electrochim Acta* 20:603–605
47. Strasser P, Lübke M, Eickes C, Eiswirth M (1999) Modeling galvanostatic potential oscillations in the electrocatalytic iodate reduction system. *J Electroanal Chem* 462:19–33
48. Li Z, Cai J, Zhou S (1997) Potential oscillations during the reduction of $\text{Fe}(\text{CN})_6^{3-}$ ions with convection feedback. *J Electroanal Chem* 432:111–116
49. Li Z, Cai J, Zhou S (1997) Current oscillations in the reduction or oxidation of some anions involving convection mass transfer. *J Electroanal Chem* 436:195–201
50. Kiss IZ, Kazsu K, Gáspár V (2005) Experimental strategy for characterization of essential dynamical variables in oscillatory systems: effect of double-layer capacitance on the stability of electrochemical oscillators. *J Phys Chem A* 109:9251–9257

51. Bockris JO'M, Reddy AKN (1973) *Modern electrochemistry*, vol 2. Plenum, New York, NY
52. Inzelt G, Kertész V (1997) Effect of poly(aniline) pseudocapacitance on potential and EQCM frequency oscillations arising in the course of galvanostatic oxidation of formic acid on platinum. *Electrochim Acta* 42:229–235
53. Nikitas P (1991) The origin of polarization catastrophe: the improper choice of the independent electrical variable. *J Electroanal Chem* 306:13–19
54. Nikitas P (1991) Stability conditions at charged interphases. *J Electroanal Chem* 316:23–25
55. Nikitas P, Anastopoulos A, Papanastasiou G (1991) Phase transitions in models for adsorption on electrodes. Further examination of the polarization catastrophe. *J Electroanal Chem* 317:43–76
56. Nikitas P (1997) Comparison between charged, charged at the pzc and uncharged interfaces: a peculiar case related to the origin of the polarization catastrophe. *J Electroanal Chem* 426:167–176
57. Thom R (1972) *Stabilité structurelle et morphogénèse*. Benjamin, New York, NY
58. Zeeman EC (1977) *Catastrophe theory: selected papers 1972-1977*. Addison-Wesley, Reading, MA
59. Poston T, Stewart I (1978) *Catastrophe theory and its applications*. Pitman, London
60. Gilmore R (1981) *Catastrophe theory for scientists and engineers*. Wiley-Interscience, New York, NY
61. Okninski A (1992) *Catastrophe theory*, vol 33, *Comprehensive chemical kinetics*. Elsevier Science, Amsterdam
62. Laviron E (1979) A.c. polarography and faradaic impedance of strongly adsorbed electroactive species. Part II. Theoretical study of a quasi-reversible reaction in the case of a Frumkin isotherm. *J Electroanal Chem* 105:25–34
63. Armstrong RD (1994) The impedance of an electrode for the situation where there is a discontinuous change of the electrode condition with potential due to the formation of a two-dimensional condensed phase. *J Electroanal Chem* 372:27–32
64. Wandlowski T, de Levie R (1993) Double-layer dynamics in the adsorption of tetrabutyl ammonium ions at the mercury water interface. III. The admittance of the needle peak. *J Electroanal Chem* 352:279–294
65. Berthier F, Diard JP, Montella C (1996) Discontinuous impedance near a saddle-node bifurcation. *J Electroanal Chem* 410:247–249
66. Berthier F, Diard JP, Le Gorrec B, Montella C (1998) Discontinuous immitance due to a saddle node bifurcation I. 1-, 2- and 3-part immitance diagrams. *J Electroanal Chem* 458:231–240
67. Berthier F, Diard JP, Montella C (1999) Discontinuous immitance due a saddle-node bifurcation. II Tangent bifurcation and critical slowdown during isotherm branch switching. *J Electroanal Chem* 460:226–233
68. Berthier F, Diard JP, Montella C, Volovik I (1996) Bifurcation analysis for the Volmer–Heyrovský mechanism. *J Electroanal Chem* 402:29–35
69. Heyrovský J (1927) A theory of overpotential. *Rec Trav Chim* 46:582–585
70. Bockris JO'M, Drazic DH (1972) *Electrochemical science*. Taylor and Francis, London
71. Bockris J, O'M DDH, Despic AR (1961) The electrode kinetics of the deposition and dissolution of iron. *Electrochim Acta* 4:325–361
72. Sadkowski A (1998) Large signal (global) analysis of non-linear response of electrocatalytic reaction. I. Multiple steady-states. *J Electroanal Chem* 447:97–107
73. Sadkowski A (2004) On some dynamic peculiarities of the charge transfer with adsorption and attractive interactions. *Electrochim Acta* 49:2259–2269
74. Berthier F, Diard JP, Nuges S (1997) On the nature of the spontaneous oscillations observed for the Koper–Sluyters electrocatalytic reaction. *J Electroanal Chem* 436:35–42
75. Baer SM, Erneux T, Rinzel T (1989) The slow passage through a Hopf bifurcation: delay, memory effects, and resonance. *SIAM J Appl Math* 46:55–71

76. Holden L, Erneux T (1993) Slow passage through a Hopf bifurcation: from oscillatory to steady state solutions. *SIAM J Appl Math* 53:1045–1058
77. Koper MTM, Aguda BD (1996) Experimental demonstration of delay and memory effects in the bifurcations of nickel electrodisolution. *Phys Rev E* 54:960–963
78. Berthier F, Diard JP, Montella C (1997) La résistance de transfert d'électrons d'une réaction électrochimique peut-elle être négative? *CR Acad Sci Paris Ser IIB* 325:21–26
79. Berthier F, Diard JP, Montella C (1999) Hopf bifurcation and sign of the transfer resistance. *Electrochim Acta* 44:2397–2404
80. Naito M, Tanaka N, Okamoto H (1999) General relationship between complex impedance and linear stability in electrochemical systems. *J Chem Phys* 111:9908–9917
81. Sadkowski A (2004) On specific properties of electrochemical imittance close to discontinuity points. *Electrochim Acta* 49:2653–2659
82. Sadkowski A (2004) On benefits of the zero-pole representation of electrochemical impedance spectroscopy data close to discontinuity point. *Polish J Chem* 78:1245–1253
83. Sadkowski A (2004) CNLS fits and Kramers–Kronig validation of resonant EIS data. *J Electroanal Chem* 573:241–253
84. Darowicki K, Kawula J (2004) Validity of impedance spectra obtained by dynamic electrochemical impedance spectroscopy verified by Kramers–Kronig transformation. *Polish J Chem* 78:1255–1260
85. Popkirov GS (1996) Fast time-resolved electrochemical impedance spectroscopy for investigations under nonstationary conditions. *Electrochim Acta* 41:1023–1027
86. Popkirov GS, Schindler RN (1995) Effect of sample nonlinearity on the performance of time domain electrochemical impedance spectroscopy. *Electrochim Acta* 40:2511–2517
87. Hazi J, Elton DM, Czerwinski WA, Schiewe J, Vicente-Beckett VA, Bond AM (1997) Microcomputer-based instrumentation for multi-frequency Fourier transform alternating current (admittance and impedance) voltammetry. *J Electroanal Chem* 437:1–15
88. Yoo JS, Park SM (2000) An electrochemical impedance measurement technique employing Fourier transform. *Anal Chem* 72:2035–2041
89. Yoo JS, Song I, Lee JH, Park SM (2003) Real-time impedance measurements during electrochemical experiments and their application to aniline oxidation. *Anal Chem* 75:3294–3300
90. Barsoukov E, Ryu SH, Lee H (2002) A novel impedance spectrometer based on carrier function Laplace-transform of the response to arbitrary excitation. *J Electroanal Chem* 536:109–122
91. Ragoisha GA, Bondarenko AS (2003) Potentiodynamic electrochemical impedance spectroscopy. Copper underpotential deposition on gold. *Electrochem Commun* 5:392–395
92. Sacci RL, Harrington DA (2009) Dynamic electrochemical impedance spectroscopy. *ECS Trans* 19:31–42
93. Darowicki K (2000) Theoretical description of the measuring method of instantaneous impedance spectra. *J Electroanal Chem* 486:101–105
94. Darowicki K, Orlikowski J, Lentka G (2000) Instantaneous impedance spectra of a non-stationary model electrical system. *J Electroanal Chem* 486:106–110
95. Darowicki K, Ślepski P (2004) Instantaneous electrochemical impedance spectroscopy of electrode reactions. *Electrochim Acta* 49:763–772
96. Mecklenbauer W (1989) Non-parametric time-frequency representation. In: Longo G, Picinbono B (eds) *Time and frequency representation of signal and systems*. Springer, Wien, p 11
97. Darowicki K, Ślepski P (2003) Dynamic electrochemical impedance spectroscopy of the first order electrode reaction. *J Electroanal Chem* 547:1–8
98. Darowicki K, Orlikowski J, Arutumow A (2003) Investigations of the passive layer cracking by means of dynamic electrochemical impedance spectroscopy. *Electrochim Acta* 48:4189–4196
99. Darowicki K, Zieliński A, Krakowiak A (2003) Analysis of spontaneous electrochemical oscillations by energy distribution technique. *Electrochim Acta* 48:1559–1566

100. Darowicki K, Ślepski P (2004) Determination of electrode impedance by means of exponential chirp signal. *Electrochem Commun* 6:898–902
101. Ślepski P, Darowicki K (2009) Optimization of impedance measurements using ‘chirp’ type perturbation signal. *Measurement* 42:1220–1225
102. Bonnefont A, Morschl R, Bauer P, Krischer K (2009) Electrochemical impedance spectroscopy of patterned steady-states on electrode surfaces. *Electrochim Acta* 55:410–415
103. Koper MTM, Schmidt TJ, Markovic NM, Ross PN (2001) Potential oscillations and S-shaped polarization curve in the continuous electro-oxidation of CO on platinum single-crystal electrodes. *J Phys Chem B* 105:8381–8386
104. Morschl R, Bolten J, Bonnefont A, Krischer K (2008) Pattern formation during CO electrooxidation on thin Pt films studied with spatially resolved infrared absorption spectroscopy. *J Phys Chem C* 112:9548–9551

Chapter 4

Temporal Instabilities in Cathodic Processes at Liquid and Solid Electrodes

4.1 Electroreduction of Peroxodisulfate Ions

4.1.1 *The N-NDR Region as a Double Layer Effect*

In this chapter, examples of temporal instabilities (oscillations and multistability) reported for cathodic processes carried out at both liquid and solid electrodes are described. With respect to liquid ones, the oscillations of the current associated with the electrode processes occurring at mercury have been quite intensively studied for several decades, especially when classical polarography was still the most popular experimental technique in electrochemistry. Therefore, studies of polarographic oscillations greatly contributed to the understanding of the mechanisms of electrochemical oscillations. A big advantage of mercury electrode is its smooth, uniform, and easily renewable surface and a high overvoltage for hydrogen evolution at negative potentials. The structure of the mercury–liquid electrolyte solution is thus much easier to define than, e.g., the structure of the passive layer on corroding solid electrodes. Hence, not only the general source of instability, but also a more detailed (electro)chemical mechanism of oscillations or multistability can be suggested. Based on the characteristics of the polarographic systems one can excellently show the different origins of the negative differential resistance in electrode processes: the potential-dependent repulsion of charged reactant particles from the reaction site in the double layer, the adsorption of an inhibitor of a charge-transfer process, or the desorption of a catalyst of this process (see Sect. 2.1.4). Such studies were later extended for solid electrodes, provided that the region of potential corresponding to instabilities was positive enough to avoid hydrogen evolution. One of the model electrode reactions that served for numerous studies of mechanisms and bifurcation scenarios of dynamic instabilities was the electroreduction of $S_2O_8^{2-}$ ions in which the negative differential resistance (N-NDR region) was caused by repulsive interaction of these anions with negatively charged electrode surface. This *Frumkin effect* was first reported as early as 1933 [1]. In order to understand the detailed origin of this effect, one has to take into account the spatial distribution of the electric potential in the double

layer, varying from ϕ_M at the metal electrode surface up to ϕ_s —the potential in the bulk of the solution. The bulk potential ϕ_s is usually considered a reference potential, with respect to which other potentials are expressed, or in other words, ϕ_s is then assumed to be of zero value. The distance at which the potential profile develops in the solution depends on the concentration of ionic salt which can be introduced intentionally as the so-called supporting electrolyte. Considering the electroactive particles, if they are not specifically adsorbed on the electrode surface, they undergo reduction or oxidation close to the physical metal–solution interface, at the distance of closest approach, usually denoted as x_2 , where the electric potential attains the ϕ_2 value. In the classical Gouy–Chapman–Stern model of the double layer, x_2 means the position of the so-called outer Helmholtz plane and is determined by the properties (solvated ion radii) of the supporting electrolyte, often present in excess compared to the electroactive species. Note that for typical concentrations of the supporting electrolyte and conditions of the electrochemical measurements, the x_2 value is much smaller than the thickness of the diffusion layer that develops during concentration polarization.

Here we shall consider the case of such a relatively low concentration of supporting electrolyte that the electric potential profile enters relatively deeply in the solution and the ϕ_2 value substantially differs from its bulk value (Fig. 4.1) [2].

Let us further assume that the reactant Ox undergoes practically irreversible electroreduction with the rate constant $k_f(E)$, so the reoxidation of the Red species at the potentials considered can be neglected:



This assumption which simplifies mathematical considerations is also quite realistic, considering the case of the N-NDR formation due to the double layer effect. In terms of this assumption, one considers thus two important effects of the spatial distribution of the electric potential across the double layer:

1. If the reactant particle (here Ox) possesses a charge $z_{\text{ox}}e$, then its local concentration at the reaction site is different than *immediately outside* the diffuse part of the double layer¹ c_{ox}^b (*static* double layer effect):

$$c_{\text{ox}}(x_2, t) = c_{\text{ox}}^b \exp(-z_{\text{ox}}F\phi_2/RT) \quad (4.2)$$

2. The rate constant k_f of the electron-transfer process at $x = x_2$ is determined not by the $E = \phi_M - \phi_s$ interfacial potential drop, but by the effective drop $E - \phi_2 = \phi_M - \phi_s - \phi_2$ (*dynamic* double layer effect):

$$k_f(E, \phi_2) = k_s \exp(-\alpha nF(E - \phi_2 - E^0)/RT) \quad (4.3)$$

¹ Since x_2 is usually much smaller than the thickness of the diffusion layer, c_{ox}^b is considered a “surface concentration”, generally dependent on time t , and in diffusion-oriented problems is usually presented in the notation: $c_{\text{ox}}(0, t)$. Thus, here $c_{\text{ox}}^b \approx c_{\text{ox}}(0, t)$ [2].

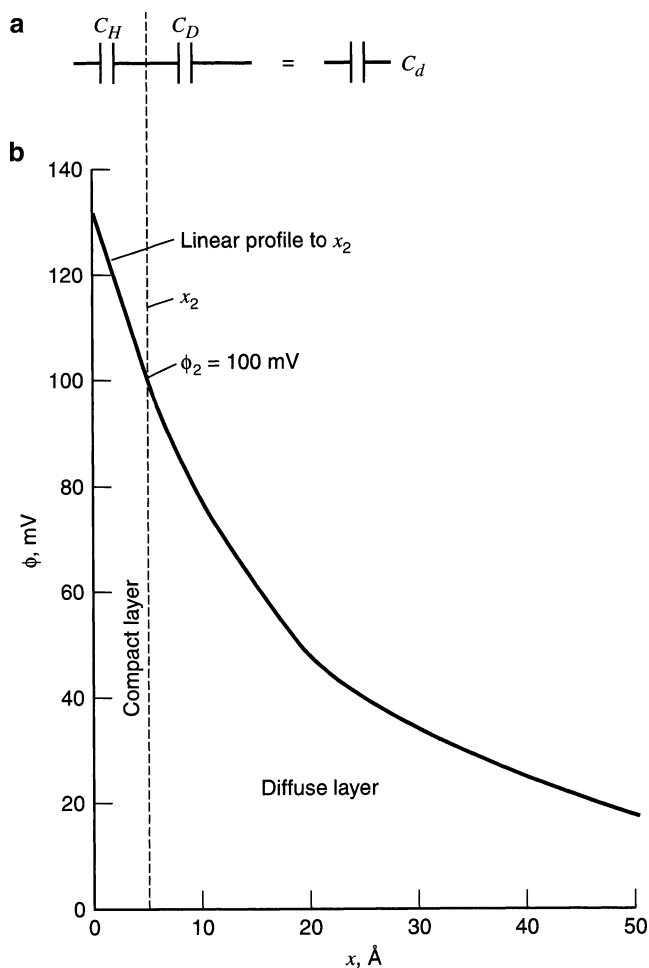


Fig. 4.1 (a) A view of the differential capacitance in the Gouy–Chapman–Stern (GCS) model of a series network of Helmholtz-layer and diffuse-layer capacitances. (b) Potential profile through the solution side of the double layer, according to GCS theory. Calculated for 0.01 M 1:1 electrolyte in water. Reprinted from [2] with permission of John Wiley & Sons, Inc. Copyright 2001 John Wiley & Sons, Inc.

where k_s is the standard rate constant of heterogeneous electron transfer, αn is a generalized cathodic transfer coefficient for the n -electron process, and E^0 is the formal potential of the Ox/Red redox couple.

Due to those double layer effects the directly determined standard rate constant, dependent on the concentration of inert supporting electrolyte, is however only an “apparent” value k_s^{app} . The “true” value k_s^{true} can be obtained by taking into account

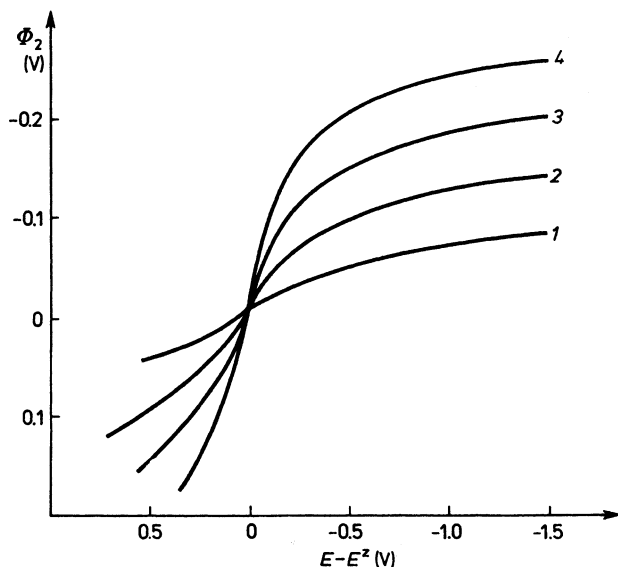


Fig. 4.2 Dependence of ϕ_2 on electrode potential referred to the zero-charge potential E_z . Mercury electrode at 25 °C in NaF solutions: (1) 1.0 M, (2) 0.1 M, (3) 0.01 M, and (4) 0.001 M [3, 4]. Reprinted from [3] with permission of John Wiley & Sons, Inc. Copyright 1961 John Wiley & Sons, Inc.

both corrections for the static and dynamic effects of the double layer which lead to the following dependence for the (cathodic negative) faradaic current of reaction (4.1):

$$I_f = -nFA[k_s^{\text{true}} \exp(-\alpha nF(E - \phi_2 - E^0)/RT)] \times [c_{\text{ox}}^b \exp(-z_{\text{ox}}F\phi_2/RT)] \quad (4.4)$$

from which, for $c_{\text{ox}}^b = c_{\text{ox}}(0, t)$, the following relationship between the “apparent” and “true” standard rate constants, known as the “Frumkin correction” follows [2]:

$$k_s^{\text{app}} = k_s^{\text{true}} \exp\left[\frac{(\alpha n - z_{\text{ox}})F\phi_2}{RT}\right] \quad (4.5)$$

Since k_s^{true} is constant for given temperature, Eq. (4.5) describes how the apparent or “observed” rate constant (and in this way also the faradaic current) vary depending on the concentration of supporting electrolyte which affects ϕ_2 . Furthermore, since ϕ_2 increases nonlinearly with imposed potential (crossing zero at the potential of zero charge, cf. Fig. 4.2), k_s^{app} calculated from Eq. (4.5), may show a minimum at a given imposed electrode potential, producing thus before it the negative dI_f/dE slope, i.e., the NDR region.

This $I-E$ shape can happen for the negatively charged ions undergoing an electron transfer at negatively charged electrode surface or for positively charged ions reacting

at positively charged electrodes. For example, for the electroreduction of ions of particle charge $z_{\text{ox}} = -2$, when the transfer coefficient $\alpha n = 0.5$, then $(\alpha n - z_{\text{ox}}) > 0$. Equation (4.4) indicates then that in certain region of electrode potential, when $\phi_2 < 0$, there exists region of a negative slope of the I - E dependence. At more negative potentials the rate of the electrode process passes through a minimum and increases due to predominating effect of the rising $\exp(-\alpha n F(E - E^0)/RT)$ term over the decrease of the apparent standard rate constant. This is the simplest explanation of the shape of the I - E dependence observed for the electroreduction of several anions, such as $\text{S}_2\text{O}_8^{2-}$, $\text{S}_4\text{O}_6^{2-}$, PtCl_4^{2-} , CrO_4^{2-} , or $\text{Fe}(\text{CN})_6^{3-}$, at the Hg, Pt, or Cu electrode, provided that supporting electrolyte concentration is sufficiently low, since only then the ϕ_2 potential differs significantly from that in the region outside the double layer (for results on Hg electrode, cf. e.g., [5]). Also the presence of surface active ions modifies the electric potential distribution in the double layer and appropriately affects the shape of the N-NDR region in the $\text{S}_2\text{O}_8^{2-}$ electroreduction; such studies for Hg electrode were described by Frumkin et al. [6]. Of course, the concept of the Frumkin correction is very simple among others because it neglects the discreteness of charge distribution in the double layer which were later discussed in electrochemical literature by Fawcett et al. (cf. e.g. [7]).

From the point of view of dynamic instabilities, it is also important that low concentration of supporting electrolyte means also the relatively high solution resistance, so it may happen that for the destabilization of the electric circuit toward the oscillatory behavior it may be not necessary to insert any additional, external resistor in series with the working electrode. In fact, spontaneous current oscillations were observed under such conditions for $\text{S}_2\text{O}_8^{2-}$ electroreduction without any additional resistance applied, i.e., for 0.02 M $\text{K}_2\text{S}_2\text{O}_8$ [8]. Nevertheless, in the same pioneer paper of the year 1960, Gokhstein and Frumkin [8] have also indicated the role of additional external resistance in the onset of sustained oscillations, implying the necessity of the electrode potential oscillations, associated with the current oscillations. If the electronic circuit was changed into the three-electrode potentiostatic arrangement, compensating the ohmic drops, when the variations of the Hg electrode potential became negligible, the oscillations ceased. The entire picture corresponds closely to the conditions of the onset of the oscillations caused by coupling of the NDR characteristics of the electrode process with the ohmic drops in the circuit, with the participation of the reactant transport dynamics between the electrode surface and the bulk of the solution (see Chap. 2). Further studies of the same group indicated current oscillations also during the polarographic electroreduction of $\text{Fe}(\text{CN})_6^{3-}$, PtCl_4^{2-} , CrO_4^{2-} , when appropriate composition of the diluted supporting electrolyte and serial resistance was applied [5].

4.1.2 Bifurcation Analysis

In line with increasing incorporation of methods of nonlinear dynamics in chemistry, Wolf et al. [9] have performed an extensive model study of the oscillatory reduction of $\text{S}_2\text{O}_8^{2-}$ on different electrodes by combining the electrochemical mechanism of the

double layer effects with the formalism of nonlinear dynamics. The work involved also experimental studies of $\text{S}_2\text{O}_8^{2-}$ electroreduction at rotating disk electrodes of Cu and Pt, with the SCE as a reference electrode and Pt counterelectrode. Of course, in this potentiostatic mode the external serial resistance had to be inserted in the circuit of the working electrode, in order to cause appropriate ohmic potential drops. The solution studied was 1–10 mM $\text{Na}_2\text{S}_2\text{O}_8$ in the presence of diluted, 1 mM Na_2SO_4 as the supporting electrolyte.

The dynamical system considered involved two dynamical variables: the concentration of $\text{S}_2\text{O}_8^{2-}$ at the electrode surface (c), and the potential drop across the double layer denoted below as ϕ , according to original reference. The reader is asked to accept these multiple notations for the same quantity in various papers. For the sake of mathematical simplicity of stability analysis, the model involved further not partial, but ordinary differential equations derived based on the concept of the Nernst diffusion layer (Sect. 2.2.2). In terms of this formalism, the temporal dynamics of the surface concentration of $\text{S}_2\text{O}_8^{2-}$ was expressed as proportional to the difference between its charge-transfer controlled current I_{red} expressed by Butler–Volmer relationship with the Frumkin correction term [i.e., analogously to (4.4)] and its diffusion-controlled current (in A) defined as:

$$I_{\text{dif}} = -\frac{nFAD}{\delta}(c^0 - c) \quad (4.6)$$

where c^0 [mol cm^{-3}] means the bulk concentration of $\text{S}_2\text{O}_8^{2-}$ ions, while δ [cm] is the Nernst diffusion layer thickness determined by the Levich equation for the rotating disk electrode [2, 10]:

$$\delta = 1.61D^{1/3}\nu^{1/6}\omega^{-1/2} \quad (4.7)$$

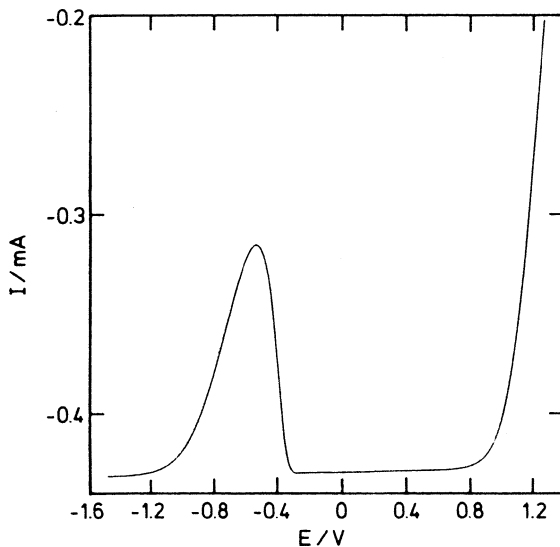
with D being the diffusion coefficient of $\text{S}_2\text{O}_8^{2-}$ ions [$\text{cm}^2 \text{s}^{-1}$]; ν , the kinematic viscosity of the solution [$\text{cm}^2 \text{s}^{-1}$]; and ω is the angular velocity of disk rotation (rad s^{-1}). As in Chap. 2, the expression for the dynamics of the electrode potential was derived from the charge conservation principle. The final forms of both equations defining the actual dynamical system are:

$$\frac{dc}{dt} = \frac{2}{nFA\delta} \times \left(-nFAk_{\text{red}}c \left[\exp\left(-\frac{\alpha nF\phi}{RT}\right) \exp\left(\frac{(\alpha n - z)F\phi_2}{RT}\right) + \frac{nFAD}{\delta}(c^0 - c) \right] \right) \quad (4.8)$$

$$\frac{d\phi}{dt} = \frac{1}{AC_d} \left(\frac{U - \phi}{R_s} + nFAk_{\text{red}}c \left[\exp\left(-\frac{\alpha nF\phi}{RT}\right) \exp\left(\frac{(\alpha n - z)F\phi_2}{RT}\right) \right] \right) \quad (4.9)$$

with U being the externally applied voltage and C_d is the double layer capacitance of the working electrode (per unit area) assumed here independent of the electrode potential; k_{red} is analogous to the true standard rate constant (cf. Eq. 4.4) of $\text{S}_2\text{O}_8^{2-}$ electroreduction. Although the model seems to be physically very simple, the

Fig. 4.3 Stationary states as a function of the externally applied potential E (vs. SCE) at $f = \omega/2\pi = 25$ Hz, $R_s = 100 \Omega$, $\alpha = 0.2$, $k_{\text{red}} = 384.7 \text{ cm s}^{-1}$, $A = 0.28 \text{ cm}^2$. Reprinted from [9] with kind permission of Deutsche Bunsen-Gesellschaft für Physikalische Chemie



implicit mathematical relation between the potentials φ and φ_2 requires application of numerical techniques to its stability analysis. The calculated dependence of the steady-state currents on the electrode potential, exhibiting N-NDR region, is shown in Fig. 4.3.

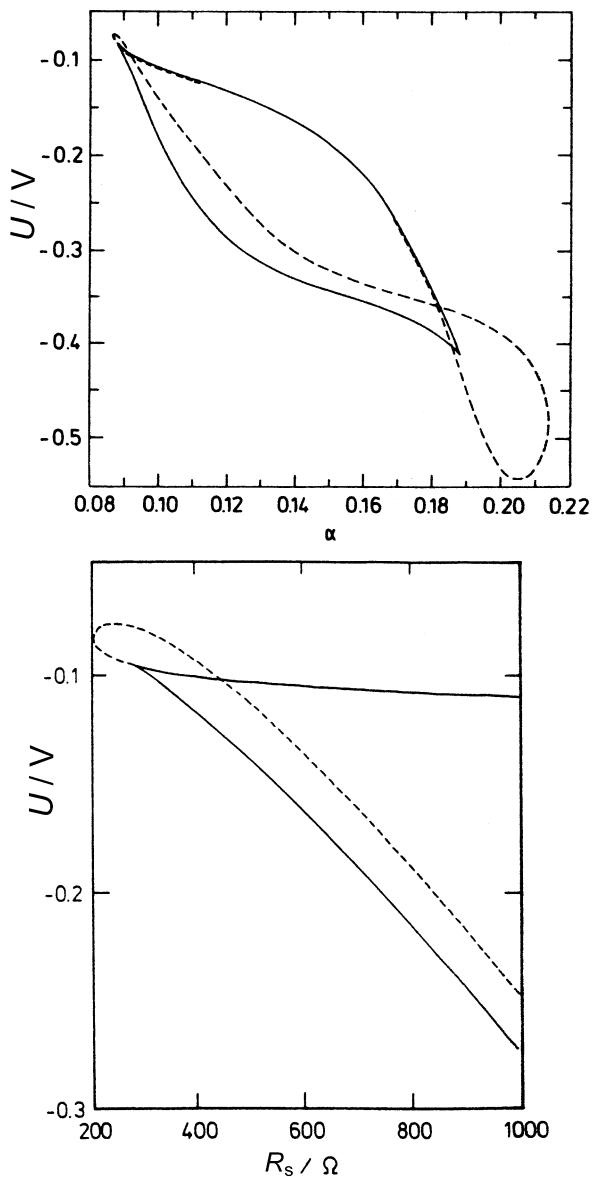
The linear stability analysis of those states indicated the stable/unstable nodes/foci or saddles, including the localization of the Hopf and saddle–node bifurcations. The corresponding bifurcation diagrams are shown in Fig. 4.4.

Since linear stability analysis supplies only limited information on the local dynamics, the numerical integration of original nonlinear ODEs was necessary to obtain a more complete picture of possible bifurcations. This allowed to detect a rich variety of dynamic behaviors depending not only on the control parameters, but also on the initial values of the surface concentration and electrode potential. The corresponding bifurcation portrait is shown in Fig. 4.5.

However, even numerically it was not possible to locate all of the different phase portraits predicted by this diagram. Table 4.1 collects the theoretically possible phase portraits with the indication of those ones which were detected or not in the model studied.

Analysis of bifurcations occurring in dependence on varying external voltage, for the following other parameters fixed: $c^0 = 1 \text{ mM}$, $\alpha = 0.2$, $f = \omega/2\pi = 10 \text{ Hz}$, $R_s = 900 \Omega$, $C_d = 25 \mu\text{F cm}^{-2}$, $A = 0.28 \text{ cm}^2$, $D = 1 \times 10^{-5} \text{ cm}^2 \text{ s}^{-1}$, and $k_{\text{red}} = 384.7 \text{ cm s}^{-1}$, allowed to detect a supercritical Hopf bifurcation at about -0.390 V , followed by a *canard explosion*, described also in Sects. 1.6 and 3.6.2. This apparent bifurcation manifested itself here as the sudden rise of the oscillation amplitude (as well as of the oscillation frequency) located in a very narrow range of voltage between -0.3904576 and $-0.3904577 \text{ V vs. SCE}$ (see Table 4.2).

Fig. 4.4 Local bifurcations [Hopf (*dashed line*) and saddle–node (*solid line*)] in the α – U parameter plane with $R_s = 900 \Omega$, $f = \omega/2\pi = 10$ Hz, $c^0 = 1$ mM (a) and in the R_s – U parameter plane for $\alpha = 0.1$, $f = \omega/2\pi = 25$ Hz and $c^0 = 1$ mM (b) (U vs. SCE). Reprinted from [9] with kind permission of Deutsche Bunsen-Gesellschaft für Physikalische Chemie



Exemplary, representative shapes of the simulated oscillations are shown in Fig. 4.6a–c. At $U \approx -0.539$ V a *subcritical* Hopf bifurcation occurs which leads to the formation of an unstable limit cycle that could be found by integrating in negative time direction (Fig. 4.6d). Finally, the stable and unstable limit cycles annihilate themselves in a *saddle–node bifurcation of cycles* (cf. Sect. 1.4.1) (or saddle–node of periodic orbits, denoted above as snp bifurcation).

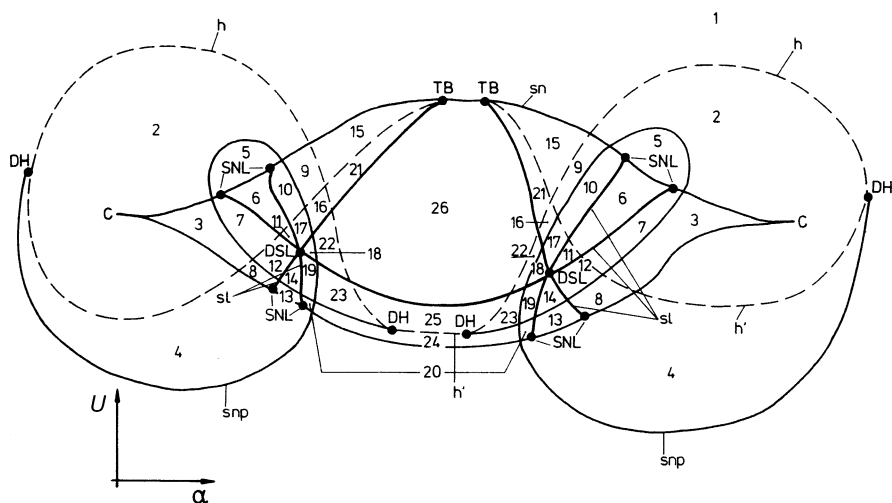


Fig. 4.5 Schematic drawing of the complete bifurcation diagram in the α - E parameter plane. (Codimension-1-bifurcations: h (supercritical-) Hopf, h' (subcritical-) Hopf, sn saddle-node, sl saddle-loop, snp saddle-node of periodic orbits; Codimension-2-points: TB Takens-Bogdanov, SNL saddle-node loop, DH degenerate Hopf, DSL double saddle loop. Reprinted from [9] with kind permission of Deutsche Bunsen-Gesellschaft für Physikalische Chemie

One should emphasize that experimental studies of $S_2O_8^{2-}$ reduction at a Cu disk electrode performed by the same authors [9] confirmed the existence of all dynamic behaviors predicted by the theoretical analysis, including the sequence of bifurcations observed upon increasing external voltage. Even the hysteresis, indicating the coexistence of a stable stationary state and stable limit cycle, separated by unstable limit cycle (cf. Fig. 1.14), was observed. The coexistence of these states was also directly detectable: when the external voltage was varied slowly to the subcritical Hopf bifurcation from the cathodic side, the steady-state behavior was reported that upon a perturbation (applied by a short temporary increase of the rotation speed) led to sustained oscillations (Fig. 4.7).

Also, the transition resembling the canard explosion was observed, but due to limited resolution of the potentiostatic system it was not possible to quantitatively confirm such behavior. It was also difficult to record experimentally the bistable behavior, but model calculations showed that the saddle-node bifurcations occur only for rather low values of transfer coefficient α (cf. Fig. 4.4a) which do not characterize the real electroreduction of $S_2O_8^{2-}$.

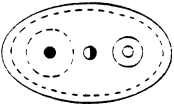
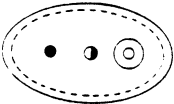
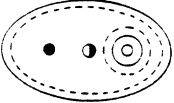
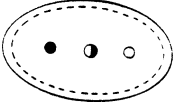




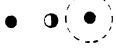

Concluding, a physically simple model, involving the Frumkin correction, appeared to reproduce successfully the complex dynamics of the $S_2O_8^{2-}$ electroreduction at the rotating disk electrode. It is, however, an extremely simple approach that does not involve any mechanistic details of this electrode process. That is why in recent years studies of the oscillatory electroreduction of $S_2O_8^{2-}$ ions at the solid electrodes, including single-crystal ones, were continued.

Table 4.1 Collection of possible dynamical phase portraits with the indication of those found for the model (4.8), (4.9)

No.	Phase portrait	Found	No.	Phase portrait	Found
1		+	2		+
3		+	4		+
5		-	6		-
7		-	8		+
9		+	10		-
11		-	12		-
13		-	14		-
15		+	16		-

(continued)

Table 4.1 (continued)

No.	Phase portrait	Found	No.	Phase portrait	Found
17		—	18		—
19		—	20		—
21		+	22		+
23		—	24		+
25		—	26		+

Full points (•): stable steady states; empty points (o): unstable steady states; half-filled points: saddles. Full circles stand for stable limit cycles and dashed circles for unstable limit cycles. Numbers of rows correspond to locations indicated in Fig. 4.5. Reprinted from [9] with kind permission of Deutsche Bunsen-Gesellschaft für Physikalische Chemie

Table 4.2 Manifestation of the canard explosion in the model of $S_2O_8^{2-}$ electroreduction

U (mV)	Current amplitude (mA)
−390.0	0.21
−390.4	0.47
−390.45	0.64
−390.457	0.90
−390.4576	1.30
−390.4577	6.8
−390.458	7.0
−390.46	7.5
−390.5	7.6
−391.0	8.0

Reprinted from [9] with kind permission of Deutsche Bunsen-Gesellschaft für Physikalische Chemie

Oscillations were then reported also under high ionic strength conditions, when the source of the oscillations could not be caused by the Frumkin effect. The essential points of those investigations are briefly described below.

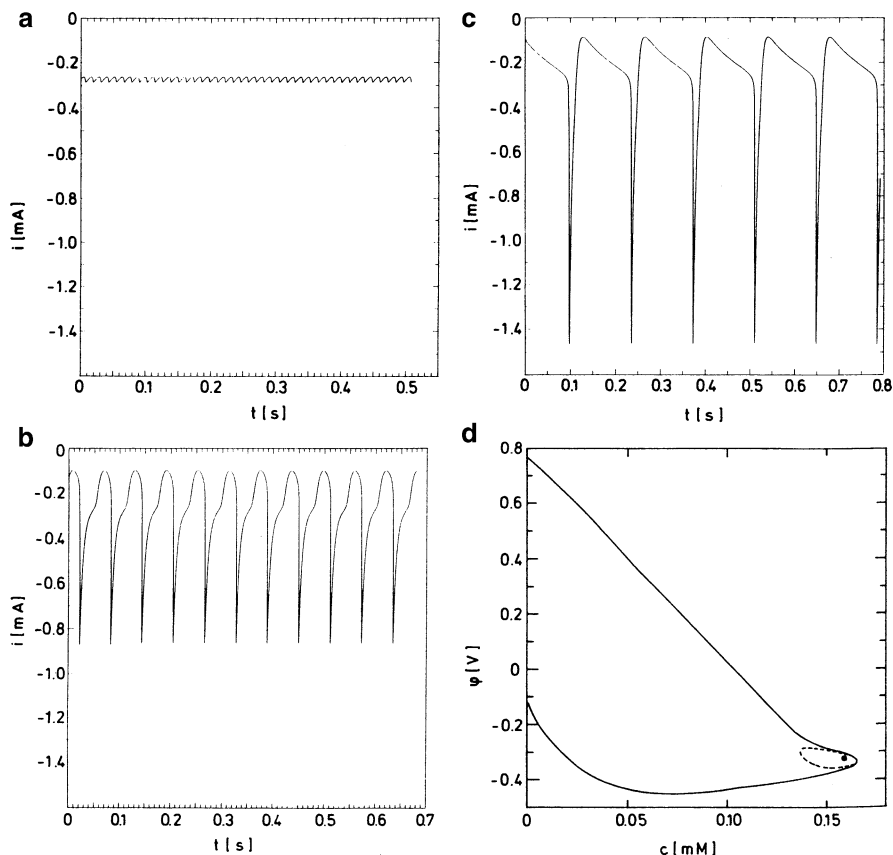


Fig. 4.6 Integrated time series at $U = -0.3901$ V (a), -0.391 V (b), and -0.530 V (c), phase portrait at $U = -0.532$ V (d); U expressed vs. SCE; (dashed line) unstable limit cycle, (solid line) stable limit cycle, (filled circle) stable focus. Other parameters: $c^0 = 1$ mM, $R_s = 900 \Omega$, $\alpha = 0.2$. Reprinted from [9] with kind permission of Deutsche Bunsen-Gesellschaft für Physikalische Chemie

4.1.3 Mechanistic Aspects of $S_2O_8^{2-}$ Electroreduction

In the course of mechanistic electrochemical studies, it was established that the electroreduction of $S_2O_8^{2-}$ at polycrystalline gold electrode [11, 12] and platinum electrode [13, 14] proceeds via *two parallel* pathways. In particular, Samec and Doblhofer [12] have shown that the first pathway has an electrocatalytic character, involving relatively strong interaction of $S_2O_8^{2-}$ with the electrode surface and giving rise to a current at positively charged electrodes. The second pathway, predominating at more negative potentials, is represented by the outer sphere, direct reduction of $S_2O_8^{2-}$ from solution and for this pathway the repulsive interaction between the anion and the negatively charged electrode can cause a double layer effect of the Frumkin type. Further analysis [15] has shown that the rate of the

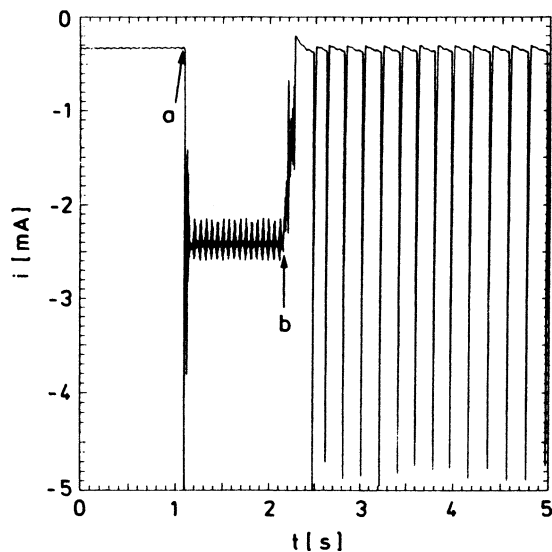


Fig. 4.7 Coexistence of stationary behavior and oscillations in the experiment (Pt electrode, $c^0 = 5$ mM, $U = 0.9429$ V vs. SCE): before (a) and after (b) the rotating speed of the electrode was $f = \omega/2\pi = 20$ Hz, the stationary state before (a) was reached varying the externally applied voltage to more cathodic values just to leave the oscillatory region, and then slightly shifting U back in the anodic direction. At point (a) the rotating frequency was raised for a short time, so that between (a) and (b) $f = \omega/2\pi \approx 150$ Hz. After (b) the same conditions as before (a) are valid, and the system is now in an oscillating state. Reprinted from [9] with kind permission of Deutsche Bunsen-Gesellschaft für Physikalische Chemie

electrocatalytic pathway is, on Au(111) electrode, for about two orders of magnitude higher than at Au(poly), presumably due to enhanced adsorption of $S_2O_8^{2-}$ on Au(111), caused in turn by better matching of the anion structure with trigonal structure of the Au(111) surface. In contrast, the direct reduction of $S_2O_8^{2-}$ at Au(111) proceeds with approximately the same rate as at Au(poly). These suggestions were corroborated by measurements involving combination of stationary and rotating disk electrode measurements with ex situ STM and electrochemical impedance spectroscopy, for both Au(111) and Au(110) electrodes [16]. The stronger electrocatalytic effect of Au(111), compared with Au(110), was explained in terms of more effective overlap of the electronic wave functions of Au(111) and the adsorbed peroxodisulfate. Both parallel pathways are shown in Fig. 4.8.

From mechanistic point of view, the electrocatalytic effect in the case of pathway (1a) is presumably caused by the fact that adsorption of $S_2O_8^{2-}$ causes its reduction with the intervening or following O–O bond breakage. The scheme indicates also the experimentally found catalytic effect of H^+ ions on this route (although the detailed mechanism of this particular process was not clarified). If $HClO_4$ is used as a source of protons, the inhibition of this pathway by ClO_4^- ions is also observed. This was explained by coadsorption of ClO_4^- ions, although relatively weak, but significant enough due to high excess of $HClO_4$ (10–1,000 times more than concentration of $S_2O_8^{2-}$) as a supporting electrolyte. In complement to

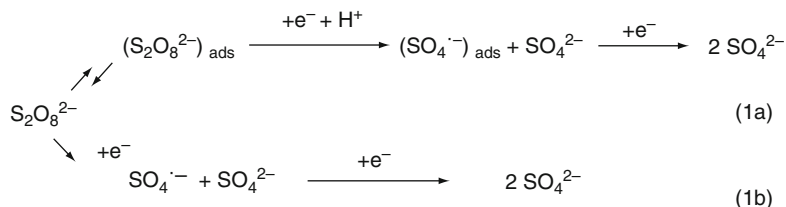


Fig. 4.8 Mechanism of $\text{S}_2\text{O}_8^{2-}$ electroreduction on Au(111) and Au(poly) electrodes, involving the electrocatalytic (1a) and direct (1b) pathways. Reprinted from [16], Copyright 1997, with permission from Elsevier

this reaction scheme, one should add that besides the adsorption of $\text{S}_2\text{O}_8^{2-}$, also the (not indicated there) adsorption of SO_4^{2-} can play a certain role in the reduction mechanism of $\text{S}_2\text{O}_8^{2-}$. Adsorption studies of SO_4^{2-} at the single crystal Au electrodes have been reported by Cahan et al. [17] and Lipkowski et al. [18, 19].

Coming back to nonlinear dynamic phenomena, one should note that Koper [20] has reported mixed-mode oscillations (MMO) during the peroxodisulfate reduction on polycrystalline Pt and Au electrodes, in addition to previously found mono-periodic, relaxation oscillations. Furthermore, bistability and transient oscillations of current of $\text{S}_2\text{O}_8^{2-}$ electroreduction were reported by Treindl et al. [21] for the Au (110) electrode in dilute solutions of NaF (Fig. 4.9).

The concentration of NaF (supporting electrolyte) was relatively low (5 mM), only a bit higher than the concentration of electroactive $\text{S}_2\text{O}_8^{2-}$ ions (2 mM). The potential was stepped from 0 V to a desired value. Following the induction time and the transient oscillations, the current eventually dropped to a final, negligible value, indicating the complete passivation of the electrode. Figure 4.9 shows that the oscillations occurred around the I - E branch with a positive charge-transfer resistance and it was found that this potential region is positive to the point of zero charge (PZC) of the bare gold electrode, equal to -0.45 V (all potentials referred to mercurousulfate electrode of the potential $+0.65$ V vs. SHE). Note that both above-mentioned reduction pathways (Fig. 4.8) have a maximum rate close to the pzc, so they overlap in this region. Although apparently the above facts could qualify the studied oscillator at once as of the hidden negative resistance (HN-NDR) type, the true mechanism of the oscillations seems to be more sophisticated. Even the detection of galvanostatic oscillations did not confirm the HN-NDR character of the system studied, since the amplitude of the oscillating electrode potential was reaching the far negative region of hydrogen evolution, i.e., not correlating with the potential region of the oscillations shown in Fig. 4.9. In the opinion of Treindl et al. [21], the asymptotic passivation of the electrode surface is premise for identification of the process responsible also for the oscillations. As Cahan et al. reported [17], sulfate ions may be chemically incorporated into the surface oxide layer on cycling the electrode potential, while Desilvestro and Weaver [11] using SERS technique have detected the stronger adsorption of oxygen species on Au in the presence of $\text{S}_2\text{O}_8^{2-}$. Taking into account the above findings, it is now assumed that the highly oxidizing $\text{SO}_4^{\cdot-}$ radical, as the intermediate in $\text{S}_2\text{O}_8^{2-}$ reduction, causes a strong passivation of Au surface by

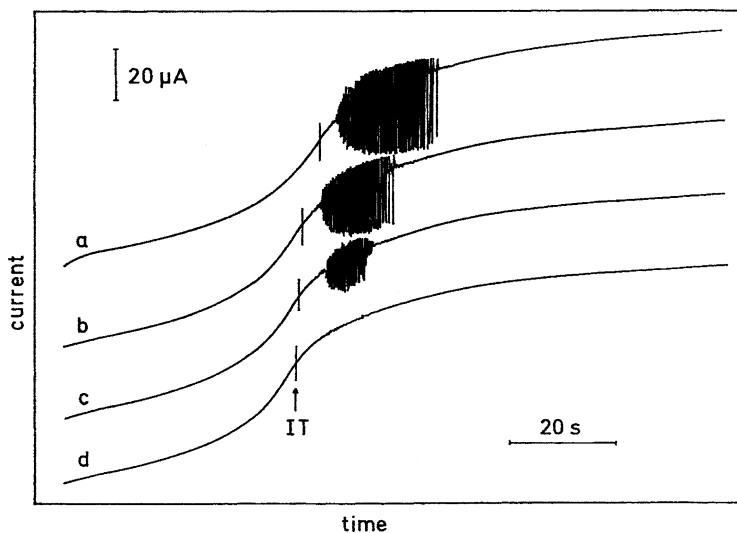
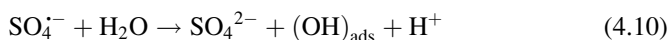


Fig. 4.9 Current transients and oscillations observed during potentiostatic $\text{S}_2\text{O}_8^{2-}$ (2 mM) reduction on the Au(110) electrode rotated at 1,000 rpm. $[\text{NaF}] = 5$ mM. The following electrode potentials were applied: (a) -0.38 V; (b) -0.37 V; (c) -0.36 V; (d) -0.35 V. IT is the inflection time. Note that the current density is negative, i.e., the current decreases with time. In all four cases, the transients are shown up to a current of $-10 \mu\text{A}$. Reprinted from [21], Copyright 1999, with permission from Elsevier

transforming it into a state which either binds the SO_4^{2-} or OH^- ions more strongly than in regular adsorption experiments. The following reaction is proposed:



with the chemisorbed $(\text{OH})_{\text{ads}}$ species considered responsible for the inhibition of $\text{S}_2\text{O}_8^{2-}$ reduction and further—for the oscillations. In order to explain their existence at a positive slope of I - E characteristics, the outline mechanism involving the variation of φ_2 potential (double layer effect) was proposed [21] which also postulated the variation of pzc during the oscillations. The $\text{S}_2\text{O}_8^{2-}/\text{Au}(110)$ oscillator remains probably one of these mysterious dynamic electrochemical systems which await further mechanistic studies.

One of the detailed problems which can be important for the mechanism of $\text{S}_2\text{O}_8^{2-}$ reduction on gold electrodes is the eventual role of surface oxides which, under appropriate conditions (in alkaline, neutral, or moderately acidic solutions) can undergo reduction at the potentials more negative than $\text{S}_2\text{O}_8^{2-}$. In [11], the reaction mechanism involving chemical oxidation of Au(poly) electrode by $\text{S}_2\text{O}_8^{2-}$ in an alkaline solution, followed by electrochemical reduction of surface oxides, was proposed. More recently, Samec et al. [22] have analyzed the electroreduction of $\text{S}_2\text{O}_8^{2-}$ on Au(111) covered by surface oxides and found the nontrivial characteristics of this system. First, the strong inhibition of the reduction process was observed but the extent of this effect did not correlate with the oxide surface coverage through a simple geometric blocking factor $(1 - \theta_T)$, where θ_T

denotes the total oxide coverage. Instead, it was necessary to consider the relative role of two main oxide species, the more stable of which presumably blocked the reaction sites for the $S_2O_8^{2-}$ reduction and was located probably on the surface step edges. Furthermore, the difference between the kinetics of the reduction of two oxide species suggested a coupling between these two processes, involving the diffusion-controlled proton catalysis. If dynamic instabilities are found for such systems, in the diagnosis of their origin it will be necessary to take into account those electrochemical processes.

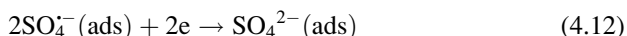
4.1.4 Studies at High Ionic Strength

Recent developments in the area of dynamic instabilities in the reduction of $S_2O_8^{2-}$ on solid electrodes have been published by Nakanishi et al. [23] who have reported oscillatory $S_2O_8^{2-}$ reduction on Pt(poly) and Au(poly) electrodes, but under such high ionic strength conditions, that the Frumkin double-layer effects could not operate. The mechanistic aspects of these oscillations are related to the mechanism of the dissociative adsorption of H_2O_2 through the concept of the autocatalytic effect of adsorbed OH [24] (cf. Sect. 4.7). Actual studies involved both dc and ac (impedance) techniques. For both electrodes, four types of electrochemical oscillations, named α , β , γ , and δ , were found (see Figs. 4.10 and 4.11); note that not all types of oscillations are existing for each electrode.

The fact that the oscillations were observed for galvanostatic (for Pt—also for potentiostatic) conditions suggests that the reported dynamics can correspond to a HN-NDR-type oscillator. The oscillations of type γ which appear upon cathodic current scan first (i.e., exhibiting the amplitude involving the most positive potentials) were further studied in more detail. Impedance measurements for $S_2O_8^{2-}$ reduction at Au(poly) electrode (Fig. 4.12) clearly proved the existence of the hidden negative real impedance for the potential located within the amplitude of the oscillations.

In dc studies, the NDR regions were found in the potentiodynamic $I-E$ characteristics, for sufficiently high scan rates (100 mV/s), only for atomically flat Au(111), and not for Au(100) and Au(110). Analogous phenomena were observed for the H_2O_2 reduction at atomically flat Pt(111), but not for Pt(100) and Pt(110), which is the premise for similarities in the reduction of both compounds.

Due to relatively positive potentials of their occurrence, the mechanism of oscillations γ was assumed to occur according to a catalytic pathway, in which $S_2O_8^{2-}$ reduction proceeds via its dissociative adsorption:



It is further suggested that NDR region arises from a catalytic effect of adsorbed OH on the dissociative adsorption of $S_2O_8^{2-}$ [Eq. (4.11)] (see below for more detailed description). Finally, the NDR-hiding species is most probably adsorbed SO_4^{2-} ions produced in the above electroreduction step (4.12).

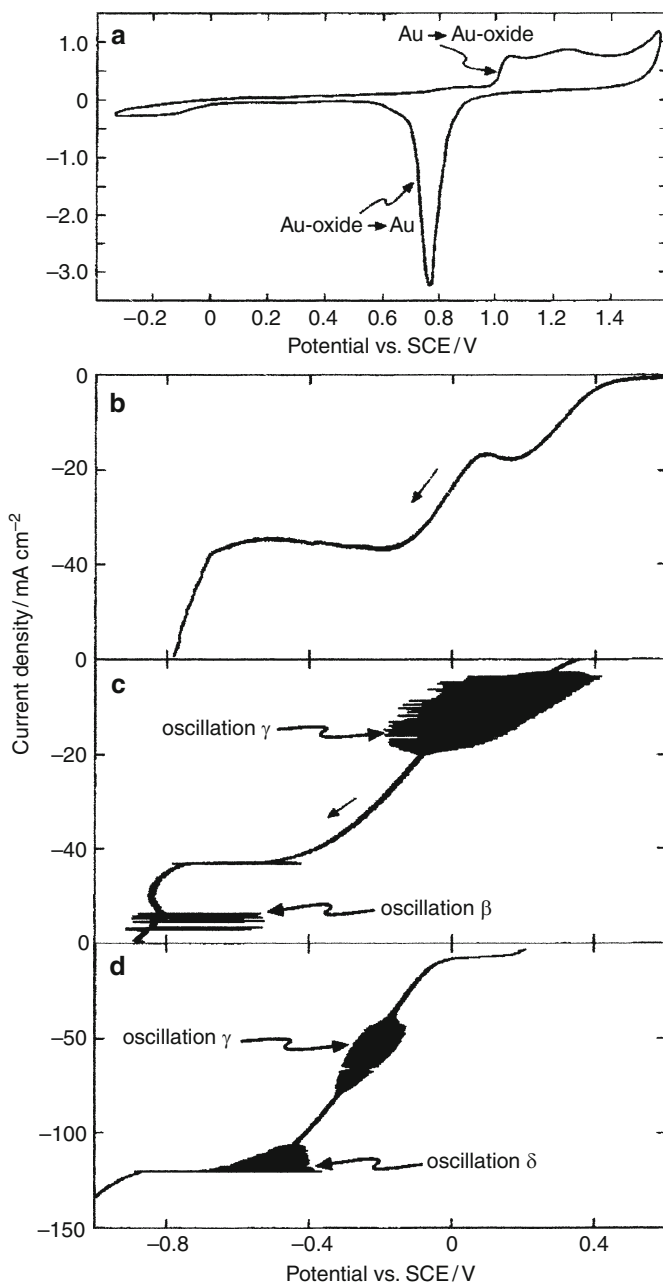


Fig. 4.10 Current-density (j) vs. potential (U) curves for poly-Au under (a, b) potential-controlled and (c, d) current-controlled conditions. Electrolyte: (a) 0.5 M HClO₄; (b–d) 0.5 M HClO₄ + 0.5 M Na₂S₂O₈. Scan rate: (a) 100 mV s⁻¹; (b) 10 mV s⁻¹; (c) 1 mA s⁻¹; (d) 10 mA s⁻¹. Reprinted with permission from [23] Copyright 2002 American Chemical Society

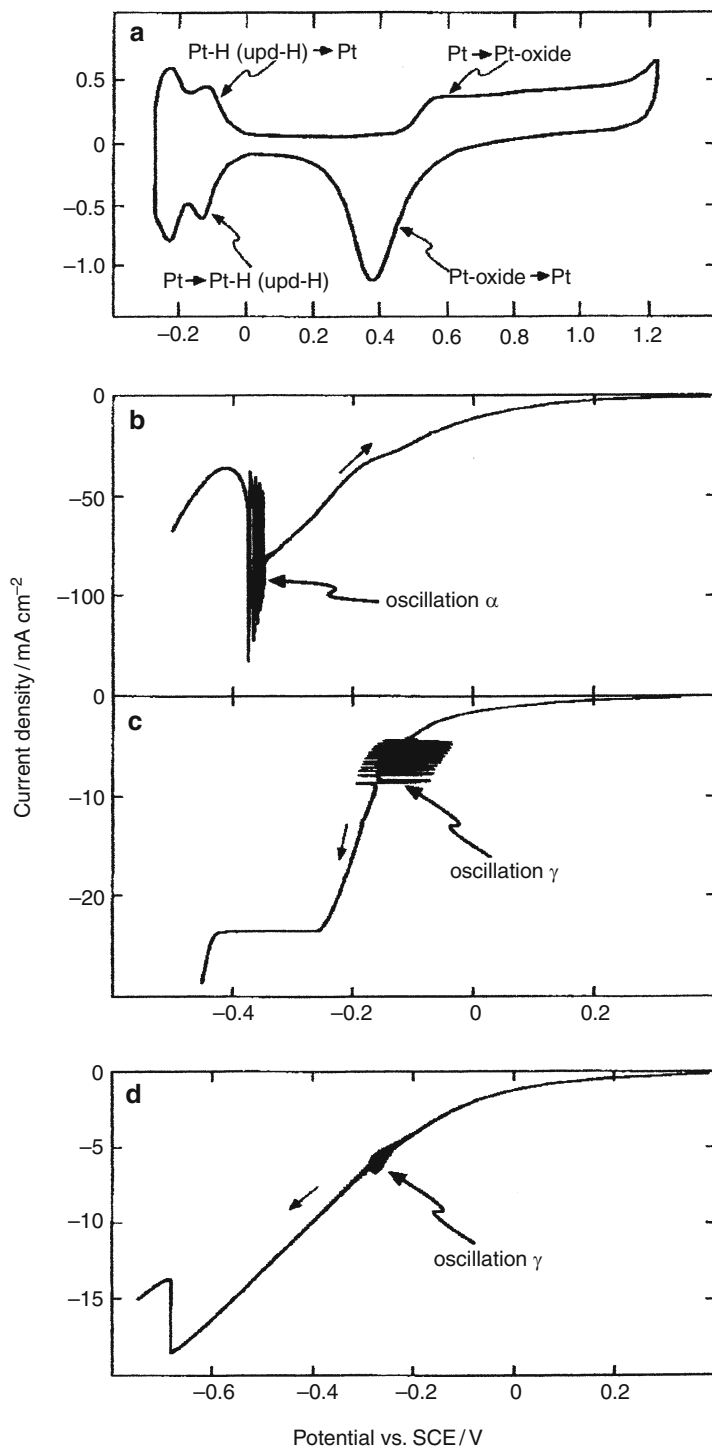


Fig. 4.11 (continued)

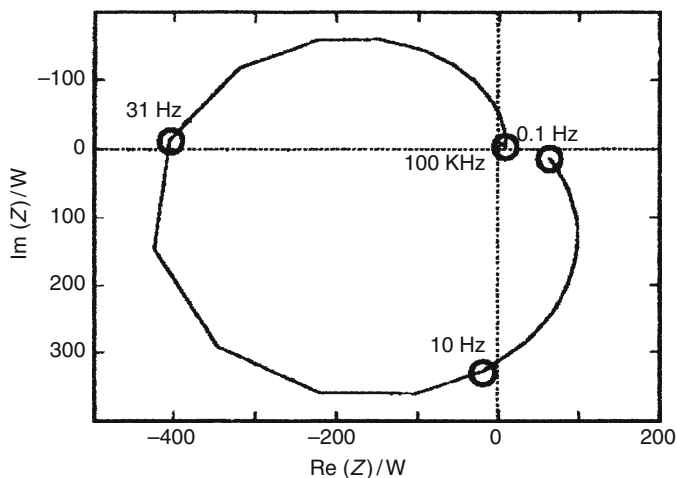


Fig. 4.12 Impedance diagram for poly-Au at -0.16 V vs SCE in 0.5 M HClO_4 + 0.7 M $\text{Na}_2\text{S}_2\text{O}_8$. Reprinted with permission from [23] Copyright 2002 American Chemical Society

Analogously to H_2O_2 electroreduction (cf. Section 4.7), the role of adsorbed OH was explained in the following way. First, the surface coverage of adsorbed OH, acting as a catalyst for reaction (4.11), decreases with increasing negative potential, causing the decrease in the $\text{S}_2\text{O}_8^{2-}$ reduction current and thus the appearance of NDR region. If we assume a *slow* desorption of produced $\text{SO}_4^{2-}(\text{ads})$ ions, we can understand why the NDR region manifests itself on the dc curves only at fast scan rates. If the scan rate is low, the decrease in the amount of adsorbed OH is compensated by an increase in empty surface sites by desorption of SO_4^{2-} and then NDR region does not form. SO_4^{2-} ions are thus a “slow species.” Furthermore, the formation of NDR on only Au(111) surface is explained in terms of high effectiveness of the catalytic role of adsorbed OH on this surface, in terms of the partial charges induced on the surface metal atoms (Fig. 4.13).

In order to confirm this outline mechanism in a quantitative way, the mathematical simulation of galvanostatic oscillations γ was performed. This required addition of two more reaction steps to Eqs. (4.11) and (4.12):

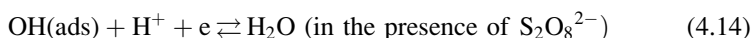
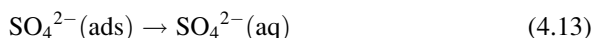


Fig. 4.11 j - U curves for poly-Pt under (a), (b), and (d) potential-controlled and (c) current-controlled conditions. Electrolyte: (a) 0.5 M HClO_4 ; (b) 0.5 M HClO_4 + 0.7 M $\text{Na}_2\text{S}_2\text{O}_8$; (c, d) 0.5 M HClO_4 + 0.5 M $\text{Na}_2\text{S}_2\text{O}_8$. Scan rate: (a) 100 mV s^{-1} ; (b, d) 10 mV s^{-1} ; (c) 1 mA s^{-1} . An external resistance of 120Ω is added for (d). Reprinted with permission from [23] Copyright 2002 American Chemical Society

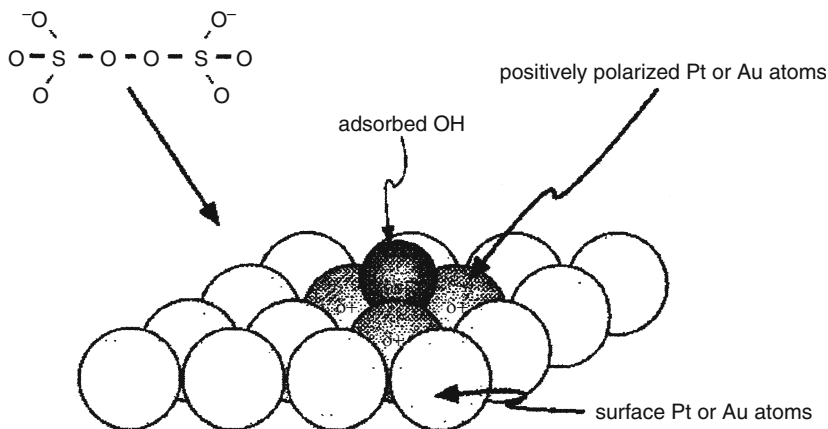


Fig. 4.13 Schematic illustration of a catalytic effect of adsorbed OH for the dissociative adsorption of $S_2O_8^{2-}$. Reprinted with permission from [23] Copyright 2002 American Chemical Society

Also, in some simulations the hydrogen evolution reaction was added: $H^+ + e \rightleftharpoons H(\text{ads})$; $2H(\text{ads}) \rightarrow H_2$, which improved the shape of modeled oscillations. The detailed construction of the model, including the kinetic equations, the reader can find in the original reference [23]. Here we shall only summarize the qualitative description of the oscillation mechanism, invoking the ideas summarized earlier. Under galvanostatic regime, at relatively positive potentials, the surface coverage of adsorbed OH (θ_{OH}) is large and therefore the $S_2O_8^{2-}$ reduction occurs efficiently. This leads to an increase in the coverage of adsorbed SO_4^{2-} ions (θ_2), since their desorption is relatively slow. The increase in θ_2 leads to a decrease in vacant surface sites at which the dissociative adsorption of $S_2O_8^{2-}$ ions occurs, thus leading to a shift of the electrode potential toward more negative values to promote the SO_4^{2-} desorption and keep constant imposed current density. This, in turn, leads to a decrease in θ_{OH} and hence a decrease in the rate of catalyzed dissociative adsorption of $S_2O_8^{2-}$ and due to this positive feedback the potential moves to even more negative values, in order to keep a constant current density. In this way, the maximum negative potential is eventually reached. At this state the rate of desorption of SO_4^{2-} is significantly enhanced, which leads to an increase in vacant surface sites for $S_2O_8^{2-}$ reduction and to a shift of the electrode potential back to positive values. This leads to an increase in θ_{OH} , and thus in the rate of the catalyzed dissociative adsorption of $S_2O_8^{2-}$, causing, by this positive feedback, further positive shift of the electrode potential which eventually reaches the maximum value.

Concerning oscillations of type α , β , and δ , the following characteristics can be outlined: oscillations α resemble those named oscillations A in the H_2O_2 electroreduction (Sect. 4.7), and the formation of NDR is therefore supposed to occur based on the same mechanism: from the suppression of the $S_2O_8^{2-}$ reduction by the *underpotential deposition* of hydrogen. For oscillations of type β and δ , impedance measurements revealed their HN-NDR characteristics. These instabilities need, however, further studies.

In this section, only temporal instabilities involving $\text{S}_2\text{O}_8^{2-}$ electroreduction were described. It is noteworthy that this process was used also for the studies of conditions for the electrochemical pattern formation, as described in Sect. 2.2 of volume II.

4.2 Electroreduction of Iodate(V) Ions

4.2.1 *The Role of Additional Current Carrier in the Onset of Instabilities*

Following the instabilities in $\text{S}_2\text{O}_8^{2-}$ electroreduction, it is now useful to consider potential oscillations in the galvanostatic reduction of IO_3^- ions in alkaline solution at Ag electrode. This process appears to be an interesting dynamical system, the features of which definitely extend our understanding of electrochemical oscillators. In particular, for this system one can achieve the ability of the continuous transition between the N-NDR and HN-NDR oscillator. Note that the characteristics of IO_3^- electroreduction were mentioned in the classification of electrochemical oscillators suggested by Strasser et al. [25] (Sect. 3.5), in a subgroup IV.3, involving the so-called additional current carrier. This idea will be now developed in more detail. The content of this section is based largely on another work by Strasser et al. [26] which includes both dc and ac experimental studies as well as extensive numerical modeling. The presented results refer to 0.15 M or 0.05 M NaIO_3 in the medium of 1 M NaOH as supporting electrolyte, with Ag(poly) wire, the Pt-wire, and Hg– Hg_2SO_4 – K_2SO_4 electrode employed as the working, counter, and the reference electrode, respectively.

The set of typical I – U curves, recorded for different scan rates, is shown in Fig. 4.14. In this case, since potentiostatic control was employed and no external resistor was inserted, the external voltage U , used in original notation, should be considered close to the interfacial potential drop E at the working electrode. Figure 4.14 shows that only for relatively low scan rates (2 mV s^{-1}) a quasi-stationary, diffusion limited plateau was observed, followed by the steep current increase due to hydrogen evolution process, confirmed by the observation of gas bubbles. At higher scan rates, the N-shaped voltammogram forms during the cathodic scan, indicating the sharp decrease of the iodate reduction rate in the respective potential region, presumably due to the decrease in surface concentration of iodate ions. On the reverse scan, this NDR region is not observed which effect can be understood in terms of recovery of iodate ions at the electrode due to convection caused by evolving hydrogen bubbles. This also suggests that intentional stirring of the solution should affect the voltammetric response of the process studied.

Figure 4.15 shows respective oscillatory courses recorded upon current scans, and the caption informs also that the onset of mechanical (magnetic) stirring completely suppressed the oscillations. Furthermore, upon increasing current density (j), the onset of potential oscillations occurs in a subcritical way

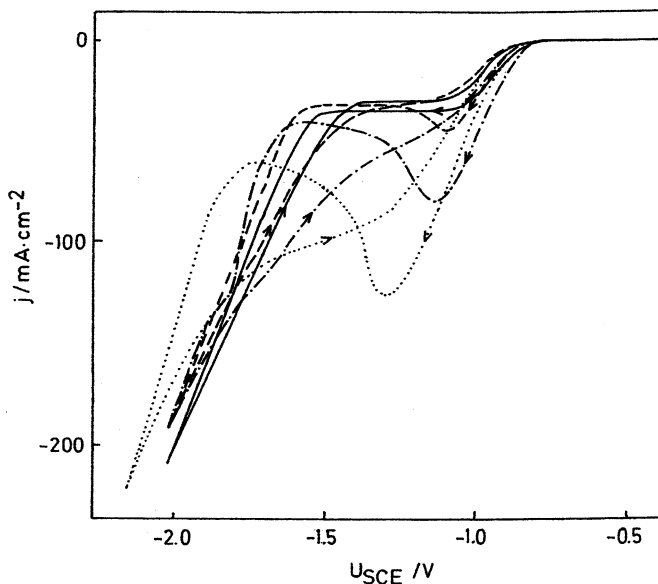


Fig. 4.14 Experimental cyclic voltammometric profiles of iodate reduction on Ag in alkaline solution (0.15 M NaIO₃ + 1 M NaOH) at various scan rates. *Solid*: 2 mV s⁻¹, *dashed*: 10 mV s⁻¹, *dot-dashed*: 50 mV s⁻¹, *dotted*: 200 mV s⁻¹. Reprinted from [26], Copyright 1999, with permission from Elsevier

(the oscillations start from significant amplitude), while their gradual decay at high j resembles the supercritical Hopf bifurcation. The potentials observed at currents right above and below the oscillatory region correspond to reduction of iodate and hydrogen evolution, respectively.

Under potentiostatic conditions, when the system is stable (nonoscillatory) it is possible to perform impedance analysis and the representative impedance spectra, arranged in sequence of increasing negative potentials, are shown in Fig. 4.16.

Figure 4.16a ($U = -1.06$ V) shows two capacitive loops indicating a stable electrochemical system with two processes on different time scales. Figure 4.16b ($U = -1.26$ V) represents drastically different characteristics: the low-frequency capacitive loop disappears in favor of an inductive one; furthermore, the extrapolation of the spectrum to $\omega = 0$ would yield negative real impedance, meaning also the negative slope (NDR) of the dc $I-U$ ($I-E$) curve. At even more negative potential (Fig. 4.16c, $U = -1.56$ V), the spectrum typical of negative impedance hidden in the dc $I-U$ response (HN-NDR) is visualized, since the negative real impedance occurs on this spectrum only for intermediate region of ω . Finally, at $U = -1.66$ V (Fig. 4.16d), the spectrum does not reveal any negative real impedance; instead, the high-frequency capacitive loop dominates and is followed by a small inductive one.

These results of dc and ac experiments should now be confronted with the electrochemical mechanism of IO₃⁻ reduction. Generally, in strongly alkaline

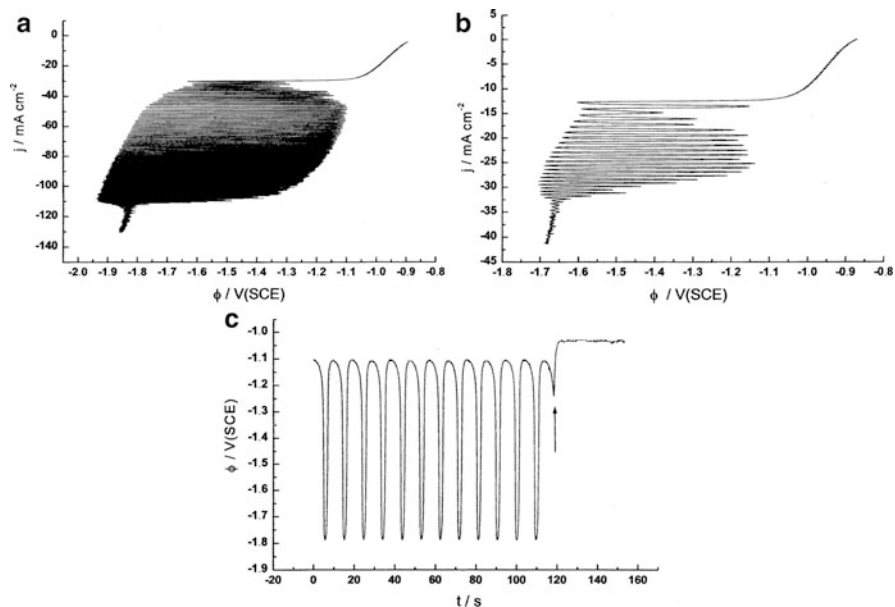
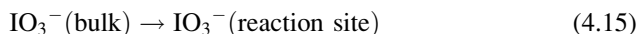


Fig. 4.15 Experimental I/U behavior during current scans (0.05 mA s^{-1}) in the absence of stirring. 1 M NaOH, (a) 0.15 M NaIO₃, (b) 0.05 M NaIO₃, (c) stationary potential oscillations at $I = -17 \text{ mA}$ without stirring (0.15 M NaIO₃ + 1 M NaOH). Upon (magnetic) stirring, the potential stabilizes at high values (arrow). Reprinted from [26], Copyright 1999, with permission from Elsevier

media, iodate(V) ions undergo a stepwise electrocatalytic reduction to IO⁻ via the reactive intermediate IO₂⁻, followed by a disproportionation reaction yielding I⁻ and IO₃⁻ [27]. Thus, essentially IO₃⁻ is reduced to the final product which is I⁻. In terms of this general scheme, two models (A and B) were proposed in order to explain the reported dynamic instabilities.

The simplest model A consists of the following steps:

1. Diffusion of IO₃⁻ ions from the solution bulk to the reaction place (just outside the double layer):



2. Potential-dependent reduction of IO₃⁻ at the reaction site:



the rate of which is modified by the coulomb repulsion of the IO₃⁻ ions from the reaction site within certain potential range [i.e., due to the Frumkin effect, analogous to described for S₂O₈²⁻ reduction in Eq. (4.4)].

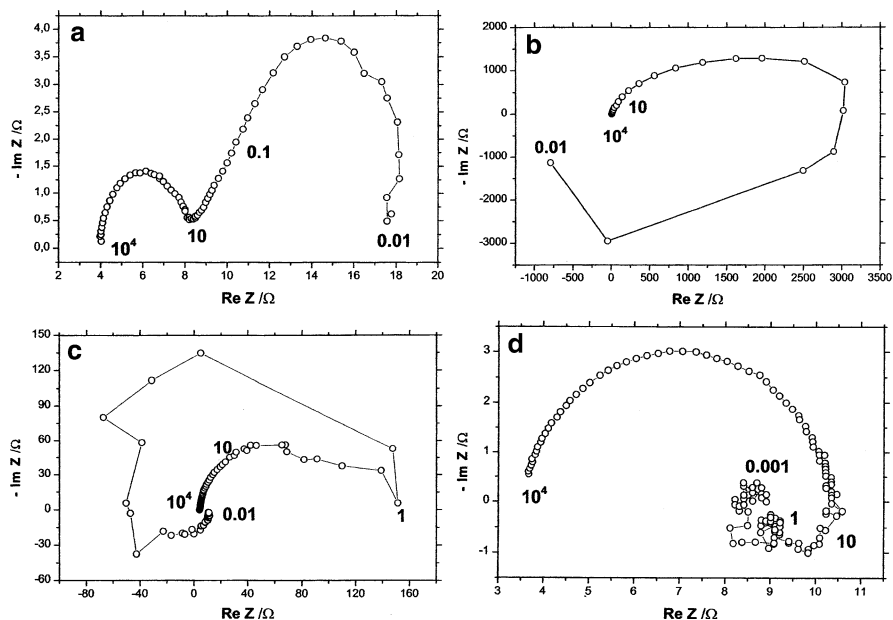
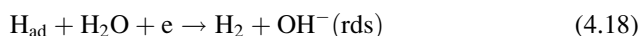
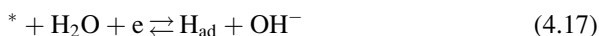


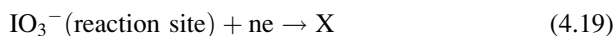
Fig. 4.16 Impedance behavior of the experimental iodate system illustrated in terms of Nyquist diagrams at various potentials, frequency range 10 kHz to 0.01 Hz, (a) $U = -1.06$ V; (b) $U = -1.26$ V; (c) $U = -1.56$ V; (d) $U = -1.66$ V. Reprinted from [26], Copyright 1999, with permission from Elsevier

3. Potential-dependent electrocatalytic reduction of protons as an *additional current-providing* process:



where $*$ denotes the bare Ag surface site and H_{ad} represents atomically adsorbed hydrogen. Based on the steady-state approximation (Bodenstein principle), the concentration of H_{ad} can be eliminated, leaving only the simple dependence of hydrogen evolution on the electrode potential [28]. It will be shown that adding step (3), (i.e., additional current providing process) contributes to interesting new dynamics, compared to the system composed of only steps 1 and 2.

The model B is made a bit more complicated by considering the simultaneous transfer of six electrons in step (2) as arguable and therefore the single reduction step (4.16) is replaced with the model sequence involving the intermediate species X (being, e.g., the IO_2^- or IO^-):



Again, if step (4.20) is relatively fast, compared to (4.19), application of the Bodenstein principle adiabatically eliminates the species X from kinetic considerations and the above mechanism becomes essentially equivalent to model A.

Coming back to mechanism A, the corresponding two-variable mathematical model was formulated in terms of the linear approximation of the Nernst diffusion layer of the thickness δ . As the two dynamic variables essential for the oscillatory and bistable dynamics, the concentration of IO_3^- at the reaction site (“surface concentration”, c) and the interfacial potential drop (electrode potential E , denoted here in terms of an alternative symbol φ , as it often happens in the papers on electrochemical instabilities) were chosen and the following ordinary differential equations were derived:

$$\frac{dc}{dt} = \frac{2D}{\delta^2}(c_b - c) - \frac{2}{\delta}ck_r^0k_r(\varphi, k_1^0) \quad (4.21)$$

$$C_d \frac{d\varphi}{dt} = J_{\text{tot}} + n_1Fck_r^0k_r(\varphi, k_1^0) + n_2k_{\text{icc}}^{00}\tilde{k}_{\text{icc}}(\varphi) \quad (4.22)$$

where subscript “icc” means “iodate-independent current carrier,” i.e., the species yielding the hydrogen evolution current. Furthermore, J_{tot} is the total current density, composed of the n_1 —electron iodate reduction and n_2 —electron hydrogen ion reduction. For every of these electrode processes, its rate constant is represented as the product of the potential-independent part (k_r^0 and k_{icc}^{00} , respectively) and the potential-dependent (Butler–Volmer type) part ($k_r(\varphi, k_1^0)$ and $\tilde{k}_{\text{icc}}(\varphi)$, respectively). Finally, c_b , D , and C_d denote bulk concentration of iodate, its diffusion coefficient, and double layer capacitance, respectively. It was convenient to transform these equations into the dimensionless form indicating the difference in time scales of the c and φ dynamics through the value of parameter ε :

$$\frac{dc'}{d\tau} = a(1 - c') - c'k_r(\varphi', k_1^0) \quad (4.23)$$

$$\varepsilon \frac{d\varphi'}{d\tau} = I + c'k_r(\varphi', k_1^0) + k_{\text{icc}}^{00}\tilde{k}_{\text{icc}}(\varphi') \quad (4.24)$$

where:

$$I = \frac{J_{\text{tot}}}{n_1Fc_bk_r^0} \quad (4.25)$$

$$\varepsilon = \frac{2C_dRT}{\delta n_1Fc_b} \quad (4.26)$$

$$\varphi' = \frac{\varphi}{1V} \quad (4.27)$$

$$c' = \frac{c}{c_b} \quad (4.28)$$

$$a = \frac{D}{\delta k_r^0} \quad (4.29)$$

$$k_{\text{icc}}^0 = \frac{n_2 k_{\text{icc}}^{00}}{n_1 F C_b k_r^0} \quad (4.30)$$

$$\tau = \frac{2}{\delta} k_r^0 t \quad (4.31)$$

Of five system parameters involved in this model, three of them: the total current I and the rate constants k_{icc}^0 and k_1^0 are treated as the bifurcation parameters. While $\tilde{k}_{\text{icc}}(\varphi)$ dependence was described in terms of classical Butler–Volmer dependence, the repulsive interaction of IO_3^- anion with the reaction site was expressed in terms of formal mathematical dependence:

$$k_r(\varphi, k_1^0) = k_1^0 \exp[-\alpha f \varphi] + \frac{\exp[-\alpha f \varphi]}{1 + 250 \exp[-f(\varphi - \varphi_0)]} \quad (4.32)$$

Linear stability analysis of the steady state ($c_{\text{ss}}, \varphi_{\text{ss}}$) led to the Jacobian matrix:

$$\mathbf{J} = \begin{bmatrix} -a - k_r(\varphi', k_1^0) & -c' \frac{\partial k_r(\varphi', k_1^0)}{\partial \varphi'} \\ \frac{k_r(\varphi', k_1^0)}{\varepsilon} & \frac{c'}{\varepsilon} \frac{\partial k_r(\varphi', k_1^0)}{\partial \varphi'} + \frac{k_{\text{icc}}^0}{\varepsilon} \frac{\partial \tilde{k}_{\text{icc}}(\varphi')}{\partial \varphi'} \end{bmatrix}_{\text{ss}} \quad (4.33)$$

In view of conditions for the Hopf bifurcation [$\text{Tr}(\mathbf{J}) = 0$ with $\text{Det}(\mathbf{J}) > 0$], one concludes that they can be met simultaneously owing to positive and negative terms in the determinant:

$$\text{Tr}(\mathbf{J}) = \underbrace{-a - k_r(\varphi', k_1^0)}_{<0} + \underbrace{\frac{c'}{\varepsilon} \frac{\partial k_r(\varphi', k_1^0)}{\partial \varphi'}}_{>0} + \underbrace{\frac{k_{\text{icc}}^0}{\varepsilon} \frac{\partial \tilde{k}_{\text{icc}}(\varphi')}{\partial \varphi'}}_{<0} \quad (4.34)$$

$$\text{Det}(\mathbf{J}) = \underbrace{-a \frac{c'}{\varepsilon} \frac{\partial k_r(\varphi', k_1^0)}{\partial \varphi'}}_{<0} \underbrace{-a \frac{k_{\text{icc}}^0}{\varepsilon} \frac{\partial \tilde{k}_{\text{icc}}(\varphi')}{\partial \varphi'}}_{>0} \underbrace{-k_r(\varphi', k_1^0) \frac{k_{\text{icc}}^0}{\varepsilon} \frac{\partial \tilde{k}_{\text{icc}}(\varphi')}{\partial \varphi'}}_{>0} \quad (4.35)$$

Note that both positive terms in the determinant (4.35) are related to the icc process, i.e., to the additional hydrogen evolution which crucial role in the system's dynamics is in this way confirmed. For this process, the derivative $\partial \tilde{k}_{\text{icc}}(\varphi') / \partial \varphi'$ is

negative, since the rate constant of H^+ electroreduction rises with increasing negative electrode potential. In turn, $\text{Tr}(\mathbf{J})$ can change sign only if for iodate electroreduction, the derivative $\partial k_r(\varphi', k_1^0)/\partial \varphi' > 0$ which is true for the NDR region. As in Chap. 2, the galvanostatic conditions considered here can be easily transformed to potentiostatic ones by replacing the imposed current with the expression $(U' - \varphi')/\rho$, with U' and ρ meaning the dimensionless external voltage and a dimensionless serial resistance, respectively.

For appropriate constant parameters, by variation of the rate constant of hydrogen evolution reaction k_{icc}^0 one can show, how the voltammetric $I-U$ response smoothly switches from the explicit N-NDR characteristics of the iodate reduction to the HN-NDR characteristics, when the hydrogen current becomes predominant in the NDR region. This is the illustration of the above-mentioned idea of smooth transformation of the N-NDR to the HN-NDR system. For the parameters ensuring the HN-NDR characteristics, it is further possible to obtain numerically the oscillations of the electrode potential upon current scan (Fig. 4.17).

In view of these model calculations, one can imagine the sequence of events composing the single oscillation of the electrode potential under galvanostatic conditions. If initially the electrode potential is less negative than the N-NDR region, the surface concentration of IO_3^- drops due to their fast consumption in the reduction process until it reaches the zero value and then the current of IO_3^- reduction ($j_{\text{IO}_3^-}$) attains limiting value. If the imposed current I exceeds this limiting value, the electrode is further charged to more negative potential values, first slowly, but when it enters the N-NDR region, its further decrease undergoes autocatalytic acceleration. In the N-NDR region the reduction of iodate drops, while the rate of the electrode process of hydrogen evolution (j_{H_2}) increases until the condition $I = j_{\text{IO}_3^-} + j_{\text{H}_2} = \text{const}$ is met. Further decrease of negative potential is then stopped, and now the diffusion can gradually replenish the preelectrode layer with consumed IO_3^- ions. Their reduction current increases and when it exceeds the imposed total current, the electrode potential moves back toward more positive values, i.e., the initial state is restored and the whole cycle can repeat. It is clear that without the independent current carrier the mechanism of recovery of surface IO_3^- concentrations would not exist and the system would then be bistable.

The above model of galvanostatic IO_3^- oscillations is further corroborated by the calculated impedance spectra which, for appropriate potentials, exhibited the shape typical of the HN-NDR systems. In order to obtain optimum concordance between the experimental and calculated Nyquist plots, it appeared necessary to invoke model B, i.e., to introduce the intermediate species X, which fast transformation (4.20) to the final product constitutes the additional fast chemical process explaining the additional capacitive loop observed at high ac frequencies in the impedance experiments.

The model allows further for the systematic bifurcation analysis, both for galvanostatic and potentiostatic conditions. As mentioned earlier, the increase in the hydrogen evolution current switches the system from the N-NDR to the HN-NDR oscillator and hence, under galvanostatic conditions, upon increasing

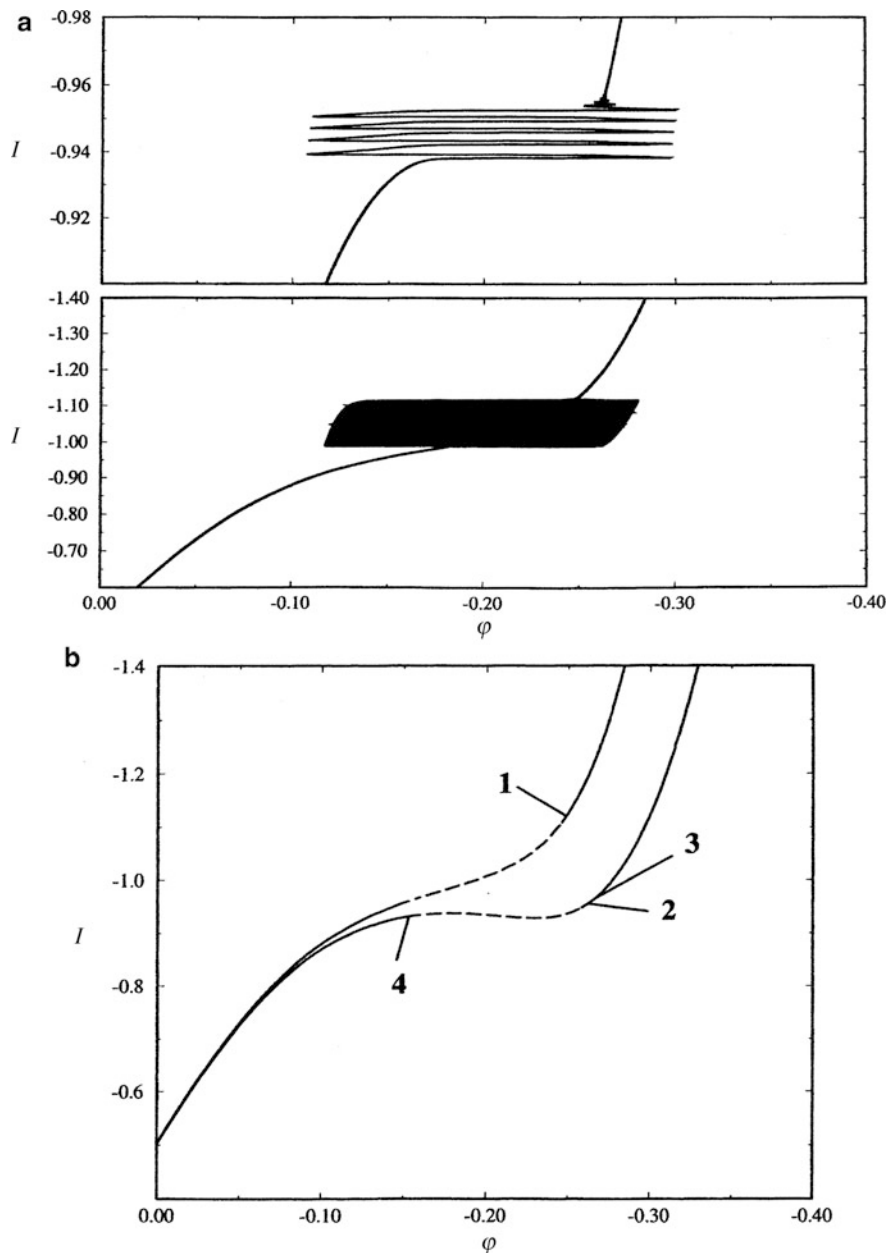


Fig. 4.17 (a) I/ϕ profiles of Eqs. (4.23) and (4.24) upon galvanostatic current scanning, scan rate = 0.001, $k_1^0 = 0.01$, $k_{\text{icc}}^0 = 0.3$ (upper graph) and 0.8 (lower graph), $I_{\text{initial}} = -0.4$, $I_{\text{final}} = -1.4$. (b) Stationary I/ϕ profiles and local stability of steady states under galvanostatic conditions, $k_1^0 = 0.01$, $k_{\text{icc}}^0 = 0.3$ (lower graph) and 0.8 (upper graph), solid (dashed) lines indicate stable (unstable) steady states. Labels 1–4 indicate the steady states on the I/ϕ curves where impedance spectra (see [26]) were calculated. Reprinted from [26], Copyright 1999, with permission from Elsevier

model rate constant of hydrogen evolution, first only the bistability and then also potential oscillations should be obtained. Accordingly, for low values of k_{icc}^0 only the saddle–node bifurcations should be possible, while for sufficiently high k_{icc}^0 also bifurcations leading to limit cycle are expected. For model A, the corresponding two-parameter bifurcation diagrams reveal the high sensitivity of the oscillatory region to the k_1^0 values which must be included in a small region of values (from $10^{-1.2}$ to $10^{-1.7}$). Thus, the existence and the location of galvanostatic oscillations are strongly contingent upon the balance of reaction rates of both the dependent and independent current carriers.

In turn, for $k_{\text{icc}}^0 = 0$, the cross-shaped phase diagram (XPD), typical of N-NDR oscillators, is obtained. When nonzero value of k_{icc}^0 is assumed, the corresponding bifurcation diagram is no longer of an XPD type, as should be expected for the HN-NDR system. The corresponding diagrams, as well as a more detailed analysis of the bifurcation scenarios in this model, including the Takens–Bogdanov (TB) bifurcation, the reader can find in the original work [26].

The occurrence of galvanostatic oscillations in the course of iodate(V) electroreduction emphasizes thus the destabilizing role of the second current carrying process—the hydrogen evolution. One should note that the suggested mechanism of instabilities would operate regardless the NDR region is visible or not (HN-NDR case) in the stationary I – E characteristics of the process [26]. In a more general sense, the importance of the model by Strasser et al. consists in an extension of a number of mechanisms in which galvanostatic oscillations can occur. Earlier, Koper and Sluyters [29] have described a purely theoretical mechanism in which, instead of an additional current carrier, a potential dependent ad- and desorption of the slow chemical species was assumed (see Sect. 3.4). In that case the current could be provided only by single current carrier at all times, and the recovery of its concentration was possible due to potential-dependent adsorption of chemical species which would act as the inhibitor of the electrode process. Coming back to experimental systems, besides the IO_3^- oscillatory reduction, the model by Strasser et al. could explain the fact that the electrocatalytic reduction of $\text{S}_2\text{O}_8^{2-}$ (also exhibiting the Frumkin-type effect of the double layer, cf. Sect. 4.1), if performed under galvanostatic conditions, exhibits only bistability in an alkaline medium, but in acidified solution also the oscillations of the electrode potential set in. The explanation is that in alkaline solutions the hydrogen evolution can be shifted too far negatively to overlap with the $\text{S}_2\text{O}_8^{2-}$ reduction current, whereas at low pH it approaches the appropriate, less negative potential range [26].

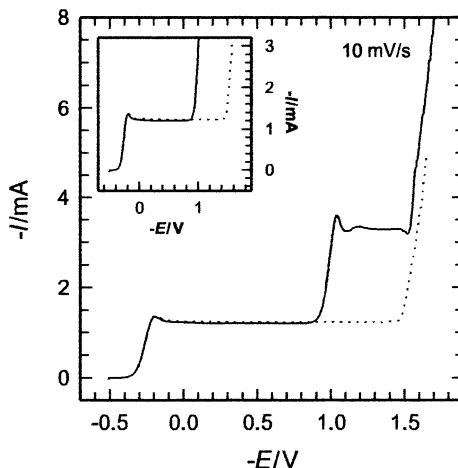
4.2.2 The NDR-Based vs. the Electrochemical Reactions and Diffusion–Convection Approach

One should note that the model based on the concept of additional current carrier triggered an interesting discussion in the literature on the role of convection in the

onset of electrochemical instabilities. Alternative explanation also recalls hydrogen evolution as a process crucial for the onset of instabilities, but as a source of convection, as Li et al. have suggested, e.g., for the electroreduction of $\text{Fe}(\text{CN})_6^{3-}$ on a Pt electrode [30]. Strasser et al. [26] did not invoke the convection as the process essential for the oscillations in the electroreduction of iodate(V), on the contrary, they have shown that increasing rate of transport, caused by stirring, eventually canceled the oscillations. Li et al. [30] have elaborated the mechanism of galvanostatic oscillations which should operate in the region of diffusion-limited current plateau, according to the following sequence (a more detailed description is given in Sect. 5.8 of volume II). As long as the current originating from primary electrode process equals the imposed current, the electrode potential is stable. However, continuous depletion of the diffusion layer, caused by electrode process and relatively slow diffusion, causes a continuous decrease of a faradaic current which causes charging the electrode to more (in this case) negative potentials, at which the additional process (hydrogen evolution) sets in. The resulting bubbles of hydrogen cause the sudden convection which replenishes the surface concentration of the primary reactant, and the current again rises above diffusion-limited plateau, causing the return of the electrode potential to less negative values. This mechanism has an important quantitative aspect: if the convective force associated with gas bubbling is on the same or on smaller timescale as the variation of E , sustained periodic behavior is impossible, since then the stationary (intermediate) potential, at moderate bubbling rate, would be reached in a damped oscillatory transient. In the opinion of Strasser et al. [26], the very fast detachment of bubbles, necessary for sustained oscillatory regime as causing almost instantaneous increase of the diffusion limited current from an undercritical to an overcritical value, seems to be unrealistic. Furthermore, also unlikely seems to be high reproducibility of the nucleation and detachment of bubbles, necessary to assume in view of reproducibility of the oscillations. Last but not least, it is difficult to find a source of negative impedance in the case of the superposition of the diffusion-controlled current of one species and of the current exponentially rising with the potential (Butler–Volmer kinetics) originating from another species. In conclusion, Strasser et al. [26] claim that their nonconvective model can explain oscillations in the electroreduction of $\text{Fe}(\text{CN})_6^{3-}$ in the presence of hydrogen evolution, as well as the oscillatory electrocatalytic oxidation of $\text{Fe}(\text{CN})_6^{4-}$ in the presence of O_2 evolution on a Pt electrode [31], where the Frumkin effect has to be excluded. Instead, the NDR (and thus the negative real impedance in the Nyquist spectrum) could result from the adsorption of oxygen species on Pt, causing certain inhibition of $\text{Fe}(\text{CN})_6^{4-}$ oxidation, compared to bare Pt surface. Then the combination of this effect with the oxygen evolution current could create conditions for the galvanostatic oscillations, analogously as for the reduction of iodates or $\text{Fe}(\text{CN})_6^{3-}$.

Different points of view of these two groups of researchers on the role of convection, associated with the faradaic contribution from the additional current carrier, hiding the NDR region, led to the more recent response of Li et al. [32]. A new experimental evidence was presented for the decisive role of convection in triggering the oscillations during the galvanostatic reduction of $\text{Fe}(\text{CN})_6^{3-}$ in

Fig. 4.18 Voltammograms of 1 M NaOH solutions containing 0.6 M $\text{Fe}(\text{CN})_6^{3-}$ (dashed line) or 0.15 M $\text{IO}_3^- + 0.6 \text{ M Fe}(\text{CN})_6^{3-}$ (solid line). The inset is a portion of the figure below the second limiting current. Reprinted from [32], Copyright 2001, with permission from Elsevier

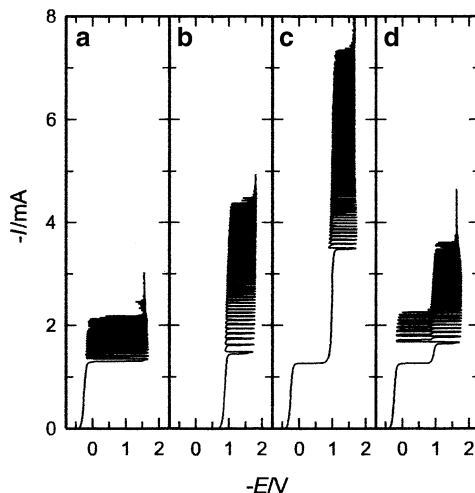


alkaline solution which is accompanied by hydrogen evolution when the oscillating Pt electrode potential reaches sufficiently negative value. The experimental strategy involved simply a replacement of the hydrogen evolution with IO_3^- reduction as additional current carrier and then the oscillations vanished. This replacement did not remove the electrostatic repulsion of $\text{Fe}(\text{CN})_6^{3-}$ ions from the reaction site within the double layer, i.e., the principal source of NDR characteristics survived, but only the hydrogen bubbling did not occur. If the sample contained both $\text{Fe}(\text{CN})_6^{3-}$ and IO_3^- , the hydrogen evolution was also observed at sufficiently negative potentials (see Fig. 4.18), so it could be considered then a third current carrier, the only one which can be associated with convection. If the oscillating electrode potential reached the IO_3^- reduction region, but did not enter yet the hydrogen evolution process, the IO_3^- took over the role of second current carrier from the water molecules.

Li et al. have presented the following experimental facts as the proof for the role of convection caused by H_2 bubbles in the galvanostatic oscillations (see Fig. 4.19). Upon the current scan, these oscillations appear only above the limiting current containing either $\text{Fe}(\text{CN})_6^{3-}$ (a) or IO_3^- (b), or above the *second* limiting current for the mixed system containing both reactants (c and d). In all these cases, the oscillations are accompanied with hydrogen evolution, when the potential reaches the most negative values, corresponding to the plateau of *all* of the systems. No oscillations were found between the first and the second limiting current plateaus (Fig. 4.19c, d), where the hydrogen evolution did not occur yet, but was replaced by the IO_3^- reduction as the second current carrier. Finally, oscillations for the system containing both $\text{Fe}(\text{CN})_6^{3-}$ and IO_3^- (Fig. 4.19d) were observed if the second limiting current was lower than the upper current limit for the potential oscillation in the reduction of $\text{Fe}(\text{CN})_6^{3-}$ (Fig. 4.19a), otherwise only potential oscillations from IO_3^- remained (Fig. 4.19c) with a much larger second limiting current [30].

In consequence, the oscillations mechanism involving the negative feedback supported by convection induced by H_2 , called ERDC (*Electrochemical Reactions*

Fig. 4.19 Potential oscillations by current scan at 0.01 mA s^{-1} in 1 M NaOH solutions containing: (a) $0.6 \text{ M Fe(CN)}_6^{3-}$, (b) 0.15 M IO_3^- , (c) $0.15 \text{ M IO}_3^- + 0.6 \text{ M Fe(CN)}_6^{3-}$, and (d) $0.03 \text{ M IO}_3^- + 0.6 \text{ M Fe(CN)}_6^{3-}$. Reprinted from [32], Copyright 2001, with permission from Elsevier

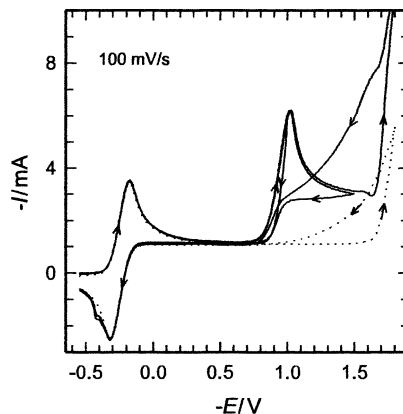


and Diffusion–Convection), was suggested for both separate reduction of Fe(CN)_6^{3-} and IO_3^- . In the latter case, when due to the double layer effect of the Frumkin type, the rate of electroreduction of IO_3^- drops (in the N-NDR region), reduction of H_2O supplies the additional current necessary to meet the conditions of the galvanostatic experiment, and IO_3^- surface concentration gets a chance to be replenished by diffusion from the bulk. Several arguments are presented to support the suggestion that the mechanism proposed by Strasser et al. [26] is mathematically correct, but of limited validity with respect to real physical properties of the systems considered.

In conclusion, there arises an important final question: If either the ERDC or NDR-based mechanisms can be assumed for the given oscillator, how to distinguish between them? Li et al. [32] suggest a simple criterion based on the course of cyclic voltammograms of the studied system. In the simplest case of the interplay of charge-transfer and diffusion processes, the I – E courses in the forward scan (when the depletion of the diffusion layer from the reactant occurs) and in the backward scan (when the replenishment takes place) do not cross. However, if during the backward scan such a crossing point is observed, i.e., if the current is anomalously enhanced, this means the existence of an extra transport, i.e., indicates the convection switched only in the final region of forward scan by hydrogen (or oxygen for anodic processes) evolution. So, the existence of the *crossing point* is a criterion for the ERDC mechanism. Such characteristics are observed for the cyclic voltammogram of Fe(CN)_6^{3-} or both Fe(CN)_6^{3-} and IO_3^- , but only if the negative scan reached the far enough cathodic region of hydrogen evolution (Fig. 4.20).

Li et al. [32] considered the presence of this crossing point as the criterion even more convincing than the presence of negative impedance for this category of oscillators. In other words, the presence of negative real impedance, evidently detectable in the whole potential range of the limiting current plateau, is not directly connected with the galvanostatic oscillations in the case of the systems considered.

Fig. 4.20 Cyclic voltammograms of 1 M NaOH solutions containing 0.6 M $\text{Fe}(\text{CN})_6^{3-}$ (dashed line) or 0.15 M IO_3^- + 0.6 M $\text{Fe}(\text{CN})_6^{3-}$ (solid lines). Reprinted from [32], Copyright 2001, with permission from Elsevier



A more general consequence of this interesting discussion of various mechanisms is the suggestion that not all galvanostatic oscillations can be explained in terms of the hidden negative impedance or, alternatively, the mechanistic classification of the oscillators, based on impedance spectra, may not cover all possible mechanisms of such instabilities. This problem is evidently worth of further analysis, particularly when the mechanisms of newly discovered electrochemical oscillators will be analyzed and classified into respective categories.

4.3 The Indium–Thiocyanate Polarographic Oscillator

4.3.1 Basic Experimental Characteristics of $\text{In}(\text{III})\text{--SCN}^-$ Oscillator

The polarographic reduction of $\text{In}(\text{III})$ to indium(0) amalgam in thiocyanate media constitutes one of classical electrochemical oscillators, characterized with the N-NDR region on the $I\text{--}E$ curve. In order to understand the origin of this NDR region, one has to recognize first the mechanism of the electrode process. The electroreduction of $\text{In}(\text{III})$ aquo-ions is characterized with such a high cathodic overpotential that it can occur only at very negative potentials close to the cathodic limit of polarography in aqueous media. Considerably lower overpotential characterizes the electroreduction of $\text{In}(\text{SCN})_2^+$ species adsorbed on the mercury surface, with the SCN^- ions bound to $\text{In}(\text{III})$ ion via the nitrogen atom and to Hg surface via the sulfur atom. The adsorbed SCN^- ions act thus as a catalyst for the $\text{In}(\text{III})$ reduction. This and other examples of such anion bridging and anion electrocatalysis on mercury were reviewed by de Levie [33] and Turowska [34] based also on personal contribution of those researchers to this area.

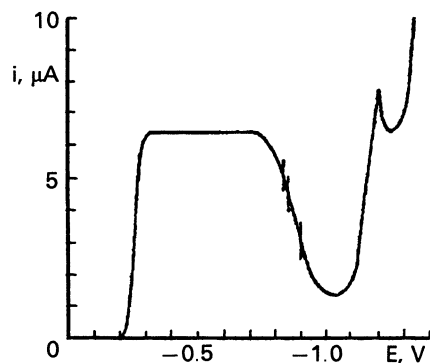
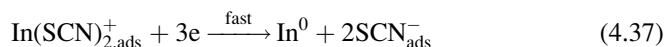


Fig. 4.21 Polarogram of the solution 1.2 mM $\text{In}(\text{NO}_3)_3$ + 5 M NaSCN, pH adjusted to 3.6 with HNO_3 . Two-electrode system was employed, with dropping mercury electrode as the working one, and Ag–AgSCN as the reference electrode. The adjustable serial resistance was inserted in the circuit. *Vertical bars* indicate the potentials from the N-NDR region for which oscillatory courses were reported. Reprinted from [36] Copyright 1970, with permission from Elsevier

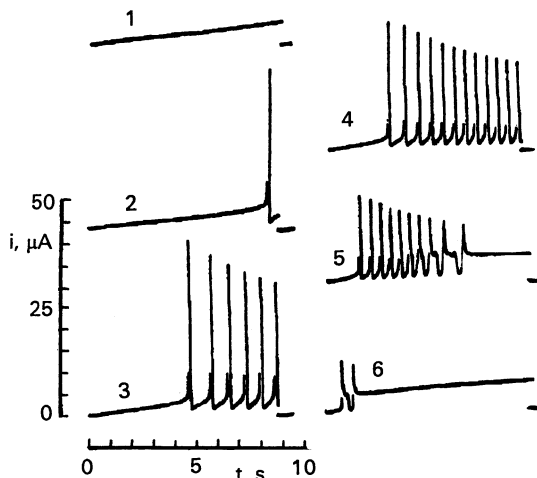
Pospišil and de Levie [35] have diagnosed the following mechanism of the electrocatalytic In(III) electroreduction in thiocyanate media:



Since in this reaction sequence the first chemical step is the rate-determining one, the potential-dependent surface concentration of adsorbed SCN^- ions controls the rate of the overall process. The catalytic SCN^- ions, liberated after reduction of In(III) to indium amalgam, can bind next In(III) ions from the solution and facilitate their reduction. The N-NDR region forms when, upon scan of the electrode potential toward negative direction, the point of zero charge is passed. Then, upon further potential scan, due to increasing negative charge of the mercury surface, the electrostatic repulsion causes desorption of SCN^- ions. This means also the gradual decrease in surface concentration of electroactive $\text{In}(\text{SCN})_2^+$ species, leading to decrease in current of the In(III) electroreduction (Fig. 4.21) [36]. Such a mechanism of the N-NDR formation was used by Jakuszewski and Turowska [37] in their discussion of various possible mechanisms of polarographic oscillations.

The explanation of the increase in the In(III) reduction current observed at high negative potentials, following the NDR region, is more sophisticated. The simplest explanation, which is being made in some theoretical models of the oscillations in this process, can assume the noncatalytic electroreduction of In(III) ions, characterized with large cathodic overpotential, as suggested earlier. However, as de Levie et al. indicate [38], in the absence of SCN^- ions (or, more generally, in noncomplexing solutions), and in acidic solution at $\text{pH} \leq 3.5$, In(III) is not polarographically reduced, until the potential is reached where hydrogen ions are reduced and, in consequence,

Fig. 4.22 Current–time curves observed at -0.900 V and with decade box resistances of 10, 11.3, 15, 20, 30, and 50 $k\Omega$, respectively, for curves (1)–(6). Reprinted from [36] Copyright 1970, with permission from Elsevier



the local pH of the solution increases. Therefore, it is reasonable to postulate that in such medium, a reducible form of In(III) is its hydroxy complex [39].

Coming back to In(III)–SCN[−] electroreduction, as for other N-NDR systems, the onset of the current oscillations under potentiostatic conditions required the presence of sufficient ohmic resistance in the circuit of the working electrode. Tamamushi [40] was probably the first researcher who built up an electronic-electrochemical circuit, consisting of the connection of the electrolytic cell, in which the polarographic reduction of In(III)–SCN[−] occurred in a two-electrode system, with appropriate serial inductance and ohmic resistance. Under dc polarization sustained sinusoidal oscillations of current were generated, like in purely electronic equivalent circuit in which the electrolytic cell was replaced by the tunnel diode or tetrode, the element with the NDR characteristics.

Further systematic studies in this area have been undertaken by de Levie and coworkers. At those times, when stationary Hg electrodes were not yet in common use, the dropping mercury electrodes of long lifetime were employed, as in the case of oscillations shown in Fig. 4.22, recorded for given value of the external voltage U and various serial resistances [36].

Even before application of the formalism of nonlinear dynamics to such processes it was possible to understand the sequence of processes engaged in the oscillation cycle. Starting, e.g., from the plateau of the I – E polarographic curve just before the NDR region one considers a relatively large faradaic current of In(III) electroreduction, which causes relatively large ohmic potential drops IR_s in the circuit. When the effective potential of Hg electrode (E) enters the region of the negative resistance, the current drops due to lower rate constant of the electron transfer and the decreasing ohmic drops shift the electrode potential toward even more negative values. Since the current is then lower, from the kinetic point of view this is a typical autocatalytic decrease in the faradaic current (or an increase in the negative electrode potential) which occurs up to the minimum of the I – E polarographic curve. At this potential the electroreduction

of In(III) ions is already so slow that their renewal at the electrode surface through the diffusion from bulk of the solution becomes possible. Thus, with a certain delay, because diffusion is relatively slow, the surface concentration of In(III) increases and their electroreduction current rises again. But this means that the ohmic drops also rise, so the effective electrode potential shifts toward less negative values. In the NDR region, this means the enhancement of the rate constant of the electron transfer, so the current rises again autocatalytically until it reaches the maximum value, when the initial situation repeats again, due to the increasing concentration polarization. This mechanism is just a clear example of how the coupling of the NDR characteristics and of the ohmic potential drops, with the participation of (relatively slow) variations of the surface concentration of In(III) gives rise to the oscillations. The In(III)–SCN[−] system became also a subject of pioneer impedance analysis described by de Levie et al. In [41], de Levie and Husovsky have analyzed theoretically the impedance characteristics of this process and derived the expression for the faradaic admittance, indicating the negative value in the region of polarographic minimum. In turn, in [42] de Levie and Pospíšil have discussed the coupling of interfacial and diffusional impedance in the equivalent circuits (see also Chap. 3). Evidently those works remained for two decades the classical papers on the polarographic In(III)–SCN[−] oscillator and on impedance characteristics of potentially unstable electrochemical systems of that type.

The recent progress in understanding of the In(III)–SCN[−] oscillator, particularly in terms of its nonlinear dynamical characteristics, was made due to experimental and theoretical studies, published in a series of papers by Koper, Sluyters, and Gaspard. Experimental characteristics, collected also with the use of the stationary Hg electrode (Fig. 4.23), included the discovery of mixed-mode (MMO) and chaotic oscillations (Fig. 4.24) [43].

Simultaneously, various bifurcations were identified. The stepwise increase of amplitude of oscillations starting from zero and increasing further proportionally to the square root of the external voltage treated as a bifurcation parameter indicated the presence of a supercritical Hopf bifurcation. Under other conditions, the decay of oscillations through the increase of their frequency up to infinity, with the oscillation amplitude practically constant, suggesting either the saddle–loop (homoclinic) bifurcation of cycles or the saddle–node infinite period (SNIPER) bifurcation. In turn, MMO suggest the dynamics involving the homoclinic orbits in the phase space, i.e., the trajectories associated with the steady state of the saddle-focus type, from which the unstable spiraling trajectory develops, jumps into a third dimension and after an extensive trip is reinjected to the same steady state (cf. Sect. 1.4.3). The reader of other chapters of this book will note that this type of oscillations/orbits was found also for other electrochemical systems as well as for the homogeneous Belousov–Zhabotinsky oscillator. Extensive studies of the In(III)–SCN[−] oscillators allowed Koper et al. to formulate several theoretical models of this system which have revealed how the instabilities in this system can be described in terms of general concepts of nonlinear dynamics.

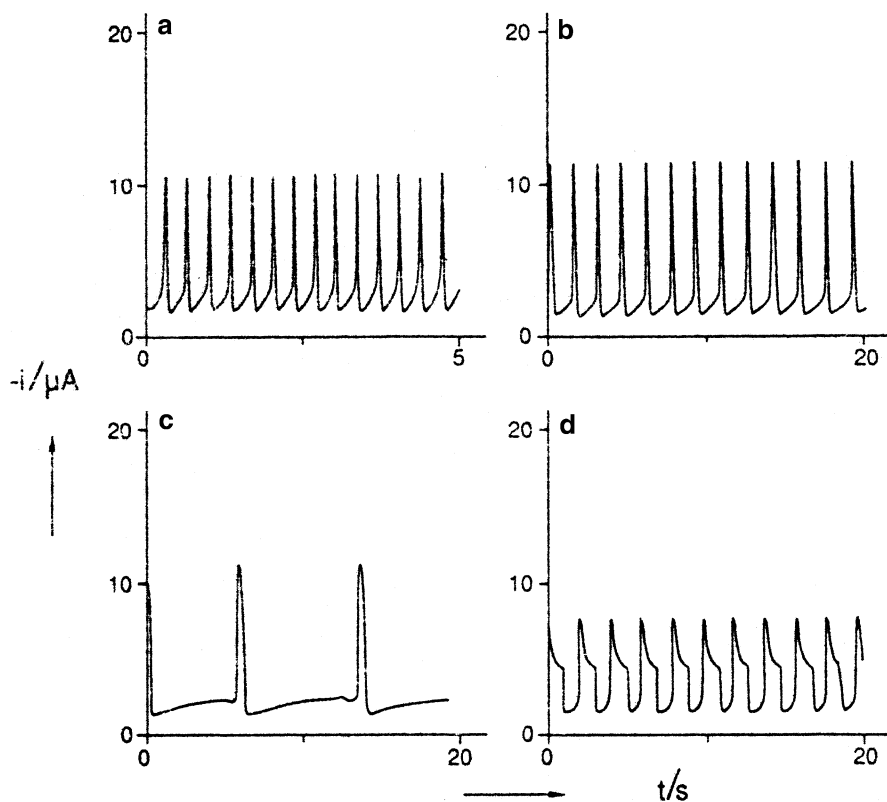


Fig. 4.23 Some typical oscillation profiles observed at the HMDE for 1.2 mM In^{3+} in 5 M NaSCN solution. The HMDE was polarized with respect to a large mercury pool in a two-electrode circuit, containing adjustable ohmic resistor. (a) $U = -0.95$ V, $R_s = 35$ k Ω ; (b) $U = -1.05$ V, $R_s = 50$ k Ω ; (c) $U = -1.10$ V, $R_s = 60$ k Ω ; (d) $U = -1.15$ V, $R_s = 90$ k Ω . Reprinted from [43], Copyright 1991, with permission from Elsevier

4.3.2 Models of the $\text{In(III)}\text{-SCN}^-$ Polarographic Oscillator

We shall describe the models in a sequence corresponding to its rising mathematical complexity, allowing thus to reproduce oscillations of also increasing complexity.

4.3.2.1 The Simplest 2D Model of $\text{In(III)}\text{-SCN}^-$ Polarographic Oscillator

Koper and Sluyters model [44] have proposed the 2D model, the construction of which aims to be of quite general importance for the NDR “cathodic” oscillators, at least as long the modeling of only periodic oscillations is requested. Reducing the

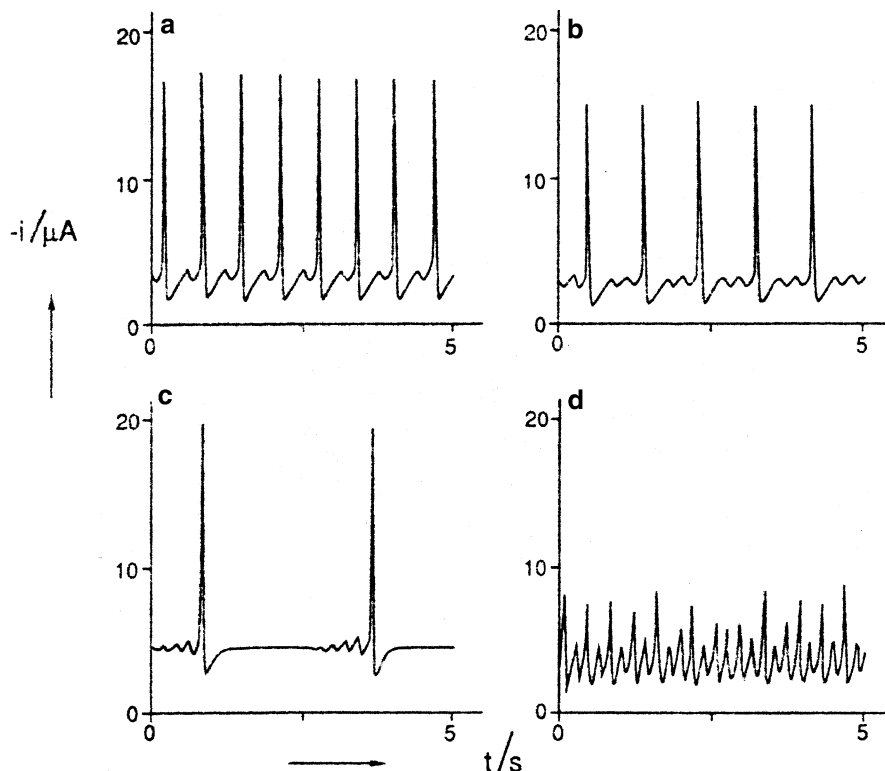


Fig. 4.24 Multiperiodic and aperiodic oscillations observed at the HMDE for 1.2 mM In^{3+} in 5 M NaSCN solution. (a) $U = -0.95$ V, $R_s = 25$ k Ω ; (b) $U = -0.95$ V, $R_s = 30$ k Ω ; (c) $U = -0.90$ V, $R_s = 25$ k Ω ; (d) $U = -0.92$ V, $R_s = 25$ k Ω . Reprinted from [43], Copyright 1991, with permission from Elsevier

number of dynamical variables to two, and thus expressing the dynamics in terms of two ordinary differential equations (ODEs), makes the stability analysis particularly simple. In this simplified approach, the authors neglected the effects of the double layer relaxation, i.e., contrary to the model developed earlier by Keizer and Scherson [45]; instead, the role of double layer (of assumed potential-independent average capacity) was now limited to the generation of the charging current flowing when the electrode potential underwent variation.

The principle of derivation of the equation for the dynamics of the electrode potential (dE/dt), coming from the charge conservation principle to the circuit from Fig. 2.6, was already presented in Sect. 2.2 [cf. Eq. (2.29)]. Similarly, derivation of equation for the dynamics of surface concentration of the reactant was described in the same section [cf. Fig. 2.7 and Eq. (2.31)]. Thus, Eqs. (2.29) and (2.31) define the actual dynamical systems with the $\text{In(III)}-\text{SCN}^-$ polarographic reduction. Also analogously to Sect. 2.2, those equations were transformed into nondimensional forms, using now the following substitutions:

$$\text{Dimensionless external voltage :} \quad v = (F/RT)U \quad (4.38)$$

$$\text{Dimensionless electrode potential:} \quad e = (F/RT)E \quad (4.39)$$

$$\text{Dimensionless surface reactant concentration :} \quad x = c(0, t)/c_{\text{bulk}} \quad (4.40)$$

$$\text{Dimensionless time :} \quad \tau = (k't/\delta) \quad (4.41)$$

where k' means the dimensioned (cm s^{-1}) part of the electron-transfer rate constant k_f , expressed formally as the product $k_f = (kk')/2$, with k being the dimensionless, but potential-dependent part of k_f . Then the system of dimensionless ODEs takes a form:

$$\frac{de}{d\tau} = \frac{v - e}{r} - cx \quad (4.42)$$

$$\frac{dx}{d\tau} = -kx + d(1 - x) \quad (4.43)$$

where:

$$r = \frac{AC_d k' R_s}{\delta} \quad (4.44)$$

$$c = \frac{nF^2 c_{\text{bulk}} \delta k}{2RTC_d} \quad (4.45)$$

$$d = \frac{2D}{\delta k'} \quad (4.46)$$

The dimensionless current is calculated from the dependence:

$$i = \frac{v - e}{r} \quad (4.47)$$

Note that in above derivation the dimensioned form of the faradaic current was expressed as $I_f = nFAk_f c_{\text{ox}}(0, t)$, meaning positive current in spite of cathodic reduction of $\text{In(III)}\text{-SCN}^-$ complex. Hence E and U will have further positive values. The model formulated in this way of course produces correct bifurcation scenarios, as they do not depend on the direction of the electron flow, so it can be considered a certain generalized construction. Its adaptation to the $\text{In(III)}\text{-SCN}^-$ electrochemical oscillator, in view of Pospíšil and de Levie mechanism (4.36, 4.37), involves the following dependences:

$$\frac{dc(0, t)}{dt} = -k_1 c(0, t) [\text{SCN}_{\text{ads}}^-]^2 = -k_f c(0, t) \theta^2 \quad (4.48)$$

where $c(0,t)$ is the actual surface concentration of indium(III) ions and θ is the electrode coverage of the adsorbed SCN^- ions:

$$\theta = [\text{SCN}_{\text{ads}}^-]/[\text{SCN}_{\text{ads}}^-]_{\text{max}} \quad (4.49)$$

and

$$k_f = k_1[\text{SCN}_{\text{ads}}^-]_{\text{max}}^2 \quad (4.50)$$

Although Koper and Sluyters [44] discuss several versions of their model, differing with degree of complexity, we shall focus here on its most realistic formulation. This includes not only the SCN^- -catalyzed, but also noncatalyzed (at high overpotentials) reduction of indium(III), described with a Butler–Volmer-type exponential dependence of the electroreduction rate constant on the dimensionless electrode potential, with e^0 meaning the dimensionless formal potential of the In(III)/In(amalgam) couple and αn being the electrochemical transfer coefficient, assumed further as being equal to 0.5. The following dimensionless ODEs were then obtained:

$$\frac{de}{d\tau} = \frac{v - e}{r} - c_1 x \theta^2 - c_2 x \exp[\alpha n(e - e^0)] \quad (4.51)$$

$$\frac{dx}{d\tau} = -k_1 x \theta^2 - k_2 x \exp[\alpha n(e - e^0)] + d(1 - x) \quad (4.52)$$

with obvious relation: $k_2 \ll k_1$. The model $\theta(E)$ dependence was chosen so that it generates the region of the negative differential resistance in the appropriate potential range:

$$\theta = \begin{cases} 1 & e \leq e_d \\ \exp[-b(e - e_d)^2] & e > e_d \end{cases} \quad (4.53)$$

with e_d parameter being a kind of “transition potential” for the coulostatic repulsion of SCN^- ions from the electrode surface and parameter b controlling the steepness of that dependence. Numerical integration of ODEs system (4.51, 4.52), using classical Runge–Kutta algorithm, showed either oscillations or steady state, depending on the parameters values. Exemplary oscillatory shapes and the stability diagram in the v – r space are shown in Figs. 4.25 and 4.26, respectively.

A deeper insight into the bifurcation scenario is revealed by analysis of the i – u dependences, for various fixed values of r , which is the model representation of the voltammetric experiments, each performed for different serial resistance in the circuit (Fig. 4.27a–c). Figure 4.27a shows the steady-state current (of a global stability) for the entire range of voltage applied, so no bifurcation occurs for such a low value of $r = 0.4$. Figure 4.27b, corresponding to higher resistance $r = 0.5$, shows the onset of oscillations through a supercritical Hopf bifurcation, followed

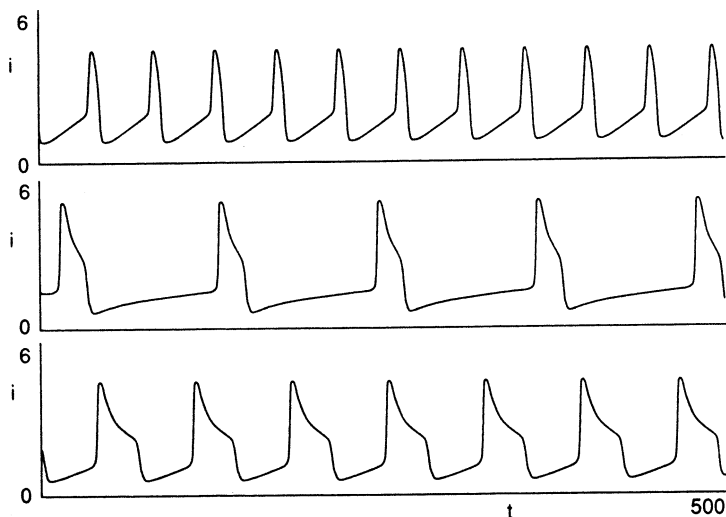
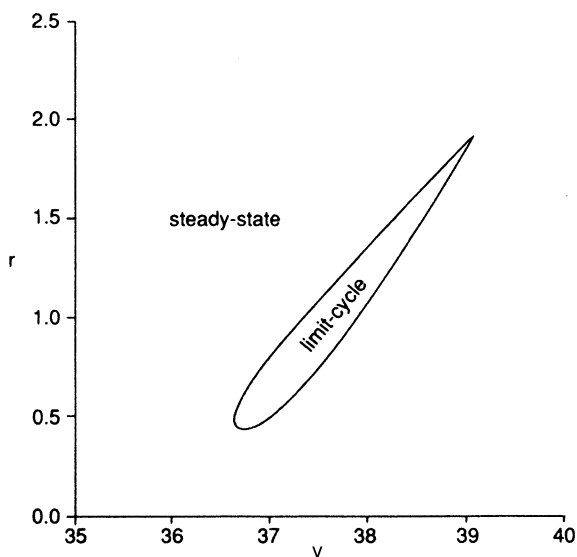


Fig. 4.25 Computed oscillation profiles of $i(t)$ dependence, for model dimensionless Eqs. (4.51)–(4.53) with parameter values $c_1 = 12$, $c_2 = 0.48$, $k_1 = 0.1$, $k_2 = 0.004$, $d = 0.02$, $e^0 = 34$, $e_d = 35$, $b = 0.5$ and (from top to bottom): $v = 37/r = 0.5$, $v = 38/r = 1.1$, $v = 38/r = 1.3$. Reprinted from [44], Copyright 1991, with permission from Elsevier

Fig. 4.26 Stability diagram of model equations (4.51)–(4.53) with parameter values as in Fig. 4.25. Reprinted from [44], Copyright 1991, with permission from Elsevier



by abrupt decay of oscillations due to subcritical bifurcation. In Fig. 4.27c, corresponding to even higher $r = 1.0$, the oscillations set in according to the subcritical Hopf bifurcation, followed by SNIPER bifurcation, according to which the oscillations cease due to increasing their period to infinity. Finally, Fig. 4.27d

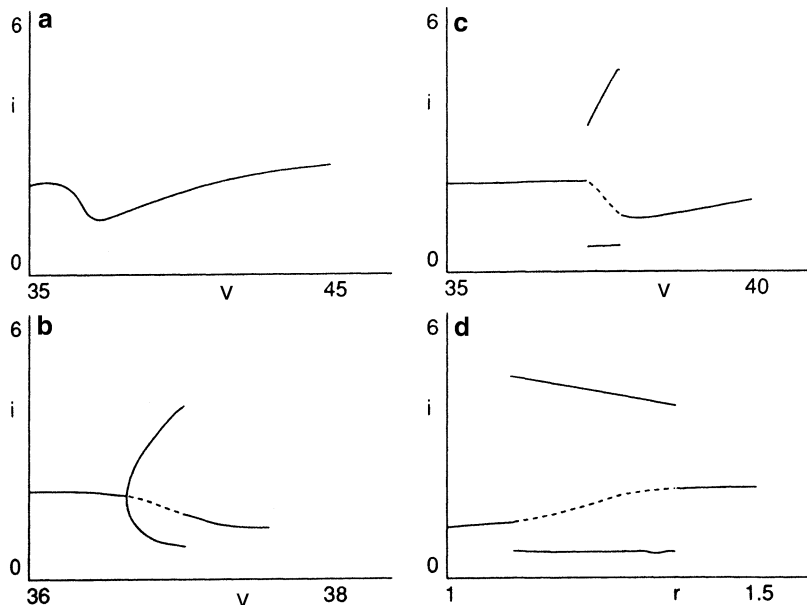


Fig. 4.27 Bifurcation diagrams for model equations (4.51)–(4.53). (a) $r = 0.4$; (b) $r = 0.5$; (c) $r = 1.0$; (d) $v = 38$ (all other parameters as in Fig. 4.25). Reprinted from [44], Copyright 1991, with permission from Elsevier

shows the effect of increasing r as a bifurcation parameter, for fixed voltage $v = 38$: a SNIPER bifurcation occurs at low r , while a subcritical Hopf bifurcation takes place at higher r .

Extension of this 2D model to polarographic conditions (rising Hg drop) and inclusion of the dependence of double layer capacitance on the electrode potential produced oscillatory shapes $i-t$ resembling better those observed experimentally by de Levie [36], but the changes were of rather quantitative than qualitative nature, so no new bifurcations were discovered. In order to reproduce more complex oscillations, the distribution of the concentration in the diffusion layer no longer can be assumed linear, and the thickness of this layer should also vary during the oscillations. This suggests the development of the present model, if still defined in terms of ODE, toward engaging more than two dynamical variables.

4.3.2.2 The 3D Model with Spherical Geometry of Diffusion

The constant thickness of the Nernst diffusion layer (δ) was one of the most serious simplifications of the previous 2D model assuming linear diffusion to planar stationary electrode, since under such conditions δ should constantly increase with the electrolysis time. In other words, the true steady-state current could not be observed and also the oscillations should exhibit certain drift in their characteristics.

However, if the planar electrode is replaced with the spherical one, in the case of semi-infinite diffusion to such an electrode, the current will asymptotically tend to a constant, nonzero value [2, 4]:

$$I = \lim_{t \rightarrow \infty} \left[nFADc^0 \left(\frac{1}{\sqrt{\pi Dt}} + \frac{1}{a} \right) \right] = \frac{nFADc^0}{a} \quad (4.54)$$

where a is the radius of the spherical electrode. Accordingly, also the periodic oscillations recorded with the use of such an electrode should asymptotically attain the steady-state characteristics, but the problem remains how much time this will take (furthermore, oscillations can also exist only in transient regime). For that reason, and in order to make the description of the reactant transport more realistic, Koper et al. [46–48] have introduced the spherical geometry to the previous model. The first equation is again the charge conservation principle, but now involving the surface concentration of a reactant at the surface of the electrode of radius a :

$$C_d \frac{dE}{dt} = \frac{U - E}{R_s} - nFAk_f(E)c_{r=a}(t) \quad (4.55)$$

The second equation describes the spherical diffusion transport:

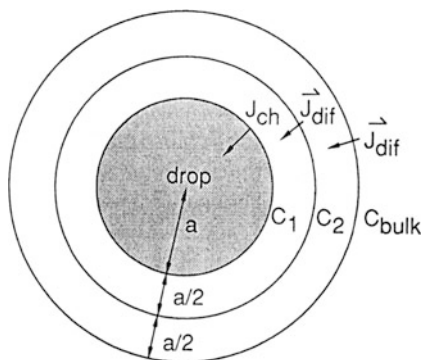
$$\frac{\partial c}{\partial t} = D \left(\frac{\partial^2 c}{\partial r^2} + \frac{2}{r} \frac{\partial c}{\partial r} \right) \quad (4.56)$$

with the boundary conditions for (4.56):

$$D \left(\frac{\partial c}{\partial r} \right)_{r=a} (t) = k_f(E)c_{r=a}(t), \quad c_{r \rightarrow \infty} = c_{\text{bulk}} \quad (4.57)$$

There is no doubt that in classical electrochemistry the partial differential equation (PDE) (4.56) would be numerically integrated in time and space, which approach is usually termed “digital simulation of electrode processes” [49, 50] and allows to calculate the realistic concentration profiles of the species involved in the electrochemical and transport processes (see below for the description of such model). Koper and Gaspard have chosen however an approach based on ODE, in order to construct the model that could be relatively easy subjected to stability analysis. This was done by approximation of the realistic diffusion profile with the two fictive spherical diffusion layers, each of thickness $a/2$ [justified by Eq. (4.54) indicating that the thickness of the diffusion layer adjacent to the spherical electrode can be estimated by the drop radius]—see Fig. 4.28. The third, external layer extends from $r = 2a$ to (formally) infinity, when the reactant concentration is equal to its bulk value (c_{bulk}). In turn, in the $(a, 3a/2)$ layer adjacent to the electrode this concentration is equal to $c_1 = u \times c_{\text{bulk}}$ and in the $(3a/2, 2a)$ layer—equal to $c_2 = w \times c_{\text{bulk}}$, where u and w are appropriate fractions of the bulk concentration. Physically, introducing the concentration of the reactant halfway in the diffusion

Fig. 4.28 The two-diffusion-layer model geometry for the hanging mercury drop electrode. J_{ch} —chemical flux at the interface, J_{dif} —diffusion flux in the solution phase. Reprinted with permission from [48]. Copyright 1992, American Institute of Physics



layer may cause deviation of the diffusion concentration profile from the linear one, a situation being a rather *crude* approximation of the curved profile in real systems.

Further derivations, the details of which can be found in [48], and which include among others the balance of matter diffusing through the surfaces of these virtual spheres, led to the following equations of the c_1 and c_2 concentrations evolution [51]:

$$\frac{dc_1}{dt} = -\frac{24k_f(E)}{19a}c_1 + \frac{108D}{19a^2}(c_2 - c_1) \quad (4.58)$$

$$\frac{dc_2}{dt} = \frac{12D}{37a^2}(16c_{\text{bulk}} - 25c_2 + 9c_1) \quad (4.59)$$

The above two ODEs, together with the charge conservation principle (4.55) form a set of *three* ordinary differential equations, i.e., from mathematical point of view such a system may offer more complex than only simple periodic oscillations. After introducing dimensionless variables:

$$e = (F/RT)E \quad (4.60)$$

$$u = c_1/c_{\text{bulk}} \quad (4.61)$$

$$w = c_2/c_{\text{bulk}} \quad (4.62)$$

$$\tau = 108Dt/19a^2 \quad (4.63)$$

equations (4.55), (4.58), and (4.59) were transformed into their dimensionless forms:

$$\frac{de}{d\tau} = \frac{v - e}{r} - mk(e)u \quad (4.64)$$

$$\frac{du}{d\tau} = -k(e)u + (w - u) \quad (4.65)$$

$$\frac{dw}{d\tau} = \frac{19}{333}(16 - 25w + 9u) \quad (4.66)$$

with:

$$v = (F/RT)U \quad (4.67)$$

$$r = \frac{432}{19}\pi R_s C_d D \quad (4.68)$$

$$k(e) = \frac{2a}{9D}k_f(E) \quad (4.69)$$

$$m = \frac{19nF^2 c_{\text{bulk}} a}{24RTC_d} \quad (4.70)$$

As above, the dimensionless current can be calculated from $i = (v - e)/r$. Application of this model to the In(III)–SCN[−] oscillator involved further the appropriate definition of the rate constant of the electron transfer, expressing both the SCN[−] catalyzed and uncatalyzed reduction pathways:

$$k(e) = k_1\theta^2 + k_2 \exp[an(e - e^0)] \quad (4.71)$$

In Eq. (4.71), the electrode coverage with adsorbed SCN[−] ions (θ) depended on the electrode potential in a way defined by Eq. (4.53), generating thus the region of an N-shaped negative differential resistance.

Numerical integration of Eqs. (4.64)–(4.66) yielded a variety of dynamic behaviors, observed upon increasing model ohmic resistance (r value): from small-amplitude oscillations, resulting from the supercritical Hopf bifurcation, the low-resistance and high-resistance MMO, incomplete Farey sequences (resembling very much those for the copper dissolution in phosphoric acid, cf. Sect. 6.1.3), large amplitude relaxation oscillations, and aperiodic (chaotic) oscillations. Selected examples of these model oscillatory courses are shown in Fig. 4.29 [46]. The notation L^m means number of m small amplitude oscillations separated by L large-amplitude oscillations in the mixed mode.

In spite of simplifications of the model, analogous transitions were reported by Koper et al. [47] in the experimental realization of the same methodology of bifurcation analysis, i.e., by varying the external resistance for the In(III)–SCN[−] electroreduction at the static mercury drop electrode. Figure 4.30 is the corresponding experimental bifurcation diagram, constructed as the dependence of the maximum oscillation amplitude vs. the serial resistance. Note that the

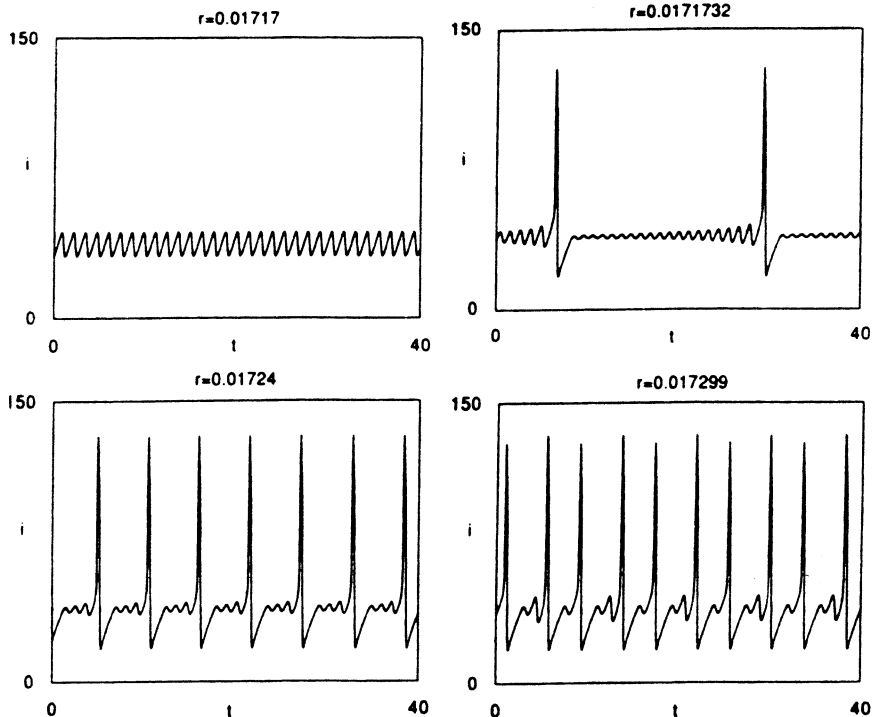


Fig. 4.29 Typical oscillatory time series for the current i obtained for Eqs. (4.64)–(4.66). Depicted are, for the indicated values of r , a small-amplitude oscillation, a MMO state 1^{19} , a MMO state 1^3 , and a typical “Farey” state $1^1 1^2$. Note the small r domain in which these transitions take place. All other parameter values were fixed at $\nu = 37$, $d = 1$, $m = 120$, $k_1 = 2.5$, $k_2 = 0.01$, $e_d = 35$, $b = 0.5$, $an = 0.5$, and $e^0 = 30$. Reprinted with permission from [46]. Copyright 1991 American Chemical Society.

supercritical Hopf bifurcation, leading to small amplitude oscillations, is soon followed by an explosion of large amplitude oscillations, being a part of MMO which mode is followed by simple relaxation oscillations. This region is, in turn, closed by high-resistance MMOs, and then oscillations cease due to the reverse of the period-doubling bifurcation.

The “low-resistance” and “high-resistance” MMO were identified as *dynamically fundamentally different* regimes. The representative time series, showing their morphological differences are shown in Fig. 4.31, while the interpretation of these courses in terms of the corresponding phase space trajectories is shown in Fig. 4.32, respectively [52]. As in the case of other systems, MMO of type 1 suggest the occurrence of *canard explosion* (cf. Sects. 1.6, 3.6.2, 4.1). Furthermore, “type 1” MMOs are related to the so-called *incomplete homoclinic scenario*, and “type 2” to the so-called Shil’nikov behavior of homoclinic trajectories [53]. While it can be a rather advanced, specialized problem for the regular (electro)chemists, it is noteworthy that analogous characteristics can be detected also for other heterogeneous and homogeneous

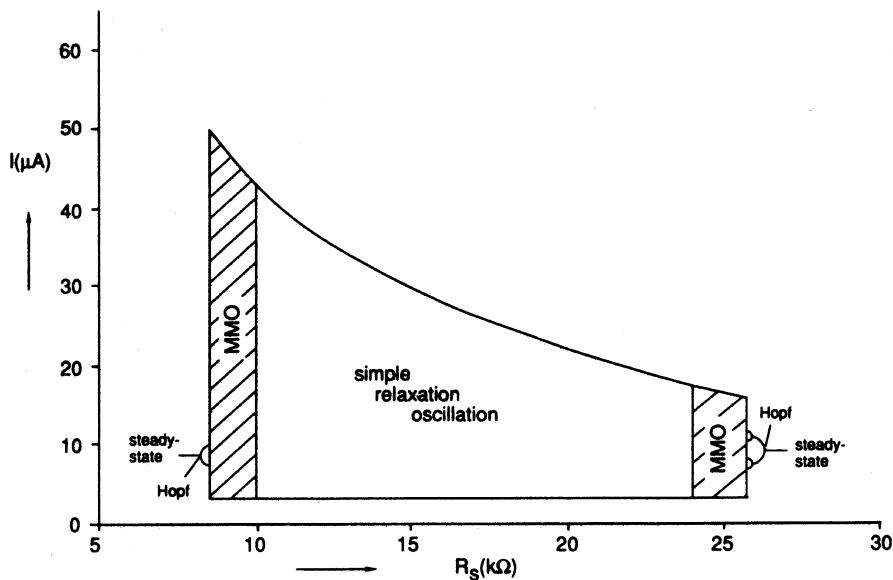


Fig. 4.30 Schematic bifurcation diagram of the minimum and maximum of the oscillating or stationary current as a function of the external resistance R_s . Reprinted with permission from [47]. Copyright 1992 American Chemical Society

oscillators, so the readers interested in universalities in the nonlinear systems' dynamics are encouraged to study this problem in more detail. The model (4.64)–(4.66) reveals in fact quite complex bifurcation scheme, in which besides the Hopf and saddle–node bifurcations loci, also the Shil'nikov saddle focus, and SUN—the saddle–unstable node bifurcation, not mentioned before, were detected; the interested reader is thus advised to consult the original reference [48].

For typical electrochemists, it will be probably of primary importance to learn that systematic experimental measurements of the dynamics observed for the In(III)–SCN[−] reduction at the static mercury electrode, together with additional analysis and transformation of experimental data, allowed Koper et al. to construct a bifurcation diagram shown in Fig. 4.33 [52].

Finally, the 3D model (4.64)–(4.66) was also adapted to hydrodynamic conditions of the rotating disk electrode [48]. It is, however, clear that for comparison of obtained theoretical predictions with the real system, not the In(III)/SCN[−] polarographic oscillator, but rather anodic dissolution of rotating metal disk in appropriate medium system should be used. We shall only mention here that quite a good concordance was found between theory and dynamical instabilities observed for the Cu/H₃PO₄ system, including the existence of MMOs and Farey sequences, extensively studied earlier by Albahadily and Schell, whose works are described in Sect. 6.1.3.3.

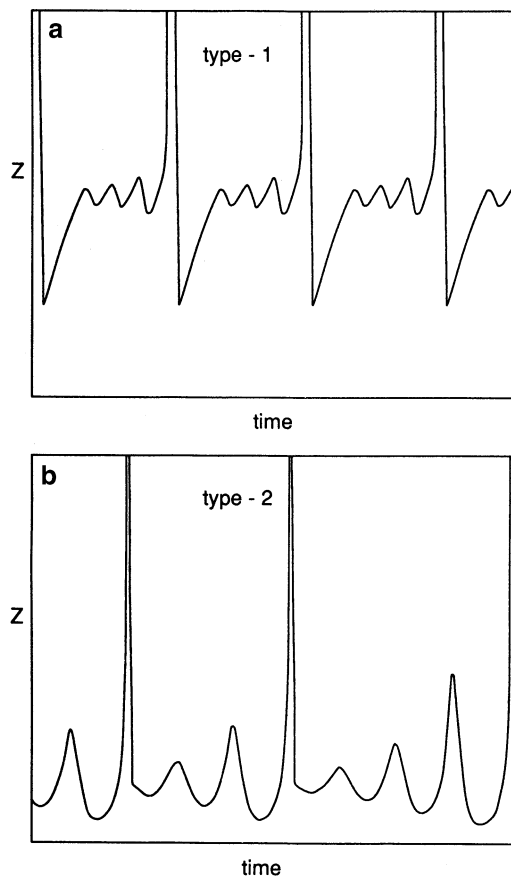


Fig. 4.31 Time series illustrating the different behaviors of the reinjection variable for (a) type 1 and (b) type 2 mixed-mode oscillations (cf. Fig. 4.32). Reprinted with permission from [52]. Copyright 1992, American Institute of Physics

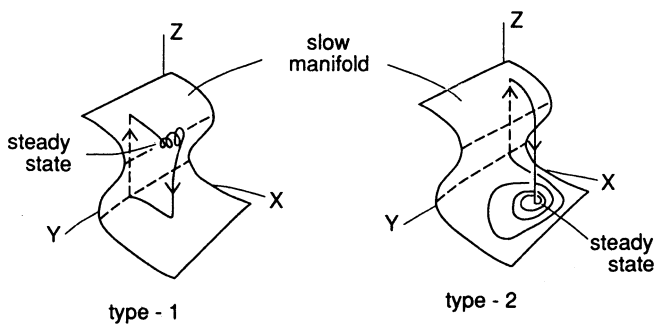


Fig. 4.32 Phase-space trajectories corresponding to type 1 and type 2 mixed-mode oscillations. Reprinted with permission from [52]. Copyright 1992, American Institute of Physics

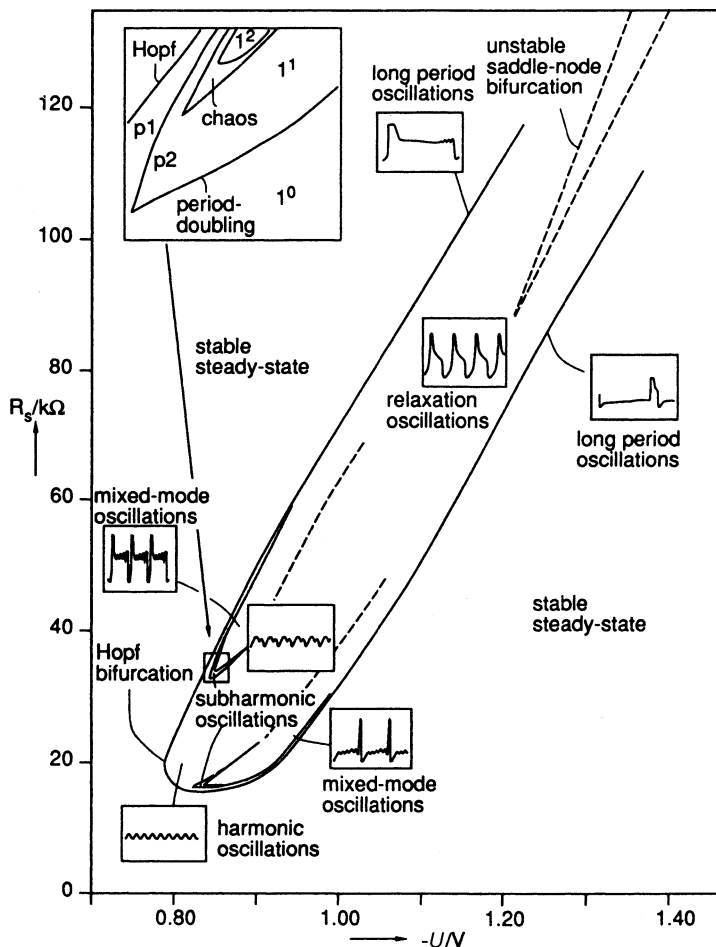


Fig. 4.33 Bifurcation phase diagram for the In/SCN system where regions of stationary, oscillatory, or complex behavior are mapped onto the U - R_s plane. Reprinted with permission from [52]. Copyright 1992, American Institute of Physics

4.3.2.3 Digital Simulation of the In(III)-SCN⁻ Polarographic Oscillator

At the end of this section devoted to model representations of the In(III)-SCN⁻ oscillator, it is useful to confront the above approaches with recent comments by de Levie et al, included in the paper of intriguing title “Demystifying an Electrochemical Oscillator” [38]. In this work, the oscillations during polarographic reduction of In(III)-SCN⁻ were carefully reproduced using the digital simulation technique. Accordingly, discretization was applied to both the time and spatial coordinates and numerical integration of *partial* differential equation for the transport of this species was performed, with appropriate initial and boundary conditions. In the crucial

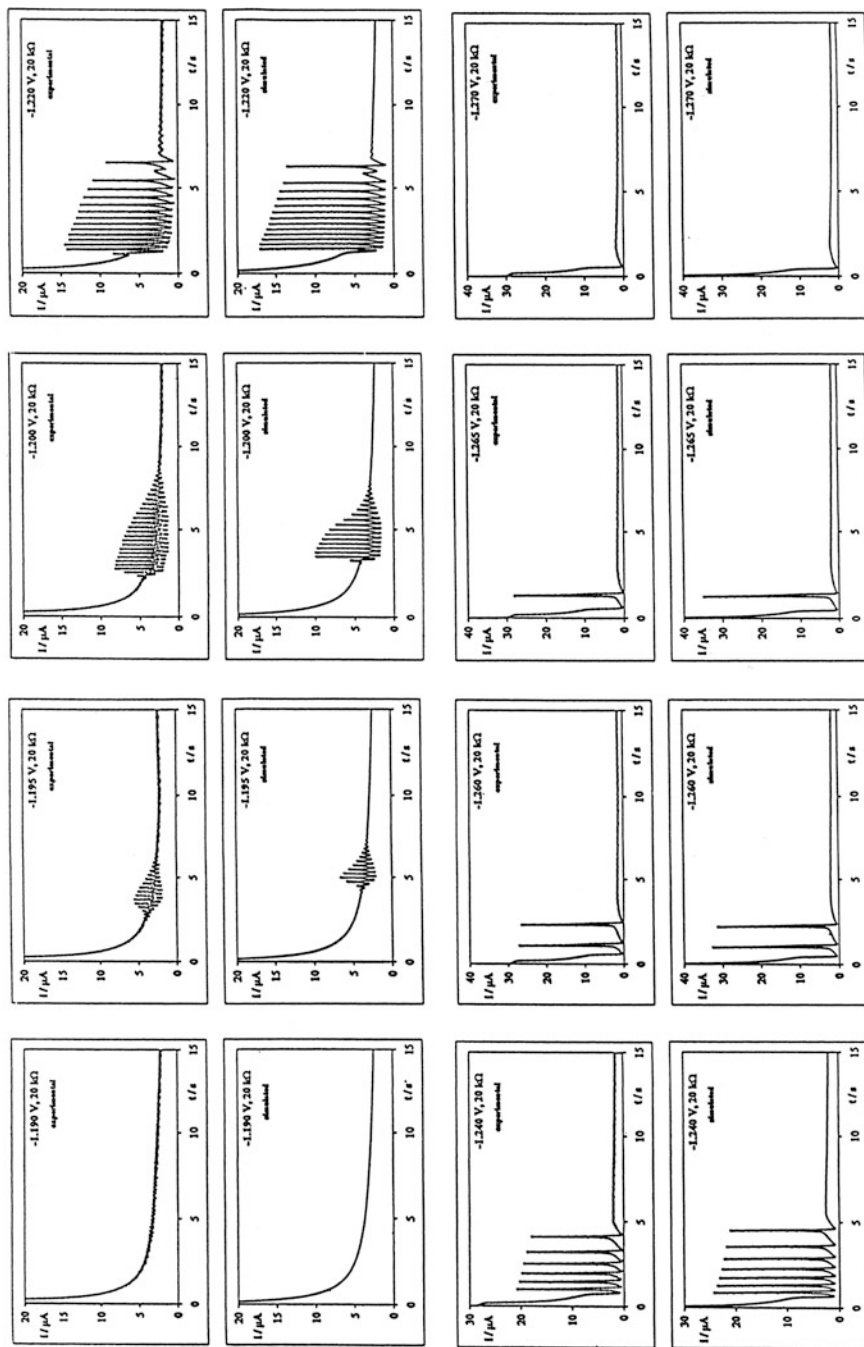


Fig. 4.34 First and third rows: oscillatory transients obtained on a hanging mercury drop electrode (HMDE) at the potentials indicated with the data, in V vs. SCE, when a 20 k Ω resistance was inserted in series with the working electrode. Second and fourth rows: oscillatory transients

region of negative differential resistance, the dependence of the electroreduction rate constant (k_f) on the applied potential was found from experimental polarographic data (in the absence of external ohmic resistance), using the classical Koutecký formalism [2, 4, 54, 55] combined with an extension of the Oldham–Parry algorithm [56]. In order to achieve possibly good concordance with experimental courses, the dependence of the double layer capacitance on the electrode potential in the NDR region was experimentally determined. Furthermore, the simulations were performed for the spherical geometry of HMDE using fast implicit finite differences algorithm [50]. The procedure applied was just like for the simulation of any classical, nonoscillatory system: first the kinetic (k_s , α) and thermodynamic (E^0) parameters of a given electrochemical system were determined as accurately as possible and then they were incorporated into the numerical model in which other parameters can be added or varied, in order to optimally reproduce an experimentally observed behavior. The oscillatory behavior appears then so naturally, as any other nonoscillatory behavior in digital simulation approach that in a realistic manner reproduces both the kinetics of the electron transfer and the transport of reagents in solution. The reader interested in such approach is advised to consult also similar approach employed for the oscillatory electroreduction of Ni(II)–SCN[−] complexes (see Sect. 4.4).

Figures 4.34 and 4.35 show comparisons of the experimental and simulated oscillatory variations of current, corresponding to potentiostatic ($U = \text{const}$) reduction of In(III)–SCN[−] at HMDE.

Quite a good concordance between the experimental and simulated oscillations shows the advantages of such an approach (long ago established in classical electrochemistry) which in this case also minimizes the number of simplifications of the models involving ODEs, if applied to nonstationary conditions. Furthermore, to cite de Levie et al. [38]: “*there is nothing strange, mysterious, or unexpected* in such oscillations: they simply follow the generally accepted formalism given these particular rate parameters.” And further: “To understand oscillatory processes, each system must be understood in terms of its individual chemistry and physics and preferably be amenable to reconstitution from its independently determined rate parameters.” In his more recent paper, de Levie [57] has clarified his point of view: models based on the assumption of the steady state (like those promoted by Koper) are useful for experiments enforcing stationary mass transport conditions, as with rotating disk electrodes, but do not apply to measurements on hanging or dropping mercury electrodes; in the latter case digital simulations are recommendable, among others because they do not require steady-state approximation. In this paper also conditions for the oscillations are summarized and several polarographic

← **Fig. 4.34** (continued) *simulated* using the independently obtained rate parameters plus the applied potential. Experimental data rates: 100 points s^{−1}; simulation: 1,000 points s^{−1}. Reprinted with permission from [38]. Copyright 1998 American Chemical Society

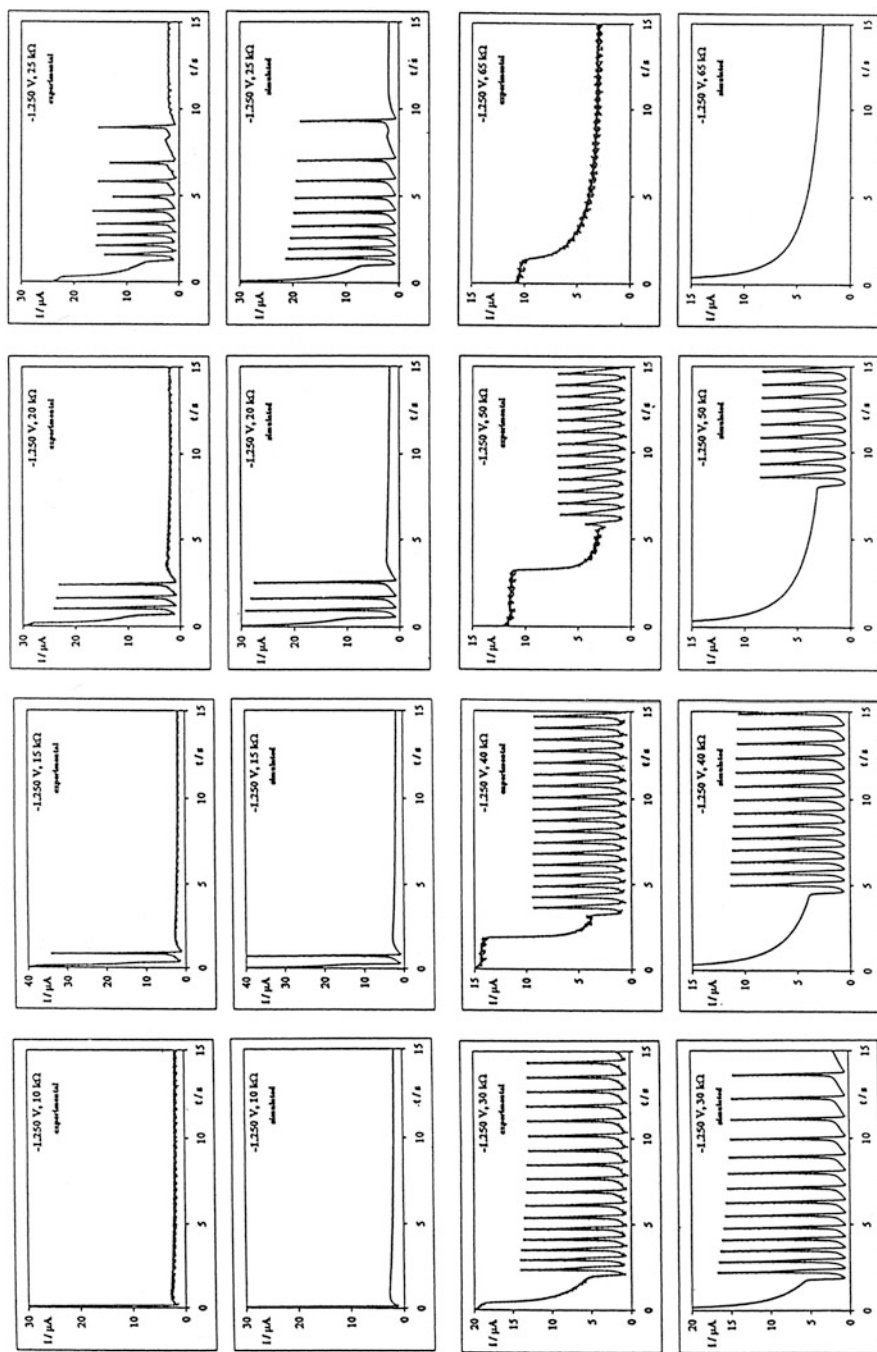


Fig. 4.35 First and third rows: oscillatory transients obtained on a hanging mercury drop electrode (HMDE) at -1.25 V vs. SCE upon insertion of a resistance of indicated value (in $\text{k}\Omega$) in series with the working electrode. Second and fourth rows: the corresponding simulated

oscillators are re-analyzed. Concerning In(III)–SCN[−] system, the author emphasizes that its oscillatory behavior was understood, *in terms of its principles*, three decades before recent digital simulations were made, which only confirmed the early mechanism. What can the author of the present monograph add, having some experience with both types of the models? The advantages of digital simulation should obviously be appreciated, but one can pose a question, whether this approach is sufficient to discover and understand the universalities typical of dynamic instabilities in various systems. Let us try the compromise solution: simplification toward the core of the dynamics of the process, expressed in terms of ODEs for temporal instabilities, is useful for recognizing the universalities in nature, but every such simplification must be preceded with the deep understanding of the physical and chemical mechanism of a given process.

At the end of this section we shall mention that polarographic current oscillations were reported also for reduction of In(III), as well as of Ga(III), in other media (0.02 M chloride and nitrate solutions), as Kariuki et al. have recently reported [58, 59]. However, those instabilities occurred at potentials around the polarographic maximum, so they most probably are of completely different, hydrodynamic origin.

4.4 Oscillations and Bistability in the Nickel(II)–SCN[−] Electroreduction

4.4.1 Origin of the N-NDR Region in the Ni(II)–SCN[−] Electroreduction

Following the previous section about the In(III)–SCN[−] oscillator, we will describe dynamic instabilities in the electroreduction of thiocyanate complexes of nickel(II) at mercury electrodes. Nickel(II) forms with SCN[−] ions a series of complexes, with the number of SCN[−] ligands changing (as the mean value) from 1 to 3.8, for SCN[−] concentration varying from 0.1 to 4.8 M, at constant [Ni(II)] = 0.001 M [60]. The polarographic wave of Ni(II) in the presence of excess of thiocyanates has a shape similar to that for the electroreduction of In(III)–SCN[−] complexes, including the N-NDR region in the similar potential range (Fig. 4.36) [61]. This suggests a similar mechanism of the NDR formation:

← **Fig. 4.35** (continued) oscillatory transients for the same series resistances. Experimental data rates: 100 points s^{−1}; simulation: 1,000 points s^{−1}. Reprinted with permission from [38]. Copyright 1998 American Chemical Society

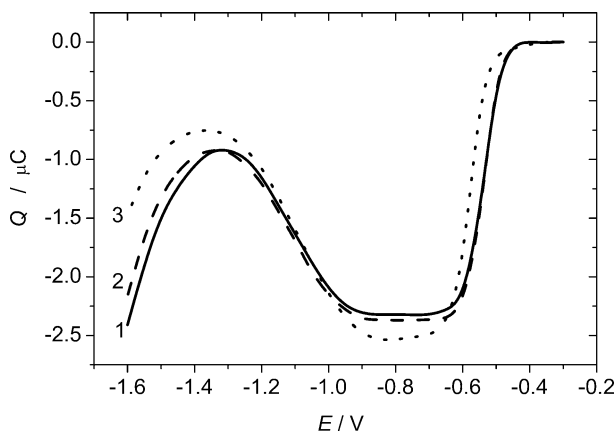


Fig. 4.36 Normal pulse chronocoulometric (voltcoulometric) waves of solutions of $1 \times 10^{-3} \text{ mol dm}^{-3}$ $\text{Ni}(\text{ClO}_4)_2$ with constant ionic strength: (1) $[\text{NaSCN}] = 2 \text{ mol dm}^{-3}$, (2) $[\text{NaSCN}] = [\text{NaClO}_4] = 1 \text{ mol dm}^{-3}$. For comparison curve (3) for $[\text{NaSCN}] = 1 \text{ mol dm}^{-3}$; $[\text{NaClO}_4] = 0$, was also included. Current sampling time $t_2 = 100 \text{ ms}$. The NDR region occurs within potential range $(-0.95 \text{ V}, -1.3 \text{ V})$. Reprinted from [61] Copyright 1999, with permission from Elsevier

the electrostatic repulsion of adsorbed, electrocatalytically acting SCN^- anions from negatively charged electrode surface.

Early report on the oscillations of the polarographic current of reduction of Ni(II)– SCN^- complexes, suggesting such an origin of NDR, has been published by Tamamushi and Matsuda [62] and the phenomenon was confirmed later by Koper and Sluyters [63]. More recent classical electrochemical works, performed by Krogulec et al. [60, 64, 65], have indicated however that the mechanism of the Ni(II)– SCN^- electroreduction is more complex than that of In(III)– SCN^- , since it includes, besides relatively simple reduction of Ni(II) to Ni(0)(Hg), also a parallel reduction of SCN^- ions: $5\text{Ni}^{2+} + 4\text{SCN}^- + 8\text{e}^- \rightarrow 4\text{NiS} + \text{Ni}(\text{CN})_4^{2-}$. The solid NiS phase was found to adsorb strongly on Hg electrode surface and, with increasing electrolysis time, it could even (auto)inhibit the entire electrode process. More recent experiments and model calculations [61] have shown that NiS is not a main (if any) source of the N-NDR region which is thus presumably due to the same mechanism, as for the In(III)– SCN^- electroreduction. Thus, the side formation of NiS should be considered a factor disturbing rather than causing the oscillations, with this effect increasing with time, when NiS accumulates on the mercury surface. In order to complete the electrochemical characteristics of the Ni(II)– SCN^- electroreduction, it was further suggested that the increase of the cathodic current, following the minimum at ca. -1.3 V is caused by the noncatalytic outer sphere electroreduction of Ni(II) ions in their complexes with SCN^- ions [61].

4.4.2 Oscillations at the HMDE

As for the N-NDR systems, the insertion of appropriate serial ohmic resistance in the circuit of the working hanging (or static) mercury electrode causes the spontaneous current oscillations which are however transient, not only because they occur when the system still tends to the steady state determined by the characteristics of the spherical diffusion. Also continuous side formation of NiS gradually blocks the electrode surface and eventually accelerates the decay of the oscillations by suppressing effect on the flowing current. Exemplary experimentally obtained oscillatory $I-t$ courses of the Ni(II)–SCN[−] electroreduction, reported by Jurczakowski and Orlik [66], are shown in Fig. 4.37a.

Clearly, since these oscillations occur in a nonsteady state regime, the only model approach which at least semiquantitatively can match the experimental $I-t$ courses has to invoke partial differential equations, i.e., engage the digital simulation technique [49, 50]. Exemplary principles of implementation of such approach to model electrochemical instabilities, which allows to generate realistic variations of the concentration profiles during the oscillations, were outlined in [67] and applied to the discussed Ni(II)–SCN[−] oscillator at HMDE [66]. Below they are briefly summarized. The Ni(II)–SCN[−] electroreduction was schematically expressed in the form of a model process:



where Ox \equiv electroactive Ni(II)–SCN[−] species and Red \equiv nickel(0) amalgam. The dependence of the rate constants k_f and k_b on the electrode potential was assumed in a way explaining the full $Q-E$ shape, like that in Fig. 4.36. The rise of the current prior to the NDR region and the formation of this region (i.e., the current of the SCN[−]-catalyzed process) is generated by term with the $K_{s,1}$ preexponential factor, while the term with $K_{s,2}$ factor explains the re-increase of current at far negative potentials, due to noncatalyzed reduction of Ni(II):

$$k_f = K_{s,1} \exp[-(\alpha n)_1 f(E - E_f^0)] + K_{s,2} \exp[-(\alpha n)_2 f(E - E_f^0)] \quad (4.73)$$

where

$$K_{s,1} = k_{s,1}^{\text{app}} \left\{ \frac{\exp[-k_{\text{NiS},1}At]}{1 + \exp[P_1(E - P_2)]} \right\} \quad (4.74)$$

$$K_{s,2} = k_{s,2}^{\text{app}} \exp[-k_{\text{NiS},2}At] \quad (4.75)$$

and with the rate constant of the reverse process described by the thermodynamic relationship:

$$k_b = k_f \exp[nf(E - E_f^0)] \quad (4.76)$$

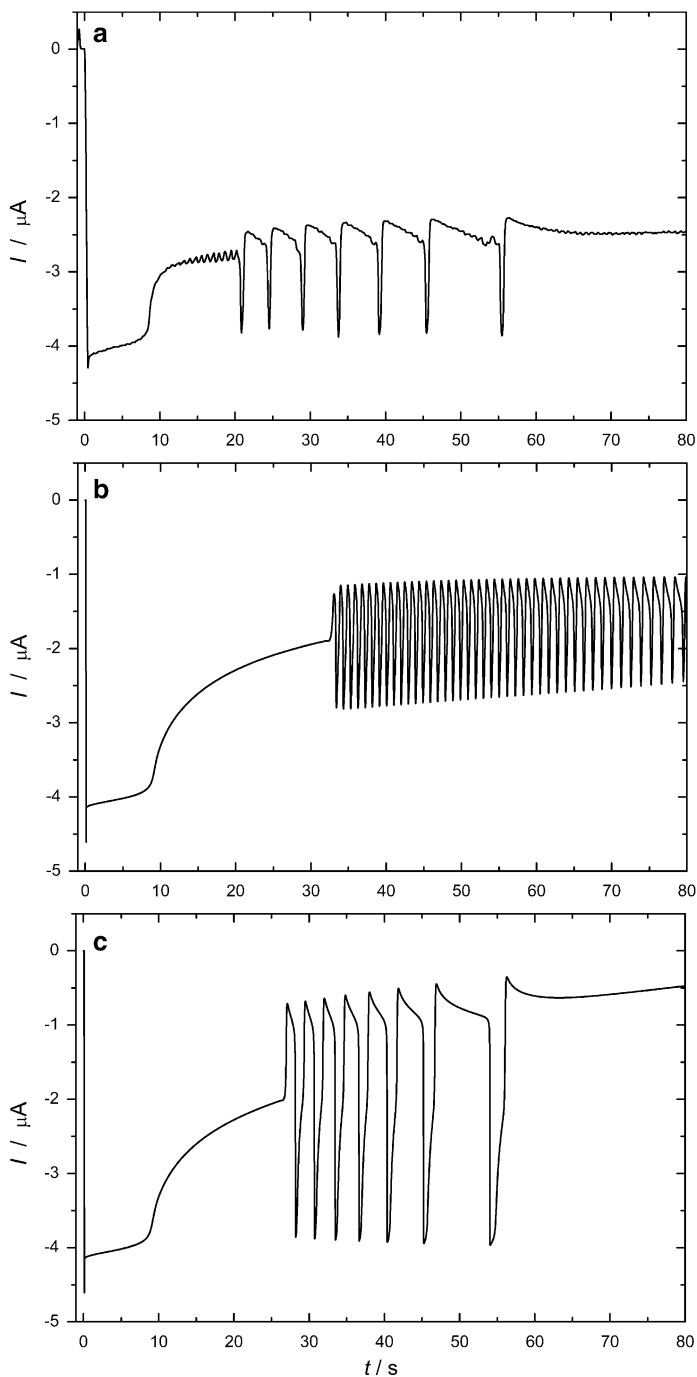


Fig. 4.37 Experimental (a) and simulated (b, c) courses of the chronoamperometric electroreduction of $2.1 \times 10^{-3} \text{ mol dm}^{-3} \text{ Ni(ClO}_4)_2 + 2.0 \text{ mol dm}^{-3} \text{ NaSCN}$. External voltage $U = -1.6 \text{ V}$, serial resistance $R_s = 250 \text{ k}\Omega$, $A = 1.17 \times 10^{-2} \text{ cm}^2$; the formation of inhibitory

In Eqs. (4.73)–(4.76) $f = F/RT$, A is the electrode surface, P_1 is a parameter which determines the I – E (or Q – E) slope in the region of the negative resistance, while P_2 , having some correspondence to the potential of zero charge of mercury in contact with SCN[−] ions, decides from what potential the negative slope of the I – E (or Q – E) curve starts to manifest itself. The rate constants $k_{\text{NiS},1}$ and $k_{\text{NiS},2}$ determine the rate with which the electrode kinetics is being affected (slowed down) by the inhibitory layer of NiS. The numerical values of most parameters were determined from the short-pulse (100 ms) normal pulse chronocoulometric studies of the Ni(II)–SCN[−] electroreduction [61], assuming that for such short sampling times the generation of NiS could be considered negligible (i.e. then $k_{\text{NiS},1} = k_{\text{NiS},2} = 0$). The latter values were modified when simulating the oscillations for given conditions.

The electrode potential E differs from the externally applied voltage U for the ohmic drops, caused by the serial resistor R_s in the circuit (the solution resistance was assumed negligible due to high concentration of NaSCN):

$$E = U - R_s(I_f + I_c) \quad (4.77)$$

with the faradaic and capacitive currents defined, respectively, as:

$$I_f = nFAf_{\text{ox}}(0, t) \quad (4.78)$$

and

$$I_c = C_d(E) \frac{dE}{dt} = C_d(E) \frac{d[U - (I_f + I_c)R_s]}{dt} \quad (4.79)$$

$f_{\text{ox}}(0, t)$ being the flux of Ox species at the electrode surface ($x = 0$), at time t . Finally, the spherical geometry of the HMDE implies the relevant equations of transport:

$$\frac{\partial c_{\text{ox}}}{\partial t} = D_{\text{ox}} \left(\frac{\partial^2 c_{\text{ox}}}{\partial r^2} + \frac{2}{r} \frac{\partial c_{\text{ox}}}{\partial r} \right) \quad (4.80)$$

$$\frac{\partial c_{\text{red}}}{\partial t} = D_{\text{red}} \left(\frac{\partial^2 c_{\text{red}}}{\partial r^2} + \frac{2}{r} \frac{\partial c_{\text{red}}}{\partial r} \right) \quad (4.81)$$

Fig. 4.37 (continued) layer of NiS was neglected in (b) ($k_{\text{NiS},1} = k_{\text{NiS},2} = 0$) and taken into account in (c) ($k_{\text{NiS},1} = 0.9 \text{ cm}^{-2} \text{ s}^{-1}$, $k_{\text{NiS},2} = 4.5 \text{ cm}^{-2} \text{ s}^{-1}$). $T = 298 \text{ K}$. Other parameters of the model: $[\text{NaSCN}] = 2.0 \text{ mol dm}^{-3}$, $T = 298 \text{ K}$, $D_{\text{ox}} = 5.3 \times 10^{-6} \text{ cm}^2 \text{ s}^{-1}$, $A = 0.0150 \text{ cm}^2$, $k_{s,2}^{\text{app}} = 1.6 \times 10^{-5} \text{ cm s}^{-1}$, $(\alpha n)_2 = 0.176$, $E_f^0 = -0.564 \text{ V}$, $P_1 = -70.6 \text{ V}^{-1}$, $P_2 = -0.703 \text{ V}$; $D_{\text{red}} = 6.5 \times 10^{-6} \text{ cm}^2 \text{ s}^{-1}$, $k_{s,1}^{\text{app}} = 10^{-3} \text{ cm s}^{-1}$, $n = 2$, $(\alpha n)_1 = 1.5$, $(\beta n)_1 = 0.5$. Reprinted from [66], Copyright 2000, with permission from Elsevier

with the following initial boundary conditions (r_0 meaning here the radius of HMDE and c_{ox}^0 the bulk concentrations of the Ni(II)–SCN[−] reactant):

$$t = 0 \quad r \geq r_0 \quad c_{\text{ox}}(r, t) = c_{\text{ox}}^0 \quad c_{\text{red}}(r, t) = 0 \quad (4.82)$$

These equations were solved numerically by means of the explicit finite differences method. The general form of finite difference equations, describing the discrete progress of diffusion in the solution, within every time step Δt and the spatial step Δx can be found in the relevant literature [49, 50]. We shall give here only specific form of equations that allow to calculate the total current as a function of time, i.e., to reproduce the oscillatory courses. If the model time of duration of the electrochemical experiment is denoted by $j\Delta t$, with $j = 1, \dots, N$, then the capacitive current (4.79) is expressed in the form:

$$\begin{aligned} I_c(j) &= C_d[E(j-1)] \left[\frac{E(j) - E(j-1)}{\Delta t} \right] \\ &= C_d[E(j-1)] \left[\frac{U - [I_c(j) + I_f(j)]R_s - E(j-1)}{\Delta t} \right] \end{aligned} \quad (4.83)$$

where indices (j) and ($j-1$) indicate the values of the current calculated for the actual time step and the preceding time step, respectively. The double layer capacitance is determined based on preceding E . Taking into account Eq. (4.77) one derives then the final expression for the actual capacitive current $I_c(j)$:

$$I_c(j) = C_d[E(j-1)] \left[\frac{U - R_s I_f(j) - E(j-1)}{\Delta t + R_s C_d [E(j-1)]} \right] \quad (4.84)$$

The dependence of C_d on the electrode potential was realized through the spline interpolation of available C_d – E data [66], for given $E(j-1)$ potential. In turn, the faradaic current I_f was calculated from the following nonlinear equation, the general mathematical form of which comes from the combination of the expression for the faradaic current (4.78) with the condition of the net zero surface fluxes of Ox and Red: $f_{\text{ox}}(0, t) + f_{\text{red}}(0, t) = 0$, valid for the absent or negligible adsorption of Ox and/or Red species at the electrode surface:

$$I_f(j) = -nFA \frac{k_f [I_f(j), I_c(j), U] c_{\text{ox}}(1, j) - k_b [I_f(j), I_c(j), U] c_{\text{red}}(1, j)}{1 + [(k_f [I_f(j), I_c(j), U] / 2D_{\text{ox}}) + (k_b [I_f(j), I_c(j), U] / 2D_{\text{red}})] \Delta x} \quad (4.85)$$

In this particular case the equation for I_f is implicit, since the faradaic current depends on the actual electrode potential which, due to ohmic drops, is dependent also on that current. Thus, for every j th time step Δt of the simulation, Eq. (4.85) was solved with respect to I_f as a root by the Müller method (a highly recommended, quickly convergent, optimized classical bisection procedure followed by inverse

parabolic interpolation [68]); in this way also I_c was simultaneously calculated. The calculation of current was coupled with the calculation of the diffusion progress of Ox in the solution and Red in the amalgam phase, distinguished by different (experimentally determined) diffusion coefficients of both species.

Representative results of calculations are shown in Fig. 4.37b, c. One should note that oscillatory solution appeared *spontaneously* when the decreasing current reached a value similar to that, for which the onset of oscillations was observed in the experiment. This confirms the realistic nature of the simulations. The shapes of the oscillatory courses in part (b) of Fig. 4.37 differ, however, from those shown in part (a), since the side formation of NiS was not yet taken into account in the model [i.e., for part (b), $k_{\text{NiS}, 1} = k_{\text{NiS}, 2} = 0$], while due to prolonged duration time of the oscillatory experiment one should expect detectable accumulation of NiS. It is thus not surprising that much better concordance is reached if appropriate nonzero values of $k_{\text{NiS}, 1}$ and $k_{\text{NiS}, 2}$, treated then as adjustable model parameters, are assumed in the simulations. This effect is clearly illustrated by the improved model oscillatory courses shown in part (c) of Fig. 4.37. Of course, the implementation of NiS in the form of the exponential term is a very simplified tool which can only express the net effect of this solid species which nucleates and grows probably inhomogeneously on the Hg electrode surface. More experimental and model data can be found in original reference [66].

The presented model seems to be a useful introduction into a subject of possibly precise modeling of the electrochemical oscillations under nonstationary conditions, which involves even the dependence of the double layer capacitance on the electrode potential. As de Levie has indicated [57], introducing this dependence may be quite significant in modeling of the oscillations for the diluted solutions of the supporting electrolyte, when the oscillating electrode potential can traverse the region of substantial $C_d(E)$ dependence.

Finally, in spite of certain criticism, recommending that mathematically strict would be the use of implicit, instead of explicit numerical integration of PDE [69], one should note that the approach presented earlier yields satisfactory results not only for the dynamically unstable systems. The same algorithm applied to simulation of cyclic voltammetric curves affected by significant ohmic drops (as for nonaqueous solutions) produces $I-E$ shapes perfectly matching the experimentally recorded patterns, if the C_d-E dependence is invoked [70, 71].

4.4.3 Oscillations and Bistability at the Streaming Mercury Electrode

4.4.3.1 Construction of the Streaming Electrode. Experimental Results

The transient regime of diffusion transport and continuous production of NiS disturbing the oscillatory course made the steady-state behaviors impossible to obtain using the HMDE. Using such an electrode type it is also difficult to unambiguously detect the bistability upon cyclic variation of the external voltage, as the

system in transient regime never returns to the same situation. In fact, up to the year 2002, apparently no reports on the *true* stable oscillations at mercury electrodes have been published. The problem was recently solved by Jurczakowski and Orlik [72] who first have applied the *streaming mercury electrode* for the studies of electrochemical instabilities in the Ni(II)–SCN[−] electroreduction. Such an electrode was in use rather in 1950s with the hope that it will allow to make short-time experiments in electrode kinetics, but later it lost competition with the pulse techniques. Up to middle of sixties (1960's) it was used for the precise determination of the potential of zero charge of Hg electrode by Paschen, Erdey-Gruz, Grahame, Damaskin, Payne et al., and it is interesting to know that this method was introduced already by Helmholtz and Ostwald at the end of nineteenth century [73].

The advantage of application of the streaming Hg electrode to the studies of the oscillations in the Ni(II)–SCN[−] electroreduction is not limited to the fact that it ensures the constant convective-diffusion transport of electroactive species from the solution bulk to the electrode surface, which allows one to obtain both true steady states and sustained oscillations of constant amplitude and period. Also, the constantly refreshing itself stream of mercury means permanent and fast removing of reaction products: nickel amalgam and irreversibly adsorbing NiS. For both these reasons the streaming Hg electrode seems to be the ideal, if not the only electrode type for the studies of stable steady states and stable oscillations in the Ni(II)–SCN[−] electroreduction. Furthermore, it allows one to report bistability in this process that was not described before, but obviously has to manifest itself due to its N-NDR characteristics.

The core of the streaming electrode is a glass capillary through which the stream of mercury is flowing, in this case vertically. The construction of the streaming electrode used in [72] was specially adapted to the studies of dynamic instabilities: the pressure of mercury was maintained constant over prolonged time, and the droplets of mercury formed at the end of the stream were collected and directed toward the peripheral area of the solution, in order to avoid fluctuations of the electrode surroundings, caused by the falling mercury drops. Details of that construction are shown in Fig. 4.38 in which the region of the streaming electrode being in contact with the solution is denoted as section B.

The idealized geometric and dynamic properties of the mercury stream were already shown in Fig. 3.3. Typical characteristics of such electrode, used in the measurements, described in this section, are: stream diameter $\phi = 0.11$ mm, stream length $l_{\max} = 2.85$ mm, stream velocity $v = 1.64$ ms^{−1}, meaning that the electrolysis time varies from zero at the orifice of the glass capillary to $t_{\max} = l_{\max}/v = 1.74$ ms at the solution surface. For the typical diffusion coefficient $D = 6 \times 10^{-6}$ cm² s^{−1}, the corresponding maximum thickness of the Nernst diffusion layer $\delta_{\max} = \sqrt{\pi D t_{\max}}$ reaches then only 1.7×10^{-4} cm. Practice shows that in order to obtain reliable, reproducible results of measurements, the streaming electrode has to exhibit characteristics close to the above, exemplary values, but this also means that the sampling time has to be as short as a few milliseconds only.

Before switching to nonlinear dynamic phenomena it is useful to recognize in more detail the basic features of the transport of reactant particles from the bulk of the solution toward the surface of such streaming electrode. The basic analytical mathematical theory of the streaming mercury electrodes was published by Koryta

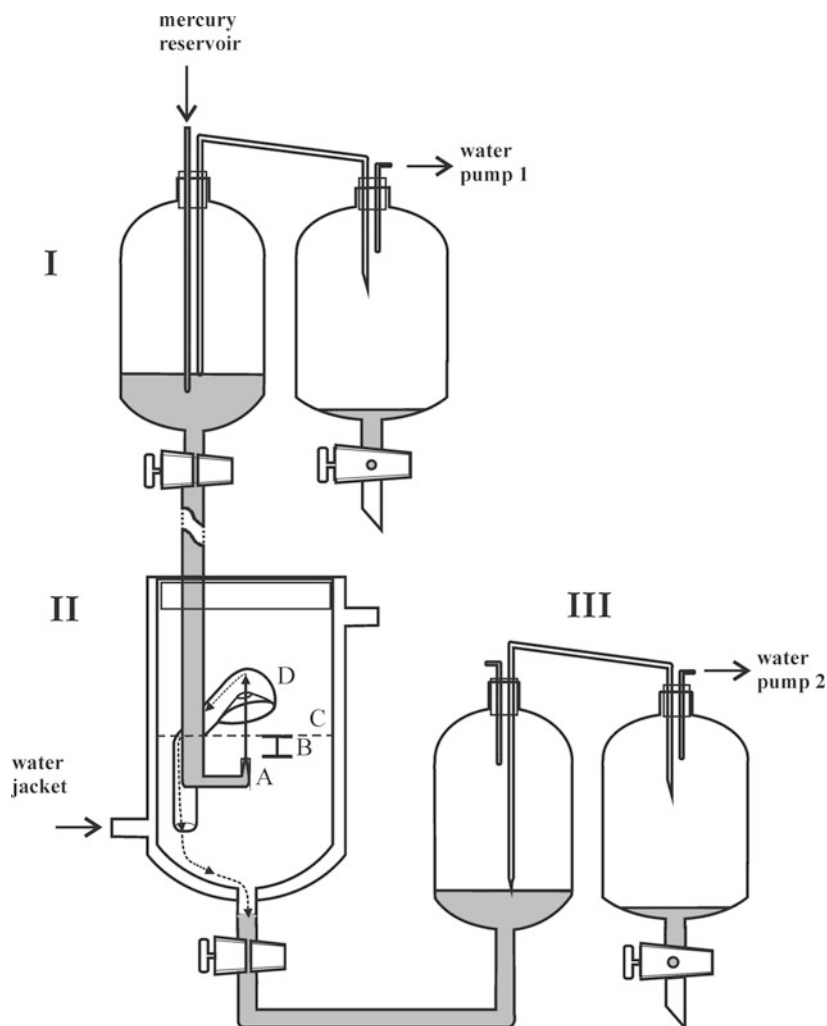


Fig. 4.38 Schematic construction of the experimental setup with the streaming mercury electrode for studying dynamic instabilities in the electroreduction of the Ni(II)–SCN[−] complexes. I—system of maintaining the constant mercury pressure in the flowing stream, II—the electrolytic cell, III—system of mercury collection, maintaining the constant level of the solution in the electrolytic cell; A—glass capillary tip, at which the thin mercury jet is formed, B—the proper streaming electrode, i.e., the range of mercury jet of a length l_{\max} being in contact with studied solution, C—solution surface. The stream of the used mercury is further captured by the fixed element D and directed to the bottom part of the cell. Reprinted with permission from [72], Copyright 2002 American Chemical Society

[74] and by Weaver and Parry [75, 76]. The idealized description of the streaming electrode (like that shown in Fig. 3.3) is based on the following assumptions [72]: (1) the layer of the electrolyte solution in the close vicinity of the electrode, set to

motion by the stream of mercury, follows exactly its surface speed, (2) the thickness of this hydrodynamic layer of the dragged solution is greater than that of the diffusion layer; (3) due to a short contact of the electrolyzed solution with the electrode surface the diffusion layer is so thin, that the strict cylindrical geometry of diffusion may be well approximated by a linear one, i.e., $\partial c/\partial t = D(\partial^2 c/\partial x^2)$; (4) all concentration gradients in the solution, other than those perpendicular to the electrode surface, are negligible.

The next crucial step is the expressions for a faradaic and the capacitive currents. Since the electrolysis time increases along the stream length (l), the local faradaic current varies accordingly. For a given element of the cylindrical surface area $dA = 2\pi r dl$, located at the distance l from the capillary outlet, the *local* faradaic current is thus generally given by:

$$dI_f(l) = nFD(dA) \left(\frac{\partial c_{\text{ox}}}{\partial x} \right)_{0,l} \quad (4.86)$$

while the *total* faradaic current is an integral of this expression along the entire electrode length:

$$I_f = 2\pi r n F D \int_0^{l_{\text{max}}} \left(\frac{\partial c_{\text{ox}}}{\partial x} \right)_{0,l} dl \quad (4.87)$$

The general solution for the current controlled by the charge-transfer step at time t , under linear diffusion conditions, is known [4]:

$$I_f = -nFAc_{\text{ox}}^0 k_f \exp(\kappa^2 t) \text{erfc}(\kappa t^{1/2}) \quad (4.88)$$

where $\kappa = k_f/D_{\text{ox}}^{1/2} + k_b/D_{\text{red}}^{1/2}$ and c_{ox}^0 is the bulk concentration of the reducible reactant. As Weaver and Parry [76] have shown, the integration of $dI_f = -nF(dA)c_{\text{ox}}^0 k_f \exp(\kappa^2 t) \text{erfc}(\kappa t^{1/2})$ with $dA = 2\pi r dl$ and $t = l/v$, over l varying from 0 to l_{max} yields the following expression for the steady-state faradaic current at the streaming mercury electrode:

$$I_{f,ss} = -2\pi r n F c_{\text{ox}}^0 k_f v \left[\frac{2}{\kappa} \sqrt{\frac{t_{\text{max}}}{\pi}} + \frac{\exp(\kappa^2 t_{\text{max}}) \text{erfc}(\kappa t_{\text{max}}^{1/2}) - 1}{\kappa^2} \right] \quad (4.89)$$

which for the case of diffusion-limited value simplifies to [74]:

$$I_{f,\text{lim}} = - \frac{4nFD_{\text{ox}}^{1/2} m^{1/2} l_{\text{max}}^{1/2} c_{\text{ox}}^0}{\rho_{\text{Hg}}^{1/2}} \quad (4.90)$$

In turn, the steady-state *capacitive* current, which—contrary to the electrodes of constant and not renewing itself surface—flows even at constant potential, due to permanent charging of the new portions of flowing mercury to an externally imposed potential, is given by Eq. (3.17) [77]. For exemplary data: $K = 25 \mu\text{F cm}^{-2}$, $(E - E_{\text{pzc}}) = 1 \text{ V}$ and typical parameters of the streaming electrode one gets $I_C = 0.14 \text{ mA}$, i.e., quite significant baseline of the capacitive current, compared to the faradaic current for typical reactant concentrations.

Using the streaming electrode from Fig. 4.38, it was obtained the steady-state I – E characteristics for the Ni(II)–SCN[−] electroreduction, exhibiting the NDR region, with in fact significant baseline contribution from the capacitive current (Fig. 4.39). This figure represent the steady states which are stable, since the small solution resistance appears to be insufficient to induce any instabilities.

When appropriate serial resistance R_s is inserted in the circuit, it is possible to record both sustained oscillations (Fig. 4.40) and bistability (Fig. 4.41).

In Fig. 4.41 only stable steady states, as the only observable ones, are visualized, but one can easily find the missing unstable steady states by the translation of the original I – E characteristics from Fig. 4.39 along the potential axis, point by point, for the actual ohmic potential drops and presentation of the results in the I – U coordinate system. The resulting diagram of all steady states attains the characteristic shape of a double fold (Fig. 4.42).

Systematic studies of the occurrence of oscillations, mono- and bistable behavior as a function of varying voltage U and serial resistance R_s led to the experimental stability (bifurcation) diagram shown in Fig. 4.43. This diagram indicates that oscillations occur in a very tiny region of the parameter space.

For reproduction of the above experimental results in terms of appropriate theoretical models, both digital simulation and linear stability analysis of steady states were performed. Based on the experimental steady-state I – E characteristics from Fig. 4.39, the following parameters of the dependence $k_f(E)$, producing the N-NDR region:

$$k_f = k_{s,1}^{\text{app}} \left\{ \frac{1}{1 + \exp[P_1(E - P_2)]} \right\} \exp[-(\alpha n)_1 f(E - E_f^0)] + k_{s,2}^{\text{app}} \exp[-(\alpha n)_2 f(E - E_f^0)] \quad (4.91)$$

were found: $k_{s,1}^{\text{app}} = 1 \times 10^{-3} \text{ cm s}^{-1}$, $k_{s,2}^{\text{app}} = 4 \times 10^{-4} \text{ cm s}^{-1}$, $(\alpha n)_1 = 1.50$, $(\alpha n)_2 = 0.12$, $E_f^0 = -0.662 \text{ V}$, $P_1 = -67.4 \text{ V}^{-1}$, $P_2 = -0.798 \text{ V}$, and $f = F/RT$ (with $T = 298.15 \text{ K}$).

4.4.3.2 Digital Simulation of Bistability in the Ni(II)–SCN[−] Electroreduction

For the numerical integration of partial differential equations of reagents transport to the model streaming electrode (Fig. 4.44a), the space discretization scheme, shown in Fig. 4.44b, was used. Accordingly, there is the spatial current distribution

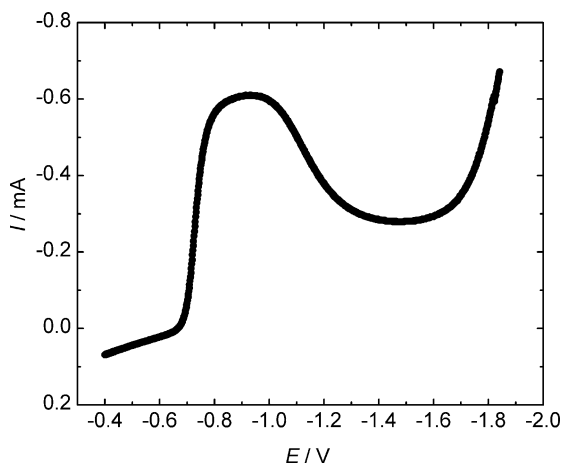


Fig. 4.39 Exemplary steady-state I - E dependence for the sample: $5.0 \text{ mol dm}^{-3} \text{ Ni}(\text{ClO}_4)_2 + 2.0 \text{ mol dm}^{-3} \text{ NaSCN}$, recorded at the streaming mercury electrode. Serial resistance $R_s = 0$. The region of a negative differential resistance (NDR) is observed within the potential range: ca. -1.0 and -1.5 V . Parameters of the streaming electrode: capillary flow $m = 210 \text{ mg s}^{-1}$, internal glass capillary (=mercury electrode) diameter $\phi = 0.11 \text{ mm}$, length of mercury jet (directed upwards) $l_{\text{max}} = 2.5 \text{ mm}$. Temperature 298.0 K . Reprinted with permission from [72], Copyright 2002 American Chemical Society

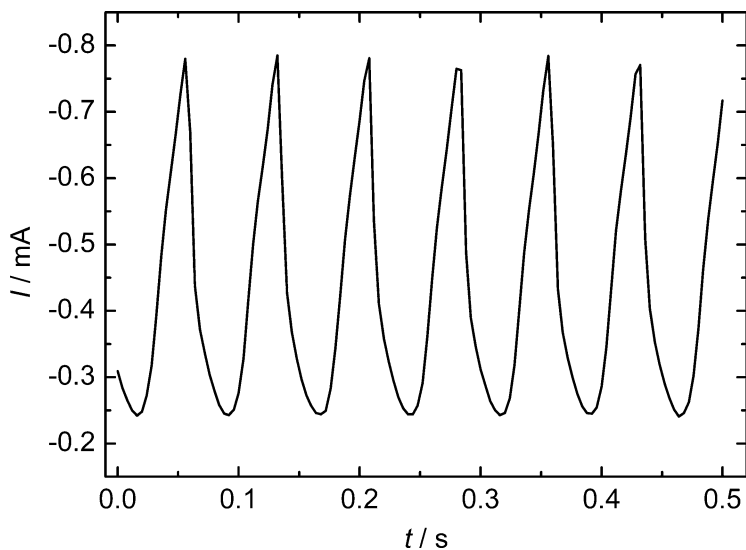


Fig. 4.40 Exemplary sustained oscillations reported for the electroreduction of $\text{Ni}(\text{II})\text{-SCN}^-$ complexes at a streaming mercury electrode, for $U = -1.47 \text{ V}$, $R_s = 0.82 \text{ k}\Omega$. Other parameters as in the caption to Fig. 4.39. Reprinted in part with permission from [72], Copyright 2002 American Chemical Society

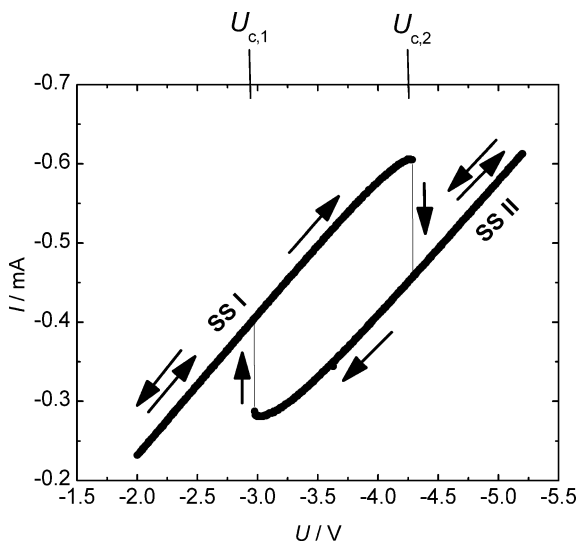


Fig. 4.41 Bistable behavior in the electroreduction of the thiocyanate complexes of nickel(II) at a streaming mercury electrode, manifesting itself as the *hysteresis* in attaining the sets of “high-current” (SS I) or “low-current” steady states (SS II) as a function of the direction of the linear voltage (U) scan. Within the interval $[U_{c,1} U_{c,2}]$ the system is bistable, whereas outside this region remains monostable. Serial ohmic resistance $R_s = 5.5 \text{ k}\Omega$ in the electric circuit of the streaming electrode. Other parameters as in the caption to Fig. 4.39. Reprinted with permission from [72], Copyright 2002, American Chemical Society

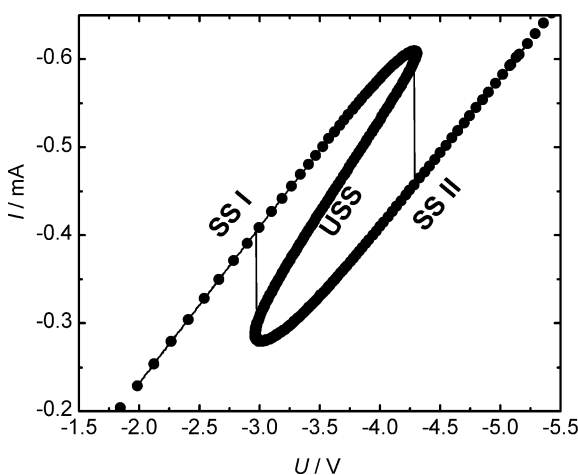


Fig. 4.42 Full diagram of the stable (SS I, SS II) and unstable (USS) steady states for the electroreduction of $5.0 \text{ mmol dm}^{-3} \text{ Ni}(\text{ClO}_4)_2 + 2.0 \text{ mol dm}^{-3} \text{ NaSCN}$ at the streaming mercury electrode: (filled circle) points obtained by the translation, on the voltage axis, of the I - E curve from Fig. 4.39, for ohmic drops IR_s (with $R_s = 5.5 \text{ k}\Omega$); (solid line) experimental curve from Fig. 4.41. Reprinted with permission from [72], Copyright 2002 American Chemical Society

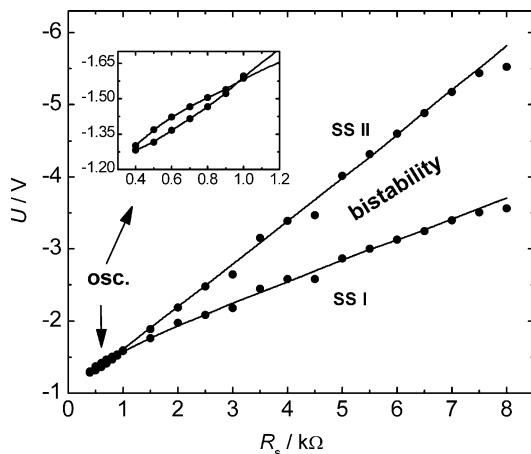


Fig. 4.43 Stability diagram of the dynamic nonequilibrium states (*filled circle*) observed for the electroreduction of the thiocyanate complexes of nickel(II) at a streaming mercury electrode. The *lines*, led through these points, for $R_s > 1 \text{ k}\Omega$ correspond to the position of the saddle-node bifurcations between the monostable and bistable behavior. **SS I**—“high current” steady state, **SS II**—“low current” steady state, **osc**—tiny region of oscillations. In the *inset*, the enlarged region of the occurrence of sustained oscillations, encircled by the curve corresponding to the Hopf bifurcation, is shown. Composition of the sample and parameters of the streaming electrode—the same as for Fig. 4.39. Reprinted with permission from [72], Copyright 2002 American Chemical Society

along the electrode which is due to the increasing electrolysis time, calculated for every electrode segment according to the formula:

$$t_{\text{res},j} = [0.5 \times \Delta l + (j - 1)\Delta l] \times \pi \rho_{\text{Hg}} r^2 / m \quad (4.92)$$

with $j = 1, \dots, N$ and assuming that the faradaic current is calculated in the middle of every discrete $\Delta l = l_{\text{max}}/N$ segment.

The total faradaic current is a sum of those partial currents. The ohmic drops are assumed to be due only to the serial resistance R_s in the external electric circuit, so for all segments of the streaming electrode the interfacial potential drop E is the same, at given time. The essential point of the simulation is the calculation of the total faradaic and capacitive currents [72]. As for HMDE (Sect. 4.4.2), due to IR_s drops, the actual interfacial potential drop E for the Hg electrode is dependent on both the faradaic I_f and the capacitive I_c currents which are also interrelated because the electrode has to be charged to that potential. The combination of expression (4.77) with the formula for the capacitive current (3.17) yields the following dependence for the latter current:

$$I_c = \frac{2\pi r K v (U - I_f R_s - E_{\text{pzc}})}{1 + 2\pi r K v R_s} \quad (4.93)$$

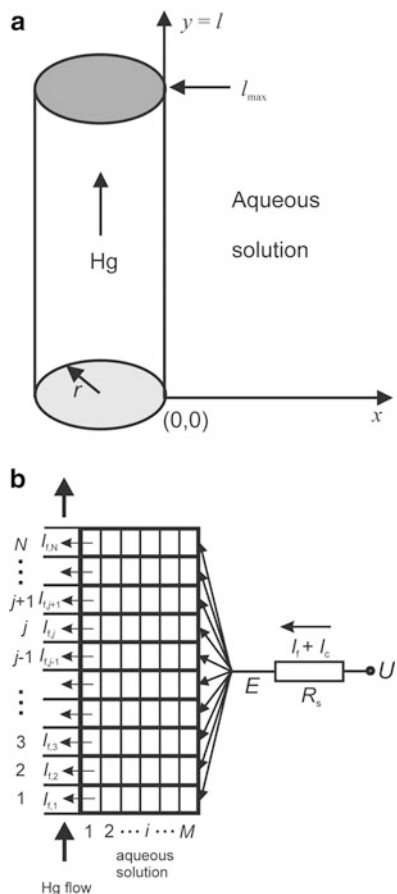


Fig. 4.44 (a) Model geometry of the idealized streaming electrode. The mercury jet appears at the end of glass capillary at $y = 0$ and moves upward along the y coordinate, whereas the diffusion layer in the dragged electrolyte solution develops only along the x -coordinate; (b) the corresponding scheme of the space discretization for the mercury surface and the adjacent aqueous solution, where the distances along the x and y coordinates are divided into $i = 1, \dots, M$ and $j = 1, \dots, N$ spatial elements, respectively. The total faradaic current I_f consists of partial faradaic currents $I_{f,j}$ flowing through discrete segments of a surface area $\Delta A = 2\pi r \Delta l$. The permanent renewal of the electrode surface is associated with the flow of the capacitive current I_c . The potential drop $E = U - (I_f + I_c)R_s$ at the mercury–solution interface is common for all spatial elements. Reprinted with permission from [72], Copyright 2002 American Chemical Society

where I_f is a sum of all partial faradaic currents flowing through discrete electrode segments:

$$I_f = \sum_{j=1}^N I_{f,j} \quad (4.94)$$

In turn, every partial faradaic current $I_{f,j}$, as being dependent on the actual E value, is simultaneously dependent on the sum of all partial faradaic currents and the capacitive current:

$$I_{f,j} = \mathbf{f} \left[E = U - R_s \left(I_c + \sum_{m=1}^N I_{f,m} \right) \right] \quad (4.95)$$

where function \mathbf{f} relates the faradaic current with the potential-dependent diffusion j th flux $f_{\text{ox},j}$ of the reactant Ox at the electrode surface:

$$I_{f,j} = nF(\Delta A)f_{\text{ox},j}(E) \quad (4.96)$$

In Eq. (4.96), the surface area of the electrode segment $\Delta A = 2\pi r\Delta l$ and the partial flux of Ox species, $f_{\text{ox},j}$ is given by:

$$f_{\text{ox},j} = - \frac{k_f c_{\text{ox},j}(1, t) - k_b c_{\text{red},j}(1, t)}{1 + \left[\frac{k_f}{2D_{\text{ox}}} + \frac{k_b}{2D_{\text{red}}} \right] \Delta x} \quad (4.97)$$

where $c_{\text{ox},j}(1, t)$ and $c_{\text{red},j}(1, t)$ denote the concentrations of the respective reagents in the j th discrete spatial cell of the solution, adjacent (i.e., for $i = 1$) to the electrode surface (cf. Fig. 4.44b), for a model time $t = k\Delta t$ of the development of the diffusion profile. Equation (4.95) means that calculation of all the partial faradaic currents requires solving of the set of N nonlinear equations. For nonzero R_s it is an iterative (e.g., Newton's) procedure. Simultaneously with I_f , one calculates the actual capacitive current I_c .

Calculations begin from the initial value of externally applied voltage U , low enough to correspond to the monostable regime of corresponding low current, composed of reasonable first approximations of all partial faradaic currents. The iteratively found partial currents become further the first approximations in the calculations for the next external voltage $U + \Delta U$, etc. The system thus always "remembers" the preceding solution, like the real system remembers its history upon voltage scan. The course of calculations, when the direction of U is eventually reversed, is shown in Fig. 4.45. When the upper (1) branch of the stable steady states (SS I) ends, further steady-state solutions automatically switch (2) to a lower (3) branch of steady states, just like in the real experiment (cf. Fig. 4.45). When the direction of U variations is then reversed, the numerical system exhibits hysteresis due to the fact that the preceding solution is used as the first approximation for the present one: in this way the numerical system exhibits its "memory" typical of bistability. In the course of further calculations, the stable steady-states SS II are being revealed until this branch also finishes (5) and the only steady-state solutions possible are again those belonging to the upper branch. In this way, the realism of this numerical modeling manifests itself, as the course of calculations matches exactly the course of experimental observation of hysteresis associated with bistable behavior.

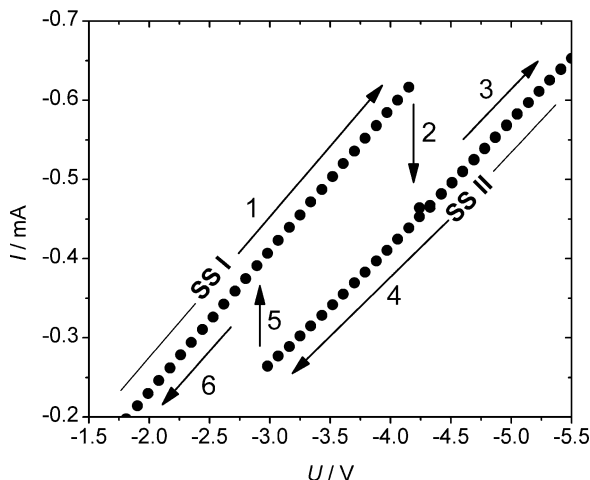


Fig. 4.45 Hysteresis loop (bistability) in the simulated potentiodynamic behavior of the Ni(II)–SCN[−] electroreduction at a streaming mercury electrode in the presence of serial ohmic resistance ($R_s = 5.5 \text{ k}\Omega$) in the electric circuit. The numbers at the respective *arrows* show the sequence in which the points, corresponding to stable steady states, appear during the forward and the reverse voltage scan during model calculations. Characteristics of the model solution and of the streaming electrode correspond to experimental data specified in the caption to Fig. 4.39. The potential-dependent double-layer capacitances [66] were used for calculations of the capacitive currents. Reprinted with permission from [72], Copyright 2002 American Chemical Society

The realistic concentration profiles, corresponding to the “high current” steady-states SS I and “low current” steady-states SS II, calculated for the first and the last segment of the model electrode, are shown in Fig. 4.46.

4.4.3.3 Linear Stability Analysis of Processes at Streaming Electrode

Following the theoretical description of instabilities in the Ni(II)–SCN[−] electroreduction in terms of purely electrochemical terms, one can extend the analysis for application of such standard technique of nonlinear dynamics, as the linear stability analysis [78]. Such an analysis is an extension of the approach elaborated earlier for the nonstreaming electrodes, since it takes into account the specific feature of the streaming electrode: the permanently flowing steady-state capacitive current, the impedance characteristics of which, involving the virtual resistor R_d (3.20), the definition of which will now be expressed in term of integral double layer capacitance, suitable for discussed here dc conditions:

$$R_d = \frac{1}{2\pi r K(E) v} \quad (4.98)$$

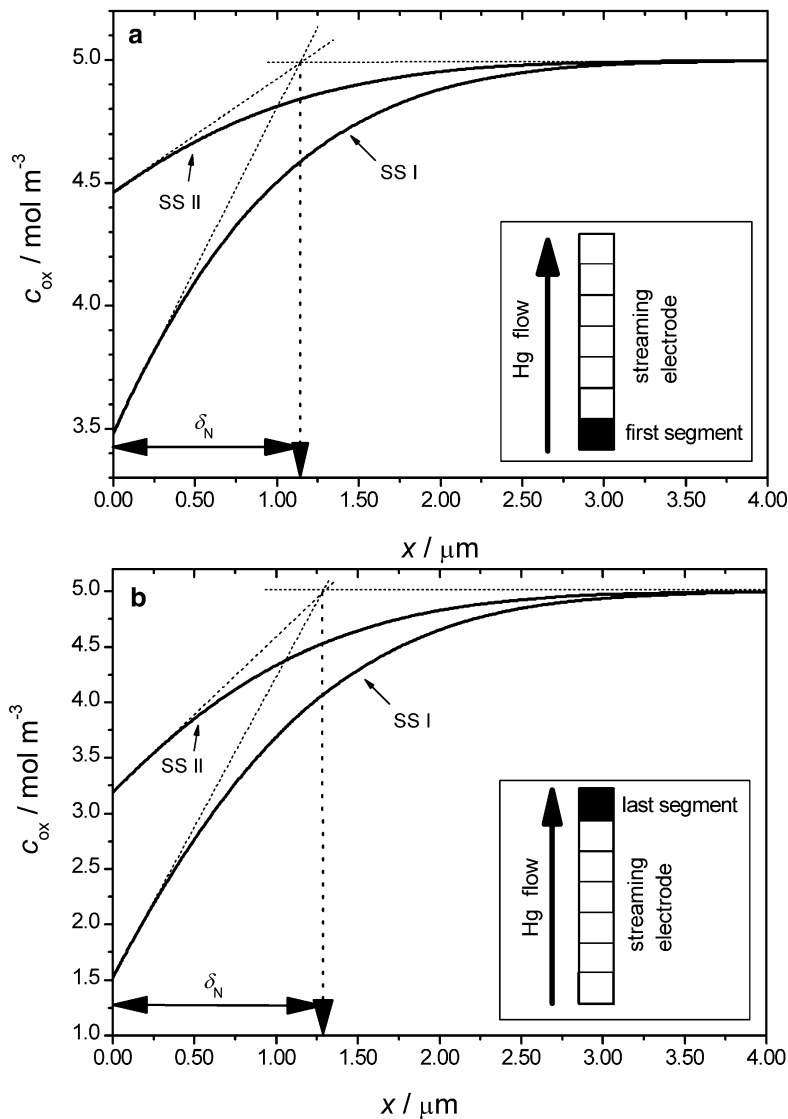


Fig. 4.46 Exemplary simulated realistic concentration profiles for the electroreduction of Ox (Ni(II)-SCN⁻ complex) in the bistable region ($U = -3.5$ V, $R_s = 5.5$ k Ω) for: (a) the first and (b) the last discrete segment of a model streaming mercury electrode, shown schematically in the insets. For the full discretization scheme and other mathematical details of the simulation procedure—see Section 4.4.3.1 and [72]. Reprinted with permission from [72], Copyright 2002 American Chemical Society

In the presence of the faradaic process, the equivalent circuit from Fig. 3.5 must be extended for the corresponding branch with the faradaic impedance Z_f , as shown in Fig. 4.47.

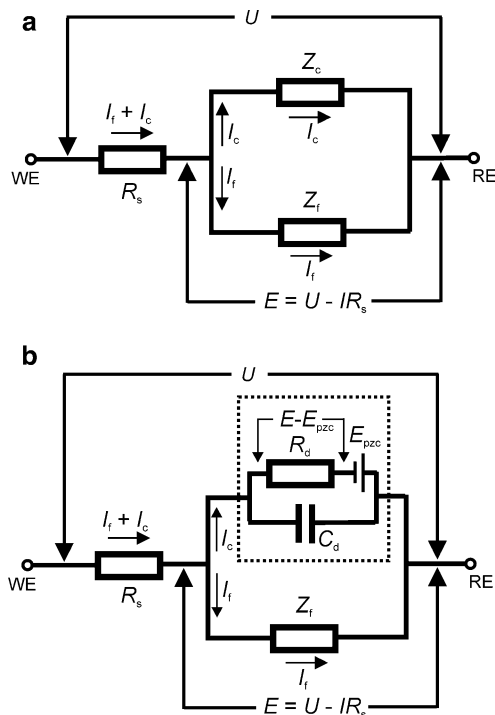


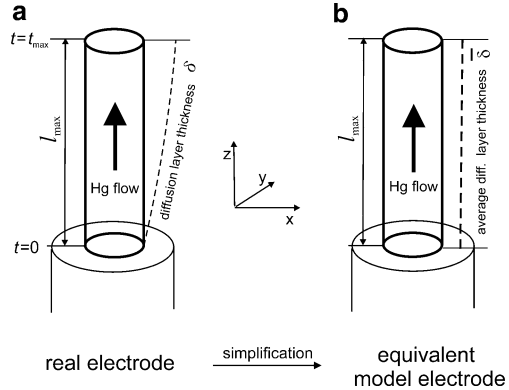
Fig. 4.47 (a) General equivalent circuit for the electrode process occurring at the streaming mercury electrode, represented by the parallel connection of the elements of the (zero-frequency for dc conditions) impedance Z_f and Z_c , associated with the flow of the faradaic I_f and capacitive I_c currents, respectively. The capacitive current I_c flows through the element of impedance Z_c even at the steady-state potential E_{ss} and in the absence of the faradaic process; (b) the equivalent circuit from figure A extended for the exemplary equivalent subcircuit (in dotted rectangle) for the complex element of an impedance Z_c : in the steady state the capacitive current flows through the resistor $R_d = (2\pi rKv)^{-1}$ to which the electrode potential E , decreased for the electromotive force E_{pzc} , is applied; r radius of the mercury stream, flowing with the velocity v . Reprinted with permission from [78], Copyright 2002 American Chemical Society

Stability analysis of the steady state requires its perturbation, so for this purpose the total capacitive current is expressed by the sum of steady-state value [Eq. (3.17)] and the term associated with the small perturbation of this steady state, characterized with the differential double layer capacity:

$$I_{c,ss} = 2\pi rK(E) \times (E - E_{pzc})v + 2\pi rI_{\max}C_d(E) \frac{dE}{dt} \quad (4.99)$$

In practice, for 2 M NaSCN, within the potential range of NDR formation for the Ni(II)–SCN[−] electroreduction, the K/C_d ratio varies from ca. 1.1 to 1.4 [79] and in calculations (especially if other simplifications are also used in the model) can be assumed as equal to 1.

Fig. 4.48 Principle of replacing the realistic streaming electrode, sketched in Part a, with its simplified model construction (Part b) of a constant (average) diffusion layer thickness [cf. Eq. (4.102)]. The diffusion transport is assumed to occur only along x direction. Reprinted from [80], Copyright 2007, with permission from Elsevier



As before, for two dynamic variables defining the system: electrode potential E and surface concentration of the reactant $c_{\text{ox}}(0, t) \equiv c_s$, one derives the following equations for their dynamics [78, 79]:

$$F[E(t), c_{\text{ox}}(0, t)] \equiv \frac{dE}{dt} = \frac{U - E}{2\pi r R_s l_{\text{max}}} \left(\frac{1}{C_d} \right) - \frac{(E - E_{\text{pzc}})v}{l_{\text{max}}} \left(\frac{K}{C_d} \right) + nFk_f c_{\text{ox}}(0, t) \left(\frac{1}{C_d} \right) \quad (4.100)$$

$$G[E(t), c_{\text{ox}}(0, t)] \equiv \frac{dc_{\text{ox}}(0, t)}{dt} = -\frac{2k_f c_{\text{ox}}(0, t)}{\bar{\delta}_N} + \frac{2D_{\text{ox}}[c_{\text{ox}}^0 - c_{\text{ox}}(0, t)]}{\bar{\delta}_N^2} \quad (4.101)$$

In Eq. (4.101), due to the variation of the diffusion-layer thickness along the mercury stream (see Fig. 4.48), its average value [cf. Eq. (3.26)] was used:

$$\bar{\delta}_N = (1/t_{\text{max}}) \int_0^{t_{\text{max}}} \delta(t) dt = (2/3) \times (\pi D_{\text{ox}} t_{\text{max}})^{1/2} = 1.21 \mu\text{m} \quad (4.102)$$

It is instructive to consider the stability of both 1D and 2D models of the present dynamical systems, remembering that 1D case can offer at most bistability (saddle–node bifurcation), and not the oscillations (Hopf bifurcation).

In **1-D case** the only dynamic variable is the electrode potential E . Then the following equation for the temporal evolution of perturbation δE was derived [78, 79]:

$$\frac{d(\delta E)}{dt} = -\frac{\delta E}{2\pi r C_d l_{\text{max}}} \left[\frac{1}{R_s} + \frac{1}{Z_f} + 2\pi r K v \right] \quad (4.103)$$

in which Z_f means now the slope of the I_f – E dependence under dc conditions, i.e., the so-called zero frequency impedance or the polarization resistance of the faradaic process. From Eq. (4.103) the following condition for the *instability* of the steady state through the saddle–node bifurcation was found:

$$\frac{1}{R_s} + \frac{1}{Z_f} + 2\pi rKv < 0 \quad (4.104)$$

or, equivalently, in terms of definition of virtual R_d resistor (4.98):

$$\frac{1}{R_s} + \frac{1}{Z_f} + \frac{1}{R_d} < 0 \quad (4.105)$$

One should note that if the electrode is nonstreaming, then $v = 0$ (or $R_d = \infty$), and conditions (4.104) or (4.105) reduce to the condition of the consequence of the saddle–node bifurcation, defined by Eq. (2.19). For the streaming electrode, the presence of $2\pi rKv$ term means that the destabilization of the steady state, for given negative slope of the I_f – E characteristics, requires higher serial resistance R_s than for the nonstreaming electrode:

$$R_s > \frac{1}{(-1/Z_f) - 2\pi rKv} = \frac{1}{(-1/Z_f) - (1/R_d)} > 0 \quad (4.106)$$

This is because the entire I – E characteristics of the process at the streaming electrode include also the capacitive baseline, i.e., the contribution from the permanently flowing capacitive current. The net negative dE/dI slope is then appropriately enhanced (in the sense of its absolute value) and therefore higher serial resistance is necessary for the onset of instability. In view of that, one concludes, based on Eq. (4.104), that in the region of negative Z_f the instability of the steady states will be switched off, if the stream velocity exceeds the critical value:

$$v > \frac{-1}{2\pi rKZ_f} \quad (4.107)$$

since then the negative slope of the I – E characteristics will be (over)compensated by the positive slope $dE/dI_c = (2\pi rKv)^{-1}$. In other words, the net dI/dE slope becomes then positive and the NDR region effectively ceases to exist.

Switching now to more realistic **2D case**, involving both Eqs. (4.100) and (4.101), one calculates the parameters of possible steady states from the condition $dE/dt = dc_{\text{ox}}/dt = 0$ in the following way. Combination of both obtained algebraic equations leads to the following nonlinear dependence:

$$\frac{U - E_{\text{ss}}}{2\pi rR_s C_d l_{\text{max}}} - \frac{(E_{\text{ss}} - E_{\text{pzc}})v}{l_{\text{max}}} \left(\frac{K}{C_d} \right) + \frac{nFk_f(E_{\text{ss}})c_{\text{ox}}^0 D_{\text{ox}}}{C_d [D_{\text{ox}} + k_f(E_{\text{ss}})\bar{\delta}_{\text{N}}]} = 0 \quad (4.108)$$

from which one can determine (as a root) the numerical value of the steady-state potential E_{ss} , and hence the corresponding steady-state concentration c_{ss} , for given values of the control parameters U and R_s . These values are then used to calculate the numerical values of the elements of the Jacobian matrix:

$$\mathbf{J} = \begin{bmatrix} a_{11} & a_{12} \\ a_{21} & a_{22} \end{bmatrix} = \begin{bmatrix} \left(\frac{\partial F}{\partial E}\right)_{ss} & \left(\frac{\partial F}{\partial c_s}\right)_{ss} \\ \left(\frac{\partial G}{\partial E}\right)_{ss} & \left(\frac{\partial G}{\partial c_s}\right)_{ss} \end{bmatrix}$$

$$= \begin{bmatrix} \frac{-1}{2\pi r R_s C_d l_{max}} - \frac{v}{l_{max}} \left(\frac{\mathbf{K}}{C_d}\right) + \frac{nF c_{ss}}{C_d} \left(\frac{dk_f}{dE}\right)_{ss} & \frac{nF k_f(E_{ss})}{C_d} \\ -\frac{2c_{ss}}{\bar{\delta}_N} \left(\frac{dk_f}{dE}\right)_{ss} & -\frac{2k_f(E_{ss})}{\bar{\delta}_N} - \frac{2D_{ox}}{\bar{\delta}_N^2} \end{bmatrix} \quad (4.109)$$

The trace Tr and the determinant Det of matrix \mathbf{J} are given by:

$$\text{Tr}(\mathbf{J}) = \frac{-1}{2\pi r R_s C_d l_{max}} - \frac{v}{l_{max}} \left(\frac{\mathbf{K}}{C_d}\right) + \frac{nF c_{ss}}{C_d} \left(\frac{dk_f}{dE}\right)_{ss} - \frac{2k_f(E_{ss})}{\bar{\delta}_N} - \frac{2D_{ox}}{\bar{\delta}_N^2} \quad (4.110)$$

$$\text{Det}(\mathbf{J}) = \left[\frac{-1}{2\pi r R_s C_d l_{max}} - \frac{v}{l_{max}} \left(\frac{\mathbf{K}}{C_d}\right) + \frac{nF c_{ss}}{C_d} \left(\frac{dk_f}{dE}\right)_{ss} \right] \left[-\frac{2k_f}{\bar{\delta}_N} - \frac{2D_{ox}}{\bar{\delta}_N^2} \right]$$

$$+ \left[\frac{nF k_f(E_{ss})}{C_d} \right] \left[\frac{2c_{ss}}{\bar{\delta}_N} \left(\frac{dk_f}{dE}\right)_{ss} \right] \quad (4.111)$$

Systematic studies of the range U and R_s parameters, for which the conditions for the saddle–node bifurcation: $\text{Det}(\mathbf{J}) = 0$ and for the Hopf bifurcation: $\text{Tr}(\mathbf{J}) = 0$ with $\text{Det}(\mathbf{J}) > 0$ were found, allowed one to construct the theoretical bifurcation diagram. Its comparison with the experimental one (Fig. 4.43), visualized for convenience again in Fig. 4.49, shows close similarities. In these calculations, the simplification $K = C_d$ was applied.

Such a quite satisfactory concordance confirms both the understanding of the electrochemical source of instabilities in the Ni(II)–SCN[−] electroreduction and the construction of the linear stability model of processes at the streaming electrode. Since no more complex dynamic behaviors were reported in the experiment, the linear stability model is sufficient to their description.

Furthermore, one can illustrate the system's dynamics through the nullclines $dE/dt = 0$ and $dc_s/dt = 0$ derived from Eqs. (4.100) and (4.101):

dE/dt nullcline:

$$c_s = \frac{1}{nF k_f(E) l_{max}} \left[C_d v (E - E_{pzc}) - \frac{U - E}{2\pi r R_s} \right] \quad (4.112)$$

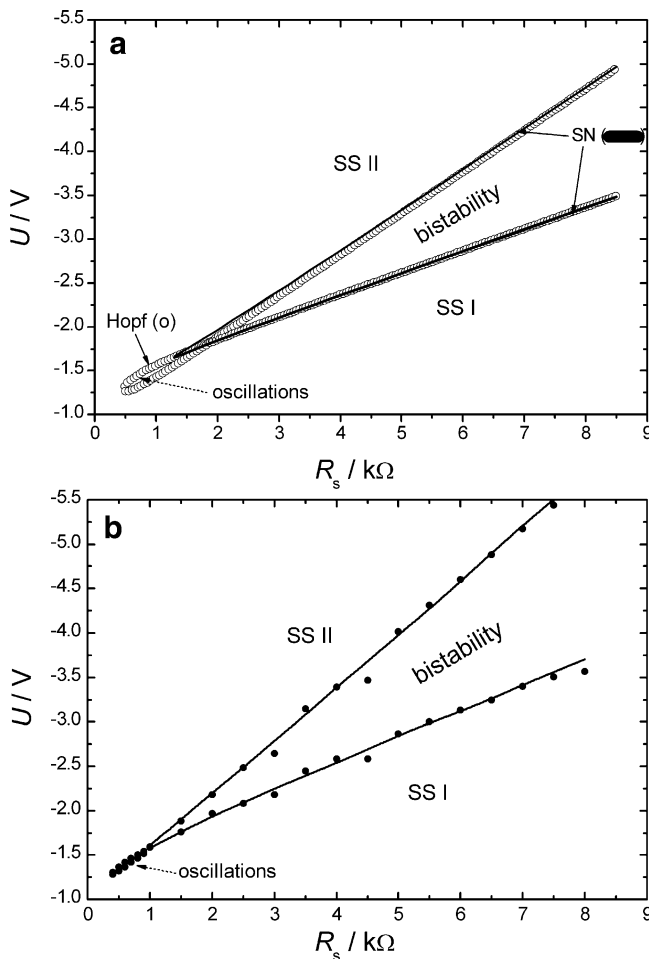


Fig. 4.49 (a) Theoretical bifurcation diagram for the Ni(II)–SCN⁻ electroreduction, corresponding to the system of differential equations (4.100) and (4.101), with $k_f(E)$ dependence given by Eq. (4.91): (solid line) points of the saddle–node bifurcation ($\text{Det}(\mathbf{J}) = 0$), (open circle) points of the Hopf bifurcation ($\text{Tr}(\mathbf{J}) = 0$ with $\text{Det}(\mathbf{J}) > 0$); (b) the corresponding experimental bifurcation diagram from Fig. 4.43. Reprinted with permission from [78]. Copyright 2002 American Chemical Society

dc_s/dt nullcline:

$$c_s = \frac{c_{\text{ox}}^0}{1 + \frac{k_f(E)\bar{\delta}_N}{D_{\text{ox}}}} \quad (4.113)$$

The exemplary, representative courses of these nullclines, for the four combinations of control parameters: U and R_s , are shown in Fig. 4.50.

Finally, as for the models described in Chaps. 1 and 2, in order to reveal the difference in time scales of both dynamical variables through the parameter ε , it is useful to represent the Eqs. (4.100) and (4.101) in dimensionless representation [78]:

$$\varepsilon \left(\frac{de}{d\tau} \right) = \frac{u - e}{\rho} - \frac{e - e_{pzc}}{\sigma} + k' \chi \quad (4.114)$$

$$\frac{d\chi}{d\tau} = (1 - \chi) - k' \chi \quad (4.115)$$

The dimensionless variables are defined as:

$$\text{Electrode potential : } e = \frac{nF}{RT} E \quad (4.116)$$

$$\text{External voltage : } u = \frac{nF}{RT} U \quad (4.117)$$

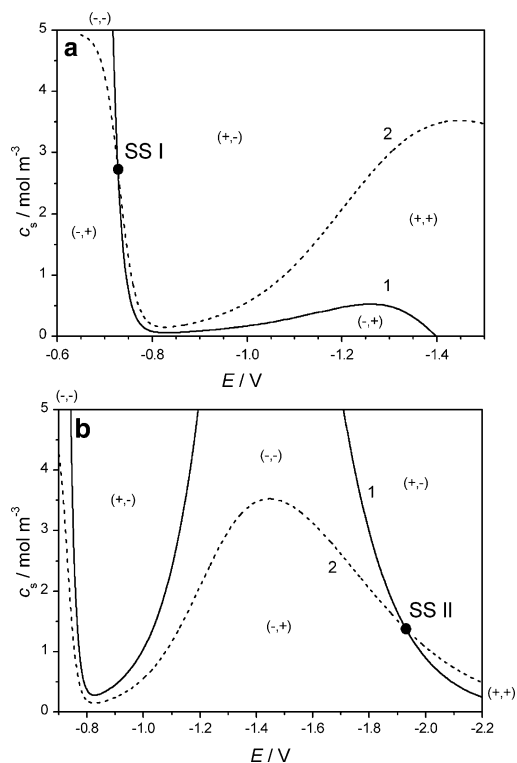


Fig. 4.50 (continued)

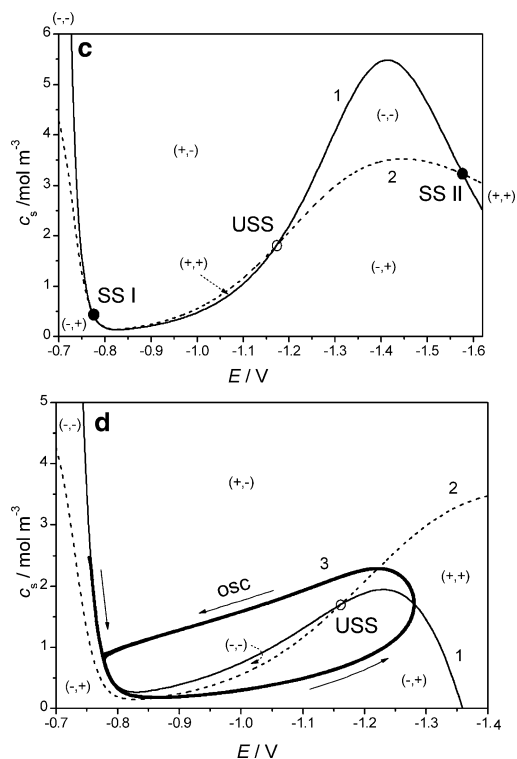


Fig. 4.50 Analysis of steady states (fixed points) of the differential equations (4.100) and (4.101) in terms of the dE/dt nullcline [Eq. (4.112), curve 1] and dc_s/dt nullcline [Eq. (4.113), curve 2]; (a) stable steady state SS I (filled circle, $E_{ss} = -0.728$ V; $c_{ss} = 2.727$ mol m^{−3}) for $U = -2$ V, $R_s = 6.0$ k Ω , (b) stable steady state SS II (filled circle, $E_{ss} = -1.930$ V; $c_{ss} = 1.381$ mol m^{−3}) for $U = -3.5$ V, $R_s = 3.0$ k Ω , (c) bistability SS I (filled circle, $E_{ss} = -0.776$ V; $c_{ss} = 0.410$ mol m^{−3})/SS II (filled circle, $E_{ss} = -1.578$ V; $c_{ss} = 3.216$ mol m^{−3}) with medium unstable steady state SS III (open circle, $E_{ss} = -1.172$ V; $c_{ss} = 1.795$ mol m^{−3}) for $U = -3.2$ V, $R_s = 5.5$ k Ω , (d) unstable steady state USS (open circle, $E_{ss} = -1.162$ V; $c_{ss} = 1.694$ mol m^{−3}) for $U = -1.425$ V, $R_s = 0.7$ k Ω , surrounded by the stable limit cycle, corresponding to sustained oscillations. The symbols in brackets, e.g., (+, −) denote the signs of the dE/dt and dc_s/dt derivatives in the appropriate regions of the plots, indicating the stability or instability of the steady state considered. Reprinted with permission from [78]. Copyright 2002 American Chemical Society

$$\text{Time : } \tau = \frac{2D_{\text{ox}}}{\delta_N^2} t \quad (4.118)$$

$$\text{Surface concentration : } \chi = \frac{c_{\text{ox}}(0, t)}{c_{\text{ox}}^0} \quad (4.119)$$

In turn, dimensionless parameters, the values of which correspond to the experimental characteristics of the Ni(II)–SCN[−] electroreduction (assuming again $K = C_d$) are defined as:

$$\varepsilon = \frac{2RTC_d}{n^2 F^2 c_{\text{ox}}^0 \bar{\delta}_N} \cong 6 \times 10^{-3} \quad (4.120)$$

$$\rho = \frac{2\pi n^2 F^2 D_{\text{ox}} c_{\text{ox}}^0 r l_{\text{max}}}{RT \bar{\delta}_N} \times R_s \cong 0.0368 \times R_s [\Omega] \quad (4.121)$$

$$\begin{aligned} \sigma &= \frac{n^2 F^2 D_{\text{ox}} c_{\text{ox}}^0 l_{\text{max}}}{RT v \bar{\delta}_N} \times \frac{1}{C_d} \\ &\cong 65.49 / C_d [\text{F m}^{-2}] = 245.28 \\ &= \frac{2\pi n^2 F^2 D_{\text{ox}} c_{\text{ox}}^0 l_{\text{max}}}{RT \bar{\delta}_N} \times R_d \end{aligned} \quad (4.122)$$

$$k' = \frac{\bar{\delta}_N}{D_{\text{ox}}} k_f \cong 1764.71 \times k_f [\text{m s}^{-1}] \quad (4.123)$$

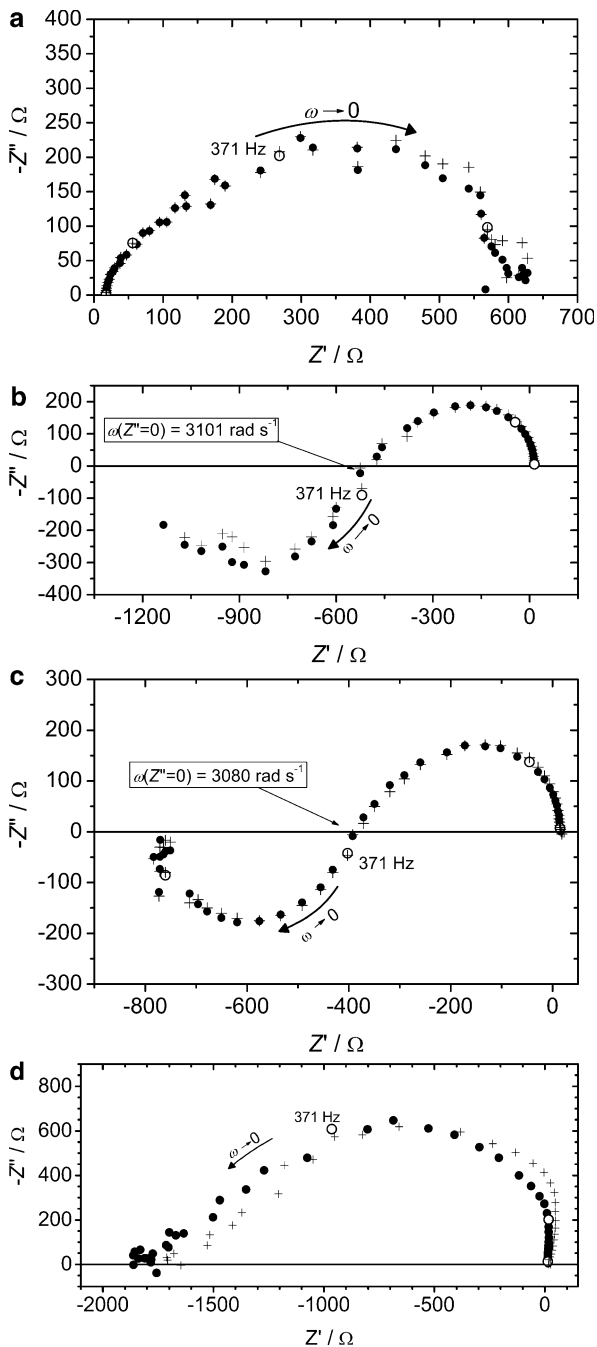
The ε parameter equal here to 0.006 shows that e (potential) is a fast variable compared to χ (surface concentration), but ε appears to be for 1–2 orders of magnitude higher than that for the instabilities studied at the nonstreaming electrodes. This is because of a very short electrolysis time at the streaming electrode which determines the appropriately small (average) Nernst diffusion layer thickness $\bar{\delta}_N$ and thus an appropriately enhanced transport. Accordingly, the stable limit cycle trajectory (cf. Fig. 4.50d) is a rather smooth curve, without straight-line sections, typical of relaxation oscillations. In fact, also in the experiment only quasi-sinusoidal oscillations of the current were reported (Fig. 4.40). The tiny region of the oscillations in the bifurcation diagram suggests that they are almost at the limit of existence. If the rate of the electrode process were only a bit lower, the (then relatively faster) transport could suppress the oscillations. Such a case will be described in the next section devoted to the electroreduction of azide complexes of nickel(II).

4.4.3.4 Impedance Studies of Ni(II)–SCN[−] Electroreduction

In order to complete the experimental characteristics of instabilities in the electroreduction of Ni(II)–SCN[−] complexes at the streaming mercury electrode, we shall briefly review its impedance studies, performed by Jurczakowski and Orlik [80]. Theoretical description of the impedance response of such an electrode type was given in Sect. 3.2. Figure 4.51 shows representative impedance spectra of the Ni(II)–SCN[−] system, recorded for four dc potentials that correspond to various regions of the dc steady-state I – E characteristics from Fig. 4.39, including the NDR region.

The spectrum in Fig. 4.51a, corresponding to the electrode potential, at which the slope of the I – E characteristics is still positive, exhibits a shape typical of the Butler–Volmer kinetics at the streaming electrode. In figures (b) and (c), the region of negative real impedance manifests themselves in line with the potential region of the occurrence of NDR on the dc curve. Thus, for both $E = -1.05$ V and -1.1 V

Fig. 4.51 Exemplary experimental impedance spectra (Nyquist diagrams) (*filled circle*) and their Kramers–Kronig transforms (+) of the Ni(II)–SCN⁻ electroreduction at the streaming mercury electrode, for zero serial external resistance R_s and various dc potentials: (a) -0.80 V, (b) -1.05 V, (c) -1.10 V, (d) -1.30 V. Applied frequency range: $f = \omega / 2\pi = 50$ Hz to 100 kHz. *Open symbols* represent impedances for the frequencies differing for the decade. Reprinted from [80], Copyright 2007, with permission from Elsevier



the real impedance axis is crossed, at its negative side, for nonzero frequency (ω_H) which means, according to Sect. 3.3.2, a Hopf bifurcation which will occur, if we insert in the circuit the serial resistance of the magnitude compensating the negative real impedance indicated by the cross-section. Furthermore, for frequencies lower than ω_H and tending to zero, the plot aims to cross the real impedance axis at more negative values which case, in turn, indicates the saddle–node bifurcation, leading to bistability. Finally, Fig. 4.51d shows the possibility of only saddle–node bifurcation, as the zero imaginary impedance occurs only for $\omega \rightarrow 0$.

Based on these impedance diagrams, one can thus determine the serial resistances R_s necessary to destabilize the system through the Hopf and saddle–node bifurcations. From the steady-state dc I – E curve one finds the steady-state current I_{ss} corresponding to each potential E , for which the given impedance spectrum was collected. The product of I_{ss} and R_s , added to E , yields the external voltage U that should be applied in order to achieve the bifurcation point, and the pair of (U, R_s) values determines its position on the stability diagram. In this way, one can reconstruct the full stability diagram that should be concordant with the one obtained from dc measurements. Figure 4.52 shows partial reproduction of this diagram in the region of oscillations and adjacent region of bistability compared with the analogous diagrams determined from dc measurements and theoretical calculations (cf. Figs. 4.43 and 4.49).

In terms of the model of the impedance response of the streaming electrodes, described in Sect. 3.2, one can calculate the theoretical shapes of the impedance spectra for the Ni(II)–SCN[−] electrochemical system, based on the equivalent circuit shown in Fig. 3.7, the expressions (3.33)–(3.36), and the dependence of the rate constant k_f on the electrode potential, defined by Eq. (4.91). The concentrations of Ox and Red were calculated as the single values averaged over the entire streaming electrode, according to Eqs. (3.27) and (3.28). The calculated Nyquist diagrams appeared to be reasonably well concordant with the theoretical ones. A better concordance between the theoretical and experimental dependences was observed for the phase angle Bode plots [80]. Anyhow, the theoretical model of the impedance of processes at the streaming electrodes is in this way at least semiquantitatively confirmed. Further details of the experimental procedure and theoretical calculations can be found in the original paper [80].

4.5 Tristability in the Ni(II)–N₃[−] System

4.5.1 Two N–NDR Regions as a Source of Tristability

It seems natural to compare the electroreduction of the Ni(II)–SCN[−] complexes with the electroreduction of Ni(II) complexes with other pseudohalogenide ligand—the azide anion. Such studies were performed by Jurczakowski and Orlik [81] using again the streaming Hg electrode which was earlier successfully applied to the Ni(II)–SCN[−] system. First, one has to recognize the form in which Ni(II) exists in

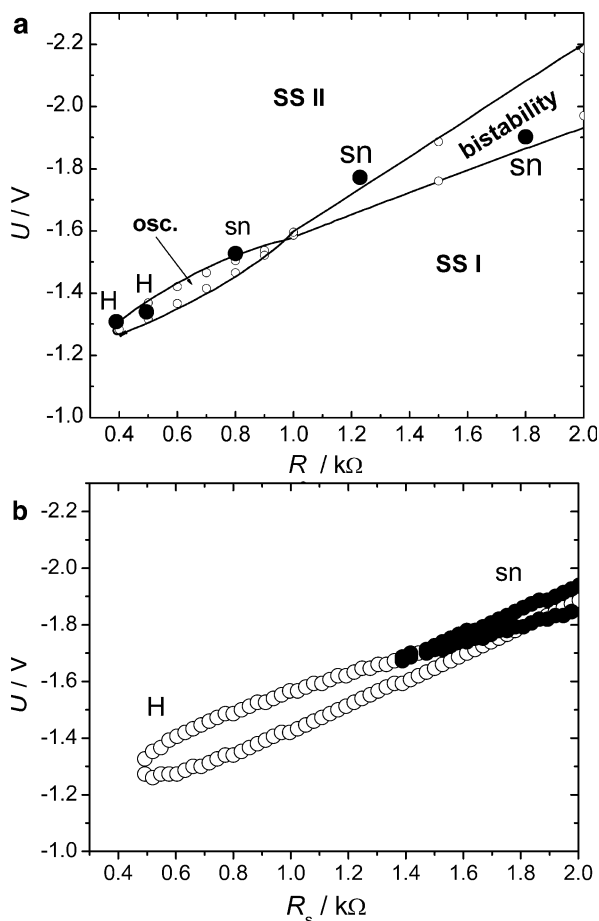


Fig. 4.52 (a) Comparison of the course of the *experimental* bifurcation diagram for the Ni(II)–SCN[−] electroreduction obtained from dc measurements (points “open circle” were connected with *solid line* for better visualization of the diagram shape) with the selected points of the Hopf (*filled circle*, H) and saddle–node bifurcations (*filled circle*, sn) determined from the experimental impedance spectra shown in Fig. 4.51b–d. SSI and SSII stand for the stable steady states coexisting in bistable regime; (b) the respective enlarged fragment of the *theoretical* bifurcation diagram showing the cusp of the saddle–node bifurcation points (*filled circle*), partially overlapping with the loop of a Hopf bifurcation points (*open circle*). Slight discrepancies in the loop size and the cusp position in (a) and (b) are caused by the simplification of the model, but their relative position is similar. Reprinted from [80], Copyright 2007, with permission from Elsevier

the presence of excess azides. Based on literature studies [82–84] one concludes that in the solution of a few mM Ni(ClO₄)₂ and 2 M NaN₃ most of nickel(II) ions are present in the form of anionic [Ni(N₃)₄]^{2−} complex, while for 1 M NaN₃ some amounts of Ni(N₃)₂ and Ni(N₃)⁺ also coexist. A simple mixing of Ni(ClO₄)₂ and NaN₃ solutions yields, however, a slightly turbid solution which also produces

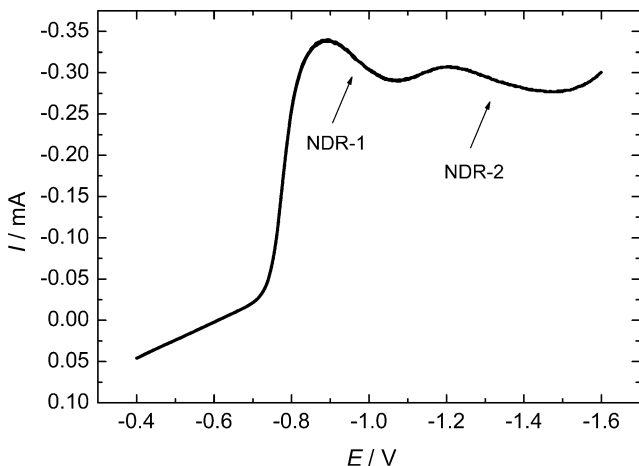


Fig. 4.53 Current–potential (I – E) dependence for the sample of an initial composition: $4.0 \text{ mmol dm}^{-3} \text{ Ni}(\text{ClO}_4)_2 + 2.0 \text{ mol dm}^{-3} \text{ NaN}_3 + 12 \text{ mmol dm}^{-3} \text{ HClO}_4$, recorded at the streaming mercury electrode for zero serial resistance ($R_s = 0$) in the circuit of the working electrode. The regions of the negative differential resistance (NDR, $dE/dI < 0$) starting from ca. -0.85 V are distorted by the extra faradaic current which leads to the formation of two (NDR-1, NDR-2) sequential regions of negative resistance. Parameters of the streaming electrode: capillary flow $m = 212 \text{ mg s}^{-1}$, internal glass capillary (= cylindrical mercury electrode) diameter $\phi = 0.11 \text{ mm}$, length of mercury jet (directed upward) $l_{\text{max}} = 2.85 \text{ mm}$. Reprinted partly with permission from [81]. Copyright 2003 American Chemical Society. Due to volatility of HN_3 the given concentrations are the initial ones; the true concentration of N_3^- , as well as of H^+ can therefore be slightly lower

irregular and irreproducible electrochemical response. An addition of small amount of HClO_4 is necessary to make the sample transparent. This obvious procedure produces a solution, the electrochemical characteristics of which appear to be particularly interesting, depending on the composition of the sample. One should only note that the exact concentrations of azide species are difficult to control since during the prolonged deaeration of the sample with nitrogen or argon, some amount of volatile HN_3 , formed upon acidification with HClO_4 , leaves the solution. It is however possible to find such conditions in which either only single or even two sequential N-NDR regions form on the steady-state I – E curve recorded at a streaming mercury electrode. The latter case is shown in Fig. 4.53.

Figure 4.53 immediately implies the possibility of not only bistability, but also of rather rarely experimentally reported phenomenon of **tristability**. The conditions of occurrence of mono-, bi-, and tristability, depending on the external voltage, for given fixed serial resistance R_s , are clearly explained by the schematic Fig. 4.54, in which the moving load line crosses such I – E characteristics with two successive region of the negative differential resistance.

Accordingly, insertion of the appropriate serial resistance to the circuit with the I – E characteristics from Fig. 4.53 allowed to record both the bistable and tristable behavior (see Fig. 4.55).

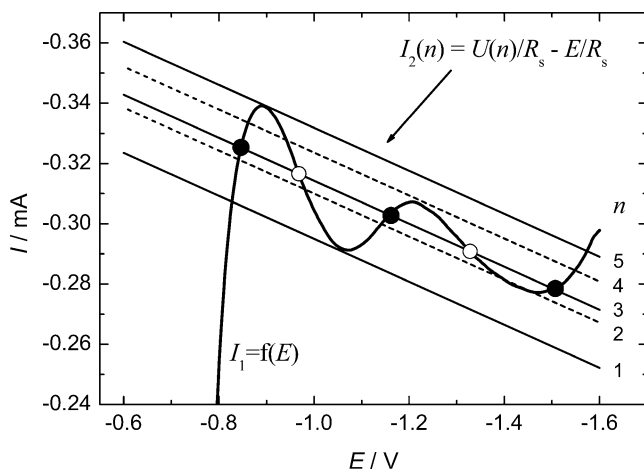


Fig. 4.54 The intersections of the enlarged part of the experimental N -shaped characteristics from Fig. 4.53 [denoted here as $I_1 = f(E)$] with the load line $I_2 = (U - E)/R_s$, explaining the occurrence of tristability and bistability, for the exemplary constant serial $R_s = 14 \text{ k}\Omega$ and different externally applied voltages U : (1) -5.130 V , (2) -5.340 V , (3) -5.400 V , (4) -5.531 V , (5) -5.646 V . As an example, for the load line (3) the associated stable (filled circle) and unstable (open circle) steady states were indicated. Reprinted with permission from [81]. Copyright 2003 American Chemical Society

Systematic studies for varying U and R_s led to the experimental bifurcation diagram shown in Fig. 4.56 which also does not contain any oscillatory region. In fact, the oscillations were not found for the Ni(II)-N₃⁻ electroreduction for any experimental conditions, also even if only single N-NDR region was formed on the steady-state I - E characteristics.

4.5.2 The Source of Two N-NDR Regions in the Ni(II)-N₃⁻ Electroreduction

For the understanding of the origin of tristability, one has to establish the electrochemical mechanism underlying the formation of the steady-state characteristics in Fig. 4.53. The formation of the first region of the negative differential resistance (NDR-1) can be understood in terms of the mechanism analogous to that operating for both Ni(II)-SCN⁻ and In(III)-SCN⁻ electroreduction. This means that this part of the curve visualizes the electroreduction of Ni(II) to nickel amalgam, electrocatalyzed by adsorbed N₃⁻ ions, the surface concentration of which decreases with increasing negative charge of the mercury electrode. The formation of the second NDR region (NDR-2) is more sophisticated. Jurczakowski and Orlik [85] have shown that in the complex particle $[\text{Ni}(\text{N}_3)_p]^{(2-p)+}$ not only the central ion is electroactive, but also, at more negative potentials, the coordinated azide ligands, provided that excess H⁺ ions

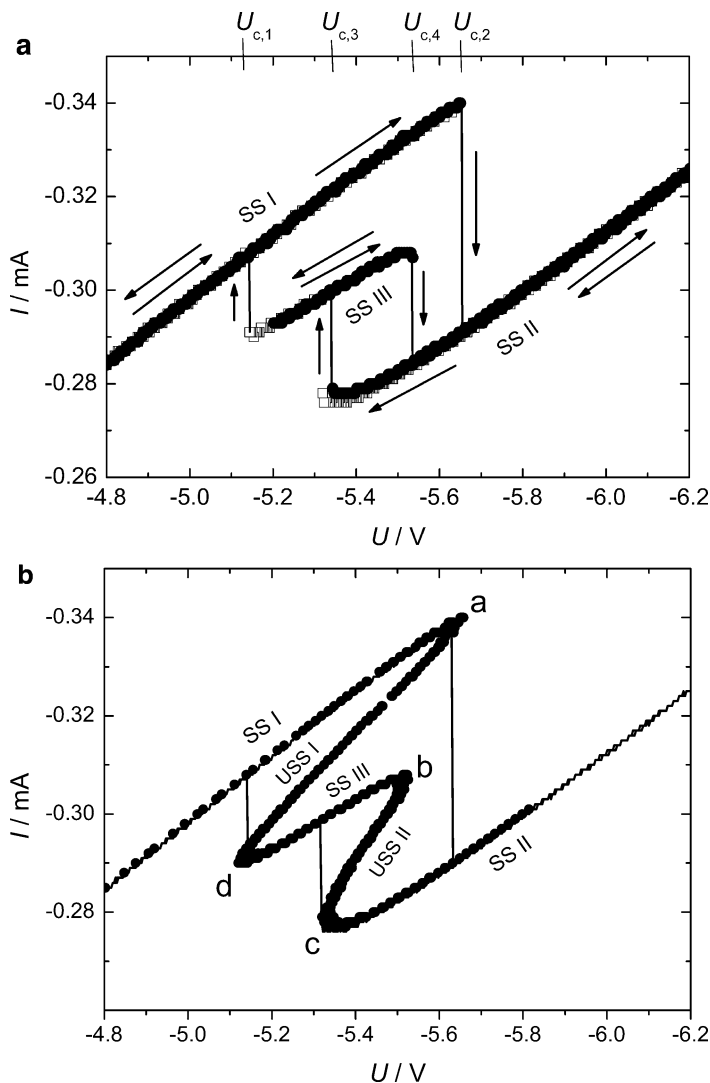


Fig. 4.55 (a) Bistable and tristable behaviors for the electroreduction of the azide complexes of nickel(II) at a streaming mercury electrode. Tristability manifests itself as the complex scheme of hysteresis, indicating the coexistence of sets of SS I, SS II, and SS III stable steady states for the same control parameter (U), for the exemplary constant serial resistance $R_s = 14$ k Ω ; (b) the corresponding full diagram of stable (SS I, SS II, SS III) and unstable (USS I, USS II) steady states obtained by translation, along the voltage axis, of the I - E curve from Fig. 4.53 for the actual ohmic drops IR_s ; symbols (a, b, c, d) denote the edges of the folds at which the monostable/bistable and bistable/tristable transitions occur, for comparison with the experimental stability (bifurcation) diagram in Fig. 4.56. Reprinted with permission from [81]. Copyright 2003 American Chemical Society

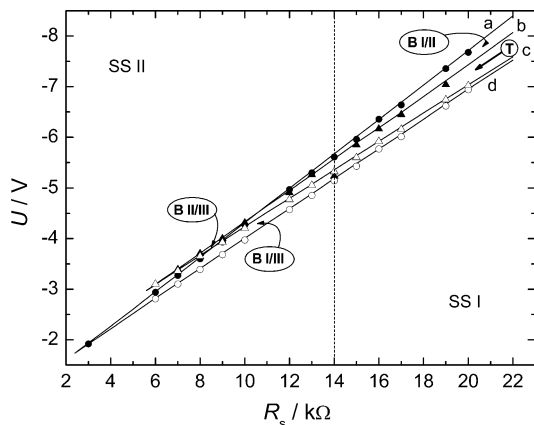


Fig. 4.56 The experimental stability (bifurcation) diagram of the monostable, bistable (**B I/II**, **B I/III**, **B II/III**), and tristable (**T**) regions involving stable steady states SS I, SS II, SS III for the electroreduction of azide complexes of nickel(II), represented by I – E characteristics from Fig. 4.53. The (a, b, c, d) symbols at the corresponding lines refer to edges of folds in Fig. 4.55b, the positions of which on the voltage axis determine the borderlines of the monostable/bistable and bistable/tristable transitions (saddle–node bifurcations). The vertical dotted line at $R_s = 14$ k Ω indicates such transitions as shown in Fig. 4.55. Reprinted with permission from [81]. Copyright 2003 American Chemical Society

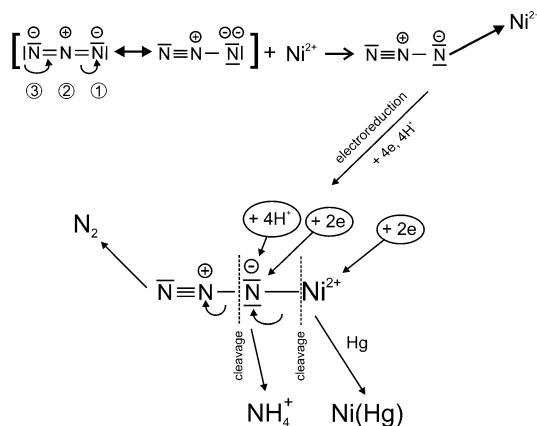


Fig. 4.57 Possible molecular mechanism of $[\text{NiN}_3]^+$ electroreduction explaining the formation of ammonium cations (ammonia) and molecular nitrogen N_2 in the presence of a sufficient amount of H^+ ions. Reprinted from [85], Copyright 2005, with permission from Elsevier

are present in the sample which are required to form ammonia as one of the products. In other words, the azide ligands linked to Ni(II) ions become reducible (although in the unbound state they are hardly reducible on mercury), with the formation of (experimentally detectable) NH_3 (or NH_4^+ ions) (see Fig. 4.57).

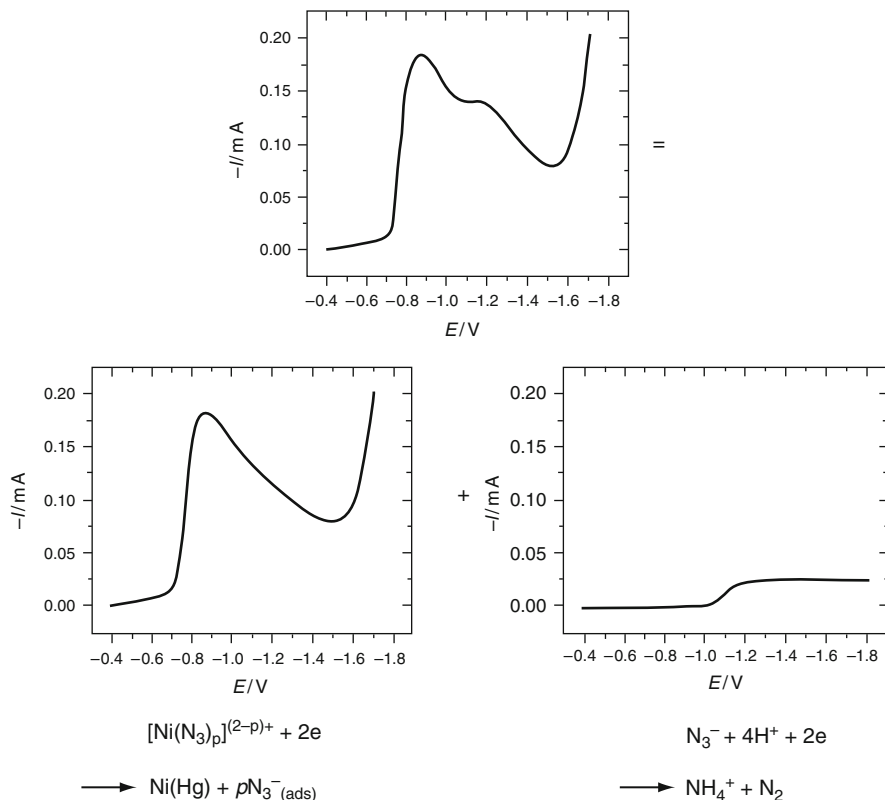


Fig. 4.58 Schematic representation of the $I-E$ curve from Fig. 4.53 (top) as the superposition of the electroreduction of Ni(II) catalyzed by adsorbed N_3^- ions (bottom left) and of the electroreduction of a small fraction of coordinated N_3^- ligands (bottom right), controlled by the amount of $HClO_4$ added. The two consecutive N-NDR regions are thus formed by the single N-NDR region of the first process, disturbed by a small postwave of the second process

For the explanation of the shape of $I-E$ curve from Fig. 4.53 it is crucial to note that the amount of H^+ (as $HClO_4$) added to the sample was relatively small, so the electroreduction of only *small fraction* of coordinated azide ligands was possible. Therefore, this electroreduction manifested itself as only a small postwave overlapping with the NDR-1 region. This deformation of the NDR-1 region resulted in the formation of two regions of negative differential resistance. The schematic decomposition of the full $I-E$ curve into the respective components is shown in Fig. 4.58.

Finally, the rise of the current following both NDR regions is presumably caused by the noncatalyzed electroreduction of Ni(II) to nickel amalgam which in this case occurs with lower overpotential than for the $Ni(II)-SCN^-$, so the current minimum is not as deep as in the latter case. One concludes that the electrochemical mechanism responsible for the steady-state $I-E$ characteristics, leading further to tristability is largely recognized. It is quite interesting that a single complex

molecule offers a possibility of two electrochemical processes, the overlapping of which leads to two regions of negative differential resistance.

Accordingly, one can construct the theoretical model [81] of the [Ni(N₃)_p]^{(2-p)+} electroreduction as involving two parallel processes engaging complex species [Ox₁ + Ox₂], consisting of Ox₁ ≡ Ni(II) and Ox₂ ≡ coordinated *protonated* N₃[−] ligand:



The total steady-state faradaic current at given potential is thus generally a potential-dependent sum of contributions from the Ox₁ and Ox₂ electroreductions:

$$I_{f,ss} = -2\pi r n F v \times \left\{ c_{\text{ox},1}^0 k_{f,1} \left[\frac{2}{\kappa_1} \sqrt{\frac{t_{\text{max}}}{\pi}} + \frac{\exp(\kappa_1^2 t_{\text{max}}) \text{erfc}(\kappa_1 t_{\text{max}}^{1/2}) - 1}{\kappa_1^2} \right] \right. \\ \left. + c_{\text{ox},2}^0 k_{f,2} \left[\frac{2}{\kappa_2} \sqrt{\frac{t_{\text{max}}}{\pi}} + \frac{\exp(\kappa_2^2 t_{\text{max}}) \text{erfc}(\kappa_2 t_{\text{max}}^{1/2}) - 1}{\kappa_2^2} \right] \right\} \quad (4.126)$$

with $n = n_1 = n_2 = 2$, and the kinetic parameters κ_1, κ_2 expressing the ratio of the charge-transfer rate to the diffusion transport rate:

$$\kappa_1 = \frac{k_{f,1}}{D_{\text{ox},1}^{1/2}} + \frac{k_{b,1}}{D_{\text{red},1}^{1/2}} \quad (4.127)$$

$$\kappa_2 = \frac{k_{f,2}}{D_{\text{ox},2}^{1/2}} \quad (4.128)$$

Of course, since Ox₁ and Ox₂ are the components of the same molecule, $D_{\text{ox},1} = D_{\text{ox},2}$. In order to generate the first and, in consequence, the second NDR region on the I – E curve, the following dependence of the charge-transfer rate constants on the electrode potential was assumed:

$$k_{f,1} = k_{s,1}^{\text{app}} \left\{ \frac{1}{1 + \exp[P_1(E - P_2)]} \right\} \exp[-(\alpha n)_I f(E - E_{f,1}^0)] \\ + k_{s,II}^{\text{app}} \exp[-(\alpha n)_{II} f(E - E_{f,1}^0)] \quad (4.129)$$

$$k_{b,1} = k_{f,1} \exp[nf(E - E_{f,1}^0)] \quad (4.130)$$

$$k_{f,2} = k_{s,2}^{\text{app}} \exp[-(\alpha n)_2 f(E - E_{f,2}^0)] \quad (4.131)$$

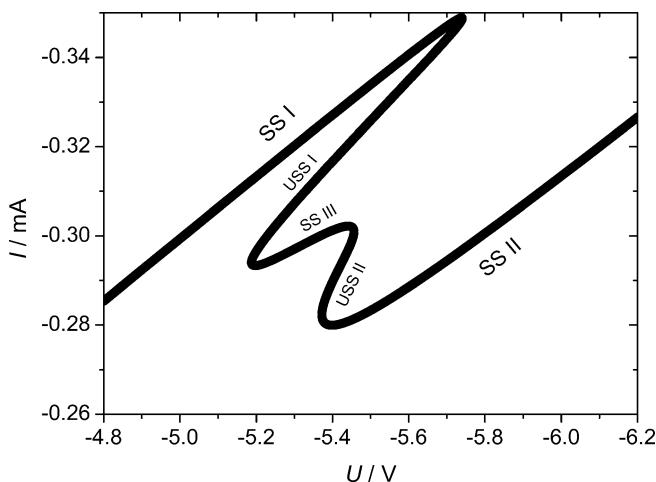


Fig. 4.59 Theoretically calculated folded diagrams of stable and unstable multiple steady states for the model (4.124, 4.125) electrochemical system: bistable and tristable behavior for the I - E characteristics from Fig. 4.53, with serial resistance $R_s = 14$ k Ω (cf. Fig. 4.55b). Reprinted in part with permission from [81]. Copyright 2003 American Chemical Society

and, for simplification: $k_{b,2} = 0$ (meaning neglected reversed anodic process of azide reduction products at high negative overpotential). Numerical values of all the parameters were found by fitting the theoretical I - E dependence to the respective experimental I - E curve from Fig. 4.53. Then, by introducing the appropriate ohmic resistance and constructing the diagram in the coordinate system I - U , one can obtain theoretical folded diagrams of steady states, exhibiting bistability and tristability, quite well concordant with experimentally determined shapes (Fig. 4.59). This concordance confirms the validity of the model description of the $\text{Ni(II)}\text{-N}_3^-$ electroreduction at the streaming mercury electrode.

In terms of this model electrochemical mechanism, one can now perform the stability analysis which should confirm the existence of bistable and tristable behavior. Also, this analysis should answer the question, whether for the studied system the oscillatory behavior is possible but was only not found in the experiment or it is completely excluded for fundamental dynamic reasons.

4.5.3 Linear Stability Analysis of the $\text{Ni(II)}\text{-N}_3^-$ Electroreduction

Compared to analogous approach presented in Sect. 4.4.3 for the $\text{Ni(II)}\text{-SCN}^-$ electroreduction, now, in addition to the dynamics of the electrode potential, the surface dynamics of the concentrations of *two* reactants: $c_{\text{ox},1}$ and $c_{\text{ox},2}$ have to be considered. Although Ox_1 and Ox_2 are the components of the same complex species, which diffuse in the solution together with the same diffusion coefficient, they react electrochemically with different rates at given potential, and this is the reason for which their surface concentrations vary differently. In this way,

the dynamical system acquires the third dimension which theoretically opens a possibility of complex dynamical behaviors, but in the experiments only saddle-node bifurcations were detected.

According to the above electrochemical reaction mechanism, the following three ordinary differential equations, defining the present dynamic system, were derived [81]:

$$F[E, c_{\text{ox},1}(0, t), c_{\text{ox},2}(0, t)] \equiv \frac{dE}{dt} = \frac{U - E}{2\pi r R_s K l_{\text{max}}} - \frac{(E - E_{\text{pzc}})v}{l_{\text{max}}} + \frac{nFk_{f,1}c_{\text{ox},1}(0, t)}{K} + \frac{nFk_{f,2}c_{\text{ox},2}(0, t)}{K} \quad (4.132)$$

$$G[E, c_{\text{ox},1}(0, t)] \equiv \frac{dc_{\text{ox},1}(0, t)}{dt} = -\frac{2k_{f,1}c_{\text{ox},1}(0, t)}{\bar{\delta}_N} + \frac{2D_{\text{ox},1}[c_{\text{ox},1}^0 - c_{\text{ox},1}(0, t)]}{\bar{\delta}_N^2} \quad (4.133)$$

$$H[E, c_{\text{ox},2}(0, t)] \equiv \frac{dc_{\text{ox},2}(0, t)}{dt} = -\frac{2k_{f,2}c_{\text{ox},2}(0, t)}{\bar{\delta}_N} + \frac{2D_{\text{ox},2}[c_{\text{ox},2}^0 - c_{\text{ox},2}(0, t)]}{\bar{\delta}_N^2} \quad (4.134)$$

In these equations, for further simplification, the differential double layer capacity C_d was assumed constant and equal to the integral double layer capacitance K (25.7 $\mu\text{F cm}^{-2}$) at certain potential within the first NDR region. The corresponding (3 \times 3) Jacobian matrix was determined, in which, in order to enhance legibility, any surface concentrations of Ox₁ and Ox₂ (variables) were denoted as $c_{s,1}$ and $c_{s,2}$, whereas these concentrations at the steady state—as $c_{ss,1}$ and $c_{ss,2}$, respectively:

$$\mathbf{J} = \begin{bmatrix} \left(\frac{\partial F}{\partial E}\right)_{ss} & \left(\frac{\partial F}{\partial c_{s,1}}\right)_{ss} & \left(\frac{\partial F}{\partial c_{s,2}}\right)_{ss} \\ \left(\frac{\partial G}{\partial E}\right)_{ss} & \left(\frac{\partial G}{\partial c_{s,1}}\right)_{ss} & \left(\frac{\partial G}{\partial c_{s,2}}\right)_{ss} \\ \left(\frac{\partial H}{\partial E}\right)_{ss} & \left(\frac{\partial H}{\partial c_{s,1}}\right)_{ss} & \left(\frac{\partial H}{\partial c_{s,2}}\right)_{ss} \end{bmatrix} = \begin{bmatrix} -\frac{1}{2\pi r R_s K l_{\text{max}}} - \frac{v}{l_{\text{max}}} + \frac{nF c_{ss,1}}{K} \left(\frac{dk_{f,1}}{dE}\right)_{ss} + \frac{nF c_{ss,2}}{K} \left(\frac{dk_{f,2}}{dE}\right)_{ss} & \frac{nF k_{f,1}(E_{ss})}{K} & \frac{nF k_{f,2}(E_{ss})}{K} \\ -\frac{2c_{ss,1}}{\bar{\delta}_N} \left(\frac{dk_{f,1}}{dE}\right)_{ss} & -\frac{2k_{f,1}(E_{ss})}{\bar{\delta}_N} - \frac{2D_{\text{ox},1}}{\bar{\delta}_N^2} & 0 \\ -\frac{2c_{ss,2}}{\bar{\delta}_N} \left(\frac{dk_{f,2}}{dE}\right)_{ss} & 0 & -\frac{2k_{f,2}(E_{ss})}{\bar{\delta}_N} - \frac{2D_{\text{ox},2}}{\bar{\delta}_N^2} \end{bmatrix} \quad (4.135)$$

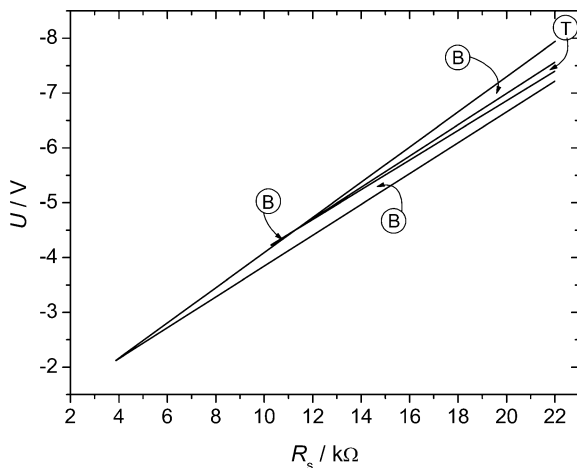


Fig. 4.60 Theoretical bifurcation diagram corresponding to the I - E characteristics from Fig. 4.53, showing the regions of bi- and tristability, denoted with letters B and T, respectively. The lines separating different regions correspond to the saddle-node bifurcations. The Hopf bifurcations were not detected, which confirms the experimentally observed lack of oscillations. Reprinted with permission from [81]. Copyright 2003 American Chemical Society

Based on criteria of the saddle-node and Hopf bifurcation for the 3D system, the theoretical bifurcation diagrams for various experimental I - E courses (composition of the samples) were calculated. Figure 4.60 shows the diagram corresponding to the experimental diagram from Fig. 4.56.

The striking similarity between this and the experimental diagrams manifests itself in the position of the points of saddle-node bifurcations, determining the regions of mono-, bi-, and tristability. Also, it is remarkable that the theoretical bifurcation diagrams do not contain the points of the Hopf bifurcations, so they exclude the birth of oscillations, at least according to this scenario. One can judge that under conditions of the measurement at the streaming mercury electrode, the rate of transport of reactant is too fast, compared to the charge-transfer rate of the $\text{Ni(II)}-\text{N}_3^-$ system, so the latter process is thus too slow to be able to drive the system away from the steady state in an oscillatory manner. Already for the $\text{Ni(II)}-\text{SCN}^-$ electroreduction, characterized with the standard rate constant of electron transfer $k_s = 10^{-3} \text{ cm s}^{-1}$ [60], oscillations occurred in a very tiny region of (U, R_s) control parameters. Since for $\text{Ni(II)}-\text{N}_3^-$ the standard rate constant $k_{s,1}$ was found to be much lower: $5.6 \times 10^{-5} \text{ cm s}^{-1}$ [82], the above argumentation is at least semiquantitatively confirmed.

4.5.4 Impedance Studies of the $\text{Ni(II)}-\text{N}_3^-$ Electroreduction

Similarly as for the $\text{Ni(II)}-\text{SCN}^-$ system, one can complement dc studies of instabilities in the $\text{Ni(II)}-\text{N}_3^-$ electroreduction at the streaming Hg electrode with the relevant impedance characteristics, studied by Orlik and Jurczakowski [86].

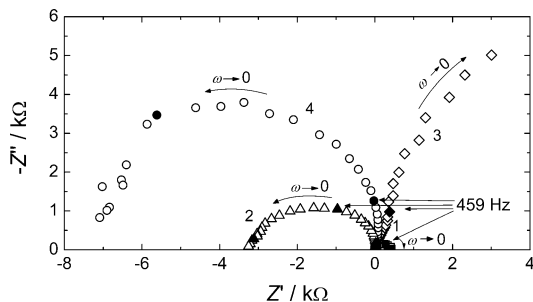


Fig. 4.61 Exemplary impedance spectra for the Ni(II)–N₃[−] electrode processes at the streaming Hg electrode at various electrode potentials: (1) −0.8 V; (2) −0.95 V, (3) −1.20 V, (4) −1.40 V. Points represented by full symbols correspond to impedances for the frequencies differing for the decade. Reprinted from [86]. Copyright 2008, with permission from Elsevier

Figure 4.61 shows a set of typical impedance spectra recorded for this process which should be confronted with Fig. 4.53, showing the dc steady-state I – E dependence measured under identical conditions.

Evidently curves 2 and 4, corresponding to NDR regions on the dc I – E curves, exhibit negative real impedance. However, compared to analogous spectra for the Ni(II)–SCN[−] system, the real negative impedance axis is attained only at ac frequency $\omega \rightarrow 0$ which fact means that only the saddle node, and not the Hopf bifurcation, can occur in this system under appropriate conditions (i.e., upon insertion of appropriate serial resistance R_s). This conclusion, drawn here from impedance spectra, is of course fully consistent with the experimentally observed lack of oscillations for this system, confirmed also by theoretical linear stability analysis of the dc characteristics.

Theoretical model of these Nyquist plots was constructed based on the assumptions which were partly invoked already when discussing the dc conditions [cf. Eqs. (4.124)–(4.128)]. In view of the concept of the effective mean diffusion layer thickness (cf. Fig. 4.48), the surface concentrations of Ox₁, Red₁, Ox₂, and Red₂ species, averaged over the entire length of the streaming electrode, were calculated according to Eqs. (3.30) and (3.31). In the equivalent circuit (Fig. 3.7), the sum of faradaic currents, originating from the central ion and the ligand electroreductions, was expressed in terms of parallel connection of two faradaic impedances: one related to Ni(II) electroreduction: $Z_1 \equiv Z_f(\text{Ni}) = R_{ct}(\text{Ni}) + Z_w(\text{Ni})$ and the other one—to the N₃[−] electroreduction: $Z_2 \equiv Z_f(\text{N}_3^-) = R_{ct}(\text{N}_3^-) + Z_w(\text{N}_3^-)$ (Fig. 4.62).

Accordingly, for every redox couple Ox₁/Red₁ and Ox₂/Red₂, the individual charge-transfer resistances $R_{ct,1}$ and $R_{ct,2}$ were calculated using Eq. (3.32), and Warburg impedances using Eqs. (3.34)–(3.36). The total impedance of the Ni(II)–N₃[−] system was expressed by the following dependence (for notation of particular quantities, see Sect. 3.2):

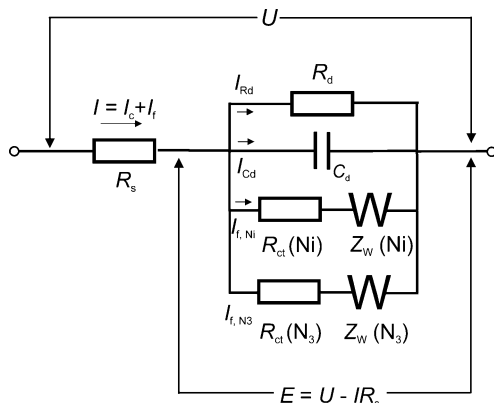


Fig. 4.62 Equivalent circuit for the impedance response in the Ni(II)–N₃ electroreduction. R_s serial solution resistance, R_{ct} charge-transfer resistance, Z_w mass-transfer (Warburg) impedance, C_d differential double layer capacity per unit area, $R_d = (2\pi r C_d \nu)^{-1}$ —the virtual resistance, where r is the mercury stream radius and ν is the mercury flow velocity. Reprinted from [86], Copyright 2008, with permission from Elsevier

$$\begin{aligned}
 Z &= R_s + [Z_f(\text{Ni})^{-1} + Z_f(\text{N}_3)^{-1} + X_c^{-1} + R_d^{-1}]^{-1} \\
 &= R_s + \left\{ [R_{ct,1} + G_{ox,1} + G_{red,1} + j(H_{ox,1} + H_{red,1})]^{-1} \right. \\
 &\quad + [R_{ct,2} + G_{ox,2} + G_{red,2} + j(H_{ox,2} + H_{red,2})]^{-1} \\
 &\quad \left. + \left(\frac{1}{j\omega AC_d} \right)^{-1} + 2\pi r C_d \nu \right\}^{-1} \quad (4.136)
 \end{aligned}$$

Theoretical spectra, calculated from Eq. (4.136) indicated the possibility of only saddle–node bifurcations, but excluded Hopf bifurcations, as Fig. 4.63 illustrates. These spectra show reasonable concordance with experimental ones from Fig. 4.61 and, what is most important, predict the same type of bifurcation.

Besides the diagnosis of nonlinear dynamic behaviors, the combination of dc and ac techniques, supported by the above model calculations, allowed also to determine the following characteristics of the redox process of the coordinated azide ligand: formal potential $E_f^0 = -1.113 \pm 0.004$ V (vs. SCE), standard heterogeneous rate constant $k_s = (3.51 \pm 0.38) \times 10^{-2}$ cm s⁻¹, cathodic transfer coefficient (αn) = 0.513 ± 0.040 . For the multistep n -electron transfer, with a single i th rate determining step characterized with a transfer coefficient α_i (equal to 0.5 for symmetrical activation barrier in the adiabatic process), the experimentally available generalized cathodic transfer coefficient (αn) is defined as [4]: $\alpha n = i - 1 + \alpha_i$. Hence one concludes that $i = 1$, i.e., the transfer of the first electron is the rate determining step, and the following mechanism of the

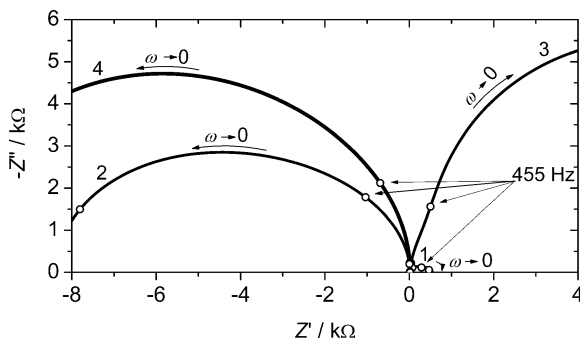
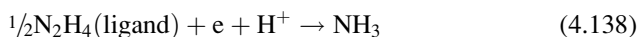
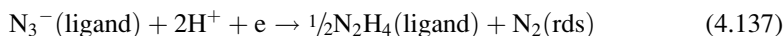


Fig. 4.63 Theoretical Nyquist plots for the electroreduction of Ni(II)-N₃⁻ at the streaming electrode, calculated using Eq. (4.136) at different potentials: (1) -0.80 V; (2) -0.95 V; (3) -1.20 V; and (4) -1.40 V. Open symbols correspond to impedances for the frequencies differing for the decade. Reprinted from [86], Copyright 2008, with permission from Elsevier

electroreduction of coordinated N₃⁻ ligand, involving hydrazine as a intermediate, was suggested:



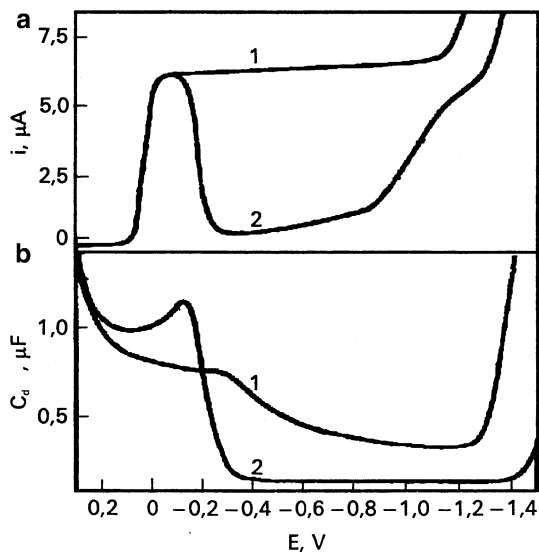
This mechanism should be considered as an expansion of reaction sequences shown in Fig. (4.57) for the nature of the intermediates in the coordinated azide electroreduction. More details of both the experimental procedure and theoretical analysis of the Ni(II)-N₃⁻ electroreduction the reader can find in the original reference [86].

4.6 Oscillations in Polarographic Processes Inhibited by Surfactants

4.6.1 The Cu²⁺-Tribenzylamine Oscillator

In this section we briefly describe the dynamic instabilities, in which the negative differential resistance of the faradaic process is caused by the potential-dependent adsorption of an organic inhibitor on the mercury electrode surface. The electroneutral molecules of such an inhibitor adsorb around the potential of zero charge (pzc) and at more extreme charges they are replaced by dipole water molecules. Thus, taking into account that pzc of mercury in contact with aqueous

Fig. 4.64 (a) Dc polarograms of (1) 1 mM CuSO_4 + 0.1 M H_2SO_4 without TBA and (2) with addition of 0.2 mM TBA; (b) Ac polarograms rescaled into differential double layer capacitance for the solutions: (1) 0.1 M H_2SO_4 and (2) 0.1 M H_2SO_4 + 0.2 mM TBA. Reprinted from [89], Copyright 1977, with permission from Elsevier



solutions not containing specifically adsorbing ions is close to -0.45 V (vs. SCE), the electroreduction process has to begin at more positive potentials, in order to produce the NDR region that will be able to manifest itself. Oscillations can therefore occur within the potential region of the diffusion-controlled limiting current in the absence of the inhibitor. Under potentiostatic ($U = \text{const}$) conditions, where ohmic drops IR_s are present, during the current I and electrode potential E oscillations, the surface concentration of reactant particles also varies periodically due to alternating adsorption/desorption of the inhibitor molecules, modifying the rate of the faradaic process. We shall describe here the typical system of that type which is characterized with the explicit (i.e., not hidden) N-NDR region: polarographic reduction of Cu^{2+} or Bi^{3+} ions in acidic medium (H_2SO_4), in the presence of tribenzylamine (TBA) as an inhibitor, as reported by Jehring and Kürschner [87–89]. These authors also mentioned other similar systems with the reported NDR region, but not exhibiting oscillations: Cu^{2+} /triethylphosphate and Cu^{2+} /Triton X-100.

Figure 4.64 compares the dc polarograms of Cu^{2+} ions in the absence and in the presence of TBA with the potential dependence of the differential double layer capacitance C_d . The formation of the NDR region within the limiting current of Cu^{2+} electroreduction correlates well with the potential region in which the significant depression of C_d , due to specific adsorption of TBA molecules, is observed. In the acidic medium, TBA molecules are largely protonated and therefore electrostatic forces favor the extension of the adsorption region of TBA molecules toward negative surface electrode charges. The measurements were made in the conventional two-electrode system consisting of the dropping mercury electrode (of a prolonged lifetime) and the calomel reference electrode.

When the appropriate serial resistance was inserted in the electric circuit, the spontaneous relaxation oscillations of the current and of the Hg electrode potential, of a frequency ca. 3 Hz, set in, as Fig. 4.65 illustrates.

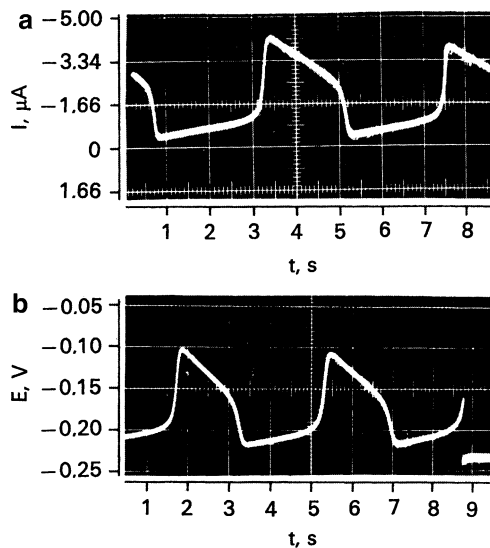


Fig. 4.65 Oscillations of the current (a) and (b) the voltage measured between the working and the reference electrode, for the 1 mM CuSO_4 + 0.1 M H_2SO_4 + 0.2 mM TBA. The externally applied voltage $U = -0.24$ V, serial resistance $R_s = 30$ k Ω . Reprinted from [89], Copyright 1977, with permission from Elsevier

Oscillogram	Electrode surface	$[\text{Cu}^{2+}]_0$	Adsorption/inhibition	Current (I)	Electrode potential (E)
1		↑↑	↓	↑	⊕ ↑
2		↓↓	↓↓↓	↑↑↑	⊕ ↑↑
3		↓↓↓	↑	↓↓	↓ ⊖
4		↑	↑↑↑	↓↓	↓ ⊖

Fig. 4.66 Schematic representation of the oscillations in the polarographic reduction of Cu^{2+} cations (*filled circle*) inhibited by surface active tribenzylamine cations (*open circle*); the direction and number of arrows symbolize the sign and the slope of appropriate changes (based on [89]). Reprinted partly from [89], Copyright 1977, with permission from Elsevier

The sequence of processes occurring during the oscillations is pictorially shown in Fig. 4.66 [89].

Picture 1 corresponds to the arbitrarily chosen starting point of the oscillatory cycle, for the electrode potential at which the electrode surface is largely covered with the inhibitor particles and the faradaic current is therefore relatively low. Therefore, the actually low concentration of Cu^{2+} ions, formed earlier in high-current state, can be replenished by their diffusion inflow from the solution bulk. Accordingly, the current slowly rises, and the electrode potential, due to increasing ohmic drops, shifts to the more positive values, at which fast desorption of TBA^+ ions occurs, associated with abrupt (autocatalytic) increase of the current (Picture 2). Then, when the electrode surface becomes largely free of inhibitor particles, the surface concentration of Cu^{2+} strongly decreases due to their fast electroreduction, but its reduction current decreases relatively slowly, proportionally to $t^{-1/2}$ (according to the increase of the diffusion layer thickness) (Picture 3). At certain moment simultaneously decreasing ohmic potential drops become so low, that the electrode potential attains again the sufficiently negative value, at which fast adsorption of an inhibitor occurs and the current drop becomes faster due to this kind of an autoinhibition mechanism (Picture 4). Now the diffusion recovers the chance to replenish the diffusion layer in Cu^{2+} ions, i.e., the situation goes back to Picture 1 and the single oscillatory cycle is closed. One should emphasize that in this mechanism the adsorption/desorption of an inhibitor is a relatively fast process (practically immediately responding to the variations of the electrode potential) compared to the slower time scale of diffusion of Cu^{2+} ions.

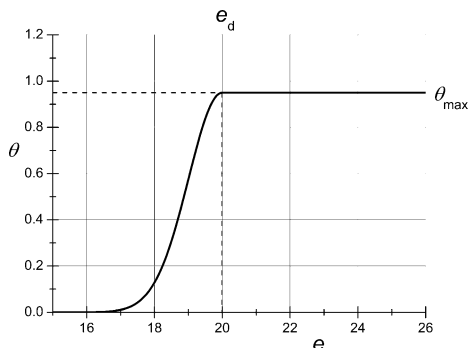
Oscillatory phenomena of that type were later analyzed also by Dörfler and Müller who studied the polarographic reduction of Cu^{2+} , Cd^{2+} , and Tl^+ ions in the presence of different surfactants: alcohols, phosphonium perchlorates, phosphonium bromides, phosphine oxides, phospholipids, and various alcohols, using the dropping Hg electrode exhibiting the drop time longer than 80 s or hanging mercury drop electrode (HMDE) [90, 91]. In some cases of the adsorbates, for the interpretation of dynamic instabilities it can be necessary to take into account the reorientation of the adsorbed molecules with varying electrode potential, the phenomenon which also can give rise to polarographic maxima of the third kind.

Another experimental system of the analogous source of oscillations is the polarographic reduction of Cu^{2+} ions in the presence of thymol as a surface-active inhibitor, described by Jakuszcwski and Turowska (sample composition: 6 mM CuSO_4 + 1 M H_2SO_4 + 3 mM thymol) [37].

4.6.2 The Mathematical Model of the “Inhibitor Oscillator”

For the quantitative description of the $\text{Cu(II)}\text{--TBA}$ polarographic oscillator, or the “inhibitor oscillator,” Koper and Slutyers [44] have elaborated the model approach, involving two dynamical variables which is the variation of the model of the $\text{In(III)}\text{--SCN}^-$ system described in Sect. 4.3. Now, if the inhibition at the electrode

Fig. 4.67 Model dependence of the electrode coverage θ of the inhibitor on the electrode potential e , calculated from Eq. (4.142)



surface covered by the organic species is very efficient, the faradaic current of copper(II) ions can be regarded as proportional to the fraction of the uncovered part of the surface, i.e., $(1 - \theta)$, with the rate constant of the electron transfer obeying there the Butler–Volmer dependence. Accordingly, the respective ODEs attain the form [44]:

$$\frac{de}{d\tau} = \frac{v - e}{r} - cx(1 - \theta) \exp[zn(e - e^0)] \quad (4.140)$$

$$\frac{dx}{d\tau} = -k_1x(1 - \theta) \exp[zn(e - e^0)] + d(1 - x) \quad (4.141)$$

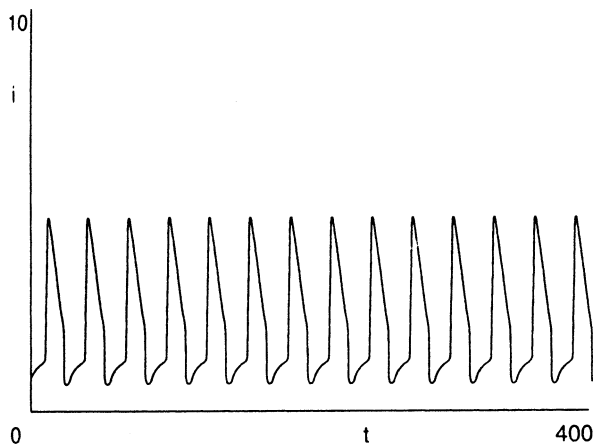
in which the electrode coverage with an inhibitor, θ , depends on the electrode potential in a way ensuring the formation of the negative differential resistance on the i - e curve of the electrode reaction of the metal ions:

$$\theta = \begin{cases} \theta_{\max} & e \geq e_d \\ \theta_{\max} \exp[-b(e - e_d)^2] & e < e_d \end{cases} \quad (4.142)$$

The value of θ_{\max} was chosen as equal to 0.95, instead of 1, in order to account for the fact that even at a saturation of the electrode surface with the inhibitor molecules, there is still some faradaic current flowing. The shape of $\theta(e)$ dependence and current oscillations calculated for the exemplary set of parameters are shown in Figs. 4.67 and 4.68, respectively.

Besides the systems described in Sects. 4.3–4.6, other electrochemical oscillators involving mercury electrode include, among others, the current oscillations at the Hg electrode in the H_2SO_4 solution, in the presence of NaBrO_3 and phenol [92], as well as in the absence of phenol [93], within the appropriate range of electrode potentials (e.g., from 0.06 to 0.01 V against Hg–1.5 M Hg_2SO_4 electrode). The probable mechanism assumed simultaneous electroreduction of bromate ions and the electrooxidation of mercury to Hg_2SO_4 and Hg_2Br_2 . Formation of these surface films affected also the surface tension at the Hg/solution interface. In the next example, the open circuit potential of a HMDE in an aqueous

Fig. 4.68 Computed oscillation profile of dimensionless current i for model equations (4.140) and (4.141) with parameter values $c = 0.12$, $k = 0.1$, $d = 0.02$, $e^0 = 15$, $e_d = 20$, $b = 0.5$, $v = 21$, and $r = 0.8$. Reprinted from [44], Copyright 1991, with permission from Elsevier



solution containing a complex cobalt ion: $\text{Co}(\text{NH}_3)_5\text{Cl}^{2+}$ was reported. These phenomena were interpreted in terms of response of Hg electrode to cyclic changes of pH near the electrode [94].

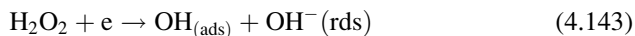
4.7 Oscillatory Reduction of Hydrogen Peroxide

Oscillatory reduction of H_2O_2 has been quite intensively studied by several groups of researchers at both noble metal and semiconductor electrodes. The works, which appeared up to mid-1990s, were reviewed by Hudson and Tsotsis [95] and Koper [51]. Here we shall briefly summarize the main points of those investigations and describe in more detail selected recent studies in this area.

4.7.1 Oscillations on Metal Electrodes

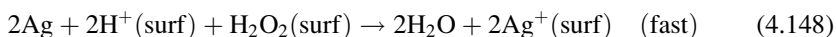
4.7.1.1 Ag electrodes

The oscillatory reduction of H_2O_2 in O_2 -free solutions at polycrystalline Ag electrode was studied by Honda et al. [96]. The large-period and large-amplitude oscillations of the electrode potential were explained in terms of the following electrochemical reaction sequence involving both H_2O_2 reduction and oxidation of Ag surface:





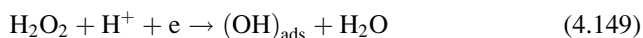
Also chemical oxidation of Ag by H_2O_2 was assumed to occur:



In terms of the above reaction scheme, the following mechanism of the electrode potential oscillations was suggested. When the electrode potential moves toward negative values, the electroreduction of H_2O_2 [Eqs. (4.143)–(4.145)] occurs at the Ag surface, the state of which simultaneously changes, enhancing its reactivity toward reaction (4.148) which eventually commences. The fast formation of $\text{Ag}^+(\text{surf})$ abruptly moves the Ag electrode potential toward more positive values, where the electrode processes (4.146) and (4.147) take place. The Ag electrode surface becomes then again deactivated (presumably due to the adsorbed O and OH species) with respect to reaction (4.148) which eventually stops to occur. The presented mechanism is of course rather introductory and required deeper insight to the (not necessarily oscillatory) mechanism of H_2O_2 reduction on Ag electrodes, in particular with respect to the existence of above-mentioned adsorbed species. Such studies were performed later by Flätgen et al. [97]. Using cyclic voltammetry and electrochemical quartz crystal microbalance (EQCM) technique, it was shown that the cathodic reduction of H_2O_2 on polycrystalline Ag electrodes in acidic electrolyte can proceed by two parallel mechanism: in addition to the well-known “normal” one, occurring at an overvoltage of about -1.5 V, a second, novel pathway was discovered, that occurs at significantly more positive potentials. This second mechanism involves the activating adsorbate $(\text{OH})_{\text{ads}}$ that forms as an unstable intermediate in the course of the H_2O_2 reduction. The process of formation of $(\text{OH})_{\text{ads}}$ is autocatalytic. At more negative potentials its coverage decreases as the rate of adsorbate reduction/desorption rises. This effect leads to the NDR region, and thus to dynamic instabilities, e.g., the oscillations under appropriate conditions. The representative cyclic voltammograms showing the two reduction pathways of H_2O_2 , are given in Fig. 4.69.

In turn, Fig. 4.70 shows the effect of the rotation rate of the Ag disk electrode in contact with 0.02 M $\text{H}_2\text{O}_2 + 0.1$ M HClO_4 solution; for the intermediate (1,000 rpm) rotation rate potentiostatic current oscillations were observed.

The formation of the activating adsorbate $(\text{OH})_{\text{ads}}$ occurs in the process:



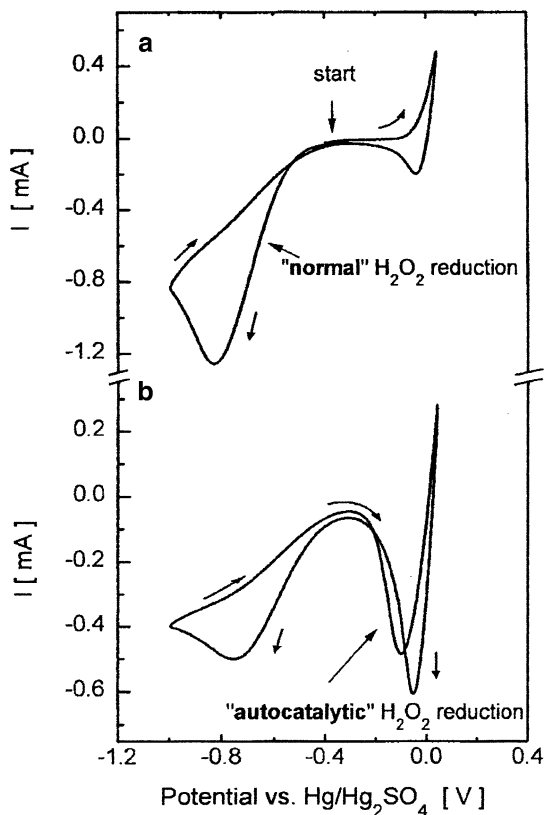
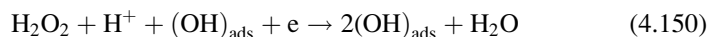


Fig. 4.69 Cyclic voltammograms of a stationary Ag electrode in an electrolyte containing 0.1 M HClO₄ + 0.02 M H₂O₂. Sweep rate 100 mV/s. Electrode area 0.28 cm² (a) First sweep, beginning at “start” in positive direction; (b) subsequent sweeps. Reprinted from [97], Copyright 1999, with permission from Elsevier

In its presence the “activated” H₂O₂ reduction proceeds at an enhanced rate:



[autocatalytic formation of (OH)_{ads}]

In the following electrochemical reaction step, (OH)_{ads} is reduced to H₂O:



For a quantitative description of the electrode coverage with (OH)_{ads}, its temporal dynamics were expressed in terms of the following dependence, taking into account both reaction pathways of H₂O₂ electroreduction:

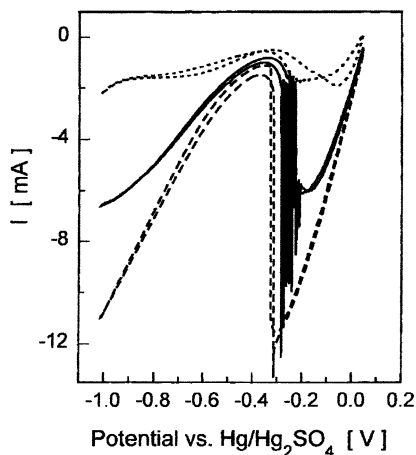


Fig. 4.70 Effect of the electrode rotation (in rpm) on the cyclic voltammograms of a stationary silver electrode in 0.1 M HClO₄ + 0.02 M H₂O₂ at 50 mV/s, no Ag⁺ added. Electrode area 0.28 cm². (Dashed line) 200 rpm; (solid line) 1,000 rpm; (dot dashed line) 5,000 rpm. Reprinted from [97], Copyright 1999, with permission from Elsevier

$$\begin{aligned} \frac{d\theta}{dt} &= j_1(\text{H}_2\text{O}_2 \rightarrow \text{OH}) - j_2(\text{OH} \rightarrow \text{OH}^-) + j_a(\text{H}_2\text{O}_2 \xrightarrow{\text{OH}} \text{OH}) \\ &= k_1 c(1 - \theta) \exp\left(\frac{-\alpha_1 FE}{RT}\right) - k_2 \theta \exp\left(\frac{-\alpha_2 FE}{RT}\right) + k_a c \theta(1 - \theta) \exp\left(\frac{-\alpha_a FE}{RT}\right) \quad (4.152) \end{aligned}$$

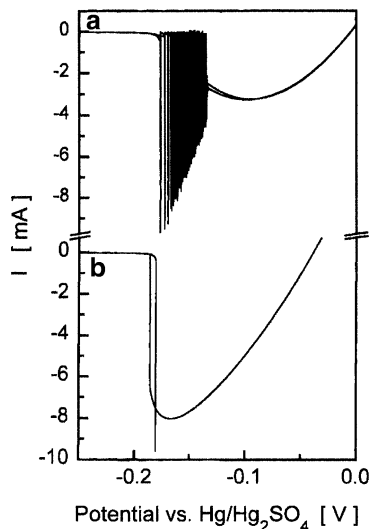
where j_i denotes the fluxes of (OH)_{ads} associated with the respective process indicated in the brackets: subscript (1) corresponds to (4.149), (2) to (4.151), and (a) to (4.150). By setting $d\theta/dt = 0$ one calculates the steady-state values of θ and the corresponding current density:

$$\begin{aligned} i_{\text{H}_2\text{O}_2} &= -2 \times q_{\text{mono}}(j_1 + j_a) \\ &= -2 \times q_{\text{mono}} \times c \left[k_1(1 - \theta) \exp\left(\frac{-\alpha_1 FE}{RT}\right) + k_a \theta(1 - \theta) \exp\left(\frac{-\alpha_a FE}{RT}\right) \right] \quad (4.153) \end{aligned}$$

where q_{mono} is the charge of one monolayer of the (OH) adsorbate on the electrode surface. The course of $i_{\text{H}_2\text{O}_2} = f(E)$ dependence exhibits is *N*-shaped as a result of superposition of the two pathways of H₂O₂ electroreduction.

In order to verify the existence of dynamic instabilities in this mechanism, the numerical model was constructed which involved two dynamic (essential) variables: the interfacial potential drop E , different from the external voltage U due to ohmic drops in the electrolyte of a resistance R_{e1} and the concentration of H₂O₂ at the electrode surface (c). The mathematical form of the respective ordinary differential equations is [97]:

Fig. 4.71 Numerical simulations of cyclic voltammograms at different rotation rates: (a) 1,000 rpm; (b) 50,000 rpm; $c_b = 0.02$ M H_2O_2 . Reprinted from [97], Copyright 1999, with permission from Elsevier



$$C_d \frac{dE}{dt} = \frac{U - E}{R_{cl}} - i_{\text{H}_2\text{O}_2} - i_{\text{Ag}} \quad (4.154)$$

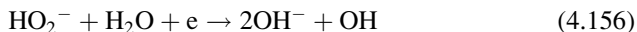
$$\frac{dc}{dt} = -\frac{1}{\delta} \frac{i_{\text{H}_2\text{O}_2}}{F} + D \frac{c_b - c}{\delta^2} \quad (4.155)$$

where c_b is the bulk concentration of H_2O_2 , δ is the thickness of Nernst diffusion layer, and other symbols have their usual significance. Equation (4.154) takes into account both pathways of H_2O_2 electroreduction, as well as anodic Ag dissolution as sufficiently positive potentials. In the derivation of Eq. (4.155), the typical assumption of Nernst diffusion layer of thickness δ , dependent on the disk rotation rate, was used (cf. Sect. 2.2.1). Further details of the model can be found in the original paper [97], while here we shall show only representative results of modeling, revealing current oscillations for the same disk rotation rate as in the experiment (Fig. 4.71).

4.7.1.2 Au Electrodes

Štrbac and Adžić [98] have reported the oscillatory behavior in oxygen and hydrogen peroxide solution on a rotating Au(100) electrode in alkaline solutions. For electrodes with other crystallographic orientations, oscillations were not observed, and the specific role of (100) surface was related to its best catalytic properties for the O_2 reduction in alkaline solutions, even better than the polycrystalline Pt electrodes. In the potential range of formation of the partly discharged $\text{Au}(\text{OH})^{-(1-\lambda)}$ layer, O_2 reduction takes place with the exchange of four electrons to OH^- , but at more negative potentials, at which $\text{Au}(\text{OH})^{-(1-\lambda)}$ is not present at the

surface, the two-electron reduction, leading to HO_2^- , occurs. It was found that this was the oscillatory reduction of HO_2^- which caused the oscillations also during O_2 reduction. Furthermore, the state of electrode surface was a crucial factor responsible for the oscillations. It was suggested that the following reaction sequence:



initiated a straight chain mechanism forming the HO_2 radical. Note that HO_2 radical was shown also by Tributsch [99] to be a direct participant in oscillatory reduction of H_2O_2 on Cu_5FeS_4 , occurring through two autocatalytic chemical reactions between metal atoms and surface-bound reactants (see next section). The first autocatalytic mechanism involves metal and metal-hydroxide sites as reaction pairs and leads to removal of OH^- from the electrode surface. The additional metal sites released in this way undergo oxidation by hydrogen peroxide. This activates the other autocatalytic reaction which involves metal-oxide sites and metal-hydroxide sites and produces the increase of the OH coverage of the Au (100) surface. As the principal reason for the oscillations a periodical covering and depletion of the electrode surface with OH groups was considered.

4.7.1.3 Pt Electrodes

It seems that the majority of studies of oscillatory reduction of H_2O_2 was carried out for Pt electrodes, including, among others, the works by Fetner and Hudson [100] and van Venrooij and Koper [101] who described bursting and MMO in this system. More recently, intensive studies of the H_2O_2 electroreduction on Pt electrodes, including single-crystal ones, were performed by the group of Japanese researchers (Nakanishi, Nakato et al.), the selected works of whose [24, 102–105] will be briefly described below. In these studies, the reduction of H_2O_2 in acidic aqueous H_2SO_4 medium was investigated, with an emphasis on surface chemistry and effects of microscopic structures of the electrode surfaces on the oscillations, and vice versa. It turned out that the oscillatory reduction of H_2O_2 at Pt electrodes of various crystallographic orientation is a particularly interesting process, revealing the dynamics of several types of oscillators, some of them classified as their new types. Based on [105], the results of these studies can be summarized in the following way. **Five types of oscillations**, named **A**, **B**, **C**, **D**, and **E**, were found for the H_2O_2 reduction, with their shapes and conditions of occurrence concisely shown in Fig. 4.72 [104].

The complicated dynamics of H_2O_2 reduction on Pt is caused, among others, by the fact that this process exhibits two types of NDR regions: (1) the one (named below the NDR-1) arising from decrease in the coverage of adsorbed OH, when the potential moves into negative direction and (2) the other one (named below the

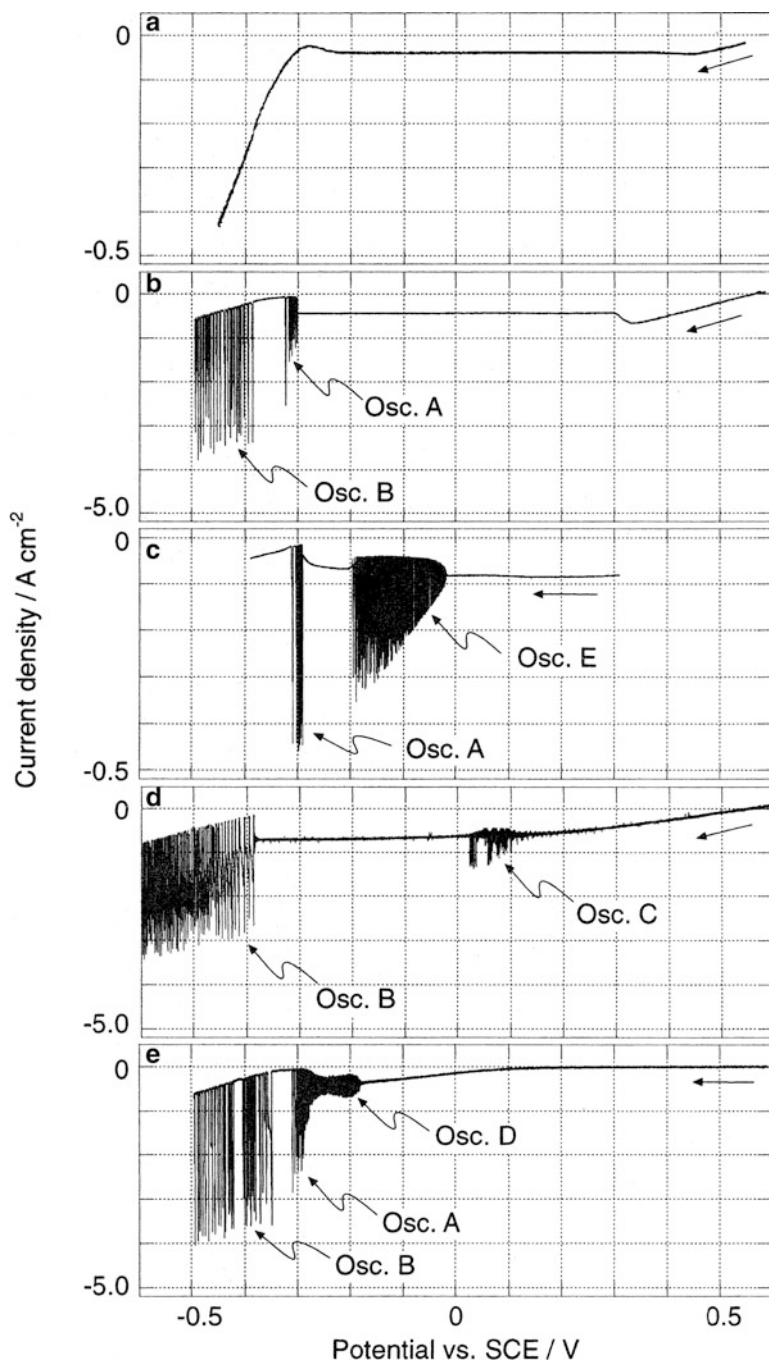


Fig. 4.72 General view of oscillations A, B, C, D, and E observed under potential-controlled conditions for H_2O_2 reduction on Pt in an acidic solution. Electrode: poly-Pt, except (c) for which single-crystal Pt(111) was used. The solution: 0.3 M H_2SO_4 containing (a) 0.1 M H_2O_2 , (b) 0.7 M H_2O_2 , (c) 1.0 M H_2O_2 , (d) 1.2 M H_2O_2 + 1.0×10^{-3} M KCl, and (e) 0.7 M H_2O_2 + 1.0×10^{-4} M KBr. Reprinted with permission from [104]. Copyright 2001 American Chemical Society

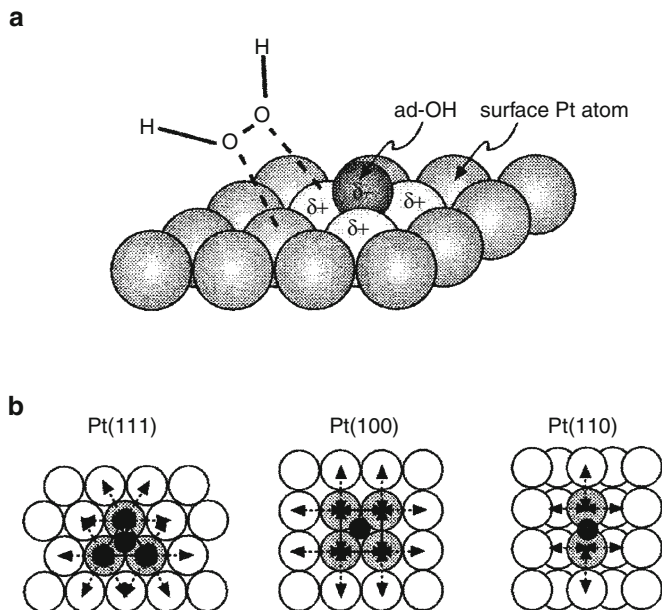
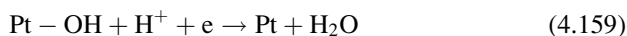
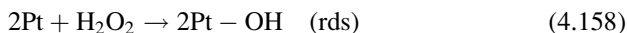


Fig. 4.73 Schematic illustration of an autocatalytic mechanism in which the dissociative adsorption of H_2O_2 is accelerated on surface Pt atoms in the neighborhood of adsorbed OH. Reprinted with permission from [24]. Copyright 2000 American Chemical Society

NDR-2) occurring at more negative potentials and caused by the suppression of the H_2O_2 reduction by formation of the underpotential deposited hydrogen (upd-H) in a potential region just before hydrogen evolution. Adsorbed OH species, being the intermediate of the first step of the H_2O_2 reduction, act as an autocatalyst in the dissociative adsorption of H_2O_2 , according to mechanism shown in Fig. 4.73, with efficiency of this autocatalysis assumed to vary in the following series: $\text{Pt}(111) > (100) \approx (110) \geq \text{poly-Pt}$ [102].

The essential mechanism of the autocatalytic effect of OH species can be imagined in the following way: if adsorbed OH is present at hollow sites of surface Pt atoms and H_2O_2 is adsorbed with negatively polarized oxygen atoms of H_2O_2 directed to surface Pt atoms, the H_2O_2 adsorption should be accelerated in the neighborhood of adsorbed OH, because these Pt atoms are more or less positively polarized by an electronegative difference between the Pt atom and OH group [102]. The electrochemical mechanism of H_2O_2 reduction involves thus the following reaction sequence:



in terms of which the NDR-2 region originates from suppression of step (4.158) by the formation of upd-H of nearly full coverage.

Below we shall describe the nature of particular A–E oscillations. Oscillations of type A are due to NDR-2, oscillations of type E—due to NDR-1, but the latter ones were observed only for atomically flat Pt(111) electrodes (see Fig. 4.72c).

Thus, both A and E oscillations are caused by explicit NDR regions (Class III of the oscillators in Sect. 3.5). Here it is also useful to note that oscillations E are strongly enhanced by the iodine atoms, adsorbed on atomically flat Pt(111) surface in a submonolayer amount; then the region of the oscillations E extends toward positive potentials [103]. Furthermore, in the presence of adsorbed iodine, the oscillations E were observed even for atomically flat Pt(100), for which they never occurred in the absence of iodine. Such a role of adsorbed iodine was explained in terms of the catalytic role of I_2 on the dissociative adsorption of H_2O_2 , in addition to the site-blocking effect (cf. Fig. 4.73). It is suggested that within the potential range from 0.2 V to 0.4 V there occurs a cooperation between the catalytic effect of adsorbed iodine and the autocatalytic effect of adsorbed OH, originating from similar phenomena: since iodine atoms, as O atoms from OH groups, exhibit higher electronegativity than Pt atoms, the induced positive charge on Pt atoms favors the dissociative adsorption of H_2O_2 through its oxygen atoms and thus the autocatalytic formation of OH species. The catalytic effect of adsorbed iodine decreases in the order: Pt(111) \gg Pt(100) \gg Pt(110) [103].

Oscillations of types C and D were observed only in the presence of small amount of halide ions in the solution and were *both* classified into HNDR oscillators [104]. In the case of oscillation type C, the NDR-1 region is hidden by the adsorption of halides, the electrode coverage of which (θ_x) decreases with increasing negative potential. However, for oscillations type D, the NDR-2 region is hidden by *both* the decreasing adsorption of halide ions and the transient cathodic current flowing due to the upd-H formation. This relatively complex scheme of hiding the NDR justifies, in the opinion of the authors, the nature of oscillation D as corresponding to a *new type* of the HN-NDR oscillator, suggesting thus the extension of their classification scheme, given in Sect. 3.5.

In order to get more systematic view into the characteristics of these oscillations, let us note that under galvanostatic conditions only potential oscillations of types B, C, and D were observed, while oscillations A and E were not, confirming that the latter two ones are typical N-NDR oscillators (Fig. 4.74).

A comparison of dc dependences with the corresponding impedance spectra confirms those diagnostic conclusions. In particular, the spectra recorded for parameters corresponding to oscillations C and D are typical of the HN-NDR oscillator: the negative resistance is observed only in a region of intermediate frequencies [104]. Further information on the system's dynamics was supported by the light reflectance changes which had revealed that variation of the electrode coverage with the bromide ions was slower than the variation of the electrode potential (i.e., that θ_{Br^-} is a slow variable). Taking into account the basic features of the system: the site-blocking effect of adsorbed halide ions, autocatalytic effect of adsorbed OH, and the site-blocking effect of upd-H, the numerical model was

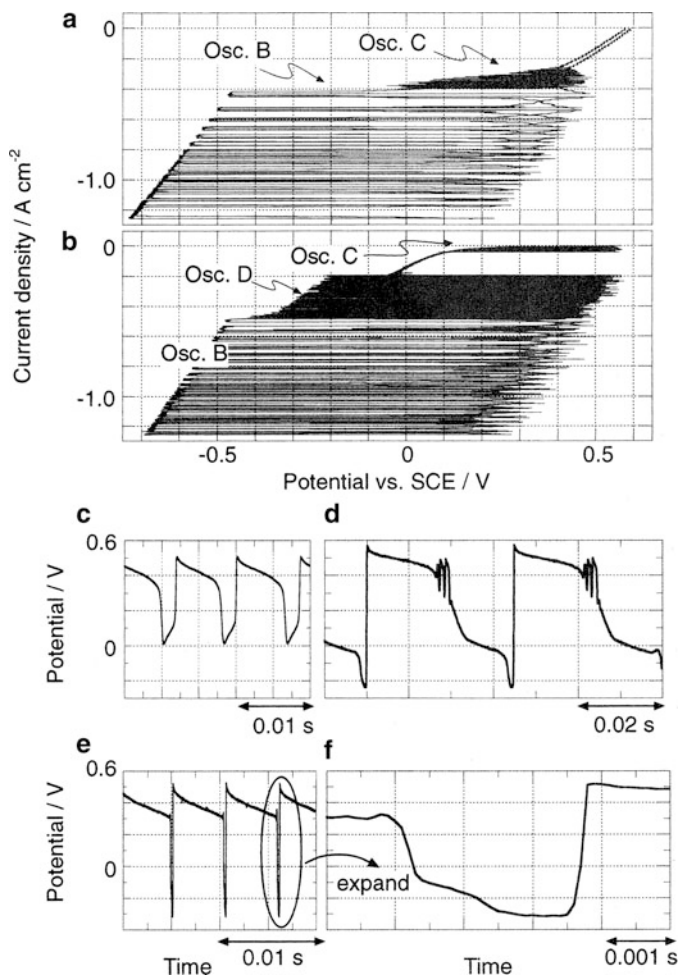
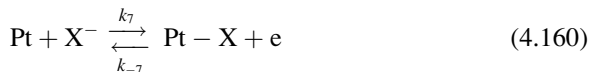


Fig. 4.74 Oscillations B, C, and D under current-controlled conditions: (a) and (b) j - U curves and (c)-(f) time courses (U - t courses) where (c) is for oscillation C at $j = -0.32$ A cm⁻² in (a), and (d) and (e) are for oscillation D at $j = -0.25$ and -0.38 A cm⁻², respectively, in (b). Curve (f) is a simple expansion of curve (e). Electrode: poly-Pt. The solution: 0.3 M H₂SO₄ containing (a) 0.7 M H₂O₂ + 1.0×10^{-3} M KCl and (b) 0.7 M H₂O₂ + 1.0×10^{-4} M KBr. Reprinted with permission from [104]. Copyright 2001 American Chemical Society

constructed and results of such calculations allowed one to distinguish between the essential features of the source of oscillations C and D. The mathematical details of this model are described in the original reference [104]. Here we shall mention that although the construction of the model was common for oscillations C and D, that which of those oscillation types was reproduced in the calculations, depended essentially on the equilibrium potential (parameter E_{70}) of the halide adsorption reaction:



which in turn was determined by its relation to the NDR-1 or NDR-2 potential regions. If E_{70} is near (or within) the potential region of the NDR-1 (due to autocatalytic effect of adsorbed OH), oscillations C are reproduced. Accordingly, if E_{70} is close to the potential region of NDR-2 (due to upd-H), oscillations of type D are reproduced, but only if additional important condition was met, namely if the *transient current due to the upd-H formation was included*. This is the above-mentioned mechanistic detail that suggests the essential difference between C and D oscillations, even if both are considered to originate from HN-NDR oscillators. More precisely, oscillations C are considered to belong to the Class IV-2, according to Strasser's et al. classification (see Sect. 3.5). For oscillations D, it was concluded that the mechanism of their formation was more complex and, moreover, oscillations D did not fall within any of the existing categories, so they have to belong to a new Class IV-4 of HN-NDR oscillators. A very detailed analysis of these problems, justifying such conclusions, is given in the original reference [104]. Here we only show the schematic waveforms of type C and D oscillations, revealing the variations of main factors, affecting their shapes (Fig. 4.75). The symbols used have the following meaning: HP—high-potential state, LP—low-potential state, IP—intermediate potential state.

Finally, oscillations of type B require more detailed explanation since they are suggested to represent a new type of electrochemical oscillator [105]. For that it will be useful to compare oscillations of type B with those of type A. Oscillations of type A occur in the region of the NDR-1, i.e., within -0.25 V to -0.30 V, while oscillations B appear at more negative potential, where the hydrogen evolution occurs and is characterized with the positive slope of the I - E dependence. Upon addition of trace amounts of halides, the oscillations B were quenched, with oscillations A almost intact. The significant effect of surface roughening of Pt electrodes has been noticed: oscillations of both A and B types were reported for the atomically roughened polycrystalline Pt electrode, while for atomically flat poly-Pt electrodes only oscillations A remained. Analogous observations were made for atomic flat and roughened single-crystal Pt (111), (110), and (100) electrodes. Next, when the solution was stirred with magnetic stirrer, oscillation A disappeared completely, whereas oscillation B remains practically unaffected. Finally, impedance measurements, made for the potential corresponding to oscillations B indicated neither explicit NDR, nor hidden NDR. In conclusion, although both potentiostatic and galvanostatic oscillations of type B were observed in the studied system, they could not be classified as the HN-NDR type oscillator. Based on these findings, the following reasoning has been suggested for the origin of oscillations B. Since they appear only for atomically roughened Pt surface, one can assume that certain specific "active" areas of such surface play a crucial role in their formation and that these places are "deactivated" by the strong, preferential adsorption of halide anions from the solution. Thus, one has to consider two types

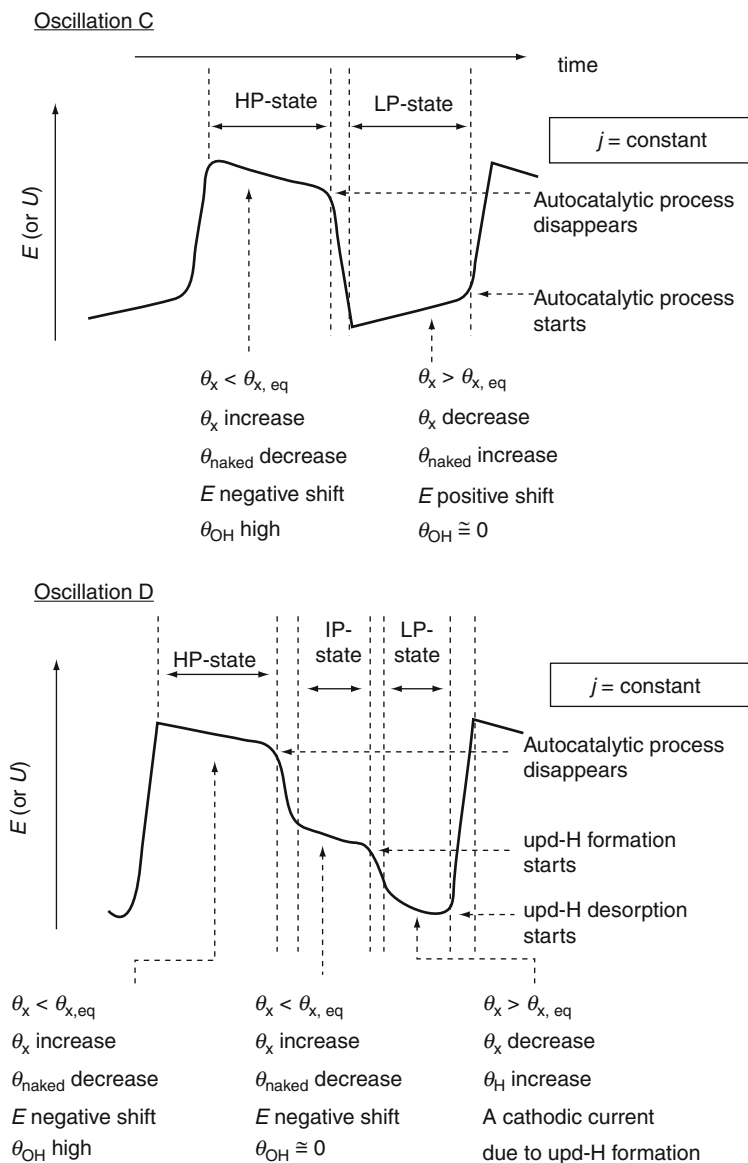
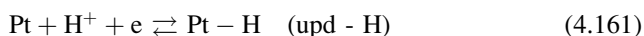


Fig. 4.75 Schematic waveforms of observed oscillations C and D under constant current densities (j) together with main factors affecting the waveforms. Reprinted with permission from [104]. Copyright 2001 American Chemical Society

of sites at the electrode surface: one type (I) is involved in oscillations A and the second type (II)—in oscillations B. The number of sites of type II is much smaller than the number of sites I. In the absence of halides, and for sufficiently negative potentials, where the oscillations B occur, practically all sites of type I are fully

covered by hydrogen atoms, generated during their underpotential deposition, so oscillations A are then not possible. However, at the active places of type II, both the hydrogen evolution and the H_2O_2 reduction occur. The occurrence of the oscillations can then be qualitatively understood in the following way, involving the “high-current” and “low-current” states of the system and the occurrence of ohmic drops which affect the effective electrode potential $E = U - IR_s$. In the “high-current” state, owing to large ohmic drops, the electrode potential E is enough positive to remove upd-H and therefore the reduction of H_2O_2 occurs at the whole electrode surface. This extensive reduction, faster than the rate of H_2O_2 diffusion from the bulk of the solution, leads however to the gradual decrease of surface H_2O_2 concentration and thus to the decrease in the faradaic current. This means the decrease in ohmic drops and thus the shift of the electrode potential E toward more negative values, at which underpotential of H sets in and the sites active for H_2O_2 reduction become gradually blocked; the process of upd-H is autocatalytic, since the decrease of current caused by adsorption of H shifts the potential toward more negative values, at which the upd-H is more advanced and this moves further the potential into the same direction. As soon as a full coverage of upd-H is formed, the Pt electrode moves to a low-current state. Since in this state the H_2O_2 reduction occurs only for small fraction of active states, the diffusion is now able to replenish gradually the surface concentration of H_2O_2 and therefore the local current density at the active sites increases, causing an increase of ohmic drops. The electrode potential moves to more positive values, at which the underdeposited H is removed and the oscillatory cycle is completed. This mechanism explains also why stirring of the solution affects and even quenches the oscillations B, since the slow diffusion transport, required for the oscillations, is then superposed with the more intensive convective transport, setting the system into the stable state. Also, it becomes understandable why appearance of oscillations B requires higher H_2O_2 concentrations than oscillations A—simply large enough ohmic drops, i.e., high enough currents are necessary. The mechanism outlined earlier is schematically shown in Fig. 4.76. In a more general sense, it indicates that in some cases the temporal oscillations of current or potential requires invoking the inhomogeneous, patterned state of the electrode surface (note that the formation of spatiotemporal patterns in two coupled $\text{H}_2\text{O}_2/\text{Pt}$ oscillators is described in Sect. 3.1.2 of volume II).

In a more detailed description of the above mechanism, one should also take into account the electrical coupling between the active area and the surrounding nonactive area of the electrode surface (see [105] for details). Based on the above mechanism for the formation of oscillations B, their mathematical model was constructed based on reactions (4.158) and (4.159) and the following additional steps:



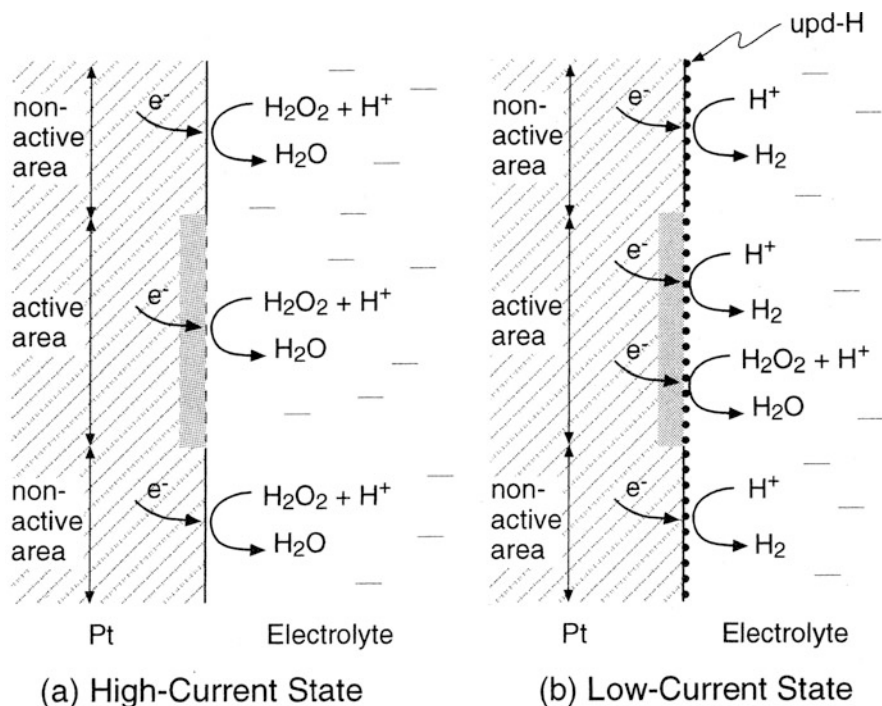
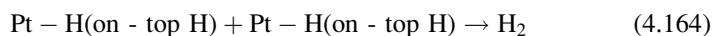
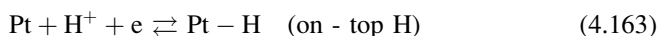


Fig. 4.76 Schematic illustration of an inhomogeneous structure of the electrode surface to explain the appearance of oscillation B, together with reactions in (a) high- and (b) low-current states. Reprinted with permission from [105]. Copyright 2001 American Chemical Society



Further mathematical details of the model can be found in the original reference [105]. Here we shall only mention that numerical calculations reproduced oscillations A and B under both potentiostatic and galvanostatic conditions, provided that both the stirring of the solution by hydrogen evolution and the presence of active areas with electric coupling with the surroundings were assumed.

In the opinion of the authors, their mechanism justifies the conclusion that oscillations of type B originate from a new type of electrochemical oscillator, which was called “coupled NDR” or CNDR oscillator, since it appears in a potential region of positive differential resistance by coupling with an NDR existing in another potential region. Accordingly, Mukouyama et al. [104] have suggested the update of the classification of electrochemical oscillators being the extension of earlier scheme proposed by Strasser et al. [25] (cf. Fig. 3.24). The present scheme, shown in Fig. 4.77, includes both the (discussed earlier) subclass IV-4 (oscillations C) and the presently introduced Class V (oscillations B). One can suppose that with the

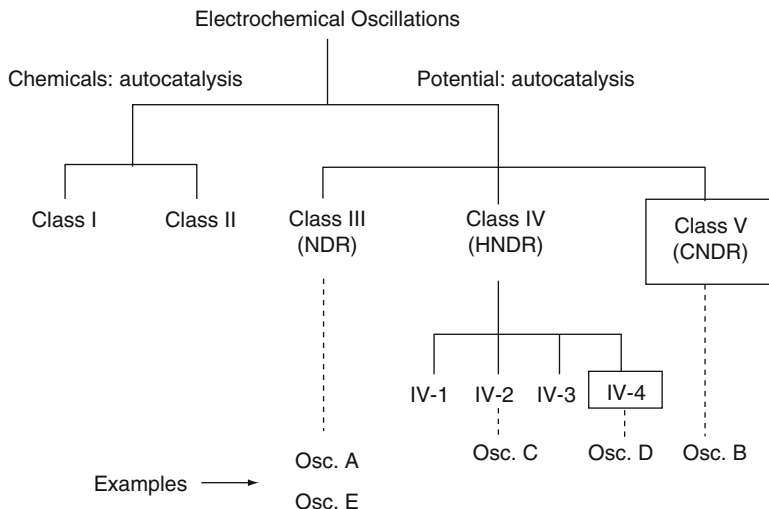


Fig. 4.77 Improved classification of electrochemical oscillations on the basis of mechanisms, with newly added categories indicated by enclosure with rectangles. Reprinted with permission from [104]. Copyright 2001 American Chemical Society

progress in mechanistic studies of other electrochemical oscillators, this classification may undergo further extension.

4.7.2 Oscillatory Reduction of H_2O_2 on Semiconductor Electrodes

4.7.2.1 Reduction on Cu-Containing Semiconductors

The oscillatory reduction of H_2O_2 under potentiodynamic, potentiostatic, and galvanostatic conditions, occurring on various Cu-containing semiconductors: CuS, Cu_2S , Cu_5FeS_4 , $CuFeS_2$, $CuInS_2$, $CuInSe_2$ have been a subject of intensive studies, led by the Berlin group of Tributsch (cf. e.g. [99, 106–112]). For the diagnosis of the oscillatory mechanism of this process, it is important that they were *not* reported for such copper-free electrode materials, as FeS, FeS_2 , PbS, MoS_2 , and CdS. In consequence, the presence of Cu(I) ions was suggested as crucial for the oscillatory mechanism. This view was corroborated by the cathodic photoeffect found for all copper-containing sulfides (particularly Cu_2S): the irradiation of the electrode surface with visible light affected the amplitude and frequency of the oscillations, in certain cases causing even their decay. This effect was explained in terms of the role of Cu(I)-oxide species in the mechanism of oscillations. The crucial role of Cu(I) ions was discussed in spite of the fact that oscillatory reduction of H_2O_2 was not observed on metallic Cu and semiconducting Cu_2O electrode. The exemplary oscillations are shown in Fig. 4.78, for the H_2O_2

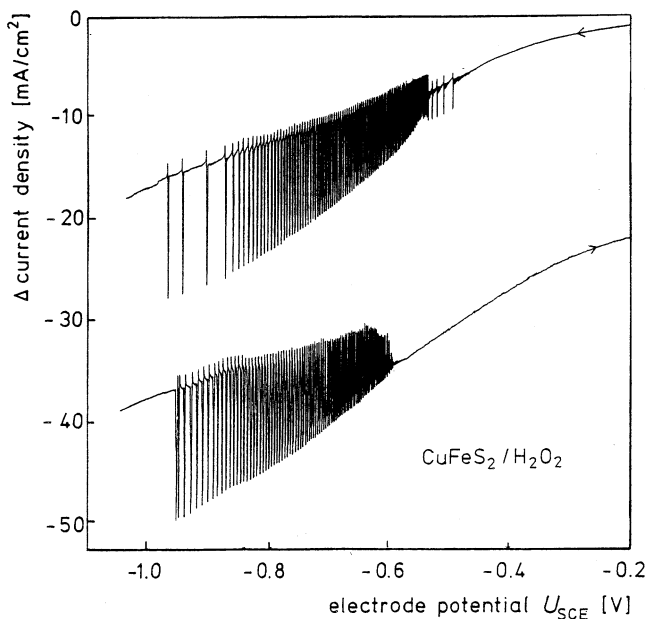


Fig. 4.78 Dynamical reduction curves of H_2O_2 on CuFeS_2 electrodes (10 mV/s sweep into opposite potential directions). Electrode rotation: 10 rps; pH = 9; 0.4 M H_2O_2 , 0.1 M KCl. Reprinted from [108] with kind permission of Deutsche Bunsen-Gesellschaft für Physikalische Chemie

reduction on CuFeS_2 (composed of Cu^+ , Fe^{3+} and S^{2-} ions) [108]. In turn, Fig. 4.79 shows the photosensitivity of the H_2O_2 reduction on Cu_2S , interpreted in terms of photosensitivity of Cu_2O as the reactant in the oscillation mechanism [108].

We shall here briefly summarize the main features of the proposed oscillatory mechanism [95, 108]. This requires first the description of two possible paths of decomposition of H_2O_2 in contact with Cu(I) containing heterogeneous catalyst, the one which is “trivial,” i.e., nonoscillatory and the other one, which occurs in an oscillatory manner. Obviously, the electrochemical oscillations should be related to the oscillatory catalytic pathway. It is thus crucial to understand under which conditions and why this oscillatory catalytic pathway prevails. We shall consider the semiconducting Cu_2S electrode a crystal set of Cu(I) ions being in electronic contact with a well-conducting sulfide matrix. The formation of Cu(I) ion from Cu atom occurred through the transfer of a single 4s electron onto the sulfur atom, and in this way the ionic bond was created. But Cu(I) ions have further bonding capabilities—they can participate also in the covalent bond, engaging their remaining 3d electrons. It is further considered that upon cathodic polarization of Cu_2S electrode the positive charge of Cu(I) ions is reduced, i.e., the electrons are transferred back from sulfur ions, when a Fermi level in the sulfide is sufficiently raised to fill electrons into antibonding 4s orbitals of Cu^+ surface atoms. Thus, the strength of ionic bonding will be significantly affected, whereas the contribution from the covalent bond is expected to remain

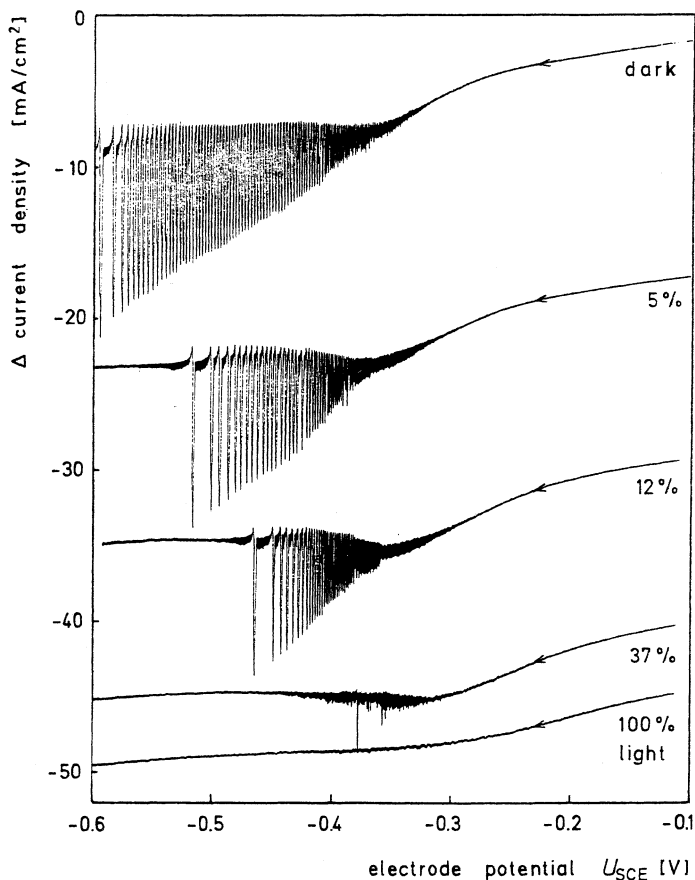


Fig. 4.79 Qualitative example of light-induced frequency changes on Cu_2S electrodes in contact with a hydrogen peroxide solution. Electrode rotation: 10 rps; $\text{pH} = 9$; $0.2 \text{ M H}_2\text{O}_2$; 0.1 M KCl . Reprinted from [108] with kind permission of Deutsche Bunsen-Gesellschaft für Physikalische Chemie

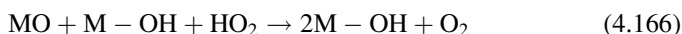
rather independent of the electrode potential. It is important to note that the oscillations set in when the extent of Cu(I) ions reduction exceeds certain critical level, i.e., when the electrode potential reaches a sufficiently negative value. In turn, at relatively positive electrode potentials, in contact with the copper-containing electrode surface, the ordinary (i.e., nonoscillatory) catalytic decomposition of H_2O_2 occurs, which involves the electron exchange with the surface bonded copper catalyst, i.e., the copper ions will then alternatively be reduced and oxidized. However, when a positive character of surface bonded copper ions becomes gradually reduced through the increase of the negative electrode potential, a point is reached at which electron transfer to the copper ions ceases to be energetically favorable and therefore the ordinary heterogeneous catalytic decomposition of H_2O_2 stops to proceed. Instead, a less efficient, but energetically possible oscillatory catalytic reaction path can manifest

itself. At this point it is useful to indicate that the absence of electrochemical oscillations in the case of reduction of H_2O_2 at FeS , FeS_2 , MoS_2 , CdS , and PbS was explained by the fact that for these compounds the ordinary, nonoscillatory catalytic activity could *not* be stopped and transformed into a periodical one through a cathodic potential. This was presumably because of too high energy level of metal ions, which would have to be filled up by electrons coming from the Fermi level, during cathodic polarization. In a particular case of CdS , the space charge layer was too large to permit an adequate shift of the Fermi level in the surface, similarly as for Cu_2O .

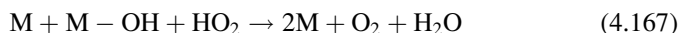
With respect to catalytic decomposition of H_2O_2 , experimental evidences were found for the following reaction steps (with $\text{M} = \text{Cu}^+$ ions) [99, 107, 108]:



(the copper sites on the Cu_2S are oxidized by H_2O_2)



(autocatalytic covering of the surface with OH groups, involving HO_2 radical)



(autocatalytic cleaning of the electrode surface of OH groups, making possible reaction (4.165) again)

This mechanism, in which a special attention should be given to the HO_2 and OH species, shows that during the oscillations an oxide layer is periodically formed and destroyed. This process is, however, not considered essential for the oscillations. Rather, the presence of surface hydroxyl groups that are formed and cathodically reduced is a source of instabilities. From the point of view of nonlinear dynamics, it is also interesting that the reaction steps found constitute the oscillatory system of the Lotka–Volterra type [99].

The above reaction scheme should be complemented with the microscopic view of the processes at the semiconductor solution surface. Let us take into account the autocatalytic process (4.167). Figure 4.80a shows then schematically that the HO_2 radical forms a ring complex, within which the cyclic electron transfer occurs and molecular oxygen is liberated. In other words, there are two neighboring copper centers involved in this autocatalytic process associated with the oscillatory catalytic pathway. An increase of the positive charge of the electrode (at the copper ions) inhibits this pathway, according to the above considerations. At sufficiently positive potential, the electron transfer to copper ions takes place (Fig. 4.80b) and then the HO_2 radical dissociates into molecular oxygen and proton; then the neighboring Cu ions stop to cooperate in electron transfer and only the ordinary catalytic decomposition of O_2H radical takes place.

Now, one should show how the periodical catalysis in H_2O_2 decomposition is related to the observed electrochemical oscillations. This point is schematically explained in Fig. 4.81, which refers to Cu(I) containing sulfides.

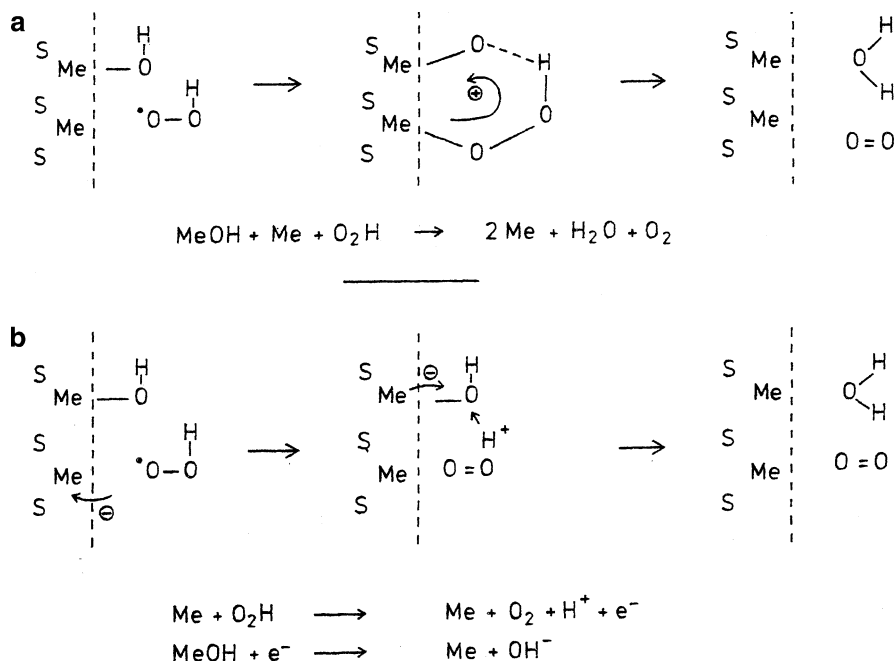
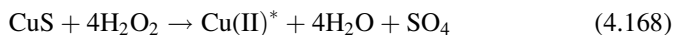


Fig. 4.80 Reaction scheme for the catalytic decomposition of HO_2 radical: (a) in an autocatalytic reaction leading to oscillations; (b) in a simple catalytic reaction, not leading to oscillations. Reprinted from [108] with kind permission of Deutsche Bunsen-Gesellschaft für Physikalische Chemie

According to the above discussed reaction sequence (4.165)–(4.167), the copper sites on a copper sulfide are first oxidized through reaction (4.165). Then the autocatalytic reaction (4.166) involving the HO_2 radicals leads to the covering of the surface with OH groups. Reaction (4.167), also involving HO_2 radicals, is then cleaning the surface from OH groups and the oxidation of the copper by H_2O_2 can again occur. As indicated earlier, in this reaction sequence the oxide layer is periodically destroyed and formed, but the oscillations of current are caused by the periodical presence of surface-bonded hydroxide groups which can be cathodically reduced [108].

In the course of further studies, the above electrochemical mechanism was found to be too simple. By means of combination of cyclic voltammetry with ex situ XPS and EDX analysis of the corrosion products, it was established for CuFeS_2 electrode [95, 110] that to the list of species important for H_2O_2 decomposition, also certain “active” species Cu(II)^* , or active copper site (denoted as Cu(II)^*) should be added, formed in the following process:



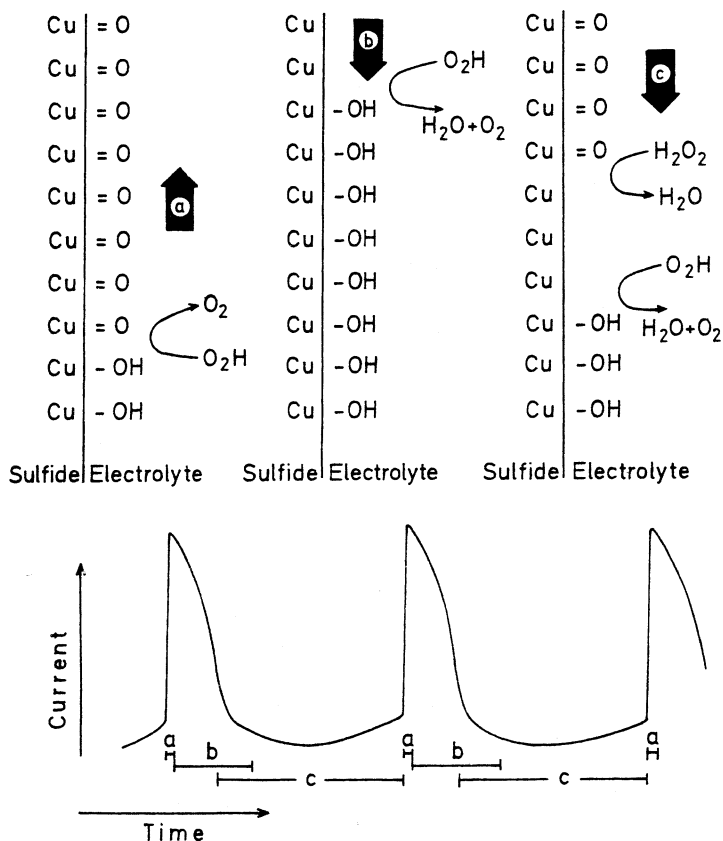


Fig. 4.81 Scheme for the explanation of the periodicity of catalysis and proposed relation between partial reactions and current oscillations. Reprinted from [108] with kind permission of Deutsche Bunsen-Gesellschaft für Physikalische Chemie

The importance of Cu(II)^* species lies in the assumption that H_2O_2 reduction requires less overpotential if occurs on this site and the process continues until its conversion into inert CuO oxide. It is thus clear that further, more advanced studies of this oscillatory mechanism are required, particularly in view of significant progress in understanding of electrochemical instabilities.

In order to understand better the oscillatory reactions on the semiconductor surface, it is useful to monitor its electronic structure which can be diagnosed from electroreflectance spectra. In this way, Cattarin et al. [113] have investigated the effect of the electrode potential on the band bending in the semiconducting phase, at the $\text{CuInSe}_2\text{-H}_2\text{O}_2$ interface. The correlation of the negative differential resistance with the negative slope of relative reflectivity $\Delta R/R$ indicated the possible band bending anomaly (see below for analogous effect for reduction of H_2O_2 on GaAs [51]). Furthermore, in this NDR region also intriguing, rather unique and not completely understood phenomena were observed: nonproportionality of the

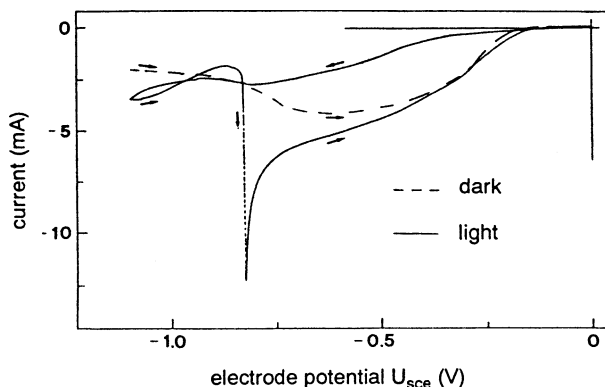
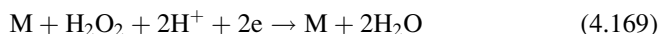


Fig. 4.82 Cyclic voltammograms (20 mV/s) of H_2O_2 reduction at p-CuInSe₂ electrode, stationary, under white light (*solid line*). Fifth cycle after polishing and etching. *Dashed line*: curve recorded during positive sweep in the dark, after polarization for 20 s under light at negative limit. Reproduced from [111] by permission of The Electrochemical Society

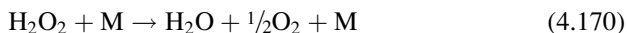
photocurrent response to photon flux and even a change in its sign (inverted photoeffect), occurring in the potential region from -0.9 to -0.75 V (see Fig. 4.82).

Further significant progress in understanding of the potentiostatic and galvanostatic oscillatory reduction of H_2O_2 on p-CuInSe₂ electrode was made by Pohlmann et al. [114] who have elaborated a model for oscillating hydrogen liberation in this process. Thus, the parallel existence of two electrode processes was considered. The hydrogen mass signal was experimentally recorded via differential electrochemical mass spectrometry (DEMS) and it was shown that, under galvanostatic conditions, the hydrogen mass oscillated in phase with the electrode potential. Evidently, the oscillatory mechanism of H_2O_2 reduction required taking into account also the process of hydrogen evolution. The particular task was to derive such a dependence of the rate constant of the electrode process on the potential which would express the essential combination of the oscillatory H_2O_2 reduction and hydrogen evolution. The proposed mechanism, leading to the expression for $k(E)$, involved the following steps (with the rate constants k_1 – k_5 of the processes used for model calculations indicated in the brackets):

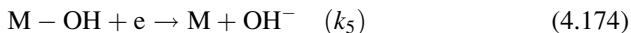
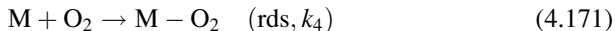
(i) The direct reduction of H_2O_2 :



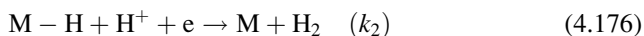
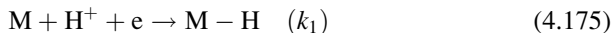
(ii) The catalytic decomposition of H_2O_2 , with the evolution of oxygen:



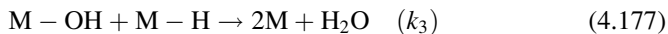
(iii) The reduction of dissolved oxygen through the rate-determining step of adsorption



(iv) Hydrogen evolution reaction:



(v) Recombination of adsorbed hydrogen and hydroxyl radicals:



The role of hydrogen evolution can be summarized in the following points: (1) it ensures the relatively high current density and introduces the diffusional time delay required for the relaxation oscillations (slow variable), (2) it leads to adsorbed hydrogen which acts as an inhibitor for the H_2O_2 reduction due to blocking of available surface areas. Due to assumed competitive adsorption of OH radicals (which is strongly potential dependent) it is possible to understand the effect of potential on the electrode coverage with H. Finally, summarizing of reactions (iv) and (v) reveals an additional feedback loop: an autocatalytic generation of free surface area sites. As the essential dynamic variables of the model there were considered the electrode coverages with M-OH and M-H, denoted as x and y , respectively. The corresponding ordinary differential equations attain then the following form:

$$\frac{dx}{dt} = k_1(E)(1 - x - y) - k_2(E)x - k_3xy \quad (4.178)$$

$$\frac{dy}{dt} = k_4(1 - x - y) - k_5(E)y - k_3xy \quad (4.179)$$

where every potential-dependent rate constant follows the Butler–Volmer dependence:

$$k_i(E) = k_{i,0} \exp\left(-\frac{\alpha FE}{RT}\right) \quad (4.180)$$

To these two differential equations, two other ones, describing the dynamics of the electrode potential (E) and surface concentration (c) of H_2O_2 , analogous to those used by Koper and Sluyters [Eqs. (2.29) and (2.31)], were added, forming thus a system of four differential equations. In the expression for the faradaic current of the direct hydrogen peroxide reduction, the crucial $k(E)$ dependence was expressed in the following way:

$$k(E, t) = k_0 \exp\left(-\frac{\alpha n F E}{RT}\right) [1 - x(t, E) - y(t, E)] \quad (4.181)$$

After some simplifications, the presented model was used to simulate the current oscillations during the potentiostatic H_2O_2 electroreduction. In conclusion, specific semiconducting properties of the CuInSe_2 electrode appeared to be *not* crucial for the oscillations, since they were not incorporated in the model. The same is probably true for other Cu-containing semiconductors described earlier.

At the end of this subsection, in relation to the content of Chaps. 1–4 of volume II, describing the pattern formation phenomena, it is useful to come back to the work by Tributsch [99]. In this work it was also reported that the onset of oscillations (occurring on a millisecond time scale) was limited by the velocity of propagation of the electrochemical signal across the electrode surface which became eventually entirely engaged in this process. This propagation velocity was found to be as high as ca. 10 m s^{-1} , thus not possible to explain in terms of purely diffusion transport. The possible variants of coupling, which include the migration contribution, and leading, e.g., to propagating fronts, were described theoretically in Chap. 1 of volume II and illustrated with experimental examples in Chap. 2 of volume II.

4.7.2.2 Reduction on GaAs Electrode

An important point is that, contrary to copper(I)-containing semiconductors, for the electroreduction of H_2O_2 on GaAs electrode, its semiconducting properties are *crucial* for the dynamic instabilities. The relevant experiments were performed using both n -type and p -type GaAs semiconductors, for which different dynamical regimes were discovered. Typical cyclic voltammogram of H_2O_2 reduction on n -GaAs is shown in Fig. 4.83 [115]. Starting from -0.2 V (vs. SCE), one observes, specific for the semiconductor electrode, a steady increase in the cathodic current in the cathodic scan, which is associated with a decrease in the semiconductor band bending and a resulting increase of conduction band electrons at the surface [51].

In turn, a current plateau observed from -0.6 to -1.0 V , proportional to bulk H_2O_2 concentration, appears to be independent of the electrode rotation rate, so its value is controlled by the charge-transfer kinetics. Oscillations of the current are observed on the return scan, also if potential scan is stopped, and are also accompanied with oscillating light emission. Detailed analysis of the oscillation

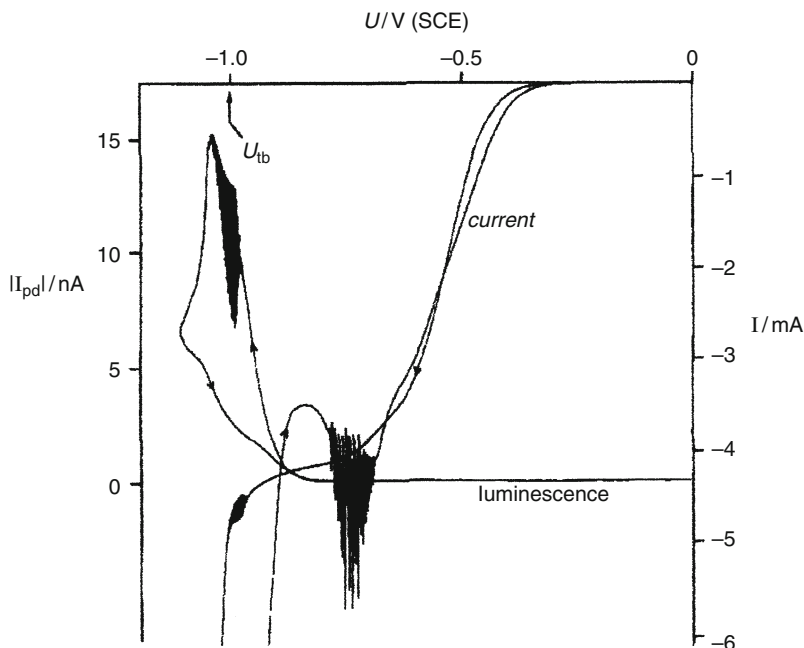


Fig. 4.83 Cathodic current–potential scan for an *n*-GaAs electrode in 1.0 M H₂O₂, 1 M H₂SO₄ solution at 40 °C. Scan rate 2 mV/s. Also shown is the light emission of the electrode detected as a photodiode current. Reprinted with permission from [115]. Copyright 1993 American Chemical Society

regimes indicated that they were born in a Hopf bifurcation, exhibit period-doubling route to chaotic oscillations, followed by sudden transition to MMO [51]. Figure 4.84 shows the corresponding bifurcation diagram.

Furthermore, it was found that insertion of the external resistor could also cause oscillations in a way typical of the systems with the negative faradaic resistance. Accordingly, under galvanostatic conditions, the electroreduction of H₂O₂ on *n*-GaAs electrode exhibited bistability. In the bistable region there were also detected oscillations of the electrode potential, when the imposed current was slowly increased toward more negative values; then, an oscillatory escape occurred toward the opposite potential branch.

Regarding now the *p*-GaAs, the oscillations of the current were observed *only under intensive illumination*, when the light intensity was so high that the cathodic photocurrent equaled the (limiting) cathodic current observed at *n*-type electrodes. Such photocurrent oscillations occurred over a large potential range, in both the forward and reverse scans (see Fig. 4.85).

The mechanism of these processes takes into account both the well established role of the OH[•] intermediate in the H₂O₂ reduction at both metal and semiconducting electrodes, as well as the specific properties of the semiconducting phase. According to Memming [116] who studied the H₂O₂ electroreduction at *p*-GaP

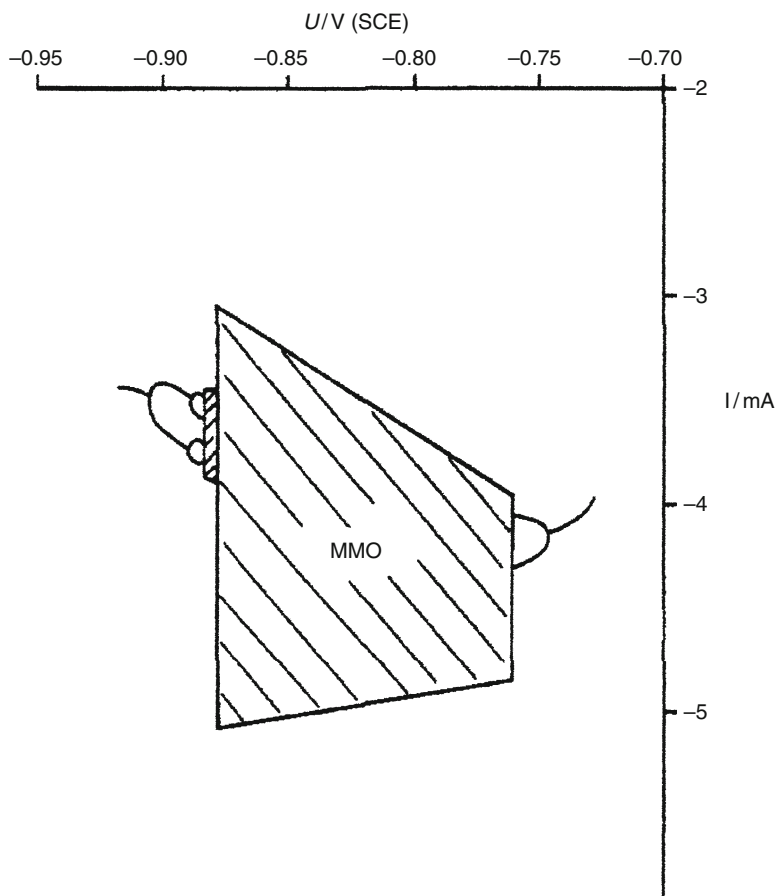
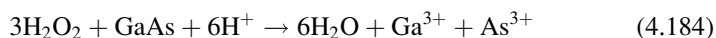


Fig. 4.84 Schematic bifurcation diagram giving the minima and maxima of the oscillatory or stationary current as a function of the applied cell potential U (n -GaAs, 1 M H_2O_2 + 1 M H_2SO_4 , 40 °C). Reprinted with permission from [115]. Copyright 1993 American Chemical Society

semiconductors one can conclude that (since at p -type semiconductors H_2O_2 is reduced only under illumination) at least one step of this process involves the photoexcited conduction band electron:



Furthermore, in parallel to processes (4.182, 4.183), the chemical etching of GaAs occurs:



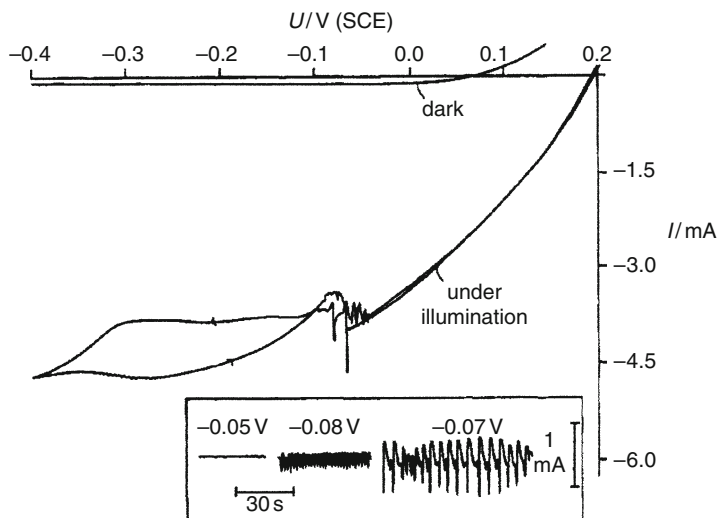
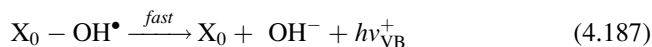
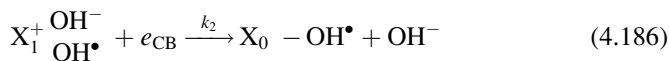
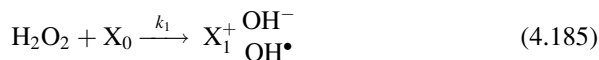


Fig. 4.85 Current–potential scan for *p*-GaAs in 1 M H₂O₂ + 1 M H₂SO₄ solution in the dark and under illumination (maximum incident light intensity). Scan rate 1 mV/s, *T* = 40 °C. In the *inset*, some typical oscillatory photocurrent time series are shown for the indicated values of the applied cell potential. Reprinted with permission from [115]. Copyright 1993 American Chemical Society

Further works (e.g., [117]) led to the conclusion that in order to explain the experimentally observed correlation between both above processes, one had to assume the existence of their common precursor, i.e., the chemisorbed H₂O₂ intermediate. Then the complete mechanism is composed of the following steps, starting from adsorption of H₂O₂ on *n*-GaAs surface [51]:



where X₀ is a free GaAs surface site and X₁⁺ is an electron-deficient GaAs surface bond. Also, surface state X₁⁺ corresponds to the postulated precursor of chemical etching of GaAs. The rate constant *k*₁ is relatively small, i.e., kinetic limitations arise in the corresponding adsorption step and the electrode coverage with the X₁ surface complex becomes one of the dynamic variables in this system. The other dynamic variable is the electrode potential *E*, but in the case of the semiconductors,

contrary to the metal phase, one has to take into account the spatial, diffuse distribution of charge in the semiconducting phase. Typically, the Debye length of this region is larger than the analogous length for the electrolyte phase, so the specific capacitance of the semiconductor depletion layer (C_{sc}) is much smaller than that of the electrolyte layer. In consequence, a change in the interfacial potential E is realized almost entirely across the semiconductor depletion layer. Furthermore, the product of the electrical potential difference between the surface and the bulk (ϕ_{sc}) and the elementary charge (band bending) decides, through the Boltzmann distribution, the concentration of free conduction band electrons at the surface (n_s) of n -type semiconductor (available for electrochemical reactions), in relation to the concentration of conduction band electrons in the bulk (n_b):

$$n_s = n_b \exp(-e\phi_{sc}/kT) \quad (4.189)$$

The two ordinary differential equations, that define the present dynamical system, have the following form [51]:

$$C_{sc} \frac{dE}{dt} = \frac{U - E}{AR_{\Omega}} + e\Gamma_m v_2 \quad (4.190)$$

$$\frac{d\theta}{dt} = v_1 - v_2 \quad (4.191)$$

where Γ_m is the total number of sites per unit area of GaAs, $E = \phi_{sc} + \phi_H$ (with the latter term meaning the potential drop in the electrolyte, across the Helmholtz layer) and v_1 and v_2 denote the rates of kinetically crucial steps (4.185) and (4.186).

In search of the oscillatory mechanism, another key point is the understanding the origin of the negative differential resistance. Its existence in the studied process, as well as decisive role for the oscillations, in conjunction with the serial resistance, was unambiguously confirmed in the impedance measurements, complemented with the appropriate model construction and its linear stability analysis [118]. It was also shown that the source of this negative impedance was the *anomalous* dependence of the band bending on the electrode potential. This anomaly means that in a certain range of the voltammogram, a shift in the applied potential to the negative values does not lead to a decrease in the semiconductor band bending (as expected for n -type semiconductor/electrolyte interface [119]), but to its *increase* which causes a decrease in the reduction current. Chemically, this effect is believed to be caused by the intermediate hydride layer formed electrochemically during the concomitant proton reduction, occurring through the Volmer reaction:



In other words, the hydride intermediate changes the charge distribution such as to increase the depletion layer band bending.

Although the presented approach is a significant step toward understanding of the oscillatory reduction of H_2O_2 at GaAs electrode, it requires further development, since it does not explain all its dynamic features, as, e.g., the experimentally observed galvanostatic oscillations. Therefore, in search of further mechanistic details of the process, Koper et al. [120] have performed later the electroreflectance (EER) study of the oscillatory hydrogen peroxide reduction on *n*-GaAs from aqueous sulfuric acid solutions. In the experiment, the normalized field-induced change in reflectivity $\Delta R/R$ is measured by application of a periodic modulation of the interfacial potential $\Delta E = \Delta E_{\text{max}} \sin(\omega t)$ and studied as a function of the light wavelength, the modulation frequency and the dc electrode potential E . The authors showed how this technique was useful to follow electrochemical oscillations at semiconductor electrodes indicating that the reflectivity and electroreflectance oscillated with qualitatively different patterns. By measuring the electroreflectance at varying frequency of the potential modulation, at least two contributions to the EER signal were detected: one stemming from the semiconductor space charge layer and one stemming from surface compounds. Based on comparison of experimentally measured photocurrent, total current, and reflectivity, supported by numerical calculations invoking the principles of the above model, it was possible to determine the quantitative characteristics of the relaxation oscillations, i.e., to identify the electrode potential as a fast dynamical variable (reflecting the fast variations of the surface states presumably due to hydride formation) and the electrode coverage with H_2O_2 surface intermediate (θ) as a slow variable.

References

1. Frumkin AN (1933) Wasserstoffüberspannung und Struktur der Doppelschicht. *Z physik Chem* 164A:121–133
2. Bard AJ, Faulkner L (2001) *Electrochemical methods. Fundamentals and applications*. Wiley, New York
3. Parsons R (1961) The structure of the electrical double layer and its influence on the rates of electrode reactions. *Adv Electrochem Electrochem Eng* 1:1–64
4. Galus Z (1994) *Fundamentals of electrochemical analysis*, 2nd edn. Ellis Horwood, New York
5. Frumkin AN, Petri OA, Nikolaeva-Fedorovitch NV (1961) Current-time curves of reduction of anions at the dropping electrode. *Dokl Akad Nauk SSSR* 136:1158–1161 (in Russian)
6. Frumkin A, Nikolayeva-Fedorovich N, Ivanova R (1959) The influence of surface active anions on the electroreduction of the persulphate anion at negative potentials. *Can J Chem* 37:253–256
7. Fawcett WR, Levine S (1973) Discreteness-of-charge effects in electrode kinetics. *J Electroanal Chem* 43:175–184
8. Gokhstein AY, Frumkin AN (1960) Autooscillations in reduction of $\text{S}_2\text{O}_8^{2-}$ anions on mercury. *Dokl Akad Nauk SSSR* 132:388–391 (in Russian)
9. Wolf W, Ye J, Purgand M, Eiswirth M, Doblhofer K (1992) Modeling the oscillating electrochemical reduction of peroxodisulfate. *Ber Bunsenges Phys Chem* 96:1797–1804
10. Levich VG (1962) *Physicochemical hydrodynamics*. Prentice-Hall, Englewood Cliffs

11. Desilvestro J, Weaver MJ (1987) Redox mediation involving oxide films as examined by surface-enhanced Raman spectroscopy: peroxodisulfate reduction at oxide-modified gold electrodes. *J Electroanal Chem* 234:237–249
12. Samec Z, Doblhofer K (1994) Mechanism of peroxodisulfate reduction at a polycrystalline gold electrode. *J Electroanal Chem* 367:141–147
13. Müller L (1967) Über die beschleunigende Wirkung von Pt-oberflächen-oxiden auf die Geschwindigkeit der kathodischen Reduktion von $S_2O_8^{2-}$ an einer Pt-elektrode in alkalischer Lösung. *J Electroanal Chem* 13:275–279
14. Müller L, Wetzel R, Otto H (1970) Die Bestimmung des Bedeckungsgrades von $S_2O_8^{2-}$ und Jodat an Platin. *J Electroanal Chem* 24:175–185
15. Samec Z, Bittner AM, Doblhofer K (1996) Electrocatalytic reduction of peroxodisulfate anion on Au(111) in acidic aqueous solutions. *J Electroanal Chem* 409:165–173
16. Samec Z, Bittner AM, Doblhofer K (1997) Origin of electrocatalysis in the reduction of peroxodisulfate on gold electrodes. *J Electroanal Chem* 432:205–214
17. Cahan BD, Villulas HM, Yeager ER (1991) The effects of trace anions on the voltammetry of single crystal gold surfaces. *J Electroanal Chem* 306:213–238
18. Shi Z, Lipkowski J, Gamboa M, Zelenay P, Wieckowski A (1994) Investigations of SO_4^{2-} adsorption at the Au(111) electrode by chronocoulometry and radiochemistry. *J Electroanal Chem* 366:317–326
19. Shi Z, Lipkowski J, Mirwald S, Pettinger B (1995) Electrochemical and second harmonic generation study of SO_4^{2-} adsorption at the Au(111) electrode. *J Electroanal Chem* 396:115–124
20. Koper MTM (1996) Mixed-mode oscillations in the peroxodisulfate reduction on platinum and gold rotating disk electrodes. *Ber Bunsenges phys Chem* 100:497–500
21. Treindl L, Doblhofer K, Krischer K, Samec Z (1999) Mechanism of the oscillatory reduction of peroxodisulfate on gold(110) at electrode potentials positive to the point of zero charge. *Electrochim Acta* 44:3963–3967
22. Samec Z, Krischer K, Doblhofer K (2001) Reduction of peroxodisulfate on gold(111) covered by surface oxides: inhibition and coupling between two oxide reduction processes. *J Electroanal Chem* 499:129–135
23. Nakanishi S, Sakai S, Hatou M, Mukouyama Y, Nakato Y (2002) Oscillatory peroxodisulfate reduction on Pt and Au electrodes under high ionic strength conditions, caused by the catalytic effect of adsorbed OH. *J Phys Chem B* 106:2287–2293
24. Nakanishi S, Mukouyama Y, Karasumi K, Imanishi A, Furuya N, Nakato Y (2000) Appearance of an oscillation through the autocatalytic mechanism by control of the atomic-level structure of electrode surfaces in electrochemical H_2O_2 reduction at Pt electrodes. *J Phys Chem B* 104:4181–4188
25. Strasser P, Eiswirth M, Koper MTM (1999) Mechanistic classification of electrochemical oscillators – an operational experimental strategy. *J Electroanal Chem* 478:50–66
26. Strasser P, Lübke M, Eickes C, Eiswirth M (1999) Modeling galvanostatic potential oscillations in the electrocatalytic iodate reduction system. *J Electroanal Chem* 462:19–33
27. Holleman A, Wiberg E (1985) *Lehrbuch der Anorganischen Chemie*. Walter de Gruyter, New York
28. Rieger PH (1994) *Electrochemistry*. Chapman-Hall, New York, p 334
29. Koper MTM, Sluyters JH (1994) Instabilities and oscillations in simple models of electrocatalytic surface reactions. *J Electroanal Chem* 371:149–159
30. Li Z, Cai J, Zhou S (1997) Potential oscillations during the reduction of $Fe(CN)_6^{3-}$ ions with convection feedback. *J Electroanal Chem* 432:111–116
31. Li Z, Cai J, Zhou S (1997) Current oscillations in the reduction or oxidation of some anions involving convection mass transfer. *J Electroanal Chem* 436:195–201
32. Li ZL, Yuan QH, Ren B, Xiao XM, Zeng Y, Tian ZQ (2001) A new experimental method to distinguish two different mechanism for a category of oscillators involving mass transfer. *Electrochem Commun* 3:654–658

33. de Levie R (1971) Anion bridging and anion electrocatalysis on mercury. *J Electrochem Soc* 118:185C–192C, and references cited therein
34. Turowska M (1984) Catalytic effect of anions undergoing specific adsorption on the electrode on the mechanism and kinetics of electrode reactions. In: Libuś W, Dutkiewicz E (eds) *Electrochemistry of interfaces and ionogenic media*. PWN, Warsaw (in Polish), pp 183–191 (and references cited therein)
35. Pospíšil L, de Levie R (1970) Thiocyanate electrocatalysis of the reduction of In(III). *J Electroanal Chem* 25:245–255
36. de Levie R (1970) On the electrochemical oscillator. *J Electroanal Chem* 25:257–273
37. Jakuszewski B, Turowska M (1973) Voltammetric minima and electrochemical oscillations. *J Electroanal Chem* 46:399–410
38. Rudolph M, Hromadova M, de Levie R (1998) Demystifying the electrochemical oscillator. *J Phys Chem A* 102:4405–4410
39. Engel AJ, Lawson J, Aikens DA (1965) Ligand-catalyzed polarographic reduction of indium(III) for determination of halides and certain organic sulfur and nitrogen compounds. *Anal Chem* 37:203–207
40. Tamamushi R (1966) An “electrochemical oscillator” – an electrochemical system which generates undamped electric oscillation. *J Electroanal Chem* 11:65–68
41. de Levie R, Husovsky AA (1969) On the negative faradaic admittance in the region of the polarographic minimum of In(III) in aqueous NaSCN solution. *J Electroanal Chem* 22:29–48
42. de Levie R, Pospíšil L (1969) On the coupling of interfacial and diffusional impedances, and on the equivalent circuit of an electrochemical cell. *J Electroanal Chem* 22:277–290
43. Koper MTM, Sluyters JH (1991) Electrochemical oscillators: an experimental study of the indium/thiocyanate oscillator. *J Electroanal Chem* 303:65–72
44. Koper MTM, Sluyters JH (1991) Electrochemical oscillators: their description through a mathematical model. *J Electroanal Chem* 303:73–94
45. Keizer J, Scherson D (1980) A theoretical investigation of electrode oscillations. *J Phys Chem* 84:2025–2032
46. Koper MTM, Gaspard P (1991) Mixed-mode and chaotic oscillations in a simple model of an electrochemical oscillator. *J Phys Chem* 95:4945–4947
47. Koper MTM, Gaspard P, Sluyters JH (1992) A one-parameter bifurcation analysis of the indium/thiocyanate electrochemical oscillator. *J Phys Chem* 96:5674–5675
48. Koper MTM, Gaspard P (1992) The modeling of mixed-mode and chaotic oscillations in electrochemical systems. *J Chem Phys* 96:7797–7813
49. Feldberg SW (1969) Digital simulation: a general method for solving electrochemical diffusion-kinetic problems. In: Bard AJ, Rubinstein I (eds) *Electroanalytical chemistry*, vol 3. Dekker, New York, pp 199–296
50. Britz D (2005) *Digital simulation in electrochemistry*, 3rd edn. Springer, Berlin
51. Koper MTM (1996) Oscillations and complex dynamical bifurcations in electrochemical systems. In: Prigogine I, Rice SA (eds) *Adv Chem Phys* XCII:161–298
52. Koper MTM, Gaspard P, Sluyters JH (1992) Mixed-mode oscillations and incomplete homoclinic scenarios to a saddle focus in the indium/thiocyanate electrochemical oscillator. *J Chem Phys* 97:8250–8260
53. Shil’nikov LP (1965) A case of the existence of a denumerable set of periodic motions. *Sov Math Dokl* 6:163–166
54. Koutecký J (1953) Theorie langsamer elektrodenreaktionen in der polarographie und polarographisches verhalten eines systems, bei welchem der depolarisator durch eine schnelle chemische reaktion aus einem elektroinaktiven stoff entsteht 18:597–610
55. Weber J, Koutecký J (1955) Über die kinetik der elektrodenvorgänge. XV. Tabellen der funktion für den polarographischen strom bei einem depolarisationsvorgang mit vorgeschalteten oder nachfolgenden sehr schnellen monomolekularen chemischen reaktionen 20:980–983

56. Oldham KB, Parry EP (1968) Use of polarography and pulse-polarography in the determination of the kinetic parameters of totally irreversible electroreductions. *Anal Chem* 40:65–69
57. de Levie R (2003) On some electrochemical oscillators at the mercury/water interface. *J Electroanal Chem* 552:223–229
58. Kariuki S, Dewald HD (1998) Current oscillations in the reduction of indium(III) and gallium (III) in dilute chloride and nitrate solutions at the dropping mercury electrode. *Electrochim Acta* 43:701–704
59. Kariuki S, Dewald HD, Thomas J, Rollins RW (2000) Current oscillations of indium(III) at a dropping mercury electrode. *J Electroanal Chem* 486:175–180
60. Krogulec T, Barański A, Galus Z (1979) The electrode kinetics of nickel in thiocyanate solutions at mercury electrodes. *J Electroanal Chem* 100:791–800
61. Jurczakowski R, Orlik M (1999) On the source of oscillatory instabilities in the electroreduction of thiocyanate complexes of nickel(II) at mercury electrodes. *J Electroanal Chem* 478:118–127
62. Tamamushi R, Matsuda K (1966) Experimental studies of negative resistance of galvanic cells and the undamped electric oscillation generated by electrochemical oscillators. *J Electroanal Chem* 12:436–442
63. Koper MTM, Sluyters JH (1993) On the mathematical unification of a class of electrochemical oscillators and their design procedures. *J Electroanal Chem* 352:51–64
64. Krogulec T, Barański A, Galus Z (1974) On the formation of sulphides in the electroreduction of thiocyanate complexes of nickel(II) at mercury electrodes. *J Electroanal Chem* 57:63–75
65. Krogulec T, Galus Z (1981) On the electroreduction of thiocyanates bound to Ni(II). *J Electroanal Chem* 117:109–118
66. Jurczakowski R, Orlik M (2000) The oscillatory course of the electroreduction of thiocyanate complexes of nickel(II) at mercury electrodes – experiment and simulation. *J Electroanal Chem* 486:65–74
67. Orlik M (1998) Digital simulation of electrochemical oscillations and associated reagents concentration profiles with the finite differences method. *Pol J Chem* 72:2272–2293
68. Kristiansen GK (1963) Zero of arbitrary function. *BIT* 3:205–207
69. Bieniasz LK, Britz D (2004) Recent developments in digital simulation of electroanalytical experiments. *Pol J Chem* 78:1195–1219
70. Orlik M (2005) An improved algorithm for the numerical simulation of cyclic voltammetric curves affected by the ohmic potential drops and its application to the kinetics of bis(biphenyl)chromium(I) electroreduction. *J Electroanal Chem* 575:281–286
71. Fuchs G, Kišova L, Komenda J, Gritzner G (2002) The influence of tetraethylammonium perchlorate on the electrode kinetics of Eu^{3+} in dimethylsulfoxide. *J Electroanal Chem* 526:107–114
72. Jurczakowski R, Orlik M (2002) Bistable/oscillatory system based on the electroreduction of thiocyanate complexes of Nickel(II) at a streaming mercury electrode. Experiment and simulation. *J Phys Chem B* 106:1058–1065
73. Galus Z (ed) (1979) *Electroanalytical methods of determination of physico-chemical constants*. PWN, Warsaw, pp 64–67 (in Polish)
74. Koryta J (1954) Diffusion and kinetic currents at the streaming mercury electrode. *Collect Czechoslov Chem Commun* 19:433–442
75. Weaver JR, Parry RW (1954) Reduction at the streaming mercury electrode. I. The limiting current. *J Am Chem Soc* 76:6258–6262
76. Weaver JR, Parry RW (1956) Reduction at the streaming mercury electrode. II. Current-voltage curves. *J Am Chem Soc* 78:5542–5550
77. Delahay P (1965) Electrode kinetics at open circuit at the streaming mercury electrode: I. Theory. *J Electroanal Chem* 10:1–7
78. Orlik M, Jurczakowski R (2002) On the stability of nonequilibrium steady-states for the electrode processes at a streaming mercury electrode. *J Phys Chem B* 106:7527–7536

79. Orlik M, Jurczakowski R (2004) On the role of specific characteristics of the streaming mercury electrode in the generation of the nonlinear electrochemical dynamical phenomena. *Polish J Chem* 78:1221–1234
80. Jurczakowski R, Orlik M (2007) Experimental and theoretical impedance studies of oscillations and bistability in the Ni(II)–SCN[−] electroreduction at the streaming mercury electrode. *J Electroanal Chem* 605:41–52
81. Jurczakowski R, Orlik M (2003) Experimental and theoretical studies of the multistability in the electroreduction of the nickel(II)-N₃[−] complexes at a streaming mercury electrode. *J Phys Chem B* 107:10148–10158
82. Kutner W, Galus Z (1974) Electrode reactions of nickel(II) at mercury electrodes in aqueous solutions of azides. *J Electroanal Chem* 51:363–376
83. Maggio F, Romano V, Pellerito L (1967) Potentiometric studies on the nickel(II)-azide complex system. *J Electroanal Chem* 15:227–230
84. Senise P, Godinho OES (1970) Spectrophotometric study of cobalt(II) and nickel(II) monoazido complexes in aqueous solution. *J Inorg Nucl Chem* 32:3641–3645
85. Jurczakowski R, Orlik M (2005) The electroreduction of azides bound to nickel(II) ions in weak acidic media. *J Electroanal Chem* 574:311–320
86. Orlik M, Jurczakowski R (2008) The kinetic parameters of the electrocatalytic reduction of the coordinated azide anions found from comparison of dc and ac measurements for the tristable Ni(II)-N₃[−] system. *J Electroanal Chem* 614:139–148
87. Jehring H, Kürschner U (1974) Der elektrochemische Elektrosorptions-Inhibitions-Oszillator als neues Biomembran Model. *Studia Biophysica*, Berlin 42:225–228
88. Jehring H, Kürschner U (1975) Durch Spannungsimpulse eines Elektrosorptions-oszillators hervorgerufene Eigenschaftensänderungen mit Hysterese in Elektrosorptionsschichten (Biomembranmodell der Informationsaufnahme und Speicherung). *Studia Biophysica*, Berlin 48:81–84
89. Jehring H, Kuerschner U (1977) Elektrochemische Oszillationen bei der inhibierten Kupferabscheidung an der Quecksilberelektrode. *J Electroanal Chem* 75:799–808
90. Dörfler HD, Müller E (1982) The analysis of current oscillations on the basis of the retardation of electrode processes by different surfactants. *J Electroanal Chem* 135:37–53
91. Dörfler HD (1989) Elektrochemische Oszillationserscheinungen durch inhibierte Elektrodenreaktionen. *Nova acta Leopoldina NF* 61:25–49
92. Treindl L', Olexová A (1983) Electrochemical oscillations of the system Hg|HSO₄[−]|BrO₃[−] and phenol. *Electrochim Acta* 28:1495–1499
93. Olexová A, Treindl L' (1984) Electrochemical oscillations of the system Hg|HSO₄[−]|BrO₃[−]. *Chem zvesti* 38:145–150
94. Schlegel JM, Parette RF (1992) An electrochemical oscillator: the mercury/chloropentamine cobalt(III) oscillator. *J Electroanal Chem* 335:67–74
95. Hudson JL, Tsotsis TT (1994) Electrochemical reaction dynamics: a review. *Chem Eng Sci* 49:1493–1572
96. Honda M, Kodera T, Kita H (1986) Electrochemical behavior of H₂O₂ at Ag in HClO₄ aqueous solutions. *Electrochim Acta* 31:377–383
97. Flätgen G, Wasle G, Lübke M, Eickes C, Radhakrishnan G, Doblhofer K, Ertl G (1999) Autocatalytic mechanism of H₂O₂ reduction on Ag electrodes in acidic electrolyte: experiments and simulations. *Electrochim Acta* 44:4499–4506
98. Šr̂bac S, Adžić RR (1992) Oscillatory phenomena in oxygen and hydrogen peroxide reduction on the Au(100) electrode surface in alkaline solutions. *J Electroanal Chem* 337:355–364
99. Tributsch H (1975) Sustained oscillations during catalytic reduction of hydrogen peroxide on copper-iron-sulfide electrodes I. *Ber Bunsenges Phys Chem* 79:570–579
100. Fetner N, Hudson JL (1990) Oscillations during the electrocatalytic reduction of hydrogen peroxide on a platinum electrode. *J Phys Chem* 94:6506–6509

101. van Venrooij TGJ, Koper MTM (1995) Bursting and mixed-mode oscillations during the hydrogen peroxide reduction on a platinum electrode. *Electrochim Acta* 40:1689–1696
102. Mukouyama Y, Nishimura T, Nakanishi S, Nakato Y (2000) Roles of local deviations and fluctuations of the Helmholtz-layer potential in transitions from stationary to oscillatory current in an “ H_2O_2 – acid – Pt” electrochemical system. *J Phys Chem B* 104:11186–11194
103. Nakanishi S, Mukouyama Y, Nakato Y (2001) Catalytic effect of adsorbed iodine atoms on hydrogen peroxide reduction at single-crystal Pt electrodes, causing enhanced current oscillations. *J Phys Chem B* 105:5751–5756
104. Mukouyama Y, Nakanishi S, Chiba T, Murakoshi K, Nakato Y (2001) Mechanisms of two electrochemical oscillations of different types, observed for H_2O_2 reduction on a Pt electrode in the presence of a small amount of halide ions. *J Phys Chem B* 105:7246–6253
105. Mukouyama Y, Nakanishi S, Konishi H, Ikeshima Y, Nakato Y (2001) New-type electrochemical oscillation caused by electrode-surface inhomogeneity and electrical coupling as well as solution stirring through electrochemical gas evolution reaction. *J Phys Chem B* 105:10905–10911
106. Cattarin S, Tributsch H (1988) Light-sustained cooperative mechanisms observed at liquid junctions of chalcopyrite semiconductors. *Chem Phys Lett* 148:221–225
107. Tributsch H (1975) Sustained oscillations during catalytic reduction of hydrogen peroxide on copper-iron-sulfide electrodes II. *Ber Bunsenges Phys Chem* 79:580–587
108. Tributsch H, Bennett JC (1976) Hydrogen peroxide induced periodical catalysis on copper-containing sulfides. *Ber Bunsenges phys Chem* 80:321–327
109. Cattarin TH (1990) Interfacial reactivity and oscillating behavior of chalcopyrite cathodes during H_2O_2 reduction I. Electrochemical phenomena. *J Electrochem Soc* 137:3475–3483
110. Cattarin S, Fletcher S, Pettenkofer C, Tributsch H (1990) Interfacial reactivity and oscillating behavior of chalcopyrite cathodes during H_2O_2 reduction. II. Characterization of electrode corrosion. *J Electrochem Soc* 137:3484–3493
111. Cattarin S, Tributsch H (1992) Reduction of H_2O_2 at CuInSe_2 (photo)cathodes II. Sustained and triggered oscillations. *J Electrochem Soc* 139:1328–1332
112. Cattarin S, Tributsch H (1993) Non-linear and pulse phenomena during H_2O_2 reduction at chalcopyrite (photo)cathodes. *Electrochim Acta* 38:115–122
113. Cattarin S, Tributsch H, Stimming U (1992) Reduction of H_2O_2 at CuInSe_2 (photo)cathodes I. Characterization of the electrode-electrolyte interface. *J Electrochem Soc* 139:1320–1328
114. Pohlmann L, Neher G, Tributsch H (1994) A model for oscillating hydrogen liberation at CuInSe_2 in the presence of H_2O_2 . *J Phys Chem* 98:11007–11010
115. Koper MTM, Meulenkamp EA, Vanmaekelbergh D (1993) Oscillatory behavior of the H_2O_2 reduction at GaAs semiconductor electrodes. *J Phys Chem* 97:7337–7341
116. Memming R (1969) Mechanism of the electrochemical reduction of persulfates and hydrogen peroxide. *J Electrochem Soc* 116:785–790
117. Minks BP, Vanmaekelbergh D, Kelly JJ (1989) Current-doubling, chemical etching and the mechanism of two-electron reduction reactions at GaAs: Part 2. A unified model. *J Electroanal Chem* 273:133–145
118. Koper MTM, Vanmaekelbergh D (1995) The origin of oscillations during hydrogen peroxide reduction on GaAs semiconductor electrodes. *J Phys Chem* 99:3687–3696
119. Morrison SR (1990) *Electrochemistry at semiconductors and oxidized metal electrodes*. Plenum, New York
120. Koper MTM, Chaparro AM, Tributsch H, Vanmaekelbergh D (1998) *Langmuir* 14:3926–3931

Chapter 5

Temporal Instabilities in Anodic Oxidation of Small Molecules/Ions at Solid Electrodes

5.1 Oscillations in Anodic Oxidation of Molecular Hydrogen

5.1.1 *Experimental Results and Oscillation Mechanism*

Oscillations and multistability in oxidation processes at solid electrodes are important for several reasons. First, they were reported for species that are (or can appear) important in chemical engineering of fuels, including the fuel cells: hydrogen, carbon monoxide, formaldehyde, formic acid/formate ions, 2-propanol, 1-butanol, hydrazine, or ethylene glycol. It can be useful to know how to avoid instabilities involving these species or, on the contrary, to profit from them. Second, electrooxidation of these molecules exhibits rich variety of nonlinear dynamic behaviors which can be treated in a model way for the sake of generalization. Third, some of these processes, under appropriate conditions, can become a source of spatial or spatiotemporal patterns on electrodes which phenomena only recently gained satisfactory explanation and description. In this chapter, we shall summarize the *temporal* phenomena associated with the oxidation of the above-mentioned molecules, while pattern formation will be discussed in separate Chap. 2 of volume II.

Current research data indicate that such processes should be qualified as electrocatalytic, i.e., the electrode surface is actively engaged in the kinetics of the electron transfer reaction, usually involving the process taking place via the adsorbed intermediate. As in the case of other types of electrochemical oscillators, one can observe the evolution of the understanding of the source of chemical instabilities—from early, sometimes oversimplified explanations oriented exclusively on the properties of the electrode/electrolyte interface toward more recent concepts, involving the analysis of the system's stability in terms of nonlinear dynamics. In particular, oscillations under galvanostatic conditions could be understood only recently in terms of the concept of the HN-NDR oscillator [1] (cf. Chap. 3).

The anodic oxidation of H₂ on Pt electrode is an electrocatalytic process, in which the electron transfer is preceded by the adsorption of H₂ molecule on the active surface site. Hence, the oscillatory course of this process can be associated

with the periodic blocking and freeing of these adsorption sites, as a common mechanism for all electrocatalytic processes. If the electrode surface is activated and there are no adsorbed impurities, then the rate of oxidation of hydrogen at Pt electrode is diffusion controlled. It is instructive to review the development of understanding the mechanism of oscillations in this important process.

The first report on the oscillations of current during the oxidation of H_2 on polycrystalline Pt electrode, under potentiostatic conditions and in the presence of sufficient serial ohmic resistance, was published by Thalinger and Volmer in 1930 in *Zeitschrift für physikalische Chemie* [2]. In turn, oscillations of the electrode potential during the galvanostatic oxidation of H_2 were first reported by Armstrong and Butler in 1947 [3]. Noteworthy, these authors mentioned the possible role, in the onset of oscillations, of adsorption and deposition of dissolved metal ion impurities, which was in fact confirmed in more recent studies. But before it had happened, Sawyer and Seo [4] have attributed these galvanostatic oscillations to the temporal formation, at sufficiently positive potentials, of the surface oxides which are then reduced by the gaseous hydrogen. On such activated electrode surface the hydrogen oxidation proceeds at nearly the equilibrium potential of H_2/H^+ redox couple, but the continuous exposure to hydrogen deactivates the electrode and hence its potential again shifts to positive values. In search of the role of surface oxide layer, Conway and Novak [5] performed later a series of studies of H_2 oxidation from the “almost anhydrous solvent”—the trifluoroacetic acid (TFA) containing controlled traces of water. Under such conditions only the small fraction of Pt electrode, controlled by the amount of water, could be anodically oxidized, as TFA is an electrochemically very inactive solvent. It was found that the periodic oxidation of H_2 begins when the potential, scanned from the range of existence of the Pt oxide layer toward cathodic direction, reaches a value at which the oxide layer can begin to reduce and readsorption of trifluoroacetate anion can occur. The role of the surface oxide was thus confirmed and anion adsorption/desorption was inferred from the observations of periodic changes of relative reflectance—in phase with the current oscillations (Fig. 5.1).

Based on these studies, an important mechanistic conclusion was drawn: although oscillations in H_2 oxidation arise from periodic inhibition and reactivation of the Pt surface, coupled with diffusion transport of H_2 from the solution bulk, it is unlikely that only oxide layer formation/destruction can cause such instabilities, simply because the electrode coverage with this oxide would then be too small to cause substantial inhibition of the H_2 oxidation. More significant for the inhibition/reactivation cycle, involved in the oscillatory behavior, appeared to be the process of the anion adsorption. Altogether, the following factors were considered for the formulation of kinetic equations, representing the oxidation of H_2 under such conditions: (a) diffusion of H_2 proved by the effect of the stirring of the solution; (b) the reactivity of an incomplete oxide film at Pt; (c) the electrode potential; (d) the free surface area ($1 - \theta$) available for direct electrocatalytic oxidation of H_2 ; (e) the inhibition of catalytic activity by anion adsorption; and (f) reversibility and irreversibility (hysteresis) in the formation and reduction of the oxide film on Pt.

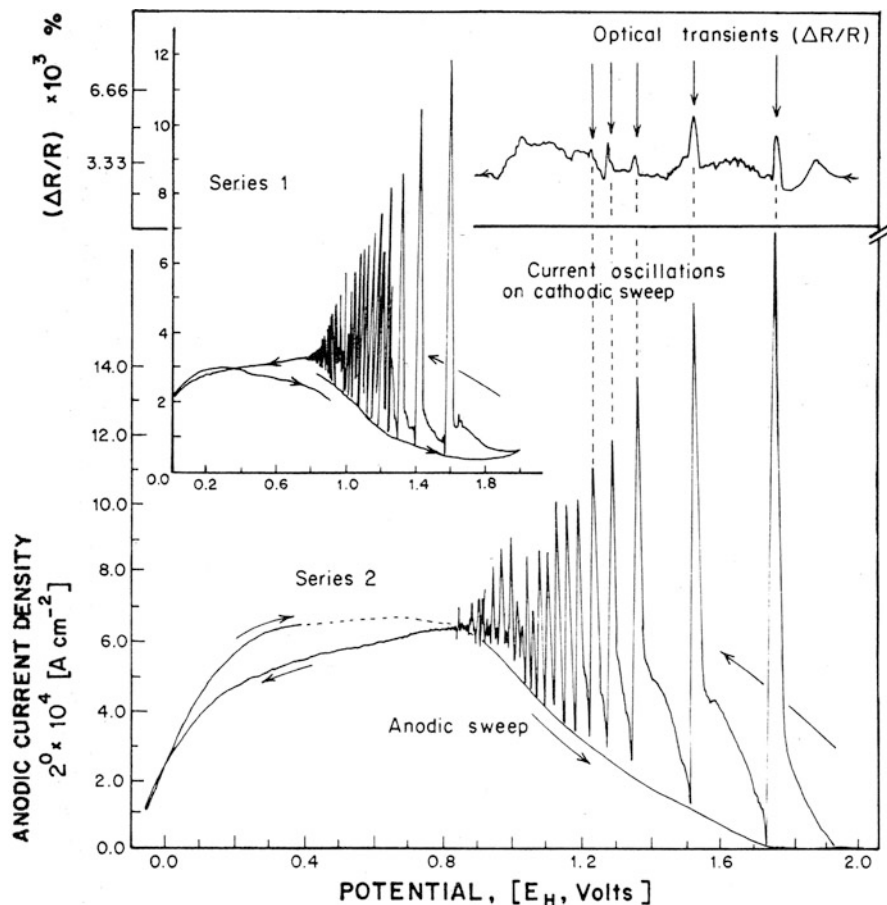


Fig. 5.1 Current oscillations in H_2 oxidation on the cathodic sweep in two potentiodynamic experiments on H_2 oxidation at Pt in almost dry TFA + 0.6 M KTFA ($s = 8 \times 10^{-2} \text{ V s}^{-1}$, $T = 298 \text{ K}$). *Note:* potential scale of series 1 is half the sensitivity of that for series 2 to accommodate the results on a single graph. *Upper curve:* relative reflectance changes $(\Delta R/R)_t$ measured simultaneously with the oscillations. Reprinted with permission from [5]. Copyright 1977 American Chemical Society

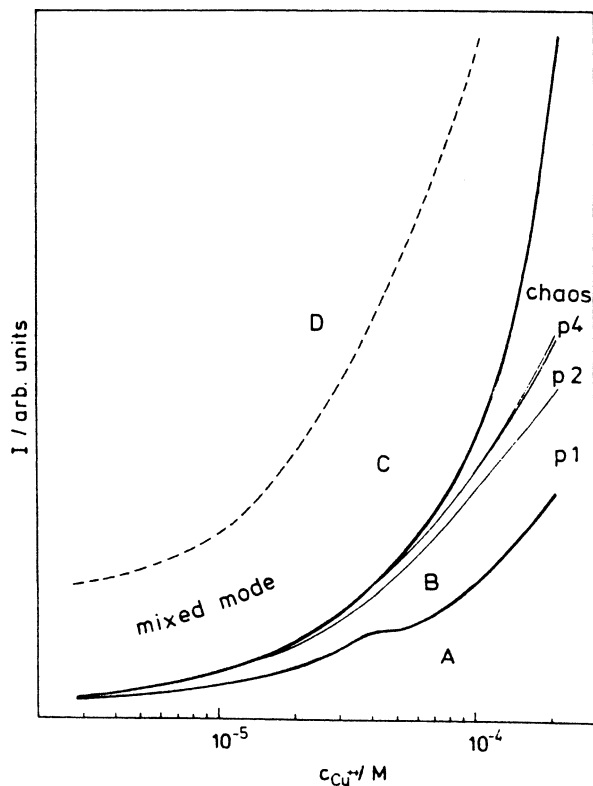
Evidently the above results inspired Horányi and Visy [6] to study the problem, whether the oscillations (in their case—under galvanostatic conditions) can be caused by coupling of hydrogen oxidation with the electroadsorption or underpotential deposition of metal ions, according to the following assumed mechanism: the electroadsorbed cations inhibit the oxidation of hydrogen by blocking the surface sites which in this way become unavailable for the adsorption and oxidation of hydrogen; as a result of this inhibition, under galvanostatic conditions, the electrode potential shifts to more positive values at which desorption of cations takes place; consequently, the rising numbers of free adsorption sites allow the flow

of higher hydrogen current, the electrode potential becomes less positive when the metal cations readsorb and the oscillatory cycle is closed. Note that this explanation cannot be alternative to the mechanism of potentiostatic oscillations given by Conway and Novak, since in the latter case the electrode potential was always so positive that the significant adsorption of cations could be excluded. In the present work, Horányi and Visy have investigated the effect of Cd^{2+} , Cu^{2+} , Sn^{2+} , Bi^{3+} , and Ag^+ ions, using different base electrolytes (H_2SO_4 , HCl , HClO_4) on the potentiostatic oscillations under galvanostatic conditions. Generally, an addition of the metal ions lowered the current of hydrogen oxidation and upon cycling variation of the electrode potential a hysteresis in the current response was observed, reflecting the limited rate of establishing the potential-dependent adsorption/desorption equilibria of metal cations. Considering the amplitude of the variation of the electrode potential during the oscillations, one concludes that Cd^{2+} ions undergo only adsorption with partial charge transfer, whereas, e.g., Cu^{2+} ions, due to much more positive standard potential $E^0(\text{Cu}/\text{Cu}^{2+})$, undergo also periodic underpotential deposition, enhancing the surface concentration of copper species. Therefore, the bulk concentration of $\text{Cu}(\text{II})$ ions can be significantly lower (e.g., 10^{-6} – 10^{-5} M) than that of $\text{Cd}(\text{II})$ ions (e.g., 10^{-2} M). Similar approach was developed by Kodera et al. [7–10] who also have proposed a mathematical model involving two dynamical variables: the electrode potential E and electrode coverage θ with deposited metal, under assumption that the oscillations in the oxidation of H_2 are caused by the attractive forces between the underpotential deposited metal atoms. Like in other approaches of that type (cf. Chap. 3), the attractive lateral interactions in the adsorption layer, leading to the bistable isotherm of the Frumkin type, constitute the autocatalytic step, necessary for the onset of instabilities. In fact, in the absence of autocatalysis, the oxidation of H_2 would not oscillate between the activated and poisoned states, but would establish at the steady-state, intermediate potential.

In later works, Krischer, Eiswirth, Ertl, Hudson et al. [11–13] have revealed further complexity in the galvanostatic H_2 oxidation, interpreting it as the periodic poisoning and activation transitions of the Pt electrode by underpotential deposition and dissolution of a passivating Cu monolayer, in the presence of chloride ions. Thus, both cations and anions added are involved in this instability. Upon increase in current density there was observed the transition from steady state to harmonic oscillations via the supercritical Hopf bifurcation, followed by a series of period doublings (Feigenbaum scenario, cf. Sect. 1.9.2) leading eventually to chaos. Figure 5.2 shows the respective bifurcation diagram.

Moreover, further increase of current density caused an emergence of another, qualitatively different chaotic regime through the *interior crisis* and finally, before the end of the oscillatory behavior, the latter chaos broke down to the periodic mixed-mode oscillations (MMO). Such a sequence of events was found also for some other oscillators, not only chemical ones [11], but also for the logistic map analyzed by Feigenbaum or for the forced Duffing oscillator with a dc bias [14]. Thus, it is an example of universalities observed in various dynamical systems. It is useful to mention here that the *interior crisis* (cf. also Sect. 1.9.2), named also an

Fig. 5.2 Experimental bifurcation diagram of the existence regions of different oscillation forms during the galvanostatic H_2 oxidation on Pt as a function of the Cu^{2+} concentration; pN means period-N oscillations. Reprinted from [13], Copyright 1993, with permission from Elsevier



explosion, is a kind of global bifurcation which manifests itself as the sudden qualitative change in the chaotic attractor size and shape. This is usually caused by its collision with unstable periodic orbit. The *interior crisis* is caused by the tangent collision of strange attractor with an unstable periodic orbit that is contained within the *interior* of the basin of attraction of this attractor, so the new attractor contains a locus of the former attractor [11, 15, 16]. In more detail, upon variation of the control parameter (here: increasing the current density) first the strange attractor is formed which does not contain the unstable periodic orbit; the latter one is created only for a critical value of the control parameter.

Studies described earlier suggest strongly that, besides underpotential deposition of Cu, also the presence of halide anions is significant for the occurrence of galvanostatic oxidation of H_2 on Pt electrodes. The fact, that specifically adsorbing Cl^- and Br^- ions can lead to splitting of the Cu-upd peaks in cyclic voltammetry [17, 18] is a strong premise that one can expect such an influence. This point was elaborated in detail by Krischer et al. [19]. Experiments with the single-crystal Pt electrodes showed that regardless of the orientation of the single crystal or the shape (wire, plate) of the polycrystalline Pt electrodes no oscillations were detectable in *suprapure* H_2SO_4 solution. One had to add at least a small amount of chlorides or bromides, so one could suppose that at the times when such *suprapure* reagents

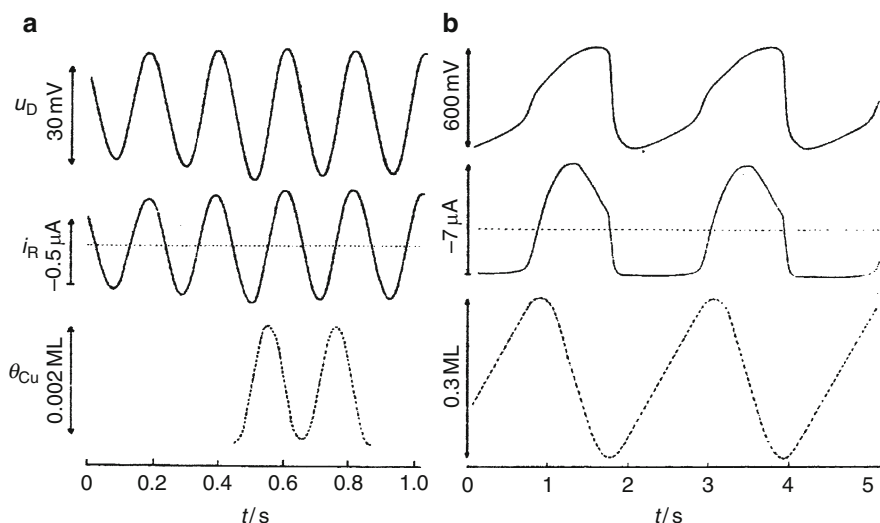
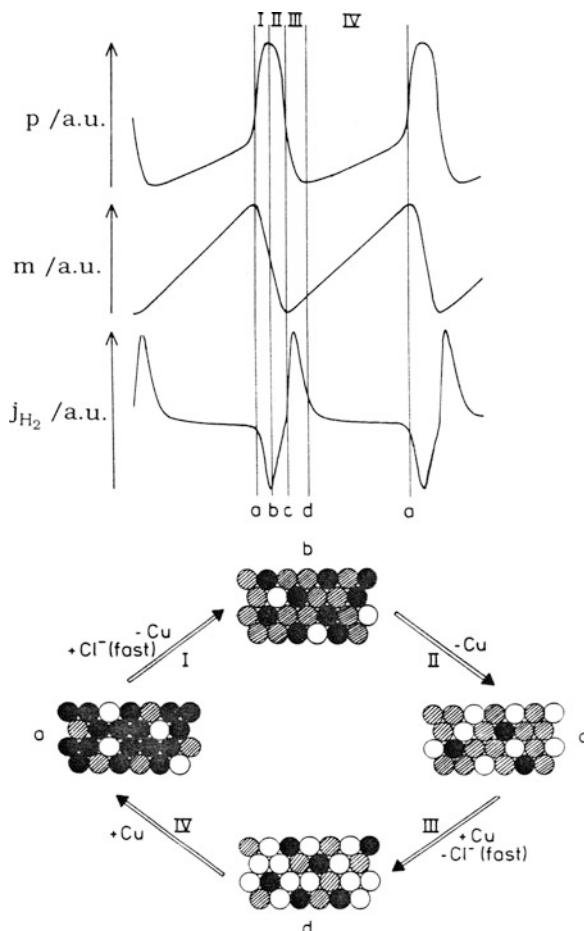


Fig. 5.3 Oscillations at the Pt-disk electrode with two different amplitudes at different current densities (*upper curves*). *Middle*: corresponding ring currents proportional to Cu^{2+} concentration at the ring. *Lower*: the integrated ring currents corresponding to the relative Cu coverage ($\Delta\theta$) at the disk. Electrolyte: $0.5 \text{ H}_2\text{SO}_4$; (a) $1 \times 10^{-4} \text{ M Cu}^{2+}$; $2 \times 10^{-3} \text{ M HCl}$; (b) $5 \times 10^{-5} \text{ M Cu}^{2+}$; $3 \times 10^{-2} \text{ M HCl}$; disk current densities: (a) $1,120 \mu\text{A cm}^{-2}$; (b) $1,440 \mu\text{A cm}^{-2}$. Reprinted from [19], Copyright 1995, with permission from Elsevier

were not yet available, at least in some experiments the unknown amounts of Cl^- or Br^- impurities could take part in the oscillatory oxidation of H_2 . On the other hand, in the presence of appropriate amount of Cl^- ions, the oscillatory course of H_2 oxidation was strongly dependent on the crystallographic orientation of the electrode: for Pt(110) oscillations were not detected, for Pt(111)—simple, single-periodic oscillations were reported, whereas for Pt(100) a large variety of oscillatory courses was found: single-periodic, undergoing further period-doubling bifurcations to chaos and followed eventually by the periodic MMO (similarly to the sequence described earlier for the polycrystalline Pt electrode). Compared to Cl^- ions, Br^- ions were able to induce complex oscillations at much lower concentration level, and for all three low-index surface orientations of Pt electrode. Additional experiments, involving two different ring-disk polycrystalline electrodes: Pt-disk/Au-ring and Pt-disk/Pt-ring, allowed to trace the variations of the electrode coverage with Cu atoms and of the current of H_2 oxidation, as well as their phases relative to the electrode potential. The crucial result of these studies is the finding that during the oscillations, the coverage of copper lags about ca. 90° behind the hydrogen oxidation current, and this phase shift was interpreted as caused by the specific adsorption of halide ions, which together with Cu atoms block the H_2 oxidation on Pt electrode (Fig. 5.3) [19].

In this way, the essential role of strongly adsorbed halide anions in the onset of the oscillatory course of H_2 oxidation was clearly confirmed. The interaction of

Fig. 5.4 Schematic drawing of an oscillation cycle: the *upper diagram* is the time series of the experimentally observed variables p , j_{H_2} and m ; the *lower diagram* is a qualitative view of the electrode surface where the *open circles* represent free adsorption sites, and the *full and shaded circles* represent metals and anions, respectively (see text for explanation). Reprinted from [20], Copyright 1995, with permission from Elsevier



both Cl^- and Br^- is strongest for Pt(100), less pronounced for Pt(111), and weakest for Pt(110)—so weak that the oscillations were not detected. This sequence correlates with the oscillations which are only observed if anions adsorb so strongly that they lead to a decrease of the H_2 -oxidation current in the Cu-upd region in the Cu-free solutions. Thus, the oscillations of current of H_2 oxidation are associated with the formation of anion/Cu coadsorbate structures, and not with Cu layer alone. The full oscillatory cycle is schematically depicted in Fig. 5.4 [19–21].

Let us start the analysis of the oscillatory cycle from the picture (a), corresponding to negative potential, with a relatively high (too high) surface concentration of metal atoms which inhibit the hydrogen oxidation. The actual value of the H_2 oxidation current is thus too low to equal the preset galvanostatic current, so this difference is compensated by the flow of capacitive current associated with charging of the electrode to more positive potential during the step (I). During this increase of the potential, the Cu atoms gradually (but relatively slowly) desorb from the electrode

surface, while the Cl^- ions adsorb then quickly. Due to this *difference in time scale* of both surface processes, the effective number of free surface sites decreases and therefore the hydrogen current also decreases. This even accelerates further increase in the electrode potential which overshoots the value, for which the actual current of H_2 oxidation under potentiostatic conditions equals the imposed current. Starting from this point (b), through step (II), the system will tend to stationary electrode coverage, ensuring this enhanced hydrogen current. The higher current causes the shift of the electrode potential back to less anodic values. Upon decrease of the potential within step (II) the electrode charge is still positive enough to cause slow desorption of metal, but starting from state (c), when step (III) begins, upon further decrease in electrode potential, the slow deposition of Cu returns and the fast desorption of halide anions begins. The effective number of free adsorption sites then increases and the potential now overshoots in the negative direction, leading to situation (d) where too many free adsorption sites are available. The continued slow adsorption of Cu returns the system to state (a) with too few adsorption sites (because the potential is below the stationary state).

In a more concise way, the above mechanism can be summarized as follows [20]: the oscillations occur due to the coupling of two processes which inhibit the hydrogen oxidation: the slow underpotential deposition of copper (favored at low potentials) and the fast specific adsorption of chloride (occurring at more positive potentials). For low surface coverage, maintaining of the preset current through the hydrogen oxidation is possible at relatively low potentials, at which however the slow underpotential deposition of Cu occurs. With increasing Cu coverage the galvanostat forces the shift of the electrode potential toward more positive values, at which Cu desorbs slowly but Cl^- ions adsorb quickly, and due to this difference in time scale the potential overshoots the steady-state value. The same reasoning applies for the, following this step, decreasing potential.

It is important to compare this mechanism with the impedance characteristics. The elementary process of H_2 oxidation is characterized with the positive differential resistance, since its rate increases exponentially with electrode potential. Simultaneously, on a comparable time scale (fast variables), an increase in the electrode coverage with halide ions, which inhibit the H_2 oxidation, occurs and this is the source of the negative differential resistance developing at sufficiently positive potential. There is also a third potential-dependent process, *overlapping* with the two previous ones: the dissolution of the metal (Cu) monolayer, also inhibiting the H_2 oxidation; this process thus does not give rise to the negative resistance, but delays the manifestation of the rise of current in the region in which it would already exhibit negative resistance. Consequently, the NDR region remains hidden in this region of the $I-E$ dependence which exhibits the net positive slope. Since the experiments, performed under galvanostatic conditions, showed that the oscillations of the electrode potential occur in the region of this positive slope, it becomes clear that the H_2 oxidation on Pt electrode, in the presence of Cu^{2+} and Cl^- ions, is an example of the HN-NDR oscillator (cf. Chap. 3). One also concludes that early explanations of these phenomena were too simple.

The above mechanism was further mathematically described in terms of three ordinary differential equations, involving the following dynamical variables: electrode coverage with Cu ($\theta_{\text{Cu}} \equiv m$), competing with the electrode coverage with Cl^- ($\theta_{\text{Cl}^-} \equiv x$), and the electrode potential ($E \equiv p$). Calculations showed that this model sufficed to generate oscillations under both galvanostatic [20] and (in the presence of ohmic potential drops) potentiostatic conditions [21].

5.1.2 Modeling the Galvanostatic Oscillations

The model of the galvanostatic conditions derived by Wolf et al. [20] consists of the following ODEs:

$$\frac{dm}{dt} = v_{\text{ads}}^m - v_{\text{des}}^m \quad (5.1)$$

$$\frac{dx}{dt} = v_{\text{ads}}^x - v_{\text{des}}^x \quad (5.2)$$

$$\frac{dp}{dt} = \frac{1}{C_d} (j_{\text{tot}} - j_m - j_{\text{H}_2}) \quad (5.3)$$

expressing the temporal variation of the surface coverage with the metal atoms [Eq. (5.1)] and halide ions [Eq. (5.2)], respectively, as due to the difference between the rate of adsorption (v_{ads}) and desorption (v_{des}) of these species. Furthermore, the temporal variation of the electrode potential p [Eq. (5.3)], characterized with the double layer capacitance C_d is due to charging current, given by the expression in the bracket, which was obtained from the following dependence:

$$j_{\text{tot}} = j_{\text{cap}} + j_{\text{ct}} = j_{\text{cap}} + j_{\text{H}_2} + j_m \quad (5.4)$$

In Eq. (5.4), j means the densities of the following currents: j_{tot} is the the total current; j_{cap} , the capacitive current; j_{ct} , the charge-transfer (faradaic) current; the latter one consisting of j_{H_2} , the hydrogen oxidation current; and j_m is the current of the underpotential deposition of metal, assuming almost complete discharge of metal ions during this process. The flow of any current associated with the partial discharge of specifically adsorbed halogen anions was neglected.

Detailed forms of particular equations are given below. The faradaic current of hydrogen oxidation was assumed to be in the diffusion-controlled region and proportional to the square of the free adsorption sites, assuming dissociative adsorption (cf. e.g., [22–24]):

$$j_{\text{H}_2} = \frac{k_{\text{ads}}^{\text{H}_2} c_{\text{H}_2} (1 - m - x)^2}{1 + (k_{\text{ads}}^{\text{H}_2} / k_{\text{diff}}^{\text{H}_2}) (1 - m - x)^2} \quad (5.5)$$

where $k_{\text{ads}}^{\text{H}_2}$ is the rate constant of the hydrogen adsorption process and $k_{\text{diff}}^{\text{H}_2}$ is the effective diffusion constant defined as the ratio of the diffusion coefficient D_{H_2} to the assumed width of the assumed diffusion layer δ .

The current of underpotential deposition of Cu monolayer is given by (note the minus sign indicating the electroreduction process):

$$j_m = -q_{\text{mono}} k_m \{ c_m (1 - m - x) \exp[-a_m(p - p_0^m)] + m \exp[a_m(p - p_0^m)] \} \quad (5.6)$$

The adsorption and desorption rates (normalized to maximum coverage) of underpotential deposited metal and of the halide ions, respectively, are given by the following dependences:

$$v_{\text{ads}}^m = k_m \{ c_m (1 - m - x) \exp[-a_m(p - p_0^m)] \} \quad (5.7)$$

$$v_{\text{des}}^m = k_m m \exp[a_m(p - p_0^m)] \quad (5.8)$$

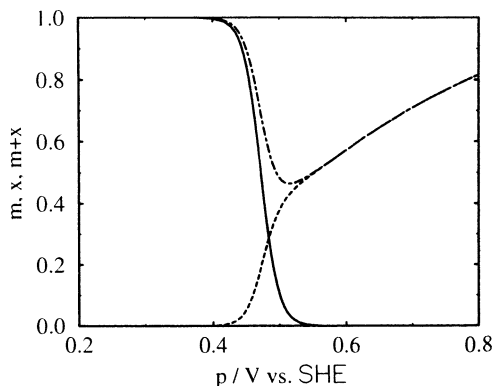
$$v_{\text{ads}}^x = k_x c_x (1 - m - x) \exp[a_x(p - p_0^x)] \quad (5.9)$$

$$v_{\text{des}}^x = k_x x \exp[-a_x(p - p_0^x)] \quad (5.10)$$

where c_m and c_x denote the (normalized to standard value of 1 M) bulk concentrations of the metal ions and of halide ions, respectively, in the solution, a_m —the (Tafel) slope for the electrode process of Cu^{2+} , including the transfer coefficient α : $a_m = \alpha n_m F / RT$, with α set here to 0.5 (symmetrical activation barrier). Analogous equations hold for the halide species X. Furthermore, q_{mono} means the electric charge flowing during the formation of adsorbed monolayer of metal under conditions of underpotential deposition. p_0^m and p_0^x denote the electrode potentials, at which, in the absence of other species, and at unit bulk concentrations, the electrode coverage with the deposited metal or adsorbed halide ions, respectively, becomes 0.5 (which assumption means the equality of rate constants for both species: $k_m = k_x$). The values of other parameters, used in the actual calculations, the reader can find in the original references (see Table 1 in [20]).

The above equations allowed to calculate the potentiostatic (or potentiodynamic) characteristics of the system, as well as its oscillatory response under galvanostatic conditions. By setting $dm/dt = 0$ and $dx/dt = 0$ separately and introducing the linear variation of the electrode potential with time one obtains the isolated isotherms of metal (m - p dependences) and of halide ions (x - p dependences), respectively. It appears that under potentiodynamic conditions ($v = 20 \text{ mV s}^{-1}$), both the metal and halide ions isotherms exhibit hysteresis upon cycling variation of the electrode potential which is however much more remarkable for the Cu isotherm, as it should be, due to assumed, fundamental for this system's dynamics, lower adsorption rate of

Fig. 5.5 Calculated coverages for a solution with $c_m = 10^{-4}$ and $c_x = 10^{-3}$; solid line m , dashed line x ; dot-dashed line $m + x$. Reprinted from [20], Copyright 1995, with permission from Elsevier



metal, compared to halide anions. In turn, taking both zeros of dm/dt and dx/dt simultaneously, one obtains the individual and summary coverages of both species competing for the same set of adsorption sites on the electrode surface which clearly show, how upon increasing potential the total number of available adsorption sites passes through the minimum (Fig. 5.5).

Thus, it becomes understandable that the hydrogen oxidation current in the cyclic voltammogram passes through a maximum, located, under steady-state conditions, at the potential of minimum total ($m + x$) coverage from Fig. 5.5, and that the whole voltammogram exhibits hysteresis if recorded under potentiodynamic conditions. Figure 5.6 shows cyclic voltammograms, calculated for both steady-state and potentiodynamic conditions, with $v = 20 \text{ mV s}^{-1}$ [20].

Let us also note an important detail of this j - p dependence—the hysteresis is pronounced much more in the region 0.25–0.50 V, when the electrooxidation of current is governed mainly by the (slowly establishing) metal coverage, than above 0.7 V, when the metal monolayer does not exist and the rate of H_2 oxidation is determined largely by the (quickly establishing) surface coverage with halide anions. Concluding, the model representation of electrochemical H_2 oxidation is coherent with the experimental characteristics, and the dynamical system, defined by Eqs. (5.1)–(5.3) can become a subject of bifurcation analysis. The bifurcation diagrams were constructed in various coordinate systems, e.g., p - j_{tot} , j_{tot} - C_m , j_{tot} - C_x , indicating the Hopf, saddle–node, saddle–loop, and the Takens–Bogdanov bifurcations. For example, Fig. 5.7 shows the bifurcation sequence, when the system's behavior is represented by the electrode potential. With increasing current density as a control parameter in the galvanostatic experiment, the stable steady state loses its stability via the Hopf bifurcation. The amplitude of oscillations born out of this transition increases with increasing current density. The middle steady state which is now unstable eventually collides with the limit cycle in the region of high amplitude oscillations and as a result of that collision, leading to the saddle–loop bifurcation, the oscillations disappear.

Numerical integration of Eqs. (5.1)–(5.3) shows that upon increasing total current density, the increase in the oscillation amplitude is accompanied with the

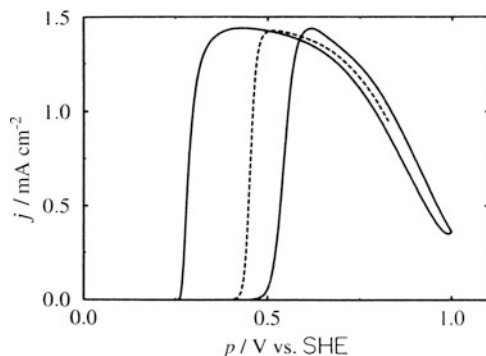


Fig. 5.6 Calculated hydrogen oxidation current density as a function of potential in a solution with $c_m = 10^{-4}$ and $c_x = 10^{-3}$; *dashed line* stationary state; *solid line* calculated cyclic voltammogram at a scan rate of 20 mV s^{-1} . Reprinted from [20], Copyright 1995, with permission from Elsevier

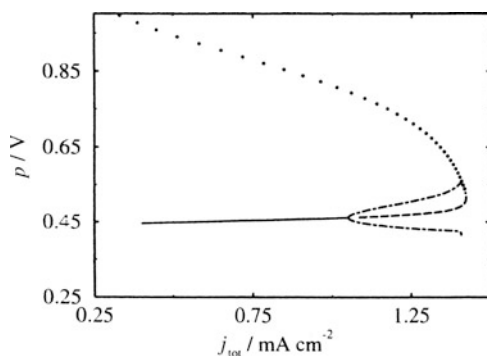


Fig. 5.7 Single-parameter continuation of the system (5.1)–(5.3) with $c_m = 10^{-4}$ and $c_x = 10^{-3}$ as a function of the applied current density j_{tot} : *solid line* stable stationary state; *dashed line* unstable stationary state; *dotted line* saddle point; *dot-dashed line* maximum and minimum of the potential oscillations. Reprinted from [20], Copyright 1995, with permission from Elsevier

decrease in their frequency and the gradual change of the shape of the peaks from harmonic to relaxation ones. These trends are quite well concordant with the experimental findings. Furthermore, for certain set of parameters various MMO, involving period-doubling bifurcations and meeting the Farey sequence (see Sect. 6.1.3), were also obtained. Such MMOs were found also in the experimental studies. Concordant with the experimental findings (at least for not too low metal concentrations in the solution) are also the phase shifts between the theoretical courses of coverages m , x , and electrode potential p .

Since the reliability of the model was in this way confirmed, one can further vary the parameter values, in order to check which of (reasonable) changes or simplifications do not kill the oscillations. One of the most important conclusions,

also concordant with the above extensively described experimental characteristics, was that the oscillations can occur only when (1) the anions adsorb and desorb faster than metal cations and (2) there is at least a minimal overlap between the electrode coverage with the metal phase and halide ions, i.e., during the positive potential scan the anions should start to desorb when there is still some metal deposited.

In spite of these concordances, in order to make the model more realistic, one can enrich the ODE's system (5.1)–(5.3) with the fourth equation, describing the dynamics of the concentration of metal ions in the solution at the electrode surface: $c_{m,0}$. This new variable may exhibit dynamics on a different time scale as being determined by the rate of diffusion which, under appropriate conditions can become a rate-determining step.

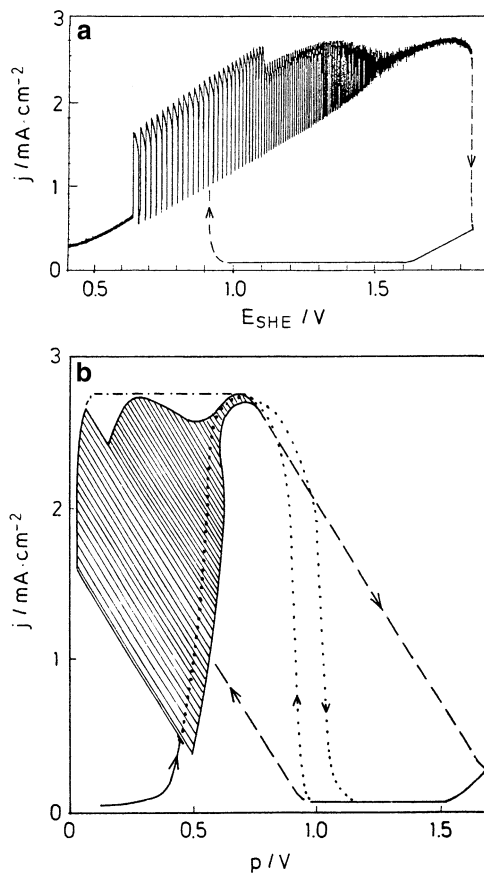
$$\frac{dc_{m,0}}{dt} = k'_m(v_{\text{des}}^m - v_{\text{ads}}^m) + k_{\text{diff}}^m(c_m - c_{m,0}) \quad (5.11)$$

In Eq. (5.11) k'_m describes the change in the c_m concentration upon dissolution of one monolayer of metal, k_{diff}^m is a ratio of diffusion coefficient of metal ions in the solution to the thickness of the Nernst diffusion layer in which the m concentration gradient is assumed linear, c_m is, as before, the metal ions concentration in the solution bulk. Contrary to Eq. (5.7), the rate of adsorption v_{ads}^m is now dependent on the local, surface concentration $c_{m,0}$, and not on bulk value c_m . When the bulk metal concentration is so low that the rate of diffusion of metal ions becomes a rate-determining step, the amplitude of the oscillations extends in negative direction so that it is necessary to include the dependence of the hydrogen oxidation current on the electrode potential:

$$j_{\text{H}_2} = \frac{k_{\text{H}_2}[\exp(a_{\text{H}_2}p) - 1]c_{\text{H}_2}(1 - m - x)^2}{1 + (k_{\text{H}_2}[\exp(a_{\text{H}_2}p) - 1]/k_{\text{diff}}^{\text{H}_2})(1 - m - x)^2} \quad (5.12)$$

The fourth-variable model, constructed in this way, is able to reproduce almost quantitatively the experimental oscillation courses, as well as the experimentally reported dependence of the periods on the current densities at low metal ion concentration. The open problem is which mechanistic nuances should be yet implemented in the model in order to reproduce chaotic oscillations, exhibiting interior crisis. As always in the case of models assuming homogeneous distribution of concentration and current distribution along the electrode surface, one can pose a question whether taking into account the spatial distribution of variables could generate more complex dynamical phenomena.

Fig. 5.8 (a) Experimental cyclic voltammogram; scan rate $\nu = 1 \text{ mV s}^{-1}$, $R_s A = 375 \Omega \text{ cm}^2$, $c_{\text{Cu}^{2+}} = 10^{-6} \text{ M}$, $c_{\text{Cl}^-} = 3 \times 10^{-4} \text{ M}$. (b) The same measurement plotted against $p = E - IR$ together with an experimental cyclic voltammogram without additional resistance (scan rate $\nu = 2 \text{ mV s}^{-1}$, $c_{\text{Cu}^{2+}} = 3 \times 10^{-6} \text{ M}$) (dotted line) and without copper (dot-dashed line) ($c_{\text{Cl}^-} = 3 \times 10^{-4} \text{ M}$) [21]. Note that symbols p and E are here equivalent to electrode potential (usually denoted as E) and external voltage (usually denoted as U), respectively. Reprinted from [21], Copyright 1995, with permission from Elsevier



5.1.3 Experimental Observation and Modeling the Potentiostatic Oscillations

According to the characteristics of the systems with the hidden negative resistance, the oscillations of current are possible under potentiostatic conditions provided the appropriately high serial resistance is present in the circuit (see Sect. 3.4). Representative experimental illustration of such oscillations in the H_2 oxidation on the rotating disk Pt electrode, in the presence of both Cu^{2+} and Cl^- ions, and under condition of the slow scan cyclic voltammetric experiment, are shown in Fig. 5.8 [21]. In the first anodic cycle, the oscillations begin after the initial region of quasi-linear rise of the current, controlled largely by the circuit ohmic resistance and finish at about 1.83 V, when the current drops abruptly due to the oxide layer formation on Pt surface. During the return scan the hysteresis is observed—the current returns to higher values only at ca. 930 mV. Thus, the system exhibits a special kind of bistability, in which the oscillatory (high-current) and steady-state

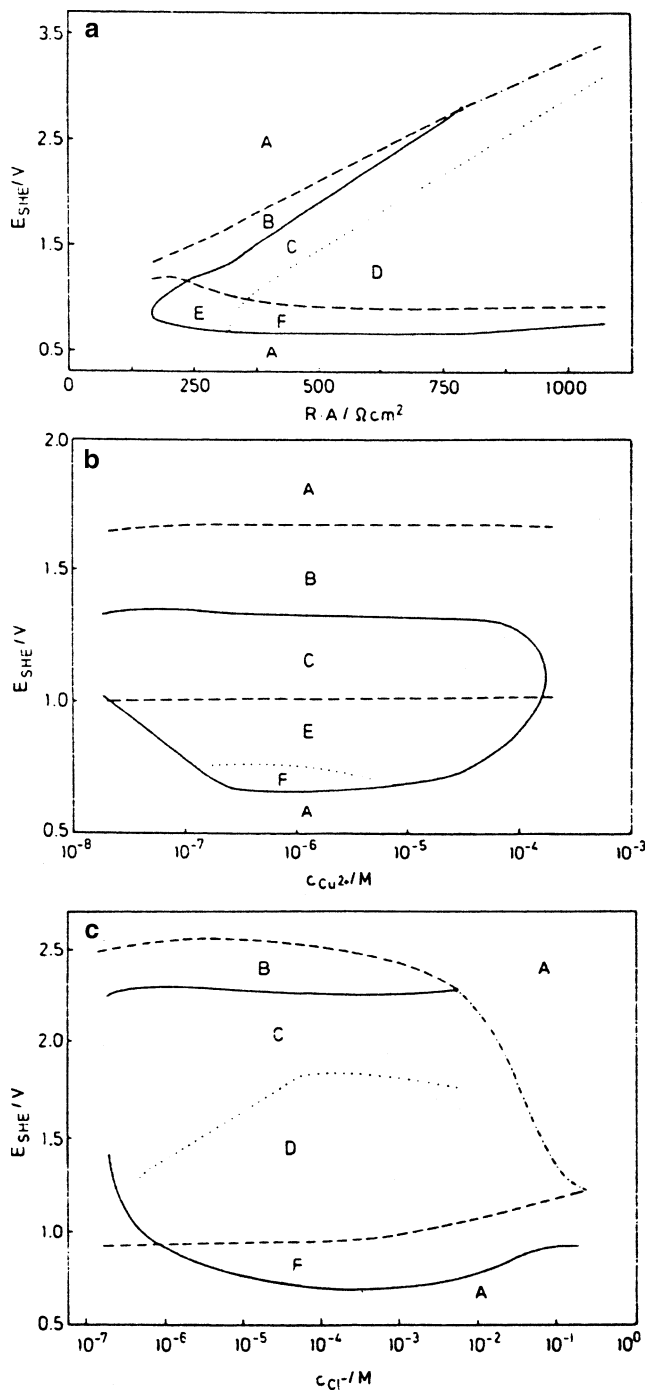


Fig. 5.9 Regions of different dynamic behavior (a) at $c_{Cu^{2+}} = 10^{-5}$ M and $c_{Cl^-} = 3 \times 10^{-4}$ M as a function of externally applied potential E (for the present notation, see remark in caption to Fig. 5.8) and $R_s A$ (b) at $c_{Cl^-} = 3 \times 10^{-4}$ M, $R_s A = 312 \Omega \text{ cm}^2$ as a function of E and $c_{Cu^{2+}}$ and

(low-current) regimes coexist for the same range of control parameters. Obviously, the high current states correspond to the Pt surface not covered with the oxide layer, whereas the low current states begin from the formation of oxide layer and end with the reduction of this layer. Due to ohmic potential drops the high-current states correspond to relatively low interfacial potential drops, whereas for the low-currents state the interfacial potential drop is quite high and therefore the oxide layer persists until, upon decreasing the externally applied voltage, it is reduced at U equal to ca. 930 mV.

Systematic studies of these oscillations revealed the four basic parameters that affect their dynamical features: besides the serial resistance R_s (which will be further multiplied by the electrode surface area A , in order to obtain the resistance parameter independent of electrode geometry) and the externally applied voltage U the other two ones are: the copper ions concentration $c_{\text{Cu}^{2+}}$ and the chloride ions concentration c_{Cl^-} in the solution. The bifurcation diagrams, constructed in the coordinate systems: $U-R_sA$; $U - c_{\text{Cu}^{2+}}$ and $U - c_{\text{Cl}^-}$, are shown in Fig. 5.9. These diagrams not only indicate, for which parameter values the oscillations exist, but also separate the regions of the small-amplitude and large-amplitude oscillations.

It is useful to correlate the observed instabilities with the impedance measurements for the same system which also indicate the possibility of the galvanostatic instability. The impedance spectra, shown in Fig. 5.10 for three different potentials (indicated on the enclosed dc $j-E$ dependence), clearly prove the negative impedance at the potential indicated by (c), visible at intermediate ac frequencies, but hidden at the dc steady-state response which exhibits a positive slope at this potential. This of course means the existence of potential oscillations under galvanostatic conditions. In turn, the explicit negative slope of the dc response at potential (d) turns into the negative real impedance for ac frequency tending to zero, giving rise to bistability in the presence of appropriate serial resistance.

In order to obtain potentiostatic instabilities in terms of the model described earlier, one can use essentially the system of equations (5.1)–(5.3). The difference is the expression for the total current density which is not imposed constant, but may vary together with the applied external voltage (in the present notation $j_{\text{tot}} = (E - p)/AR_s$). Also, the formation of the oxide layer on Pt surface was neglected, since it has qualitatively similar characteristics to the specific adsorption of chlorides. Based on these equations, the cyclic voltammograms, the bifurcation diagrams, and impedance spectra were calculated, yielding results similar to essential experimental observations. In particular, the bifurcation

Fig. 5.9 (continued) (c) $c_{\text{Cu}^{2+}} = 10^{-5}$ M, $R_sA = 625 \Omega \text{ cm}^2$ as a function of E and c_{Cl^-} . (A) One stable stationary state; (B) coexistence between a stable stationary state at high currents and one at low currents; (C) coexistence between small oscillations at high currents and a stationary state at low currents; (D) coexistence between large oscillations at high currents and a stationary state at low currents; (E) small oscillations; (F) large oscillations. Reprinted from [21], Copyright 1995, with permission from Elsevier

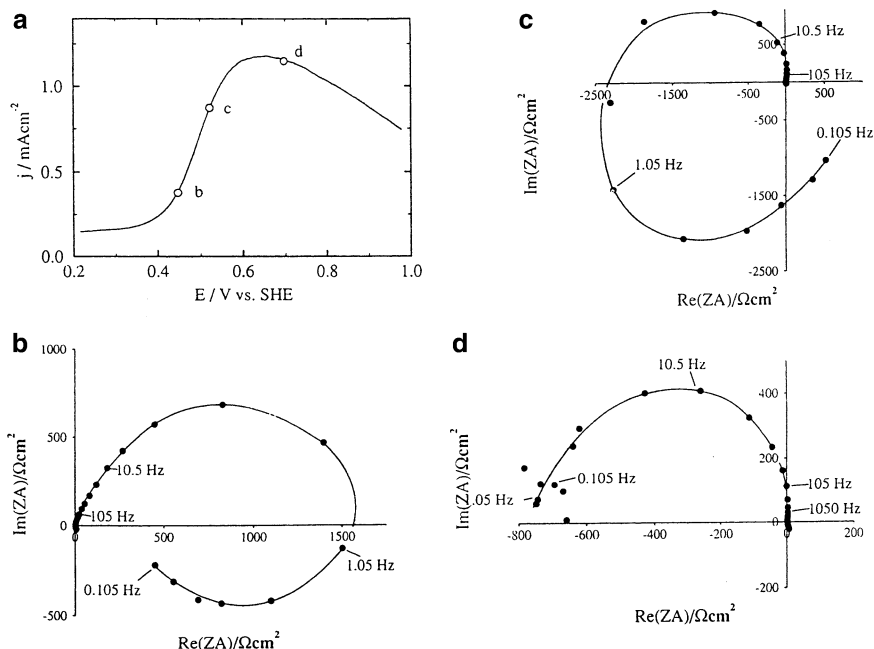


Fig. 5.10 (a) Experimental positive potential scan with a scan rate $\nu = 2 \text{ mV s}^{-1}$, $c_{\text{Cu}^{2+}} = 1 \times 10^{-4} \text{ M}$, $c_{\text{Cl}^{-}} = 1 \times 10^{-4} \text{ M}$, no additional resistance. (b)–(d) refer to the potentials where the impedance spectra were recorded. Impedance Z plotted in the complex plane as a function of the frequency f . $E =$ (b) 447, (c) 522 and (d) 697 mV. Reprinted from [21], Copyright 1995, with permission from Elsevier

mechanism for the onset and decay of the oscillations was found, depending on Cl^{-} concentration: for $3 \times 10^{-3} \text{ M}$, the oscillations are born via the Hopf bifurcation, but decay due to a saddle–loop bifurcation; for 10^{-3} M Cl^{-} , the oscillations develop from small amplitude ones, and cease in a similar, but reversed manner, indicating in both cases the Hopf bifurcation. All these findings are also concordant with experimental observations. The collection of possible bifurcations is collected in the theoretical diagrams shown in Fig. 5.11.

The bifurcation scheme on Fig. 5.11a is quite well concordant with that in Fig. 5.9a. In particular, the point of Takens–Bogdanov (TB) bifurcation is also concordant with the earlier suggestion on the saddle–loop bifurcation which is born when TB takes place. Figure 5.11b shows that the concentration of Cu^{2+} ions affects the position of the borders of the Hopf bifurcation, but does not have any influence on the occurrence of the saddle–node bifurcations which in this way never meet (again similarly to experimental results shown in Fig. 5.9b). On the contrary, Fig. 5.11c shows that two borderlines of the saddle–node bifurcations are almost parallel only for relatively low Cl^{-} concentrations but upon its increase, they converge and eventually end in a *cusp point* (being a codimension–2 bifurcation). In this case, the experiment shows that for low concentrations of Cl^{-} the position of

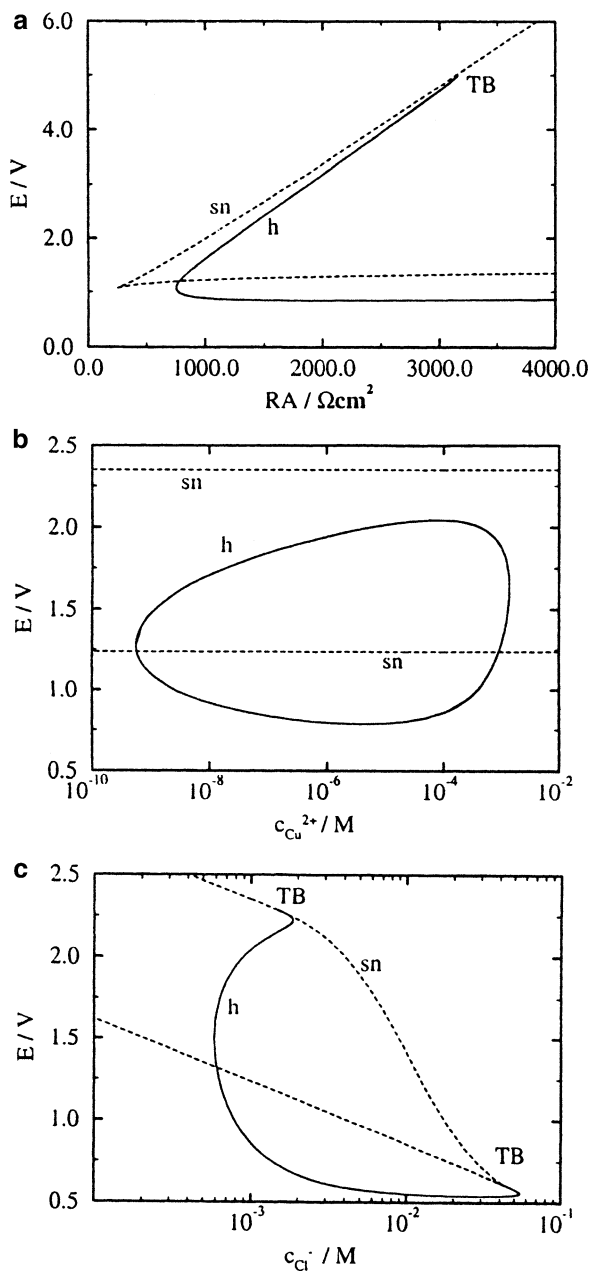


Fig. 5.11 Calculated bifurcation diagram (a) in the E - $R_s A$ plane (note again that E means here external voltage, denoted in most other cases by U) at $c_{\text{Cu}^{2+}} = 10^{-4} \text{ M}$ and $c_{\text{Cl}^-} = 10^{-3} \text{ M}$, (b) in the E - $c_{\text{Cu}^{2+}}$ plane at $c_{\text{Cl}^-} = 10^{-3} \text{ M}$ and $R_s A = 1,250 \Omega \text{ cm}^2$ and (c) in the E - c_{Cl^-} plane at $c_{\text{Cu}^{2+}} = 10^{-4} \text{ M}$ and $R_s A = 1,250 \Omega \text{ cm}^2$; h Hopf bifurcation, sn saddle-node bifurcation, TB Takens-Bogdanov bifurcation point. Reprinted from [21], Copyright 1995, with permission from Elsevier

saddle–node bifurcation lines should be rather horizontal (cf. Fig. 5.9c), but this discrepancy is due to neglecting of the formation of surface oxide layer at positive potential which would cause the poisoning of the electrode independent of Cl^- concentration.

In turn, impedance spectra were calculated for assumed $R_s = 0$, so the equivalent circuit consisted of only parallel connection of the double layer capacitance C_d and the faradaic impedance Z_f , yielding the total impedance given by the expression $Z = (j\omega C_d + Z_f^{-1})^{-1}$. Details of these calculations the interested reader can find in original paper [21], while here we shall only mention a good concordance of theoretical and experimental impedance spectra. Evidently in this way the validity of the model mechanism of oscillatory H_2 oxidation was additionally confirmed.

As a final comment of the above analysis of the oscillatory H_2 electrooxidation one concludes that oscillations occurring under both galvanostatic and potentiostatic conditions originate from the same mechanism. If the oscillations are born in the Hopf bifurcations, like in this process, the system which oscillates under galvanostatic conditions (i.e., for the infinite serial resistance characterizing the ideal galvanostat) will oscillate also under potentiostatic conditions, in the presence of appropriate finite serial resistance. The H_2 oxidation on Pt, in the presence of Cu^{2+} and Cl^- ions, is thus a typical example of a HN-NDR type oscillator.

At the end of this section devoted to hydrogen oxidation we shall only briefly mention another, special case of the oscillatory process in which hydrogen and oxygen, dissolved in a stirred solution of dilute sulfuric acid, combine to form water on the surface of a submerged Pt catalyst. The electrochemical aspect of this process exists through the polarization of this Pt electrode (vs. the smooth Pt counterelectrode) with the cathodic or anodic current. While cathodic polarization of the catalytic Pt electrode was ineffective in changing the reaction rate between hydrogen and oxygen, the anodic polarization caused a periodic change of the current, under appropriate conditions. Furthermore, the reaction rate was increased by ac polarization at frequencies <10 Hz. Such periodic behavior was observed also for palladium, but not for rhodium and iridium. The origin of these oscillations was ascribed to periodic buildup and decomposition of oxide on the catalyst surface [25].

5.2 Oscillations in Anodic Oxidation of Carbon Monoxide

Although studies of the electrooxidation of CO on Pt electrodes have been a subject of very intensive studies, dynamic nonlinear self-organization in electrochemical processes involving CO as a reactant is rather modestly represented in the literature. However, electrochemistry of CO plays an important role in the oxidation of formic acid or formaldehyde on Pt electrodes since CO is then an intermediate species, poisoning the electrode surface and in this way involved in the so-called *indirect pathways* of the reaction mechanism. For this reason, CO oxidation will constitute

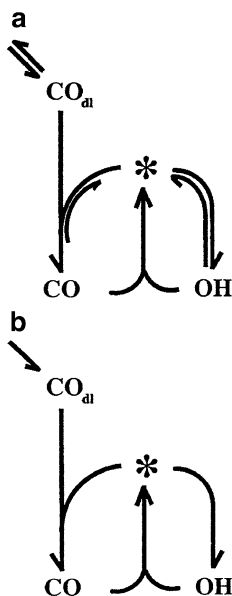


Fig. 5.12 (a) Network diagram of the CO oxidation mechanism. CO_{dl} , *asterisk*, CO and OH denote CO at the double layer, the vacant surface sites, adsorbed CO and adsorbed OH, respectively. The *arrows* indicate the chemical (pseudo)reactions. The total number of *barbs* and *arrows* encodes the stoichiometric coefficient of the respective species. (b) Diagram of unstable steady state subnetwork which is contained in the CO model. This unstable network leads to bistability in some region of parameter space. Since no electrical quantity is involved, the instability is purely chemical and thus numerically observable under truly potentiostatic conditions, i.e., for constant electrode potential (denoted as ϕ or E). Reprinted with permission from [26]. Copyright 1997 American Institute of Physics

an important subsystem in the oscillatory reaction mechanisms of both formaldehyde and formic acid (see Sects. 5.3 and 5.4). Strasser et al. [26] have elaborated the reaction scheme of this subsystem (Fig. 5.12), being a part of their mechanism for the oxidation of formic acid on single-crystal platinum electrode (see again Sect. 5.4 for the explanation of its construction). Note that this scheme includes a well-established, potential-dependent recombination of adsorbed CO and OH species which leads to unblocking of the adsorption sites (*), according to Eq. (5.16).

In the following, we shall briefly describe selected studies of temporal self-organization in the oxidation of CO being not an intermediate of any process, but a principal reactant. Ross et al. [27, 28] have reported bistability in the electrode reactions of CO under cyclic voltammetric conditions. More recently, the origin of S-shaped polarization curve in the continuous electrooxidation of CO on Pt single-crystal electrodes was analyzed, both theoretically and experimentally, by Koper et al. [29], who continued the work by Strasser et al. [26]. The model involved the following reaction steps, with the symbols of their rate constants included in the brackets:

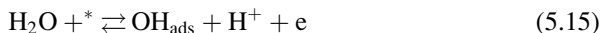
1. Slow transport of CO toward the electrode surface:



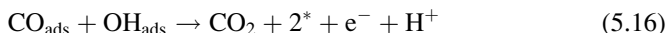
2. Irreversible (as assumed here) adsorption of CO ($k_{\text{CO,ads}}$):



3. Reversible oxidative adsorption of OH ($k_{\text{OH,ads}}$, $k_{\text{OH,des}}$):



4. Mutual removal of CO_{ads} and OH_{ads} with the release of two adsorption sites (k_{r}):



The mathematical model involved three dynamical variables: θ_{CO} , θ_{OH} , and $c_{\text{CO,s}}$ —the CO concentration in the solution at (close to) the electrode surface, i.e., at the place, from which molecules of CO adsorb. Without discussing the details of further assumptions and the mathematical form of differential equations, which the reader can find in the original paper [29] (see also Section 2.10 of vol. II), we shall focus on the most important results. The numerically generated cyclic voltammetric curves are shown in Fig. 5.13. The potential region of hysteresis (bistability) increases either if the electrode rotation rate is low (thick Nernst diffusion layer) or if the bulk CO concentration is low. Both cases correspond to significant limitations from the rate of transport of CO from the solution bulk toward the electrode surface. On the other hand, when the mass transport of CO is sufficiently efficient, the bistability completely disappears, so it appears to be due to only transport limitations, and *not* of chemical origin. Similar dependences were observed in the experimental studies.

Figure 5.14 shows the full S-shaped steady-state I – E polarization curve which was computed for the parameters listed in the caption. The arrows indicate the potentials at which the saddle–node bifurcations occur.

In terms of these model calculations, indicating the role of the (slow) CO transport in the creation of the bistable region, the search for the positive feedback loop, responsible for this instability, cannot be limited to chemical reaction mechanism. The fact that it involves interaction of adsorbed intermediates: CO_{ads} and OH_{ads} , qualifies it as a *Langmuir–Hinshelwood* (LH) mechanism. This scheme, together with the condition of a *slow mass transport* of CO from the bulk of the solution, creates a positive feedback in the number of free surface sites (see below for more detailed explanation). Experimentally it is not possible to record full, S-shaped I – E dependence due to the instability of the middle states under such potentiostatic conditions, but it is possible to do that under galvanostatic conditions (see Chap. 2). Such experiments were also performed, additionally

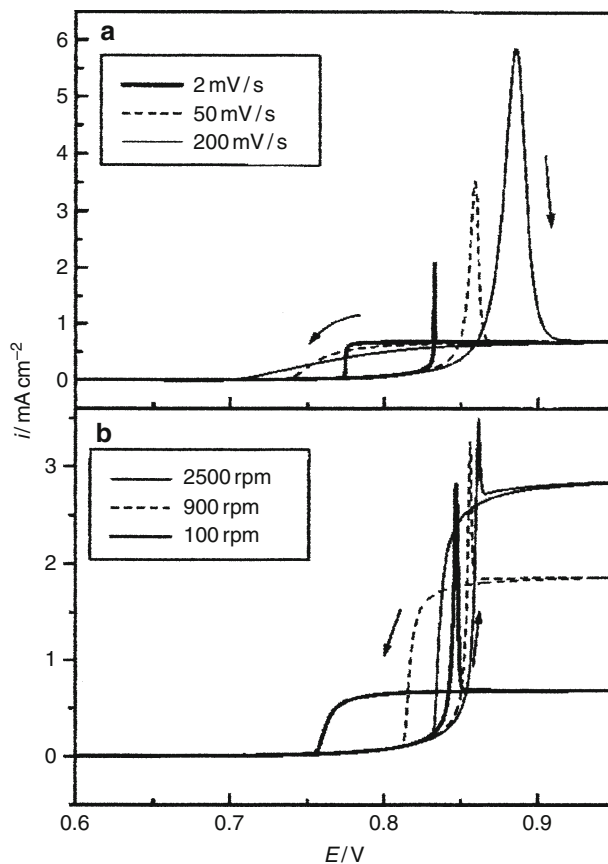


Fig. 5.13 Cyclic voltammetry of CO electrooxidation in the model. (a) Influence of voltage scan rate; (b) influence of disk rotation rate. The following values for the model parameters were used: $k_{\text{OH, ads}} = 10^{-4} \text{ s}^{-1}$, $k_{\text{OH, des}} = 10^5 \text{ s}^{-1}$, $k_{\text{r}} = 10^{-5} \text{ s}^{-1}$, $k_{\text{CO, ads}} = 10^8 \text{ cm}^3 \text{ mol}^{-1} \text{ s}^{-1}$, $c_{\text{CO, bulk}} = 10^{-6} \text{ mol cm}^{-3}$, $D_{\text{CO}} = 5 \times 10^{-5} \text{ cm}^2 \text{ s}^{-1}$, $\theta_{\text{CO}}^{\text{max}} = 0.333$, $S_{\text{tot}} = 2.2 \times 10^{-9} \text{ cm}^{-2}$ (total number of adsorption sites per cm^2), the Nernst diffusion layer thickness $\delta = 1.34 \times 10^{-3} \text{ cm}$ (at 2,500 rpm), $\delta = 2.23 \times 10^{-3} \text{ cm}$ (at 900 rpm), $\delta = 6.7 \times 10^{-3} \text{ cm}$ (at 100 rpm). Reprinted with permission from [29]. Copyright 2001 American Chemical Society

confirming the validity of the described model. Noteworthy, also recent studies by Samjeské et al. [30] of the dynamics of CO oxidation on polycrystalline Pt electrode, made with the fast time-resolved, surface-enhanced infrared absorption spectroscopy, confirmed the LH mechanism for the interaction of the adsorbed CO and (most likely) OH species. Coming back to nonlinear dynamic phenomena, Koper et al. [29] have reported also potential oscillations for the oxidation of CO from H_2SO_4 medium, at the Pt(111) RDE, which instabilities were presumably caused by the adsorption of sulfate ions on Pt surface, competing with H_2O and CO molecules for the adsorption sites. In fact, such a role of anions can be a source of the negative feedback loop, meaning the inhibition of the CO electrooxidation occurring from adsorbed state [31]. Interestingly, if BF_4^- are these anions, the

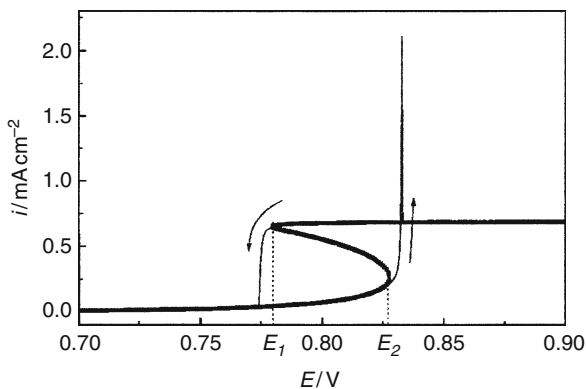


Fig. 5.14 S-shaped polarization curve observed for $\delta = 6.7 \times 10^{-3}$ cm (at 100 rpm), other parameter values as in Fig. 5.13. The *thin line* shows the cyclic voltammogram observed at low scan rate of 2 mV/s. Reprinted with permission from [29]. Copyright 2001 American Chemical Society

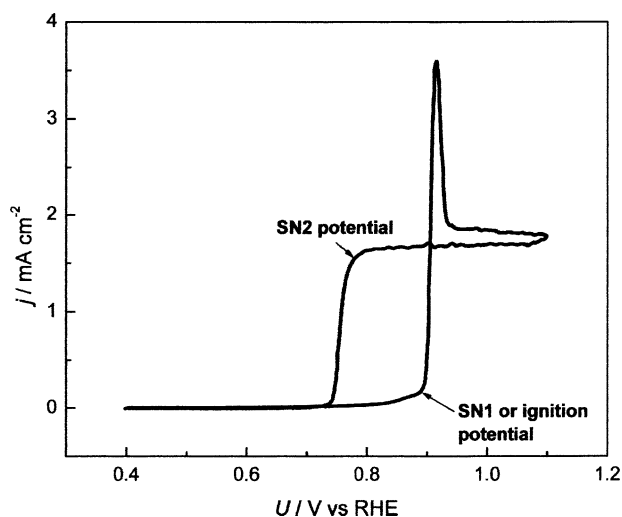


Fig. 5.15 Cyclic voltammogram of a rotating polycrystalline Pt disk electrode in CO saturated 0.1 M HClO₄ solution. Scan rate: 50 mV/s; rotation rate 1,200 rpm. Reprinted from [32], Copyright 2009, with permission from Elsevier

relation between time scales of dynamic variables is modified so that one can report the current oscillations for such a low (vanishing) ohmic resistance of the solution that this system can be qualified as a rare example of a *truly potentiostatic* oscillator (Class I oscillator). Analogous phenomena are observed if BF₄⁻ ions are replaced with Cl⁻ ions, both for the polycrystalline and single-crystal Pt electrodes. This case will be analyzed below in more detail.

Typical cyclic voltammogram of CO bulk oxidation on a rotating disk polycrystalline Pt electrode is shown in Fig. 5.15, as reported by Krischer et al [32].

Starting from less positive potentials, at which the electrode surface is poisoned with CO_{ads} , during the anodic sweep one observes the steep rise of current density that occurs only after the so-called ignition potential, at which one of the saddle–node bifurcations (SN1) occurs. Around this potential the sudden oxidative removal of CO_{ads} begins and the released adsorption sites become now available for OH_{ads} . The rising current visualizes the progress of oxidation of CO molecules arriving at the electrode surface from the solution bulk. The current density reaches the maximum value rather soon and then drops to lower (but still high) value which is almost independent of the rising anodic potential. When the potential sweep is reversed in this region, the hysteresis is observed: the current density is almost constant in spite of crossing the ignition potential and drops to negligible values at much less anodic potentials, at which the electrode becomes again entirely covered with adsorbed CO, as prior to the experiment (saddle–node bifurcation point SN2). The mechanistic basis for this bistability is the above-mentioned competitive Langmuir–Hinshelwood mechanism between CO_{ads} and OH_{ads} which, together with mass transport limitation of CO, induces a positive feedback in the number of free surface sites. Close to the ignition potential, a fluctuation to a larger number of free adsorption sites allows for some OH formation, and consecutive reaction with CO_{ads} . The incipient continuous oxidation reaction causes a decrease of the CO concentration in front of the electrode, which favors OH formation over CO adsorption, promoting further CO oxidation and thereby creating more free surface sites. In turn, close to the second critical potential, the decrease in the OH formation rate with decreasing potential causes an autocatalytic built-up of the CO adsorbate layer [32]. One should add that SN2 potential appeared to be sensitive to the value of the positive turning potential of the cyclic voltammogram, to the bulk CO concentration in the solution, determined by the partial pressure of CO in the purging gas, and (relatively slightly) to the change of supporting electrolyte from H_2SO_4 to HClO_4 .

Noteworthy, oscillations set in this system after addition of small amounts of chloride ions. The relevant cyclic voltammogram, collecting the voltage and current density changes as a function of time, is shown in Fig. 5.16.

During the anodic sweep, the onset of oscillations occurs just when the adsorbed CO begins to react and is followed by their decay to the quasi-stationary state. Upon reversed scan the return of the oscillations takes place with certain, small hysteresis, and finally, the nonoscillatory low current re-establishes when the electrode becomes covered with nonreacting CO. When the electrode potential is fixed in the interval corresponding to the oscillations, they exhibit the sustained nature, but of degree of complexity dependent on the acid: in H_2SO_4 medium oscillations are regular, while in HClO_4 always irregular ones were reported. This shows certain role of anions of these acids in the qualitative characteristics of the oscillations, although they are not able to induce them, since for that Cl^- ions are necessary.

Since the oscillations mean generally the interplay of the positive and negative feedback loops, it remains to identify the latter one. In the opinion of the authors [32] this negative feedback comes from the reversible, potential-dependent adsorption of Cl^- anions: when the system is on reactive branch, the adsorption of Cl^-

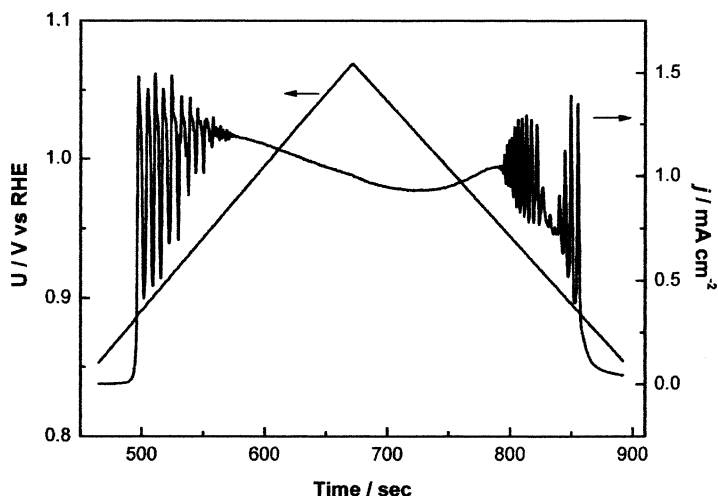


Fig. 5.16 Current and voltage time trace of a rotating polycrystalline Pt electrode in CO saturated 0.5 M $\text{H}_2\text{SO}_4 + 10^{-6}$ M Cl^- . The voltage was scanned with 1 mV/s. Reprinted from [32], Copyright 2009, with permission from Elsevier

ions reduces the number of free surface sites and thus slows down the faradaic process. Conversely, Cl^- ions are displaced if the surface becomes more and more covered with CO. Hence, on both branches Cl^- adsorption counteracts the positive feedback in the free surface sites.

Since it is well known that adsorption of CO and various anions depend on the crystallographic orientation of the Pt (and other metal) electrode, analogous comparative experiments were performed for the electrodes of the Pt(110), Pt(100), and Pt(111) plane surfaces [32]. For all these electrodes, the bistable region in the absence of Cl^- ions was recorded. For H_2SO_4 medium, upon addition of ca. 10^{-6} M Cl^- the strongest modification (shrinking) of this region, being a change toward the onset of oscillations, was observed for Pt(110); the oscillations were found for $[\text{Cl}^-] = \text{ca. } 10^{-5}$ M, when the bistable region disappeared completely. The other extreme case is Pt(111) electrode for which the CV response is almost unaffected by this amount of Cl^- . One accepts that sulfate ions adsorb most strongly (through three oxygen atoms) on Pt(111) surface, and then the OH_{ads} formation, as well as Cl^- adsorption, become hindered. Figure 5.17 compares the shape of sustained current oscillations (or only current fluctuations) recorded for all three Pt plane orientations, under fixed potential conditions.

The courses shown in Fig. 5.17 are representative since they illustrate the following experimental facts: for single-crystal Pt electrodes one does not report regular oscillations, contrary to the polycrystalline Pt. Next, the frequency of the oscillations, for the cases where they occur [Pt(110), Pt(100)], significantly depends on the crystallographic orientation of the electrode plane, presumably due to difference in the rate constant of adsorption of Cl^- ions [larger on Pt(110) than on Pt(100)]. Evidently not all aspects of the oscillatory mechanism in the studied

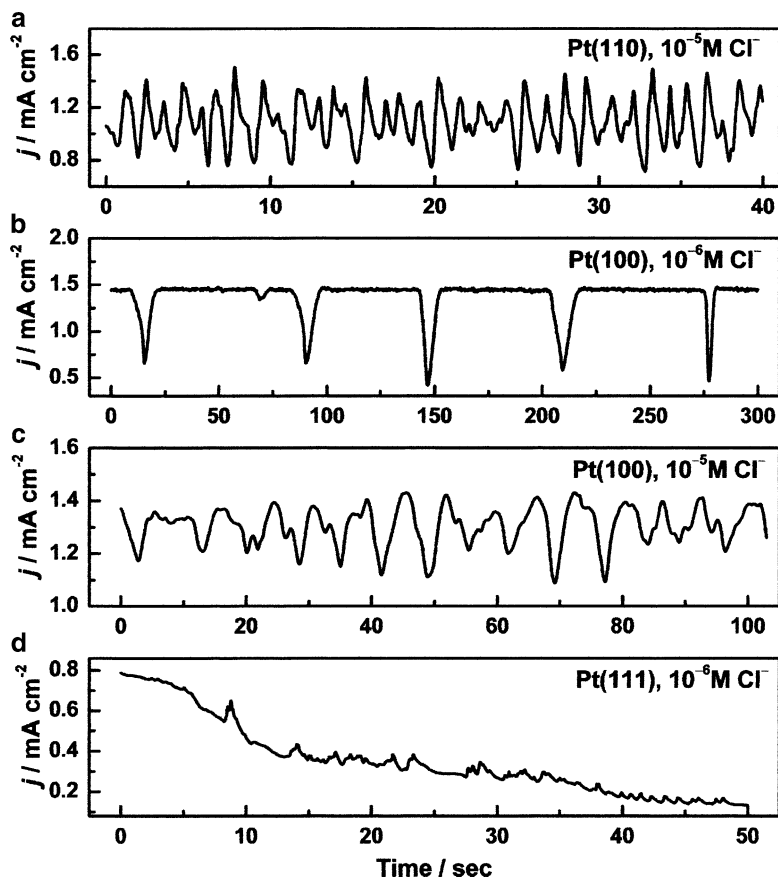


Fig. 5.17 Time series of rotating single crystalline Pt electrodes in CO-saturated 0.5 M H_2SO_4 solution containing small amounts of HCl at a constant applied voltage U . From top to bottom: $U = 840, 920, 900, 910$ mV. Reprinted from [32], Copyright 2009, with permission from Elsevier

system are clear and there remains open the question whether this temporal dynamics translates into spatial or spatiotemporal patterns—regular or irregular, like the oscillations reported earlier. In the opinion of the authors [32], if such patterns can form, it would be particularly interesting to find out whether their variety is as rich, as for chemical CO oxidation under UHV conditions and whether the surface reconstruction of Pt electrode is also involved in these phenomena under conditions of electrochemical experiment.

For better understanding of the latter sentence it is useful to invoke at least basic aspects of the self-organized, chemical catalytic oxidation of CO with oxygen. Such chemical oxidation of CO with O_2 on the surfaces of heterogeneous catalysts has been one of the most intensively studied catalytic processes. The source of the positive feedback in the kinetics of this process is, as in electrochemical systems, the type of the Langmuir–Hinshelwood (LH) mechanism, meaning that the

chemical transformation of reactants occurs between the reactant particles only in their adsorbed state (a situation prevailing in heterogeneous catalysis). In the case considered, the LH mechanism involves the following steps:



Not only temporal oscillations in the course of this process were observed (cf. e.g., [33, 34]). Impressive studies of CO oxidation on Pt(110) for ultrahigh vacuum (UHV) conditions, performed by the Berlin's group of Ertl (cf. e.g., [35–39]), have revealed the formation of various surface patterns, including spiral waves, target patterns, standing waves, and turbulent behavior. In brief, the oscillations are associated with the structural reorganization of the Pt(110) surface between the (1×1) structure (stabilized by CO adsorption) and (1×2) reconstructed structure (developing under UHV conditions) (the 1×2 symbol means that the unit cell is in the latter case twice as large in one direction). Thus, the reconstruction of the surface is CO dependent or CO induced.

An important difference is that on the reconstructed (1×2) surface the O_2 molecule hardly dissociates, compared to (1×1) structure, so then the oxidation of CO is slowed down. When the Pt surface is in the (1×1) state, the molecules of O_2 readily dissociate to atoms of oxygen which react with adsorbed CO. This process causes the decrease of CO surface concentration below the critical value, at which the Pt surface undergoes reconstruction to less reactive (1×2) state. Now, due to weak adsorption of O_2 , CO can accumulate on the surface, even removing the O atoms, so the oxidation rate drops. When the surface concentration of CO rises up to a critical value, the surface switches back to (1×1) state, in which O_2 adsorbs, dissociates into atomic oxygen and oxidizes adsorbed CO (Fig. 5.18) [40].

Since the surface dynamics is affected also by the transport rate of reactants from the system's bulk, the existence and degree of complexity of these oscillations depend on the feed rate of the reacting species. More detailed and advanced description of the oscillations in this system can be found in [35, 36] and references cited therein. One should also note that Eiswirth, Ertl et al. have formulated sufficient and necessary conditions for the oscillating Langmuir–Hinshelwood mechanism, i.e., for occurrence of a Hopf bifurcation in such reaction mechanism [41]. Krischer et al. have shown also that the electrooxidation of CO on polycrystalline Pt electrodes leads to the formation of Turing patterns and domain patterns under galvanostatic conditions [42–44]. These experimental results confirmed earlier theoretical predictions about the conditions of formation of such patterns (cf. Sect. 1.2, volume II). These phenomena are also additionally described in Chap. 2 of volume II.

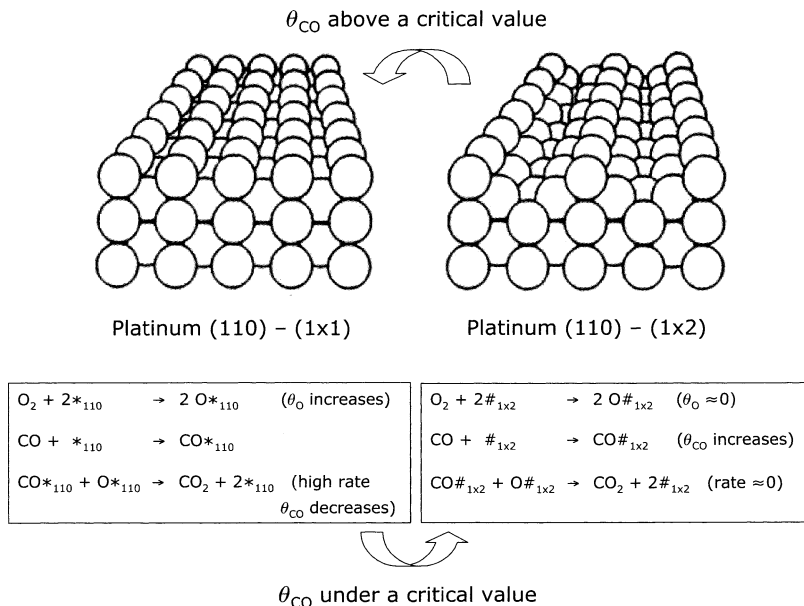


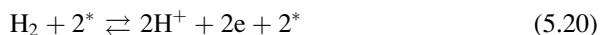
Fig. 5.18 Reaction mechanisms for the oxidation of CO on the (110) surface of platinum (*left*) and on the reconstructed surface (*right*). Reproduced with permission from [40]. Copyright Wiley-VCH GmbH & Co. KGaA

Another important process, studied in the Berlin group, was the catalytic oxidation of CO with NO, yielding CO_2 and N_2 and exhibiting the oscillatory course, as well as spatiotemporal patterns on the surface of the catalyst, but detailed description of this process is beyond the scope of this monograph [37, 45, 46].

5.3 Bistability and Oscillations in Anodic Oxidation of $\text{H}_2 + \text{CO}$ Mixture

Following the instabilities in separately carried out processes of H_2 and CO anodic oxidation, in this section we describe the bistability and oscillations reported by Krischer et al. [47] for both these processes occurring simultaneously on polycrystalline Pt electrodes. Thus, the oxidation of the ($\text{H}_2 + \text{CO}$) mixture on Pt electrodes is considered as composed of two dynamically unstable subsystems: the CO system, belonging to S-NDR class and the H_2 system which (in the presence of Cl^- and Cu^{2+} ions) belongs to HN-NDR class. For the S-NDR systems, the electrode potential is a negative feedback variable, and the destabilizing autocatalytic loop is of chemical origin (see Chap. 2). For HN-NDR systems, the situation is opposite: the electrode potential is a positive feedback variable and negative feedback comes from chemical reaction steps. The connection of such two systems

should thus give rise to interestingly complex dynamic instabilities. Also, understanding of the interaction of H_2 and CO oxidation has tremendous practical significance for the efficiency of fuel cells based on the oxidation of hydrogen. When hydrogen stream, feeding the low-temperature fuel cell, is contaminated with only traces of CO (which are usually present if hydrogen is produced from hydrocarbons), the efficiency of such a cell drastically decreases [47]. Of course, this nuisance triggered numerous studies how to avoid it, but most of works were not oriented for the associated dynamic instabilities; only a few papers discussed the voltage or current oscillations. The first one, noteworthy, appeared as early as in 1969 [48] and was later followed by a few others reports [49–55]. Interestingly, in [52] Zhang and Datta have reported that time-averaged cell voltage, cell efficiency, and power density of the proton exchange membrane fuel cell (PEMFC) operating in the presence of CO in the anode feed reformat gas were, in an autonomous oscillatory state, higher (up to twice) than that in stable steady state. The explanation of that gain was explained in terms of the decrease of the time-averaged anode overpotential in the oscillatory state. In later work, Zhang et al. [54] have performed mechanistic and bifurcation analysis of anode potential oscillations in PEMFC with CO in anode feed, concluding that the oscillator belongs to the HN-NDR type, and the oscillations were born via a supercritical Hopf bifurcation. In the latter work, Kiss et al. [55] have studied the spatial nonuniformity during CO and CO/ H_2 oxidation on coupled Pt electrodes which analysis will be briefly described in Chap. 2 of volume II. Below we shall concentrate on recent work by Krischer et al. [47] in which the modeling and the theoretical bifurcation analysis of bistability and oscillations during H_2 –CO mixtures were described. The presented approach is based on the Koper model for CO electrooxidation [29], described in the previous section, extended for the implementation of the hydrogen oxidation current. Thus, to Eqs. (5.13)–(5.16) the following surface process was added:



meaning that the oxidation of hydrogen molecule requires two adsorption sites which are released after that process. Further assumption and mathematical construction of the model the reader can find in the original paper, while here we shall summarize most representative results of calculations. The following four dynamical variables were taken into account: θ_{CO} , θ_{OH} , surface concentration of CO in the solution (c_{CO}) and electrode potential (ϕ_{DL}), so the surface concentrations and electrode coverage with hydrogen were not considered. The dynamic properties of the system were studied as a function of the following parameters: external voltage U , the specific electrolyte resistance ρ , the diffusion layer thickness δ , the specific double layer capacitance C , and the percentage of CO in the H_2 –CO gas mixture. The representative bifurcation diagram in the U – ρ coordinate system is shown in Fig. 5.19. In this diagram, the “reduced system” means the system simplified by considering only the contribution from H_2 oxidation to the faradaic current, whereas the dot line refers to even more simplified system,

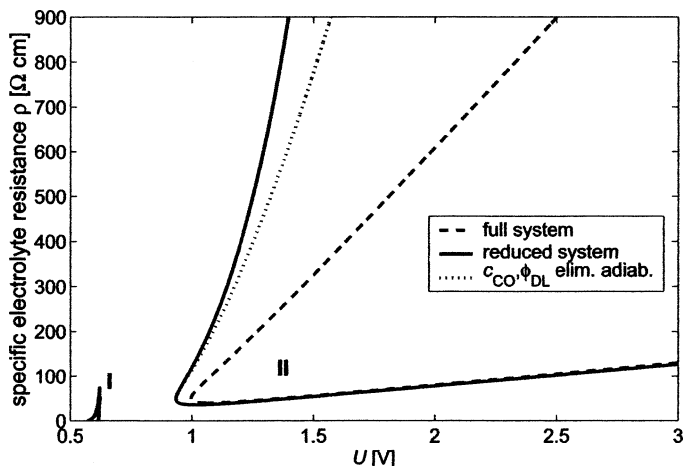


Fig. 5.19 Location of saddle–node (region I) and Hopf bifurcations (region II) in the ρ – U parameter plane for the full model (*dashed line*), the reduced model (*solid line*), and a two-variable model in which c_{CO} and ϕ_{dl} (interfacial potential drop) were adiabatically eliminated (*dotted line*). See [47] for other parameters. Reprinted with permission from [47]. Copyright 2007 American Chemical Society

from which the variables—surface concentration of CO and the electrode potential—were adiabatically eliminated.

The striking feature of this diagram is the large area of oscillations (region II), determined by the lines of the Hopf bifurcations, compared to relatively small area of bistability, determined by the lines of the saddle–node bifurcations terminated by cusp point (region I), disconnected from the oscillations region. Furthermore, the effect of increasing resistance is opposite in both these regions: upon increasing resistance the bistable region narrows, while the oscillation region widens. Further analysis of these regions led to the following conclusions. For the bistable region, the underlying feedback mechanism is the same as in the pure CO system (the autocatalysis stemming from the Langmuir–Hinshelwood mechanism, coupled to the limitations of the slow mass transfer); in other words, the bistability is generated by the S-NDR mechanism. For the oscillatory region, three types of the oscillations (A, B, C) were found, and the regions of their existence were collected on the U – C diagram (Fig. 5.20).

Region A, corresponding to relatively low double layer capacitances, includes the oscillations typical of the HN-NDR systems. Region B, for which double layer capacitance attains relatively high values, includes the S-NDR type oscillations (chemical autocatalysis) assisted by a positive feedback in the electrode potential (electrical autocatalysis). Finally, Region C covers the hybrid oscillations resulting from two positive feedback loops (i.e., being the hybrids between those in Region A and those in Region B). In conclusion, as expected, the system possesses the characteristic features of both S-NDR and HN-NDR systems, with the relative contribution to the observed dynamics dependent on the parameters. In other

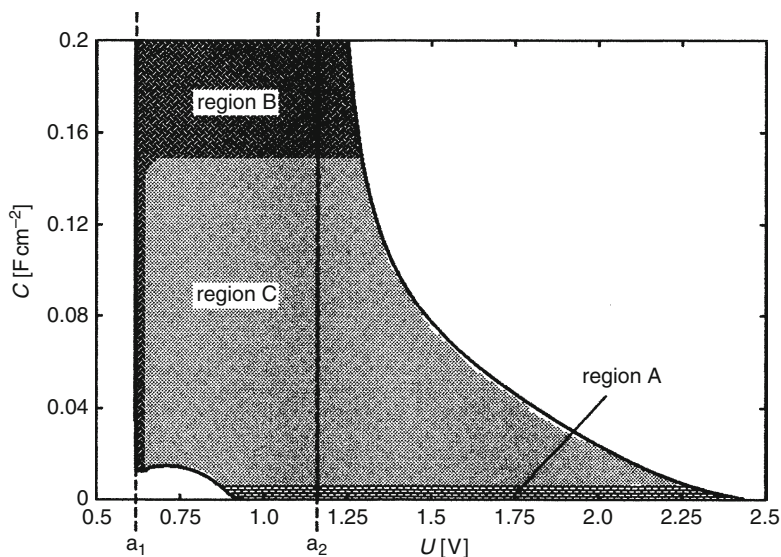


Fig. 5.20 Regions with oscillations of different phenotype in the C - U parameter plane. a_1 - a_2 : voltage interval, in which the steady state lies on the autocatalytic branch of the polarization curve ($\rho = 100 \Omega \text{ cm}$). Reprinted with permission from [47]. Copyright 2007 American Chemical Society

words, the system contains two different pairs of activator-inhibitor loops. These theoretical predictions require experimental validation. Also, it would be interesting to check whether the system under study can give rise to spatial or spatiotemporal patterns, through, e.g., the Turing bifurcation or the interaction of Hopf and Turing bifurcations. And, hopefully, based on such considerations the conditions can be found, under which the negative role of CO contaminations in the hydrogen stream feeding the low-temperature fuel cell will be diminished, so the anodes of such cell become more CO tolerant [47].

5.4 Instabilities in the Anodic Oxidation of Formate Ions

5.4.1 Experimental Results and Outline Oscillation Mechanism

Let us cite first Beden and Bewick [56] who remind us: “since the early work of Morgan [57] it has been known that formic or formate species can produce oscillations during their decomposition, either chemically [58, 59], or electrochemically on Pt, Pd or Pt-Rh electrodes [60, 61].” Beden et al. also have described the experimental [56] and mechanistic [62] studies of high-amplitude oscillations of the current reported for the formate oxidation in neutral aqueous medium, at or above 60°C , under potentiostatic conditions, during the deposition of rhodium on a gold substrate electrode. These oscillations were found to occur in the oxide region

and thus attributed to the rapid changes in the oxide coverage of their layer thickness. At sufficiently high positive potentials the formed compact oxide layer completely inhibited the oxidation of formate ions, thus also the oscillations. So, it is one more of early works in which decisive role of the oxide layer formation/destruction in the oscillatory course of formate oxidation was postulated.

The first report on the oscillations of the electrode potential in this system, under galvanostatic conditions, comes from above cited paper from the year 1928 [60]. Later studies of the oscillations and bistability on solid electrodes were reported by Wojtowicz et al. [61], Bockris et al. [63], and Schell et al. [64–67]. In addition to classical electrochemical methods, Inzelt and Kertész [68] have employed electrochemical quartz crystal microbalance (EQCM) technique to show that the potential oscillations in the course of galvanostatic oscillations of formic acid at Pt electrode are associated with accumulation and consumption of strongly bound species. In later work, these authors [69] have used the same technique to study the effect of added Cu^{2+} ions on that process by choosing the experimental conditions in such a way that the region of the oscillatory potential variations overlaps the underpotential deposition (upd) of copper. In consequence, the deposition of Cu^{2+} ions and dissolution of Cu adatoms followed the potential changes related to the formation and removal of species engaged in the electrode processes of formic acid. One should note that deposition/dissolution of metal adatoms caused relatively substantial frequency (mass) changes, detected by EQCM, compared to more subtle mass variations caused by the formation/destruction of chemisorbed layer of organic species. It appeared that addition of Cu^{2+} caused the modification of the oscillations, including the transition to the mixed-mode regime (Fig. 5.21), as well as the occurrence of bistability. The explanation of the complication in the system's dynamics, caused by addition of Cu^{2+} ions, was based on the idea of the presence of an additional feedback loop in which Cu adatoms and Cu^{2+} ions participate.

Oscillatory oxidation of formic acid can occur also in the presence of conducting polymer. Inzelt and Kertész [70] have monitored the simultaneous periodic changes of the potential and of the electrochemical quartz crystal frequency response in the course of this process under galvanostatic conditions, when the platinized platinum electrode was partially covered with poly(aniline) film. The layer of this conducting polymer acted as a pseudocapacitance which increased the period of the oscillations. This way of regulation the oscillation period indicates the role of capacitance in the generation of the oscillatory instabilities (note the paper by Kiss et al. discussed in Sect. 2.3, where an analogous effect was considered in terms of application of the differential controller to detect the essential dynamical variables in the oscillatory systems). Besides these capacitance effects, due to electrochromic nature of the poly(aniline) redox reaction, periodical changes of the color of the electrode were observed, constituting thus the studied system also the *electrochromic oscillator*. Simultaneous mass changes, detected by EQCM, were enhanced due to sorption/desorption of counterions accompanying these redox transformations.

Systematic experimental studies of oscillatory formic acid oxidation on Pt (and Pt-group) rotating disk electrodes have revealed their complicated dynamics. In the above cited work, Xu and Schell [65] have reported the period-doubling phenomena,

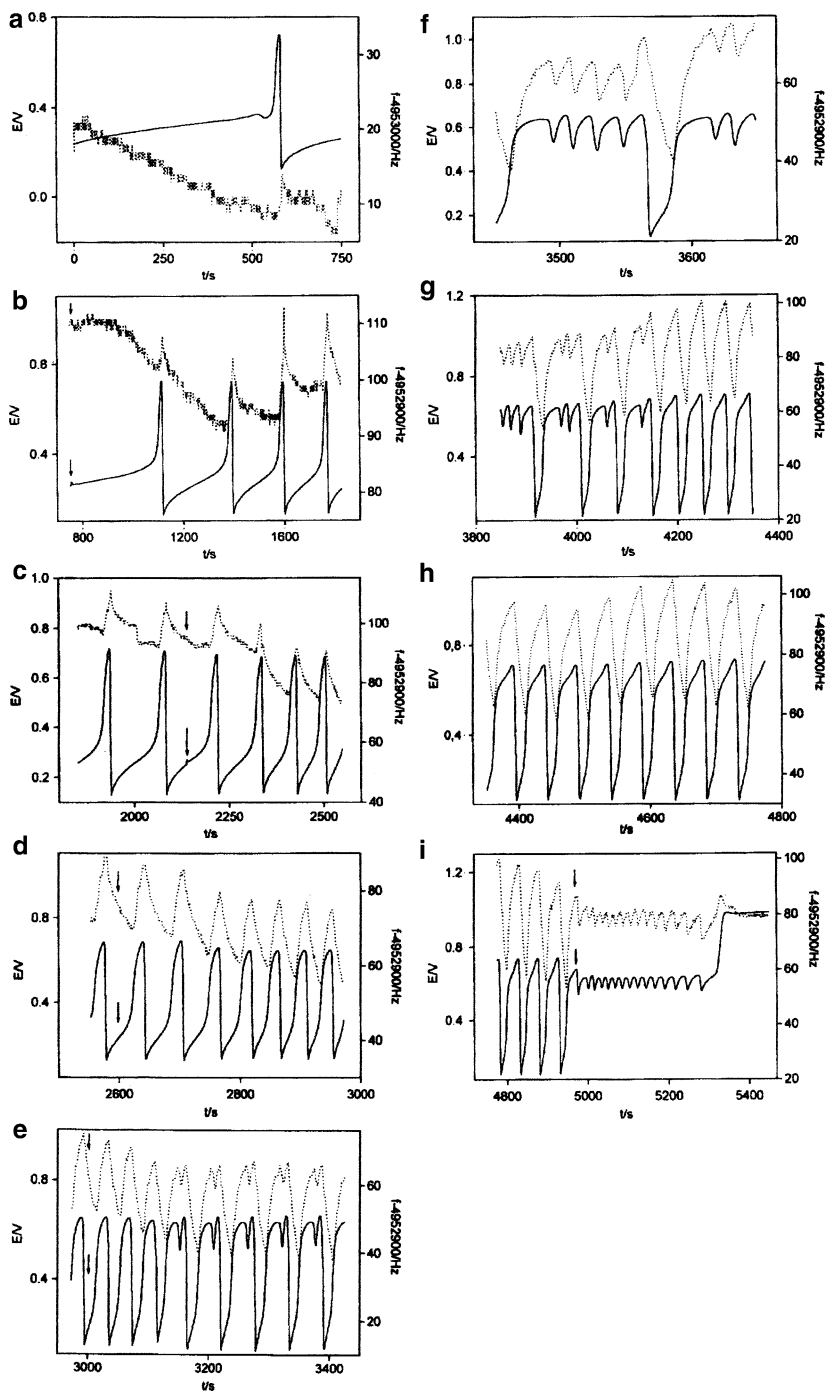


Fig. 5.21 Effect of Cu^{2+} ions on the potential (*continuous line*) and frequency (*points*) changes in the course of the galvanostatic oxidation of formic acid at Pt/Pt. Current 0.5 mA. Solution: 0.6 mol dm^{-3} HCOOH. CuSO_4 stock solution was added to the solution phase at the moments

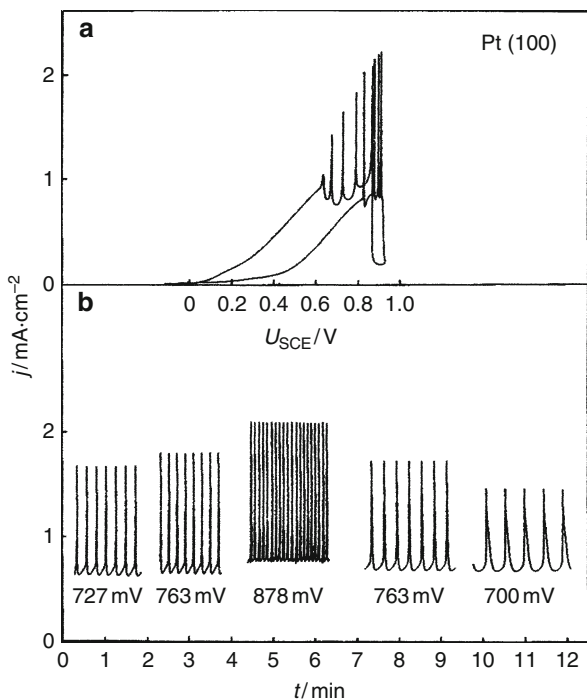


Fig. 5.22 (a) Cyclic voltammogram of formic acid (FA) oxidation on Pt(100) with external resistance $R_s = 600 \Omega$ at low FA concentrations. Bulk solution: 0.05 M HCOOH , 10^{-3} M HClO_4 . Scan rate 5 mV/s . Sharp current spikes appear on both the anodic and the cathodic scan indicating oscillatory behavior of the current. (b) Current oscillations after holding the scan at different potentials U . From left to right, the first three time series were obtained when stopping on the anodic scan, the remaining two ones when stopping on the cathodic scan. Reprinted with permission from [76]. Copyright 1997 American Institute of Physics

with the sequence of periodic states obeying the Farey sequence (cf. Sect. 6.1.3). In more recent studies, the single-crystal, low-index Pt electrodes were employed, for which the oscillatory instabilities were reported under potentiostatic conditions and discussed in terms of several possible mechanisms [26, 71–76]. In these papers a very rich set of experimental data was collected, including the role of concentration of formic acid, the magnitude of ohmic drops, and of the solution stirring intensity. All these experimental facts contributed to the explanation of the oscillatory instabilities in the process considered. As Markovic and Ross concluded in 1993 [75] based on their thorough studies for Pt(100) electrode: “the current oscillations in this reaction are certainly more complex than was thought earlier, particularly in the number of variables contributing to the periodic behavior.” Certainly this sentence inspired other researchers to further studies. Figure 5.22

Fig. 5.21 (continued) indicated by the arrows. Final concentrations of Cu^{2+} ions were: (a) 0 , (b) 10^{-3} , (c) 3×10^{-3} , (d) 5×10^{-3} , (e)–(h) 7×10^{-3} and (i) $10^{-2} \text{ mol dm}^{-3}$. Reprinted from [69], Copyright 1995, with permission from Elsevier

shows the exemplary oscillatory courses of current, under potentiostatic conditions—for both the linear potential scan and the steady-state dynamics for the stopped electrode potential [76]. Note that appropriate serial resistance was necessary to induce oscillations under such conditions.

Obviously the understanding of the source of the oscillations requires first the understanding of the electrochemical mechanism of the oxidation of formic acid on Pt-group electrodes. Since this process involves carbon monoxide as the intermediate, it is also useful to recognize the mechanism of the oxidation of CO, taken as the reactant of the separate studies (see Sect. 5.2). The inspection of the above-given references reveals that over the years several mechanisms of HCOOH oxidation on Pt electrode were proposed. Some points of these mechanisms could have been resolved only recently, due to the progress in the techniques of surface studies, complementing the purely electrochemical investigations. Therefore, we shall not review all proposed mechanisms, but focus on the description on most recent achievements in this area which seem to be consistent with available experimental data [26, 76], cf. also [77]. Since the oscillations were reported for both galvanostatic and potentiostatic conditions (in the latter case with appropriate serial resistance), this clearly suggests that the electrooxidation of formic acid on Pt, either polycrystalline or single-crystal electrode, is an example of the process characterized with the hidden negative resistance (HN-NDR system). If so, the amplitude of the potential oscillations should cover the I - E region with a positive slope, while the negative resistance at these potentials should be detected in the impedance measurements, for intermediate ac frequencies (cf. Chap. 3).

The source of instabilities in the electrooxidation of formic acid, proposed by Strasser et al. [26, 76], is based on the earlier, well-established electrochemical mechanism of this process, involving the “direct” and “indirect” paths [78, 79], similarly as proposed by Wojtowicz et al. [61] and Schell et al. [64–67].

The *direct* path involves oxidation of the formic acid via a reactive intermediate which is presumably the $\cdot\text{COOH}$ radical:

1. The HCOOH molecule arrives from the bulk to the electrode surface:



2. Fast, equilibrium adsorption of FA:



3. Oxidation of adsorbed FA:

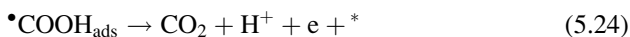
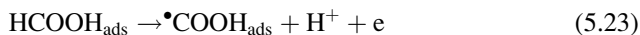
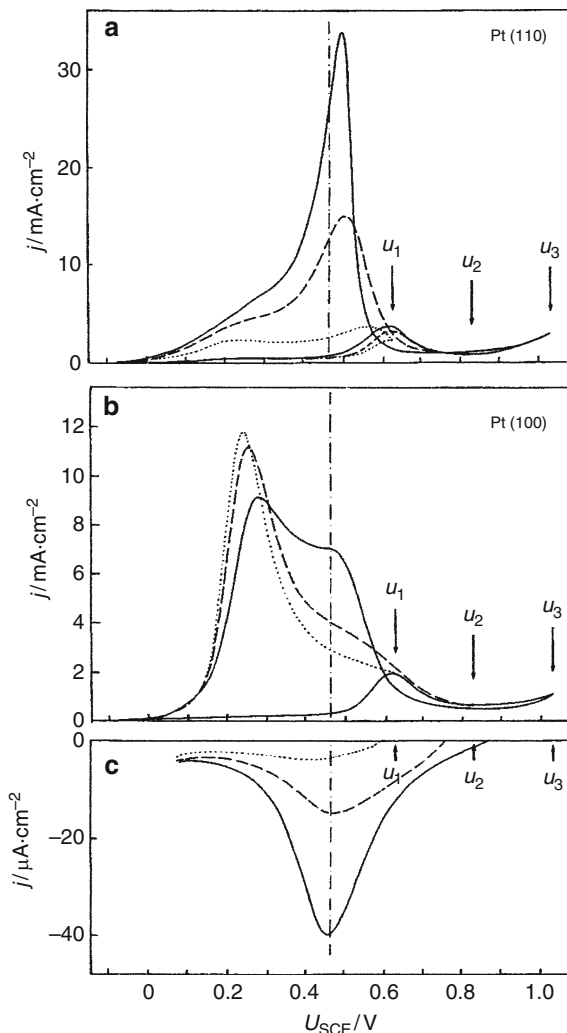
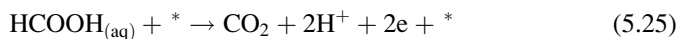


Fig. 5.23 i/U curves of the formic acid oxidation (a) and (b), and OH desorption (c) at Pt(110) and Pt(100).

Electrolyte: 1 M HCOONa + 0.5 M H₂SO₄, pH 2.6 (a) and (b), 1 M Na₂SO₄, pH 2.6. The scan (20 mV/s) was reversed at different anodic potentials as indicated by the arrows. Reprinted with permission from [76]. Copyright 1997 American Institute of Physics

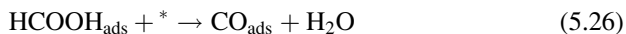


where * denotes the free adsorption site at the electrode surface. Summarizing of the above steps leads to the overall reaction of oxidation which, in the notation useful for illustrating the kinetic mechanism, includes those adsorption sites:



Reaction (5.23) is considered relatively slow compared to reaction (5.24), but can be of similar rate than the adsorption process [Eq. (5.22)]. It also important that this direct reaction path provides the necessary current density to account for the measured current of the formic acid oxidation (cf. Fig. 5.23). This is important for the later form of the expression for the faradaic current.

The parallel *indirect* path involves first the surface chemical decomposition of adsorbed HCOOH molecule into H₂O and CO, the latter one adsorbing on the electrode:



The formation of CO, confirmed by in situ IR spectrometry [78–80], is of particular importance since it is a molecule poisoning the Pt surface, and thus inhibiting the direct oxidation through the occupation of the active reaction sites, at which this direct oxidation would occur. Furthermore, it is also very important for the system's dynamics that the CO adsorption is a relatively slow process. The adsorbed CO is assumed to be removed from the surface at sufficiently positive potentials through its oxidation, involving the OH_{ads} species, stemming from oxidation of water molecule, according to Eqs. (5.15) and (5.16). Note that adsorption of OH also means the poisoning of the Pt surface, if it occupies (as it is assumed in the model) the same adsorption sites, as CO and HCOOH. The OH poisoning (5.15) is a relatively fast process, compared to above-mentioned slow CO poisoning. Reaction (5.16) means the release of two adsorption sites, and the sum of both equations indicates the autocatalytic recovery of adsorption sites:



Therefore in some earlier concepts, this process, being a source of positive feedback loop, was considered a principal source of dynamic instabilities which would then be of purely chemical, not electrochemical origin. However, in view of recent experimental results this idea found no confirmation.

5.4.2 The Model of Oscillations Under Potentiostatic Conditions

The mechanism elaborated by Strasser et al. [26, 76] explained the current oscillations under potentiostatic conditions, in the presence of appropriate ohmic drops. In particular, this model involves a separate study of the CO oxidation subsystem prior to the analysis of the oxidation of formic acid (cf. Sect. 5.2). On the other hand, this approach is based on some simplifications, e.g., it is assumed that the electrode potential does not attain such positive values (i.e., >ca 1.0 V vs. SCE), at which surface oxygen species, such as PtO, PtO₂, or PtO(O), subsurface hydroxide and oxygen can be formed, and in consequence, all these species are not considered in the model. This is, however, a reasonable assumption since under the experimental conditions the electrode potential remains within only 0.1–0.7 V. The reader interested in all details (including the differences in the characteristics of the process occurring at various crystallographic planes of Pt) is advised to consult the original references, while below we shall summarize the most important points

which will clarify the basic source of the oscillations under considered conditions, generally on Pt or Pt-group metals.

Typical simplification of the kinetic law for the direct pathway, taking into account the role of OH_{ads} from the indirect pathway, assumes that step (5.24) is so fast, that one can apply steady-state approximation to the COOH_{ads} species. The faradaic current, stemming mainly from the *direct* path of HCOOH oxidation, can then be expressed by the simple expression which takes into account the poisoning of the electrode surface by both the CO_{ads} and OH_{ads} species [77]:

$$J_{\text{direct}} = nFK(E, c_{\text{HCOOH}})(1 - \theta_{\text{CO}} - \theta_{\text{OH}}) \quad (5.28)$$

with $K(E, c_{\text{HCOOH}})$ being the factor dependent on both the electrode potential E and formic acid concentration, c_{HCOOH} . When, for given HCOOH concentration, E is increased, $K(E)$ also increases, so the direct path, in the absence of surface poisoning, would produce only the positive dJ/dE slope. Thus, the explanation of the negative resistance lies in the variation of θ_{CO} and θ_{OH} with the electrode potential.

Let us analyze what happens if the Pt electrode is immersed into the HCOOH solution and the potential is first scanned from small values (e.g., 0 V vs. SCE) toward anodic direction, and compare the description of processes with the course of curves shown in Fig. 5.23.

The electrode is initially significantly covered with the adsorbed CO poison, so only a residual number of vacant adsorption sites allows the oxidation of HCOOH via the direct path. At ca. 0.5 V the formation and electrode coverage of OH radicals becomes so advanced that due to oxidative interaction of CO_{ads} and OH_{ads} certain number of adsorption sites is regenerated, giving rise to an increase in the current of direct oxidation of HCOOH. However, upon further increase of the potential, the surface concentration of OH_{ads} becomes so high that all adsorbed CO molecules are removed. Upon further increase of E , the increasing amounts of OH_{ads} lack the reactant for removal, so they now in turn increasingly poison the electrode surface—thus **the increase of θ_{OH} with E is believed to cause the region of the negative differential resistance**. One should note that Fig. 5.23 illustrates the differences in the shapes of the peaks recorded for Pt(110) and Pt(100) electrodes which are explained by faster course of the direct path of HCOOH oxidation on the Pt(100) surface. At potentials following the NDR region, i.e., up to 0.8–0.9 V, the current does not drop to zero which fact means that, in spite of high electrode coverage with adsorbed OH, the inhibition is not total. Since the inhibitive effect of CO_{ads} and OH_{ads} is thus not equally strong, this phenomenon is called the “asymmetric inhibition.” Upon reversed (negative) scan of the electrode potential, one observes certain hysteresis which is however of purely kinetic nature, caused by interaction of the time scale of the potential sweep with the slow CO adsorption process. In other words, for the steady-state experiments, for each value of the electrode potential there exists only one value of the current, so under such conditions—potentiostatic, with negligible (vanishing) ohmic drops there are no any electrochemical dynamic instabilities present. Such monostability is true for all three single-crystal Pt

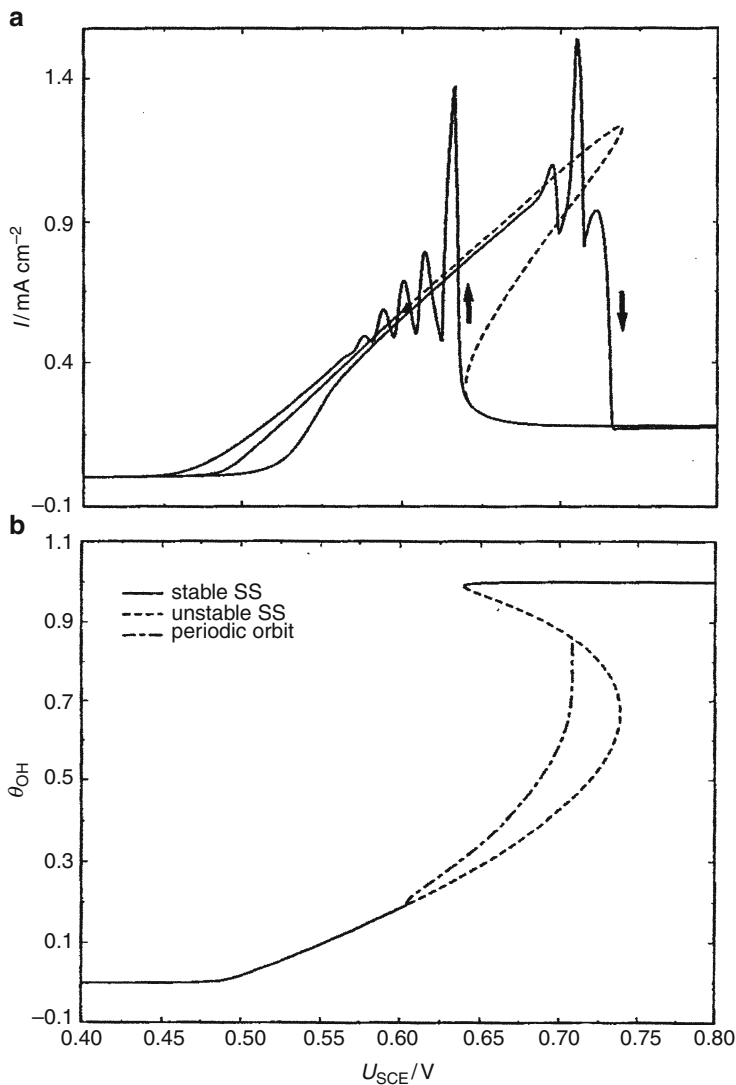


Fig. 5.24 (a) Calculated cyclic voltammograms and stationary I/U curve for the FA oxidation model [Eqs. (5.29)–(5.36)]. The anodic and cathodic scans are indicated by arrows. Sharp current spikes are seen during both scan directions. Furthermore, a hysteresis between a low-current steady state and an oscillatory high-current state is observed. Model parameters (see also [26]): $T = 298$ K, $\text{pH} = 1$, $\delta = 3 \times 10^{-2}$ cm, $R_s = 300 \Omega$, $k_{\text{poison}} = 60 \text{ dm}^3/\text{mol s}$, scan rate 10 mV/s . The stationary curve corresponds to an infinitely slow scan rate. The transition between stable current behavior and oscillatory current behavior was found to be a Hopf bifurcation point (solid triangle, $U = 0.6$ V) at low values of U . The stationary curve further shows the experimentally unaccessible unstable steady state branch (dashed line) which undergoes two saddle–node bifurcations ($U = 0.74$ V, $U = 0.64$ V) before regaining stability on the low-current branch. (b) Calculated one-parameter bifurcation diagram of the FA model for the model parameters as

electrodes considered. In other words, this is why no chemical source of instabilities is confirmed, and the oscillator studied cannot be qualified as *truly* potentiostatic, or Class-1 oscillator [76], although such suggestions were made earlier in the literature.

Accordingly, only in the presence of sufficiently high ohmic resistance either the bistability or oscillations were reported under potentiostatic conditions. The mathematical model of Strasser et al. [26] was elaborated in stepwise manner, starting from the mechanism of the CO oxidation as a crucial subsystem (cf. Fig. 5.12). Here we shall focus on the final results for the HCOOH oxidation. In order to replace the partial differential equations (PDEs) with the ordinary ones (ODEs), the linear Nernst layer approximation was applied for the transport of HCOOH from the solution bulk toward the electrode surface (the approach being one more application of the Koper's approach, cf. Sect. 2.2.2). The following dynamical variables were chosen: $[FA]_{dl}$: the concentration of formic acid in the solution at the electrode surface (i.e., at the reaction site in the double layer on the solution side), θ_{CO} (the electrode coverage with CO), θ_{OH} (the electrode coverage with OH) and E : the electrode potential, differing from externally applied voltage U for ohmic drops IR_s (for all other details see the original reference [26]). The 4D dynamical system was defined with the following equations. The first one is Eq. (5.29):

$$\frac{d[FA]_{dl}}{dt} = \frac{2D_{FA}}{\delta^2} \{ [FA]_{bulk} - [FA]_{dl} \} - \frac{2 \times 1,000 \times S_{tot}}{\delta} (v_{direct} + v_{poison}) \quad (5.29)$$

where D_{FA} is the diffusion coefficient of FA, δ is the thickness of the Nernst diffusion layer, and the factor 1,000 in the numerator comes from the differences in the units: the total number adsorption sites S_{tot} was given in mol cm^{-2} , while $[FA]_{dl}$ was expressed in mol dm^{-3} . The rates of two reactions of HCOOH decay, through the direct oxidation v_{dir} [cf. Eq. (5.25)] and through the surface decomposition leading to CO poison, v_{poison} [cf. Eq. (5.26)], are defined as, respectively:

$$v_{direct} = \chi(E, k_{ads}, k_d, [FA]_{dl}) \times (1 - \theta_{CO} - f\theta_{OH}) \quad (5.30)$$

$$v_{poison} = k_{poison}[FA]_{dl} \times (1 - \theta_{CO} - \theta_{OH}) \quad (5.31)$$

Fig. 5.24 (continued) given in (a). The steady-state coverage of OH, θ_{OH} is plotted against the applied potential U . The *solid and dashed lines* indicate stability and instability, respectively. The *dotted-dashed line* shows the amplitude of the stable periodic orbits born in the Hopf bifurcation. At the value of U where the *dotted-dashed line* disappears the limit cycle collides with the saddle in a saddle-loop bifurcation. Beyond the potential value there is no stable state other than the low current, OH-covered steady state. Reprinted with permission from [26]. Copyright 1997 American Institute of Physics

where

$$\chi(E, k_{\text{ads}}, k_{\text{d}}, [\text{FA}]_{\text{dl}}) = \frac{k_{\text{d}} \exp[\alpha_3 FE/RT] \times k_{\text{ads,FA}} [\text{FA}]_{\text{dl}}}{k_{\text{d}} \exp[\alpha_3 FE/RT] + k_{\text{ads,FA}} [\text{FA}]_{\text{dl}}} \quad (5.32)$$

with k_{d} and α_3 being the (standard) rate constant and the transfer coefficient of reaction (5.23), and $k_{\text{ads,FA}}$ is the adsorption constant of formic acid on the Pt surface [26]. In turn, k_{poison} is the rate constant of reaction (5.26). Finally, the *empirical* factor f in Eq. (5.30) reflects the above-mentioned asymmetry in the inhibition of the formic acid oxidation by CO (complete) and OH (incomplete), manifesting itself by assumption only in the direct path.

The second equation of the model is (5.33):

$$\begin{aligned} \frac{d\theta_{\text{OH}}}{dt} = & k_{\text{ads,OH}}(1 - \theta_{\text{CO}} - \theta_{\text{OH}}) \exp[\alpha_1 (FE/RT)] \\ & - k_{\text{r}} S_{\text{tot}} \theta_{\text{CO}} \theta_{\text{OH}} \exp[\alpha_2 (FE/RT)] - k_{\text{des,OH}} \theta_{\text{OH}} \exp[-(1 - \alpha_1) \\ & \times (FE/RT)] \end{aligned} \quad (5.33)$$

where $k_{\text{ads,OH}}$, $k_{\text{des,OH}}$, and k_{r} are the rate constants of OH adsorption, OH desorption and of reaction between OH_{ads} and CO_{ads} [Eq. (5.16)].

The third equation is (5.34):

$$\frac{d\theta_{\text{CO}}}{dt} = v_{\text{poison}} - k_{\text{r}} S_{\text{tot}} \theta_{\text{CO}} \theta_{\text{OH}} \exp[\alpha_2 (FE/RT)] - k_{\text{des,CO}} \theta_{\text{CO}} \quad (5.34)$$

Finally, the fourth equation (5.35) comes from the charge conservation principle applied to the faradaic and capacitive currents:

$$\frac{dE}{dt} = \frac{1}{C_{\text{d}}} (j_{\text{tot}} - j_{\text{direct}} - j_{\text{ads,OH}} - j_{\text{r}} + j_{\text{des,OH}}) \quad (5.35)$$

where C_{d} is the double layer capacity, $j_i = nFS_{\text{tot}}v_i$ are the partial current densities for the particular electrochemical processes and the total current density flowing through the cell is given by:

$$j_{\text{tot}} = \frac{U - E}{AR_{\text{s}}} \quad (5.36)$$

Of course, some of the parameters were *a priori* unknown and had to be adjusted in the course of the simulation procedures. Table III in [26] collects values of parameters used in the simulations. Figure 5.24 shows exemplary results of simulations corresponding to the characteristics of the Pt(100) electrode, with $R_{\text{s}} = 300 \Omega$: the cyclic voltammetric and steady-state $I-U$ responses for the model system, as well as the respective bifurcation diagram. Let us note that relatively high value of the rate

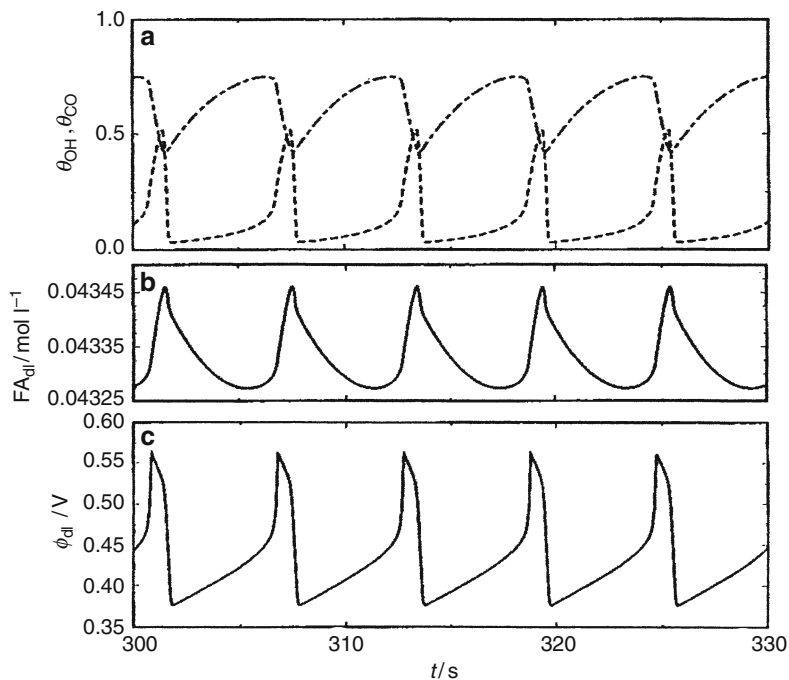


Fig. 5.25 Calculated time series of the four model variables at constant outer potential ($U = 0.9$ V) and for other parameters: $T = 298$ K, $\text{pH} = 1$, $\delta = 3 \times 10^{-2}$ cm, $R_s = 700$ Ω , $k_{\text{poison}} = 6$ $\text{dm}^3/\text{mol s}$. (a) *dashed line*: θ_{OH} , *dotted dashed line*: θ_{CO} , (b) $[\text{FA}]_{\text{dl}}$, (c) $\phi_{\text{dl}} \equiv E$. Reprinted with permission from [26]. Copyright 1997 American Institute of Physics

constant for the poisoning of the electrode ($k_{\text{poison}} = 6\text{--}60$ $\text{dm}^3 \text{mol}^{-1} \text{s}^{-1}$) was assumed, in agreement with experimental findings.

In the bifurcation diagram (Fig. 5.24b), the oscillations are born in a Hopf bifurcation at $U = 0.6$ V and decay when their amplitude collides with the branch of unstable steady states (of saddle type) which situation corresponds to the saddle–loop infinite period bifurcation.

If one wants to model the dynamics resembling the experimental observations for other single crystal electrodes, it is possible through assuming different rate constant for the poisoning of electrode surface with CO (5.26), since this value was found to be a crucial structure-sensitive parameter, largely determining the shape of the calculated voltammograms and the wave forms of the current oscillations. Thus, for Pt(111) the rate constant $k_{\text{poison}} = 6$ $\text{dm}^3 \text{mol}^{-1} \text{s}^{-1}$ was assumed. Respective simulations (corresponding to $R_s = 600$ Ω) have shown that in this case the sequence of the Hopf and saddle–loop bifurcation on the voltage axis was reversed, compared to Pt(100) [26]. Taking further the model Pt(111) system as an example, it is further very informative to compare the temporal variations of all four dynamical variables involved in the model: θ_{OH} , θ_{CO} , surface concentration of formic acid $[\text{FA}]_{\text{dl}}$ and electrode potential E (Fig. 5.25).

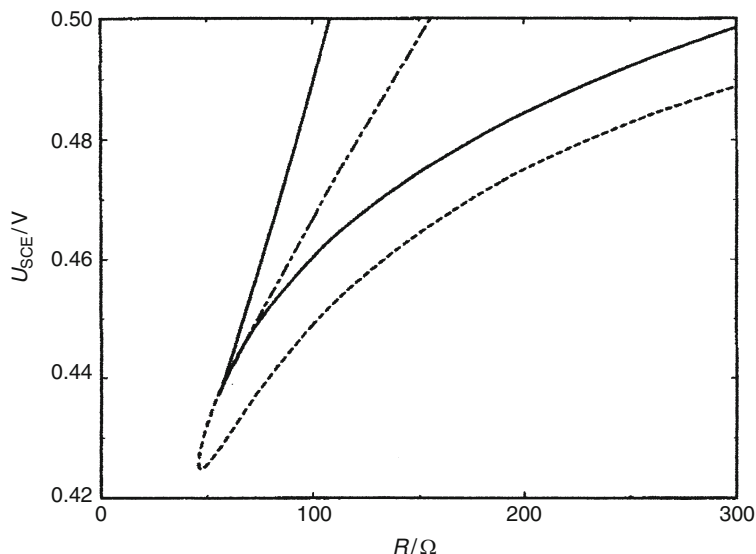


Fig. 5.26 Two-parameter bifurcation diagram of the complete FA model using $\delta = 3 \times 10^{-2}$ cm, $k_{\text{poison}} = 10 \text{ dm}^3/\text{mol s}$, $\text{pH} = 3$. All other parameters as before. The *solid line*, *dashed line*, and the *dotted-dashed line* indicate the location of the saddle–node bifurcations, the Hopf bifurcations, and the saddle–loop bifurcations, respectively. All three *curves* meet in a Takens–Bogdanov point close to the cusp. Reprinted with permission from [26]. Copyright 1997 American Institute of Physics

The dynamical variables θ_{OH} and E appear to be nearly in phase, suggesting that θ_{OH} is, as the electrode potential, the fast variable, which almost without a delay matches the variation of E . On the contrary, the electrode coverage of CO, θ_{CO} , formed in the potential-independent reaction (5.26) appears to be a relatively slow variable, exhibiting also a significant phase shift with respect to θ_{OH} variations. This is concordant with the above qualitative description of the CO and OH surface dynamics. At certain threshold value of E , a sudden increase of both θ_{OH} and E takes place, since the high degree of poisoning of the electrode causes the decrease in the oxidation current and thus in the ohmic potential drops. Then also the surface concentration of formic acid in the solution increases, as its consumption in the oxidation reaction slows down.

It is further customary and useful to construct the bifurcation diagram in the U – R_s coordination system, for other parameters fixed at appropriately chosen values. Such an exemplary diagram is shown in Fig. 5.26.

Note that a relatively large value of the Nernst diffusion layer ($\delta = 3 \times 10^{-2}$ cm) models the condition of the (practically) unstirred solution. The corresponding substantial development of the diffusion profile of the formic acid in the solution means that its surface concentration undergoes significant changes during the oscillations, so $[\text{FA}]_{\text{dl}}$ is one of the essential dynamic variables under such conditions. If δ was assumed as small as, e.g., 2×10^{-4} cm, this would model the conditions of strong stirring through the generation of an intensive flux of formic acid toward the electrode surface; the $[\text{FA}]_{\text{dl}}$ will be in this case nearly constant, close to the bulk

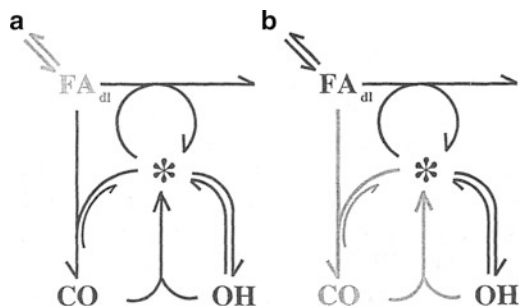


Fig. 5.27 (a) Network diagram of suboscillator 1. Only the *black species* and reactions are essential for the model dynamics. The *gray species* and reactions, i.e., the variable $[FA]_{dl}$, as well as the diffusional transport reactions, have become nonessential by setting δ to a very small value thereby keeping $[FA]_{dl}$ at its bulk concentration. (b) Network diagram of suboscillator 2. Similar to (a), only the *black species* and reactions are essential for the dynamics and are responsible for the observed dynamics. The rate of poisoning reaction has been set to zero. Consequently, θ_{CO} as well as the rate of the removal reaction is zero. Reprinted with permission from [26]. Copyright 1997 American Institute of Physics

value ($[FA]_{bulk}$). Obviously in the latter case, the $[FA]_{dl}$ is no longer an essential dynamical variable for our model system. These conclusions constitute a useful introduction to the next paragraph.

5.4.3 The Oxidation of Formic Acid as the System of Two Suboscillators

Before it was said that the oxidation of CO forms a subsystem for the HCOOH oxidation at Pt electrode, Strasser et al. [26] have elaborated this problem in terms of the stoichiometric network analysis (SNA) [81, 82] in which, based on the stoichiometric and kinetic coefficients of a chemical reaction mechanism expressed in the relevant network diagram, one can diagnose the system's ability to exhibit dynamical instability. On such diagrams, the arrows connecting the chemical species symbolize the chemical (pseudo)reactions, while the number of feathers and barbs corresponds to the stoichiometric coefficients in relevant chemical reactions (for the stoichiometric coefficient of the consumed species equal to 1, no feather is drawn at the corresponding reaction arrow). In the case considered here, the full mechanism of formic acid electrooxidation was decomposed into two suboscillators (subnetworks of reactions) which consist of the same source of instability (autocatalysis) but exhibit different negative feedback loops. These networks diagrams are shown in Fig. 5.27, where the essential species and reactions are indicated as black symbols and arrows, while the nonessential elements are shown in gray. These suboscillators can be considered as two "minimal oscillators."

The suboscillator 1 (Fig. 5.27a) corresponds to the thin diffusion layer, when the $[FA]_{dl}$, as practically equal to the constant bulk value, is no longer an essential dynamical variable. The system dynamics is then reduced to the subsystem

involving CO, OH, and available adsorption sites (*). The fact that these species constitute the oscillatory surface subsystem means also that suboscillator 1 is independent of stirring. Essential for the oscillations is the fast reversible adsorption of OH species.

The suboscillator 2 corresponds to the situation when the poisoning of the electrode with CO is completely neglected. This condition, in terms of the model mechanism, means setting both of the rate constant of poisoning reaction and electrode coverage θ_{CO} to zero. Obviously it also means that θ_{CO} becomes now a nonessential variable. In turn, the essential role of $[\text{FA}]_{\text{dl}}$ is now recovered by setting the diffusion layer thickness back to a large value: $\delta = 3 \times 10^{-2}$ cm. As for suboscillator 1, the essential for the oscillations remains the fast reversible adsorption of OH species, but now, due to $[\text{FA}]_{\text{dl}}$ role which is dependent on the rate of formic acid transport, the dynamics of suboscillator 2 is sensitive to stirring.

It is instructive to compare bifurcation diagrams of both suboscillators, shown in Fig. 5.28.

The diagram for suboscillator 1 is evidently similar to that for the full FA oscillator, shown in Fig. 5.26. In turn, the diagram for the suboscillator 2 reveals the cross-shaped morphology, typical of systems in which oscillations and bistability are interrelated, with the oscillatory region being now very tiny. Further analysis shows the following important facts. In both cases, the Hopf bifurcations appear to occur for such parameters which correspond to the **positive** slope of the I - E curve of the formic acid oxidation. In the case of suboscillator (2), if the thickness of the diffusion layer is changed to an intermediate value $\delta = 2 \times 10^{-4}$ cm, only the saddle-node bifurcations are detected, with the $[\text{FA}]_{\text{dl}}$ concentration kept at nearly constant bulk value. Thus, the bistability is caused only by the fast, potential-dependent ad/desorption of OH, in the presence of ohmic resistance, and the oxidation of formic acid is only a current providing process. When the conditions are chosen so that $[\text{FA}]_{\text{dl}}$ can vary, the system can become oscillatory (in the sense of minimal oscillator).

In terms of this approach, let us consider the full dynamics of the formic acid electrooxidation, under unstirred conditions, as the result of interaction of both suboscillators. Let us note again the similarity of the full bifurcation diagram (Fig. 5.26) and the diagram for suboscillator 1 (Fig. 5.28a) which suggests that for U and R_s far from the cusp bifurcation, the system's dynamics should be determined largely by the suboscillator 1. In turn, near the cusp point, the interaction of both suboscillators, exhibiting in these (U , R_s) regions stable limit cycles, leads to complex: mixed-mode (MMO) and aperiodic oscillations (Fig. 5.29). The analysis of oscillations generated by either of two minimal oscillators shows that in the MMO sequence, the small-amplitude (quasi-sinusoidal) oscillations stem from suboscillator 2, where the large-amplitude ones (relaxation spikes) are generated by the dynamics of the suboscillator 1.

Finally, the positive and feedback loops in both suboscillators are schematically depicted in Fig. 5.30.

These diagrams help to understand the experimentally observed effect of stirring on the oscillatory oxidation of formic acid. Since in the dynamics of the

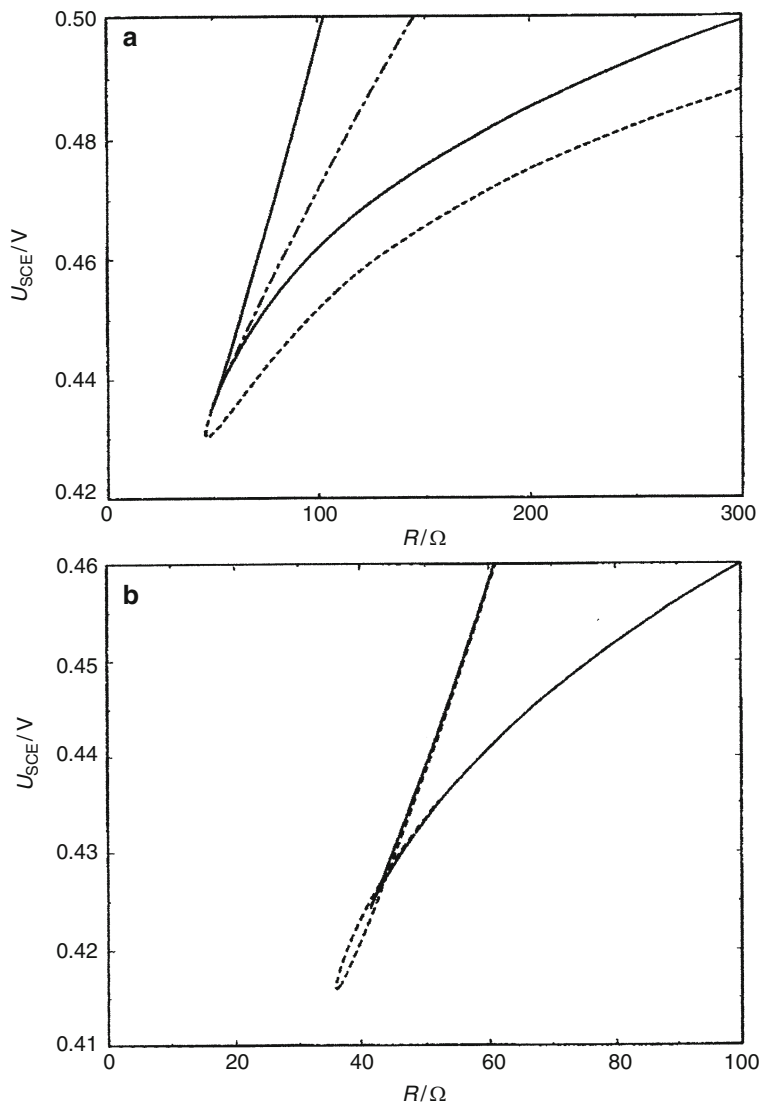


Fig. 5.28 (a) Two-parameter bifurcation diagram of suboscillator 1 using $\delta = 2 \times 10^{-4}$ cm, $k_{\text{poison}} = 10$ dm³/mol s, pH = 3. All other parameters and linestyles as in Fig. 5.26. (b) Two-parameter bifurcation diagram of suboscillator 2 using $\delta = 3 \times 10^{-2}$ cm, $k_{\text{poison}} = 10$ dm³/mol s, pH = 3. All other parameters and linestyles as in Fig. 5.26. Reprinted with permission from [26]. Copyright 1997 American Institute of Physics

suboscillator 1, $[\text{FA}]_{\text{dl}}$ is not an essential variable, this submodel produces simple, period-1 oscillations, insensitive to stirring, as reported experimentally. In turn, under such conditions, where MMOs were experimentally reported, stirring was

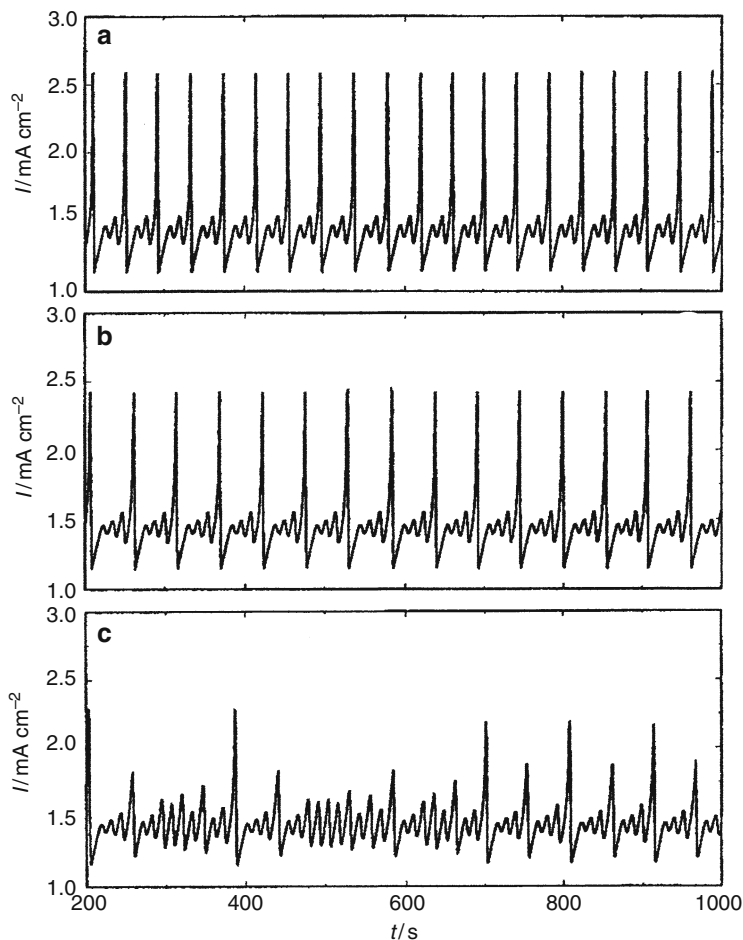


Fig. 5.29 Time series for $R_s = 50 \Omega$ at different values of U . All other parameters as in Fig. 5.26. (a) Mixed-mode oscillations (MMOs) characterized by one large-amplitude and two small-amplitude oscillations (1^2 state) at $U = 432.1$ mV, (b) mixed-mode oscillations characterized by one large-amplitude and three small-amplitude oscillations (1^3 state) at $U = 432.1155$ mV, (c) aperiodic oscillations at $U = 432.118$ mV. Reprinted with permission from [26]. Copyright 1997 American Institute of Physics

found to switch MMOs into period-1 oscillations. It is easy to understand this in terms of the above considerations: in the absence of stirring MMOs are caused by the interplay of suboscillators 1 and 2; when stirring is switched on, the negative feedback in suboscillator 2 is suppressed, as discussed earlier, and the dynamics of only suboscillator 1 dominates the oscillatory behavior of the entire process.

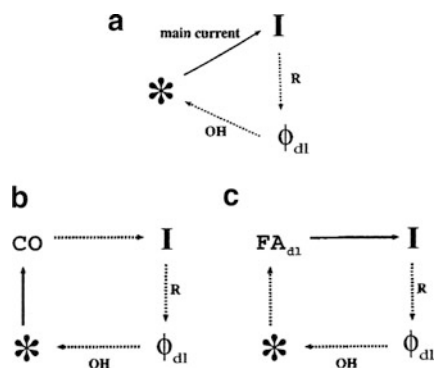


Fig. 5.30 (a) Positive feedback loop of both suboscillators. *Solid arrows* represent a positive, whereas *dashed arrows* indicate negative effect. The regulations can be viewed as matrix elements of a jacobian. Free surface sites affect the total current via the direct oxidation path. I effects the electrode potential $\phi_{dl} \equiv E$ via the ohmic resistance and ϕ_{dl} feeds inversely back to the free surface sites due to negative differential resistance. (b) Negative feedback loop of suboscillator 1. The loop contains the slow chemical species CO_{ads} . (c) Negative feedback loop of suboscillator 2. The loop includes the slow chemical species $[FA]_{dl}$. Reprinted with permission from [26]. Copyright 1997 American Institute of Physics

5.4.4 Mechanism of Oscillations Under Galvanostatic Conditions

Since it was experimentally found that the oxidation of formic acid on Pt electrodes proceeds in an oscillatory manner also under galvanostatic conditions, one should check that the model of Strasser et al. is able to provide a hidden negative impedance, revealed in the experimentally obtained spectra. As stated earlier, the full mechanism of the oscillatory oxidation of the formic acid on Pt electrodes can be decomposed into the suboscillators 1 and 2 which are characterized with common positive feedback loop, but different negative feedback loops. Analysis shows that the hidden negative impedance is provided by the suboscillator 1 and this view is supported by appropriate numerical simulations which show that the oscillations of the electrode potential, under galvanostatic conditions, occur on branches of positive dI/dE slope of the $I-E$ dependence recorded under dc conditions [26]. According to the theory of HN-NDR oscillators (Sect. 3.4), the system considered involves: (1) the current-carrying process, i.e., the direct path of the oxidation of formic acid to CO_2 and H_2O , (2) a process on a time scale comparable to that of (relatively fast) variations of the electrode potential, which is responsible for the generation of the NDR region and which will be visualized as the negative real impedance for the intermediate ac frequencies, i.e., a fast potential-dependent adsorption/desorption of OH species, and (3) a relatively slow potential-dependent process exhibiting a positive $I-E$ characteristic, hiding the NDR region under dc conditions, i.e., the adsorption and reactive removal of CO poison. Therefore, for low ac frequencies, when both CO and OH respond to ac perturbation, the dI/dE is positive, like under dc conditions. In turn, for sufficiently

high ac frequencies, the CO stops to respond, but OH still does, and hence only the increase of θ_{OH} with increasing potential determines the negative dJ/dE slope [77]. It is also instructive to find a mechanistic correlation between the galvanostatic formate and hydrogen oxidation: fast OH ad/desorption plays analogous role like Cl^- ad/desorption in the latter case, slow poisoning and reactive removal of CO corresponds to the potential-dependent ad/desorption of the metal cations, and direct oxidation path of formic acid constitutes the current carrying process, analogously to the diffusion-limited H_2 oxidation current [26].

In order to complete the above description, one should indicate that suboscillator 2 does provide only an explicit, not-hidden NDR region. In this case there is involved the faradaic process (direct electrooxidation of formic acid) involving the slow variable (concentration of the reactant), dependent on the electrode potential as a fast variable and coupled with the potential-dependent, comparably fast adsorption/desorption of an inhibitor: OH species. Numerical simulations, performed for the suboscillator 2, confirmed that the current oscillations occur only around the negative dJ/dE slope, at sufficiently low stirring rates, when $[\text{FA}]_{\text{dl}}$ can become an essential variable, and in the presence of appropriate serial resistance. Under galvanostatic conditions, as should be expected for this type of the oscillator, no oscillations of the electrode potential could be generated.

One can conclude that the mechanism of Strasser et al. [26], in spite of some simplifications, represents the realistic model of dynamic instabilities reported for this process. In spite of apparent stoichiometric simplicity of this process, its dynamics is interestingly complicated through the coexistence of two suboscillators, the relative contribution to the overall mechanism depends on experimental conditions, with the important role of the rate of transport, controlled by the intensity of stirring of the solution.

5.4.5 *Recent Suggestions for the Formic Acid Oxidation Mechanism*

All the above phenomena described in this chapter were interpreted in terms of well-established dual-path of the formic acid oxidation. One should note that in some very recent papers, in which the modern spectroscopic methods were employed to study the reaction intermediates, this mechanism is questioned. For example, Osawa et al. [83–85] have conducted measurements with the *Surface Enhanced Infrared Absorption Spectroscopy* (SEIRAS). Contrary to earlier views, they have suggested that formic acid was oxidized to CO_2 on Pt electrodes via adsorbed formate (utilizing both oxygen atoms to take two surface sites). Thus, the formate is the main active intermediate during the electrooxidation of formic acid on Pt, with the rate of this process being a nonlinear function of coverages of formate and carbon monoxide. The decomposition of formate to CO_2 is the rate determining step. Furthermore, in terms of this concept CO_{ads} is not only a surface

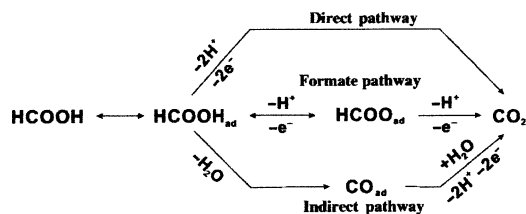


Fig. 5.31 Tentative reaction scheme for the oxidation of formic acid on Pt which includes three different reaction pathways: the “indirect” pathway, the “formate pathway,” and the “direct” pathway. The formate pathway relates to the formate species detected by IR. Reprinted from [88] with permission of John Wiley & Sons, Inc. Copyright 2006 Wiley-VCH Verlag GmbH & Co. KGaA, Weinheim

poison competing with formate form adsorption sites, but it also suppresses the decomposition of formate to CO₂. The latter effect, decreasing the imposed current, causes the shift of the electrode potential toward positive values. At sufficiently high potentials the oxidative removal of CO takes place, and then more surface sites become available for formate species. Occurring in this way acceleration of formate oxidation causes the return of the potential toward less positive values, when CO is formed again. The mechanism qualitatively expressed in this way was then successfully mathematically modeled by Osawa et al. [86]. In turn, in another recent work, Behm et al. [87], based on their IR in situ measurements of the formic acid oxidation on a Pt film/Si electrode, have stated that adsorbed bridge-bonded formates could not play a role of a main intermediate in this process. In the opinion of Behm et al., actual studies have confirmed their earlier **triple** pathway mechanism, consisting of: the *direct* pathway, the *indirect* pathway, and the *formate* pathway (Fig. 5.31) [88]

In the latter route, adsorbed formate act as the “reaction spectator” which blocks the Pt surface in the predominant, direct reaction pathway. These concepts are applicable both to the formic acid and *methanol* oxidation, since in the latter case the formic acid and formates were found also among the oxidation products (besides CO and CO₂), and formate were detected as the intermediates during the oxidation on Pt [89].

Concluding, application of modern spectroscopic methods has revealed but did not resolve yet all the mechanistic details of HCOOH oxidation on Pt electrodes. This may have further consequences also for the revision of the oscillatory mechanism of this process.

5.4.6 Temperature Overcompensation Effect in Formic Acid Oxidation

The electrooxidation of formic acid on a polycrystalline Pt electrode was used by Epstein, Varela et al. [90] to study the effect of temperature on the oscillatory

characteristics of this process. As mentioned in Sect. 2.4, the independence of biological rhythms of variation of the environmental temperature is an important feature of physiological clocks. It is thus interesting to study the influence of temperature on the oscillations in laboratory systems which usually do not exhibit such “model homeostasis.” For the electrooxidation of formic acid, galvanostatic studies of oscillations were performed within the temperature range from 5 to 25°C. A particularly interesting and novel (for the surface oscillatory reactions) observation was made: in the oscillatory region, the temperature effect on the rate constant was *not* concordant with the Arrhenius law; in most cases the temperature coefficient $q_{10} = k(T + 10^\circ)/k(T)$ was less than 1, meaning the *decrease* of rate constant with temperature (or, equivalently, negative temperature coefficient in the logarithmic scale). Only at high imposed current this coefficient was close to 1. Let us remember that for most chemical and biochemical reactions the van't Hoff prediction: $q_{10} = 2-4$, was confirmed. The non-Arrhenius behavior with $q_{10} \approx 1$ is termed the *temperature compensation*, and thus even stronger anomaly, i.e., $q_{10} < 1$ means *temperature overcompensation*.

For the purposes of intercomparison of different oscillatory courses at different temperatures, for a given applied current, the following normalization procedure was performed:

$$I_N^T = \frac{j_{\text{osc}}^T - j_{\text{osc},i}^T}{j_{\text{osc},f}^T - j_{\text{osc},i}^T} \quad (5.37)$$

where j_{osc}^T is the applied current density, and $j_{\text{osc},i}^T$ and $j_{\text{osc},f}^T$ are the initial and final current densities that define the oscillatory potential region (determined from galvanodynamic sweep experiments). Figure 5.32 shows such exemplary comparison of oscillations for $I_N^T = 0.33$.

The temperature coefficient q_{10} was defined as:

$$q_{10} = \left(\frac{p_{T_1}}{p_{T_2}} \right)^{10/(T_2 - T_1)} \quad (5.38)$$

where p means period of the oscillations at a given temperature. The overall activation energy of the oscillatory system was defined in terms of the oscillation frequency $f = 1/p$:

$$f = A \exp\left(\frac{-E_a}{RT}\right) \quad (5.39)$$

Table 5.1 shows the experimentally determined variations of the coefficient q_{10} with temperature.

In turn, under conditions of typical voltammetric conditions, when the electrode process is *nonoscillatory*, the trivial Arrhenius behavior was observed, i.e., high, positive apparent activation energies were determined from temperature

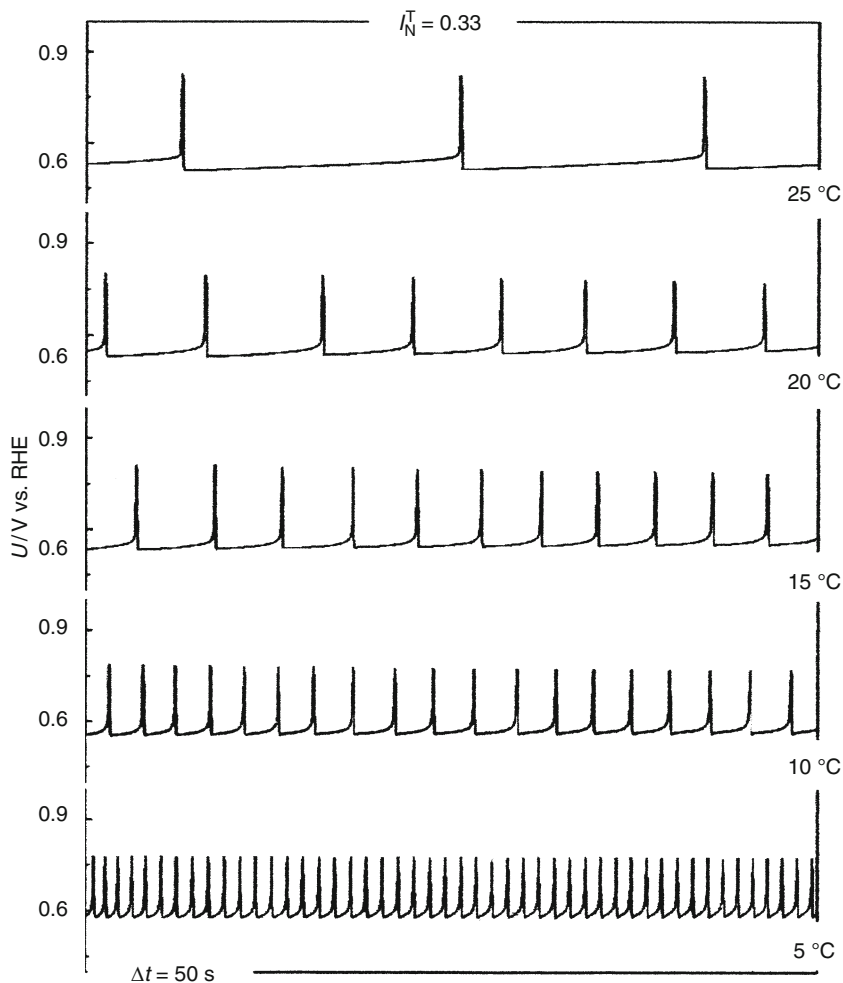


Fig. 5.32 Potential time series at different temperatures and $I_N^T = 0.33$. Electrolyte: aqueous solution with 0.60 M HCOOH and 0.10 M H₂SO₄. Reprinted with permission from [90]. Copyright 2008 American Chemical Society

Table 5.1 q_{10} values obtained for different temperature intervals and applied currents

ΔT (°C)	$I_N^T = 0.17$	$I_N^T = 0.33$	$I_N^T = 0.50$	$I_N^T = 0.67$	$I_N^T = 0.83$
20–25		0.13	0.25	0.43	0.76
15–20	0.22	0.53	0.13	0.18	0.78
10–15	0.26	0.34	0.41	0.35	1.16
5–10	0.16	0.18	0.40	0.50	0.92
5–25	0.22	0.25	0.24	0.33	0.96

Reprinted with permission from [90]. Copyright 2008 American Chemical Society

dependences of the reaction kinetics. Thus, temperature overcompensation (or at least compensation) was directly related only to oscillatory instabilities. This indicates that in the oscillatory regime there occurs a complicated interplay between reaction steps, leading to apparent negative (or zero) activation energy. Mechanistically, the effect of increase in the rate of every elementary step with temperature must there be compensated or even overcompensated by other effects of the opposite direction. For the formic acid oxidation process it has been suggested [90] that the temperature (over)compensation resulted from the interplay between the opposing effects of temperature on (1) the positive feedback loop, which includes the steps of $(H_x)O$ adsorption, (bi)sulfate adsorption, CO_{ad} oxidation by $(H_x)O_{ad}$ species, and formate adsorption and desorption/oxidation, and on (2) the negative feedback loop composed of the (nonfaradaic) step of formic acid dehydration to CO_{ad} . The above notation refers to the indirect pathway of $HCOOH$ oxidation, written in the form: $CO_{ad} + (H_x)O_{ad} \rightarrow CO_2 + xH^+ + xe + 2Pt$. Analysis of the oscillatory courses shows that the system spends most of its time in the active, low potential state and only a short time in the passive, high potential state. It was further found that changing the temperature affected only the transition from the active (low-potential) to the passive (high-potential) state, whereas the steeper passive to active transition remained nearly unaffected by temperature. This can be understood as a consequence of either a weak influence of temperature on the surface poisoning step (i.e., when CO_{ad} is formed from adsorbed $HCOOH$ molecules) or in terms of the buildup of the carbon monoxide layer in the oscillatory regime and within the studied temperature range: from 5 to 25°C.

For comparison, analogous studies of temperature coefficient of the oscillatory oxidation of methanol on polycrystalline platinum under similar conditions [91] exhibited only conventional, Arrhenius-type dynamics ($q_{10} \approx 2.3$), with the activation energy ranging between 50 and 70 kJ mol^{-1} .

5.4.7 *Oxidation of Formic Acid as an Analog of the Stimulus–Response of Neuronal Cells*

Although electrochemical models of neural transmissions are more often associated with the active/passive transitions of iron (or other metals) in acidic media, it appears that the galvanostatic oxidation of formic acid on the polycrystalline Pt electrode ($A = 2.4 \text{ cm}^2$) also may exhibit characteristics analogous to those of a nerve cell. To these characteristics there belong: a threshold for amplified excitation, a refractory period, and presumably for the first time reported directly for an electrochemical system—a dependence of the response on the slope of ramp stimulation [92]. The latter effect is important since in the real neuron, a rapid stimulation activates the ion-selective Na^+ channels faster than it does the K^+ channels, whereas a slow stimulation allows the inactivation of the Na^+ channels and the activation of the K^+ channels [92, 93]; these dependences are considered

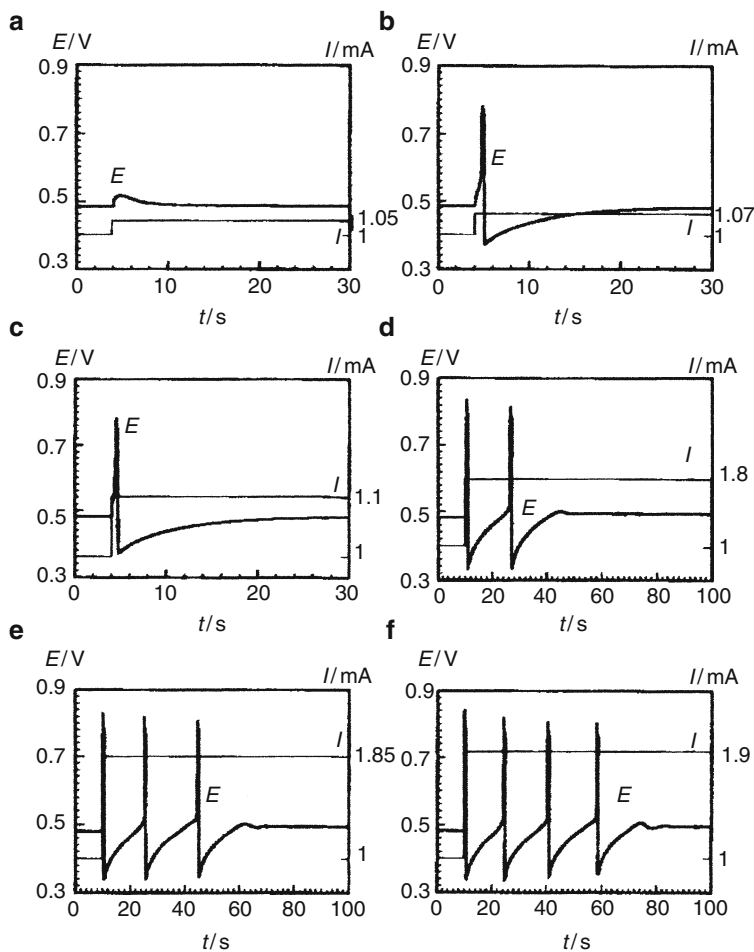


Fig. 5.33 Potential response to a quick current increase (100 mA/s). Reprinted from [92], Copyright 1995 with permission from Elsevier

important in the recognition of taste and smell, when e.g. the taste stimulus is rapidly applied (for other models of such sensors, see also Sect. 6.2 of volume II). Experiments were performed in a three-electrode configuration, for 1 M HClO_4 as a supporting electrolyte and concentration of formic acid as high as 1 M, while the temperature was enhanced to 43 °C. Figures 5.33–5.35 show the above-mentioned three characteristics, analogous to the response of a nerve cell. The threshold visualized in Fig. 5.33a, b manifests itself in this way that the large potential jump occurred only if the current, initially fixed at 1 mA, was increased for more than 0.05 mA.

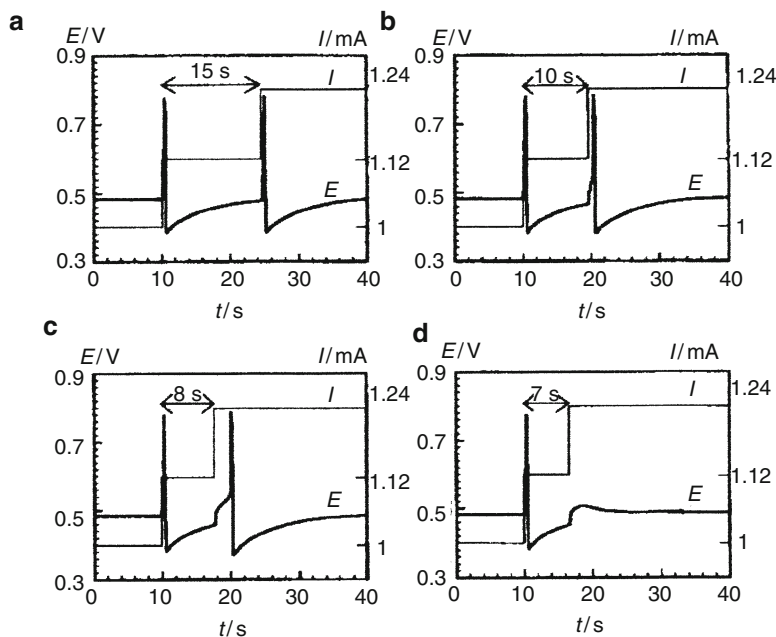


Fig. 5.34 Refractory behavior of the potential response. Reprinted from [92], Copyright 1995 with permission from Elsevier

If the current increment was even higher, the electrochemical system responded with a series of impulses (Fig. 5.33d–f) and this also can mean analogy with neural behavior; the authors indicated analogous effect in the course of numerical simulation of a single neuron's behavior [94].

In turn, the refractory period, meaning the time during which the system temporarily does not respond, or responds differently to the next stimulus, is illustrated in Fig. 5.34. Only if the interval between two subsequent current increments was sufficiently high (at least 15 s), the second potential response was as large as the first one, otherwise it could be almost completely damped.

Finally, Fig. 5.35a–f shows the effect of the rate of current increase covering the amplitude of 0.2 mA. With decreasing rate (r) the response in the form of a single pulse eventually decayed. However, even for the slowest current ramp, if the current was allowed to increase further than for 0.2 mA, a series of potential impulses were observed, but only as long as the current was increasing with time. The above effects were interpreted in terms of the potential-dependent activation and deactivation of the Pt electrode surface with adsorbed CO intermediate, in line with earlier mechanistic suggestions.

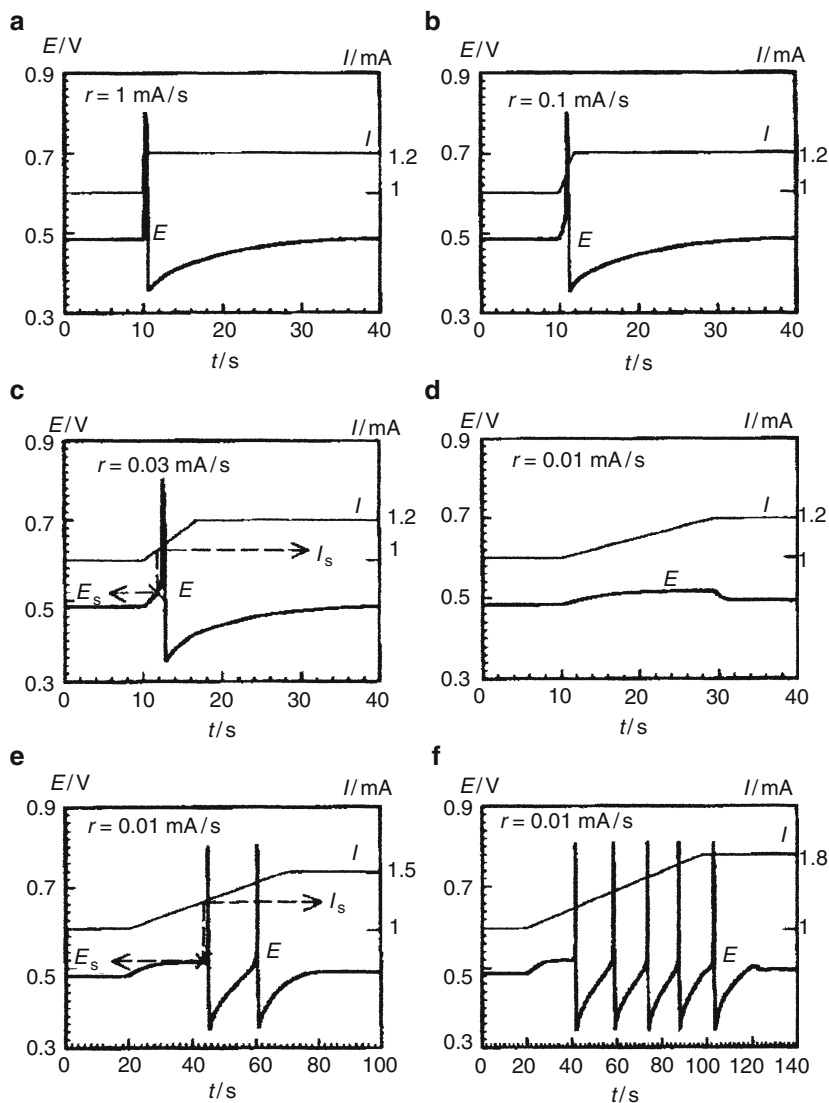


Fig. 5.35 Potential response related to the r (ramp) and the amount of the current increase. Reprinted from [92], Copyright 1995 with permission from Elsevier

5.5 Oscillatory Oxidation of Formaldehyde

Obviously the oxidation of formaldehyde to CO_2 and H_2O includes the elements of mechanism of oxidation of formic acid, discussed in detail in Sect. 5.4. Schell et al. [65, 66] have studied this process under galvanostatic conditions, at a rotating disk

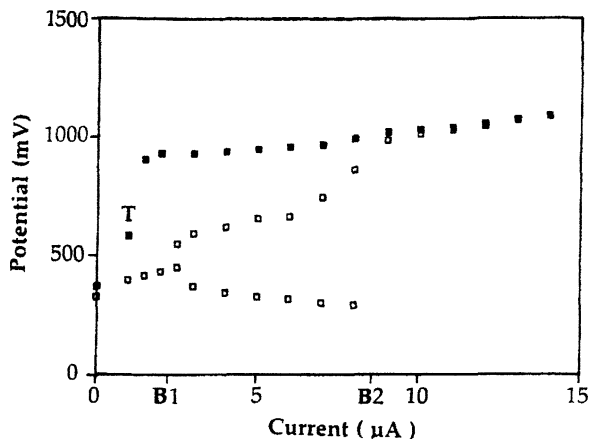


Fig. 5.36 The response of the potential (vs. SCE) plotted against the applied current. *Open squares (closed squares)* represent data collected when the applied current was changed in the forward (reverse) direction. Between B1 and B2 the system exhibited oscillations on the lower branch. The absolute minimal and maximal values of the potential are plotted for each oscillatory state. The point labeled with a T represents one case where the system had not relaxed. In separate experiments, it was found that a long relaxation, following the perturbation of the system in the vicinity of the low current end of the upper branch, was a common event. Typically, after the current was decreased, the system would immediately exhibit a rapid decrease in potential. However, the rate of change in the potential would slow and eventually the potential would begin to increase, and the system would finally return to a state on the upper branch. The working electrode disk used in the experiment was 5.0 mm diameter in platinum. Reprinted with permission from [65]. Copyright 1990 American Chemical Society

Pt electrode. The reported phenomena included simple oscillations which exhibited period-doubling bifurcation, small- and large-amplitude oscillations (MMO) and chaos, as well as bistability (Fig. 5.36).

Chaos in the oxidation of formaldehyde (and also of methanol and of methanol–formaldehyde mixtures), at Pt electrode under galvanostatic conditions, at temperature enhanced to 43 °C was also extensively analyzed by Okamoto et al. in a series of works [95–97]. The rich set of reported chaotic (and periodic) courses, caused by the cascade of period-doubling bifurcations, as well as intermittencies of type I and III, were found and analyzed in terms of return maps and calculations of the Lyapunov exponents. Intermittency, a term and its classification into types, introduced in a classical work by Pomeau and Manneville (cf. Chap. 1) [98, 99] means generally a way of generation of chaos through apparently random irregularities appearing in the periodic behavior. The phenomenon is typical of the systems in which the transition from periodic to chaotic behavior takes place by the saddle–node bifurcation of cycles (see e.g., p. 364 in [100], for an elegant illustration of this inherently deterministic phenomenon).

Also noteworthy, the oscillation patterns were time dependent, presumably due to the variation of the electrode state as a function of time. The regions of chaotic and periodic behavior are shown in Fig. 5.37.

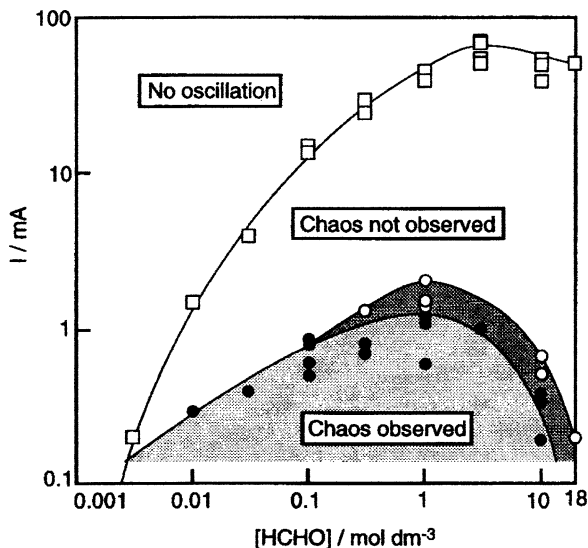
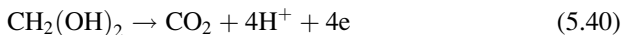
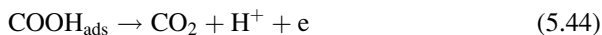
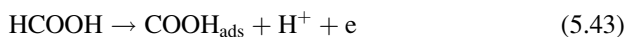
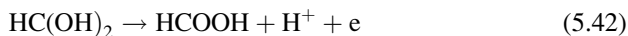
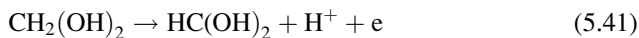


Fig. 5.37 Chaos-yielding region in the plane of formaldehyde concentration and current at 43 °C. *Open and closed circles* are, respectively, the maximal currents for the occurrence of chaos in the ascending-order sequence and in the descending-order sequence. *Open squares* are the maximal currents for the occurrence of periodic oscillations. The *dark and light gray zones*, respectively, stand for regions of chaos in the ascending-order sequence and in the descending-order sequence. [HCHO] stands for a formaldehyde concentration. Reprinted with permission from [96]. Copyright 1998 American Chemical Society

The electrochemical mechanism of oxidation of formaldehyde under studied conditions (aqueous acidic medium) takes into account its almost complete existence in the hydrated form—the methylene glycol $\text{CH}_2(\text{OH})_2$. The following mechanism was suggested to explain the oscillations in the oxidation of formaldehyde at polycrystalline Pt electrodes. It is postulated that the overall oxidation process of methylene glycol:



occurs via (at least) two paths: direct and indirect one. The direct path presumably involves short-lived intermediates that, according to one of the concepts, are involved in the following reaction sequence [101, 102]:

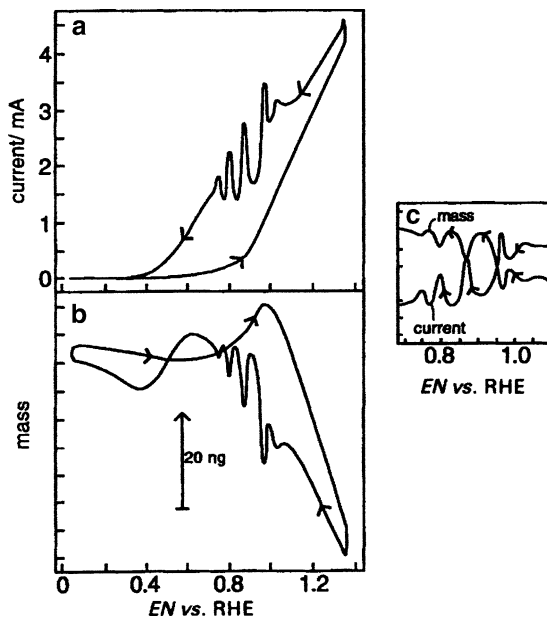


The second path involves the intermediate formation of the poisoning species which inhibits the electrode process; at the times of these studies there were several candidates for this species, but based on recent findings one can postulate that this is CO_{ads} , which, at sufficiently high potentials, when the water molecules are oxidized to OH_{ads} and H^+ , is removed from the electrode surface through the oxidative recombination with OH_{ads} [Eq. (5.16)]. Since this part of the mechanism is essentially the same as for the oxidation of CO or formic acid, discussed in previous sections (only the detailed nature of oxygen species on Pt may be different, e.g., PtO could be assumed), we shall not develop this point again in detail here. We shall only shortly say that in terms of the above mechanism the oscillations of Pt electrode potential under galvanostatic conditions were interpreted as the following sequence of processes: due to increasing electrode coverage of Pt surface with CO poison, the electrode potential moves to so high positive values, that eventually the PtOH (or PtO) species appear, which depassivate the electrode surface via reaction (5.16). The electrode potential returns then to less positive values and the oscillatory cycle repeats. In view of mechanism elaborated more recently for the HCOOH oxidation, one can consider the above explanation as introductory and requiring more quantitative characteristics of the system's dynamics, like the one be presented in Sect. 5.4.

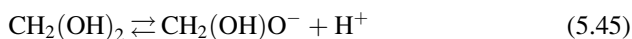
In more recent studies of the formaldehyde oxidation, performed at polycrystalline Pt and Rh electrodes, both in acidic and alkaline media, Koper et al. [103] have combined cyclic voltammetry with impedance spectroscopy and EQCM. For all these combinations both the galvanostatic and potentiostatic (in the presence of sufficient ohmic drops) oscillations were found, except in alkaline solution on Pt, where only potentiostatic oscillations were found. From practical point of view, the system: HCHO, NaOH, NaClO_4 /Rh disk electrode was found particularly suitable for experimental studies due to high reproducibility and stability of reported dynamical behaviors. As expected, the onset of the oscillations under galvanostatic conditions, with the amplitude of the potential covering the positive slope of the I - E dependence, suggested the existence of the hidden negative resistance and this was confirmed by impedance measurements (see Fig. 3.16) [77, 103, 104]. In turn, potentiostatic oscillations of the current exhibited various bifurcation scenarios: for the relatively low serial resistances both the birth and the death of the oscillations occurred through the supercritical Hopf bifurcation, while for the relatively high resistance the oscillations ceased at more anodic limit of the potential abruptly, and the current dropped to a low value corresponding to a passivated electrode state. From the point of view of nonlinear dynamics such the situation is described in terms of the homoclinic bifurcation, when the limit cycle collides with the saddle point in the phase space (Sect. 1.4.3).

In turn, monitoring of mass changes during the oscillations, using EQCM method, has demonstrated the important role of oxide layer formation in the oscillations. The correlation of the oscillatory changes of the current and the mass changes of the platinized platinum electrode, obtained for HCHO in acidic (HClO_4) solution, is shown in Fig. 5.38.

Fig. 5.38 (a) Cyclic voltammogram and (b) EQCM mass response obtained for the oxidation of 1 M HCHO in 0.1 M HClO₄ solution at a platinized platinum electrode, 50 mV s⁻¹; (c) oscillatory parts of (a) and (b). Reproduced from [103] by permission of The Royal Society of Chemistry



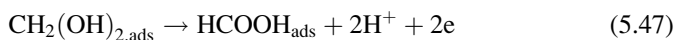
These results, compared also with other studies of the oxidation of HCHO at Pt electrodes, involving both voltammetry and IR spectroelectrochemistry [105, 106] have suggested that the formaldehyde oxidation was a more complex process than supposed earlier and should be supplemented with more mechanistic details. In an alkaline medium, in which the catalytic effect of hydroxide on the formaldehyde oxidation was proved, the product of its hydration, methylene glycol is expected to be ionized:



with $\text{p}K_{\text{a}}$ of this reaction equal to ca. 12.75. Furthermore, the nonhydrated, original form of formaldehyde, at the electrode potentials preceding the onset of its oxidation, appeared to be involved in the surface chemical decomposition, leading to the formation of adsorbed CO_{ads} :



Also the adsorption of methylene glycol and of a carboxylic acid was detected, suggesting thus the reaction pathway of the following scheme:

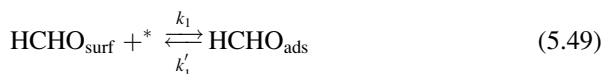


Irrespective of these (and probably also further, still unknown) mechanistic details the following main points remained unchanged: the negative differential

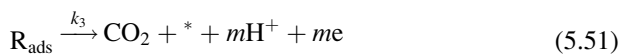
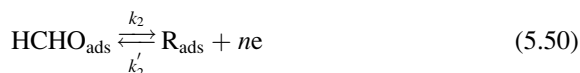
resistance is due to the, rising with the positive electrode potential, fast process of covering the electrode surface with the passivating layer of OH_{ads} . Under dc conditions, this negative resistance is hidden within a broad potential range due to an additional, relatively slow process of poisoning the electrode with CO being a traditional candidate for that effect, but in view of more recent findings, also other surface-active species (like methylene glycol or glycolate) can be involved in that process. The reaction of formation of adsorbed OH species (5.15) is treated now as an introductory step of the electrode surface oxidation, as the significant mass increase, observed in EQCM experiments, could be explained rather in terms of more advanced process: insertion of O and OH in the Pt lattice. Of course, adsorbed CO and OH remove each other in the important step (5.16). Regarding this step, one can add that in view of above-mentioned studies of Okamoto et al. [95, 96], not only OH_{ads} but also $\text{H}_2\text{O}_{\text{ads}}$ can be an important reactant for the interaction with CO, since the oscillations were found already at such small anodic potentials, at which OH_{ads} is probably not yet formed.

In a recent theoretical study, Karantonis et al. [107] have built up the model of HCHO oxidation, essentially based on the above dual-path mechanism of oscillations, but containing additional steps, in order to produce also the bistable behavior. This is thus the “extended dual-path mechanism.” Its “oscillatory part” consists of the following steps:

1. Transport of HCHO from the solution bulk and adsorption on Pt surface:

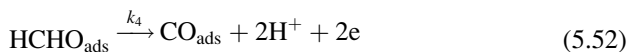


2. Direct oxidation path:



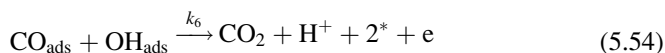
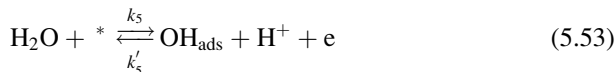
(this step and R species were ignored due to the high reaction rate)

3. Indirect oxidation path:



with CO assumed to bound linearly to the surface and act as a poison.

4. The oxidative removal of CO_{ads} , involving steps identical with Eqs. (5.15) and (5.16):



Additional, above-mentioned steps introducing bistability are the following:

5. Desorption of CO_{ads} (under assumption: $k_7 \gg k'_7 \approx 0$):



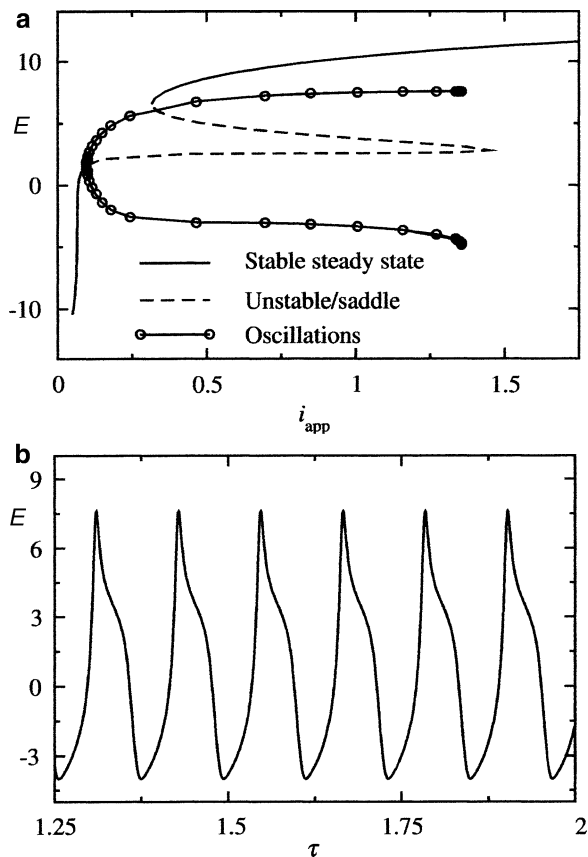
6. Irreversible formation of higher valent oxides of Pt (abbreviated as O):



Further assumption included the following points: (1) the concentration profile of HCHO is linear within the Nernst diffusion layer of a constant thickness δ ; (2) the double layer capacitance C_d is constant; (3) the electron transfer processes follow the Butler–Volmer kinetics; and (4) the adsorption–desorption processes follow the Frumkin equations. The latter assumption means introducing the coefficient of lateral interactions in the adsorbed layer. This also means that the shape of the adsorption isotherms will be a source of bistability. The bifurcation diagrams were constructed as the dependences of electrode potential E , electrode coverages of CO, OH, HCHO, and surface concentration of HCHO in the solution, on the applied current i_{app} . As an example, Fig. 5.39 shows the bifurcation diagram in the E – i_{app} coordinates which reveals the occurrence of the supercritical Hopf and saddle–node bifurcations.

In search of further details of the mechanism of formaldehyde oxidation, recently the modern spectroscopic methods were combined with electrochemical techniques. Karantonis, Nakabayashi et al. [108] have studied the oscillatory formaldehyde oxidation on Pt(111) electrodes, under potentiostatic and galvanostatic conditions, using also the optical second harmonic generation (SHG) method. The choice of SHG technique was justified by its sensitivity to the adsorption of CO, known from the studies at the polycrystalline Pt electrode. The present use of a single crystal Pt(111) gave a chance to deepen those studies for the elucidation of the variation of the surface structure during the oscillations. Under potentiostatic conditions, two surface phase transitions were observed: order–disorder and order–order (similarly as for the transitions observed at Pt (111) for CO-saturated electrolyte [109]). Under galvanostatic conditions, oscillations of the SHG field were concordant with the oscillations of the electrode potential, but only the order–disorder transition was reported in SHG spectra, occurring during the spontaneous transition from low to high potentials.

Fig. 5.39 (a) Bifurcation diagram of the electrode potential E versus the applied current i_{app} . (b) Electrode potential E temporal evolution for $i_{app} = 1.27$. Reprinted from [107], Copyright 2006, with permission from Elsevier



Nevertheless, even if not all surface transitions were detected, these studies are evidently a pioneer work in evidencing the occurrence of structural transitions under both potentiostatic and galvanostatic conditions of the oscillatory oxidation of formaldehyde.

More recently, another application of combined electrochemical and spectroscopic methods to this process was published by Samjeské, Osawa et al. [110] for the studies of the oxidation of formaldehyde on Pt (under both galvanostatic and potential sweep conditions) who employed *Time-Resolved Surface-Enhanced Infrared Spectroscopy* (SEIRAS). Based on their investigations the dual reaction path was established: the direct path via adsorbed formate, and the indirect path via CO_{ads} . (cf. analogous suggestion for the oxidation of formic acid). Both pathways are kinetically coupled through the reaction involving formic acid, as indicated in the scheme later (Fig. 5.40).

In terms of this proposal, an alternative mechanism of the formation of the NDR region is suggested as being due to the kinetic coupling of the direct and indirect paths [110]. The mechanism of the potential oscillations can be briefly presented in the following way: at the beginning, the electrode surface is almost fully covered by

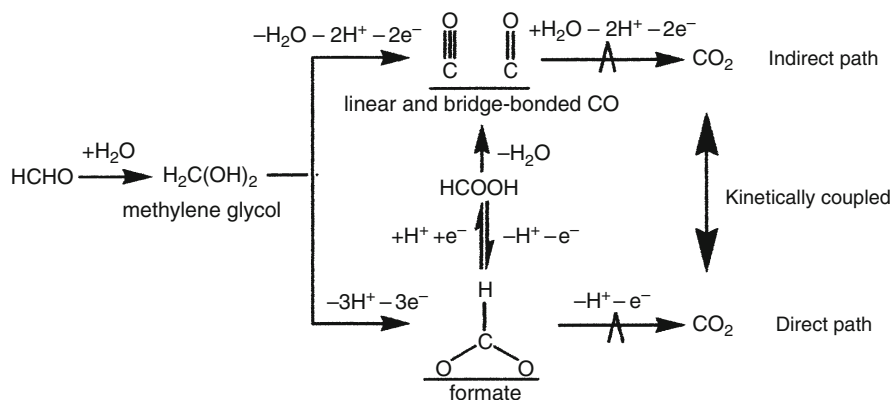


Fig. 5.40 Proposed reaction scheme for formaldehyde oxidation of Pt in acid. The direct path via adsorbed formate and indirect path via adsorbed CO are kinetically coupled (see [110] for details). Reprinted with permission from [110]. Copyright 2007 American Chemical Society

CO and the formaldehyde oxidation is practically entirely suppressed. Under galvanostatic conditions, the increase in the electrode potential takes place. Initially, when the potential is not yet positive enough, the CO oxidation is slow, so the contribution from the direct pathway, involving formate, on such passivated electrode, is still small. The two-electron formation of CO from $\text{CH}_2(\text{OH})_2$ would allow the electrode to discharge itself but since CO adsorbs and passivates the surface, the current decreases and the electrode potential effectively moves toward positive values. Upon increasing potential, CO starts to oxidize and in this way the direct path becomes unblocked. It can occur, however, on so small number of sites that the electrode potential rises even further, up to the values at which the rate of the direct path satisfies the imposed current. Then the potential decreases and the oscillatory cycle is closed. This basic explanation accounts for simple, sinusoidal oscillations, observed for relatively low imposed current densities, while more quantitative analysis of this mechanism is necessary in order to understand the relaxation oscillations observed for high current densities [110]. One should note that OH_{ads} is not explicitly shown in the reaction scheme; in fact, it can be another intermediate exhibiting fast adsorption, but slow further oxidation in the considered potential range. The reader interested in details of this recent model is advised to consult the original reference [110].

In very recent studies of the formaldehyde oxidation, Seidel, Krischer et al. [111] have applied the nanostructured Pt/glassy carbon model electrode. In other words, the electrode consisted of catalytically active Pt nanodisks supported onto a planar glassy carbon substrate (Fig. 5.41).

Systematic measurements were performed on structurally well-defined model electrodes of different Pt surface coverages, under different applied current densities. The conditions of the constant electrolyte transport were established through the application of the thin-layer flow cell connected to a differential

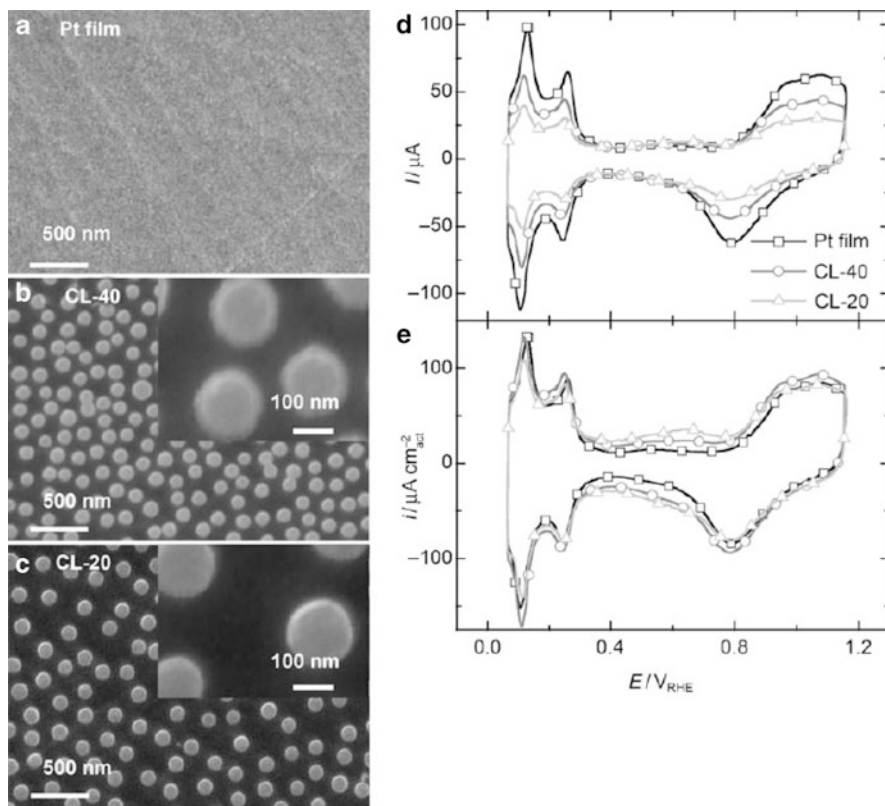


Fig. 5.41 SEM images of the nanostructured model catalysts: (a) Pristine Pt film, (b) high-density ($\sim 40\%$ coverage) nanostructures Pt/GC electrode prepared by colloidal lithography; CL-40; (c) medium-density ($\sim 20\%$ coverage) nanostructured Pt/GC electrode prepared by colloidal lithography; CL-20; (d) base cyclic voltammograms (scan rate 100 mV s^{-1}) of Pt film (*black squares*), CL-40 (*gray circles*) and CL-20 (*light gray triangles*) in $0.5 \text{ M H}_2\text{SO}_4$ base electrolyte; (e) base cyclic voltammograms normalized vs. the corresponding active surface area. Reprinted with permission from [111]

electrochemical mass spectrometry (for monitoring of CO_2 formation). Using such experimental setup it was possible to show the important role of transport processes, since the oscillation frequency of the electrode potential and the rate of CO_2 formation were lower for such nanostructured Pt/GC electrode, compared to continuous Pt film (at similar current density). In fact, over a discontinued Pt surface, the probability for formic acid intermediate to readsorb and to be further oxidized to CO_2 should be lower than for continuous surface. The considered reaction mechanism is shown in Fig. 5.42.

These studies have indicated also that all individual Pt disks, i.e., individual Pt oscillators oscillated in synchrony. In other words, in spite of its nanostructured nature, the whole electrode can be considered a single oscillator. In the interpretation of this synchronization a reasonable assumption was done that all the

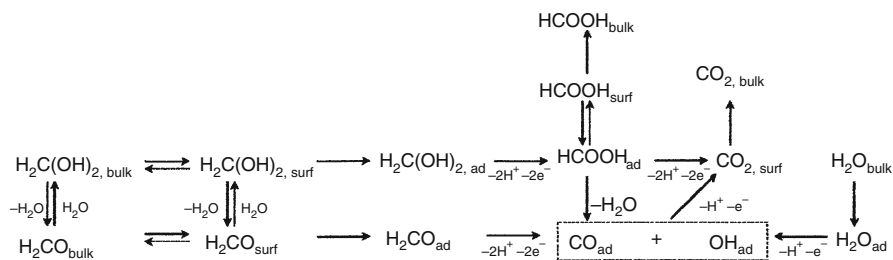


Fig. 5.42 Simplified reaction scheme for formaldehyde oxidation to formic acid (incomplete oxidation product) and CO_2 (final product). The *upper* and the *lower* sequences direct and indirect pathways, respectively [111]

oscillators face the same (bulk) concentration of formaldehyde, while the concentration of the formic acid at the electrode surface (and not present in the bulk) oscillates. It is considered that the coupling between different “nanooscillators” is not of transport (diffusional), but of electrical nature, which can include, e.g., migration effects. Note that coupled oscillators are described in Chap. 3 of volume II.

5.6 Instabilities in the Anodic Oxidation of Alcohols

In this section, we shall briefly describe dynamic instabilities associated with the oxidation of methanol, ethanol, 1-propanol, 2-propanol, and 1-butanol. One should note that in these processes, besides the oscillations and bistability, a rarely experimentally observed phenomenon of *tristability* was reported.

5.6.1 Oscillations in Alcohols Oxidation

5.6.1.1 Methanol

Galvanostatic Conditions

Early studies of oscillatory electrooxidation of methanol at Pt electrodes were rather rare [112, 113] and only in the second half of 1990s this subject attracted again the interest of researches [114], most probably due to the significance of methanol (and formic acid) for the application in the fuel cells. In more recent *galvanostatic* studies, Okamoto et al. [95] have reported, at temperature enhanced to 43°C , the chaotic temporal course of the electrode potential, being a result of a cascade of period-doubling bifurcations (Fig. 5.43).

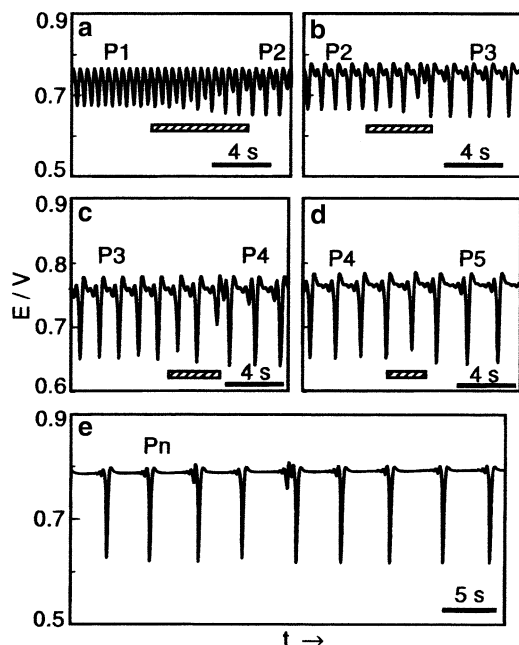


Fig. 5.43 Periodic and chaotic oscillation patterns in the oxidation of 1 mol dm⁻³ of methanol alone at 5 mA. The *hatched line* shows a duration of pattern change: (a) a pattern shift from the period-1 to the period-2 oscillation; (b) a pattern shift from the period-2 to the period-3 oscillation; (c) a pattern shift from the period-3 to the period-4 oscillation; (d) a pattern shift from the period-4 to the period-5 oscillation; and (e) a disordered periodic pattern observed after (d) Reprinted with permission from [95]. Copyright 1997 American Chemical Society

According to the general theory of oscillations under galvanostatic conditions, one should expect that the methanol oxidation belongs to the class IV, i.e., to the oscillators exhibiting hidden negative resistance (HN-NDR type oscillator). The existence of this kind of NDR region was confirmed by the impedance measurements made by Lee et al. only in 2001 [115]. An experimental system involved optimized, concentric arrangement of electrodes and the solution consisted of 0.03 M CH₃OH in 0.1 M HClO₄. Figure 5.44 shows the impedance spectra typical of HN-NDR oscillators—the maximum negative real impedance was detected for $E = +65$ mV, when the (nonzero) ac frequency was close to 1 Hz, being thus the inherent frequency of the oscillatory system in the state close to the Hopf bifurcation point (well concordant with direct observation of potential oscillations under galvanostatic conditions).

The electrochemical mechanism underlying such impedance characteristics should be concordant with earlier, well-established findings [116] that the anodic oxidation of CH₃OH proceeds via gradual, four-step electrochemical dehydrogenation, leading to adsorbed CO that poisons the electrode surface, but is removed at more anodic potentials through the reaction with adsorbed OH radicals, formed as

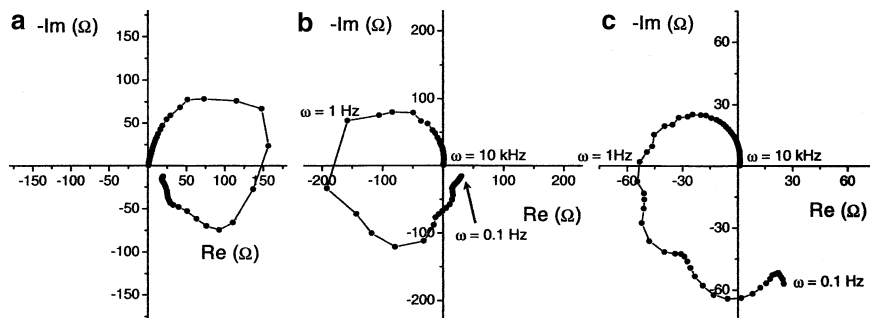
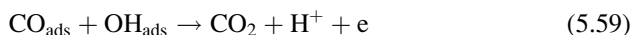


Fig. 5.44 Electrochemical impedance behavior of methanol oxidation at a Pt electrode measured at three outer potentials of: (a) +45; (b) +65; and (c) +85 mV. Reprinted from [115], Copyright 2002, with permission from Elsevier

the product of the oxidation of H_2O molecules. In the simplified notation, involving summarizing of all dehydrogenation steps into one process, the following essential reaction sequence holds [note similarities with the mechanism of formate oxidation: Eqs. (5.26) and (5.15) or (5.16)]:



According to Eq. (5.57), by imposing an appropriate anodic current one initiates the dehydrogenation reactions, as a result of which the electrode surface becomes covered with various adsorbed intermediates: $\text{CH}_2\text{OH}_{\text{ads}}$, CHOH_{ads} , COH_{ads} , and CO_{ads} . If these dehydrogenation reactions are relatively slow, only few vacant Pt sites remain and thus further dehydrogenation or oxidation of CH_3OH residues is slowed down further [115]. Under galvanostatic conditions, in order to satisfy the imposed current, the electrode potential moves to more positive values, at which step (5.58) can set in with the formation of adsorbed OH radicals. However, since this reaction also requires free Pt sites, the electrode potential increases until so many OH_{ads} are produced that the autocatalytic interaction of CO_{ads} and OH_{ads} (5.59) become efficient enough to cause the increase in the number of free sites. This effect enhances the rate of oxidation reactions, and, accordingly, the imposed current can be satisfied at lower electrode potentials. At sufficiently low potentials the OH radicals stop to form and the poisoning of the electrode surface with CO (and other intermediates) returns, closing the oscillatory cycle. More details of this mechanism and its quantitative treatment will be given below, when discussing the multistability in the methanol oxidation.

Potentiostatic Conditions

The oscillations of the current during methanol oxidation under *potentiostatic* conditions were so far only rarely studied. Hachkar et al. [117] observed such dynamics in the studies of methanol oxidation, performed at a rough ($f = 100$) rhodium electrode, in an alkaline medium and temperature enhanced to 55°C. In turn, Vielstich et al. [118] have observed such oscillations at a platinum-based gas-diffusion electrodes, polarized to relatively high potentials (>1.0 V vs. RHE); the instabilities were associated with the characteristics of a nonelectrochemical step of diffusion occurring inside the electrode pores. These two systems had thus a rather complex microscopic characteristics. One can pose a question, whether it is possible to find such oscillations in the simpler system. Let us remember that according to the theory of HN-NDR oscillators, the system which oscillates under galvanostatic conditions should exhibit the oscillations also under potentiostatic conditions ($U = \text{const}$), provided that the appropriately large serial resistance, causing ohmic potential drops, is inserted into the electric circuit of the working electrode (cf. Chap. 3). A very recent study of the oscillations in the methanol oxidation, occurring under such conditions on Pt electrode, in aqueous H_2SO_4 solution, was described by Varela et al. [119]. Figure 5.45 shows the representative oscillatory courses of the current, recorded for fixed serial resistance $R_s = 1.75$ k Ω and various externally applied voltages. The oscillations are born, starting from the small amplitude ones, through the supercritical Hopf bifurcation and their amplitude rises with increasing voltage. Simultaneously, their harmonic shape turns into more relaxation one, single peaks split into large- and small-amplitude ones, and eventually the regular MMO become aperiodic.

The corresponding bifurcation diagram is shown in Fig. 5.46.

From the mechanistic point of view, this work emphasizes also the striking difference between the oscillatory behavior of methanol electrooxidation, compared to other C1 molecules: the significantly smaller oscillation amplitude and generally the simpler dynamics for methanol. Usually, this simplicity of methanol reaction was explained in terms of its postulated relatively simple mechanism, involving practically only one, indirect pathway (involving CO_{ads}), with the direct oxidation pathway considered negligible. Then the complexity in dynamical behavior during the oxidation of other C1 compound was understood as caused by several parallel reaction pathways. The idea of predominating indirect path in CH_3OH oxidation was invoked, e.g., by Schell in his model mechanism of multistability in this process (see below). However, more recent studies of the mechanism of the methanol oxidation on Pt in HClO_4 and H_2SO_4 media (cf. e.g., [120, 121]) indicate the existence of even three parallel routes, differing with the nature of the intermediate: CO_{ads} , HCHO , and HCOOH . The products of methanol oxidation include not only CO_2 since the intermediates HCHO and HCOOH can diffuse away from the electrode. In turn, formaldehyde forms probably in a pathway involving adsorbed methoxide (CH_3O) as the intermediate. The relative efficiency of these routes is strongly dependent on the composition of a supporting electrolyte: in H_2SO_4 medium the oxidation current is significantly lower than in HClO_4 due to adsorption

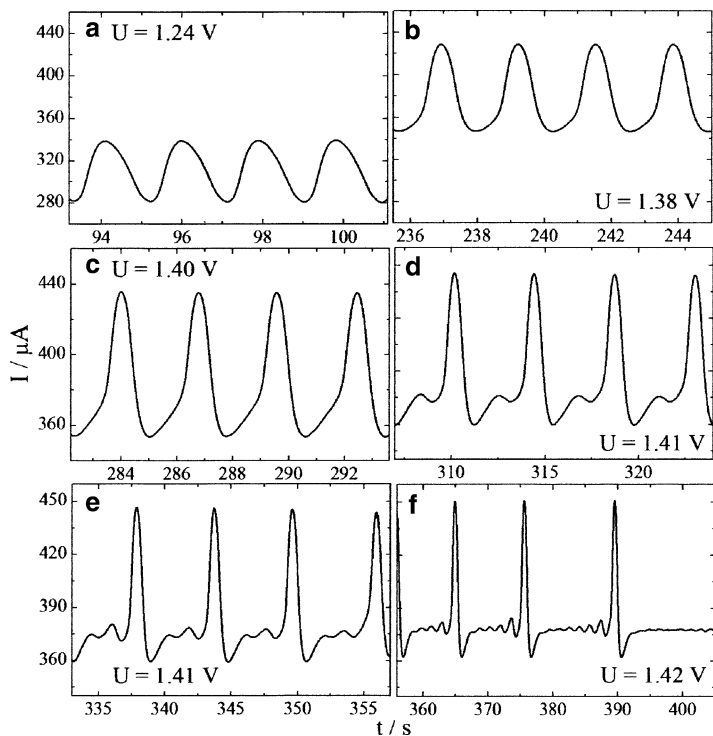


Fig. 5.45 Current time series under potentiostatic control with $R_s = 1.75 \text{ k}\Omega$. Electrolyte: $[\text{CH}_3\text{OH}] = 0.99 \text{ mol dm}^{-3}$ and $[\text{H}_2\text{SO}_4] = 0.48 \text{ mol dm}^{-3}$. Reprinted with permission from [119]. Copyright Sociedade Brasileira de Química 2008

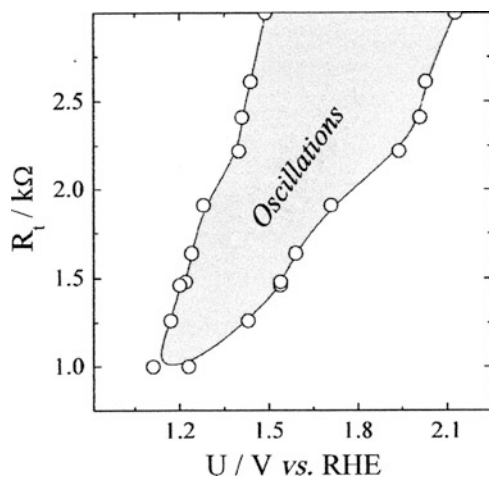


Fig. 5.46 Bifurcation diagram in the R_s vs. U plane, electrolyte: $[\text{CH}_3\text{OH}] = 0.68 \text{ mol dm}^{-3}$ and $[\text{H}_2\text{SO}_4] = 0.49 \text{ mol dm}^{-3}$. Reprinted with permission from [119]. Copyright Sociedade Brasileira de Química 2008

of sulfate ions which compete with CO_{ads} engaged in the reaction pathway requiring several neighboring Pt sites. It is thus understandable that in view of this complexity of the methanol oxidation process, Varela et al. [119] complemented electrochemical measurements of the oscillations with in situ Fourier Transform Infrared (FTIR) spectroscopy, in order to trace simultaneously the (eventual) temporal changes of adsorbed intermediates. The maximum coverage of CO which could be attained under given experimental condition was equal to 0.85 monolayer (ML) which means that the entire CO population consisted of linearly adsorbed CO, forming ca. 0.70 ML and bridge coordinated CO, occupying ca. 0.15 ML (i.e., 0.30 reaction sites, since every CO molecule requires then two adsorption sites). The most striking results of those studies are the following: (1) during the induction period preceding the oscillations the distinct increase in CO coverage is observed and (2) during the galvanostatic oscillations the electrode coverage with CO only slightly and monotonously increases, remaining close to $\theta_{\text{CO}} \approx 0.7$ ML. The latter value is rather high, so only a *small part* of the electrode, uncovered with CO, has its population changing during the oscillation. This can be considered an explanation for the small amplitude and simple oscillatory dynamics of methanol oxidation under given conditions. Analogous comparative measurements were made for the oscillatory oxidation of formaldehyde and revealed a remarkably smaller mean CO coverage (ca. 0.25–0.30 ML), similar to values found for the same system by Osawa et al. [83, 84] who employed *Surface Enhanced Infrared Absorption Spectroscopy (SEIRAS)* (cf. Sect. 5.4). This difference of CO coverage for methanol and formaldehyde is of kinetic origin, i.e., is caused by the differences in the rate constants of the reaction steps involved in the oscillatory cycle of these organic molecules [119].

5.6.1.2 Oscillations in Oxidation of Other Alcohols

We shall briefly summarize oscillatory oxidation of other alcohols. For ethanol, Novak and Visy [122] have reported the galvanostatic oscillation that included one signal of period ca. 5 s and a peak potential of ca. 700 mV (RHE), i.e., a bit less than the value corresponding to significant coverage of Pt with OH radicals, in acidic solution. Higher potential values, even beyond the onset of the production of the Pt oxide layer, were mentioned by Rao and Roy [123]. More recently, oscillations in the galvanostatic oxidation of ethanol were studied by Chen and Schell [124] who focused their research on the correlation between their characteristics and the length of time the system was allowed to relax and made relevant mechanistic suggestions.

In turn, Inzelt et al. [125] have studied the oscillations in the galvanostatic electrooxidation of 2-propanol at the platinumized Pt electrode with a roughness factor of ca. 400, employing the EQCM technique. This experimental approach allowed to formulate the first experimental evidence that the oscillations arising in the course of this process are associated with the (usually postulated in mechanistic considerations) accumulation and consumption of the chemisorbed species. One should realize that following of the mass changes of the electrode using EQCM was

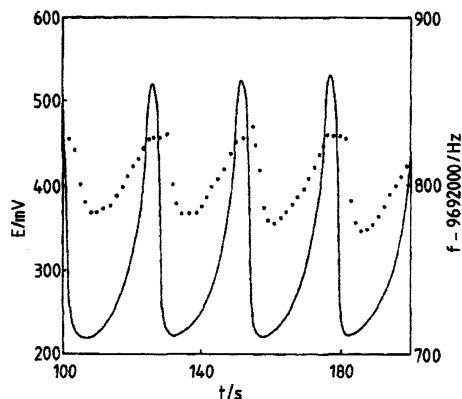


Fig. 5.47 A part of the oscillation pattern for the galvanostatic oxidation of 2-propanol in $1 \text{ mol dm}^{-3} \text{ HClO}_4$ at platinized platinum electrode: potential vs. SCE (*continuous line*), frequency (*dots*). Current density is $7 \times 10^{-4} \text{ A cm}^{-2}$, and concentration of 2-propanol is 1 mol dm^{-3} . Reprinted with permission from [125]. Copyright 1993 American Chemical Society

difficult: the minimum ac frequency ensuring accurate measurements was 1 Hz, and this frequency could be measured only once every second, so the period of electrochemical oscillations should be appropriately long. This was achieved by adjusting the current density, concentration of 2-propanol in the solution, and enhancing the roughness of the electrode surface area by its above-mentioned platinization. The choice of 2-propanol (instead of, e.g., more intensively studied formic acid) was supported by the fact that it oxidizes into acetone, and not to any gaseous product which could make the frequency response of EQCM noisy. A representative comparison of the oscillatory variations of the electrode potential and EQCM frequency response is shown in Fig. 5.47.

From this comparison it follows that the rapid decrease in the electrode potential is accompanied by a fast decrease in frequency, meaning the increase in mass on the surface. In turn, the increase in the potential is matched by the corresponding increase in frequency (decrease in mass). Also, the dynamics of the system is not a steady state: one observes gradual increase of the oscillation amplitude, mass changes amplitude, and the period of the oscillations. Finally, the oscillations cease at high positive potential, presumably due to, parallel to the oxidation of chemisorbed organic species, formation of oxygen species (PtO, PtOH) on the electrode surface. At more positive potentials (ca. 0.9 V vs. SCE), the rapid frequency decrease was observed and explained as due to the formation of PtO phase on the electrode surface. The authors give the following explanations for the reported dependences, which emphasizes the role of chemisorbed species [125]. At least three processes that simultaneously occur at the electrode surface are considered: chemisorption, oxidation of the chemisorbed species, and oxidation of 2-propanol on the free sites (not occupied by chemisorbed species). The chemisorption involves dehydrogenation which causes a decrease in electrode potential,

the rupture of bonds, possibly the splitting of molecule of 2-propanol, and considerable charge transfer. This means the oxidation process leading to the respective chemisorbed product of high degree of oxidation. The oxidation of the products of chemisorption starts only above ca. 400 mV and the chemisorbed species can be completely removed by oxidation in the potential interval 800–1,000 mV. Then the number of free sites increases and, accordingly, the rate of oxidation of 2-propanol to acetone as a final product increases.

Also for 1-butanol oscillations of the electrode potential under galvanostatic conditions were reported by Chen and Schell [126].

5.6.2 Multistability and Excitability in Alcohols Oxidation

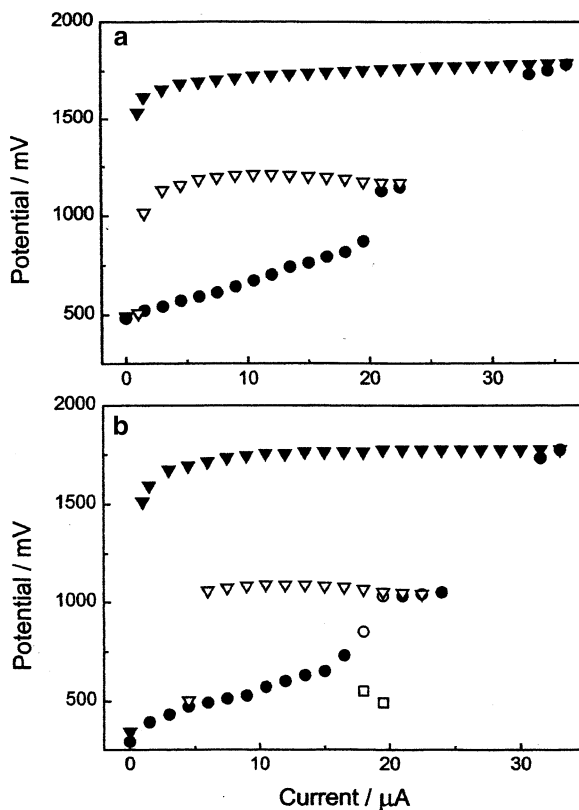
5.6.2.1 Experimental Results

Besides oscillations, electrochemical oxidation of low molar mass alcohols, as methanol, ethanol, 1-propanol, and 1-butanol, can exhibit also excitability, bistability, and tristability under appropriate conditions, as discovered and described by Schell et al. in a series of papers [124, 126–128]. One should emphasize that tristability is a rarely observed phenomenon in real systems—another electrochemical system (and probably the only other one) of such behavior was described in Sect. 4.5. Also for homogeneous systems only a few examples of tristability were reported [129–131]. This phenomenon is interesting not only because of its rare occurrence, but also because it may have substantial practical significance for the work of, e.g., fuel cells: the coexistence of different state can cause a sudden large increase in the electrode potential in the methanol half-cell (anode), causing then the large drop of the fuel cell potential.

For the sake of systematization of the nonoscillatory dynamical instabilities in the electrooxidation of alcohols, one should summarize that under galvanostatic conditions, Schell et al. have reported bistable and tristable behavior in the case of methanol, ethanol, and 1-butanol, while excitability in the case of ethanol and 1-butanol. It was also shown that the occurrence of these behaviors depended on pH, controlled by addition of either HClO₄ or NaOH. Bistable and tristable characteristics in the methanol oxidation at a stationary Pt electrode [127] are shown in Fig. 5.48a [124]. Noteworthy, the tristable behavior was reported only for the intermediate (0.5 M) concentration of HClO₄, while in alkaline (NaOH) medium tristability generally vanished and only bistable behavior persisted. Quite analogous role of HClO₄ and NaOH was found for tristability and bistability occurring in galvanostatic ethanol oxidation [128] (Fig. 5.48b).

Figure 5.48b shows that for ethanol oxidation also a narrow region of current exists, for which potentials oscillations in HClO₄ medium set in. Furthermore, careful inspection of Fig. 5.48b indicates the interplay of these oscillations with tristability. In fact, two types of tristability are observed in this case: for a substantial current range it involves coexistence of three branches of stable steady states,

Fig. 5.48 Electrode potential plotted against applied current. *Closed circles* were obtained on increasing the current, *triangles* were obtained on decreasing the current. 0.50 M HClO₄ (a) 0.2 M methanol, (b) 0.2 M ethanol. *Open circles* represent maxima of oscillations and *open rectangles* represent minima. Reprinted from [128], Copyright 1999, with permission from Elsevier



but there is a narrow current range in which tristability consists of an oscillatory state coexisting with two steady states.

Furthermore, it was ethanol oxidation which exhibited also **excitability** [124]. The experiments started from open circuit conditions and the current was gradually increased in increments of 0.25 μA. Various combinations of current increases and decreases realized in various time scales allowed to detect the response of the electrode potential vs. time typical of excitability (Fig. 5.49).

After a sequence of small current increases, the electrode potential relaxed quickly to the steady-state value of the same branch. However, when the current, from the appropriately high value, was quickly decreased for a sufficiently high interval, the potential exhibited an abrupt decrease followed by a long relaxation to the steady state. For later discussion of origin of these instabilities, it is useful to note that studies of the electrochemical oxidation of ethanol at a Pt electrode showed that its mechanism is more complicated than that of methanol. Oxidation of ethanol at Pt electrode can proceed via different pathways, including the direct one, yielding various products, not only carbon dioxide, but also acetaldehyde, acetic acid, methane, or ethane. For certain range of electrode potentials, the

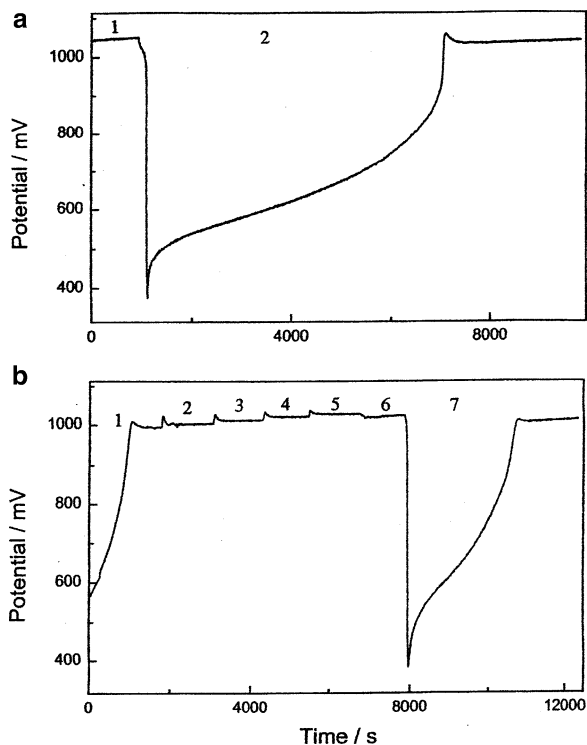


Fig. 5.49 Electrode potential plotted against time. The numbers correspond to different values of the applied current. (a) $[\text{CH}_3\text{CH}_2\text{OH}] = 0.05 \text{ M}$, 1: $I = 7.0 \mu\text{A}$, 2: $I = 6.25 \mu\text{A}$. The point at which the current was changed corresponds to the point at which the potential first decreases. (b) $[\text{CH}_3\text{CH}_2\text{OH}] = 0.15 \text{ M}$, 1: $I = 2.75 \mu\text{A}$; 2: $I = 3.00 \mu\text{A}$, 3: $I = 3.25 \mu\text{A}$, 4: $I = 3.50 \mu\text{A}$, 5: $I = 3.75 \mu\text{A}$, 6: $I = 3.50 \mu\text{A}$. This change was implemented at a slow rate. 7: $I = 3.25 \mu\text{A}$. The final current change corresponds to the point where the potential begins a large sharp increase. Reprinted from [124], Copyright 1999, with permission from Elsevier

production of acetic acid can be even five times faster than of CO_2 [132]. Carbon dioxide is the final product of one or more pathways in which adsorbed CO is an intermediate. Nevertheless, one can refer to the reaction mechanism elaborated for the methanol oxidation and apply its essential steps to the introductory explanation of instabilities in ethanol oxidation.

Finally, regarding 1-butanol, in the course of its galvanostatic oxidation on a Pt electrode, Chen and Schell [126] reported all discussed above dynamic phenomena: oscillations, bistability, tristability, and excitability, depending on acidic or alkaline medium. As in the case of ethanol, the bistable and tristable behavior involved the coexistence of not only stable steady states, but also of the oscillations in the limited current range. The main difference is of quantitative nature: the parameter range for occurrence of oscillations in acid solutions is substantially larger for 1-butanol than for ethanol.

5.6.2.2 The Common Electrochemical Mechanism of Dynamic Instabilities in Alcohols Oxidation

Since different alcohols exhibit similar dynamical nonlinear behaviors, it is natural to search for their common mechanistic origin. First the bistability involving the lowest and the middle potential branches will be analyzed. When CO_2 is the final oxidation product, the crucial intermediate is adsorbed CO. Then **bistability** is considered as caused by the *dual reactivity* of surface bonded CO which reacts with both adsorbed H_2O (at relatively low potentials) and OH radicals, formed at higher potentials [124, 126]. For the low-potential branch, the potentials are too low to cause the formation of OH radicals. Thus, under both open-circuit conditions and subsequent application of small currents in the galvanostatic mode, CO reacts only with adsorbed water molecules. Upon increase of the imposed current, in order to satisfy its actual value, the electrode is charged to more positive potentials, at which the rate of oxidation processes is appropriately higher. Eventually the electrode potential becomes so positive that the electrochemical production of adsorbed OH sets in, and since that moment the adsorbed CO can react with both $\text{H}_2\text{O}_{\text{ads}}$ and OH_{ads} . With further increase of the potential, the surface concentration of OH_{ads} becomes so high that the rate of their interaction with CO becomes higher than that of $\text{H}_2\text{O}_{\text{ads}}$. Eventually the production of OH_{ads} radicals becomes faster than their consumption in the reaction with CO. Since sites occupied by OH are inactivated, this situation means of course the progressing inhibition of the oxidation process, causing even further increase of the electrode potential, forcing acceleration of the oxidation at still vacant sites. This sequence of processes initializes the positive feedback, since the increase of electrode potential enhances the production of OH_{ads} which cause further increase of the potential. The system then jumps to a higher potential state, at which the anodic reactions occur with enhanced rate, satisfying the imposed current. In fact, experimental studies confirm that the transition to higher potential state takes place at the potentials corresponding to strong chemisorption of OH radicals. The above mechanism is applicable for the methanol oxidation, in which indirect CO pathway is dominant. For other alcohols, if there are more reaction pathways involving CO_{ads} , the extension of the above model allows one to understand multistability.

For the onset of **oscillations**, the existence of more than one reaction path is necessary. This statement already explains, why for methanol, oxidizing practically along one reaction path, oscillations are not detected or are difficult to observe (i.e., they require either large concentration or a sudden application of a large current), contrary to other two, higher alcohols. Let us consider two reaction pathways—a direct one and an indirect one—involving adsorbed CO. Upon increasing imposed current, as described earlier, the rate of both direct oxidation and formation of CO_{ads} will increase, in order to satisfy the electrochemical reaction rate with this current. The system enters the oscillatory regime if such conditions are attained that, for certain time, the rate of formation of CO_{ads} is greater than its removal. Then the effective number of vacant adsorption sites decreases and the electrode potential

moves toward more positive values, in order to enhance the direct oxidation rate at these vacant sites. When eventually the electrode potential attains the values at which adsorbed hydroxyl radicals form and quickly react with adsorbed CO molecules, a large number of vacant sites is recovered and the electrode potential returns to lower values, at which remaining OH radicals are reduced and due to these both effects the direct oxidation proceeds with the rate satisfying the imposed current. However, slow building up of CO_{ads} sets in again and the oscillatory cycle repeats. Based on that thinking, one can further judge that different parameter ranges for the oscillatory behavior in the ethanol and 1-butanol oxidation are caused by different relative efficiency of the direct and indirect pathways of this process. For methanol, in order to induce oscillations, one has to use more extreme conditions, under which the pathways other than the usually predominating, indirect one, get a chance to manifest themselves.

For the sake of generalization, the following universal aspects of the oscillatory electrooxidation (more generally: instabilities) of small organic molecules can be formulated: (1) the build up of the adsorbed poison layer (like CO_{ads}) along the indirect pathway; (2) the replenishing of the surface by reaction between the adsorbed poison intermediates (mainly CO_{ads}) and adsorbed oxygenated species (OH_{ads}), and (3) the feedback between the total surface coverage and the electrode potential [133].

In turn, the detailed mechanism of the **excitable** response is currently not well recognized. One can suppose that in the onset of this regime not only various intermediates of alcohols oxidation are involved, but certain role is played also by the formation of oxide at Pt surface, at sufficiently positive potentials. Chen and Schell [126] have suggested that excitability, manifesting itself when the imposed current is made less anodic, occurs due to the reduction processes, which however cannot be associated with the electrode reactions of alcohols, due to their significant irreversibility. Instead, the reduction of PtO to PtOH species (equivalent to OH_{ads}) was proposed. The OH_{ads} formed in this way reacts with CO_{ads} , increasing the number of vacant adsorption sites. This enhances the rate of direct oxidation of alcohol, allows the potential to shift to even lower values, at which further portion of PtO is reduced, etc.—in this way there realizes the positive feedback, explaining the fast decrease of the potential from the initial middle branch. A more detailed discussion of the assumptions underlying these suggestions the reader can find in original reference [126].

In turn, the differences of the systems' dynamics for the NaOH and HClO_4 media was explained in terms of the crucial role of adsorbed OH radicals: they take place in the oxidation of alcohols, in removing of CO and possibly are a source of oxygen atoms in the production of carboxylic ions. The point is that the (predominant) source of those radicals is different in the two of these electrolytes [126, 128]: in HClO_4 medium it is water, while in NaOH medium—the hydroxide ions present in the solution as the dissociation products. This causes different *kinetic* characteristics of OH_{ads} deposition from both media. In NaOH, this deposition occurs at lower potentials and proceeds with potential more gradually than for acidic solution. In other words, there is a considerable potential range between the

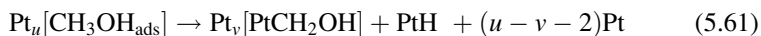
onset of OH deposition and the building up of their monolayer. In turn, in acidic solution, the OH_{ads} formation on the polycrystalline Pt surface occurs more abruptly. In consequence, and in accordance with experimental observations, for NaOH solutions, the imposed current density can be increased to relatively high values before the transition of the state to the higher potentials branch, since the point at which OH_{ads} formation exceeds their consumption and starts to inhibit the oxidation process, occurs with a delay, compared to acidic solutions. In other words, the OH_{ads} to CO_{ads} ratio favoring the alcohol oxidation is maintained for higher imposed currents, if the basic solution is used.

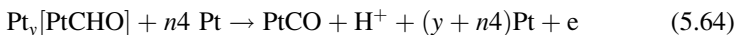
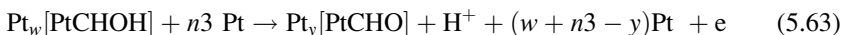
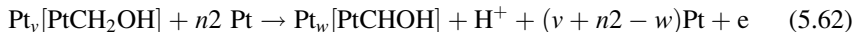
As a complement of the above mechanistic aspects of dynamic instabilities one can also mention earlier works by Schell et al. [134, 135] who observed for the oxidation of methanol, ethanol, and 1-propanol, studied under cyclic voltammetric conditions, a bifurcation upon increasing alcohol concentration in which a period-one cyclic voltammogram was replaced by a period-two cyclic voltammogram, the latter term meaning the limiting case of CV in which the current–potential curve required two potential cycles to retrace itself. The electrochemical mechanism involved the dual role of adsorbed OH radicals which can either react with CO_{ads} , as the intermediate of alcohol oxidation or undergo transformation to the oxide PtO. Upon increasing alcohol concentration in the solution, more OH_{ads} reacts with CO_{ads} , and less OH_{ads} is transformed into PtO. However, the system does not exhibit the monotonous trip toward the decrease of PtO production, but enters a two-period regime: during one cycle essentially no oxides form and during the next cycle the oxide production and reduction take place.

5.6.2.3 The Model of Multistable Oxidation of Alcohols

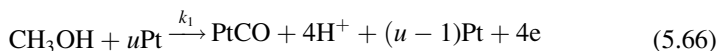
The above mechanistic considerations are included in the model reaction scheme, elaborated by Schell [127] for the oxidation of methanol, but the essential steps of this model can be used for discussion of the anodic behavior of ethanol and butanol. The model refers to earlier numerous classical studies of the electrochemical oxidation of methanol and introduces the steps responsible for the multistable behavior. In more detail, the Schell's approach explains the coexistence of the middle and the lowest branches, but did not account for the high-potential states shown in Fig. 5.48 which most probably involve both oxygen evolution and high-potential oxidation pathways of organic compounds.

The model, based on the assumption that oxidation of methanol occurs practically only along the indirect path, involves three dynamical variables: the electrode coverage of CO (θ_{CO}), OH radical (θ_{OH}), and the electrode potential (E). The formation of CO_{ads} (together with oxidation of adsorbed hydrogen) was presented as a reaction sequence (with explicit indication of engaged reaction sites at Pt):

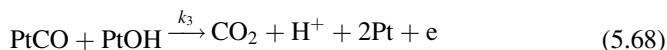
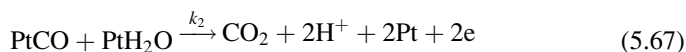




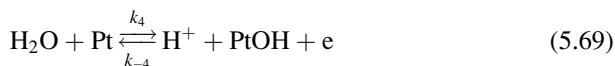
In a *simplified* version of the mechanism, sufficient for modeling of multistability, the above reaction steps were summarized into a single one:



In the model, CO is assumed to adsorb only linearly on Pt surface and therefore u decreases for one in (5.66). The adsorbed CO reacts both with adsorbed H_2O and adsorbed radical, in the potential-dependent processes characterized with the rate constants k_2 and k_3 , respectively [cf. Eq. (5.16)]:



as a result of which in each case two adsorption sites on Pt surface become vacant. Finally, the electroadsorption of OH radicals is described as:



One assumes further that the rate determining step in the reaction (5.66) uses only one surface site, and taking into account steps (5.67) and (5.68), one derives the kinetic equation for the rate of change of the surface concentration of carbon monoxide:

$$\frac{d\theta_{\text{CO}}}{dt} = k_1 S - k_2 \theta_{\text{CO}} \theta_{\text{wu}} - k_3 \theta_{\text{CO}} \theta_{\text{OH}} \quad (5.70)$$

where S means the concentration of vacant adsorption sites (assuming that each molecule occupies one site), and θ_{wu} is surface concentration of water. The rate constants k_1 to k_3 , scaled so that all concentrations are dimensionless and vary from 0 to 1, are exponentially dependent on the electrode potential:

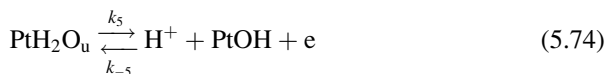
$$k_i = k_{0i} \exp[n_i F (E - E_i) / (2RT)] \quad (5.71)$$

where n_i is the number of electrons for the particular process and factor $\frac{1}{2}$ means that such value was assumed for the electron transfer coefficient (symmetrical activation barrier).

The model assumes further that not all water molecules on or near the Pt surface will be the reactants for reaction (5.67), but only those which exist in the “up-state,” i.e., for which the oxygen atoms point toward the electrode surface and the hydrogen end of the molecule points toward the solution (cf. the three-surface-state theory of Bockris et al. [136–138]). Thus, θ_{wu} in Eq. (5.70) means the surface coverage of only those “up-state,” reactive water molecules which are further assumed to remain in quasi-equilibrium state, described by the thermodynamic relationship:

$$\theta_{\text{wu}} = S \exp[-\Delta G/(k_B T)] \quad (5.72)$$

From three contributions to free Gibbs energy ΔG : (1) chemical interaction energy of the water dipole with the metal surface, (2) the electrical interaction, and (3) the energy of lateral interaction of a water molecule in the up-state with other molecules, only the third effect was taken into account, under additional simplifying assumption that only interactions with other water molecules in the same state are considered. Since the assumption on the quickly establishing equilibrium (5.69) is not valid at high positive potentials, at which the oxidation of water to adsorbed hydroxyl radicals occurs, the model took into account also this effect through introducing the following reaction scheme:



For other details of the relevant derivations, the reader is advised to consult the original reference [127] while below only the final expression for θ_{wu} will be given:

$$\theta_{\text{wu}} = \frac{SK_{\text{wu}} + \theta_{\text{OH}}K_a}{1 + K_b + UcSK_{\text{wu}}/(k_B T)} \quad (5.75)$$

where U is the lateral interaction energy; c , average coordination number of interacting particles; and d is the thickness of the double layer.

$$K_a = \frac{k_{-5}}{k_r} = \exp[-F(E - E_a)/(2RT)] \quad (5.76)$$

$$K_b = \frac{k_5}{k_r} = \exp[F(E - E_b)/(2RT)] \quad (5.77)$$

$$K_{wu} = \exp[\gamma(E - E_0)] \quad (5.78)$$

$$\gamma = \frac{\mu}{dk_B T} \quad (5.79)$$

with μ meaning the dipole moment of water, d is the thickness of the double layer, and k_B is Boltzmann's constant.

The remaining two ODEs were defined in the following way. The surface dynamics of the electrode coverage with OH radical was given by:

$$\frac{d\theta_{OH}}{dt} = k_4 S - k_{-4}\theta_{OH} + k_5\theta_{wu} - k_{-5}\theta_{OH} - k_3\theta_{CO}\theta_{OH} \quad (5.80)$$

The equation for the dynamics of the electrode potential follows from the charge conservation principle applied to the sum of the capacitive and the faradaic currents:

$$C_d \frac{dE}{dt} = -Q_0 \sum_j n_j r_j + j \quad (5.81)$$

where C_d is the (assumed constant) double layer capacitance; Q_0 , the charge corresponding to the charge transferred on depositing a monolayer of hydrogen atoms ($220 \mu\text{C cm}^{-2}$); j is the imposed current density and the sum is composed of kinetic terms:

$$\sum_j n_j r_j = 4k_1 S + 2k_2\theta_{CO}\theta_{wu} + k_3\theta_{CO}\theta_{OH} + k_4 S - k_{-4}\theta_{OH} + k_5\theta_{wu} - k_{-5}\theta_{OH} \quad (5.82)$$

Figure 5.50 shows results of the modeling for parameters listed in the caption.

Let us analyze the variation of θ_{OH} (or Pt-OH) with current density (dashed curve in Fig. 5.50c), showing the way in which the feedback, leading to instability, realizes. When current density increases, the electrode becomes charged to more positive potentials at which more OH radicals are produced and adsorbed on the Pt surface. Eventually, occupation of adsorption sites with OH species becomes so high that the interaction of CO with H_2O becomes severely inhibited. At this point, in order to satisfy the imposed current, the electrode potential must move to more positive values, at which other reactions can set in. This explanation refers only to two lowest branches of the steady states, according to the above-mentioned assumptions of the model.

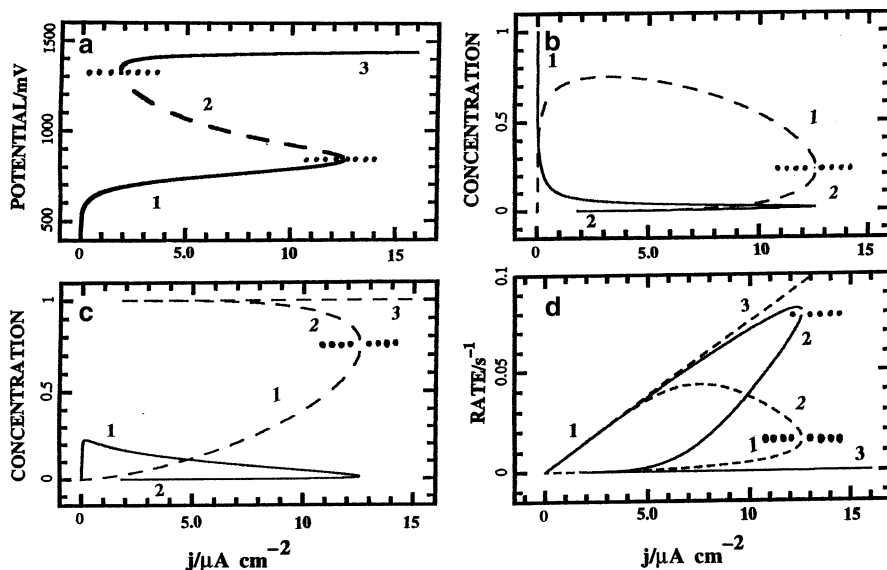


Fig. 5.50 Calculations from model, Eqs. (5.70), (5.75), (5.80), and (5.81). For all quantities, the number 1 refers to the *bottom* branch of states, the number 2 refers to the *intermediate* branch, and the number 3 refers to the *top* branch. (a) Potential is plotted against current. *Solid branches* represent stable steady states, *dashed branch* represents unstable steady states. (b) Concentration of surface bonded CO (*solid curve*) and concentration of surface sites (*dashed curve*) are plotted against current. (c) Concentration of water in the up state (*solid curve*) and concentration of PtOH (*dashed curve*) are plotted against current. (d) Rate of the reaction between water in the up state and PtCO (*solid curve*) and rate of the reaction between PtOH and PtCO (*dashed curve*) are plotted against current. Parameters: $k_{01} = 2 \times 10^{-5} \text{ s}^{-1}$, all other $k_{0i} = 0.10 \text{ s}^{-1}$, $F/(2RT) = 19.5$, $E_1 = 0.45 \text{ V}$, $E_2 = 0.68 \text{ V}$, $E_3 = 0.822 \text{ V}$, $E_4 = 0.887 \text{ V}$, $E_5 = E_a = E_b = 0.580 \text{ V}$, $\gamma = 5.1 \text{ V}^{-1}$, $E_0 = 0.44 \text{ V}$ and $Uc/(k_B T) = 2.5$. Reprinted from [127], Copyright 1998, with permission from Elsevier

At the end of this section we mention that the oscillatory oxidation of methanol under galvanostatic conditions was also observed at the nanostructured nickel hydroxide film (NNHF) electrode, where not the CO_{ads} species is the crucial intermediate, but the $\text{Ni}(\text{OH})_2/\text{NiOOH}$ redox couple acts as mediator for the electron transfer, making the NNHF electrode a better electrocatalyst than Pt [139, 140]. Since the postulated oscillatory mechanism is also essentially different from the previously discussed and involves the role of convection, a more detailed description of this process was included in Sect. 5.8 of volume II.

5.7 Oscillatory Oxidation of Sulfur Compounds

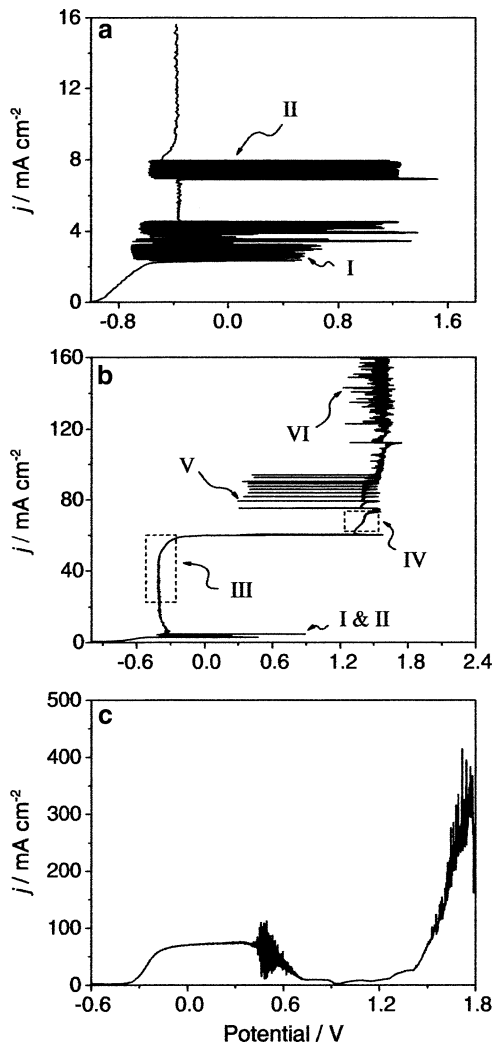
Oxidation of sulfur compounds is important for both industrial applications and the research, hence also dynamic instabilities in their redox processes are worth of studying. For example, Jansen et al. [141] have described the potential and current

oscillations during the anodic oxidation of pyrite in solutions of NaF, ascribed to the formation of a surface layer of iron(III) sulfide, decomposing into iron(II) sulfide and disulfide ions. More recently, Xu et al. [142] have described the oscillatory oxidation of thiourea on a polycrystalline Pt electrode. Both simple oscillations and their period-doubling bifurcations were found. Electrochemical impedance spectroscopy indicated the presence of the hidden negative resistance, suggesting thus the classification of this oscillatory system to the HN–NDR one. Also, the same group of researchers has described the current and potential oscillations, as well as bistability in the electrochemical oxidation of thiocyanate ions on a Pt electrode [143].

Also simpler species, as sulfide ions, can undergo oscillatory oxidation at different electrodes. The first paper about the oscillatory oxidation of sulfide ions on Pt electrode was published as early as in 1905 [144] and was followed by analyses by Bohnholzer and Heinrich [145] and Gerischer [146]. Later, apparently only in 1998 Jansen et al. [147] have described potentiostatic current oscillations at Pt electrodes and have elaborated mechanism which involved periodic formation and removal of sulfur. At low anodic potentials a surface layer of platinum sulfide, passivating the electrode surface, forms. This causes the inhibition of the oxidation of sulfide ions and the deposition of elementary sulfur. The resulting increase of the electrode potential causes the removal of the sulfide film by oxidation leading to platinum oxide and now the sulfur formation is possible on the oxide surface layer. Also other electrode types were involved for such studies. Recently, Chen and Miller [148, 149] have reported galvanostatic potential oscillations in the electrocatalytic oxidation of S^{2-} ions on a microstructured Ti/Ta₂O₅–IrO₂ electrode. Two distinct galvanostatic potential oscillations (oscillations A and B) were identified. Type A oscillations occurred for low current region and had relatively large amplitudes and very low frequencies, compared to type B oscillations which set in for the high current conditions. Furthermore, electrochemical impedance studies proved that both oscillation A and B were caused by the hidden negative resistance (HN–NDR). It was also found that periodic oxygen evolution was involved in the oscillatory mechanism. In the authors' interpretation, the source of oscillations A is the periodic variation of the S^{2-}/HS^- concentration, caused by the alternate depletion of the preelectrode layer of sulfide species due to its slow diffusion from the bulk, and its replenishment due to convection that sets in when the potential moves to sufficiently positive potentials, in search of the process that would satisfy the imposed current. Again, it is clear that this mechanism is analogous to the one suggested by Li et al. [150], or, in view of the work by Strasser et al. [151] one can also consider the formation of HN–NDR region due to the overlap of the sulfide ions and water oxidation currents. In turn, oscillations B were ascribed to the synergetic effect of sulfur formation/removal under constant oxygen evolution condition.

Also Miller and Chen, in more recent studies [152] have described the anodic oxidation of sulfide ions at the Pt electrode. Besides the type A and B (or α and β) galvanostatic oscillations (analogously to Ti/Ta₂O₅–IrO₂ electrode), current oscillations, as well as bistability were reported. The dependence of oscillations

Fig. 5.51 (a) Linear galvanic voltammogram of S^{2-} electrooxidation at a Pt(poly) electrode, collected at a scan rate of $0.01 \mu A s^{-1}$; (b) linear galvanic voltammogram collected at a scan rate of $0.02 \mu A s^{-1}$; and (c) linear voltammogram obtained under the scan rate of $0.05 mV s^{-1}$. Temperature was maintained at $20.0 \pm 0.1 ^\circ C$. Reprinted from [153], Copyright 2005, with permission from Elsevier



A and B on the current density was analogous to those found for the described above oxide electrode. Also, the existence of hidden negative resistance was found for both oscillations A and B, classifying them as belonging to HN-NDR oscillators.

Apparently independently of these studies, Feng, Wang et al. [153] have described the anodic oxidation of sulfide ions at the polycrystalline Pt electrode which process appeared to constitute both the N-NDR and HN-NDR oscillator. These studies are described below in more detail. Under galvanostatic conditions, upon varying imposed current, six distinct oscillations windows (Fig. 5.51), with very different oscillation morphology (Fig. 5.52), were observed (see e.g., “bursting oscillations” in Fig 5.52a).

Fig. 5.52 Time series of galvanostatic potential oscillations during the electrochemical oxidation of sulfide. The applied currents are (a) 2.86 mA cm^{-2} , (b) 7.27 mA cm^{-2} , (c) 31.83 mA cm^{-2} , (d) 63.66 mA cm^{-2} , (e) 95.49 mA cm^{-2} , and (f) $127.32 \text{ mA cm}^{-2}$. Other reaction conditions are $[\text{Na}_2\text{S}] = 1.0 \text{ M}$ and $T = 20.0 \pm 0.1 \text{ }^\circ\text{C}$. Reprinted from [153], Copyright 2005, with permission from Elsevier

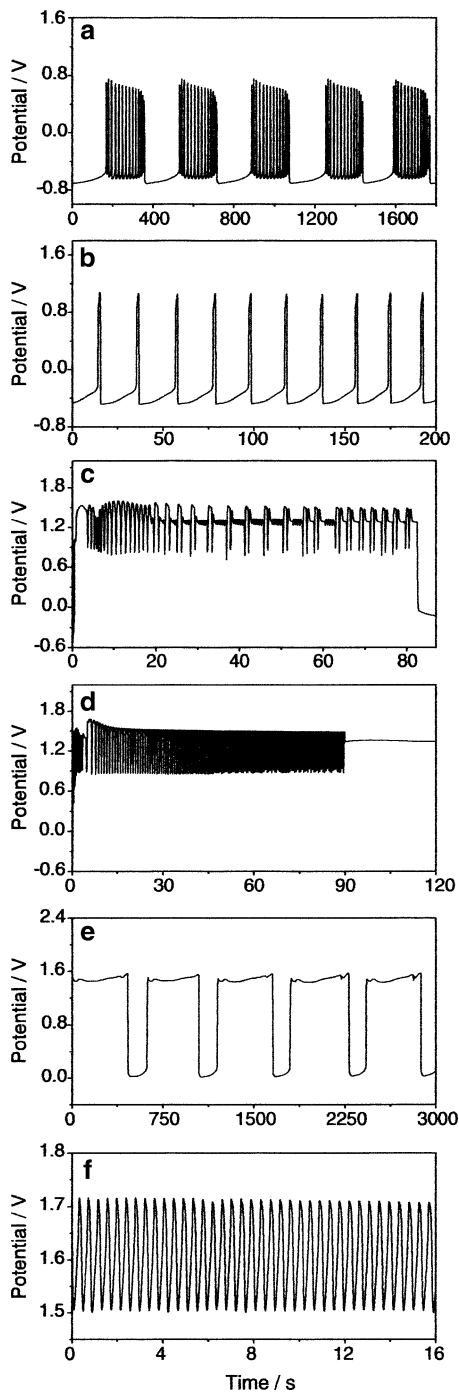
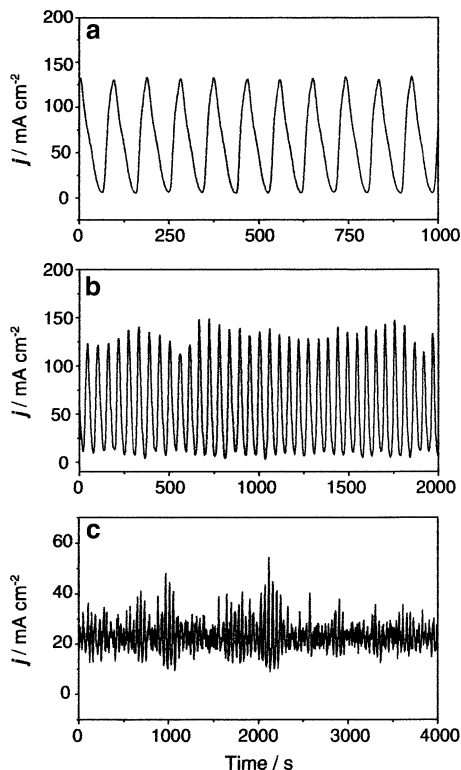


Fig. 5.53 Time series of anodic current oscillations during the electrochemical oxidation of Na_2S . The applied potential values are: (a) 0.50 V, (b) 0.525 V, and (c) 0.55 V. Other reaction conditions are $[\text{Na}_2\text{S}] = 1.0 \text{ M}$ and $T = 20.0 \pm 0.1 \text{ }^\circ\text{C}$. Reprinted from [153], Copyright 2005, with permission from Elsevier

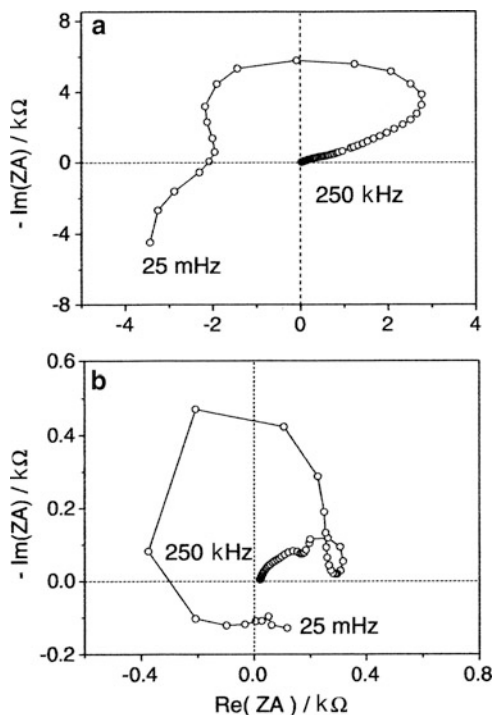


In turn, Fig. 5.53 shows the existence of also potentiostatic oscillations, shown for three exemplary voltages. Although a bit irregular, the course in Fig. 5.53b resembles quasi-periodic behavior. Then the chaotic course in Fig. 5.53c could be considered a consequence of the so-called Ruelle–Takens–Newhouse (RTN) route to chaos (cf. Sect. 1.9).

Of course, the galvanostatic and potentiostatic oscillations are related to the positive and negative slopes of the voltammograms shown in Fig. 5.51c. The presence of an explicit N-NDR region at the potential around ca. 0.57 V (vs. $\text{Hg-Hg}_2\text{SO}_4\text{-K}_2\text{SO}_4$ reference electrode) is consistent with the impedance spectrum recorded for the same potential, where the negative real impedance was found for nonzero frequency. Oscillations observed in Fig. 5.51c around the potential of ca. 1.7 V occur at the $I-E$ branch with positive slope and, accordingly, the electrochemical impedance spectroscopy indicated for this potential the loop characteristic of HN-NDR oscillator: real impedance was found negative for intermediate frequencies and returned to positive values for ω decreasing to zero, in line with positive slope of the $I-E$ curve (Fig. 5.54).

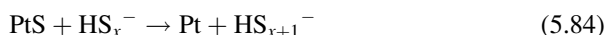
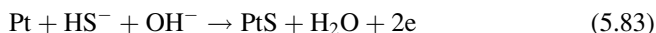
It is perhaps somewhat surprising that electrooxidation of such simple species, as S^{2-} ions, offers such a variety of oscillatory instabilities. In search of the interpretation of these phenomena, it was also noted certain effect of the temperature on the oscillation morphology, as well as the fact that the oscillations persisted

Fig. 5.54 Electrochemical impedance spectrum measured at different potential values: (a) 0.52 V and (b) 1.7 V. The frequency was varied from 250 kHz to 25 mHz. Other reaction conditions were: $[\text{Na}_2\text{S}] = 1.0 \text{ M}$ and $T = 20.0 \pm 0.1 \text{ }^\circ\text{C}$. Reprinted from [153], Copyright 2005, with permission from Elsevier



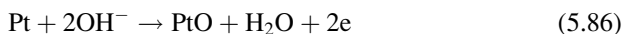
also in the absence of convection induced by oxygen evolution at high positive potentials. Under conditions of the experiments, the sulfide ions exist predominantly in the HS^- form, the oxidation of which causes alternate formation and removal of elementary sulfur layer.

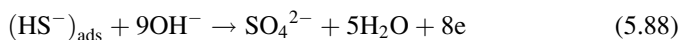
At external voltage of ca. 0.5 V the occurrence of the following processes was suggested:



The sulfur layer, formed in process (5.83) is supposed to block partly the Pt surface, leading thus to the first (explicit) NDR region at around 0.5 V.

At potentials as high as ca. 1.5 V, the sulfur precipitate is not observed and the suggested reaction pathway is the following:





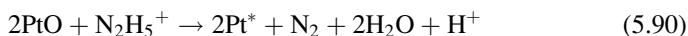
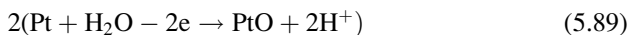
The formation of gaseous oxygen was omitted, since it was not observed within the potential range from -0.8 V to $+1.8$ V. In this case, the competition for the adsorption sites between the OH^- and HS/S^{2-} species was assumed to be responsible for the second NDR region. Although this work is of introductory character, its further development is expected, also with respect to the eventual pattern formation phenomena [153]. Very recently, Gao et al. have reported the formation of such sulfur patterns, recorded by CCD camera. For wide range of sulfide concentrations, the HN-NDR characteristics were found and the corresponding types of patterns included pulses, fronts, labyrinths, twinkling eyes, and spirals. The N-NDR oscillations occurred only at relatively high concentrations of sulfides, and under such conditions pulses and synchronization phenomena were reported [154].

5.8 Other Oscillatory Oxidation Reactions

In this section, we briefly review the oxidation of other molecules at solid electrodes.

Oscillatory anodic oxidation of **hydrazine** in acidic medium, at polycrystalline Pt electrode, under chronopotentiometric conditions, was reported by Bard in 1963 [155]. A significant role in the onset of these instabilities was ascribed to an appropriate pretreatment of the electrode. The oxidation of hydrazine follows the following overall scheme: $\text{N}_2\text{H}_5^+ - 4\text{e} \rightarrow \text{N}_2 + 5\text{H}^+$, but the overpotentials at which it occurs can be separated for as much as 0.5 V, depending on the initial Pt state. The Pt surface can attain two different states: either the *activated* one, in which it contains a layer of finely divided platinum (after, e.g., reduction of Pt oxide layer, platinization or ac activation), or the *deactivated* one (presumably with missing fine Pt particles, partly poisoned, etc., obtained after, e.g., prolonged contact with the acidic hydrazine solution or the treatment with *aqua regia*). At the activated Pt surface, direct electrooxidation of hydrazine occurs at $E = -0.1$ to -0.2 V (vs. the saturated mercury–mercurous sulfate electrode, with a potential of 0.4 V vs. SCE).

If the experiment involved Pt in the deactivated state, the oxidation of hydrazine occurred at more positive potentials, corresponding to the formation of oxide layer, of a composition simplified here to PtO. An important, experimentally confirmed fact was that this oxide layer was readily and quickly reduced by hydrazine. Thus, the sequence of reactions occurring at such positive potentials can be suggested as:



where the *activated* sites of platinum surface are symbolized by Pt*. It is of course also possible that the redox interaction of hydrazine with PtO occurs along two parallel pathways: direct chemical and electrochemical ones.

Finally, the oscillations set in sometimes, when the platinum electrode surface was first preoxidized by treatment with *aqua regia*. Upon polarization, the electrode potential moved first to high anodic values at which, together with the formation of PtO, also hydrazine undergoes oxidation. Since then [cf. Eq. (5.90)], the free active sites Pt* appear, the electrode potential moves toward less positive values, corresponding to the electrooxidation of hydrazine at the active Pt surface. However, when these sites become poisoned with, e.g., adsorbed intermediates, the electrode becomes deactivated, the potential moves again toward more positive values, and the oscillatory cycle repeats.

Wojtowicz et al. [61] have performed kinetic studies of the oxidation of **ethylene** at stationary and rotating platinized platinum disk electrodes, from its saturated solution in 1 M HClO₄, at 80°C. Current oscillations were observed in certain ranges of potential and rotation rate. Contrary to the formic acid oxidation, the oscillations could be suppressed by exceeding certain critical rotation speed which fact indicated the more, in this case, pronounced role of transport in developing the instabilities. The mechanism proposed by Wojtowicz et al. included the following steps: (1) arrival of C₂H₄ at the electrode vicinity, (2) fast (faster than that transport) equilibrium chemisorption of C₂H₄, according to the specific isotherm, (3) electrode surface oxidation: co-deposition of oxygen-containing species (O, OH) on free sites, (4) reaction between adsorbed C₂H₄ and surface oxide species. The respective kinetic model was elaborated.

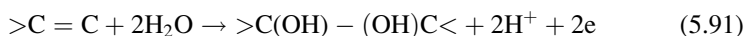
Schell et al. [156] have studied the electrocatalyzed oxidation of **glycerol** in alkaline solution upon cyclic variation of the polycrystalline Pt electrode potential and compared it with the oxidations of ethylene glycol and methanol. Based on analysis of behaviors caused by chemical instabilities, the conclusion was drawn that the elementary reactions that dominate the oxidation of glycerol are the same as those that dominate the oxidation of methanol, including the formation of surface bonded CO and its reaction with surface bonded hydroxyl radicals.

In this section, we shall only briefly mention selected works on the anodic oxidation of various species occurring at **semiconductor** electrodes [157]. An example of such processes is the oxidation of **iodide** ions at the illuminated n-type MoSe₂ electrode, described by Tributsch et al. [158]. Oscillations of the current and of the electrode reflectivity, as well as surface propagating waves were observed. For the p-type MoSe₂, metallic NbSe₂, and Pt electrodes similar phenomena were observed, but with that difference that they did not require illumination. For the semiconductor CdS electrode immersed in the aqueous solution of 0.1 M K₃Fe(CN)₆ + 0.1 M K₄Fe(CN)₆, Vainas [159] has reported the current oscillations, attributed to the formation and detachment of gas bubbles formed on metallic patches found on the CdS.

Very recently, Hammer et al. [160] have reported oscillatory oxygen evolution originating from oxidation of water molecules during anodization of Ta electrodes. In general, valve metals like also Al or Nb cover with oxide films either in a humid

environment or during anodic oxidation. The resulting oxide Ta_2O_5 has properties similar to ceramics due to their large band gap of 3–6 eV. In spite of insulating properties of Ta_2O_5 which should prevent water oxidation, under industrial conditions of Ta anodization for electrolytic capacitor fabrication, large amounts of oxygen are evolved. Hammer et al. have reported that upon anodic polarization of sintered, porous Ti anode to the potentials exceeding ca. 10 V, the current is oscillating, and accompanied by alternating strong oxygen evolution. Quantitatively, the current efficiency of the Ta_2O_5 formation was ca. 96%, so ca. 4% of the anodic charge was consumed for oxygen evolution. Its oscillatory course was explained in terms of a cyclic formation of gas bubbles, blockage of the inner electrode surface, removal of gas, further oxide growth, the whole sequence repeating cyclically. The fact that the amount of oxygen was proportional to the oxide amount formed in parallel was explained in terms of the model where mobile ions during oxide growth form interband states which allow electron tunneling.

Finally, although oxidation of **graphite** does not correspond to the electrode process of small molecules, we shall mention it here because of some analogies with the composition of chemical bonds involved in such processes with the structure of organic species, described earlier in this chapter. Beck et al. [161] have described potential oscillations during galvanostatic overoxidation of graphite electrode in aqueous solution of sulfuric acid to yield electrochemical graphite oxide (EGO). The period of these oscillations was as long as about one hour. Particularly interesting is that these oscillations were associated with the processes occurring not at the surface, but in the bulk of the solid state. The proposed oscillatory mechanism involves the novel “zone-model,” meaning the zone-like progress of the intercalation of graphite. The increasing part of the electrode potential is caused by the buildup of a *transport overvoltage* due to the formation of C–OH groups and their linkage through hydrogen bonds. In the decreasing part of the wave, further oxidation occurs, such as $\equiv C-OH \rightarrow =C=O$, the OH groups disappear and the transport overvoltage decreases. Water molecules can be transported to the next zone. A more detailed description of this mechanism is given in the original reference [161]. Also, Harrach et al. [162] have described potential oscillations during the galvanostatic oxidation of highly oriented pyrographite (HOPG) intercalated with H_2SO_4 . The complex mechanism of this process involves overcharging stage (increase in the charge of graphene layers with simultaneous expulsion of H^+). At high potentials this step is followed by the irreversible, autocatalytic overoxidation of graphite:



which results in a rapid decrease of water molecules at the reaction front, which then slows down the reaction: near the front, graphene layers collapse, preventing the further arrival of new H_2O molecules and preventing the overoxidation reaction from occurring [157, 162].

References

1. Koper MTM, Sluyters JH (1994) Instabilities and oscillations in simple models of electrocatalytic surface reactions. *J Electroanal Chem* 371:149–159
2. Thalinger M, Volmer M (1930) *Z phys Chem* 150:401
3. Armstrong G, Butler JAV (1947) Electrochemical periodicities in the anodic polarisation of platinum electrodes in the presence of hydrogen and their significance. *Disc Faraday Soc* 1:122–141
4. Sawyer DT, Seo ET (1963) Electrochemistry of dissolved gases III. Oxidation of hydrogen at platinum electrodes. *J Electroanal Chem* 5:23–24
5. Conway BE, Novak DM (1977) Oscillatory kinetics in electrochemical oxidation of hydrogen in an almost anhydrous solvent. *J Phys Chem* 81:1459–1468
6. Horányi G, Visy C (1979) Potential oscillations in the course of galvanostatic oxidation of hydrogen at platinum electrode in the presence of electrosorbing cations. *J Electroanal Chem* 103:353–361
7. Kodera T, Yamazaki T, Kubota N (1986) Verification of potential oscillation caused by metal deposition and dissolution. *Electrochim Acta* 31:1477–1478
8. Kodera T, Yamazaki T, Masuda M, Ohnishi R (1988) Limit cycle in electrochemical oscillation—potential oscillation during anodic oxidation of H₂. *Electrochim Acta* 33:537–540
9. Yamazaki T, Kodera T (1989) Potential oscillation during anodic oxidation of hydrogen at a platinum electrode. I. Experimental. *Electrochim Acta* 34:969–975
10. Yamazaki T, Kodera T, Ohnishi R, Masuda M (1990) Potential oscillation during anodic oxidation of hydrogen at a platinum electrode. II. Kinetic analysis. *Electrochim Acta* 35:431–435
11. Krischer K, Lübke M, Wolf W, Eiswirth M, Ertl G (1991) Chaos and interior crisis in an electrochemical reaction. *Ber Bunsenges Phys Chem* 95:820–823
12. Eiswirth M, Lübke M, Krischer K, Wolf W, Hudson JL, Ertl G (1992) Structural effects on the dynamics of an electrocatalytic oscillator. *Chem Phys Lett* 192:254–258
13. Krischer K, Lübke M, Eiswirth M, Wolf W, Hudson JL, Ertl G (1993) A hierarchy of transitions to mixed mode oscillations in an electrochemical system. *Physica D* 62:123–133
14. Thompson JMT, Stewart HB (1987) *Nonlinear dynamics and chaos*. Wiley, Chichester
15. Ott E (2006) Crises. *Scholarpedia* 1(10):1700. doi:[10.4249/scholarpedia.1700](https://doi.org/10.4249/scholarpedia.1700)
16. Grebogi C, Ott E, Yorke JA (1983) Crises: sudden changes in chaotic attractors and chaotic transients. *Physica D* 7:181–200
17. Michaelis R, Zei MS, Zhai RS, Kolb DM (1992) The effect of halides on the structure of copper underpotential-deposited onto Pt(111): a low-energy electron diffraction and X-ray photoelectron spectroscopy study. *J Electroanal Chem* 339:299–310
18. Markovic N, Ross PN (1993) Effect of anions on the underpotential deposition of copper on platinum(111) and platinum(100) surfaces. *Langmuir* 9:580–590
19. Krischer K, Lübke M, Wolf W, Eiswirth M, Ertl G (1995) Oscillatory dynamics of the electrochemical oxidation of H₂ in the presence of Cu²⁺: structure sensitivity and the role of anions. *Electrochim Acta* 40:69–81
20. Wolf W, Krischer K, Lübke M, Eiswirth M, Ertl G (1995) Modeling oscillations in galvanostatic H₂ oxidation at Pt in the presence of metal ions. *J Electroanal Chem* 385:85–93
21. Wolf W, Lübke M, Koper MTM, Krischer K, Eiswirth M, Ertl G (1995) Experimental and theoretical description of potentiostatic current oscillations during H₂ oxidation. *J Electroanal Chem* 399:185–196
22. Vetter KJ (1961) *Elektrochemische Kinetik*. Springer, Berlin
23. Breiter M (1962) Über die Art der Wasserstoffadsorption an Platinmetallelektroden. *Electrochim Acta* 7:25–38
24. Will FG (1965) Hydrogen adsorption on platinum single crystal electrodes. I. Isotherms and heats of adsorption. *J Electrochem Soc* 112:451–455

25. Joncich MJ, Hackermann N (1953) The reaction of hydrogen and oxygen on submerged platinum electrode catalysts. I. Effect of stirring, temperature and electric polarization. *J Phys Chem* 57:674–678
26. Strasser P, Eiswirth M, Ertl G (1997) Oscillatory instabilities during formic acid oxidation on Pt(100), Pt(110) and Pt(111) under potentiostatic control. II. Model calculations. *J Chem Phys* 107:991–1003
27. Gasteiger HA, Markovic NM, Ross PN (1995) H₂ and CO electrooxidation on well-characterized Pt, Ru and Pt-Ru. 1. Rotating disk electrode studies of the pure gases including temperature effects. *J Phys Chem* 99:8290–8301
28. Gasteiger HA, Markovic NM, Ross PN (1995) H₂ and CO electrooxidation on well-characterized Pt, Ru, and Pt-Ru. 2. Rotating disk electrode studies of CO/H₂ mixtures at 62 degree C. *J Phys Chem* 99:16757–16767
29. Koper MTM, Schmidt TJ, Marković RPN (2001) Potential oscillations and S-shaped polarization curve in the continuous electro-oxidation of CO on platinum single-crystal electrodes. *J Phys Chem B* 105:8381–8386
30. Samjeské G, Komatsu K, Osawa M (2009) Dynamics of CO oxidation on a polycrystalline platinum electrode: a time-resolved infrared study. *J Phys Chem C* 113:10222–10228
31. Maikhandi S, Bonnefont A, Krischer K (2005) Strictly potentiostatic current oscillations during bulk CO electro-oxidation on platinum in the presence of inhibiting anions. *Electrochem Commun* 7:710–716
32. Malkhandi S, Bonnefont A, Krischer K (2009) Dynamic instabilities during the continuous electro-oxidation of CO on poly- and single crystalline Pt electrodes. *Surface Sci* 603:1646–1651
33. Turner JE, Sales BC, Maple MB (1981) Oscillatory oxidation of CO over a Pt catalyst. *Surf Sci* 103:54–74
34. Turner JE, Sales BC, Maple MB (1982) Oscillatory oxidation of CO over a Pt, Pd and Ir catalysts: theory. *Surf Sci* 114:381–394
35. Ertl G (1990) Oscillatory catalytic reactions at single-crystal surfaces. *Adv Catal* 37:213–277
36. Imbihl R (1993) Oscillatory reactions on single crystal surfaces. *Prog Surf Sci* 44:185–343
37. Imbihl R, Ertl G (1995) Oscillatory kinetics in heterogeneous catalysis. *Chem Rev* 95:697–733
38. Ertl G (1995) Oscillatory kinetics and spatio-temporal self-organization in reactions at solid surfaces. *Science* 254:1750–1755
39. Ertl G, Rotermund HH (1996) Spatiotemporal pattern formation in reactions at surfaces. *Curr Op Solid State Mat Sci* 1:617–621
40. Chorkendorff I, Niemantsverdriet JW (2007) Concepts of modern catalysis and kinetics, 2nd edn. Wiley, Weinheim, p 72
41. Eiswirth M, Bürger J, Strasser P, Ertl G (1996) Oscillating Langmuir-Hinshelwood mechanism. *J Phys Chem* 100:19118–19123
42. Bonnefont A, Varela H, Krischer K (2003) Stationary small and large amplitude patterns during bulk CO electrooxidation on platinum. *ChemPhysChem* 4:1260–1263
43. Bonnefont A, Varela H, Krischer K (2005) Stationary spatial patterns during bulk CO electrooxidation on platinum. *J Phys Chem B* 109:3408–3415
44. Morschl R, Bolten J, Bonnefont A, Krischer K (2008) Pattern formation during CO electrooxidation on thin Pt films studied with spatially resolved infrared absorption spectroscopy. *J Phys Chem C* 112:9548–9551
45. Fink T, Dath JP, Imbihl R, Ertl G (1991) Kinetic oscillations in the NO + CO reaction on Pt (100): experiments and mathematical modeling. *J Chem Phys* 95:2109–2126
46. Imbihl R, Fink T, Krischer K (1992) Bifurcation analysis of the three-variable model for the NO + CO reaction on Pt surfaces. *J Chem Phys* 96:6236–6248
47. Siegmeier J, Baba N, Krischer K (2007) Bistability and oscillations during electrooxidation of H₂-CO mixtures on Pt: modeling and bifurcation analysis. *J Phys Chem C* 111:13481–13489

48. Deibert MC, Williams DL (1969) Voltage oscillations of the H₂-CO system. *J Electrochem Soc* 116:1290–1292
49. Szpak S (1970) Potential oscillations of the H₂-CO system at low CO content. *J Electrochem Soc* 117:1056–1058
50. Yamazaki T, Kodera T (1990) Potential oscillation of Pt electrode in H₂SO₄ solution during the anodic oxidation of H₂ and CO. *Electrochim Acta* 36:639–646
51. Zhang J, Datta R (2002) Sustained potential oscillations in proton exchange membrane fuel cells with Pt Ru as anode catalyst. *J Electrochem Soc* 149:A1423–A1431
52. Zhang J, Datta R (2004) Higher power output in a PEMFC operating under autonomous oscillatory conditions in the presence of CO. *Electrochem Solid State Lett* 7:A37–A40
53. Zhang J, Datta R (2005) Electrochemical preferential oxidation of CO in reformat. *J Electrochem Soc* 152:A1180–A1187
54. Zhang J, Fehribach JD, Datta R (2004) Mechanistic and bifurcation analysis of anode potential oscillations in PEMFCs with CO in anode feed. *J Electrochem Soc* 151:A689–A697
55. Kiss IZ, Brackett AW, Hudson JL (2004) Nonuniform reaction rates during CO and CO/H₂ oxidation on coupled Pt electrodes. *J Phys Chem B* 108:14599–14608
56. Beden B, Bewick A (1980) Oscillatory kinetics in the electrochemical oxidation of formate ions during the deposition of rhodium electrode. Part I. Experimental observation. *J Electroanal Chem* 107:127–145
57. Morgan JS (1916) The periodic evolution of carbon monoxide. *J Chem Soc* 109:274–283
58. Showalter K, Noyes RM (1978) Oscillations in chemical systems. 24. Oscillatory decomposition of formic acid in sulfuric acid. *J Am Chem Soc* 100:1042–1049
59. Raw CJG, Friedrich J, Perrino F, Jex G (1978) Oscillatory gas evolution from the system formic acid-concentrated sulfuric acid-concentrated nitric acid. *J Phys Chem* 82:1952–1953
60. Müller E, Tanaka S (1928) Über die pulsierende elektrolytische Oxydation der Ameisensäure. *Z Elektrochem* 34:256–264
61. Wojtowicz J, Marincic N, Conway BE (1968) Oscillatory kinetics in the electrochemical oxidation of formate and ethylene. *J Chem Phys* 48:4333–4345
62. Beden B, Lamy C, Bewick A (1981) Oscillatory kinetics in the electrochemical oxidation of formate ions during the deposition of rhodium electrode. Part II. Mechanistic considerations. *J Electroanal Chem* 121:115–124
63. Bockris JO'M, Conway BE, Yeager E, White RE (1981) *Comprehensive treatise of electrochemistry*, vol 3. Plenum, New York
64. Cai X, Schell M (1992) Observation of bistability in cyclic voltammetric experiments on ethanol, propanol, butanol and formic acid/formate. *Electrochim Acta* 37:673–680
65. Xu Y, Schell M (1990) Bistability and oscillations in the electrocatalyzed oxidation of formaldehyde. *J Phys Chem* 94:7137–7143
66. Schell M, Albahadily FN, Safar J, Xu Y (1989) Characterization of oscillatory states in the electrochemical oxidation of formaldehyde and formate/formic acid. *J Phys Chem* 93:4806–4810
67. Albahadily FN, Schell M (1991) Observation of several different temporal patterns in the oxidation of formic acid at a rotating platinum-disk electrode in an acidic medium. *J Electroanal Chem* 308:151–173
68. Inzelt G, Kertész V (1993) Experimental evidence for the periodical changes of the amount of chemisorbed species accompanying the potential oscillations produced in the course of galvanostatic oxidation of formic acid on platinum. *Electrochim Acta* 38:2385–2386
69. Inzelt G, Kertész V (1995) Enhanced frequency oscillations accompanying galvanostatic potential oscillations at Pt electrode in Cu²⁺ formic acid systems. *Electrochim Acta* 40:221–225
70. Inzelt G, Kertész V (1997) Effect of poly(aniline) pseudocapacitance on potential and EQCM frequency oscillations arising in the course of galvanostatic oxidation of formic acid on platinum. *Electrochim Acta* 42:229–235

71. Raspel F, Nichols RJ, Kolb DM (1990) Current oscillations during formic acid oxidation on Pt(100). *J Electroanal Chem* 286:279–283
72. Raspel F, Eiswirth M (1994) Current oscillations in the electrochemical oxidation of formic acid at Pt single crystal surfaces. *J Phys Chem* 97:7613–7618
73. Kita H, Lei HW (1995) Oxidation of formic acid in acid solution on Pt single-crystal electrodes. *J Electroanal Chem* 388:167–177
74. Tripkovic A, Popovic K, Adzic RR (1991) *J Chim Phys* 88:1635
75. Markovic N, Ross PN (1993) Oscillatory behavior in the electrochemical oxidation of formic acid on Pt(100). *J Phys Chem* 97:9771–9778
76. Strasser P, Lübke M, Raspel F, Eiswirth M, Ertl G (1997) Oscillatory instabilities during formic acid oxidation on Pt(100), Pt(110) and Pt(111) under potentiostatic control. I. Experimental. *J Chem Phys* 107:979–990
77. Koper MTM (1998) Non-linear phenomena in electrochemical systems. *J Chem Soc Faraday Trans* 94:1369–1378
78. Parsons R, VanderNoot T (1988) The oxidation of small organic molecules: a survey of recent fuel cell related research. *J Electroanal Chem* 257:9–45
79. Beden B, Leger JM, Lamy C (1992) In: Bockris JO'M, Conway BE, White RE (eds) *Modern aspects of electrochemistry*, vol 22. Plenum, New York, p 97
80. Beden B, Lamy C, Tacconi NRD, Arvia AJ (1991) The electrooxidation of CO: a test reaction in electrocatalysis. *Electrochim Acta* 35:691–704
81. Clarke BL (1980) Stability of complex reaction networks. *Adv Chem Phys* 42:1–213
82. Eiswirth M, Freund A, Ross J (1991) Mechanistic classification of chemical oscillators and the role of species. In: Prigogine I, Rice SA (eds) *Adv Chem Phys*, vol 80, pp 127–199.
83. Samjeské G, Osawa M (2005) Current oscillations during formic acid oxidation on a Pt electrode: insight into the mechanism by time-resolved IR spectroscopy. *Angew Chem Int Ed* 44:5694–5698
84. Samjeské G, Miki A, Ye S, Yakamata A, Mukoyama Y, Okamoto H, Osawa M (2005) Potential oscillations in galvanostatic electrooxidation of formic acid on platinum: a time-resolved surface-enhanced infrared study. *J Phys Chem B* 109:23509–23516
85. Samjeské G, Miki A, Ye S, Osawa M (2006) Mechanistic study of electrocatalytic oxidation of formic acid at platinum in acidic solution by time-resolved surface-enhanced infrared absorption spectrometry. *J Phys Chem B* 110:16559–16566
86. Mukoyama Y, Kikuchi M, Samjeské G, Osawa M, Okamoto H (2006) Potential oscillations in galvanostatic electrooxidation of formic acid on platinum: a mathematical modeling and simulation. *J Phys Chem B* 110:11912–11917
87. Chen YX, Heinen M, Jusys Z, Behm RJ (2006) Bridged-bonded formate: active intermediate or spectator species in formic acid oxidation on a Pt film electrode? *Langmuir* 22:10399–10408
88. Chen YX, Heinen M, Jusys Z, Behm RJ (2006) Kinetics and mechanism of the electrooxidation of formic acid – spectroelectrochemical studies in a flow cell. *Angew Chem Int Ed* 45:981–985
89. Chen YX, Miki A, Ye S, Sakai H, Osawa M (2003) Formate, an active intermediate for direct oxidation of methanol on Pt electrode. *J Am Chem Soc* 125:3680–3681
90. Nagao R, Epstein IR, Gonzalez ER, Varela H (2008) Temperature (over)compensation in an oscillatory surface reaction. *J Phys Chem A* 112:4617–4624
91. Carbonio EA, Nagao R, Gonzalez ER, Varela H (2009) Temperature effects on the oscillatory electro-oxidation of methanol on platinum. *Phys Chem Chem Phys* 11:665–670
92. Okamoto H, Tanaka N, Naito M (1995) Analogy between the stimulus-response characteristics of neuronal and electrochemical cells. *Chem Phys Lett* 237:432–436
93. Koester J (1985) In: Kandel ER, Schwartz JH (eds) *Principles of neural science*, 2nd edn. Elsevier, Amsterdam, p 81
94. MacGregor RJ (1987) *Neural and brain modeling*. Academic, New York, p 225
95. Okamoto H, Tanaka N, Naito M (1997) Chaos in the oxidation of formaldehyde and/or methanol. *J Phys Chem A* 101:8480–8488

96. Okamoto H, Tanaka N, Naito M (1998) Chaotic and periodic potential oscillations in formaldehyde oxidation. *J Phys Chem A* 102:7343–7352
97. Okamoto H, Tanaka N, Naito M (1998) Intermittencies and related phenomena in the oxidation of formaldehyde at a constant current. *J Phys Chem* 102:7353–7361
98. Pomeau Y, Manneville P (1980) Intermittent transition to turbulence in dissipative dynamical systems. *Commun Math Phys* 74:189–197
99. Bergé P, Pomeau Y, Vidal C (1984) Order within chaos – towards a deterministic approach to turbulence. Wiley, New York
100. Strogatz SH (1994) Nonlinear dynamics and chaos. Perseus, Massachusetts
101. Hunger HF (1968) The mechanism of oscillatory behavior during the anodic oxidation of formaldehyde. *J Electrochem Soc* 115:492–497
102. Bełtowska-Brzezińska M, Heitbaum J, Vielstich W (1985) The influence of UPD-lead on the adsorption of formaldehyde, formic acid and methanol on Pt in acid solution. *Electrochim Acta* 30:1465–1471
103. Koper MTM, Hackar M, Beden B (1996) Investigation of the oscillatory electro-oxidation of formaldehyde on Pt and Rh electrodes by cyclic voltammetry, impedance spectroscopy and the electrochemical quartz microbalance. *J Chem Soc Faraday Trans* 92:3975–3982
104. Koper MTM (1996) Oscillations and complex dynamical bifurcations in electrochemical systems. In: Prigogine I, Rice SA (eds) *Adv Chem Phys* XCII: 161–298
105. Olivi P, Bulhões LOS, Beden B, Hahn F, Léger JM, Lamy C (1992) Oxidation of formaldehyde in an alkaline medium on a polycrystalline platinum electrode. *J Electroanal Chem* 330:583–594
106. Olivi P, Bulhões LOS, Léger JM, Hahn F, Beden B, Lamy C (1994) New results in the electro-oxidation of formaldehyde on a platinum electrode in an acid medium. *J Electroanal Chem* 370:241–249
107. Karantonis A, Koutsaftis D, Kouloumbi N (2006) Bistability, oscillations and bifurcations of the electrocatalytic oxidation of HCHO on Pt. *Chem Phys Lett* 422:78–82
108. Mishina E, Karantonis A, Yu QK, Nakabayashi S (2002) Optical second harmonic generation during the electrocatalytic oxidation of formaldehyde on Pt(111): potentiostatic regime versus galvanostatic potential oscillations. *J Phys Chem B* 106:10199–10204
109. Akemann W, Friedrich KA, Stimming U (2000) Potential-dependence of CO adlayer structures on Pt(111) electrodes in acid solution: evidence for a site-selective charge transfer. *J Chem Phys* 113:6864–6874
110. Samjeské G, Miki A, Osawa M (2007) Electrocatalytic oxidation of formaldehyde on platinum under galvanostatic and potential sweep conditions studied by time-resolved surface-enhanced infrared spectroscopy. *J Phys Chem C* 111:15074–15083
111. Seidel YE, Jusys Z, Lindström RW, Stenfeldt M, Kasemo B, Krischer K (2010) Oscillatory behavior in galvanostatic formaldehyde oxidation on nanostructured Pt/glassy carbon model electrodes. *ChemPhysChem* 11:1405–1415
112. Pavela TO (1958) *Suom Kemistil* 31:138
113. Buck RP, Griffith LR (1962) Voltammetric and chronopotentiometric study of the anodic oxidation of methanol, formaldehyde, and formic acid. *J Electrochem Soc* 109:1005–1013
114. Krausa M, Vielstich W (1995) Potential oscillations during methanol oxidation at Pt electrodes. Part I: experimental conditions. *J Electroanal Chem* 399:7–12
115. Lee J, Eickes C, Eiswirth M, Ertl G (2002) Electrochemical oscillations in the methanol oxidation on Pt. *Electrochim Acta* 47:2297–2301
116. Bagotzky VS, Vassiliev YB, Khazova OA (1977) Generalized scheme of chemisorption, electrooxidation and electroreduction of simple organic compounds on platinum group metals. *J Electroanal Chem* 81:229–238
117. Hachkar M, Beden B, Lamy C (1990) Oscillating electrocatalytic systems: part I. Survey of systems involving the oxidation of organics and detailed electrochemical investigation of formaldehyde oxidation on rhodium electrodes. *J Electroanal Chem* 287:81–98

118. Vielstich W, Paganin VA, Lima FHB, Ticianelli EA (2001) Nonelectrochemical pathway of methanol oxidation at a platinum-catalyzed oxygen gas diffusion electrode. *J Electrochem Soc* 148:A502–A505
119. Martins AL, Batista BC, Sitta E, Varela H (2008) Oscillatory instabilities during the electrocatalytic oxidation of methanol on platinum. *J Braz Chem Soc* 19:679–687. http://jbcs.sbq.org.br/jbcs/2008/vol19_n4/10-07586AR.pdf
120. Batista EA, Malpass GRP, Montheo AJ, Iwasita T (2003) New insight into the pathways of methanol oxidation. *Electrochem Commun* 5:843–846
121. Batista EA, Malpass GRP, Montheo AJ, Iwasita T (2004) New mechanistic aspects of methanol oxidation. *J Electroanal Chem* 571:273–282
122. Novak M, Cs V (1980) Some observations on oscillatory phenomena in anodic oxidation. *Acta Chim Acad Sci Hung* 105:47–56
123. Rao KV, Roy CB (1977) *J Indian Chem Soc* 54:1180
124. Chen S, Schell M (1999) Bistability and excitability in the electrochemical oxidation of ethanol. *Electrochim Acta* 44:4773–4780
125. Inzelt G, Kertész V, Láng G (1993) Simultaneous oscillations of the surface mass and potential in the course of the galvanostatic oxidation of 2-propanol. *J Phys Chem* 97:6104–6106
126. Chen S, Schell M (2000) Excitability and multistability in the electrochemical oxidation of primary alcohols. *Electrochim Acta* 45:3069–3080
127. Schell M (1998) Mechanistic and fuel-cell implications of a tristable response in the electrochemical oxidation of methanol. *J Electroanal Chem* 457:221–228
128. Chen S, Schell M (1999) A comparison of multistability in the electrocatalyzed oxidations of methanol and ethanol in acid and alkaline solutions. *J Electroanal Chem* 478:108–117
129. Orbán M, Dateo C, De Kepper P, Epstein IR (1982) Systematic design of chemical oscillators. 11. Chlorite oscillators: new experimental examples, tristability, and preliminary classification. *J Am Chem Soc* 104:5911–5918
130. Nagy A, Treindl L (1989) Design of a permanganate chemical oscillator with hydrogen peroxide. *J Phys Chem* 93:2807–2810
131. Chie K, Okazaki N, Tanimoto Y, Hanazaki I (2001) Tristability in the bromate-sulfite-hydrogencarbonate pH oscillator. *Chem Phys Lett* 334:55–60
132. Leung LWH, Weaver MJ (1988) Real-time FTIR spectroscopy as a quantitative kinetic probe of competing electrooxidation pathways of small organic molecules. *J Phys Chem* 92:4019–4022
133. Krischer K, Varela H (2003) Oscillations and other dynamic instabilities. In: Vielstich W, Lamm A, Gasteiger HA (eds) *Handbook of fuel cells*, chapter 46, vol 2, Part 6, Wiley, Chichester, pp 679–701
134. Schell M, Xu Y, Amini A (1994) An electrochemical mechanism for the voltammetric oxidation of methanol and its relationship with period-doubling bifurcations. *J Phys Chem* 98:12768–12775
135. Xu Y, Amini A, Schell M (1995) Mechanistic explanation for a subharmonic bifurcation and variations in behavior in the voltammetric oxidations of ethanol, 1-propanol and 1-butanol. *J Electroanal Chem* 398:95–104
136. Habib MA, Bockris JO'M (1986) Potential-dependent water orientation: an in situ spectroscopic study. *Langmuir* 2:388–392
137. Bockris J, O'M JKT (1992) In-situ studies of adsorption of organic compounds on platinum electrodes. *J Electroanal Chem* 330:541–581
138. Bockris JO'M, Reddy AKN (1973) *Modern electrochemistry*, vol 2. Plenum, New York, pp 779–790
139. Huang W, Li Z, Peng Y, Niu Z (2004) Transition of oscillatory mechanism for methanol electro-oxidation on nano-structured nickel hydroxide film (NNHF) electrode. *Chem Commun* 1380–1381

140. Huang W, Li ZL, Peng YD, Chen S, Zheng JF, Niu ZJ (2005) Oscillatory electrocatalytic oxidation of methanol on an Ni(OH)₂ film electrode. *J Solid State Electrochem* 9:284–289
141. Helms H, Schlömer E, Jansen W (1998) Potential- und Stromoszillationen an Pyrit-Elektroden in sulfidischer Lösung. *Monatsh Chem* 129:1275–1284
142. Xu L, Gao Q, Feng J, Wang J (2004) Oscillations and period-doubling bifurcations in the electrochemical oxidation of thiourea. *Chem Phys Lett* 397:265–270
143. Liu L, Feng J, Wu G, Lu X, Gao Q (2009) Dynamical complexity in electrochemical oxidations of thiocyanate. *Chin J Chem* 27:649–654
144. Küster FW (1905) Beiträge zur Kenntnis der Polysulfide. III. Die periodischen Vorgänge bei Elektrolyse der Polysulfide. *Z anorg Chem* 46:113–143
145. Bohnholtzer W, Heinrich F (1933) Zur Kenntnis der Elektrolyse von Natriumsulfid. *Z Elektrochem* 39:939–947
146. Gerischer H (1950) Reaktionen und periodische Vorgänge an einer Platinanode in Alkalisulfidlösungen. *Z Elektrochem* 54:540–546
147. Helms H, Schlömer E, Jansen W (1998) Oszillationsphänomene bei der Elektrolyse von Alkalisulfidlösungen an Platinelektroden. *Monatsh Chem* 129:617–623
148. Chen A, Miller B (2004) Potential oscillations during the electrocatalytic oxidation of sulfide on a microstructured Ti/Ta₂O₅-IrO₂ electrode. *J Phys Chem B* 108:2245–2251
149. Miller B, Chen A (2005) Effect of concentration and temperature on electrochemical oscillations during sulfide oxidation on Ti/Ta₂O₅-IrO₂ electrodes. *Electrochim Acta* 50:2203–2212
150. Li Z, Cai J, Zhou S (1997) Current oscillations in the reduction or oxidation of some anions involving convection mass transfer. *J Electroanal Chem* 436:195–201
151. Strasser P, Lübke M, Eickes C, Eiswirth M (1999) Modeling galvanostatic potential oscillations in the electrocatalytic iodate reduction system. *J Electroanal Chem* 462:19–33
152. Miller B, Chen A (2006) Oscillatory instabilities during the electrochemical oxidation of sulfide on a Pt electrode. *J Electroanal Chem* 588:314–323
153. Feng J, Gao Q, Xu L, Wang J (2005) Nonlinear phenomena in the electrochemical oxidation of sulfide. *Electrochem Commun* 7:1471–1476
154. Wang S, Yang J, Hu X, Feng J, Gao Q, 218th ECS Meeting, Abstract #2230, ©2010, The Electrochemical Society
155. Bard AJ (1963) Chronopotentiometric oxidation of hydrazine at a platinum electrode. *Anal Chem* 35:1602–1607
156. Schell M, Xu Y, Zdraveski Z (1996) Mechanism for the electrocatalyzed oxidation of glycerol deduced from an analysis of chemical instabilities. *J Phys Chem* 100:18962–18969
157. Hudson JL, Tsotsis TT (1994) Electrochemical reaction dynamics: a review. *Chem Eng Sci* 49:1493–1572
158. Tributsch H, Sakata T, Kawai T (1981) Photoinduced layer phenomenon caused by iodine formation in MoSe₂: electrolyte (iodide) junctions. *Electrochim Acta* 26:21–31
159. Vainas B (1985) A local corrosive breakdown of surface compensated CdS electrodes. *J Electroanal Chem* 184:215–218
160. Hammer C, Walther B, Karabulut H, Lohrengel MM (2011) Oscillating oxygen evolution at Ta anodes. *J Solid State Electrochem* 15:1885–1891
161. Beck F, Jiang J, Krohn H (1995) Potential oscillations during galvanostatic overoxidation of graphite in aqueous sulphuric acids. *J Electroanal Chem* 389:161–165
162. Harrach A, Douglade J, Métrot (1992) Oscillatory behavior of HOPG during its over-oxidation in H₂SO₄-H₂O media. *Mater Sci Forum* 91:689

Chapter 6

Temporal Instabilities in Corrosion Processes

6.1 Oscillations in Anodic Dissolution of Metal Electrodes

6.1.1 General Characteristics of Passivation/Dissolution Processes

Oscillatory dissolution of metal electrodes belongs to the earliest known examples of the nonlinear dynamic phenomena, reported already in the first half of nineteenth century, as it follows from work of Fechner, dated 1828 [1]. In this section, representative examples of such corrosion systems are briefly described. Currently known examples of the corrosion processes that can exhibit oscillatory dynamics include, among others, the following experimental systems: Fe/H₂SO₄; Fe/NaClO₃; Fe/HNO₃, Fe/NaCl; Cu/H₃PO₄; Cu/HCl; Cu/NaCl, Cu/NaClO₃, Ni/H₂SO₄; Ag/KCN + K₂CO₃; Ag/HClO₄, Ag/HCl; Al (including alloys)/KOH; Au/H₂SO₄ + Cl⁻, Co/HCl + CrO₃, Co/H₃PO₄, Co/H₂SO₄ + HNO₃; Pb/LiAlCl₄; Pb/H₂SO₄, Pb/NaOH; Sn/NaOH; Zn/NaOH; Ti/H₂SO₄; Bi/NaCl; Cd/KOH; Nb/HBF₄; and W/NaOH, V/H₃PO₄. Reviews of these phenomena published up to 1994 include, among others, papers by Wojtowicz [2], Hudson and Bassett [3], and Tsotsis and Hudson [4]. Figure 6.1, taken from [2], collects some representative experimentally recorded current or potential oscillations for such systems, as well as, for comparison, examples of oscillations discussed in Chapter 5.

Early discoveries of oscillatory corrosion processes were made during the simple measurements of the *I-U polarization curves*, measured in a two-electrode arrangement, so the ohmic potential drops in the electric circuit were not compensated. Typical polarization curves for such systems are characterized with the abrupt decrease of the anodic current, caused by the passivation effect, at the potentials close to the *Flade potential* (E_F). In the simplest description of those processes, a dissolution of metal electrode to ions in the solution is represented by reaction:



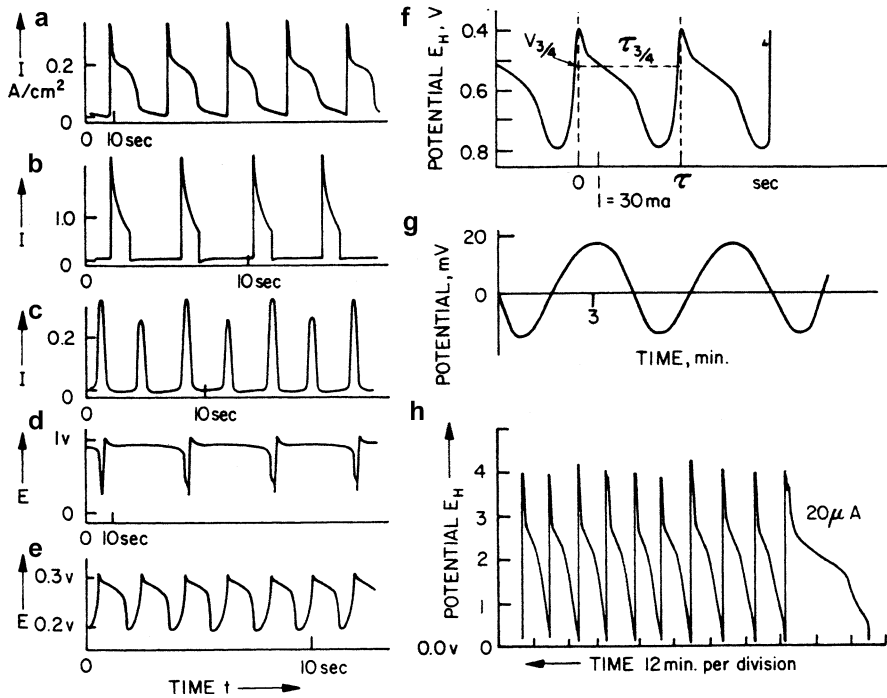
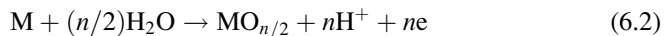


Fig. 6.1 Examples of electrochemical oscillations: (a) Fe/1 N H₂SO₄, $E_H = +0.49$ V, (b) Au/4 N HCl, $E_H = +1.8$ V, (c) Zn/4 N NaOH, $E_H = -1.1$ V, (d) Fe/14 N HNO₃, $I = -40$ mA/cm², (e) Cu/0.4 N CrO₃ + 1 N HCl (rest potential), (f) Pt-Pt/1 M CH₃O + 3.75 M H₂SO₄, $I = -30$ mA/cm², (g) Pt/0.1 M N₂H₄ + 1 M KOH (rest potential), (h) Pd/1 M HCOOK + 1 M KOH, $I = +0.2$ mA/cm² (after [2] and references cited therein). Reprinted from [2] with kind permission from Springer Science +Business Media B.V.

characterized with the formal potential E_1^0 , while the process of the formation of the passive oxide layer can be described with the reaction scheme:

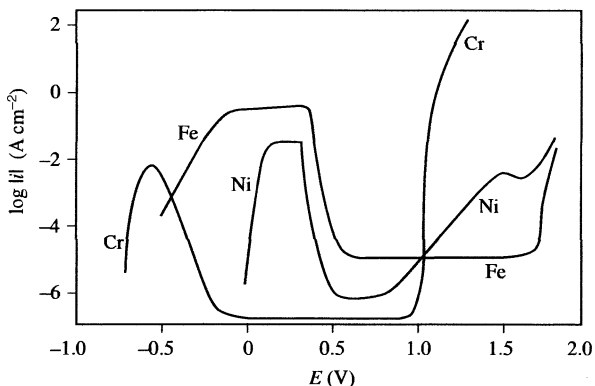


which is characterized with the respective value of E_2^0 , more positive than E_1^0 . In terms of this notation, the *thermodynamically* determined Flade potential can be considered as equal to equilibrium potential of the reaction (6.2), and at 298.15 K:

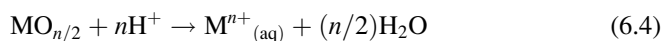
$$E_F = E_2 = E_2^0 + \frac{RT}{nF} \ln [H^+]^n = E_2^0 - 0.059\text{pH} \quad (6.3)$$

The Flade potential is thus a linear function of pH of the solution, with a negative slope being *independent of the stoichiometry of the metal oxide* (n). The Flade potential depends on pH in the same way, as the potential of the hydrogen or any pH-sensitive oxide electrode.

Fig. 6.2 Schematic anodic polarization curves of Fe, Ni, and Cr in 0.5 M H₂SO₄ [5]; (after experimental data given in: Okamoto G (1973) Passive film of 18-8 stainless steel structure and its function. Corrosion Sci 13:471–489, Fig. 10). Reproduced from [5] with permission of Taylor & Francis Group LLC. Copyright 2007



In turn, the passive oxide layer MO_n may dissolve also *chemically*, according to the equation:



The sum of Eqs. (6.2) and (6.4) is identical with the overall metal dissolution reaction (6.1) in which the passive layer is an intermediate species. In the steady-state, the oxide layer is continuously regenerating itself, with the rate of its dissolution in the electrolyte equal to the corrosion rate of the metal [5].

According to Chap. 2, the passivation of the electrode surface is one of the causes of a region of a negative differential resistance (NDR) which can be a source of instabilities if coupled to ohmic potential drops, with contribution from the reagents transport phenomena. Thus, one can expect the bistability and oscillations of current in the NDR region, under appropriate conditions. Exemplary polarization curves of several metal electrodes are collected in Fig. 6.2 [5]. In turn, Fig. 6.3 indicates schematically their three distinct sections [6]: the active region in which oxidation of metal to respective ions occurs with the rate increasing with the (positive) electrode potential; the passive region, following the Flade potential, when the current drops to negligible values; and the *transpassive region* at sufficiently positive potentials, where the oxygen evolution due to oxidation of water occurs and in which also often the destruction of passive layer, unblocking the electrode surface, takes place.

These schematic dependences and underlying chemical equations are relatively simple, but the behavior of real metal electrodes is more complicated.

6.1.1.1 Hysteresis and Bistability in the Active/Passive Transition

First, the Flade potential determined by Eq. (6.3), as a thermodynamic value, should not depend on the direction of cyclic potential changes toward negative or positive values. However, in typical experiments one often observes the hysteresis in the

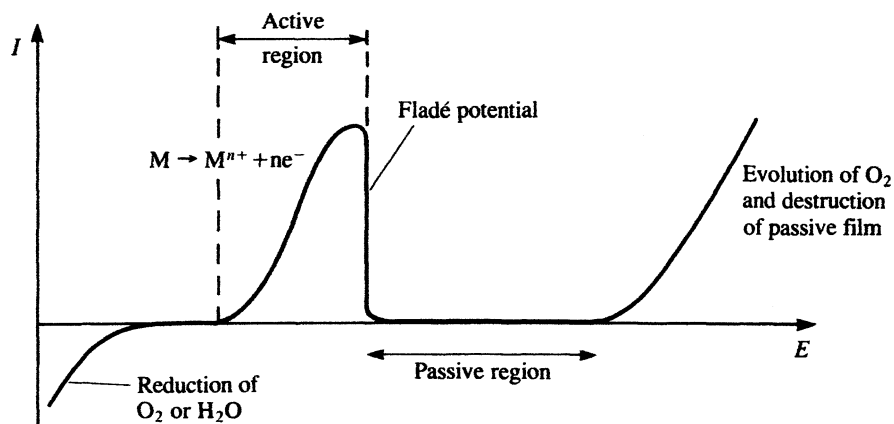


Fig. 6.3 Voltammetric curve for a metal that forms a passive film, e.g., nickel. Reprinted from [6] by permission of Oxford University Press

current–voltage response—thus also the dependence of the potential, at which the active–passive transition occurs, on the scan direction. This effect can result from trivial kinetic limitations on the way of the system toward its thermodynamic characteristics. It is also possible that in the presence of uncompensated ohmic drops, the region of the I – E characteristics with a negative dE/dI slope transforms into the set of unstable steady-states, separating the upper and lower branches of the stable steady-states; hysteresis is then a manifestation of bistability. If this is the case, the appropriate correction of the I – U curve for the ohmic drops should lead to the I – E curve without hysteresis. Such successful correction was reported, e.g., by Russell and Newman [7] for Fe dissolution in 1 M H_2SO_4 . However, Epelboin et al. [8] have observed certain hysteresis leaving even after appropriate IR correction applied to I – U curve recorded for the ring Fe electrode in the same medium. This discrepancy was explained by pointing out that such simple IR correction is a simplification since it is referred to the total current which however can be *inhomogeneously distributed* at the electrode surface. Even earlier, the inhomogeneity of the dynamics developing on the circular Fe electrode was indicated by Pigeau and Kirkpatrick [9] who have shown experimentally that the current oscillations were accompanied by the growth of a zone with higher reflectance, emerging from the outer rim of the electrode and propagating toward its center. These facts are strong premises for considering of the process of metal dissolution at a microscopic level, i.e., in terms of the dissipative pattern formation due to local and global dynamics of the process (see Sect. 1.2, volume II). In other words, a really solid explanation of reported dynamic instabilities in the passivation/dissolution systems should invoke the spatial inhomogeneity of the electrode–solution interface and such approach will be discussed in Chaps. 1–3 of volume II. Here we shall only mention, as an example, that Hudson et al. [10] have proved that the period-doubling bifurcation, observed in the oscillatory current–time series for the ring-shaped Fe electrode, originated from a *spatiotemporal* bifurcation from a ring of activity into two half-rings of alternating activity.

6.1.1.2 Porous Salt Layer as a Precursor of the Oxide Film

The next source of complexity of real passivating systems is that between the active state of metal electrode and its passive state, caused by the compact layer, often a porous layer is formed, of the composition dependent both on the metal and components of the electrolyte solution. For example, for the Fe/H₂SO₄ system this porous layer can be simplified as hydrated FeSO₄ [with possible participation of, e.g., hydroxo forms of Fe(II)]. Formally, it means that the surface concentration of Fe²⁺ ions becomes so high that the solubility product of FeSO₄ is locally exceeded and crystals of FeSO₄ precipitate on the surface. The thickness of such porous layer may increase up to 1 mm [5]. FeSO₄ is thus considered a precursor of the oxide layer that forms at more positive potentials. It is usually accepted that solid FeSO₄ is poorly conducting and the oxidation current flows largely in the pores of these species when the solution is in direct contact with the active metal surface.

Upon increasing positive potential, for given concentration of H₂SO₄, the total current can stabilize at the relatively high, limiting value, forming thus an anodic current plateau under steady-state conditions. Quite formally, one can say that although the resistance of FeSO₄ species is high, the *net* resistance of the salt layer, caused by the presence of pores, is relatively low. Significant premises for the mechanism underlying the formation of this plateau were supplied by the experiments with rotating disk electrode, which showed the increase of this plateau with increasing rotation rate (Fig. 6.4, [5]). Thus, the limiting current can be considered as determined by the rate of mass transport—in this case by the potential-independent convective diffusion of the dissolved FeSO₄ species from the solid layer at the electrode toward the bulk of the solution. The detailed picture of phenomena occurring at the interface can be even more complex. In the pores local current density may attain such high values, that increasing anodic polarization of the electrode may cause local formation of oxide layer which later dissolves, when H⁺ ions can diffuse back to the pores. Such alternate formation and dissolution of the oxide layer was observed experimentally.

Further studies show however that the origin of limiting anodic current is not always completely understood. Keddam [12], based on analysis of electrohydrodynamic (EHD) impedance data, has suggested the existence of the viscosity gradient in the boundary layer and thus that the only species that limits the dissolution rate is water. Since it is difficult to analyze the conventional ac impedance spectrum measured on the diffusion plateau of the anodic dissolution of metal, it therefore appears useful to complement such measurements with the EHD impedance data. The latter method involves perturbing the rotation speed of electrode and measuring the current; the results reveal directly the influence of mass transport on surface phenomena. The reader interested in the principles and applications of EHD impedance method, introduced by Bruckenstein at the beginning of 1970s, is advised to consult the appropriate references, e.g., [13, 14].

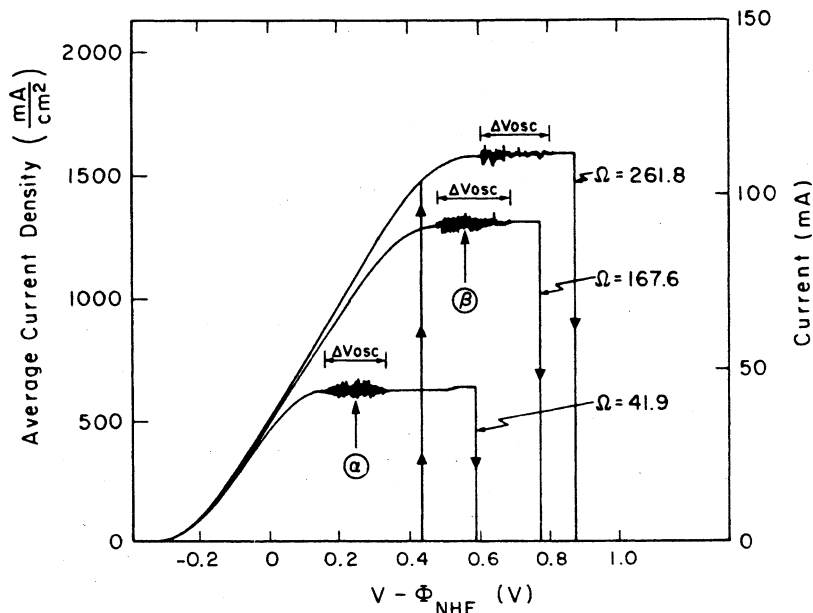


Fig. 6.4 Potentiodynamic sweep curves for an Fe rotating disk electrode, with radius = 0.149 cm, in a 1 M H_2SO_4 electrolyte. Regions in which oscillations are observed are indicated. Electrode rotation speeds are given in rad s^{-1} . Reproduced from [11] by permission of The Electrochemical Society

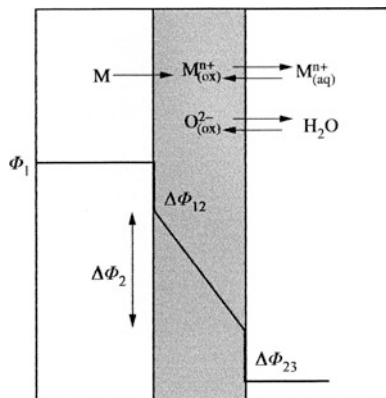
6.1.1.3 The Nature and Properties of Passive Film

The relatively small current density flowing in the passive region is called the passivation current density (i_p) which can be dependent on various factors including pH of the solution. For example, for the Fe/ H_3PO_4 system, the passivation current density decreases with increasing pH, due to decreasing solubility of $\text{Fe}(\text{OH})_2$ that precipitates at the Fe surface. Thus, pH can affect not only the Flade potential, but also the magnitude of i_p .

Typically the passive oxide layer is very thin (1–3 nm), and then the electron conductivity realizes through the tunneling across it. If the thickness of such layers increases, the probability of tunneling decreases and then they reveal the (usually) semiconducting properties, characterized with forbidden band of 2–3 eV. This is the case, e.g., for Fe oxides (n -type semiconductor) and Cu or Ni oxides (p -type semiconductors). For comparison, PbO_2 can be considered a metallic conductor, while Al_2O_3 is an insulator.

The composition and structure of passive layers (films) on metal surfaces are usually very complex and difficult to unambiguous determination, also because they may vary with experimental conditions. For example, although typically the oxidation state of the metal in the passive oxide film corresponds to the thermodynamically most stable oxide (e.g., oxides of Ni^{2+} , Al^{3+} , Fe^{3+} , Cr^{3+}), it

Fig. 6.5 Variation of potential across a passive film (schematic). Reproduced from [5] with permission of Taylor & Francis Group LLC. Copyright 2007



may happen that the most stable oxidation state varies with the electrode potential. Thus, at sufficiently high positive potentials, nickel in an alkaline medium forms passive oxide of Ni^{3+} ; for chromium, the rise of anodic current at the onset of the transpassive region is caused by the transformation of the passive layer of Cr_2O_3 into well soluble CrO_3 species [5]. Moreover, Eq. (6.1) and (formally identical) sum of Eqs. (6.2) and (6.4) may differ with the number of electrons involved, e.g., active dissolution of Fe leads to Fe^{2+} ions, while passive dissolution leads at least mainly to Fe_2O_3 as the most stable oxide under typical conditions [5].

Another chemical detail is the presence of hydroxyl groups at the surface of the oxide film which contacts with the electrolyte solution. This may be caused either by hydration of the oxide surface, or by the precipitation on it, of the thin metal hydroxide layer. Furthermore, the oxide layer can be doped with small amounts of foreign ions from the electrolyte (e.g., SO_4^{2-} or Cl^-) which enter the oxide layer during its growth and either occupy the crystal lattice sites of O^{2-} ions or are located at the defects of that lattice [5].

The growth and the dissolution of the passive oxide films involve ion-transfer reactions at the metal–film and the film–electrolyte interfaces, with the electric potential distribution sketched in Fig. 6.5.

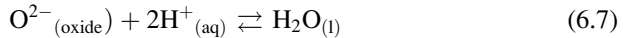
At the metal–film interface, the produced metal ions occupy the cationic sites of the oxide:



The strong (10^8 V/cm) electric field present in the film causes the migration of cations toward the solution phase, whereas the anions migrate in the opposite direction. At the film–solution interface, the metal ions move into the solution:



while the O^{2-} ions are involved in the reversible dissolution or deposition process [5]:



Reaction (6.7) controls whether the oxide film grows or thins. Since both reactions (6.6) and (6.7) involve charged particles, their rate depends exponentially on the potential difference at the film–electrolyte interface ($\Delta\Phi_{23}$ in Fig. 6.5). In turn, the current corresponding to ionic conduction through the film is exponentially dependent on the average electric field in the film, given by the $\Delta\Phi_2/L$ ratio, where L means the thickness of the film.

6.1.1.4 Transpassive Region and Pitting Corrosion

In *transpassive region* (cf. Figs. 6.2 and 6.3), the substantial rise of current density observed at the potential denoted further as E_b can be due to the following processes [5]:

1. Transpassive dissolution (oxidation) of the passive film (then E_b is the *film breakdown potential*).
2. Dissolution by *pitting* resulting from *local* film breakdown (if this process is predominating, E_b means the *(critical) pitting potential*).
3. Oxygen evolution due to water oxidation, if the latter process begins at potentials less positive than the passive film breakdown; if passive oxide film is very stable, the current in transpassive region is caused exclusively by oxygen formation.

The composition of the solution can decide which of these processes causes the initial rise of current. Cl^- ions are particularly well recognized as the species causing the pitting corrosion of the passive layer—above the critical (pitting) potential the film breakdown occurs at certain sites and enhanced localized dissolution leads to the formation of deep pits on an otherwise passive surface. The diameter and the depth of the single pit usually reach several tens of micrometers [5]. In such a case, the pitting corrosion of the passive layer can precede the oxygen evolution. On the other hand, if the aggressive anions are absent (as, e.g., for $NaNO_3$ solution) the transpassive potential of, e.g., Fe and Ni appears to be higher than the reversible potential of the oxygen evolution, which is then responsible for the rise of anodic current in the transpassive region. At more anodic potential the film dissolution begins, which is also facilitated by the earlier oxygen evolution, since the solution at the anode becomes locally acidified: $H_2O \rightarrow 2H^+ + 1/2O_2 + 2e$.

The corrosive interaction of Cl^- ions with the passive layer can occur according to three mechanisms, depicted in Fig. 6.6.

In terms of mechanism (a) the Cl^- ions, driven by electric field, penetrate the film layer, changing its properties and facilitating the dissolution after certain induction time, which is required for the migration of the anion from the film–solution interface to the metal surface. Mechanism (b) occurs when due to

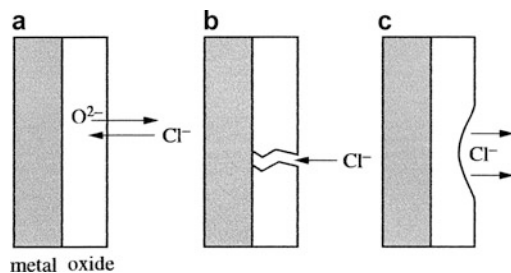


Fig. 6.6 Proposed anodic depassivation mechanisms in presence of chloride ions: (a) anion penetration into the film by exchange with O^{2-} ; (b) electrolyte penetration at the metal surface through film defects; (c) film dissolution caused by local anion adsorption. Reproduced from [5] with permission of Taylor & Francis Group LLC. Copyright 2007

the defects, the electrolyte is in direct contact with the metal surface and a local rapid dissolution occurs with the formation of a pit. Finally, according to mechanism (c), the anodic depassivation is caused by an accelerated dissolution of the passive film as a result of adsorption of aggressive anions at the outer film surface, replacing hydroxyl groups (as was experimentally proved for the iron electrode); the intensive rise of current occurs after some time, necessary for pit initiation [5]. Of course, pitting corrosion is a localized corrosion, so it is characterized with increasing heterogeneity of the metal/solution interfaces—this aspect of such processes and their consequences for nonlinear dynamic behavior will be analyzed also in Sect. 3.1.10 of volume II.

High-rate transpassive dissolution of passivated metals is used in practice for electrochemical machining and micromachining: in this case the appropriately shaped cathode is moved over the surface over the anode, with the interelectrode distance of the fraction of millimeter kept constant. Datta and Romankiw [15] have described the anodic dissolution of metals through the patterned photoresist. Another example of micromachining of Cu substrate, but based on different principle, is described in Sect. 6.2.

In order to complete these brief outline characteristics of the corrosion process, one should note that also the rate determining step can depend on the electrolyte composition. When steel corrodes in contact with acids, the bottleneck is the kinetics of the electron-transfer reaction at the metal/electrolyte interface. If the steel is contacted with the neutral, aerated solution, the rate of mass transfer of the oxidizing agent of anodic reaction products takes over the control on the reaction rate. Finally, for the stainless steel in aqueous solution, the small rate of corrosion rate is determined by the properties of the passive film [5].

The reader interested in more detailed characteristics of corrosion processes is advised to consult, e.g., the recently published monograph by Landolt [5] or earlier books by Keddam [12] and Kiss [16] and references cited there.

6.1.2 The Fe/H₂SO₄ Oscillatory System

6.1.2.1 Experimental Characteristics

Simple experiment, described in 1941 by Bonhoeffer and Renneberg [17], has proved that the active or passive states of iron are only stable. If a piece of passivated iron is touched with Fe wire in active state, the activation of passive piece occurs, provided that the surface area of the active iron wire is large enough (usually the surface as small as 0.1% of the passive surface suffices to activate it) [18]. Later, Franck and Meunier [19] have reported that if a completely passivated electrode (alone stable in this state) is coupled with the active one (also alone stable in this state), the state of either one of them, or of both begins to oscillate. It was thus another experimental proof that the mixed electrode with a two-phase structure of the surface is unstable. Moreover, it is a premise to consider the source of instabilities in coupled oscillators (Chap. 3, volume II).

According to Hudson et al. [10], based on studies to date, one can distinguish between two distinct regimes of Fe dissolution in aqueous H₂SO₄ electrolyte. The first type of the oscillations is observed on the mass-transferred controlled plateau of anodic current, just before the active–passive transition, and is presumably connected with the formation and removal of a porous salt film (cf. Fig. 6.4). These oscillations exhibit relatively small amplitude, but high frequency (0.1–1 kHz) [11, 20, 21] and the degree of their complexity is dependent on the electrode size [22]: with electrode diameter increasing from 2.0 mm to 6.35 mm regular oscillations turned into low-order chaos, followed by high-order chaos. In the authors' opinion, these transitions were due to increasing coupling between the various sites on the electrode surface, so the full explanation of these phenomena should involve the concept of coupled oscillators, as mentioned already above. Regarding chaos, quantitative analysis of respective $I-t$ courses (correlation dimension ranging from 2.4 up to 6) suggested its deterministic nature. More recently, studies of this type of oscillations have been undertaken by Sazou and Pagitsas [23] who have elaborated the mechanism indicating the role of IR drop and appropriate hydrodynamic conditions in their onset.

The second type of oscillations, observed in most reported experiments [24], is characterized with typical relaxation shape. These instabilities, ascribed to the transitions between the active and passive states of Fe electrode, reveal the oscillation periods of the order of seconds to minutes and constitute the main type of instabilities described below in this section.

Bursting Oscillations as a Model of Neural Excitation

Complex oscillations in the Fe/H₂SO₄ system can be observed upon addition of halides which cause *pitting corrosion* of the passive anodic film. In particularly interesting case, described by Sazou et al. [25], the pitting corrosion causes the

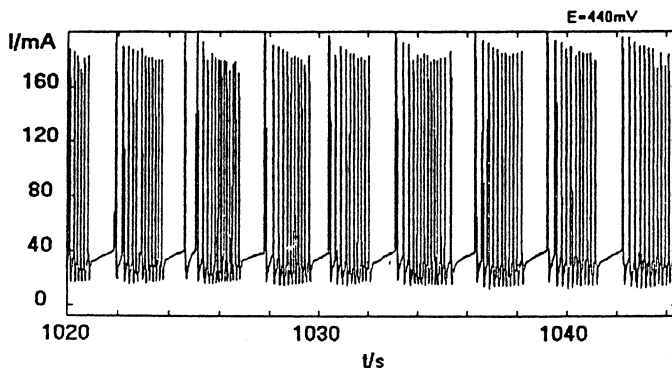


Fig. 6.7 Bursting oscillations during the dissolution of a Fe disk in 2 M $\text{H}_2\text{SO}_4 + 0.04 \text{ M Cl}^-$; rotation rate 1,000 rpm. $U = 440 \text{ mV}$ vs. SCE. Reprinted from [25], Copyright 1992, with permission from Elsevier

complex oscillatory behavior in which trains of relaxation oscillations are separated by the periods of steady-state passivity. According to Koper [24], such *bursting oscillations* (Fig. 6.7) can be explained in such a way that a relatively slow pitting corrosion process acts as a switch of the system's state between the passive and the oscillatory state.

The bursting dynamics, as occurring in neurons activity [26], is worth of theoretical and experimental studies. Mathematically, the bursting dynamics can be described as involving fast and slow essential variables, depending on the timescales over which they vary [27, 28]. The fast subsystem, described by a minimum of two variables, is responsible for the fast spiking. The slow subsystem is responsible for the slow modulation causing the periodic appearance of the fast spiking behavior (in the simplest case it involves one slow variable). More recently, Kiss et al. [29] have analyzed the bursting oscillations in the electrodisolution of iron in sulfuric acid solution. Under conditions of those experiments, this system exhibited such oscillations in which fast periodic spiking was superimposed on chaotic, slow oscillations. The role of external potential, external resistance, and electrode diameter in the transition from the chaotic to bursting oscillations was studied and the bifurcation scenarios, involving the Hopf and homoclinic bifurcations, were indicated.

Electrochemical Model of Unidirectional Synaptic Transmission

Analogies between the neural excitation and instabilities in the $\text{Fe}/\text{H}_2\text{SO}_4$ system are not limited to bursting oscillations. Karantonis et al. [30] have described the system, imitating the neural synaptic transmission, corresponding to unidirectional chemical signaling. The experimental setup consisted of an $\text{Fe}/\text{H}_2\text{SO}_4$ electrochemical oscillator stimulated by the chemical interaction achieved via the flow of chloride ions toward the electrode surface, controlled by peristaltic pump

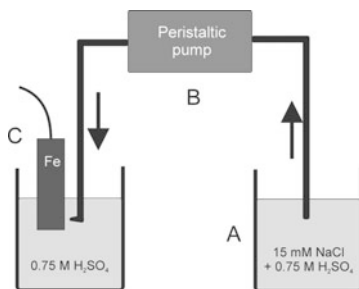


Fig. 6.8 Schematic representation of the experimental setup. A chloride containing solution: 15 mM NaCl + 0.75 M H_2SO_4 (A) is injected via a peristaltic pump (B) to the surface of an iron electrode (1 mm diameter disk) (C) immersed in 0.75 M sulfuric acid solution. The distance between the outlet of NaCl solution and the Fe electrode surface was 2 mm. SCE and a carbon rod were employed as the reference and auxiliary electrodes, respectively. Based on [30]

(Fig. 6.8). The microtube through which this solution was being introduced to the electrochemical cell was placed in a distance 2 mm away from the surface of an iron disk.

In this experimental setup, the $\text{Fe}/\text{H}_2\text{SO}_4$ interface mimicked the postsynaptic neuron that could occur in electrodissolving (active) state, passive state or exhibit oscillations between the former two extreme states, depending on the external voltage applied. In turn, the presynaptic terminal was imitated by a controlled source of chloride ions which, as interacting with the active/passive transitions of the iron electrode through the pitting corrosion, acted as chemical transmitters. Since the inflow of chloride ions is controlled externally from its source by the peristaltic pump, the purely chemical connection of the source of chemical transmitter with the $\text{Fe}/\text{H}_2\text{SO}_4$ interface was unidirectional.

The nonlinear dynamical characteristics of the electrochemical system, under given conditions, are visualized by the $I-U$ dependence, obtained upon cyclic variation of the external potential U . This diagram shows the regions of existence of the passive, active and oscillatory states of the iron electrode, including their coexistence, revealed by the hysteresis in the system's response (Fig. 6.9).

The effect of the inflow of Cl^- ions depends on the applied (fixed) voltage and in which of the states (if more than one are possible) the system initially remained. For $U = 215$ mV and the electrode in bistable region, in the active steady-state (I equal to ca. 2.5 mA), this state loses its stability and the oscillations set in (Fig. 6.10). One can say that the chemical signal in the form of Cl^- ions has been noticed by the $\text{Fe}/\text{H}_2\text{SO}_4$ interface which changed its trivial, steady-state dynamics into the oscillatory one.

In another experiment, at the same voltage $U = 215$ mV, the electrode was set initially in the oscillatory state and the same chemical signal of Cl^- ions was applied—then the dynamics of the electrochemical system returned to the trivial, active steady-state (Fig. 6.11). Thus the transition to the oscillatory regime appears to be reversible with that reservation that in the sequence: steady-state \rightarrow oscillations \rightarrow steady-state, the final steady-state current is a bit higher than the

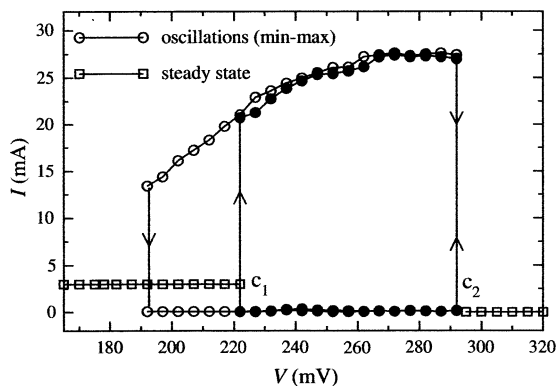
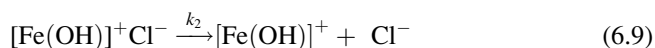
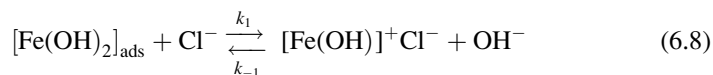


Fig. 6.9 Experimental bifurcation diagram (potentiostatic curve) of the Fe/0.75 M H₂SO₄ system. Squares represent steady-states. Black and white circles represent the minimum and maximum of stable oscillations for increasing and decreasing values of external voltage V , respectively. Reprinted from [30], Copyright 2008, with permission from Elsevier

initial one, presumably due to the progress of the pitting corrosion of iron under influence of Cl⁻ ions, causing the increase of the roughness, and thus the surface area of the electrode.

In turn, when the applied potential was close to the bifurcation value of ca. 290 mV, the dynamic response depended on that, how positive was the applied voltage vs. this critical value. In any case, the electrode remained initially in the passive state. For $U = 320$ mV, a single, narrow high-amplitude current peak is formed following a prolonged (10 s) single chemical pulse. When the voltage is very close to the bifurcation value, i.e., $U = 295$ mV, every chemical signal of even short duration time (1 s) causes an almost immediate, sharp response of the current, so the sequence of such signals, produced by peristaltic pump is matched with the corresponding series of current peaks, as long as the chemical signal is produced. Finally, if the voltage is placed in the oscillatory region (e.g., $U = 265$ mV), the perturbation of this regime with periodic chemical signal causes the significant decrease of the oscillatory period and the emergence of current *bursts* (Fig. 6.12a) or, for higher amplitude of perturbation, the temporal decay of the oscillations, followed by their return with gradually increasing amplitude (Fig. 6.12b).

As the chemical mechanism underlying the above phenomena, the destruction of adsorbed Fe(OH)₂ layer was proposed as occurring through the formation of the [Fe(OH)⁺]Cl⁻ salt exhibiting higher solubility:



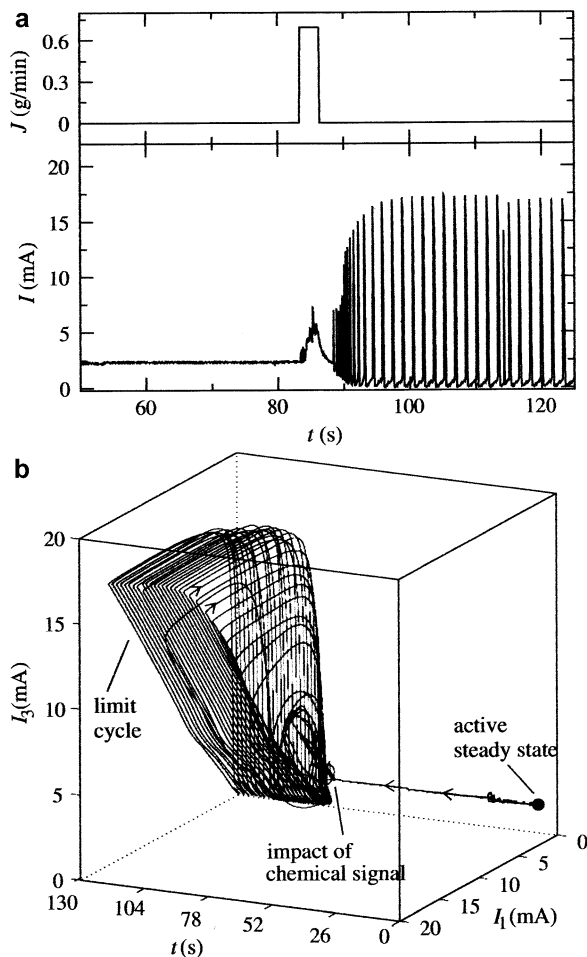
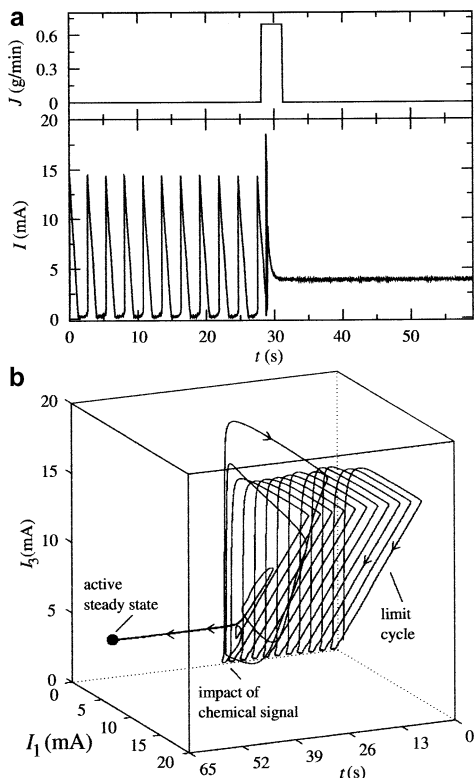


Fig. 6.10 (a) Current response of an active iron interface under the influence of a single chemical pulse. Applied potential $V = 215$ mV, pulse amplitude $J = 0.6948$ g/min, pulse duration $\Delta t = 3$ s. (b) Projection of the trajectories for embedding dimension $m = 3$ and time delay $\tau = 0.01$ s. Reprinted from [30], Copyright 2008, with permission from Elsevier

One should also note that the Fe/H₂SO₄ active/passive system was also used long ago by Franck [31] as the electrochemical model of the nerve transmission along the neuron, since both phenomena exhibit striking analogies in their dynamics. This instructive experiment is outlined in Sect. 2.1 of volume II.

The pitting (as well as the general) corrosion of iron in the H₂SO₄ medium, in the presence of halides, in the context of nonlinear dynamical phenomena still remains a subject of experimental studies, reported by Pagitsas et al. [32–36]. In these studies, the microscopic nature of processes leading to corrosion was deepened and described in terms of the point defect model. Among others, based on the

Fig. 6.11 (a) Current response of an oscillatory iron interface under the influence of a single chemical pulse. Applied potential $V = 215$ mV, pulse amplitude $J = 0.6948$ g/min, pulse duration $\Delta t = 3$ s. (b) Projection of the trajectories for embedding dimension $m = 3$ and time delay $\tau = 0.01$ s. Reprinted from [30], Copyright 2008, with permission from Elsevier



nonlinear dynamic response of passive iron surfaces, perturbed chemically by halides, it was possible to distinguish between the general and pitting corrosion.

Finally, Lou and Ogura [37] have described current oscillations observed on a stainless steel electrode in sulfuric acid solution with and without chromic acid, and attributed them to the periodic sequence of dissolution and reformation of $M(\text{OH})_3$ film, which was formed by the reaction of divalent metal ions dissolved in the earlier stage of polarization of the stainless steel.

6.1.2.2 Theoretical Models

In this section, the most important models of the oscillatory dissolution of iron electrode in aqueous sulfuric acid media, both outlining the early historical proposals and discussing in more detail the most recent achievements, are briefly described. The analysis of the evolution of these concepts is very instructive, not only because it shows increasing understanding in the mechanism of such processes. One can note that completely different mechanisms of the same electrochemical process can mathematically generate oscillations, so the choice of the

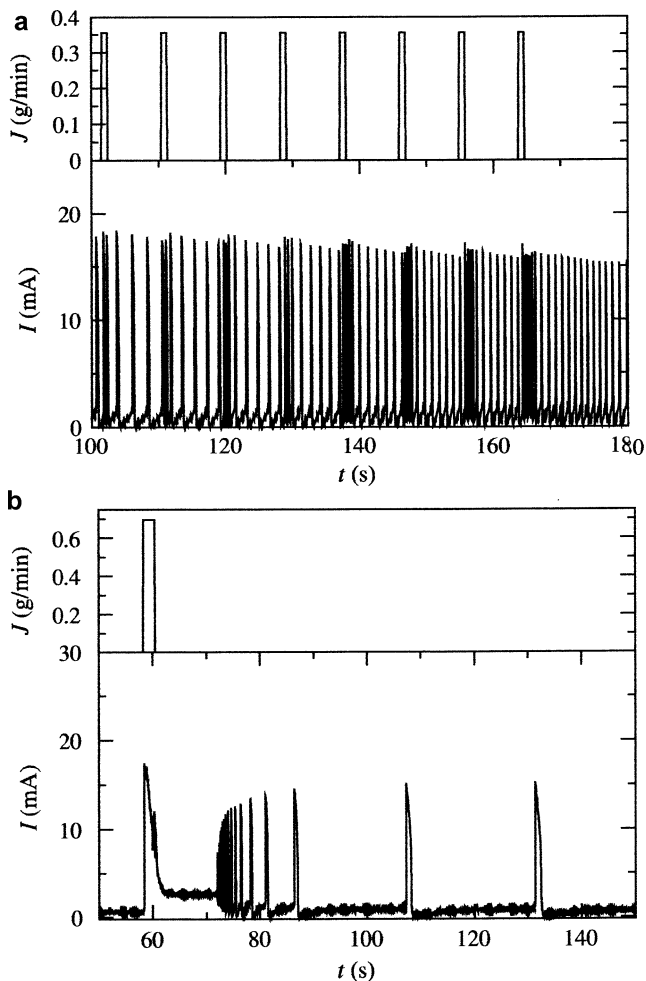


Fig. 6.12 (a) Current response of an oscillatory iron interface under the influence of a chemical pulse train. Applied potential $V = 265$ mV, pulse amplitude $J = 0.3559$ g/min, pulse duration $\Delta t = 3$ s. (b) Current response of an oscillatory iron interface under the influence of a chemical pulse for $V = 274$ mV and pulse amplitude $J = 0.6948$ g/min. Pulse duration $\Delta t = 1$ s. Reprinted from [30], Copyright 2008, with permission from Elsevier

most reliable model requires deepened knowledge on the detailed electrochemical properties of the system.

Generally, the models explaining the oscillations in the Fe/acid solution system are based on the idea of switching between the active and passive states. As mentioned above, only one of these extreme states is stable under given conditions, with the intermediate state being unstable: if two iron electrodes, one completely passivated and the other in active state, are brought into contact, either the active undergoes passivation, or the passive one becomes active, depending on the relation of the mixed potential of these two electrodes to the Flade potential [2].

The Franck–FitzHugh Model and Related Approaches

In 1961, Franck and FitzHugh [38] have published the first significant explanation of the oscillatory dissolution of Fe electrode in sulfuric media, under potentiostatic ($U = \text{const}$) conditions, based on the dependence of the Flade potential on the (periodically varying) pH of the solution in contact with the Fe surface. The mechanism of oscillations involves the following steps:

1. Initially the electrode is in its active state ($E < E_F$), meaning the flow of current of high density (reaching even tenths of A cm^{-2}), associated with the intensive dissolution of Fe surface. Since in the solution this current is conducted largely by H^+ ions which migrate toward the counter-electrode, their local concentration at Fe electrode decreases; that means that migration caused certain concentration gradient of $[\text{H}^+]$ in the solution.
2. Induced in this way local increase of pH of the solution in contact with Fe surface means progressing shift of its Flade potential toward more negative values [cf. Eq. (6.3)], and when E_F becomes more negative than the actual Fe potential E (i.e., $E > E_F$), the electrode undergoes abrupt passivation—the anodic current drops to $\mu\text{A cm}^{-2}$.
3. Due to actually low current, the migration of H^+ ions toward the cathode is significantly slowed down and the diffusion of H^+ ions from the solution bulk restores now their concentration in the vicinity of the Fe electrode.
4. The stepwise decrease of solution pH at the electrode causes chemical dissolution of the passive layer and the reactivation of the Fe electrode when its Flade potential returns to more positive values: $E < E_F$; the oxidation current then rises. The oscillation loop is completed and the whole cycle repeats. The oscillation period is thus related to the time scale of the transport of H^+ ions in the solution.

The mathematical representation of this model involves two ordinary differential equations:

$$\frac{d\varepsilon}{dt} = K_1 - K_2\varepsilon - K_3\theta + K_4\varepsilon W(\varepsilon, \theta) \quad (6.10)$$

$$\frac{d\theta}{dt} = K_5\varepsilon W(\varepsilon, \theta) \quad (6.11)$$

in which $\varepsilon = E - E_F$ measures the distance between the imposed (constant) electrode potential E and the pH-dependent Flade potential E_F , while θ is the electrode coverage with the passive film layer. K_i values ($i = 1, \dots, 5$) are the kinetic constants which include various parameters of the current–voltage dependence for Fe dissolution and both diffusion and migration characteristics of H^+ ions. The detailed form of these equations is determined by further detailed assumptions. First, the passive oxide film forms if $\varepsilon > 0$ and dissolves for $\varepsilon < 0$; the kinetics of these processes are described with different dependences:

$$W(\varepsilon, \theta) = \begin{cases} \theta & \text{for } \varepsilon < 0 \\ 1 - \theta & \text{for } \varepsilon > 0 \end{cases} \quad (6.12)$$

or, in an equivalent form:

$$W(\varepsilon, \theta) = \theta + (1 - 2\theta)U(\varepsilon) \quad (6.13)$$

where $U(\varepsilon)$ is a Heaviside staircase function, taking only two values, depending on the sign of the argument ε : $U(\varepsilon) = 0$ for $\varepsilon < 0$ and $U(\varepsilon) = 1$ for $\varepsilon > 0$. Thus, different equations describe the system's dynamics, when the electrode potential is lower and when it is higher than the actual Flade potential. For $\varepsilon < 0$ the rate of the oxide layer dissolution is proportional to the electrode coverage θ with this passive layer, while for $\varepsilon > 0$ the rate of formation of the passive layer is proportional to the fraction of the electrode surface, uncovered with oxide ($1 - \theta$). This discontinuous change of the reaction kinetics at the Flade potential is a key feature of the FFH model, but become later a main reason for its certain criticism.

Further assumptions introduce the following simplifications: the I - E dependence is considered linear, the Flade potential is linearly dependent on pH, the concentration profile of H^+ ions at the Fe electrode is linear, and the H^+ ions are considered the only charge carriers of the electric current in the solution. Finally, the rate of formation of H^+ ions during the interaction of Fe^{2+} ions and water molecules, leading to the passive oxide layer, is negligible compared to the rates of migration and diffusion transport of these ions.

Wang et al. [39] have shown that the nonphysical discontinuity of the model can be overcome by replacing the Heaviside function with the smooth dependence:

$$\chi(\varepsilon) = 1 - \frac{1}{1 + \exp(a\varepsilon)} \quad (6.14)$$

which becomes sufficiently steep for $a \geq 500$. This is however more a mathematical transformation than the enhancement of the physical sense of the model. It is further convenient to transform the dimensioned variables to their dimensionless equivalents: the potential $V = K_5\varepsilon/K_2$ and the time $\tau = K_2t$, in terms of which Eqs. (6.10)–(6.11) take a form:

$$\frac{dV}{d\tau} = bh - V - b\theta + (V/c)G(V, \theta) \quad (6.15)$$

$$\frac{d\theta}{d\tau} = VG(V, \theta) \quad (6.16)$$

where:

$$G(V, \theta) = \theta + (1 - 2\theta)\chi(V) \quad (6.17)$$

$b = K_3K_5/K_2^2$, $h = K_1/K_4$ (with $0 \leq h \leq 1$) and $c = K_2/K_4$, the latter quantity c being the *bifurcation parameter* which determines the qualitative dynamics of the system in a following way. For $c > 0.5$ only a single stable steady-state exists, defined with $(V_{ss}, \theta_{ss}) = (0, h)$. At $c = 0.5$ the *supercritical* Hopf bifurcation occurs, i.e., upon c decreasing further below 0.5 the oscillations are born, with the amplitude rising from zero at a bifurcation point. Figure 6.13 shows exemplary oscillations obtained from numerical integration of Eqs. (6.15) and (6.16) for $c = 0.25$ and other parameters specified in the caption.

This simple, only two-variable model allows to reproduce only regular, high-amplitude oscillations for the potentials close to E_F , and is not able to explain formation of low amplitude oscillations, observed also for $E < E_F$ and of aperiodic (chaotic) oscillations. Also, in contrast to more modern approaches, the Franck–FitzHugh and related models assume the oscillations between the passive and active electrode states as a *truly potentiostatic* phenomena, since the electrode potential is assumed constant, whereas only the pH-dependent Flade potential oscillates. In consequence, the model does not involve the capacitive (double layer recharging) current. The source of oscillations is limited to the characteristics of the Fe–solution interface and of the transport of H^+ ions, and thus the origin of this instability is not considered the feature of the entire electric circuit containing N-NDR element, with ohmic potential drops present. Also the chemical description of the electrode interface seems to be simplified, as in the passive state the Fe electrode surface is covered not only by the compact oxide, but also by the porous $FeSO_4$ layer, and the proportions between the amount of oxide and sulfate may depend on both the electrode potential and the concentration of sulfuric acid. Furthermore, the model assumes only a homogeneous dissolution of the entire Fe surface. Nevertheless, the Franck–FitzHugh model remains the first important step toward understanding of oscillations related to the active–passive transitions of the electrode surface and became the subject of further modifications.

The Adsorption Models

It is known that adsorption of species with strong attractive lateral interactions in the adsorption layer, which can be described in terms of, e.g., the Frumkin isotherm, may give rise to bistability (see Sect. 3.6). In 1984, Griffin [40] has proposed the simple, minimal parameter kinetic model of corrosion/passivation of metals, in which as a result of the oxidation of metal atoms, the produced cations adsorb on the surface as oxides and then dissolve into the solution. The interaction between the cations was expressed in terms of the linear dependence between the average desorption energy associated with cation dissolution and the cation coverage θ or, equivalently, as the exponential dependence of the dissolution rate constant on θ . Depending on the parameter value describing these interactions either single-valued or multi-valued (bistable) dependence between the theoretical anodic current and the electrode potential was obtained, resembling the experimental $I-U$ dependences in the active–passive transition region.

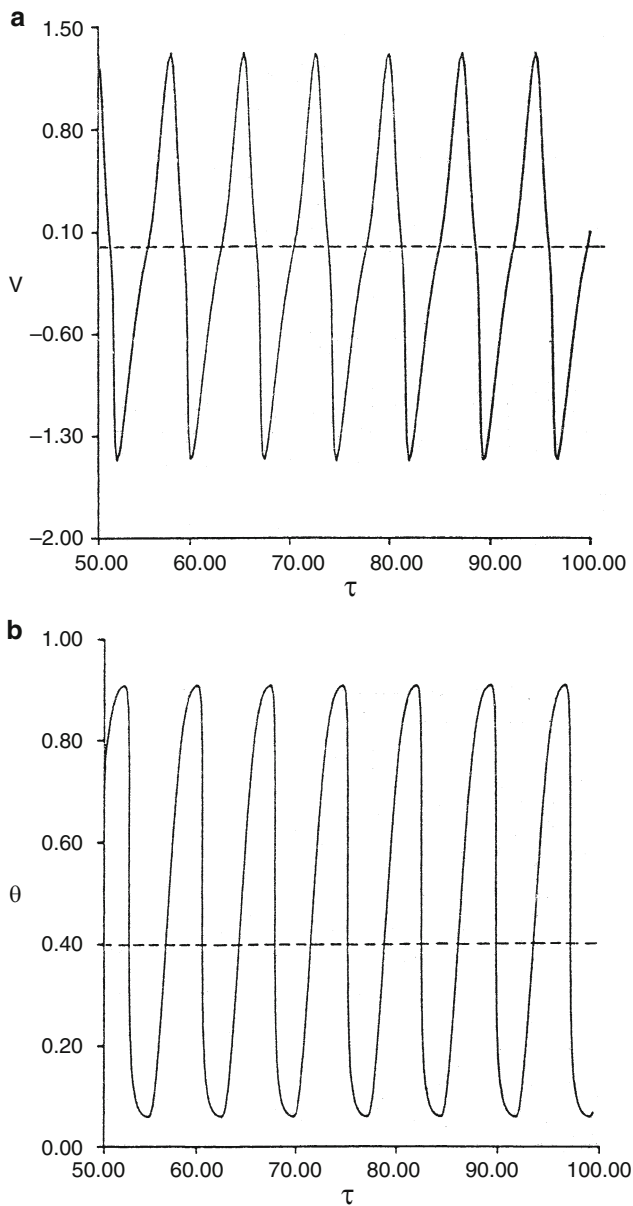
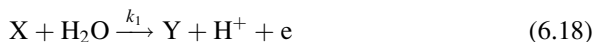


Fig. 6.13 Oscillations of (a) dimensionless potential and (b) electrode coverage, obtained from numerical integration of Eqs. (6.15) and (6.16) for $b = 1$, $h = 0.4$, $c = 0.28$ and $a = 500$. Reproduced from [39] by permission of The Electrochemical Society

Later, Talbot and Oriani [41, 42] and Kado and Kunitomi [43] have developed the models which postulated that the decisive role in oscillatory instabilities accompanying the transitions between the active and passive states was played by adsorption of various sparingly soluble species of iron at the Fe electrode surface. In the latter approach, three of adsorbed species were suggested as crucial for the onset of instabilities: $\text{Fe}^{\text{I}}(\text{OH})_{\text{ads}} \equiv \text{X}$; $[\text{Fe}(\text{OH})_2]_{\text{ads}} \equiv \text{Y}$ and $\{\text{Fe}[\text{Fe}(\text{OH})_2]\}_{\text{ads}} \equiv \text{Z}$, involved in the following model reaction scheme:



which itself can generate only steady-state and damped oscillations. In order to obtain sustained oscillations, one has to (and this is the crucial assumption for those models) introduce sufficiently strong lateral attractive interactions between the particles X, Y, and Z. Accordingly, the rate constant k_2 was replaced by k_2' by introducing the exponential factor $\exp[A/k_{\text{B}}T]$, in which A was a parameter describing the lateral (here: attractive) interactions X–X, Y–Y, Z–Z, X–Y, X–Z, Y–Z in the adsorption layer:

$$k_2' = k_2 \exp[A(x, y, z)/(k_{\text{B}}T)] \quad (6.21)$$

Expression (6.21), in which x, y, z denote electrode coverages with species X, Y, Z, respectively, introduces to the model the additional nonlinearity which appeared to be a mathematically sufficient condition for the onset of sustained oscillations (for appropriate values of other parameters). As we see, in this type of models the Flade potential and its dependence on pH of the solution at the electrode surface, as well as the ohmic drops in the circuit, are not invoked. If we want to find something common with the Franck–FitzHugh model, it is the assumption that the oscillatory regime can be explained in terms of the properties of the Fe–solution interface, without considering the instability as a feature of the entire electric circuit.

The Electrical–Electrochemical Models

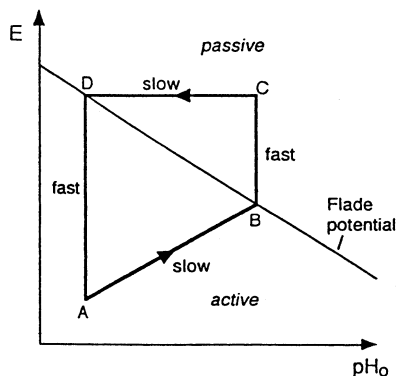
To this group of models there belong those mechanisms which take into account both the characteristics of the Fe–electrolyte interface and the ohmic drops in the electric circuit. Early model construction meeting both assumptions has been described by Degn already in 1968 [44]. The mathematical construction involved the coupling of the concentration polarization at the Fe electrode and the ohmic

drops in a following way. Let us assume that initially the external voltage U is a bit larger than the value sufficient to cause the anode passivation, but due to ohmic drops the effective electrode potential E is still too negative to cause this process. Thus, initially there flows a relatively high current which gradually decreases due to increasing concentration polarization of species A in the solution. Below certain critical value of the current, the electrode potential E becomes positive enough to initiate passivation. The current then significantly drops and now the diffusion of species A can replenish its decreased concentration in the pre-electrode layer. The gradual increase in $[A]$, i.e., the decrease in its concentration polarization, enhances the current which again rises to values, for which, due to increasing ohmic drops, the electrode potential becomes so negative that the passive layer stops to form and undergoes only dissolution. The whole cycle repeats again. Oscillations generated by this approach revealed relaxation shape. Although the Degn's model did not include explicitly the flow of capacitive current during the periodic recharging of the working electrode, it remains a valuable historical contribution to understanding of electrochemical oscillations.

In 1987, Russell and Newman [11] have suggested the approach that also included the ohmic potential drops in the electric circuit, constructing the model in which they combined the properties of the passive layer, the transport phenomena of metal and H^+ ions, and variations of the solution pH. Initially, when the Fe electrode is still in its active state, associated with the flow of current of relatively high density, the concentration of Fe^{2+} ions in the pre-electrode layer increases and the first portions of the porous $FeSO_4$ layer are formed. A high electric field associated with this high current accelerates migration of H^+ ions toward the cathode; accordingly, the pH of the solution at the anode increases. Increasing Fe^{2+} concentration makes the $FeSO_4$ layer less porous and eventually it becomes so compact that blocks the electrode surface. The current density abruptly drops, in consequence the electric field in pores of $FeSO_4$ also decreases, H^+ ions get a chance to diffuse back to the Fe electrode and dissolve the passive layer. Although the general scheme of phenomena may seem very similar to the Franck–FitzHugh model, due to taking into account the role of varying ohmic potential drops, the electrode potential and the distribution of the electric field vary periodically. Thereby, in this approach the oscillations occur under more realistic conditions that are no longer truly potentiostatic. The mathematical construction of the present model was also more complicated than the Franck–FitzHugh model, since it was based on partial differential equations. But even in spite of that more realistic description, the model oscillations did not exhibit satisfactory concordance with the experimental results and it was clear that the better understanding of the oscillations associated with the passive/active transition requires further work.

Finally, in 1993, Koper and Sluyters [45] have developed their models which is now quite widely used also by other researchers to simulate oscillations in passivation/dissolution systems. Its construction can be understood as substantial extension of earlier approaches: those by Franck and FitzHugh, the Russell and Newman, and Degn, including the role of NDR. The chemical side of the Koper and Sluyters model includes the formation of porous layer, analogous to $FeSO_4$ in real system.

Fig. 6.14 The schematic phase portrait of the oscillatory dissolution of Fe in H_2SO_4 , explaining the formation of relaxation oscillations. The interfacial potential drop of the anode ($E = U - IR_s$) is plotted against the pH of the solution near the anode surface. Reprinted from [24] with permission of John Wiley & Sons, Inc. Copyright 1996 John Wiley & Sons, Inc.



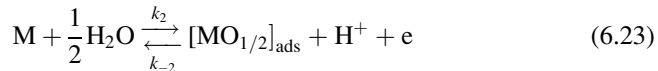
The transport of ions in the solution includes the metal ions formed due to oxidation of the electrode and the ions of the electrolyte. The instabilities are due to a negative differential resistance (N-NDR type), coupled with ohmic potential drops. Koper and Sluyters have shown the steps of development of the models, aiming to reproduce possibly well the experimental current–time courses. Thus, introducing in the first step only ohmic potential drops to the traditional Franck and FitzHugh model allowed to generate oscillations, but of shapes distinctly different from the experimentally reported dependences; moreover, the concentration of H^+ ions in the solution might attain physically unreliable values. The main reason for that seemed to be one of the crucial assumptions of the FFH model, namely that that practically only H^+ ions participate in the conduction of current in the solution. Under such crude assumption, the variations of H^+ concentration appeared to be simply too large.

Before presentation of the mathematical side of the most sophisticated version of these models it is useful to indicate the principles of its construction in terms of the phase portrait that involves fast and slow dynamic variables, explaining in this way the relaxation oscillations reported typically for the electrooxidation processes involving active/passive transitions (Fig. 6.14) [24].

The phase diagram identifies the electrode potential E as a fast variable, and pH (or $[\text{H}^+]$) as a slow variable. Furthermore, the solid straight line in this diagram indicates the Flade potential which is linearly dependent on pH, according to Eq. (6.3). Let us start the oscillation cycle at point A of the diagram, when the potential of the electrode is not too positive, and pH is sufficiently low to keep the electrode in its active state, associated with the flow of a relatively high current. The flow of current, carried out partly by H^+ ions, causes the local decrease of these ions, so pH slowly increases along the $A \rightarrow B$ direction. Simultaneously, due to the increase of the Fe^{2+} concentration in the solution, the precipitation of FeSO_4 occurs which causes the current to decrease. This means the stepwise decrease of the ohmic potential drops and, in consequence, the shift of the potential of the anodically polarized electrode to more positive values—hence the positive slope of the AB section comes from. At point B the actual Flade potential is reached and then the electrode undergoes passivation, the current abruptly drops which means

also, due to ohmic drops, the abrupt increase of the electrode potential to even more positive values (higher than E_F), at which passivation is even stronger. This means autocatalysis in the passivation rate, or, equivalently, autoinhibition in the sense of the variations of the current, anyway this is a feedback loop that has to exist in the oscillatory process. In other words, the electrode potential manifests itself here as the autocatalytic variable. The time scale of the system's trip along the BC section in Fig. 6.14 is determined by the time constant of the entire circuit which is dependent on the capacity of the double layer. The vertical course of the BC section means that the formation of the passive layer [cf. Eq. (6.2)] practically does not affect the local pH which assumption is quite realistic if only the monolayer of the oxide is formed. Now, continuing at point C, the oxidation current is so low that the (relatively slow) diffusion of H^+ ions from the solution bulk can overcome its migration in the opposite direction. The pH of the pre-electrode layer slowly decreases along the CD section, while the current, and hence the potential remain roughly constant since the electrode remains passivated (note however that due to pH changes the Flade potential becomes more positive). At point D, when the electrode potential touches the E_F value, the electrode undergoes sudden depassivation: the rising current, due to ohmic drops, again autocatalytically shifts the potential E toward less positive values, i.e., the increase of current is autocatalytic. The cycle closes at point A from which it starts again.

The mathematical construction of the model [45] was developed for the electrooxidation processes:



which are in fact Eqs. (6.1) and (6.2) for $n = 1$. The individual electron transfer rate constants k_1 , k_2 , and k_{-2} were assumed to follow the Tafel dependence:

$$k_1 = k_1^0 \exp[(e - e_1^0)/2] \quad (6.24)$$

$$k_2 = k_2^0 \exp[(e - e_2^0)/2] \quad (6.25)$$

$$k_{-2} = k_{-2}^0 \exp[-(e - e_2^0)/2] \quad (6.26)$$

where $e = FE/RT$ and $1/2$ factor indicates the value of the transfer coefficient for the activation barrier. The electrodisolution reaction (6.22) occurs to a solution of a strong HA electrolyte. This oxidation is assumed to occur homogeneously at the electrode surface, so all the gradients (i.e., of the concentrations and electric potential) develop only along the direction normal to that surface, denoted as the x axis. In every portion of the solution (excluding the region of the electrical double

layer which is not explicitly considered in the model), the electroneutrality condition is met:

$$[\text{H}^+]_x + [\text{M}^+]_x = [\text{A}^-]_x \quad (6.27)$$

These ions participate in the conduction of current proportionally to their transference numbers, which can be defined according to Eq. (6.28), with the use of the electroneutrality condition (6.27) for elimination of $[\text{A}^-]_x$ as a variable:

$$\begin{aligned} t_j(x) &= \frac{[j]_x \lambda_j}{[\text{H}^+]_x \lambda_{\text{H}^+} + [\text{M}^+]_x \lambda_{\text{M}^+} + [\text{A}^-]_x \lambda_{\text{A}^-}} \\ &= \frac{[j]_x \lambda_j}{[\text{H}^+]_x (\lambda_{\text{H}^+} + \lambda_{\text{A}^-}) + [\text{M}^+]_x (\lambda_{\text{M}^+} + \lambda_{\text{A}^-})} \end{aligned} \quad (6.28)$$

where $[j]$ denotes the molar concentration of a given, j th ion of a molar conductivity λ_j .

An important feature of the model is further the implementation of the formation of MA porous salt precipitated on the electrode surface, which takes place when the concentration of M^+ ions appearing in the solution reaches a critical value $[\text{M}^+]_{\text{crit}}$ determined by the solubility product K_{s0} :

$$[\text{M}^+]_{\text{crit}} [\text{A}^-]_0 = K_{s0} \quad (6.29)$$

where $[\text{A}^-]_0$ denotes the concentration of A^- at the electrode/electrolyte interface. Then the rate at which the salt layer dissolves into the neighboring solution determines the rate of metal electrodisolution. Using electroneutrality condition (6.27), one can express $[\text{M}^+]_{\text{crit}}$ in an equivalent form:

$$[\text{M}^+]_{\text{crit}} = -\frac{1}{2} [\text{H}^+]_0 + \left(\frac{1}{4} [\text{H}^+]_0^2 + K_{s0} \right)^{1/2} \quad (6.30)$$

In the model, it is further introduced a crude approximation that the porous layer has the same conductivity as the solution. The M^+ ions which appeared due to Eq. (6.22) travel through the porous layer and reach the salt film–solution interface, but the thickness of MA layer is not considered in the model. If the resulting local concentration of M^+ exceeds the solubility product of K_{s0} , M^+ ions remain there as the component of the precipitating MA salt, otherwise, if $[\text{M}^+] = 0$, they dissolve further into the bulk of the solution with unit probability. The intermediate situation is described through the linear dependence between the rate constant of the oxidation process (6.22) and the concentration ratio $[\text{M}^+]_0 / [\text{M}^+]_{\text{crit}}$, meaning that the k_1 constant in Eq. (6.22) is replaced with the corrected one k_1^* :

$$k_1^* = k_1 \left[1 - \frac{[\text{M}^+]_0}{[\text{M}^+]_{\text{crit}}} \right] \quad (6.31)$$

where $0 \leq [M^+]_0 \leq [M^+]_{\text{crit}}$.

Another simplifying assumption is that for the dynamics of the electrode coverage θ during the oscillations:

$$\frac{d\theta}{dt} = k_2(1 - \theta) - k_{-2}\theta[H^+] \quad (6.32)$$

the quasi steady-state approximation $d\theta/dt = 0$ can be applied, based on which the actual, instantaneously adjustable steady-state values θ_{ss} were determined.

Due to ohmic potential drops, during the oscillations the electrode undergoes recharging to the actual potential E , associated with the flow of capacitive current. In terms of the equivalent circuit shown in Fig. 2.6, the total current meets the charge conservation principle, given earlier as Eq. (2.10) and for clarity repeated here:

$$I = \frac{U - E}{R_s} = I_c + I_f = AC_d \frac{dE}{dt} + I_f \quad (6.33)$$

where R_s is the serial resistance, C_d is the differential double layer capacitance per unit area, I_f and I_c are the faradaic and capacitive currents, respectively, and A is the electrode surface. In the following, C_d will be considered potential-independent. Finally, the concentration profiles of M^+ and H^+ ions in the diffusion layer are linearized, so they correspond to the idea of the Nernst diffusion layer of the assumed thickness δ (cf. Fig. 2.7). Derivation of equations describing the dynamics of surface concentrations of respective species, in terms of the Nernst layer, was also described in Sect. 2.2.2.

Mathematical definition of the present dynamical system involves three ordinary differential equations, given by expressions (6.34)–(6.36). They describe the dynamics of (1) the dimensionless potential (e) of the anode; (2) the concentration (u) of M^+ ions in the solution at the phase boundary with the porous MA layer, and (3) the concentration of H^+ ions (h) in the same region:

$$\frac{de}{d\tau} = \frac{v - e}{r} - qk_1^*(1 - \theta) \quad (6.34)$$

$$\frac{dh}{d\tau} = d(h_b - h) - t_h d^{1/2} \left(\frac{v - e}{rq} \right) \quad (6.35)$$

$$\frac{du}{d\tau} = -\alpha du + d^{1/2}(1 - \theta)k_1^* - t_u d^{1/2} \left(\frac{v - e}{rq} \right) \quad (6.36)$$

where: $d = A/\delta^2$, $\tau = 2Dt/A$, $v = FU/RT$, $r = 2DC_dR_s$, $q = F^2A^{1/2}/2RTC_d$, $h_b = [H^+]_{\text{bulk}}$, the concentration of H^+ in the bulk of the solution, and:

$$\alpha = \frac{D_{M^+}}{D_{H^+}} = \frac{\lambda_{M^+}}{\lambda_{H^+}} = \frac{\lambda_{A^-}}{\lambda_{H^+}} \quad (6.37)$$

$$t_h = \frac{h}{h(1 + \alpha) + 2\alpha u} \quad (6.38a)$$

$$t_u = \frac{\alpha u}{h(1 + \alpha) + 2\alpha u} \quad (6.38b)$$

$$k_1^* = k_1 \left(1 - \frac{u}{u_c} \right) \quad (6.39)$$

$$u_c = -\frac{1}{2}h + \left(\frac{1}{4}h^2 + K_{s0} \right)^{1/2} \quad (6.40)$$

In line with the above assumption, the electrode coverage θ follows the assumption of the steady-state, and is equal to:

$$\theta_{ss} = \frac{1}{1 + \left(\frac{k_{-2}}{k_2} \right) h} \quad (6.41)$$

Note that the mathematical form of Eq. (6.34) comes from the assumption that the contribution to the faradaic current from process (6.23) is negligible. For readers, other details of these derivations can be found in the original paper [45]. In terms of this three-variable model it is possible to obtain not only simple periodic (Fig. 6.15), but also mixed-mode (low- and high-amplitude, MMO) and aperiodic (chaotic) oscillations (Fig. 6.16). In these figures the current was determined as equal to $(v - e)/r$ quantity, based on actually calculated values of electrode potential $e(t)$, for external voltage v and serial resistance r treated as parameters.

In turn, Fig. 6.17 shows respective stability diagrams of the studied model, diagnosed from the linear stability analysis, which indicated the regions of the single stable steady-state, oscillations, and multiple steady-states.

Since parameter d is inversely proportional to the thickness of the Nernst diffusion layer δ , the diagram in Fig. 6.17a shows different dynamic modes that can be obtained by varying the rotation rate of the disk electrode and the voltage applied. In turn, Fig. 6.17b illustrates the conditions for respective dynamic regimes if the rotation rate is fixed, with $[H^+]$ and the external voltage as the bifurcation parameters.

Another way of illustration of the dynamic instabilities is to present the dependence of the current on a selected bifurcation parameter, for all other parameters fixed (i.e., to construct the respective section of the bifurcation diagrams from Fig. 6.17). Such diagrams, shown in Fig. 6.18, indicate either the abrupt or smooth transition to oscillations, with their amplitude found from numerical integration of differential equations (6.34)–(6.36).

In the opinion of Koper and Sluyters [45], their model which does not require any discontinuity in the kinetics of the passivation/activation process, is a quite general way of description of fundamental properties of the dynamic systems with the electrodes undergoing electrooxidation, with the surface formation of the inhibiting salt layer. Some simplifications, discussed above, cause of course that

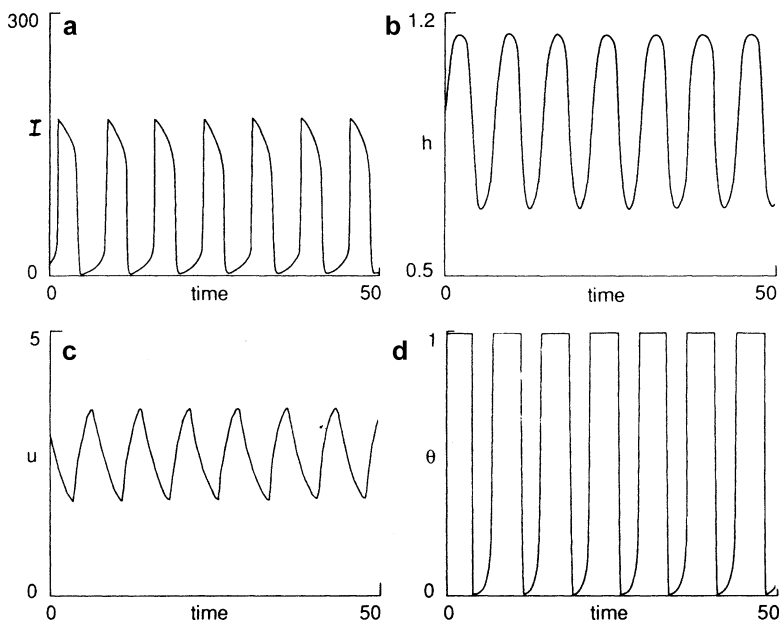


Fig. 6.15 Typical oscillatory time series for limit cycle solution of model (6.34)–(6.36) with $\nu = 30$, $r = 0.1$, $h_b = 1.2$ and other parameters $q = 100$, $k_1^0 = 0.01$, $k_2^0 = 0.01$, $k_{-2}^0 = 0.001$, $d = 1$, $h_b = 1$, $e_1^0 = 0$, $e_2^0 = 20$, $K_{s0} = 16$ and $\alpha = 0.2$; (a) I - t behavior, (b) h - t behavior, (c) u - t behavior and (d) θ - t behavior. Reprinted from [45], Copyright 1993, with permission from Elsevier

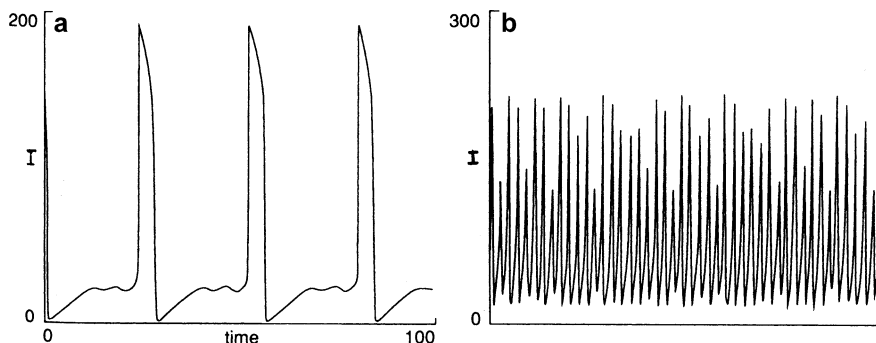


Fig. 6.16 Complex oscillations in model (6.34)–(6.36): (a) mixed-mode oscillations (MMO) for $\nu = 30.52$, $r = 0.1$, $d = 1$; (b) chaotic oscillations for $\nu = 24$, $r = 0.032505$, $d = 0.5$ and other parameters as for Fig. 6.15. Reprinted from [45], Copyright 1993, with permission from Elsevier

one should not expect a detailed concordance between the shapes of the simulated and experimental I - t oscillatory courses; the model reproduces rather *types* of the dynamic changes. Also the bistability (hysteresis) in the current–voltage response, observed for the Fe electrode under conditions of cyclic voltage variations in the

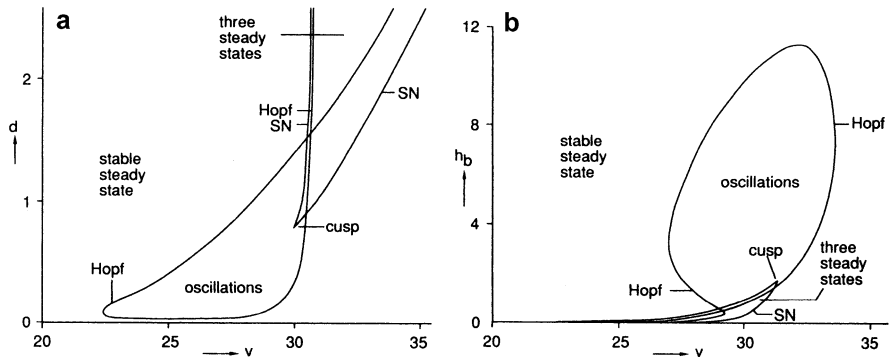


Fig. 6.17 Linear stability diagrams of the Koper and Sluyters model (6.34)–(6.36) which indicate regions of unique stable steady-state, oscillations and multiple steady-states, and associated bifurcations ($r = 0.1$): (a) $d - v$ diagram for $h_b = 1$; (b) $h_b - v$ diagram for $d = 1$. Other parameters: $K_{sol} = 16, \alpha = 0.2, q = 100, k_1^0 = 0.01, k_2^0 = 0.01, k_{-2}^0 = 0.001, e_1^0 = 0, e_2^0 = 20$. Reprinted from [45], Copyright 1993, with permission from Elsevier

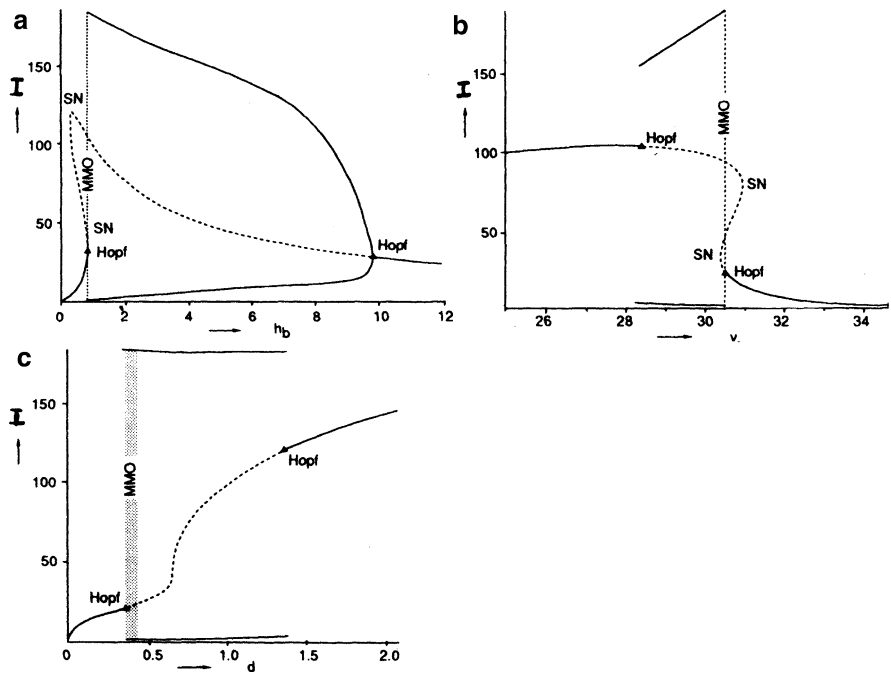


Fig. 6.18 Bifurcation diagrams for model (6.34)–(6.36): *full curves*, stable steady-states or minimum and maximum of stable oscillations; *broken curves*, unstable steady-states; *Hopf* Hopf bifurcations, *SN* saddle-node bifurcation; *shaded region* MMO, region when mixed-mode oscillations are obtained. (a) $I - h_b$ diagram, $v = 30, d = 1$; (b) $I - v$ diagram, $h_b = 1, d = 1$; (c) $I - d$ diagram, $v = 30, h_b = 1$. Reprinted from [45], Copyright 1993, with permission from Elsevier

area of the NDR could not be obtained with the present model. Finally, as all models described earlier, this one also assumes only the homogeneous dissolution of the anode surface, and thus also the use of single value for the ohmic drops IR_s . In spite of all these simplifications, the usefulness of the Koper–Sluyters model lies in its relative simplicity.

It is thus evident that more sophisticated approach to the oscillatory electrodis-solution of iron in H_2SO_4 media (and other processes of that type) should involve the role of spatial distribution of corrosion/passivation areas, with the identification of associated local and global couplings (cf. Sect. 1.2, volume II). It is remarkable that spatial inhomogeneities of the oscillating Fe electrode potential have been shown already by Franck and Meunier [19]: for the anodically polarized iron electrode, immersed in the $H_2SO_4 + HCl$ solution, there was measured not only the electrode potential (E_1), but also, using additional reference electrodes with capillary tips, the local potentials in two different places (E_2, E_3). The oscillatory variations of E_1 were then associated with the nonzero differences $E_2 - E_3$, taking a form of oscillations of different shapes than those of E_1 . Also the recent, above-mentioned works of Pagitsas et al. describe the corrosion of iron in terms of the point defect model [32–36].

Finally, Nechiporuk and Petrenko [46], using an electrochemical model of anodic dissolution of metals in acidic media, have analyzed bifurcation properties of steady-state solutions in relation to transport properties of the ionic species. In particular, it was shown how an increase in migration nonequilibrium (caused, e.g., by the change of solution conductivity, transference numbers, etc.) may give rise to oscillatory instability and complex bifurcation points.

6.1.3 The Oscillatory Electrodis-solution of Copper

6.1.3.1 The Cu/SO_4^{2-} System

Besides iron, copper was another electrode material, the oscillatory electrooxidation of which was quite intensively studied in various media. Mechanisms of those phenomena involved periodic formation and destruction of the passive layer at the copper surface. Kawczyński, Baranowski et al. [47, 48] have reported studies for the $Cu(s)-CuSO_4 + H_2SO_4(aq)-Cu(s)$ system, consisting of thin layer (0.15–0.30 cm) solution of 0.80 M $CuSO_4 + 0.46$ M H_2SO_4 solution placed between two horizontal flat and polished copper electrodes (Fig. 6.19). Under such conditions, both periodic and chaotic current oscillations are observed.

Since chaos was observed for both upper and lower copper anode, the density-driven convection, which could be present only in the former case, could not account for that aperiodicity. Instead, the complex character of nucleation phenomena in the passive (salt layer) film formation/dissolution is presumably responsible for the chaos observed. The formation of such passive layers was later confirmed by Inzelt [49] who has reported the oscillatory mass changes during the Cu dissolution

Fig. 6.19 The electrochemical cell and electrical circuit. 1—Cu anode; 2—Cu cathode; 3—reference electrode; 4— $\text{CuSO}_4 + \text{H}_2\text{SO}_4$ solution; 5—thermostat; 6—potentiostat; 7—recorder. Reprinted from [48] with kind permission of Oldenbourg Verlag

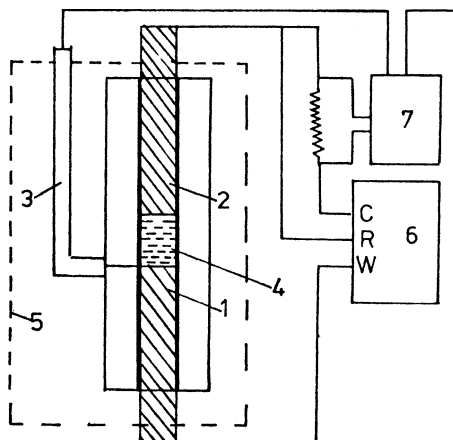
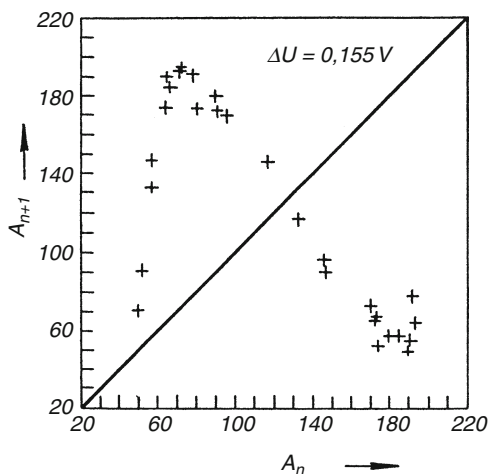


Fig. 6.20 One-dimensional Poincaré map for chaotic oscillations at $U = 0.155 \text{ V}$; A_{n+1} and A_n denote the consecutive and previous current amplitudes, respectively. Reprinted from [48] with kind permission of Oldenbourg Verlag



in $\text{H}_2\text{SO}_4 + \text{CuSO}_4$ medium, manifesting itself by oscillating electrochemical quartz crystal microbalance response. The chaotic courses were analyzed in terms of one-dimensional Poincaré maps (Fig. 6.20) [48].

6.1.3.2 The Cu/Cl^- System

The oscillatory electrooxidation of Cu anode in HCl or NaCl solutions has been studied since 1920s of the twentieth century [50–53] and some attempts to explain the mechanisms of these oscillations were made by Cooper et al. [54]. Here we shall focus on more recent studies of these oscillations in various acidic chloride solutions, performed by Lee et al. [55, 56], using rotating disk copper electrode.

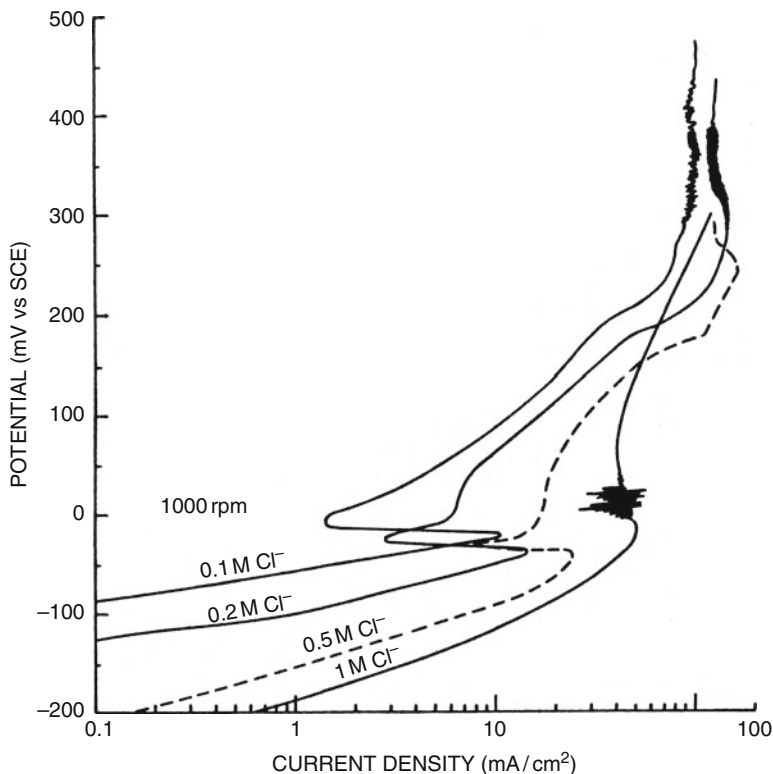


Fig. 6.21 Anodic polarization of Cu in 0.1 M NaCl + 1 N H₂SO₄, 0.2 M NaCl + 1 N H₂SO₄, 0.5 M NaCl + 1 N H₂SO₄, and 1 M HCl. Sweep rate: 0.5 mV/s. Reproduced from [55] by permission of The Electrochemical Society

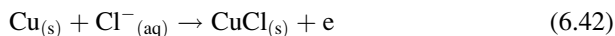
Typical dynamic I - E characteristics of the studied system, indicating the region of oscillations, are collected in Fig. 6.21 [55].

Concerning the chemical mechanism of these oscillations, it is well-known that interaction with chloride ions significantly stabilizes the first oxidation state of copper. Accordingly, two Cu(I) species were initially considered as the main components of this layer: Cu₂O and CuCl. Results obtained for the rotating disk copper electrode have suggested that formation of CuCl was thermodynamically favorable, compared to Cu₂O, and hence CuCl should be considered a crucial compound forming during Cu anodic oxidation under such conditions. For the oscillations, it is also necessary that CuCl film on the Cu surface is sufficiently thick.

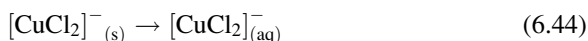
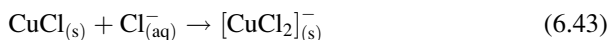
Analogously to Fe-H₂SO₄ system, for which the formation of porous FeSO₄ layer was considered, now the formation-dissolution mechanism of the porous CuCl film was suggested as the source of the oscillations. In the presence of this film, the transport of Cu⁺ ions into the solution and of Cl⁻ ions from the solution to the interface has to occur. The difference in the chemical mechanism is that CuCl can undergo dissolution due to complexation with excess Cl⁻ ions. Thus, the

following main processes are considered the basis for the electrochemical oscillations in the Cu–Cl[−] system (for [Cl[−]] < 1 mol/dm³):

1. Formation of the CuCl surface film.



2. Dissolution of CuCl through transformation to soluble complex species.



At Cl[−] concentrations higher than 1 mol dm^{−3} the formation of higher Cu(I) complexes, like [CuCl₃]^{2−}, should be also taken into account. Also, at relatively high electrode potentials the oxidation process: CuCl → Cu²⁺_(aq) + Cl[−]_(aq) + e should be considered.

Noteworthy, the rate of formation of CuCl_(s) [Eq. (6.42)] is dependent on the transport of Cl[−] toward the Cu surface and thus it is dependent on the thickness of CuCl film, while the rate of CuCl dissolution [Eqs. (6.42) and (6.43)], as occurring at the film/solution interface, is independent of the film thickness. Since reaction (6.43) is much faster than the desorption step (6.44), hence the summary process (6.43) + (6.44) constitutes a mass transfer-limited nonelectrochemical reaction.

Oscillations mean of course that the exact balance between the CuCl film formation and dissolution does not exist. Then thickness of the CuCl film changes periodically, which causes the analogous variation of the rate of transport of Cl[−] ions through this film. When its thickness is relatively high, the flow of Cl[−] ions toward the electrode surface is slowed down and, accordingly, the Cu oxidation current is then low. But low anodic current means so slow formation of CuCl, that its dissolution, both direct and through complexation with Cl[−] ions, may become predominating. After some time, when the CuCl film becomes thin enough, the transport of Cl[−] ions through it becomes so efficient that the current significantly increases. This in turn means the increased production of CuCl which after some time causes the decrease of the current, etc. Pearlstein et al. [56] have built up the respective mathematical model of this mechanism for the simplified geometry of the electrochemical system, studied at the rotating disk electrode. Partial differential equation, i.e., the Fick's law was used for calculating the diffusion of Cl[−] ions along a single coordinate, normal to the electrode surface. The “steady film solution” was obtained, i.e., the conditions under which a CuCl film of constant thickness exists on the Cu surface. Furthermore, using linear stability analysis, the conditions were found, under which the film thickness and current density will be oscillatory functions of time. Details of this procedure can be found in the original paper [56].

From the point of view of nonlinear dynamics, the electrodisolution of copper in acidic chloride solutions is a process exhibiting a variety of complex behaviors, as Bassett and Hudson have reported [57–59]. These complex regimes include,

besides simple oscillations, also: type III intermittency, period doubling to chaos, Shil'nikov chaos, and quasi-periodicity.

Later, Gu et al. [60, 61] have published the studies of the oscillatory electrooxidation of copper electrode in contact with aqueous solution of NaCl and KSCN. The system is chemically more complicated through the possible formation of the mixed CuCl and CuSCN film.

6.1.3.3 The Cu/H₃PO₄ System

The Cu/H₃PO₄ system became one of the most systematically studied examples of the oscillatory anodic dissolution of metals, starting from the first report by Jacquet in 1936 [62]. Among more recent reports, works by Glarum and Marshall [63, 64], systematic investigations performed by Albahadily and Schell [65–67], and selected works of other researchers deserve a brief description here. In contrast to the Fe/H₂SO₄ system, the anodic potentiodynamic voltammograms of Cu dissolution in 85% phosphoric acid, studied at the rotating Cu disk electrode, do not exhibit clear transition from the active to passive region, and in spite of that the current oscillations occur at the quasi-plateau of the anodic current (Fig. 6.22) [63].

In turn, Fig. 6.23 shows typical oscillatory $I-t$ courses, recorded under potentiostatic conditions.

Furthermore, the anodic current plateau, although proportional to the square root of the disk rotation rate, according to Levich equation [68]:

$$i_{\text{lim}} = 0.62nFAD^{2/3}\omega^{1/2}\nu^{-1/6}c^0 \quad (6.45)$$

[cf. also Eq. (4.7)] appears to be only apparently dependent on bulk Cu²⁺ concentration. In fact, after correction for the solution viscosity (ν) this anodic plateau becomes no longer dependent on bulk [Cu²⁺] (cf. also earlier experiments by Edwards [69]). In the opinion of Glarum and Marshall [63], this points on the role of depletion of water, consumed in the boundary layer, when the Cu²⁺ ions, appearing due to Cu disk oxidation, undergo hydration and in this way bind significant amount of water molecules.

In their mechanistic interpretation, Glarum and Marshall clearly associate the oscillations with the NDR characterizing the studied system. Although this negative resistance is not directly visible (i.e., it is hidden) at the dc $I-E$ curves of the anodic copper dissolution, it manifests itself in the impedance measurements, made for the potential region III in Fig. 6.24 [64]. Exemplary admittance spectrum is shown in Fig. 6.25. The axis of real negative admittance is intersected for low, but nonzero frequency of the ac voltage, which is a criterion for the oscillations that would set in if sufficiently high ohmic serial resistance moves the plot to the right, so that the intersection point overlaps with the origin of the coordinate system (see Sects. 3.3 and 3.4).

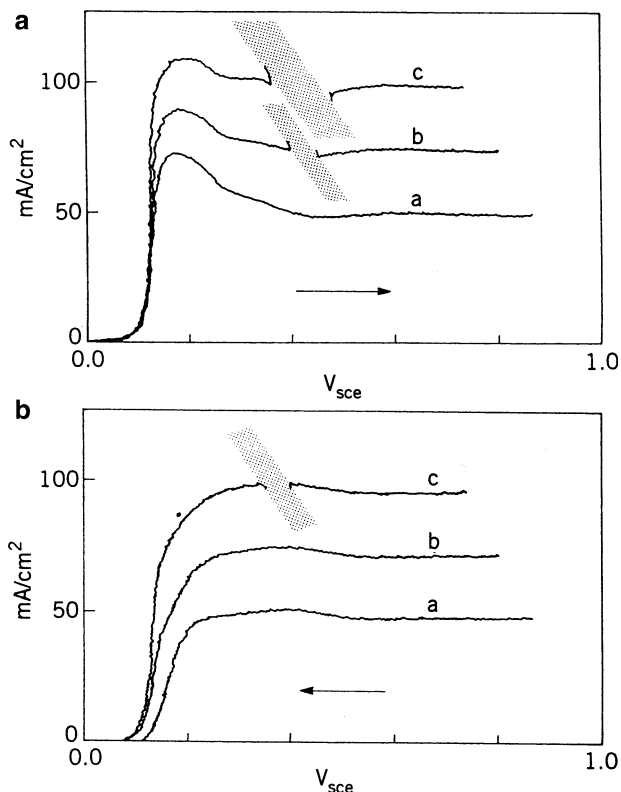


Fig. 6.22 (a) Anodic sweep voltammograms at 24 mV/s of a 1/4 in. diam. rotating copper disk electrode in 85% phosphoric acid. For plots a–c, the disk rotation speeds are 100, 225, 400 rad/s. The shaded regions indicate areas swept by oscillations. (b) Cathodic sweep voltammograms complementing the anodic sweeps. Reproduced from [63] by permission of The Electrochemical Society

In consequence, the coupling of this negative resistance with ohmic potential drops in the electrolyte is a cause of oscillatory instability under potentiostatic ($U = \text{const}$) conditions [63]. If the ohmic potential drops are too small to cause this instability, i.e., for the Cu disks of a small diameter or for low disk rotation speeds, the oscillations are not observed. Under these conditions they however can be recovered if sufficiently large, external serial ohmic resistor is inserted in the circuit of the Cu electrode. This clearly confirms the crucial role of ohmic potential drops in generation of the oscillations discussed.

This negative resistance is caused most probably by the formation of film passivating the copper surface, with the current oscillations reflecting the periodic formation/destruction of this film. This view is strongly corroborated by the in situ ellipsometric measurements, made by Tsitsopoulos et al. [70] who have found strict correlation between the period of current oscillations and the variation of the thickness and composition of the surface film. Furthermore [71], using X-ray photoelectron spectroscopy (XPS) and scanning electron microscopy (SEM) they

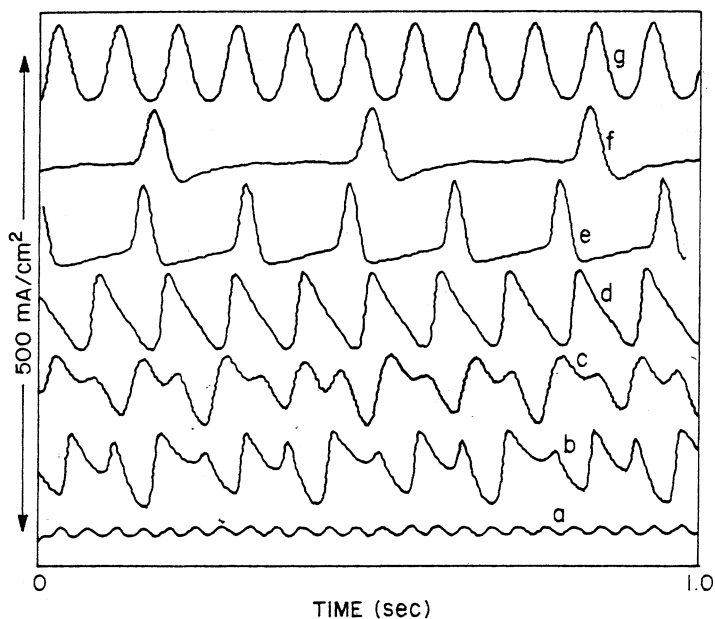


Fig. 6.23 Oscillation waveforms seen for a $\frac{1}{4}$ in. diameter copper electrode in 70% phosphoric acid. For curves a–f, the disk rotation speed is 300 rad/s and mean IR -corrected potentials are 0.36, 0.38, 0.40, 0.42, 0.54, and 0.56 V. Waveform g was found when the rotation speed was raised to 400 rad/s for the potentiometer setting giving waveform f. The corrected mean potential is 0.49 V. Reproduced from [63] by permission of The Electrochemical Society

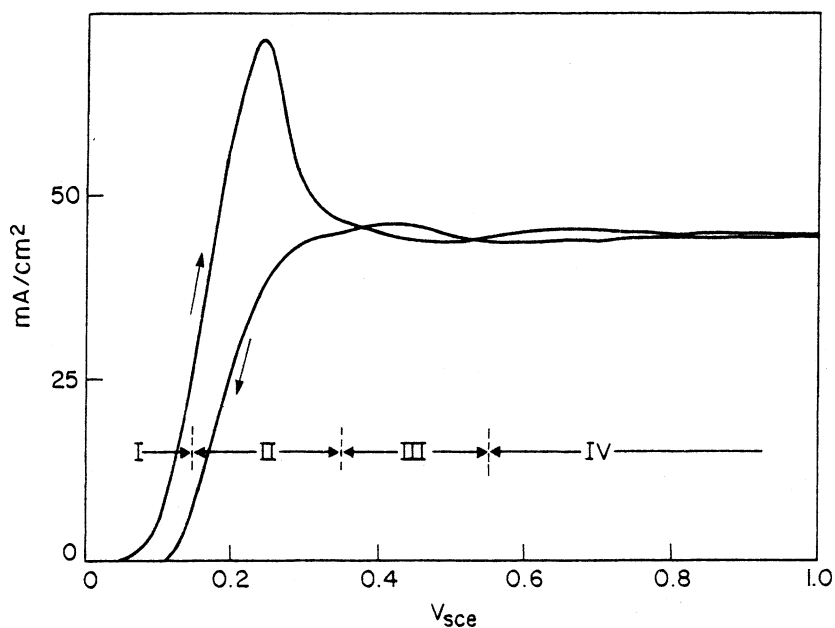


Fig. 6.24 Voltammetric behavior of the $\text{Cu}/\text{H}_3\text{PO}_4$ interface measured at 20 mV/s sweep rate and 100 rad/s disk rotation. Reproduced from [64] by permission of The Electrochemical Society

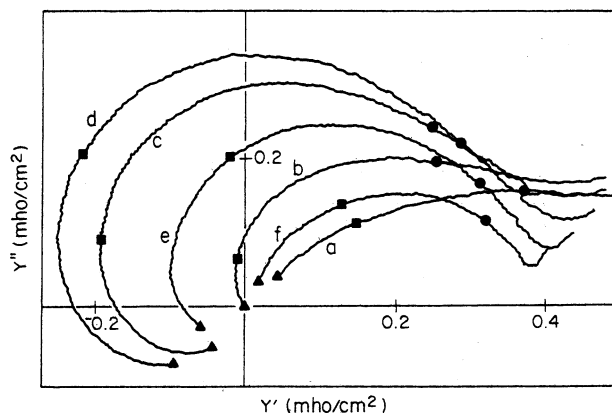


Fig. 6.25 Admittance plots for the low frequency dispersion in region III. Curves a–f correspond to potentials 0.30–0.55 V in 0.05 V increments. The plotted frequency range is 1–1,000 Hz with 1 Hz (*triangles*), 10 Hz (*squares*), and 100 Hz (*circles*) point shown. Disk rotation: 100 rad/s. Reproduced from [64] by permission of The Electrochemical Society

established the chemical composition of the layer occurring at the copper surface during the oscillations as essentially Cu_2O . The porous nature of the Cu_2O film was postulated as the explanation for the absence of complete passivation, with the pores filled with the hydroxide species $\text{Cu}(\text{OH})_2$. It was found that during the oscillations, when the current drops to relatively low values (corresponding to the passive state of the electrode), the amount of $\text{Cu}(\text{OH})_2$ increases, compared to that of Cu_2O . On that basis it was suggested that $\text{Cu}(\text{OH})_2$, as the poorly conducting phase, is the species blocking the electrode surface. In consequence, the oscillatory cycle is associated with the periodical formation and dissolution of $\text{Cu}(\text{OH})_2$, caused by periodical changes of pH of the boundary layer which, in turn, are caused by the changes in the migration current, carried largely by hydrogen ions. This explanation of oscillations, limited to the chemical processes at the interfaces, does not however include the instability of the entire electric circuit, in which ohmic potential drops should also be considered.

In spite of certain chemical complexity of the system considered, Albahadily and Schell [65–67] have performed both experimental and theoretical, extensive systematic studies of oscillations for the $\text{Cu}/\text{H}_3\text{PO}_4$ system, leading to the elaboration of the bifurcation structure of reported instabilities. The bifurcation diagrams were constructed in the coordinate system: applied external voltage–disk rotation speed, the latter parameter determining the thickness of the diffusion layer.

Nonlinear Dynamic Features of the $\text{Cu}/\text{H}_3\text{PO}_4$ System [65]

It appeared that in order to obtain satisfactorily reproducible results, it was necessary to decrease the sample temperature to ca. -24°C , presumably due to the lower amplitude of oscillations which at such temperatures decreases for about order of magnitude, compared to typical room temperature [67]. Then the copper electrode is

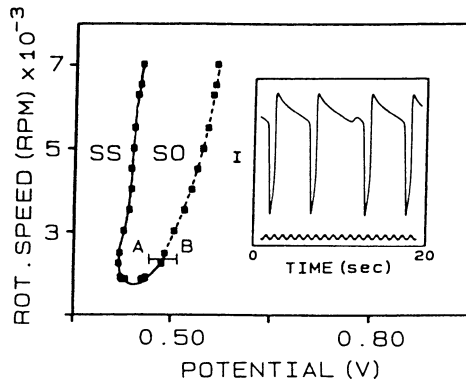


Fig. 6.26 Measured boundaries in the parameter plane, rotation speed vs. the potential set for the working electrode that separate the region for which sustained oscillations (labeled SO) were observed from the region for which only stable stationary states were found (labeled SS). *Solid lines* consist of points at which Hopf bifurcation occurred; *dashed lines* consist of points at which the mixed-mode (MMO) oscillations appear. Temperature = $-17.5\text{ }^{\circ}\text{C}$. The small amplitude oscillations shown in the *inset* were observed just inside the solid portion of the boundary: rotation speed = 2,200 rpm, potential = 427 mV, maximum absolute value of the current = 1.4 mA, minimum value = 1.2 mA. The waveform consisting of large and small amplitude oscillations was measured just inside the *dashed portion* of the boundary: rotation speed = 7,000 rpm, potential = 567 mV, maximum absolute value of the current = 5.8 A, minimum value = 1.4 mA. The dynamics of the system, studied along the section A–B, are described further in the text. Reprinted with permission from [65]. Copyright 1988 American Institute of Physics

expected to dissolve rather smoothly, compared to the large amplitude oscillations, when the current may reach such high values that it causes too extensive etching of the copper surface. Figure 6.26 shows a simple bifurcation diagram, obtained for $-17.5\text{ }^{\circ}\text{C}$ [65] in which however complex dynamics are included.

One should note different bifurcation scenarios if the solid and the dashed lines are crossed in this diagram. If the left solid line is crossed from the left (SS states) to the right (SO states), first the small amplitude, sinusoidal oscillations are observed (like those visualized at the bottom of the inset in Fig. 6.26) which only further develop into large-amplitude oscillations. This indicates the supercritical Hopf bifurcation. In turn, if the system is moved away from the steady-state SS toward SO region from the right to the left, crossing the right dashed line in Fig. 6.26, large amplitude oscillations are observed, but the detailed scenario of their appearance is complex: (1) close to the regions boundary, the oscillations are of the mixed-mode type (see upper course in the inset of Fig. 6.26), (2) upon moving inside the oscillatory region, different periodic behaviors were observed, each consisting of a mixture of both large and small amplitude (i.e., MMO) oscillations, and (3) finally, oscillations consisting of only single peaks persist. One should add that bistable behavior was not observed, either due to its nonexistence or inability to detect under given conditions.

A sequence of dynamic events occurring upon moving from the point A to B was analyzed in detail. Upon increasing voltage, the initial single-peak, large amplitude

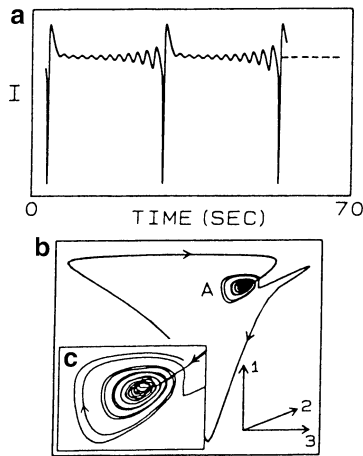


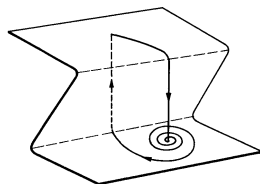
Fig. 6.27 (a) Measured current I plotted as a function of time. Rotation speed = 2,425 rpm, $U = 488.05$ mV. Dashed curve represents the unstable stationary state value of the current. (b) Phase trajectory constructed from time series in (a). Axes are labeled: 1 = $I(t + 2T)$, 2 = $I(t)$, 3 = $I(t + T)$; $T = 0.75$ s. (c) An enlargement of the surface [labeled A in (b)] on which the orbit spirals away from the fixed point (the position of the fixed point is the center of the spirals). Reprinted with permission from [65]. Copyright 1988 American Institute of Physics

oscillations at point A turned into various, both periodic and aperiodic, mixed-mode oscillations, with the average number of small amplitude oscillations increasing until only periodic small amplitude oscillations remained. Upon further movement toward point B, the amplitude of these oscillations gradually decreased up to the point of the Hopf bifurcation where only the stable steady-states survived. Figure 6.27a shows the exemplary course of mixed-mode oscillations and the corresponding phase trajectory (Fig. 6.27b, c), just before reaching the bifurcation point between A and B points in Fig. 6.26. In turn, the horizontal dashed line in Fig. 6.27a, following the oscillatory course, indicates the steady-state current that stabilizes just after crossing this bifurcation point; one can suppose that this current is close to the unstable steady-state around which the current oscillates just before the Hopf bifurcation.

This portrait shows clearly how the phase trajectory, after making an extensive trip in the phase space, is injected into a small neighborhood of the unstable steady-state (fixed point, the parameters of which are close to the value of the current indicated by the dashed line in Fig. 6.27a) and then spirals away which motion corresponds to oscillations of increasing amplitude. The enlarged crucial portion of such trajectory is shown in Fig. 6.27c. It is illustrative to look at this type of dynamics also in terms of the trip of the system's state between the two surfaces of the folded manifold, like that shown in Fig. 6.28.

Such a dynamic behavior is strictly related to the existence of the so-called homoclinic orbit (i.e., literally “the orbit from the same bed”) which means an orbit of infinite period that begins at the fixed point and returns to it after the trip in the phase space (cf. Chap. 1). Strictly speaking, the phase portrait in Fig. 6.27b, c

Fig. 6.28 The schematic representation of the system's dynamics corresponding to the homoclinic trajectory (after [72], reprinted with permission, Copyright 1993 American Chemical Society)



corresponds to *nearly* homoclinic conditions, since the trajectory is reinjected not exactly to the fixed point, but to its close neighborhood. This injection is faster than the slow local spiraling motion away from this unstable fixed point (unstable focus). Thus, the mixed-mode oscillations are related to the phase trajectories of a homoclinic type. Furthermore, such dynamic characteristics are close to the condition of generation of the so-called *Shil'nikov chaos* or homoclinic chaos (see also Sect. 1.9.2).

Similar MMO sequences, as for the electrochemical $\text{Cu}/\text{H}_3\text{PO}_4$ system, were found in both homogeneous and other heterogeneous oscillators: in the former ones the flow rate in the flow reactors (CSTR) plays a role of a bifurcation parameter analogous to, e.g., to the voltage applied between the electrodes in electrochemical systems. The formal similarity of MMO sequences does not necessarily mean exactly the same mechanism underlying their creation. Nevertheless, analysis of MMO reported for various systems allows one to categorize them as belonging to two classes [66]: (1) “periodic–chaotic sequences” meaning alternate occurrence of periodic and chaotic patterns and (2) periodic “Farey sequences.” Both these scenarios were reported for the homogeneous Belousov–Zhabotinsky reaction: the periodic–chaotic sequence was reported by Hudson et al. [73] while the Farey one by Swinney and Maseklo [74–76]. Here, we shall briefly characterize attaining the chaotic regimes for the copper electrodisolution in H_3PO_4 solution.

Route to Chaos Through Period-Doubling Bifurcations

One of the dynamic scenarios found in the SO region of Fig. 6.26 was the transition to chaos through the sequence (“cascade”) of *period-doubling bifurcations* upon increasing voltage, analogously to those observed in the logistic map upon increasing parameter r (Sect. 1.9). The corresponding phase portraits were constructed using the time-delay (T) method in the three-dimensional space: $[I(t), I(t + T), I(t + 2T)]$. Figure 6.29 shows the obtained images projected onto the $[I(t + T), I(t)]$ plane.

The deterministic nature of chaotic courses was confirmed in the following way. The three-dimensional phase portraits were found to cross the plane, $I(t + 2T) = -1.40$ mA. The current at $(n + 1)$ th intersection, $I(n + 1)$, was plotted against $I(n)$ at n th intersection: $I(n + 1) = F[I(n)]$ and a one-dimensional maps were obtained, the course of which, possessing an extremum, was typical of deterministic chaotic dynamics (Fig. 6.30) (cf. similar map in Fig. 6.20).

Systematic studies led to constructing the phase diagram showing the sequence of period-doubling bifurcations upon increasing voltage (Fig. 6.31).

Fig. 6.29 Phase trajectories constructed from the time series data, shown projected into the $[I(t), I(t + T)]$ plane; $T = 0.73$ s. (a) A period-2 orbit for $U = 487.05$ mV, (b) a period-4 orbit for $U = 487.65$ mV; (c) an aperiodic orbit for $U = 487.90$ mV. Rotation speed = 4,600 rpm. Reprinted with permission from [65]. Copyright 1988 American Institute of Physics

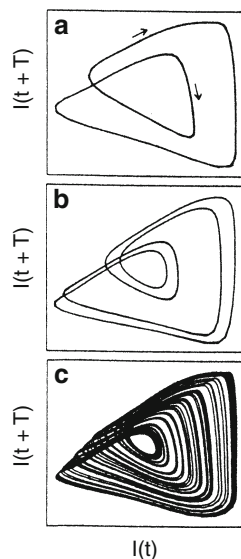
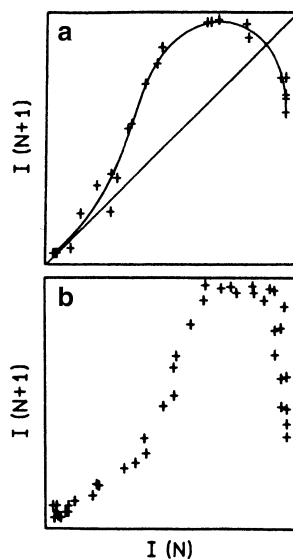


Fig. 6.30 One-dimensional maps (a) $U_0 = 445.1$ mV, (b) $U_0 = 445.0$ mV, rotation rate = 4,600 rpm. The maps demonstrate that the apparent random behavior is deterministic: for any $I(N)$, the maps give $I(N + 1)$. The presence of the extremum implies that the deterministic dynamics is chaos. Reprinted with permission from [65]. Copyright 1988 American Institute of Physics



A Periodic–Chaotic Sequence and the Tangent Bifurcation

The analysis of experimental data collected by Schell and Albahadily [67] led them to the diagnosis of the bifurcation scenario in the periodic–chaotic sequence: its periodic regimes are entered by way of *tangent bifurcations* and disappeared through *period-doubling bifurcations*. In order to understand those phenomena and, by the way, notice again their universalities in nonlinear systems, one can refer to the famous *logistic map* (1.138): $x_{n+1} = ax_n(1 - x_n)$. One of the most

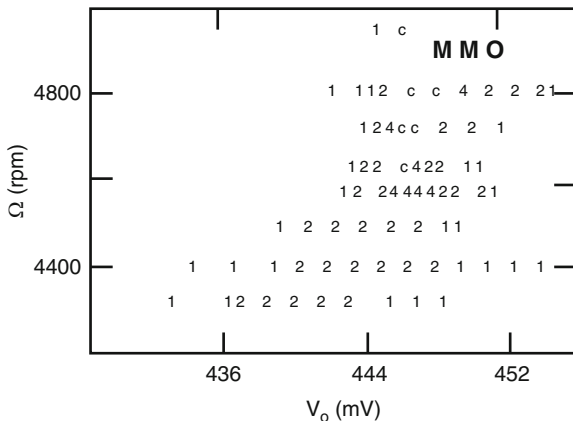


Fig. 6.31 Phase diagram [rotation speed (Ω) vs. potential set for the working electrode ($V_o \equiv U$)] showing the location of different oscillatory states; Temperature = -17.5°C . Notation: 1 = period-1 state; 2 = period-2 state; 4 = period-4 state; C = chaotic state; MMO = mixed-mode oscillations. Reprinted with permission from [65]. Copyright 1988 American Institute of Physics

intriguing features of this map, which exhibits route to chaos through the cascade of period-doubling bifurcations is the existence (temporal revival) of periodic behavior (i.e., periodic windows) within the chaotic regime, when the bifurcation parameter is changed (see Fig. 1.39a). The most intriguing is the window with period-3 cycle, existing for $3.8284\dots < r < 3.8415\dots$. The period-3 cycle means that any point p in this cycle repeats every three iterates: $p = f(f(f(p))) \equiv f^3(p)$ and is therefore a fixed point on the third-iterate map. Figure 6.32 shows such third-iterate map $x_{n+3} = f^3(x_n)$ which corresponds to $a = 3.835$ [77].

The intersections of this map with the straight line indicate eight points, of which six, indicated by dots in the figure correspond to period-3 cycle (other two are period-1 points). Stable period-3 cycles are denoted by (\bullet), while unstable by (\circ). Now, if a is slightly decreased from 3.835 toward chaotic regime, the maxima become lower and the minima become less deep, so the curve pulls away from the diagonal. For $a = 3.8$ all its six intersections with a diagonal will already not exist. So, somewhere between $a = 3.835$ and $a = 3.8$, and exactly for $a = 1 + \sqrt{8} = 3.8284\dots$, the $f^3(x)$ map must have become tangent to the diagonal, meaning therefore the occurrence of *tangent bifurcation* in which stable and unstable period-3 cycles coalesced and annihilated [77]. In fact, the tangent bifurcation is a kind of a saddle-node bifurcation.

Coming back to specific characteristics of the $\text{Cu}/\text{H}_3\text{PO}_4$ system, the transition between various dynamic modes, involving periodic and chaotic MMOs, are visualized in the phase diagram shown in Fig. 6.33 [67]. The notation L^S means the number of large amplitude oscillations (L) followed by a number (S) of small amplitude oscillations. An inspection of this diagram reveals, among others, the periodic-chaotic sequences. Further details of these transitions can be found in the original paper [78].

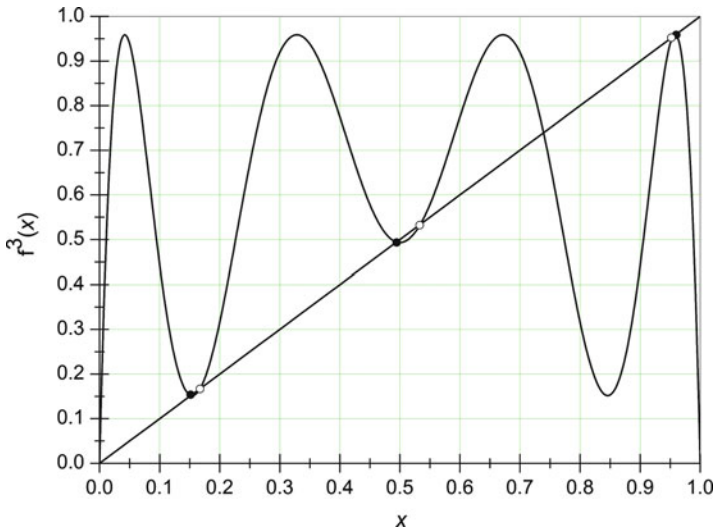


Fig. 6.32 Principle of the tangent bifurcation illustrated by the third-iterate logistic map (1.138) for $a = 3.835$

The Farey Sequence [79]

John Farey, a British geologist, has published his concept in 1816, in the *Philosophical Magazine*. The Farey sequence is a term from the number theory, which orders all rational numbers between 0 and 1 according to a specific rule. The Farey sequence of order n is a sequence of fractions between 0 and 1, arranged in order of (usually) increasing size, in which the denominator does not exceed n .

For example, the Farey sequence of orders 1–5 are, respectively:

$$\begin{aligned}
 F_1 &= \left\{ \frac{0}{1}, \frac{1}{1} \right\} \\
 F_2 &= \left\{ \frac{0}{1}, \frac{1}{2}, \frac{1}{1} \right\} \\
 F_3 &= \left\{ \frac{0}{1}, \frac{1}{3}, \frac{1}{2}, \frac{2}{3}, \frac{1}{1} \right\} \\
 F_4 &= \left\{ \frac{0}{1}, \frac{1}{4}, \frac{1}{3}, \frac{1}{2}, \frac{2}{3}, \frac{3}{4}, \frac{1}{1} \right\} \\
 F_5 &= \left\{ \frac{0}{1}, \frac{1}{5}, \frac{1}{4}, \frac{1}{3}, \frac{2}{5}, \frac{1}{2}, \frac{3}{5}, \frac{2}{3}, \frac{3}{4}, \frac{4}{5}, \frac{1}{1} \right\}
 \end{aligned} \tag{6.46}$$

The construction of Farey sequence of order n is very simple and begins from the list consisting of $\{0/0\}$ and $\{1/1\}$ fractions. Then, between every two fractions one inserts the fraction, the numerator of which is a sum of their numerators, and

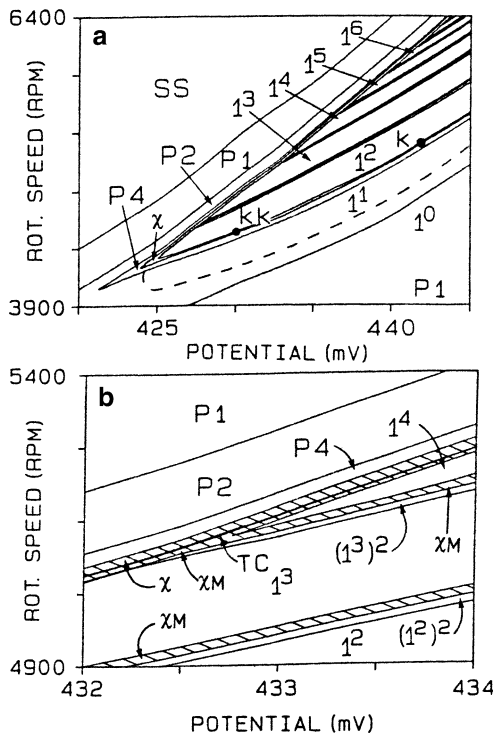


Fig. 6.33 (a) Phase diagram depicting the regions in the parameter plane, rotation speed at the working electrode vs. the potential set at the working electrode, for which different behaviors were observed. (b) An enlargement of a region in (a). L^S = periodic mixed-mode state, $L = 1, S = 1, 2, \dots, 6$; $(L^S)^2$ = subharmonic of a mixed-mode state, χ_M = chaotic mixed-mode state; SS = stationary state; P1 = small amplitude periodic oscillations; P2 = subharmonic of P1; P4 = second subharmonic of P1; χ = chaotic state with small-amplitude oscillations; TC = approximate location of the curve at which the transition from small amplitude chaos to chaotic MMOs occurred. Mesh size: rotation speed, 50–100 rpm through large windows and 1–10 rpm near boundaries; potential, 1.0–2.0 mV through large windows and 2.5×10^{-2} mV near boundaries. Boundaries should only be considered to represent general trends; the mesh size is too large to capture the small-scale turns. Reprinted with permission from [67]. Copyright 1989 American Institute of Physics

the denominator is the sum of the denominators. One continues this procedure until the set of fractions of sufficiently small denominators is exhausted, bearing in mind that for the sequence of order n the maximum value of a denominator must not exceed n .

Let us learn some terminology related to Farey sequences. The neighboring fractions in the Farey sequence are named a *Farey pair*. One of important properties of such a pair is the Farey sum: $(p_1/q_1) \oplus (p_2/q_2) = (p_1+p_2)/(q_1+q_2)$ which is the fraction which will first appear between p_1/q_1 and p_2/q_2 in the Farey sequence of the order $(q_1 + q_2)$. The $(p_1+p_2)/(q_1+q_2)$ fraction is therefore called the *Farey mediant* of p_1/q_1 and p_2/q_2 . In other words, the new term in the Farey sequence is a mediant

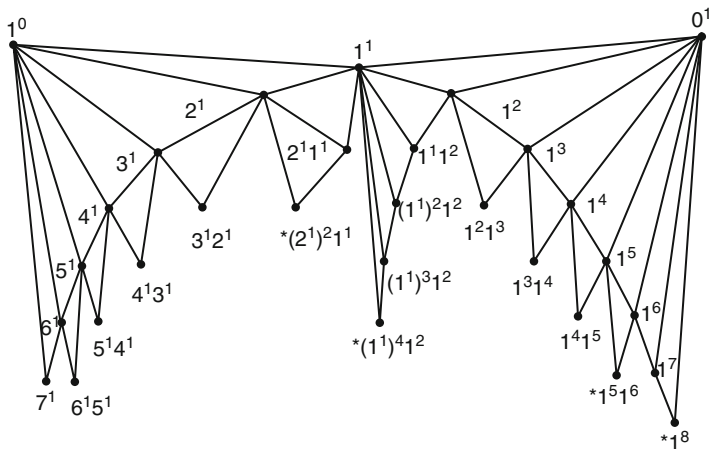


Fig. 6.34 A portion of the Farey tree constructed of observed states. States marked with a *star* were observed for only four to six cycles. Most other states were observed for many more cycles. The working electrode potential increases to the *right* (not to scale), while the *vertical dimension* is used only for diagrammatic convenience. Reprinted with permission from [66]. Copyright 1989 American Institute of Physics

of its neighbors. In fact, if $p_1/q_1 = 1/3$ and $p_2/q_2 = 1/2$, then in the Farey sequence of order 5 we find the term $2/5$ in the predicted place [cf. Eqs. (6.46)].

Which is the connection of the Farey scheme with the mixed mode oscillations? Under appropriate experimental conditions, it was found that the change in the applied voltage (the bifurcation parameter) results in increasing complexity of oscillations in a way following the Farey arithmetics. These dependences can be visualized in a form of a *Farey tree* shown in Fig. 6.34 where the pattern of each state is the concatenation of the patterns of a pair of states above it, one on either side. As above, the notation $L_1^{S_1}L_2^{S_2}...$ means the state consisting of L_1 large oscillations, followed by S_1 small oscillations, followed by L_2 large oscillations, followed by S_2 small oscillations, etc.

A correspondence between the mixed mode oscillations and the rational numbers forming the Farey sequence is established as follows: if one period of a state consists of a total of L large amplitude oscillations and S amplitude oscillations, then one assigns to that state L^S the *firing number* p/q :

$$\frac{p}{q} = \frac{S}{L + S} \tag{6.47}$$

having a sense of the fraction of the small oscillations. Since both the number of small oscillations per period and the total number of oscillations are additive under concatenation of patterns, the firing number of the Farey mediant of two states in Fig. 6.34 is the Farey sum of the firing numbers of its parents [66].

For the sake of generalization of nonlinear dynamic characteristics, one should note that, similarly as in the case of the periodic–chaotic sequences, described above, the Farey sequence was found by Maselko and Swinney [75, 76] also in the characteristics of the mixed-mode oscillations of the homogeneous Belousov–Zhabotinsky (BZ) reaction, from which works the interpretation of MMOs in terms of Farey concept originates. However, there are also differences in the detailed dynamics underlying the Farey sequences. For the BZ reaction, Maselko and Swinney have proposed the explanation based on the phase locking on a torus, involving two intrinsic frequencies of the system. The torus, corresponding to quasiperiodic oscillations, evolves from the single steady-state through two successive Hopf bifurcations. For Cu/H₃PO₄ system, the mixed-mode oscillations characterized with the Farey sequence were not related to the torus trajectory. Experimentally, it was proved by the separation between the quasi-periodic regime and MMOs through the small-amplitude chaos. In other words, before the onset of MMOs, the torus trajectory disappeared.

The above studies of Albahadily et al. were based on dc studies of the oscillatory Cu/H₃PO₄ system. Later developments in its stability analysis (including the acetate buffer medium) involved also impedance spectroscopy, as Kiss et al. have reported [80]. The Nyquist (complex plane) spectra were recorded for different electrode potentials, including the values close to the points of the Hopf bifurcations, also in the absence of external serial resistance. The critical frequencies, by which oscillations emerged at the bifurcation points, were determined. In this work, the nontraditional construction of phase diagrams was suggested, in which typically used external voltage U was replaced by the true electrode potential (E) which is a dynamic variable, and not a bifurcation parameter. The other parameter was the external resistance. In the opinion of the authors, the advantage of such novel construction of phase diagrams lies in their independence of cell geometry, so the experiments made in different laboratories can be more easily compared. For the Cu–H₃PO₄ system, the corresponding diagram between E and the (reciprocal) value of critical resistance at which Hopf bifurcation occurs (leading to or canceling the oscillations, respectively) is shown in Fig. 6.35a. In turn, Fig. 6.35b shows the diagram involving angular frequencies at the bifurcation points.

Following the above concept, Kiss et al. [81] have used the Cu–H₃PO₄ system to test numerical simulations aiming to investigate how this type of phase diagrams changes with the surface area (electrode radius) and the rotation rate of an electrode. Based on linear stability analysis of a general, two-variable model for NDR-type electrochemical oscillators, the *scaling relationship* was proposed. This scaling law predicted that all scaled data points derived from the critical values of parameters (resistance and electrode potential) characterizing the onset of oscillations should fall—independently of the size of the electrode and the rotation rate—on a *single plot*. Strictly speaking, this analysis refers to the NDR-type oscillatory systems exhibiting supercritical Hopf bifurcation. The reader interested in the details of this analysis is advised to consult the original reference, while here we shall limit our considerations to most important conclusions. Mathematical derivations referred to the skeleton model of the N-NDR oscillator, suggested by Koper and Sluyters [cf. Eqs. (2.29) and (2.31)] [82], combined with the conditions

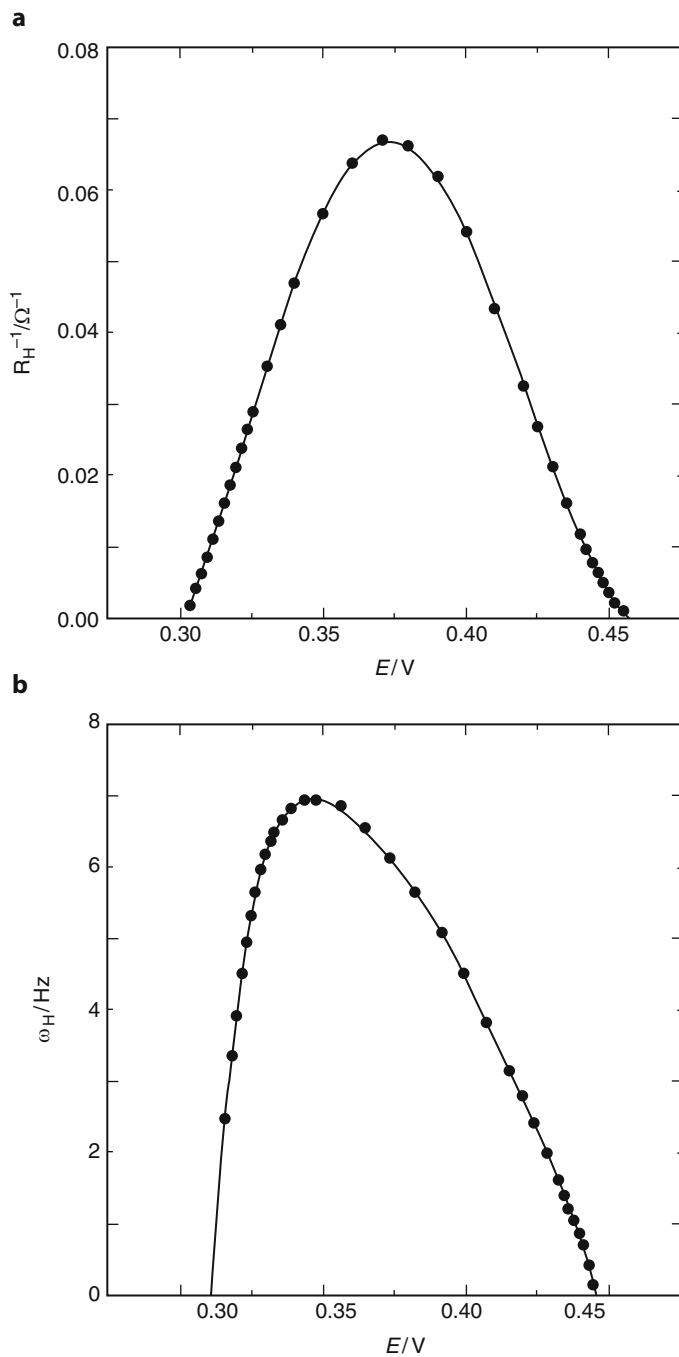


Fig. 6.35 (a) Reciprocal values of R_H and (b) ω_H values (i.e., corresponding to a Hopf bifurcation) determined by the impedance analysis of the Cu-orthophosphoric acid system as a function of true electrode potential. Reprinted with permission from [80]. Copyright 1998 American Chemical Society

for the range of mass transfer region in the steady-state, reached at the rotating disk electrode. Then, linear stability analysis predicts that the locus of a Hopf bifurcation varies with the electrode rotation rate ν according to the dependence:

$$R_{\text{H}}A - C(E_{\text{ss}}) = \frac{D(E_{\text{ss}})}{\nu^{1/2}} \quad (6.48)$$

where A is the electrode surface, ν is the rotation rate of the disk electrode, R_{H} is the solution resistance at the Hopf point and:

$$C(E_{\text{ss}}) = - \frac{1}{nFc_0 \left[\frac{dk(E)}{dE} \right]_{\text{ss}}} \quad (6.49)$$

$$D(E_{\text{ss}}) = - \frac{k(E_{\text{ss}})\beta}{nFc_0D_o \left[\frac{dk(E)}{dE} \right]_{\text{ss}}} \quad (6.50)$$

with β being the appropriate constant. The essential scaling relationship [Eq. (6.48)] was verified by both numerical calculations involving the three-variable Koper–Gaspard [83] model and the electrochemical dynamical system experimental studies of Cu–H₃PO₄ system.

At the end of section devoted to oscillatory Cu dissolution, we shall mention a recent paper by Karantonis et al. [84] who studied oscillatory electrodedissolution of copper in trifluoroacetic acid (TFA), by means of dc voltammetry and impedance spectroscopy. In the dc experiments, involving the copper disk electrode, the potentiodynamic I – E studies have indicated the oscillations which set in upon increasing anodic potential via a supercritical Hopf bifurcation. In impedance measurements, finding the specific frequency at which this process resonated with the input signal was correlated with the characteristics of neural resonators as natural band-pass filters. The Bode and the Nyquist plots, constructed for the electrode potentials close to the supercritical Hopf bifurcation point, have indicated that the minimum values of the total impedance (meaning the situation close to resonance) was observed for the ac frequency range $\omega = 0.8$ – 3 Hz. Also, Potkonjak et al. [85] have reported for this system, occurring in a part of limiting current region, a rich variety of dynamical responses, depending on temperature and applied potential, including mixed-mode oscillations. Changes of the electrode surface structure and morphology were investigated by X-ray diffraction spectroscopy, atomic force microscopy, and optical microscopy.

Finally, electrochemical oscillations were reported also for the copper-based alloys. For example, Hurtado et al. [86] have described open circuit potential oscillations for some Cu–Al and Cu–Ag–Al alloys in contact with NaOH solutions. The oscillations were explained in terms of fast Al dissolution, altering the main Cu dissolution/passivation process, and the slow transportation of produced aluminate to the solution bulk, meaning thus their temporal accumulation at the interface.

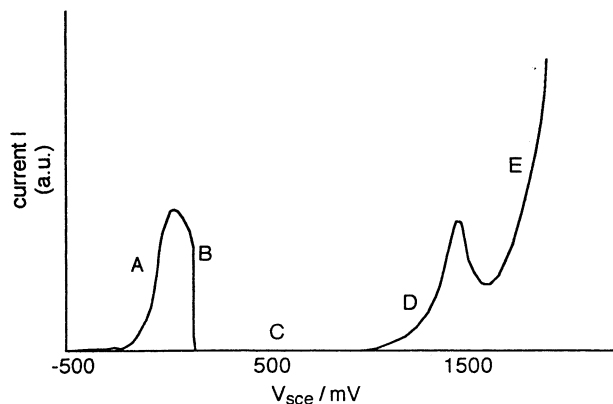


Fig. 6.36 Typical polarization curve of the anodic Ni dissolution in H_2SO_4 . Region A: potential region of active dissolution; Region B: primary passivation; Region C: passivated electrode; Region D: transpassive dissolution; Region E: oxygen evolution. Reprinted from [24] with permission of John Wiley & Sons, Inc. Copyright 1996 John Wiley & Sons, Inc.

6.1.4 Oscillatory Dissolution of Nickel in H_2SO_4 Medium

6.1.4.1 Experimental Studies

The electrodisolution of nickel in aqueous solutions of sulfuric acid is an interesting and important example of the process exhibiting complex dynamics. This process has been quite intensively studied, starting from Hoar and Mowat in 1950 [87], through papers by Osterwald from 1960 and 1962 [88, 89], up to more recent studies, published by Lev et al. in 1988 and 1989 [90–92].

For the $\text{Ni}/\text{H}_2\text{SO}_4$ system, the instabilities described in this section were reported for the *transpassive* region, denoted as D in Fig. 6.36, i.e., for the potential region between the region of a passivated electrode surface (C) and the region of oxygen evolution (E).

According to Fig. 6.36, the destruction of the passive layer precedes the oxygen evolution and, furthermore, between regions D and E there occurs a secondary passivation, leading to the second region of a negative resistance there. Investigations of Osterwald were based on parallel connection of a potentiostat and a galvanostat, with the possibility of a rapid switch of the operation modes between these devices. The advantage of such experimental methodology will be explained in view of Fig. 6.37, which shows the polarization curve recorded by Osterwald and Feller [88] under potentiostatic conditions [90].

First the I – E characteristics of the transpassive region, visualized in Fig. 6.37, were determined. Next, using the potentiostat, the electrode potential was established at a value corresponding to the positive slope of I – E curve. Then the

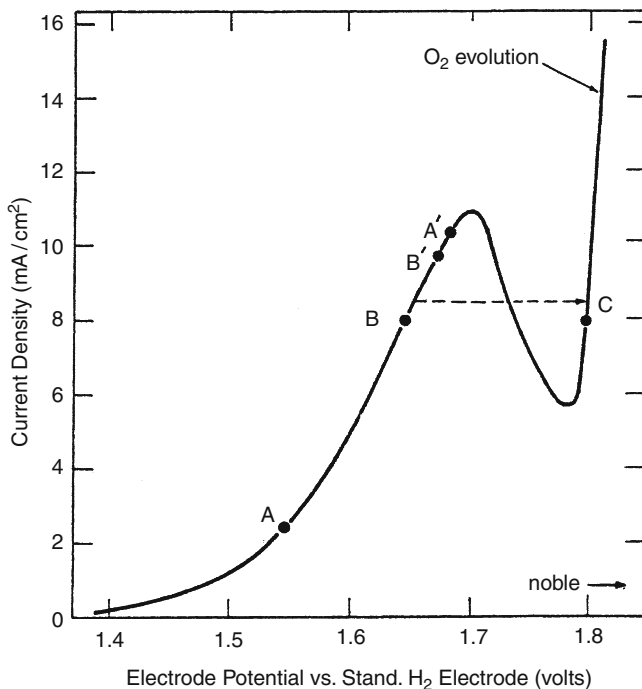
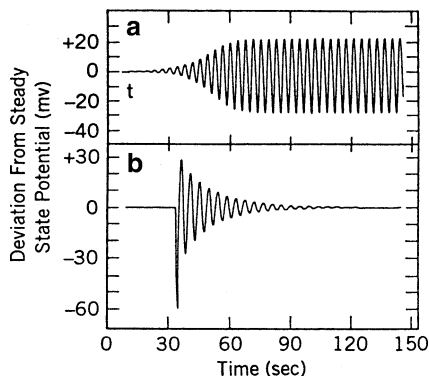


Fig. 6.37 Polarization curve obtained potentiostatically for a nickel electrode in 1 N H₂SO₄ in the transpassive region. Points A, B, A' and B' are explained in the text. Reprinted from [88] by permission of The Electrochemical Society

system's control was switched to galvanostatic, with the galvanostat set previously at a value of current identical with that measured in the potentiostatic mode. Depending on the choice of the potential, three major dynamical behaviors were observed by Osterwald [88]:

1. If the potential was chosen between the points A and B, or between A' and B' in Fig. 6.37, in the galvanostatic mode the sustained electrode potential oscillations set in (see Fig. 6.38a).
2. If the potential was lower than at point A or higher than at point A', damped oscillations set in, in course of which the system asymptotically returned to the originally chosen electrode potential (Fig. 6.38b).
3. If the potential was placed between points B and B', no oscillations in the galvanostatic mode were observed, but the potential jumped onto the right-hand ascending branch. As Koper indicates in his review [24], this behavior, reported by Osterwald in 1960, was probably the first clear manifestation of a homoclinic bifurcation in an electrochemical system, although that time such terminology, specific for nonlinear dynamics, was not yet being in use in chemistry. In fact, one can interpret this potential jump as the beginning of the oscillation leading however to the collision of a limit cycle trajectory with the

Fig. 6.38 Oscillations of potential under galvanostatic conditions of a nickel electrode in 1 N H_2SO_4 . (a) sustained oscillations for a current density of 2.87 mA cm^{-2} ; (b) Damped oscillations for a current density of 2.26 mA cm^{-2} . Reproduced from [88] by permission of The Electrochemical Society



saddle point on a negative branch of the $I-E$ curve, unstable under galvanostatic conditions. In consequence, the limit cycle is destroyed, and the system moves to another stable steady-state, placed on the stable, ascending branch of the $I-E$ characteristics. Such a decay of oscillations is qualified as a saddle-loop (or homoclinic) bifurcation, described in Sect. 1.4.3 (Fig. 1.24). Here, we shall illustrate this sequence of events in terms of another schematic diagram which shows first the birth of oscillations via a supercritical Hopf bifurcation and then their decay due to a homoclinic bifurcation (Fig. 6.39).

Note that the homoclinic bifurcation is one of the infinite-period global bifurcations, meaning that the oscillation period increases to infinity upon approaching the bifurcation point. Figure 6.40 shows the elongation of the oscillation period for the Ni/ H_2SO_4 system, when the external voltage is increasing up to critical value. The additionally reported hysteresis in the system's dynamics will be explained later in this section.

Based on Figs. 6.38 and 6.40 one immediately concludes that anodic oxidation of Ni electrode in H_2SO_4 medium exhibits oscillations of the electrode potential under galvanostatic conditions, as well as the oscillations of current under potentiostatic conditions, in the latter case in the presence of appropriate serial ohmic resistance. This qualifies the system considered as the HN-NDR type oscillator (i.e., with hidden N-shaped negative resistance). Thus, one can expect that impedance studies will reveal the existence of its negative real part at intermediate frequencies, according to properties of such systems described in Sect. 3.4.

Systematic studies led Lev et al. [91] to the bifurcation diagram of the Ni electro-dissolution in H_2SO_4 , constructed in the coordinate system: acid concentration–current density as the control parameters (Fig. 6.41). This diagram shows that, besides simplest oscillations, there were observed also complex periodic and chaotic oscillations, exhibiting period doubling bifurcations and torus bifurcations. Also the region of birhythmicity was indicated; this phenomenon, known also from the area of homogeneous oscillators [78] can be considered a generalization of bistability and means the existence of the system in different oscillatory states for the same range of control parameters, depending on the system's “history.”

Fig. 6.39 (a) Phase plane representation of a limit cycle bifurcating in a homoclinic orbit and disappearing for the critical value of bifurcation parameter μ_c . (b) Typical bifurcation diagram belonging to the situation illustrated in (a). Reproduced from [93] by permission of The Royal Society of Chemistry

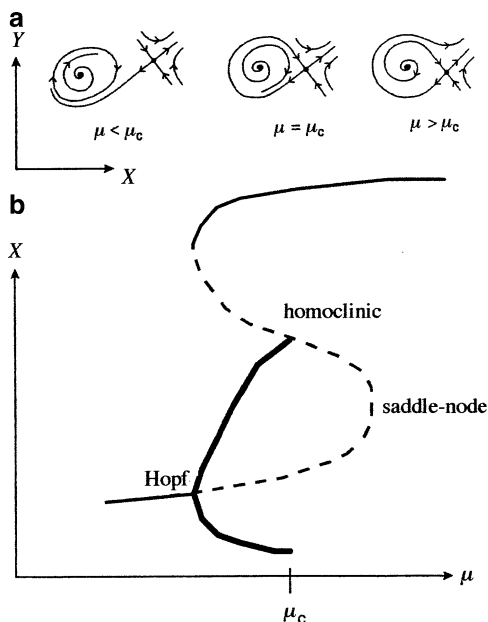
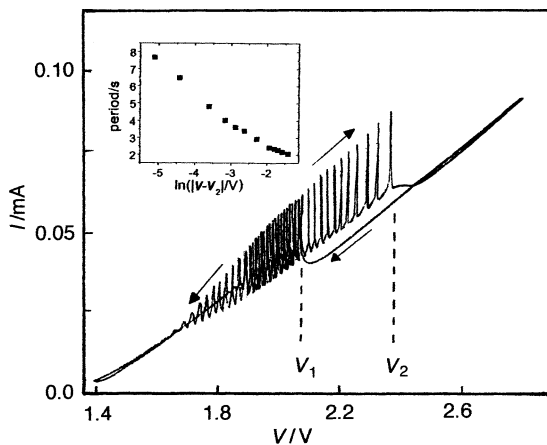


Fig. 6.40 Cyclic voltammogram of the dissolution of nickel wire in 1 M sulfuric acid. Scan rate 10 mV/s. *Inset* shows the period of the oscillation as the voltage approaches the critical value V_2 . In series with the nickel working electrode there was a 12 k Ω ohmic resistor. Reference electrode: SCE. Reproduced from [93] by permission of The Royal Society of Chemistry



Obviously, as for the bistability, this means the hysteresis in the system's oscillatory response upon cyclic variation of the control parameter(s) (cf. also Fig. 6.40).

As for other passivation/depasivation processes, chemical and structural complexity of the passive/porous layer at the electrode makes it difficult to elaborate an in-depth satisfactory, unambiguous electrochemical mechanism of the Ni/ H_2SO_4 oscillator. According to the development of trends in explanation of

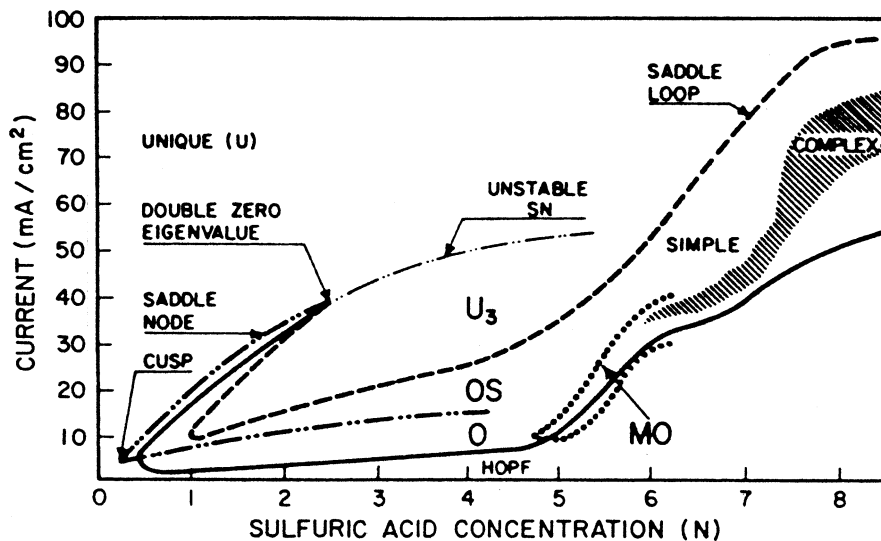


Fig. 6.41 Grand bifurcation map of the Ni dissolution: typical phase planes are unique (U), globally stable states (U_3) and oscillatory (O) states, multiplicity of oscillatory and stable states (OS), bistability (near cusp) and birhythmicity (MO). The Hopf, saddle-node, and saddle-loop bifurcations are identified in the figure; the generalized Hopf is denoted by the *dotted line*. Reprinted with permission from [91]. Copyright 1989 American Chemical Society

electrochemical instabilities, the apparently first mechanism, focusing on the properties of the Ni/H₂SO₄ interface, was published in 1969 by Indira et al. [94]. Later, another mechanism, invoking impedance characteristics, was elaborated by Keddam et al. [95]. It was followed by the model by Haim, Lev et al. [92], as the continuation of their earlier experimental research. All these models are briefly described below.

6.1.4.2 The Indira and Ross Model

The approach by Indira et al. [94], developed later also by Doss and Deshmukh [96], can be called the SR (“Stoichiometric Region”) mechanism. This concept refers generally to the conductivity of the crystalline phases, like the solid nickel oxide film at the nickel electrode. Stoichiometric NiO phase is expected to be an insulator (exhibiting bad both ionic and electronic conductivity), but can acquire certain conductivity through defects of the crystalline structure. Let us consider the state of anodically polarized metallic nickel already passivated with the compact film of nickel oxide. According to the SR model, at the film/solution interface the interaction of O²⁻ ions from the oxide with hydrogen ions in the solution causes the formation of O²⁻ vacancies (v_O^{2-}) in the oxide film. The effectively positively charged vacancies v_O^{2-} , by coulombic repulsion cause the transfer of close Ni²⁺

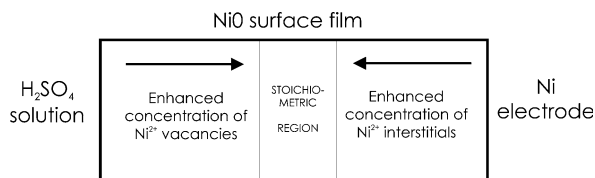


Fig. 6.42 Principle of the (SR) mechanism. Schematic structure of the NiO film layer at the surface of the anodically polarized nickel electrode in H_2SO_4 solution, indicating regions of defected, conducting phase and the middle stoichiometric region, the periodical formation and breakdown of which is considered crucial for the galvanostatically recorded oscillations of the Ni electrode potential. *Arrows* indicate the directions of migration of Ni^{2+} vacancies and interstitials in the electric field (after [94])

ions also to the solution phase. Also complex formation of Ni^{2+} ions with SO_4^{2-} ions may cause spontaneous transfer of Ni^{2+} ions into the solution. Under the influence of the electric field, the effectively negatively charged $v_{\text{Ni}^{2+}}$ vacancies migrate through the oxide film toward the metal, where the transfer of Ni^{2+} ions to the arriving vacancies occurs. Under high electric field (high anodic overpotentials) also the energy-demanding transfer of Ni^{2+} ions from the metal to the interstitial position ($i_{\text{Ni}^{2+}}$) in the oxide phase occurs, with the interstitials migrating through the oxide film toward the solution. As a consequence of these processes, the oxide film close to the metal surface has enhanced concentration of $i_{\text{Ni}^{2+}}$ and that near the solution a relatively high concentration of $v_{\text{Ni}^{2+}}$. Since these defects migrate in opposite directions, somewhere in the middle of the film the Ni^{2+} interstitials and vacancies meet and annihilate each other, forming a “stoichiometric region” (SR), the thickness of which increases in time, as recombination of charge carriers progresses (see Fig. 6.42).

The formation of this poorly conducting middle region, associated with decay of charge carriers, causes the increase of the local potential drop which is experimentally reported as the increase of the electrode potential. The intensity of the electric field cannot however increase continuously, since at its certain critical value the internal field emission takes place which means the flow of a small electronic current through the stoichiometric region. This in fact means its damage, due to the formation of Frenkel defects: interstitials and vacancies. Accordingly, the potential drop across this region decreases and this is reported as the decrease in the measured Ni electrode potential. However, the enhanced conductivity means now the possibility of migration of the interstitials and vacancies toward each other, eventually their recombination and thus regeneration of the stoichiometric region. To summarize, galvanostatic oscillations of the Ni electrode potential are considered a result of the periodic formation and destruction of the stoichiometric region inside the passive oxide layer at the Ni electrode. In other words, the explanation of the oscillations in terms of SR mechanism ascribes the crucial role to the nature of the solid-state effects.

Fig. 6.43 Complex plane impedance plots of the anodic dissolution of single crystal Ni(111) electrode in 1 M H_2SO_4 , at 25 °C, at potentials A–F indicated in the dc I – E curve, in Fig. 6.44 [24, 95]. Reproduced from [95] by permission of The Electrochemical Society

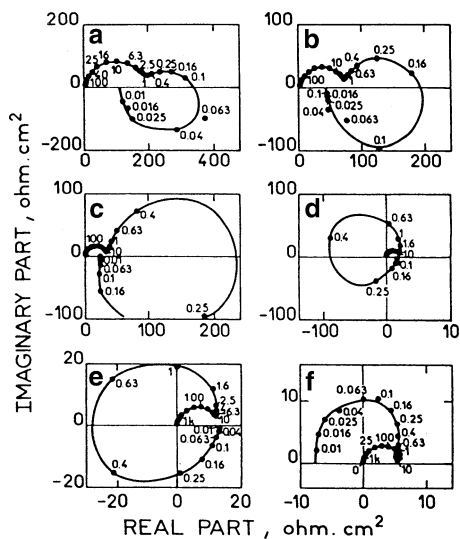
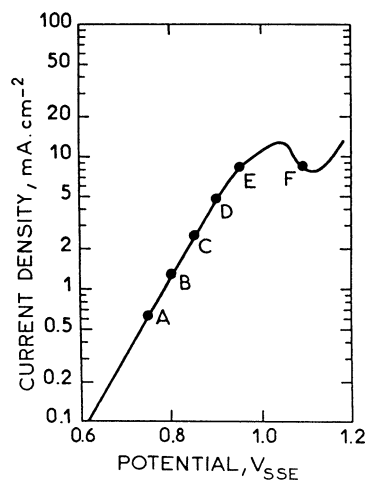


Fig. 6.44 Steady-state polarization curve of the transpassive dissolution of single-crystal Ni(111) electrode in 1 M H_2SO_4 at 25 °C. A–F correspond to the impedance diagrams (a–f) in Fig. 6.43 [24, 95]. SSE - Hg/ Hg_2SO_4 /sat. K_2SO_4 ref. electrode. Reproduced from [95] by permission of The Electrochemical Society



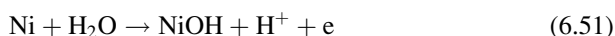
6.1.4.3 The Keddum et al. Model

For Keddum et al. [95], the results of impedance measurements were the basis for the electrochemical characteristics of the Ni/ H_2SO_4 system. The representative complex plane spectra, collected in Fig. 6.43, correspond to respective electrode potentials located in the transpassive region, indicated in Fig. 6.44.

Two spectra c and d are crucial for the diagnosis of instabilities. They both correspond to the positive I – E slope in Fig. 6.44, but spectrum d reveals the negative real impedance, hidden on the dc dependence (similarly as spectrum e). Evidently, the shape of this spectrum confirms that the Ni/ H_2SO_4 system belongs to

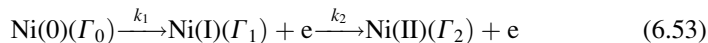
the HN-NDR oscillators (Class IV). This transition indicates the presence of a Hopf bifurcation under galvanostatic conditions, confirming thus the origin of experimentally observed oscillations. Also, in concordance with the theory of HN-NDR oscillators, the transition from plot c to plot d must be accompanied by a plot for which the real impedance Z' becomes infinitely negative for some nonzero frequency. In turn, the negative real impedance observed for $\omega \rightarrow 0$, at potential F is concordant with the explicit negative slope of the dc (zero frequency) I - E characteristics. From Sect. 3.4 we know that in the HN-NDR system a Hopf bifurcation should occur also under potentiostatic conditions ($U = \text{const}$), provided that sufficient serial ohmic resistance is inserted in the circuit of the Ni working electrode, and this was also confirmed experimentally [97] (cf. Fig. 6.40).

Concerning the chemical source of instabilities in the Ni/H₂SO₄ system, Keddama et al. have postulated NiO as the species that initially completely passivates the electrode surface, as a result of the processes:



Based on experimental observation that the dissolution rate of a passive layer increased with H₂SO₄ concentration, at constant pH, it was further suggested that dissolution of NiO layer in the transpassive region was accelerated by SO₄²⁻ and HSO₄⁻ ions. The formation of the second region of a negative resistance was explained in terms of repassivation with the species like Ni(OH)₃.

In complement to above analysis one should note a recent impedance analysis of the dissolution/passive transition in the Ni/H₂SO₄ system, reported by Keddama, Vicente et al. [98]. The research was inspired by the conclusion that this transition is a complex electrode process which strongly depends on the composition of the solution and presumably other factors which determine the course of ionic reactions, electron transfer process, mass transport phenomena, phase formation, precipitation and dissolution of various intermediates. As an illustration of possible controversies, there were recalled the recently published results of spectroscopic measurements that Ni(OH)₂ was a component of passive layer [99, 100] in contradiction with the proposed oscillation mechanisms. One can suppose that Ni(OH)₂ was indeed formed under conditions of spectroscopic measurements, but in the oscillatory experiments the detailed conditions, and thus the composition of the passive layer, could be different. The problem was approached with the analysis of electrochemical impedance spectra recorded in the active/passive transition potential range, for a polycrystalline nickel electrode in an acid sulfate medium of pH 2.7, in the absence of chloride ions, which could strongly interact with the nickel surface or participate in the formation of nickel salt layers. The experimental impedance spectra were interpreted in terms of the reaction sequence, involving two irreversible electron-transfer steps, followed by chemical dissociation and solubilization of Ni(II) species, and the transport of a solvated Ni²⁺ throughout a solvated media [98, 101, 102]:



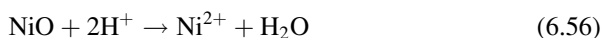
Theoretical impedance spectra, constructed for the assumption that passivating species $[\text{Ni}(\text{OH})_2]$ progressively covers the electrode surface, predicted the appearance of negative time constants for coverage of the passive species greater than 0.5. It is approximately concordant with experimental impedance spectra showing a negative constant at low frequencies, concordant in turn with the negative slope of the polarization curve, occurring for $\theta \approx 0.7$. These results are one more illustration of the difficulties in exact determination of the composition of the passive layers formed during anodic oxidation of metals.

6.1.4.4 The Haim et al. Model

Haim et al. [92] have used some ideas from the Keddam model, but their mechanism ascribes different role to various species. In the initial passive state, the Ni surface is entirely covered by the oxide layer. Three species: NiO, Ni^IOH and NiHSO₄⁻, the latter one meaning adsorbed bisulfate ions, contribute to the total coverage of the electrode surface denoted further as $\sum_i \theta_i$. The active electrodis-solution of nickel: $\text{Ni} \rightarrow \text{Ni}^{2+} + 2\text{e}$ occurs only through the surface fraction uncovered with oxide species, with a rate v_1 :

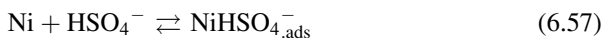
$$v_1 = k_{\text{b}} c_{\text{H}} \left(1 - \sum_i \theta_i \right) \exp \left[\frac{bFE}{RT} \right] \quad (6.55)$$

in which c_{H} means the concentration of H⁺ ions in the solution. The formation of NiO and NiOH species occurs according to Eqs. (6.51) and (6.52), with NiOH dissolving chemically:



Haim et al. assume a priori that the rate of Eq. (6.56), although being purely chemical, is strongly dependent on the electrode potential in a Tafel-like way. This (disputable) dependence appeared however to be crucial for the onset of oscillations.

Furthermore, the region of secondary passivation, observed only for Ni electrode in contact with H₂SO₄ solution is caused by adsorption of HSO₄⁻, according to equation:

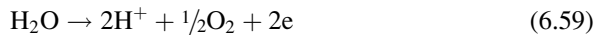


It is important to note that HSO_4^- ions exhibit greater affinity to Ni surface than SO_4^{2-} ions. The surface coverage of HSO_4^- , θ_h , follows a potential-dependent isotherm:

$$\theta_h = \frac{K_a c_h}{1 + K_a c_h} (1 - \theta) \quad (6.58)$$

where θ means the sum of the oxide and hydroxide coverage and K_a is the potential-dependent equilibrium constant: $K_a = K_a^0 \exp[\alpha E]$ which reflects the increasing adsorption of HSO_4^- with increasing positive surface charge (potential) of the electrode.

Finally, the increase of current at most positive potential is explained, as mentioned above, with the oxygen evolution reaction:



which is assumed to occur only at the electrode surface not covered with the passivating oxide layer.

Mathematical construction of the model, based on the above assumptions, involves two ordinary differential equations with the electrode potential E and the total oxide–hydroxide coverage θ_h as the dynamical variables. They could be transformed to the following forms [24]:

$$\varepsilon \frac{dE}{dt} = J - r_{\text{nd}} \quad (6.60)$$

$$\frac{d\theta}{dt} = r_{\text{of}} - r_{\text{od}} \quad (6.61)$$

where parameter $\varepsilon = C_d \Gamma_m / nF \approx 0.1$, with C_d —differential double layer capacitance and Γ_m —the total number of Ni surface sites. J is the current density, applied in the galvanostatic experiment, r_{nd} —the rate of nickel dissolution, r_{of} —the rate of oxide formation, and r_{od} —the rate of oxide dissolution. This model neglects the oxygen evolution reaction (6.59) in the region of the potential oscillations. Linear stability analysis of this system shows indeed that oscillations are possible only under assumption that the oxide layer dissolution [Eq. (6.56)] is potential-dependent, more precisely, if $\partial r_{\text{od}} / \partial E$ is sufficiently positive.

The theoretical bifurcation diagram, determined by Haim et al. for their model, is shown in Fig. 6.45.

To summarize, in terms of the Haim et al. model, the negative impedance arises from the potential-dependent bisulfate adsorption on Ni surface which blocks the nickel electrodisolution. The source of positive impedance is the chemical, but potential-dependent dissolution of oxide layer [Eq. (6.56)].

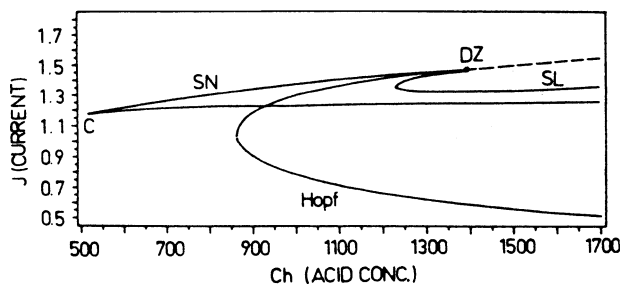


Fig. 6.45 Theoretical bifurcation diagram predicted by the model proposed by Haim et al. [92], to be compared with Fig. 6.41 [24]. Hopf Hopf bifurcation, SN saddle-node bifurcation, SL saddle-loop bifurcation, C cusp and DZ double-zero singularities. Reprinted with permission from [92] Copyright 1992 American Chemical Society

The formation of spatiotemporal patterns in Ni/H₂SO₄ system is described in Sect. 2.4 of volume II.

6.1.4.5 Delay of Bifurcations in a Potentiodynamic *I*–*E* Characteristics of the Ni/H₂SO₄ Oscillator

In 1996, Koper and Aguda [103] have analyzed the effect of the scan rate (v) in potentiodynamic studies of the oscillatory nickel electrodisolution. It was an experimental illustration of a more general theoretical problem of the change of the value of bifurcation parameter, compared to the static problem (i.e., for potentiostatic conditions in this case). In general, the parameter value μ_v ($v \neq 0$, dynamic case), where the transition due to the bifurcation occurs, is delayed with respect to the critical parameter value μ_s of the static problem. This delay $\mu_v - \mu_s$ follows a power-law dependence:

$$\mu_v - \mu_s = cv^p \quad (6.62)$$

where c is a constant and p is an exponent characteristic of the type of bifurcation, equal to $2/3$ for a saddle-node bifurcation [104, 105], and to zero for the Hopf bifurcation in the direction from the steady-state to the oscillatory regime [106]. This means that the delay in a Hopf bifurcation is insensitive to v . In turn, for the reverse Hopf bifurcation (from the oscillatory to steady-state), the amplitude of the oscillations decreases with decreasing v , and in the limit of small v , is proportional to $O(v^{1/4})$ quantity [107]. An additional prediction is the memory effect [106] meaning the dependence of the delay for the Hopf bifurcation on the initial value μ_i of the control parameter: $\mu_v - \mu_s = \mu_s - \mu_i$. These predictions were compared by Koper and Aguda with the characteristics of the Ni/H₂SO₄ system, exhibiting

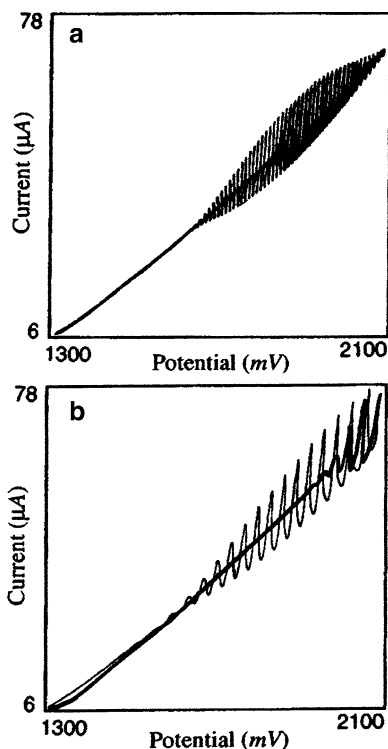


Fig. 6.46 Current–voltage scans for Ni dissolution in 1 N H₂SO₄ illustrating the effect of varying scan rate on the oscillatory behavior: (a) scan rate = 3 mV/s, (b) 10 mV/s. The Hopf bifurcation under consideration is at 1,750 mV. Note the presence of a second Hopf bifurcation near the upper potential limit of the scan. External resistance is 10 k Ω . Reprinted with permission from [103] <http://link.aps.org/abstract/PRE/v54/p960>, Copyright 1996 by the American Physical Society

both supercritical Hopf and saddle-node bifurcations. Figure 6.46 shows that the oscillations in the anodic current are significantly delayed at the higher scan rate.

The analysis of the delay vs. scan rate in the log–log coordinates yields the slope $p = 0.94$, in clear contradiction with earlier predictions of $p = 0$ [106], presumably due to effect of the internal noise of the system. An analysis of the amplitude of oscillations during the reverse scan indicated its (expected) decrease with a decrease in scan rate. In turn, studies of the memory effect showed the decrease of the potential for the onset of the oscillations, with the increase of the initial potential, i.e., the negative slope of this dependence. This was also interpreted in the following way: since noise erases memory effect [106], high scan rates are needed to minimize the integrated effect of noise.

In turn, with respect to saddle-node bifurcation, the p value close to $2/3$ was obtained, as Fig. 6.47 proves.

In conclusion, the deviations between the theoretical ($p = 0$) and experimental ($p \approx 1$) parameter of the power dependence were explained in terms of the role of

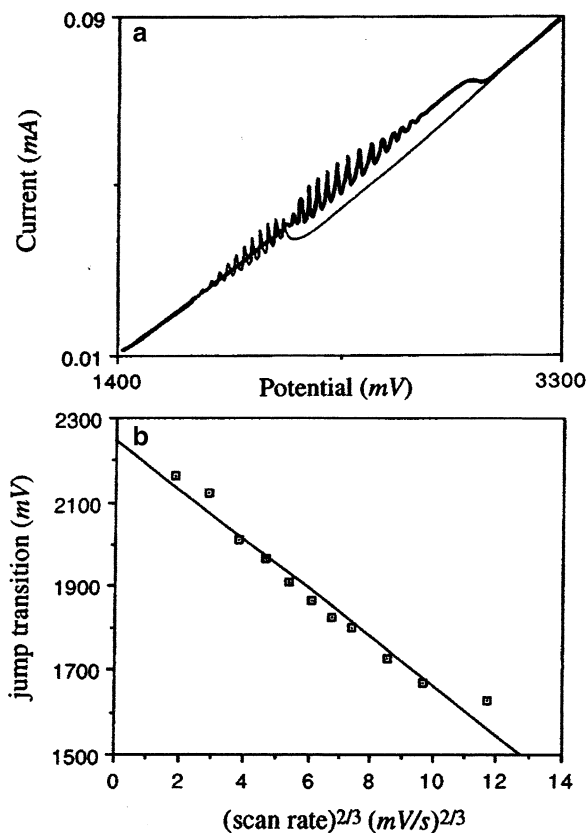


Fig. 6.47 (a) Current–voltage scan for Ni dissolution in 1 N H_2SO_4 in the presence of a 20 k Ω external resistance and scan rate of 10 mV/s. Note the presence of two Hopf bifurcations on the forward scan (*thick curve*) and two jump transitions due to saddle-node bifurcations, one on the forward and one on the reverse scan (*thin line*). (b) The potential of the jump transition during the reverse scan as a function of $(\text{scan rate})^{2/3}$. Theoretically, this plot should give a straight line in the limit of small scan rates. Reprinted with permission from [103] <http://link.aps.org/abstract/PRE/v54/p960>, Copyright 1996 by the American Physical Society

internal noise. An alternative possible explanation, based on the concept of a continuous drift of the system's characteristics, was not considered applicable for the system studied.

6.1.5 Oscillatory Oxidation of Cobalt Electrodes

6.1.5.1 The Co/HCl + CrO_3 System

The early studies of the oscillatory dissolution of Co wires immersed in hydrochloric acid/chromic acid electrolyte were conducted by Franck and Meunier [19]. More recently, Hudson et al. [108] continued investigations of this system

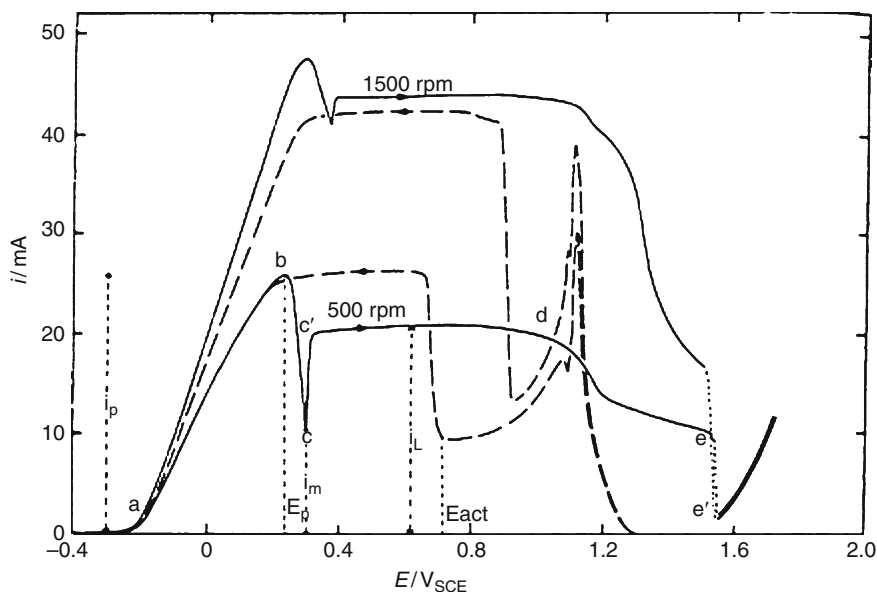


Fig. 6.48 Potentiodynamic sweep curves for a rotating disc Co electrode in 1.58 M H_2SO_4 aqueous solution at two different rotation speeds. $dE/dt = 20 \text{ mV s}^{-1}$. Reprinted from [109], Copyright 1990, with permission from Elsevier

under potentiostatic conditions, using rotating Co electrode, the potential of which was controlled with respect to the conventional saturated calomel electrode (SCE). The experimental characteristics of the $\text{Co}/\text{HCl} + \text{CrO}_3$ system are complicated by the fact that it consists of the anodic current of Co dissolution and of the cathodic current of CrO_3 electroreduction, with relative proportion dependent on the electrode potential. The $I-E$ characteristics exhibit the regions of the NDR and the oscillations set in via a subcritical Hopf bifurcation. It was also found that the lower the HCl concentration, the higher the potential of the onset of oscillations. Figure 6.48 proves also that oscillations are related to the predominating cathodic (negative) current of CrO_3 electroreduction. The mechanism of these phenomena involves formation of the chromic dichromate film on the metal surface which undergoes destruction through the pitting corrosion, with the participation of aggressive Cl^- ions, adsorbed on this film (hence the effect of HCl concentration on the onset of the oscillations). In other words, the oscillations are due to cyclic deposition and removal of a protective film on the Co surface. The dynamics of coupled oscillators of that type is described in Sect. 3.1.5 of volume II.

6.1.5.2 The $\text{Co}/\text{H}_2\text{SO}_4 + \text{NO}_3^-$, Cl^- System

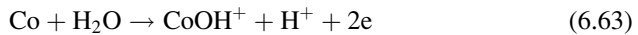
Sazou, Pagitsas et al., in the series of papers have described current oscillations occurring during Co electrodisolution in sulfuric acid solutions, with additions of

nitrate ions [109], chloride ions [110, 111], and iodide ions [112]. In all cases studied, the presence of only sulfuric acid appeared to be insufficient for the onset of oscillations which observation immediately suggests that nitrate or halide ions were involved in the pitting corrosion of the passivated Co surface, leading to the oscillations. Typical potentiodynamic curve of anodic Co polarization in H_2SO_4 media is shown in Fig. 6.48 and includes the following sections: (a–b) active dissolution region, (b–c) transition to a passive-like state due to the formation of the CoO film, characterized with the NDR; (c–c', c'–d) reactivation of the surface due to aggressive sulfate ions, with the limiting current determined by the dissolution–precipitation mechanism; (d–e) partial repassivation of Co surface, presumably due to the formation of Co_2O_3 and Co_3O_4 film; (e–e') complete passivation, and (beyond e') the oxygen evolution current.

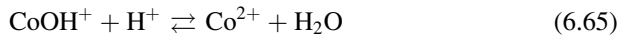
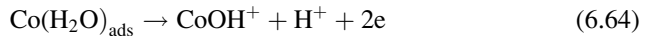
Contrary to Fe/ H_2SO_4 system, the passivation of Co is not complete, which means that the chemical properties of surface film are in both systems different.

Major processes associated with the respective region can be summarized as follows [109]:

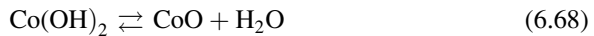
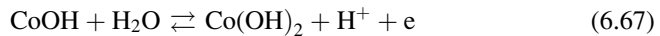
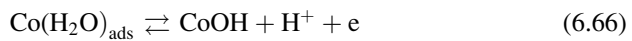
1. Activation processes:



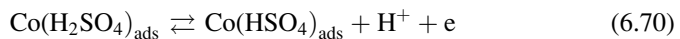
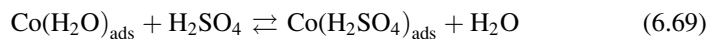
or

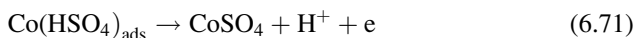


2. Passivation processes:

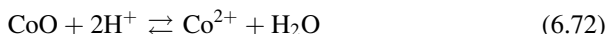


or (assuming the adsorption competition between water and sulfuric acid):





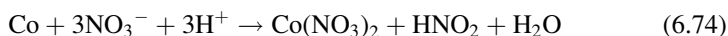
3. Reactivation processes:



As noted above, the onset of oscillations required addition of foreign ions. Typical potentiodynamic curves, showing the oscillations upon addition of nitrate ions, are shown in Fig. 6.49. Comparison of a negative (upper picture) and positive (lower picture) potential scan reveals certain hysteresis.

Longer period of run of the potentiostatic experiments indicated the gradual change in the oscillatory modes, leading from the simple periodic behavior, through the period-doubling bifurcation, up to chaotic oscillations. One should emphasize also the significant effect of temperature on the oscillatory characteristics.

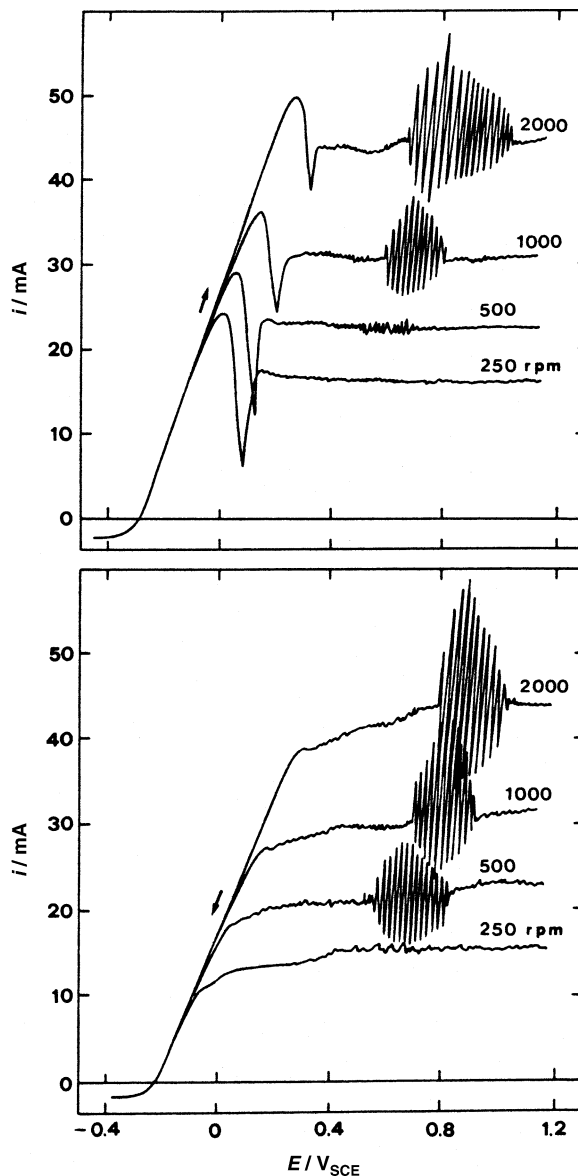
The proposed reaction mechanism was based on the deposition/dissolution mechanism of a porous film by intervention of nitrate ions. In the absence of nitrate ions, there establishes the steady-state balance between the formation and dissolution of passive film, corresponding to the formation of (quasi-)limiting anodic current within certain potential region. Let us choose, e.g., the potential 0.7 V. In the presence of sufficient concentration of nitrate ions, the passive layer undergoes pitting corrosion, i.e., the fraction of active Co surface increases. The number and size of the pits tend to increase due to the oxidizing action of NO_3^- and the autocatalytic increase of NO_3^- ions caused by the electrochemical oxidation of HNO_2 [109]:



These processes are associated with the increase of current, until local accumulation of corrosion products inhibits further dissolution of metal and then current decreases. But in other places of the porous film, the concentration of nitrate ions may become high enough to induce growing corrosion of the passive layer. This mechanism invokes thus also the role of spatial inhomogeneity of the electrode surface in the passive state. The onset of the oscillatory regime requires appropriate combination of nitrate ion concentrations, electrode potential range, and the rotation rate of the disk electrode. Explanations of qualitatively similar potentiostatic oscillations occurring during electrooxidation for H_2SO_4 solution in the presence of Cl^- and I^- ions also involved the idea of pitting corrosion [110–112].

The oscillatory dissolution of Co electrodes was also studied in phosphoric acid solution, including pioneer investigations of the role of periodic (sinusoidal) perturbation of Co – 1M H_3PO_4 system, i.e., creating the forced oscillator, as described also by Pagitsas and Sazou [113, 114].

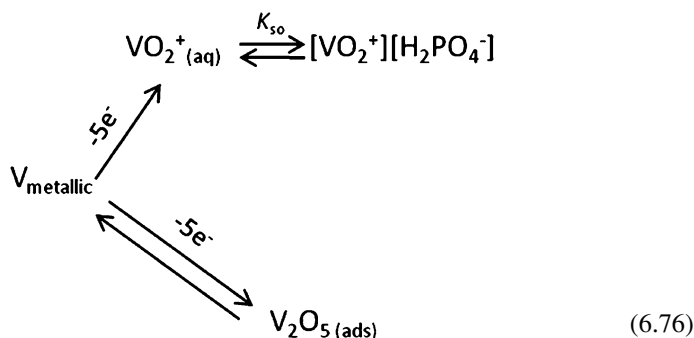
Fig. 6.49 (Top) Positive potentiodynamic sweep curves for a Co rotating disc electrode in 1.58 M $\text{H}_2\text{SO}_4 + 0.1 \text{ M NO}_3^-$. (Bottom) Negative potentiodynamic sweep curves, complementing the $I-E$ curves of (a). $dE/dt = 20 \text{ mV s}^{-1}$. Reprinted from [109], Copyright 1990, with permission from Elsevier



6.1.6 Oscillatory Oxidation of Vanadium Electrodes

Current oscillations for anodically polarized vanadium electrode were reported only recently by Alonzo et al. [115, 116], for phosphate media. These studies were later continued by Gorzkowski et al. [117] for both H_3PO_4 and other acidic media, including H_2SO_4 , HNO_3 , HClO_4 , and CF_3COOH . Application of rotating

disk vanadium electrode allowed for recording oscillations of different degrees of complexity and also of bistability. Since the passivation of the vanadium electrode was not complete, the consumption of electrode material was relatively fast and observed dynamic regimes were of transient nature. Experimental studies of the V/H₃PO₄ system were supported by numerical simulations of observed instabilities and by stability analysis of its model [118]. The model was based on Koper and Sluyters approach [45], described in Sect. 6.1.2.2. Its adaptation to V/H₃PO₄ included acid–base equilibria of H₃PO₄ which were not included in the original construction, involving the fully dissociating strong HA acid. The simplified reaction mechanism of vanadium oxidation at high positive potentials (>1 V vs. the Hg–Hg₂SO₄–0.1 M H₂SO₄ reference electrode) was assumed in the following form:



Thus, parallel electrooxidation of the metallic vanadium to VO₂⁺ cations (which formed a porous salt layer with H₂PO₄⁻ ions, characterized with the solubility product K_{s0}) and to a passive layer of V₂O₅, was assumed. In terms of this reaction mechanism, a system of two ordinary differential equations, describing the temporal dynamics of the electrode potential (E) and of the surface concentration of VO₂⁺ ions in the solution ($C_{\text{VO}_2^+}$) was derived:

$$\frac{dE}{dt} = \frac{U - E}{f_{\text{R}}AC_dR_{\text{S}}} - \frac{nFk_1(E)(1 - \theta) \times (1 - (C_{\text{VO}_2^+}/C_{\text{max}}))}{C_d} \tag{6.77}$$

$$\begin{aligned}
 \frac{dC_{\text{VO}_2^+}}{dt} = & \frac{2f_{\text{R}}k_1(E) \times (1 - \theta) \times (1 - (C_{\text{VO}_2^+}/C_{\text{max}}))}{\delta} - \frac{2DC_{\text{VO}_2^+}}{\delta^2} \\
 & - t_{\text{VO}_2^+} \frac{2nf_{\text{R}}k_1(E) \times (1 - \theta) \times (1 - (C_{\text{VO}_2^+}/C_{\text{max}}))}{z\delta}
 \end{aligned} \tag{6.78}$$

where U —external voltage, A —the vanadium electrode surface area, f_{R} —its roughness factor (assumed as equal to 5), $k_1(E)$ —the rate constant of V oxidation to VO₂⁺, C_{max} —critical concentration of VO₂⁺, at which the [VO₂⁺][H₂PO₄⁻] precipitation starts at the solution/electrode interface, D —diffusion coefficient of VO₂⁺, $z = +1$ is electric charge of VO₂⁺ ion, δ —the thickness of diffusion

layer, controlled by the rotation speed of vanadium disk [calculated from Levich equation (4.7)], $n = 5$: number of electrons involved in $V(0) \rightarrow V(V)$ electrooxidation. The transference number for VO_2^+ ions $t_{VO_2^+}$ (with the current carried altogether by VO_2^+ , H^+ and $H_2PO_4^-$ ions) is given by:

$$t_{VO_2^+} = \frac{\lambda_{VO_2^+} C_{VO_2^+}}{\lambda_{VO_2^+} C_{VO_2^+} + \lambda_{H^+} [H^+] + \lambda_{H_2PO_4^-} [H_2PO_4^-]} \quad (6.79)$$

where λ_i are the molar conductivities of respective ions. In turn, θ , the electrode coverage with passive layer of V_2O_5 was calculated from the steady-state approximation ($d\theta/dt = 0$) applied to the equation for its temporal dynamics, concordant with scheme (6.76):

$$\frac{d\theta}{dt} = k_2(E)(1 - \theta) - k_{-2}(E)\theta[H^+]^{10} \quad (6.80)$$

Finally, due to a large excess of H_3PO_4 , its equilibrium concentration $[H_3PO_4]$ at the electrode surface was considered practically constant, and the local dynamics of $[H^+]$ was found negligible, as $[H^+]$ was quickly regulated by fast dissociation/protonation equilibria of H_3PO_4 . The local concentration of $H_2PO_4^-$ ions, necessary to calculate the actual transference number of VO_2^+ ions [Eq. (6.79)], was found from the combination of the dissociation constant of H_3PO_4 (K_a) with the electroneutrality condition $C_{VO_2^+} + [H^+] = [H_2PO_4^-]$:

$$[H_2PO_4^-] = \frac{C_{VO_2^+} + \sqrt{(C_{VO_2^+})^2 + 4K_a[H_3PO_4]}}{2} \quad (6.81)$$

Numerical integration of Eqs. (6.77) and (6.78), performed for potentiodynamic conditions, yielded oscillatory and bistable behaviors, which exhibited satisfactory concordance with experimental data (Figs. 6.50 and 6.51).

Furthermore, analysis of the E and $C_{VO_2^+}$ nullclines, derived from model equations (6.77, 6.78), performed for different external voltages U and disk rotation speeds allowed for determination of stable and unstable steady-states, as shown in exemplary Fig. 6.52.

Based on that analysis a bifurcation diagram in the coordinate system $U-E$, given in Fig. 6.53, was constructed.

Analogous studies for other acidic media revealed similar dynamic behaviors, of various degrees of complexity. For the reader, further details can be found in [117, 118]. One should emphasize that the present studies reproduce only the essential sources of basic instabilities in the V/H_3PO_4 and other acidic systems. For example, the V/H_3PO_4 system is evidently of an N-NDR type, but some experimental data suggest that under appropriate conditions it may also exhibit hidden negative impedance [117]. The more comprehensive experimental and theoretical characteristics of the vanadium electrodisolution in various media evidently require further investigations.

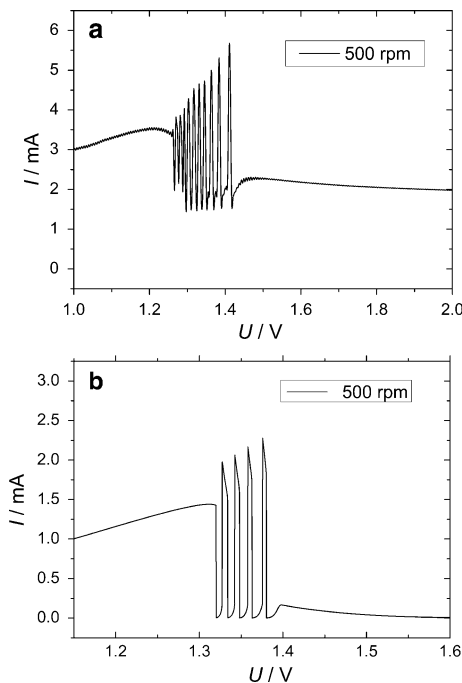


Fig. 6.50 Comparison of the experimental (a) and corresponding simulated (b) oscillatory modes of the vanadium electrooxidation in phosphate media. Experimental conditions: vanadium electrode (1 mm diameter vanadium wire, embedded in Teflon), temperature $T = 0\text{ }^{\circ}\text{C}$, scan rate $\nu = 10\text{ mV s}^{-1}$. Parameters of the model: $C(\text{H}_3\text{PO}_4) = 2 \times 10^3\text{ mol m}^{-3}$, $f_R = 5$, $T = 273\text{ K}$, double layer capacitance $C_d = 0.2\text{ Fm}^{-2}$, $A = 7.86 \times 10^{-7}\text{ m}^2$, serial resistance $R_s = 180\ \Omega$, formal potentials and rate constants of oxidations of $\text{V}(0)$ to VO_2^+ and V_2O_5 , respectively: $E_1^0 = 0.768\text{ V}$, $k_1 = 8 \times 10^{-5}\text{ mol m}^{-2}\text{ s}^{-1}$; $E_2^0 = 1.168\text{ V}$, $k_2^0/k_2^0 = 1 \times 10^{-20}\text{ mol}^{-10}\text{ m}^{30}$, $K_{\text{so}} = 5.5 \times 10^4\text{ mol}^{-2}\text{ m}^6$, scan rate $\nu = 2\text{ mV s}^{-1}$. Reproduced from [118] with kind permission from Springer Science+Business Media B.V.

6.1.7 Oscillatory Dissolution of Other Metals

In this section, we shall briefly summarize other examples of the oscillatory dissolution of some other metals. Common points with the above discussed mechanisms can be found, and therefore it is not necessary to discuss every case in great detail. The reader interested in the dissolution mechanism of particular metal is thus advised to consult the appropriate original reference.

6.1.7.1 Silver

Oscillatory dissolution of silver was reported as early as in 1942 by Gilbertson and Fertner [4, 119]. Also later Francis and Colner [120] have described oscillations during the anodization of a silver electrode in a plating bath, containing AgCN

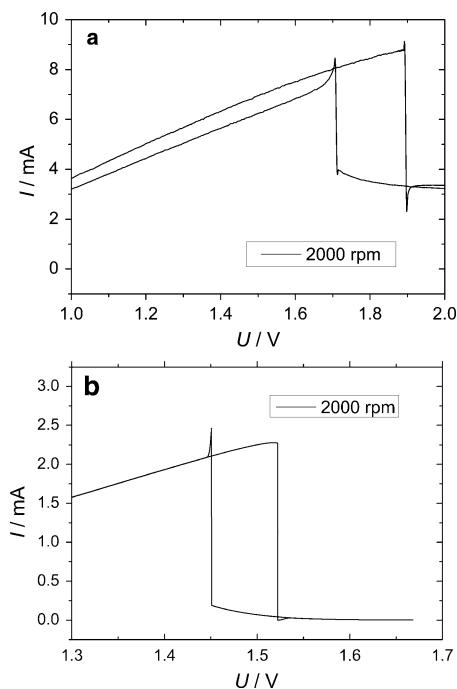


Fig. 6.51 Comparison of the experimental (a) and simulated (b) bistable modes of the vanadium electrooxidation in phosphate media. Experimental conditions: vanadium electrode (1 mm diameter vanadium wire, embedded in Teflon), temperature $T = 0\text{ }^{\circ}\text{C}$, scan rate $\nu = 10\text{ mV s}^{-1}$. Parameters of the model (see also caption to Fig. 6.50): $C(\text{H}_3\text{PO}_4) = 2,000\text{ mol m}^{-3}$, $f_R = 5$, $T = 273\text{ K}$, $C_d = 0.2\text{ F m}^{-2}$, $A = 7.86 \times 10^{-7}\text{ m}^2$, $R_s = 180\ \Omega$, $E_1^0 = 0.768\text{ V}$, $k_1 = 8 \times 10^{-5}\text{ mol m}^{-2}\text{ s}^{-1}$, $E_2^0 = 1.168\text{ V}$, $k_{-2}^0/k_2^0 = 1 \times 10^{-20}\text{ mol}^{-10}\text{ m}^{30}$, $K_{so} = 5.5 \times 10^4\text{ mol}^{-2}\text{ m}^6$, scan rate $\nu = 2\text{ mV s}^{-1}$. Reproduced from [118] with kind permission from Springer Science+Business Media B.V.

dissolved in excess KCN and with addition of K_2CO_3 . The mechanism of these oscillations assumed that the high density current, setting at the beginning of electrolysis, caused significant concentration polarization, meaning the decrease in $[\text{CN}^-]$ and the increase in $[\text{Ag}^+]$ in the pre-electrode layer. As a consequence, the current decreases and at certain moment the film of AgCN forms at the electrode surface which later dissolves, enabling the rise of current. The oscillations are thus caused by cyclic precipitation and dissolution of the AgCN film, with possible contribution also from Ag_2O .

Oscillations were also reported during anodic dissolution of Ag in chloride media [5, 121, 122], under galvanostatic conditions. The role of formation/dissolution of AgCl films in these dynamics seems to be obvious, but also the role of rearrangement and recrystallization of various forms of this solid was considered. Also, the role of Ag_2O was discussed. It is also interesting to learn that Indira et al., who proposed also the Stoichiometric Region (SR) mechanism for the galvanostatic

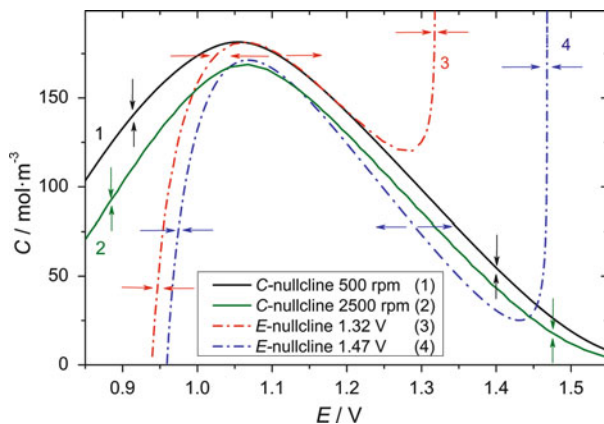


Fig. 6.52 Exemplary nullclines for the dynamical system (6.77, 6.78), constructed for two rotation speeds and two external voltages U . Direction of arrows denotes the sign of appropriate derivatives dE/dt and dC/dt . Reproduced from [118] with kind permission from Springer Science+Business Media B.V.

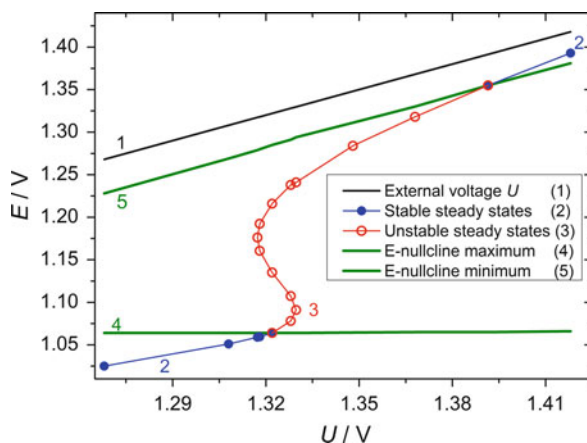


Fig. 6.53 Theoretical bifurcation diagram of Eqs. (6.77) and (6.78) with U as bifurcation parameter for rotation speed 500 rpm, constructed based on the course of nullclines. The imposed external voltage U is denoted by line (1). Steady-states (2) are stable while steady-states (3), lying between the maximum (4) and minimum (5) of E -nullcline, are unstable. Oscillations, of the amplitude defined by the distance between the lines (4) and (5), occur when no steady-state is stable for a given external voltage U . Reproduced from [118] with kind permission from Springer Science+Business Media B.V.

oxidation of nickel (see Sect. 6.1.4), have developed similar ideas for the case of Ag dissolution in dense HCl media [94]. As before, the AgCl film consists of three layers, only the middle one of which forms a stoichiometric phase, responsible for the relatively large potential drop across it. The periodic buildup and damage of SR

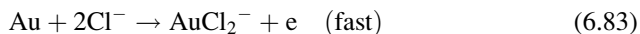
is considered to be a reason for the oscillations of the Ag electrode potential under galvanostatic conditions. Finally, the chaotic course of the oscillatory oxidation of Ag in a 1 M HClO₄ solution was reported by Corcoran and Sieradzki [123].

6.1.7.2 Gold

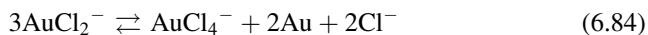
Franck [124] and Vetter [125] were probably the first researchers who reported the oscillatory electrodisolution of Au electrode in acidic electrolytes. More recent studies, mainly by Arvia et al. (e.g., [126]) cover oscillatory dissolution of Au in contact with H₂SO₄ solution, containing chloride ions, both in the absence and in the presence of stirring (in the latter case, when the limiting anodic current was developed, the oscillations were observed in this potential region). The mechanism postulated the localized corrosion, with the passivity potential (E_p), dependent on the hydrochloric acid concentration in a following way:

$$E_p = 1.630 + 2.303 \frac{RT}{F} \log c_{\text{HCl}} \quad (6.82)$$

Thus, the local HCl concentration at the Au–solution interface affected the onset of oscillations. The fast anodic Au dissolution (which thus can easily enter the diffusion-controlled regime) occurs according to the equation:



with the equilibrium potential of the Au/AuCl₂[−] couple equal to 1.154 V (at 25°C). The above electrodisolution reaction, occurring thus at relatively positive potentials, is followed by reversible, heterogeneous disproportionation of Au(I) to Au(III) and Au(0):



In the course of diffusion-controlled reaction (6.83) the pre-electrode layer becomes depleted with Cl[−] ions (i.e., with HCl) and then the formation of complex AuCl₂[−] species is replaced with the formation of the oxide layer, through discharge of water molecules, at the Au surface. The surface becomes then passivated and the current decreases. The relatively slow diffusion of HCl from the bulk restores then the acidity of the solution at the interface, the oxide layer dissolves and current rises again.

Later, Diard et al. [127] have shown the multiplicity of steady-states across the Au passive–active region, ascribing the oscillations to the periodic gold oxide film formation and dissolution. More recently, in situ Raman spectroscopic studies were combined with electrochemical studies of the oscillatory dissolution of Au in 2 M HCl [128]. The following data have been measured during the current oscillations: the vibrations bands for Au–Cl[−], AuCl₄[−] and Au–O(H) as a function of the potential, the spatial profile of AuCl₄[−] concentration in the diffusion layer, and

composition of which can be dependent on the solution composition, as this layer can incorporate, e.g., WO_4^{2-} , MoO_4^{2-} and CrO_4^{2-} ions, chosen here as the examples. Bargeron and Givens [131] have reported oscillations in the anode current, related to the potentiostatic pitting of aluminum. In the case of In containing Al alloys, Wilhelmsen et al. [132] have found both oscillations of the current under potentiostatic conditions and of the potential under galvanostatic conditions. The mechanism of these phenomena assumes that in active sites of the electrode, Al undergoes oxidation: $\text{Al} + 4\text{OH}^- \rightleftharpoons \text{Al}(\text{OH})_4^- + 3\text{e}$ until, at the critical current density, $\text{Al}(\text{OH})_3$ or Al_2O_3 deposit on these active sites, damping in this way the flow of current. Then OH^- ions, through their diffusion from the solution bulk, enhance pH in the pre-electrode layer, the aluminum oxide/hydroxide layer dissolves, current rises again, etc.

Regarding pure metallic Al, more recent studies indicate the possible correlation between its oscillatory electrodisolution and porous structure of formed Al_2O_3 . For example, Lee et al. [133] have reported the relation between the modulated nanoporous structure of aluminum oxide and the spontaneous current oscillations during the potentiostatic hard anodization of aluminum in 0.3 M $\text{H}_2\text{C}_2\text{O}_4$ medium; also, the respective oscillatory mechanism is proposed. Such correlations were found also for anodization of various semiconductors (cf. Chap. 4, volume II). Note also that pattern formation during Al electrodisolution under appropriate conditions can be interpreted as a phenomenon of convective origin, as described in Sect. 5.4.3 of volume II.

6.1.7.4 Lead

Oscillatory lead electrodisolution was observed under both potentiostatic and galvanostatic conditions. Oscillations of the current were reported for the Pb electrodisolution, in contact with hot concentrated H_2SO_4 solutions, at the electrode potentials prior to passivation region, as described by Grauer et al. [134]. In turn, in basic media of NaOH solutions containing various concentrations of ClO_3^- or ClO_4^- ions, galvanostatic oscillations of the Pb electrode potential were reported by Abd El Aal [135]. In the latter case the oscillations were found to occur within the oxygen evolution region, indicating an effect of the aggressive ClO_3^- or ClO_4^- ions on the oxygen formation/evolution process [4].

One should mention also oscillatory electrodisolution of Pb (or its alloys) in contact with nonaqueous media, not so frequently used in the studies of electrochemical instabilities. Bhaskara [136] has reported potential oscillations during the dissolution of Pb and (Pb, Ag) or (Pb, Sn) alloys in contact with the solutions of LiAlCl_4 in propylene carbonate and explained these instabilities in terms of formation and dissolution of PbCl_2 film, the existence of which was confirmed by X-ray studies of Pb anode, performed under the same conditions.

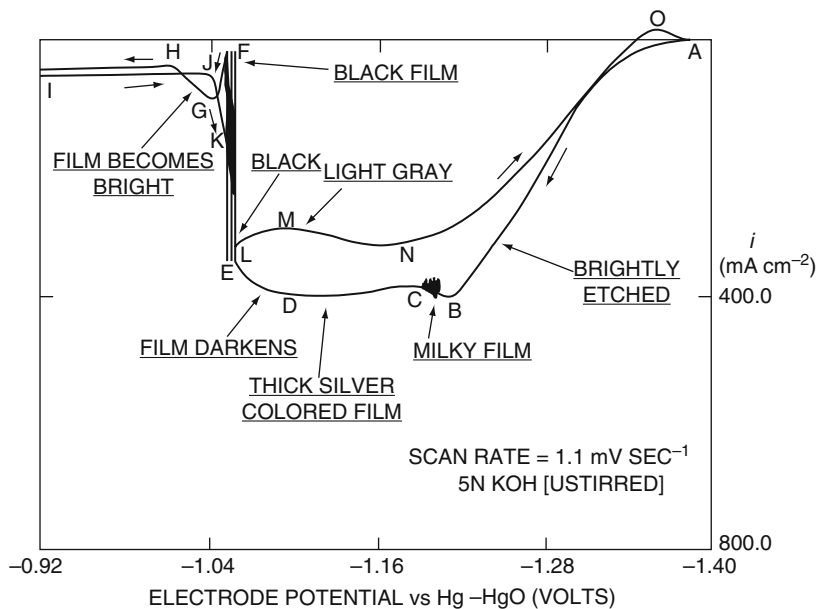


Fig. 6.54 Current–voltage *curve* of a zinc wire electrode in unstirred 5 N KOH recorded at a scan rate of 1.1 mV/s. Reproduced from [137] by permission of The Electrochemical Society

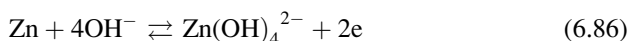
6.1.7.5 Zinc

For anodic dissolution of Zn in KOH, Hull et al. [137, 138] have constructed the diagram, which relates the I – E characteristics of the Zn wire in 5 M KOH (obtained in forward and backward slow-scan potentiodynamic experiments) with visual observation of the Zn surface (Fig. 6.54).

The oscillations were attributed to the formation of ZnO film, the dissolution of which is strongly dependent on the solution pH and the actual structure of the metal/solution interface. The role of the formation/destruction of surface films in these oscillations was further confirmed by Podesta et al. [139], who used SEM for the comparative studies of the Zn, Au, and Fe electrode surfaces in different regions of potentiostatic E/I behavior.

A more detailed insight into the mechanism of these processes was proposed by McKubre and Macdonald [140], in view of the I – E characteristics shown in Fig. 6.55.

The initial increase of current with the electrode potential is associated with the simple metal dissolution:



which further, in the range of a linear I – E dependence, turns into two-step process, involving intermediate formation and dissolution of ZnO:

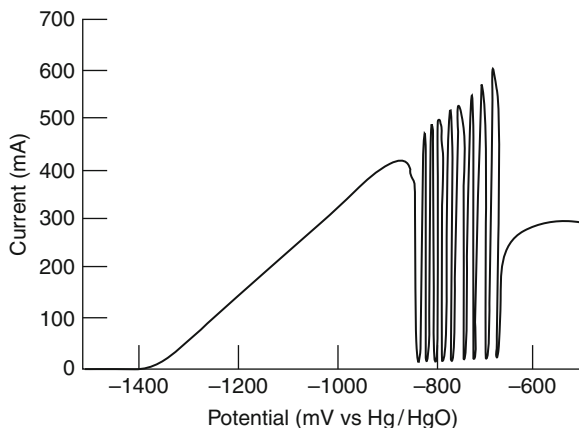
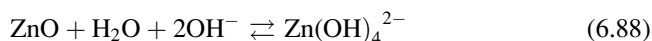
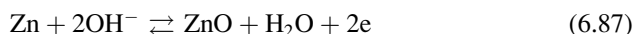


Fig. 6.55 Current oscillations of zinc during anodic potentiodynamic sweep at 5 mV/s; 28 w/o NaOH. 80 °C. 600 rpm. Reproduced from [140] by permission of The Electrochemical Society



At sufficiently anodic potentials, when solubility of $\text{Zn}(\text{OH})_4^{2-}$ reaches a saturation limit, a porous film of $\text{Zn}(\text{OH})_2$ starts to precipitate at the electrode surface and this process continues until local pH of the solution becomes so low, that ZnO , forming in the course of above reactions, becomes insoluble and thus forms a compact passivating-type film. This of course causes a decrease in the anodic current, so the production and the local concentration of $\text{Zn}(\text{OH})_4^{2-}$ decreases, the diffusion of OH^- from the bulk enhances back the pH, so the hydroxide and oxide film undergo dissolution and a new portion of $\text{Zn}(\text{OH})_2$ can be formed, completing the oscillatory cycle. Finally, oscillatory electrodedissolution of rotating zinc disk electrode in concentrated KOH solutions containing polyethylene glycol was studied by Frackowiak and Kiciak [141].

6.1.7.6 Tin

Typically, anodic oscillations reported by various authors [4] for the Sn/NaOH system were explained in terms of formation/destruction of the films of various tin oxides and hydroxides. For example, Shams El Din et al. [142, 143] have reported, under galvanostatic conditions of the anodization of Sn and Sn amalgams in NaOH solutions, the oscillations of the electrode potential, changing between the values characterizing the $\text{Sn}/\text{Sn}(\text{OH})_2$ and $\text{Sn}(\text{OH})_2/\text{Sn}(\text{OH})_4$ redox couples.

Mechanistically, these oscillations have been attributed to the competition between the anodic formation and dissolution of $\text{Sn}(\text{OH})_4$. More recent studies, like that by Strirrup and Hampson [144], involving rotating disk tin electrodes in contact with NaOH solutions, allowed to recognize the primary and secondary passivity, the former one caused by the deposition of SnO or $\text{Sn}(\text{OH})_2$ film, and the latter one due to the formation of SnO_2 , the permanent existence of which causes the oscillations to cease. In terms of this mechanism the current oscillations occur in the region of potentials corresponding to the transition between the primary and secondary passivity, i.e., between the electrodes surface states switching between Sn/SnO [$\text{Sn}(\text{OH})_2$] and SnO [$\text{Sn}(\text{OH})_2$]/ SnO_2 .

Finally, Drogowska et al. [145] have reported current oscillations at the preoxidized Sn electrodes immersed in bicarbonate or phosphate solutions in the presence of chloride ions. The mechanism of these oscillations involved alternating corrosion of the passive layer with the participation of chloride ions, followed by the repassivation of the electrode surface.

6.1.7.7 Other Metals

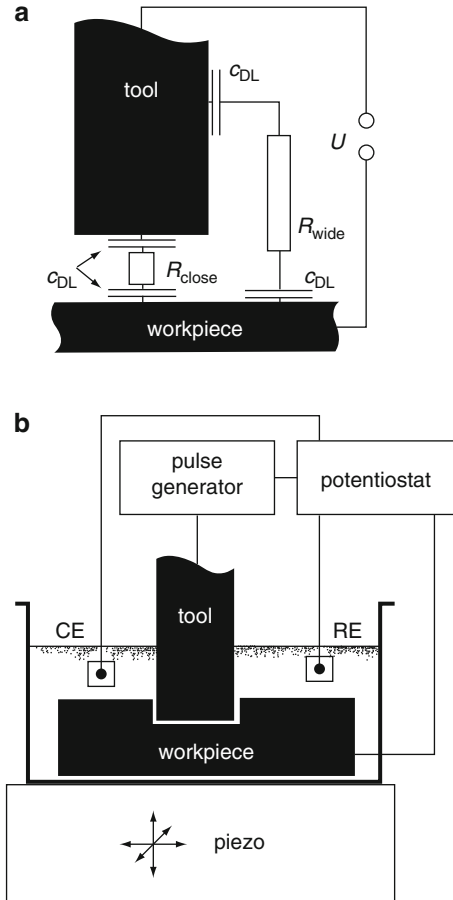
For *titanium*, the oscillatory electrooxidation was reported for H_2SO_4 solutions [146] and for bromide solutions [147]. Very recently, studies of the current oscillations accompanying the Ti anodization in H_2SO_4 medium under similar conditions were described by Warczak and Sadkowski [148]. Since for understanding of these phenomena the porosity of the forming layer of TiO_2 is significant, their characteristics will be described in more detail in Sect. 4.4 of volume II. For *bismuth*, the electrode potential oscillations have been found by Petrov et al. for both poly-Bi and single crystal electrodes (cited after [4]) and by Ammar and Khalil [149] in different media, including phosphate, borate, benzoate, and tartrate solutions. For *cadmium*, potential oscillations in KOH solutions, explained by formation/destruction of a passive surface film: either $\text{Cd}(\text{OH})_2$ or CdO finely dispersed in $\text{Cd}(\text{OH})_2$, have been published by Galushko et al. [150]. In turn, Kadaner et al. [151] have described low-frequency (0.01–0.3 Hz) potential oscillations during *niobium* electrochemical dissolution in HBF_4 electrolyte, by imposing a 50 Hz ac current equal to or larger than the passivation current of the metal under these conditions. A mechanistically interesting case appeared to be galvanostatic electrodisolution of *tungsten* in NaOH solutions, accompanied with the potential oscillations [152] which were explained as *thermokinetic* instabilities caused by the electrochemical reaction heat released on the electrode surface and the resulting large temperature gradients between the electrode surface and the electrolyte bulk. Experimental data were supported with theoretical analysis.

6.2 Application of Metal Electrodeposition Processes in Micromachining

The controlled electrodeposition of solid phases can be used in electrochemical micromachining. Schuster, Ertl et al. [153] have described such procedure for the 3D machining of conducting materials with submicronic precision. This approach seems to overcome the limitations of the commonly used lithographic techniques in the production of 3D structures. The machining system consists of an appropriately shaped tool electrode, directly molded on the workpiece in which the pattern is created. The tool electrode can move in three dimensions. The high resolution of pattern production is achieved through the application of ultrashort potential pulse, lasting for only nanoseconds. For the understanding of this method, it is necessary to invoke the basic characteristics of the electrode processes. When the voltage pulse is applied between the tool electrode and the workpiece, the capacitive current, associated with charging of both interfaces, begins to flow, decaying in time exponentially, according to the time constant being the product of (largely) the double layer capacitance and (largely) the electrolyte solution resistance. Of course, the smaller the time constant, the faster the charging of the electrode to the imposed potential. When the electrode attains the potential sufficient to induce the faradaic current of the given redox process, this current rises further exponentially with increasing potential. Taking into account these characteristics, it now becomes clear, how smart and simple was the idea of the inventors of this version of electromicromachining. The key feature of the setup sketched in Fig. 6.56 is that the time constant, deciding the rate of electrode charging is not the same for all electrode regions, i.e., it is spatially varying. The smallest time constant characterizes the region of the minimum solution resistance, i.e., the region when the very tip of the tool electrode approaches the surface of the workpiece, with the interelectrode distance ranging from nanometers to micrometers only (see Fig. 6.56a).

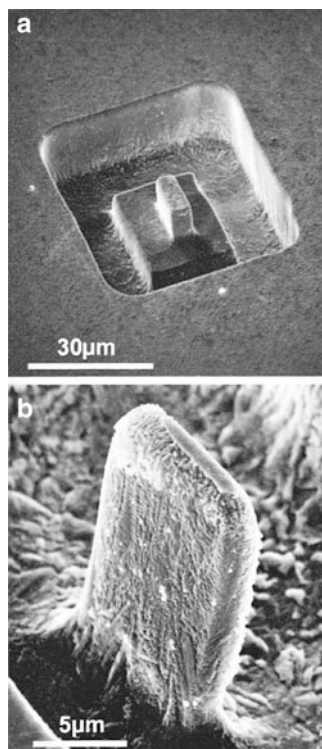
Now, if one chooses the duration of ultrashort voltage pulse so that it will be comparable (at best smaller) to this local, smallest time constant, only this tiny region of both electrodes will be charged, while other regions will remain practically unpolarized, as they would require much longer time for attaining the same potential. In other words, if the electrode potentials are chosen properly, during the ultrashort voltage pulse only this part of the workpiece will undergo electrodeposition which is placed in front of a very tip of the tool electrode. Figure 6.56b shows details of the experimental setup, involving bipotentiostat that controls the potentials of both the tool and the workpiece electrode, with respect to the common reference electrode. The pulse generator in the circuit of the tool electrode is a source of ultrashort potential jump. In the experiment, the copper substrate was used as a workpiece for micromachining, the cylindrical Pt wire (10 μm or 50 μm in

Fig. 6.56 (a) Scheme of an electrochemical cell. Upon application of a voltage pulse, the double layer capacity C_{DL} is charged via the electrolyte resistance. Because the electrolyte resistance along the current path depends on the electrode separation (R_{close} and R_{wide}), the time constants for charging the double layer become spatially varying. (b) Experimental setup for electrochemical micromachining with ultrashort voltage pulses. From [153]. Reprinted with permission of AAAS



diameter) was applied as a tool electrode, and also a Pt wire worked as a pseudo-reference electrode. The electrolyte was an aqueous, acidified solution of CuSO_4 (e.g., 0.1 M CuSO_4 and 0.01 M HClO_4). In contact with such solution the copper substrate attained the well-defined equilibrium potential of the Cu/Cu^{2+} couple, at which the electrode was kept, in order to minimize the global Cu corrosion during the whole experiment and to avoid the redeposition of dissolved Cu. The average potential of the tool electrode was adjusted to 200 mV vs. the equilibrium potential of Cu/Cu^{2+} . The local etching of Cu workpiece was caused by a sequence of 50 ns, -1.6 V pulses of the voltage applied to the tool electrode, with a pulse-to-pause ratio of 1/10. Monitoring of the current–time dependence, compared to simultaneous voltage–time dependence, indicated that only at sufficiently small interelectrode distances (i.e., smaller than $1 \mu\text{m}$) the shape of the current response indicates characteristic contribution from the exponentially decaying capacitive current, otherwise only its minor contribution is visible. Thus, only at sufficiently small

Fig. 6.57 (a) Cu structure (small prism, 5 μm by 10 μm by 12 μm) machined into the Cu sheet of an electronic circuit board upon application of 2 MHz sequence of 50-ns, -1.6-V pulses to the tool electrode (a cylindrical Pt wire 10 μm in diameter) in 0.01 M HClO_4 and 0.1 M CuSO_4 . The tool was first etched vertically into the surface and was then moved along a rectangular path like a miniature milling cutter. (b) Cu tongue with a thickness of 2.5 μm , etched as in (a). From [153]. Reprinted with permission of AAAS



distances the local capacitive current is high enough, compared to other regions of the electrodes, to cause the electrolysis in the place precisely determined by the very tip of the tool electrode.

These experimental results are concordant with theoretical estimations: for typical specific resistance $\rho = 30 \Omega \text{ cm}$ (0.1 M HClO_4), double layer capacity of metal electrodes C_d (or C_{DL}) $\approx 10 \mu\text{F cm}^{-2}$ and potential pulse duration of 30 ns, the maximum distance, for which a significant double layer charging is achieved, equals to ca. 1 μm . In other words, pulses of 30 ns duration should allow one to achieve a machining resolution of 1 μm [153].

Figure 6.57 shows the representative scanning electron micrograph of the Cu substrate treated with the micromachining method, with the appropriately programmed sequence of potential pulses and position of the tool electrode.

As the introduction to the next section, we shall note that the electrochemical micromachining described in this chapter can be applied also to *etching of semiconductors*. In this way a hole was etched in the p-Si semiconductor with a cylindrical 50- μm tool, contacting through 1% HF solution [153]. Furthermore, as the polarization of the pulse can be reversed, not only etching but also a *deposition* in a micrometer scale can be achieved with this method. In this way, a series of copper dots was deposited on a Au substrate from the acidified solution of CuSO_4 , with an elliptical, anodically polarized, Pt tool, 50 μm in diameter [153].

In conclusion, the presented approach may provide new abilities for modern micromachining technologies, due to its spatial resolution down to nanometer range, fully 3D capabilities, and the versatility of chemical reactions that can be used to produce desired patterns.

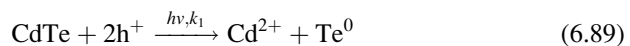
6.3 Anodic Oscillatory Dissolution of Semiconductor Electrodes

The nonlinear self-organization processes in semiconductors have been extensively described, e.g., in recent monograph by Schöll [154] which includes also the references to the original papers by this author. The book, addressed mainly to physicists, is also a concise handbook of principles of nonlinear dynamics, while its title emphasizes the importance of spatiotemporal aspects of such dynamics in the etching of semiconductors. Therefore, in this section, we only briefly discuss the examples of temporal self-organization in anodic dissolution of semiconductors, while spatiotemporal phenomena will be more extensively treated in Chap. 4 of volume II.

6.3.1 Cadmium-Based Semiconductors

One of the simplest systems of that type consists of CdS electrode immersed in the alkaline aqueous solution. For such systems Josseaux et al. [155] have reported damped photocurrent oscillations, which were explained in terms of the formation and dissolution of Cd(OH)₂ film.

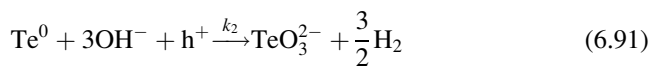
Photocurrent oscillations were described also by Marcu and Tenne [156] for single-crystal *n*-CdTe semiconductor immersed in an alkaline cesium sulfide solutions (1 M CsOH + 1 M Cs₂S). The current oscillations were characterized with a frequency of ca. 1 Hz, with the shape changing as a function of time, for constant electrode potential; among others, the transition from simple periodic course to the one resembling the consequence of the period-doubling bifurcation, was reported. In turn, the practical insensitivity of the current toward stirring rate of the solution excludes the principal role of diffusion (or more generally—transport) rate in the solution. The morphology and the amplitude of the oscillations depended strongly also on the electrode potential. In the interpretation of these phenomena it was considered, as the crucial step, the thermodynamic instability of CdTe in sulfide solutions, with respect to S/Te exchange:



The released Cd^{2+} ion diffuses into the solution, where it precipitates as CdS:



Also elementary tellurium, appearing in the semiconducting phase, is easily oxidized:



Note that the role of Te layer is by no means trivial, since it can affect the kinetics of reaction (6.89) in several ways: as the gray filter reducing the amount of light reaching the semiconductor surface or as the factor modifying the height of the semiconductor–solution Schottky barrier. Marcu and Tenne consider the changing width of the Te layer on the surface of CdTe as the possible source of the oscillations of the photocurrent. In order to justify this hypothesis, both experimental and theoretical (kinetic model) arguments were presented. Among others, the fact that analogous photocurrent oscillations were not observed with CdS and CdSe semiconductors was explained in terms of their higher stability in sulfide solutions, compared to CdTe.

The following, more detailed mechanism of the oscillations of the photocurrent was proposed for CdTe/S²⁻ system. First, the decisive role of Te layer as the gray filter for the illumination was excluded and the oscillatory mechanism was based on electrochemical properties of semiconductor. In this explanation the idea of the flat band potential will be invoked, i.e., the potential at which the potential drop associated with the space charge in the semiconductor vanishes (the concept analogous to the potential of zero charge for metals). This flat band potential of CdTe depends on local pH which varies due to reaction (6.91). Initially, the fresh crystal of CdTe has its specific flat band potential. Upon illumination, the corresponding photocurrent will produce an initial Te layer, which is responsible for the decrease of the photocurrent. The following dissolution of Te causes a local decrease in pH, associated with a decrease in the flat band potential. This in turn causes a decrease in the photocurrent of reaction (6.89) which means also the slower production of Te that is, on the other hand, continuously dissolving with relatively high rate. The consumption of OH⁻ slows down then and, accordingly, the local pH increases, shifting the flat band potential back to previous value. The rate of reaction (6.89) increases again.

If the term “flat band potential” is replaced with the “Flade potential,” the above mechanism is in principle analogous to the Franck–FitzHugh oscillatory mechanism for the dissolution/precipitation systems (Sect. 6.1.2.2). However, the discussed semiconductor system has an additional, striking specific feature which is its *nonlinear* response to the light intensity (contrary to more classical models in which linear response is usually assumed). This system was mathematically defined in terms of two ordinary differential equations, the one describing the temporal variations of the amount of Te formed on the surface and the other one the dynamics

of either the photocurrent or the local concentrations of OH^- ions, both approaches producing oscillations. It is also noteworthy that the oscillatory behavior is in this work from 1988 was already, although briefly discussed in terms of linear stability analysis. Later, Marcu and Strehblow [157] have reported current oscillations observed during anodization of $\text{Cd}_x\text{Hg}_{1-x}\text{Te}$ in alkaline solutions containing Cs^+ and S^{2-} ions; the explanation of those instabilities was essentially similar to that for CdSe, i.e., assumed the formation and dissolution of Te monolayer as the key process.

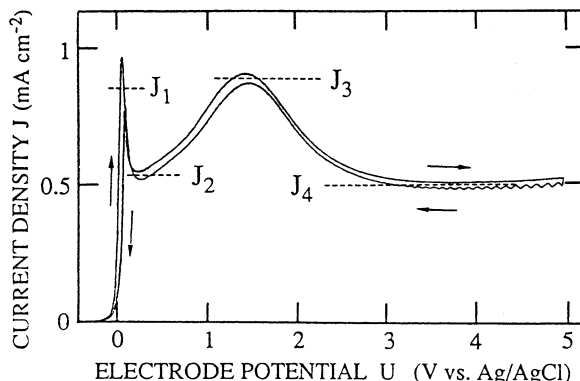
6.3.2 Silicon in Fluoride Media

Undoubtedly, electrodisolution of silicon in F^- -containing media has been one of the most intensively studied processes in semiconductor electrochemistry. A part of these studies concerns with the oscillatory course of this process in the electropolishing region ($E > 2.5$ V vs. SCE [24]). We shall first briefly summarize the early works on this subject [4].

The oscillatory electrooxidation of Si in fluoride medium, occurring under galvanostatic conditions, was first reported by Turner in 1958 [158] who also first suggested the role of SiO_2 layer in the oscillations. The next important step in this area was the paper published by Gerischer and Lübke [159] who have described and analyzed the current oscillations at *p*-Si, and the photocurrent oscillations at illuminated *n*-Si, in contact with NH_4F solutions. An important point of this work, which will be invoked in some later elaborated mechanism (see Sect. 4.1, volume II), is the postulated existence of a “sub-oxide” SiO_{2-x} between the Si surface and SiO_2 layer. With increasing thickness of the oxide layer, its composition becomes closer to SiO_2 . This “improvement” of the stoichiometry of the silicon oxide and its growth requires the electric field-assisted transport of oxygen ions through the oxide toward the $\text{SiO}_2\text{-SiO}_{2-x}/\text{Si}$ interface. In fact, transport of these ions through the oxide layer was suggested as a key process for the occurrence of the oscillations. The model of current oscillations thus involved nonlinear relation between oxide formation and its dissolution.

The above work triggered an increasing interest in the oscillatory dissolution of Si in HF media. In the following years, in a series of papers, Chazalviel et al., based on voltammetric and impedance measurements [160–163] have performed further studies of Si dissolution in NH_4F media, indicating their occurrence under potentiodynamic conditions, but ceasing for the constant electrode potential. Also small sinusoidal perturbations of the constant electrode potential were able to trigger the oscillations which were therefore considered the *resonant* oscillations. Other studies include the works by Peter et al. [164, 165] who studied Si dissolution using ring disc voltammetry and ellipsometry. They have suggested that the oscillations could not be ascribed to periodical buildup and destruction of surface oxide layers (since the fluctuations in the oxide layer thickness were not detected), but rather to periodic changes in the electrical field in the interfacial region. This, in

Fig. 6.58 Typical voltammogram of a (111) *p*-Si electrode. Electrolyte is 0.025 M HF + 0.025 NH₄F + 0.95 M NH₄Cl (*c*_F = 0.05 M, pH 3). Rotation rate 300 rpm; sweep rate 5 mV s⁻¹. Note the small current oscillations in the *J*₄ plateau. Reprinted from [161] with kind permission of Deutsche Bunsen-Gesellschaft für Physikalische Chemie

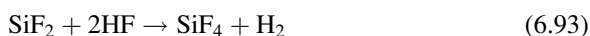


turn, could be associated with the periodic buildup and decay of space charge within the superficial oxide layer. At that stage of studies, as the authors conclude, the behavior of Si electrode in the region of oscillation “remains a challenging puzzle.” As the reader will learn from the analysis below and in Chap. 4 of volume II, the role of surface oxides will appear important for the oscillations.

Studies of the role of oxides have been undertaken also by Lewerenz and Schlichthörl [166] who have analyzed the light-induced oscillatory *n*-Si(111) dissolution in 0.2 M NH₄F media performing, among others, excess microwave reflectivity measurements, simultaneously with photocurrent measurements. In other studies Lewerenz et al. [167, 168] have used ellipsometry and *ex situ* XPS measurements to monitor the surface of *n*-Si(111) electrodes immersed in NH₄F solutions, after prior oxidation of Si surface up to a thickness of 35–40 Å. It was found that during the oscillations the oxide layer changed its thickness, but for less than 10% only. On the other hand, Ozanam and Chazalviel [169] using internal IR multiple-reflection spectroscopy observed 60% modulation of the oxide layer during the oscillations, but it is possible that the magnitude of these variations depends on particular experimental conditions.

Figure 6.58 shows typical voltammogram of a (111) *p*-Si electrode in fluoride media, taken from the work by Chazalviel et al. [161] (the curve is very similar to the one obtained for *n*-Si under intensive illumination [159]).

One should note that current oscillations are observed in the potential region corresponding to *J*₄ plateau. Let us first analyze the sequence of interfacial phenomena occurring along this *J*–*E* dependence. Upon anodic polarization first the abrupt increase of current (*J*₁) is observed which was associated with the formation of porous silicon. At the *p*-Si, according to Turner [158] and Peter et al. [165] in this potential region there occurs the oxidation of Si to Si(II) and further to Si(IV), accompanied by hydrogen evolution [24]:



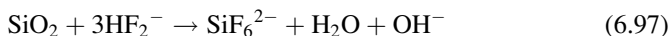
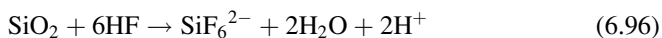
with SiF_4 complexed further to SiF_6^{2-} . However, at the n -Si electrode, holes have to be generated upon illumination, due to optical excitation [24]:



A sharp decrease in anodic current following peak J_1 , based on the works by Chazalviel et al., is ascribed to the formation, on the Si surface, of the passivating film. Its composition varies, upon increasing anodic potential, from silicon hydroxide finally to SiO_2 at potentials in the J_4 region, where the oxidation occurs according to the following equation [165]:



In turn, the SiO_2 is chemically dissolved by HF and HF_2^- in the solution:



Thus, the plateau of current density in the J_4 region is controlled predominantly by the rate of SiO_2 dissolution, according to the kinetic equation [160]:

$$J_4 = k_4[\text{HF}_2^-][\text{H}^+]^{1/2} \quad (6.98)$$

The J_4 current was later found to depend on the rotation rate of the disk electrode in a way indicating combined kinetic and mass-transfer control, involving the transport of fluoride ions from the solution bulk to the Si electrode surface [170]. At this point, one can make an introductory suggestion that the oscillations during Si anodization are due to a competition between electrochemical formation of SiO_2 layer [Eq. (6.95)] and its chemical (currentless) dissolution (etching) by fluoride ions [Eqs. (6.96), (6.97)]. In order to collect possibly direct and reliable experimental data supporting this assumption, Nast et al. [171] have monitored the surface morphology changes of silicon oxide on p -Si(111), during the oscillations, by in situ atomic force microscopy (AFM). Also, in separate in situ fast Fourier transform infrared spectroscopy (FTIR), the photoelectrochemically induced oxide coverage variations on n -Si(111) were found. A strong correlation between the photocurrents, the surface roughness, and the silicon oxide coverage was observed, as illustrated by Fig. 6.59.

Analysis of the positive and negative slopes of the Si–O signals clearly indicates a faster reaction rate for the electrochemical oxide formation than the rate of its chemical dissolution. Furthermore, since the oxide formation always takes place as long as a measurable current is observed, the oxide has to be *porous* to allow a conductive contact between the silicon and electrolyte. The qualitative properties of the oxide layer must also change during the oscillations: based on the comparison of

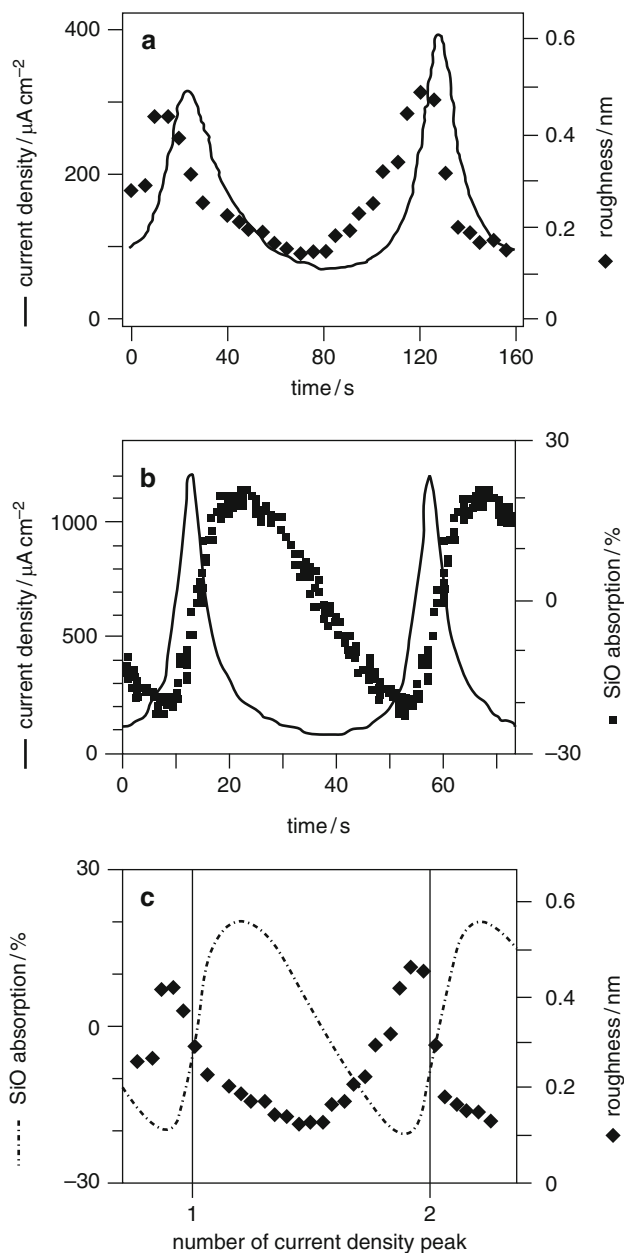


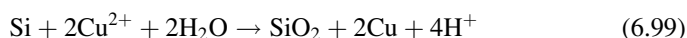
Fig. 6.59 Temporal change of (a) the roughness parameter (0.1 M NH_4F , pH 4.2, $U = 5.2$ V vs. SCE) and (b) the Si–O absorption signal (0.1 M NaF, pH 4.0, $U = 6$ V vs. SCE). The roughness parameter and the Si–O absorption signal with respect to the corresponding current density peaks are given in (c). Reprinted from [171], Copyright 1998, with permission from Elsevier

the current density and Si–O signal, one concludes that the oxide is less passivating in the increasing part of the oxide coverage transient than in its decreasing part. In the detailed explanation of the observed dependences, there was also invoked the possible role of pH of the electrolyte inside of the porous oxide layer and immediately adjacent to the oxide–electrolyte interface. Description of detailed models of the oscillations will be continued in Sect. 4.1 of volume II, due to correlation between temporal instabilities and spatial patterns of oxide on the Si surface.

Here, we shall only mention that the origin of the above-mentioned oscillations occurring after small potential perturbation was diagnosed by Chazalviel et al. based on impedance measurements [162, 172] and appropriate theoretical considerations. The resonant behavior of the system subject to external sinusoidal perturbation was ascribed exclusively to the characteristics of the Si/solution interface, i.e., they were not considered as the manifestation of the instability of the whole circuit, like in the case of interaction of the NDR with ohmic potential drops. Without going here into mathematical details of the model, we shall briefly say that Chazalviel et al. have proposed the model of the oscillations in which the electrode was considered a set of small *domains* exhibiting individually autonomous current oscillations. According to this model, each anodic current pulse results in the creation of a SiO₂ film in the small domain, and for repeating the pulse, there must pass the time necessary to chemical dissolution of this film. Since these domains are uncorrelated (unsynchronized), the macroscopically reported current is practically constant, but upon small external periodic perturbation of the potential, they become synchronized, oscillate all with the same phase, and consequently, macroscopic current oscillates, as well. The idea of complete lack of coupling between the individual domains was somewhat questioned by Koper [24], but the concept of synchronized and nonsynchronized individual oscillators was later repeated also in more recently elaborated mechanism of electrodisolution of Si, and also for some other semiconductors. Concerning the Si/fluoride system, it is noteworthy that this problem has been undertaken very recently again by Chazalviel and Ozanam [173]. In this work, the main point is that the *damped* current oscillations are attributed to a *sustained* current oscillation on a local scale. Using a combined simulation/analytical probabilistic analysis, it was examined whether an interaction between the various locations on the electrode surface may lead to such macroscopic oscillation of the total current. The main conclusion is that a short-range interaction cannot lead to a synchronization of the oscillation over the surface of a large electrode, but such a synchronization might be obtained on small electrodes, or with appropriate values of the system parameters. Thus, if the coupling occurs, it has a rather global nature and realizes due to the external resistance in series with the electrode (see Sect. 1.2, volume II). But it also means that the microscopic nature of the oscillations in the Si/fluoride system still remains an open question. The detailed studies of pore formation on Si surface under various conditions, mainly upon anodization in fluoride-containing solutions, with the emphasis on self-organization, remains the subject of intensive studies (cf. e.g., [174–180]). Various mechanisms of pore formation in electrochemical anodization of semiconductors were discussed by Chazalviel et al. [181] who have

recommended linear stability analysis of the semiconductor/solution interface as the promising approach for the initial stages of pore growth, taking into account both physical and chemical aspects of the process. Selected models related to the pore formation on Si and other semiconductor surfaces will be described in more detail in Sect. 4.1 of volume II.

As the last example of the oscillatory process involving Si dissolution, we shall mention here the chaotic oscillations of the *open-circuit potential* (OCP) observed during the immersion plating of *p*-Si with copper in electrolyte containing CuSO_4 and HF, reported and analyzed further by Parkhutik et al. [182, 183]. The processes which occur at the Si/solution interface include: the deposition of Cu film on the surface of Si: $\text{Cu}^{2+} + 2e \rightarrow \text{Cu}$ and simultaneous dissolution of Si wafer beneath the Cu film, supplying the electrons for Cu^{2+} reduction and causing local acidification of the solution: $\text{Si} + 2\text{H}_2\text{O} \rightarrow \text{SiO}_2 + 4\text{H}^+ + 4e$. These processes summarize into the overall reaction not requiring an external electron source:



The presence and stability of Cu film seems to play an essential role in the reported OCP oscillations. It is supposed that the Cu deposition in the form of clusters is associated with simultaneous growth of very thin layer of SiO_2 which, on the other hand, dissolves chemically in HF. This results in lifting off of the deposited Cu layer. The surface of silicon is autorenewed and the deposition cycle repeats [183]. The complicated interplay of copper film formation and destruction, silicon oxidation, silicon oxide dissolution, and electrolyte properties causes the irregular course of the oscillations. Finally, one should mention that currentless deposition of Cu on Si is important due to practical implications in microelectronics, e.g., in deposition of metallization lines [183].

The reader interested in various aspects of electrochemistry of silicon, including brief description of electrochemical oscillations, is advised to consult also, e.g., the specialized monograph by Lehmann [184] which covers the state of knowledge up to the year 2002.

References

1. Fechner GT (1828) Zur Elektrochemie. 1. Ueber Umkehrungen der Polarität in der einfachen Kette. Schweiger's J (Journal für Chemie und Physik) 53:129–151
2. Wojtowicz J (1973) Oscillatory behavior in electrochemical systems. In: Bockris JO'M, Conway BE, White RE (eds) Modern aspects of electrochemistry, vol 8. Plenum, New York, pp 47–120
3. Hudson JL, Bassett MR (1991) Oscillatory electrodisolution of metals. In: Luss D, Amundson NR (eds) Reviews in chemical engineering. Freund, London
4. Hudson JL, Tsotsis TT (1994) Electrochemical reaction dynamics: a review. Chem Eng Sci 49:1493–1572

5. Landolt D (2007) Corrosion and surface chemistry of metals. EPFL, Taylor and Francis, Boca Raton, FL
6. Brett CMA, Brett AMO (1993) Electrochemistry. Principles, methods and applications. Oxford University Press, Oxford
7. Russell PP, Newman J (1983) Experimental determination of the passive-active transition for iron in 1 M sulfuric acid. *J Electrochem Soc* 130:547–553
8. Epelboin I, Gabrielli C, Keddam M, Takenouti H (1975) A model of the anodic behaviour of iron in sulphuric acid medium. *Electrochim Acta* 20:913–916
9. Pigeau A, Kirkpatrick HB (1969) *Corrosion* 25:209
10. Hudson JL, Tabora J, Krischer K, Kevrekidis IG (1993) Spatiotemporal period doubling during the electrodisolution of iron. *Phys Lett A* 179:335–363
11. Russell P, Newman J (1987) Anodic dissolution of iron in acidic sulfate electrolytes. II. Mathematical model of current oscillations observed under potentiostatic conditions. *J Electrochem Soc* 134:1051–1059
12. Keddam M (2002) In: Marcus P (ed) *Corrosion mechanisms in theory and practice*. Dekker, New York, p 97
13. Deslouis C, Tribollet B (1990) Flow modulation technique and EHD impedance: a tool for electrode processes and hydrodynamic studies. *Electrochim Acta* 35:1637–1648
14. Orazem ME, Tribollet B (2008) *Electrochemical impedance spectroscopy*. Wiley, New Jersey
15. Datta M, Romankiw LT (1989) Application of chemical and electrochemical micromachining in the electronics industry. *J Electrochem Soc* 136:285C–292C
16. Kiss L (1988) Kinetics of electrochemical metal dissolution. Akadémiai Kiadó, Budapest
17. Bonhoeffer KF, Renneberg W (1941) Activity waves on passive iron wires. *Z physik Chem* 118:389
18. Kortüm G (1966) *Lehrbuch der Elektrochemie*, 4th edn. Verlag Chemie, Weinheim
19. Franck UF, Meunier L (1953) Gekoppelte periodische Elektrodenvorgänge. *Z Naturforsch* 8b: 396–406
20. Bartlett JH (1945) Transient anode phenomena. *Trans Electrochem Soc* 87:521–545
21. Diem C, Hudson JL (1987) Chaos during the electrodisolution of iron. *AIChE J* 33:218–224
22. Wang Y, Hudson JL (1991) Effect of electrode surface area on chaotic attractor dimensions. *AIChE J* 37:1833–1843
23. Sazou D, Pagitsas M (2006) On the onset of current oscillations at the limiting current region emerged during iron electrodisolution in sulfuric acid solution. *Electrochim Acta* 51:6281–6296
24. Koper MTM (1996) Oscillations and complex dynamical bifurcations in electrochemical systems. In: Prigogine I, Rice SA (eds) *Adv Chem Phys XCII*. Wiley, New York, pp 161–298
25. Sazou D, Pagitsas M, Georgolios C (1992) The influence of chloride ions on the dynamic characteristics observed at the transition between corrosion and passivation states of an iron electrode in sulphuric acid solutions. *Electrochim Acta* 37:2067–2076
26. Izhikevich EM (2007) *Dynamical systems in neuroscience. The geometry of excitability and bursting*. MIT, Cambridge
27. Rinzel J (1987) In: Teramoto E, Yamaguti M (eds) *Mathematical topics in population biology, morphogenesis and neurosciences*, Springer, Berlin, 1987, pp 267–281
28. Izhikevich EM (2000) Neural excitability, spiking, and bursting. *Int J Bifurc Chaos* 10:1171–1266
29. Kiss IZ, Lv Q, Organ L, Hudson JL (2006) Electrochemical bursting oscillations on a high-dimensional slow subsystem. *Phys Chem Chem Phys* 8:2707–2715
30. Karantonis A, Koutsaftis D, Bredaki M, Koulombi N (2008) Reception and detection of chemical signaling by electrochemical oscillators. *Chem Phys Lett* 460:182–186
31. Franck UF (1989) Periodische Strukturen und Vorgänge in gleichgewichtsfernen physikalisch-chemischen Systemen. *Nova acta Leopoldina NF* 60:109–131

32. Pagitsas M, Diamantopoulou A, Sazou D (2001) Distinction between general and pitting corrosion based on the nonlinear dynamical response of passive iron surfaces perturbed chemically by halides. *Electrochem Commun* 3:330–335
33. Pagitsas M, Diamantopoulou A, Sazou D (2003) A point defect model for the general and pitting corrosion of iron/oxide/electrolyte interface deduced from current oscillations. *Chaos Soliton Fract* 17:263–275
34. Sazou D, Pagitsas M (2003) Non-linear dynamics of the passivity breakdown of iron in acidic solutions. *Chaos Soliton Fract* 17:505–522
35. Pagitsas M, Pavlidou PS, Sazou D (2007) Chlorates induced pitting corrosion of iron in sulfuric acid solutions: an analysis based on current oscillations and a point defect model. *Chem Phys Lett* 434:63–67
36. Pagitsas M, Pavlidou M, Sazou D (2008) Localized passivity breakdown of iron in chlorate- and perchlorate-containing sulphuric acid solutions: a study based on current oscillations and a point defect model. *Electrochim Acta* 53:4784–4795
37. Lou W, Ogura K (1995) Current oscillations observed on a stainless steel electrode in sulfuric acid solutions with and without chromic acid. *Electrochim Acta* 40:667–672
38. Franck UF, FitzHugh R (1961) Periodische Elektrodenprozesse und ihre Beschreibung durch ein mathematisches Modell. *Z Elektrochem* 65:156–168
39. Wang Y, Hudson JL, Jaeger NI (1990) On the Franck-FitzHugh model of the dynamics of iron electrodisolution in sulfuric acid. *J Electrochem Soc* 137:485–488
40. Griffin GL (1984) A simple phase transition model for metal passivation kinetics. *J Electrochem Soc* 131:18–21
41. Talbot JB, Oriani RA (1985) Steady state multiplicity and oscillations in passive film formation. *Electrochim Acta* 1985:1277–1284
42. Talbot JB, Oriani RA, DiCarlo M (1985) Application of linear stability and bifurcation analysis to passivation models. *J Electrochem Soc* 132:1545–1551
43. Kado T, Kunitomi N (1991) A model for the current oscillations of iron in sulfuric acid. *J Electrochem Soc* 138:3312–3321
44. Degn H (1968) Theory of electrochemical oscillations. *Trans Faraday Soc* 545:1348–1358
45. Koper MTM, Sluyters JH (1993) A mathematical model for current oscillations at the active-passive transition in metal electrodisolution. *J Electroanal Chem* 347:31–48
46. Nechiporuk VV, Petrenko OE (1998) Effect of migration nonequilibrium on bifurcation diagrams (electrochemical dissolution of metals). *Russ J Electrochem* 34:1158–1161
47. Kawczyński AL, Przasnyski M, Baranowski B (1984) Chaotic and periodic current oscillations at constant voltage conditions in the system $\text{Cu(s)}|\text{CuSO}_4 + \text{H}_2\text{SO}_4(\text{aq})|\text{Cu(s)}$. *J Electroanal Chem* 179:285–288
48. Kawczyński AL, Raczyński W, Baranowski B (1988) Analysis of chaotic oscillations in a simple electrochemical system. *Z phys Chem Leipzig* 269:596–602
49. Inzelt G (1993) Oscillations of the EQCM frequency response in the course of open-circuit copper dissolution in aqueous solutions of H_2SO_4 and CuSO_4 . *J Electroanal Chem* 348:465–471
50. Hedges ES (1926) Periodic phenomena at anodes of copper and silver. *J Chem Soc*: 1533–1546
51. Hedges ES (1929) An enquiry into the cause of periodic phenomena in electrolysis. *J Chem Soc*: 1028–1038
52. Bonhoeffer KF, Gerischer H (1948) Periodic chemical reactions. V. Anodic behavior of copper in hydrochloric acid. *Z Elektrochem* 52:149–160
53. Cooper RS, Bartlett JH (1958) Convection and film instability copper anodes in hydrochloric acid. *J Electrochem Soc* 105:109–116
54. Cooper JF, Muller RH, Tobias CW (1980) Periodic phenomena during anodic dissolution of copper at high current densities. *J Electrochem Soc* 127:1734–1744

55. Lee HP, Nobe K, Pearlstein AJ (1985) Film formation and current oscillations in the electrodisolution of Cu in acidic media. I. Experimental studies. *J Electrochem Soc* 132:1031–1037
56. Pearlstein AJ, Lee HP, Nobe K (1985) Film formation and current oscillations in the electrodisolution of Cu in acidic media. II. Mathematical model. *J Electrochem Soc* 132:2159–2165
57. Bassett MR, Hudson JL (1987) The dynamics of the electrodisolution of copper. *Chem Eng Commun* 60:145–159
58. Bassett MR, Hudson JL (1988) Shil'nikov chaos during copper electrodisolution. *J Phys Chem* 92:6963–6966
59. Bassett MR, Hudson JL (1989) Quasi-periodicity and chaos during an electrochemical reaction. *J Phys Chem* 93:2731–2737
60. Gu ZH, Chen J, Fahidy TZ (1992) The oscillatory behavior of anodic copper dissolution into a NaCl/KSCN electrolyte. *Electrochim Acta* 37:2637–2644
61. Gu ZH, Chen J, Fahidy TZ (1994) The effect of process parameters on the anodic dissolution of copper into NaI/KSCN electrolytes. *J Electroanal Chem* 367:7–14
62. Jacquet PA (1936) On the anodic behavior of copper in aqueous solutions of orthophosphoric acid. *Trans Electrochem Soc* 69:629–655
63. Glarum SH, Marshall JH (1985) The anodic dissolution of copper into phosphoric acid. I. Voltammetric and oscillatory behavior. *J Electrochem Soc* 132:2872–2878
64. Glarum SH, Marshall JH (1985) The anodic dissolution of copper into phosphoric acid. II. Impedance behavior. *J Electrochem Soc* 132:2878–2885
65. Albadily FN, Schell M (1988) An experimental investigation of periodic and chaotic electrochemical oscillations in the anodic dissolution of copper in phosphoric acid. *J Chem Phys* 88:4312–4319
66. Albadily FN, Ringland J, Schell M (1989) Mixed-mode oscillations in an electrochemical system. I A Farey sequence which does not occur on a torus. *J Chem Phys* 90:813–821
67. Schell M, Albadily FN (1989) Mixed-mode oscillations in an electrochemical system. II A periodic-chaotic sequence. *J Chem Phys* 90:822–828
68. Bard AJ, Faulkner L (2001) *Electrochemical methods. Fundamentals and applications*. Wiley, New York
69. Edwards J (1953) The mechanism of electropolishing of copper in phosphoric acid solutions I. processes preceding the establishment of polishing conditions. *J Electrochem Soc* 100:189C–194C
70. Tsitsopoulos LT, Tsotsis TT, Webster IA (1987) An ellipsometric investigation of reaction rate oscillations during the electrochemical anodization of Cu in H₃PO₄ solutions: some preliminary results. *Surf Sci* 191:225–238
71. Tsitsopoulos LT, Webster IA, Tsotsis TT (1987) Reaction rate oscillations during the electrochemical anodization of Cu in H₃PO₄ solutions: XPS and SEM studies. *Surf Sci* 220:391–406
72. Doona CJ, Blittersdorf R, Schneider FW (1993) Deterministic chaos arising from homoclinicity in the chlorite thiourea oscillator. *J Phys Chem* 97:7258–7263
73. Hudson JL, Mankin JC (1981) Chaos in the Belousov-Zhabotinskii reaction. *J Chem Phys* 74:6171–6177
74. Swinney HL, Maseko J (1985) Comment on renormalization, unstable manifold, and fractal structure of mode locking. *Phys Rev Lett* 55:2366–2366
75. Maseko J, Swinney HL (1986) Complex periodic oscillation in the Belousov-Zhabotinskii reaction. *J Chem Phys* 85:6430–6441
76. Maseko J, Swinney HL (1987) A Farey triangle in the Belousov-Zhabotinskii reaction. *Phys Lett A* 119:403–406
77. Strogatz SH (1994) *Nonlinear dynamics and chaos*. Perseus, Massachusetts
78. Epstein IR (1989) The role of flow systems in far-from-equilibrium dynamics. *J Chem Educ* 66:191–195

79. Schuster HG, Just W (2005) *Deterministic chaos. An introduction*. Wiley-VCH, Weinheim, p 139
80. Kiss IZ, Gáspár V, Nyikos L (1998) Stability analysis of the oscillatory electrodisolution of copper with impedance spectroscopy. *J Phys Chem* 102:909–914
81. Kiss IZ, Kazsu Z, Gáspár V (2009) Scaling relationship for oscillating electrochemical systems: dependence of phase diagram on electrode size and rotation rate. *Phys Chem Chem Phys* 11:7669–7677
82. Koper MTM, Sluyters JH (1991) Electrochemical oscillators: their description through a mathematical model. *J Electroanal Chem* 303:73–94
83. Koper MTM, Gaspard P (1992) The modeling of mixed-mode and chaotic oscillations in electrochemical systems. *J Chem Phys* 96:7797–7813
84. Karantonis A, Bourbos E, Koutsaftis D (2010) Electrochemical resonance: frequency response analysis of the electrodisolution of copper in trifluoroacetic acid close to dynamic instabilities. *Chem Phys Lett* 490:69–71
85. Potkonjak NI, Potkonjak TN, Blagojević SN, Dudić B, Randlejović DV (2010) Current oscillations during the anodic dissolution of copper in trifluoroacetic acid. *Corrosion Sci* 52:1618–1624
86. Hurtado MRF, Sumodjo PTA, Benedetti AV (1993) Electrochemical studies with copper-based alloys open-circuit potential oscillations in alkaline media. *J Electrochem Soc* 140:1567–1571
87. Hoar TP, Mowat JAS (1950) Mechanism of electropolishing. *Nature (London)* 165:64–65
88. Osterwald J, Feller HG (1960) Periodic phenomena at a nickel electrode in sulfuric acid. *J Electrochem Soc* 107:473–474
89. Osterwald J (1962) Zum stabilitätsverhalten stationärer Elektrodenzustände. *Electrochim Acta* 7:523–532
90. Lev O, Wolffberg A, Sheintuch M, Pismen LM (1988) Bifurcations to periodic and chaotic motions in anodic nickel dissolution. *Chem Eng Sci* 43:1339–1353
91. Lev O, Wolffberg A, Pismen LM, Sheintuch M (1989) The structure of complex behavior in anodic nickel dissolution. *J Phys Chem* 93:1661–1666
92. Haim D, Lev O, Pismen LM, Sheintuch M (1992) Modeling periodic and chaotic dynamics in anodic nickel dissolution. *J Phys Chem* 96:2676–2681
93. Koper MTM (1998) Non-linear phenomena in electrochemical systems. *J Chem Soc Faraday Trans* 94:1369–1378
94. Indira KS, Rangarajan SK, Doss KSG (1969) Further studies on periodic phenomena in passivating systems. *J Electroanal Chem* 21:57–68
95. Keddarn M, Takenouti H, Yu N (1985) Transpassive dissolution of Ni in acidic sulfate media: a kinetic model. *J Electrochem Soc* 132:2561–2566
96. Doss KSG, Deshmukh D (1976) Electrochemical potential oscillations. The nickel-sulphuric acid system. *J Electroanal Chem* 70:141–156
97. Lev O, Sheintuch M, Yarnitzky H, Pismen LM (1990) Spatial current distribution during nickel anodic dissolution in sulfuric acid. *Chem Eng Sci* 45:839–847
98. Gregori J, García-Jareño JJ, Keddarn M, Vicente F (2007) A kinetic interpretation of a negative time constant in impedance equivalent circuits for the dissolution/passive transition. *Electrochim Acta* 52:7903–7909
99. Scherer J, Ocko BM, Magnussen OM (2003) Structure, dissolution, and passivation of Ni(111) electrodes in sulfuric acid solution: an in situ STM, X-ray scattering, and electrochemical study. *Electrochim Acta* 48:1169–1191
100. Nakamura M, Ikemiya N, Iwasaki A, Suzuki Y, Ito M (2004) Surface structures at the initial stages in passive film formation on Ni(111) electrodes in acidic electrolytes. *J Electroanal Chem* 566:385–391
101. Gregori J, García-Jareño JJ, Giménez-Romero D, Vicente F (2005) Kinetic calculations of the Ni anodic dissolution from EIS. *J Solid State Electrochem* 9:83–90

102. Gregori J, García-Jareño JJ, Giménez-Romero D, Vicente F (2006) Calculation of the rate constants of nickel electrodisolution in acid medium from EIS. *J Solid State Electrochem* 10:920–928
103. Koper MTM, Aguda BD (1996) Experimental demonstration of delay and memory effects in the bifurcations of nickel electrodisolution. *Phys Rev E* 54:960–963
104. Habermann R (1979) Slowly varying jump and transition phenomena associated with algebraic bifurcation problem. *SIAM J Appl Math* 37:69–106
105. Erneux T, Laplante JP (1989) Jump transition due to a time-dependent bifurcation parameter in the bistable iodate-arsenous acid reaction. *J Chem Phys* 90:6129–6134
106. Baer SM, Erneux T, Rinzel J (1989) The slow passage through a Hopf bifurcation: delay, memory effects, and resonance. *SIAM J Appl Math* 49:55–71
107. Holden L, Erneux T (1993) Slow passage through a Hopf bifurcation: from oscillations to steady state solutions. *SIAM J Appl Math* 53:1045–1058
108. Hudson JL, Bell JC, Jaeger NI (1988) Potentiostatic current oscillations of cobalt electrodes in hydrochloric acid/chromic acid electrolytes. *Ber Bunsenges Phys Chem* 92:1383–1387
109. Sazou D, Pagitsas M, Kokkinidis G (1990) Current oscillations during electrodisolution of a cobalt electrode induced by the presence of nitrate ions in sulphuric acid solutions. *J Electroanal Chem* 289:217–235
110. Sazou D, Pagitsas M (1991) Polarization behaviour of a cobalt rotating disc electrode in sulphuric acid solutions in the absence and presence of chloride ions. *J Electroanal Chem* 304:171–185
111. Sazou D, Pagitsas M (1991) Periodic and aperiodic current oscillations induced by the presence of chloride ions during electrodisolution of a cobalt electrode in sulfuric acid solutions. *J Electroanal Chem* 312:185–203
112. Sazou D, Pagitsas M (1993) Current oscillations associated with pitting corrosion processes induced by iodide ions on the partially passive cobalt surface polarized in sulphuric acid solutions. *Electrochim Acta* 38:835–845
113. Pagitsas M, Sazou D (1995) The effect of a sinusoidal potential perturbation on the active-passive transition region of cobalt in a phosphoric acid solution. *J Electroanal Chem* 386:89–99
114. Pagitsas M, Sazou D (1995) Experimental bifurcation analysis of the cobalt/phosphoric acid electrochemical oscillator. *Electrochim Acta* 40:755–766
115. Alonzo V, Darchen A, Le Fur E, Pivan JY (2002) Electrosynthesis of vanadophosphate by anodic oxidation of vanadium in phosphoric acid solutions. *Electrochem Commun* 4:877–880
116. Alonzo V, Darchen A, Le Fur E, Pivan JY (2006) Electrochemical behaviour of a vanadium anode in phosphoric acid and phosphate solutions. *Electrochim Acta* 51:1990–1995
117. Gorzkowski MT, Wesołowska A, Jurczakowski R, Ślepski P, Darowicki K, Orlik M (2011) Electrochemical oscillations and bistability during anodic dissolution of vanadium electrode in acidic media—Part I. Experiment. *J Solid State Electrochem* 15:2311–2320. doi:[10.1007/s10008-011-1463-z](https://doi.org/10.1007/s10008-011-1463-z)
118. Gorzkowski MT, Orlik M (2011) Electrochemical oscillations and bistability during anodic dissolution of vanadium electrode in acidic media—Part II. The model. *J Solid State Electrochem* 15:2321–2330. doi:[10.1007/s10008-011-1464-y](https://doi.org/10.1007/s10008-011-1464-y)
119. Gilbertson LI, Fertner WO (1942) *Trans Electrochem Soc* 81:199
120. Feancis HT, Colner WH (1950) Cyclic phenomena observed in the electropolishing of silver. *J Electrochem Soc* 97:237–240
121. Lal H, Thirsk HR, Wynne-Jones WFK (1951) A study of the behaviour of polarized electrodes. Part I. The silver/silver halide system. *Trans Faraday Soc* 47:70–77
122. Lal H, Thirsk HR, Wynne-Jones WFK (1951) The anodic polarization of silver in halide solutions. Part II. Periodic phenomena occurring during polarization. *Trans Faraday Soc* 47:999–1006
123. Corcoran SG, Sieradzki K (1992) Chaos during a growth of an artificial pit. *J Electrochem Soc* 139:1568–1573

124. Franck UF (1958) Instabilitäterscheinungen an passiviebaren Metallen. *Z Elektrochem* 62:649–655
125. Vetter K (1967) *Electrochemical kinetics*. Academic, New York
126. Podestá JJ, Piatti RCV, Arviá AJ (1979) Periodic current oscillations at the gold/acid aqueous interfaces induced by HCl additions. *Electrochim Acta* 24:633–638
127. Diard JP, Le Gorrec B, Saint-Aman E (1983) Etude des structures de dissolution anodique de l'or en milieu acide. *Electrochim Acta* 28:1211–1213
128. Li ZL, Wu TH, Niu ZJ, Huang W, Nie HD (2004) In situ Raman spectroscopic studies of the current oscillations during gold electrodisolution in HCl solutions. *Electrochem Commun* 6:44–48
129. Mao BW, Ren BM, Cai XW, Xiong LH (1995) Electrochemical oscillatory behavior under a scanning microscopic configuration. *J Electroanal Chem* 394:155–160
130. Zheng J, Huang W, Chen S, Niu Z, Li Z (2006) New oscillatory phenomena during gold electrodisolution in sulfuric acid containing Br⁻ or in concentrated HCl. *Electrochem Commun* 8:600–604
131. Bargeron CB, Givens RB (1977) Source of oscillations in the anode current during the potentiostatic pitting of aluminum. *J Electrochem Soc* 124:1230–1232
132. Wilhelmsen W, Arnesen T, Hasvold Ø, Størkersen WJ (1991) The electrochemical behavior of Al-In alloys in alkaline electrolytes. *Electrochim Acta* 36:79–85
133. Lee W, Kim JC, Gösele U (2010) Spontaneous current oscillations during hard anodization of aluminum under potentiostatic conditions. *Adv Funct Mater* 20:21–27
134. Grauer R, Wehr P, Engell HJ (1969) Electron-optical and electrochemical investigation into the passivation behavior of fine lead in hot concentrated sulfuric acid. *Werkst Korros* 20:94–98
135. Abd El Aal EE (1992) Effect of chlorate and perchlorate anions on lead passivity in NaOH solutions under galvanostatic conditions. *Corrosion* 48:482–488
136. Bhaskara Rao ML (1967) Electrochemical studies on lead in organic electrolytes. *J Electrochem Soc* 114:665–668
137. Hull MN, Ellison JE, Toni JE (1970) The anodic behavior of zinc electrodes in potassium hydroxide electrolytes. *J Electrochem Soc* 117:192–198
138. Hull MN, Toni JE (1971) Formation and reduction of films on amalgamated and non-amalgamated zinc electrodes in alkaline solutions. *Trans Faraday Soc* 67:1128–1136
139. Podesta JJ, Piatti RCV, Arvia AJ (1982) Comparative electron microscopy (SEM) examination of Fe, Au and Zn electrodes surfaces polarized in different regions of potentiostatic *I/E* behavior. *Corrosion NACE* 38:599
140. McKubre MCH, Macdonald DD (1981) The dissolution and passivation of zinc in concentrated aqueous hydroxide. *J Electrochem Soc* 128:524–530
141. Frackowiak E, Kiciak M (1988) Application of the rotating disk electrode for the investigation of polycrystalline zinc in concentrated alkaline solutions with admixture of polyethylene glycol. *Electrochim Acta* 33:441–443
142. Shams El Din AM, Abd El Wahab FM (1964) On the anodic passivity of tin in alkaline solutions. *Electrochim Acta* 9:883–896
143. Shams El Din AM, Kamel LA (1972) Studies on the anodic and cathodic polarization of amalgams—V. The behaviour of tin amalgams in alkaline solutions. *Electrochim Acta* 17:491–501
144. Strirrup BN, Hampson NA (1976) Anodic passivation of Sn in sodium hydroxide solutions. *J Electroanal Chem* 67:45–56
145. Drogowska M, Brossard L, Menard H (1991) Influence of chloride ions on the anodic dissolution of tin in bicarbonate and phosphate solutions at pH 8. *J Electrochem Soc* 138:1243–1250
146. Vicentini B, Sinigaglia D, Taccani G (1975) Crevice corrosion of titanium. Behaviour of galvanic cell between shielded and unshielded titanium in sulphuric acid. *Corrosion Sci* 15:479–492
147. Okada T (1981) The pitting potential of titanium in bromide solutions. *Dengi Kagaku Oyobi Kogyo Butsuri Kagaku* 49:584

148. Warczak M, Sadkowski A (2009) Oscillatory regime of titanium anodization under voltage control. *Electrochem Commun* 11:1733–1735
149. Ammar IA, Khalil MW (1971) Behavior of bismuth as valve metal in phosphate, borate, benzoate and tartrate solutions. *J Electroanal Chem* 32:373–386
150. Galushko VP, Zavgorodnaya EF, Podol'skaya NV, Tukhaya OK (1972) Cadmium behavior during an anodic oxidation in alkaline solution. *Ukr Khim Zh* 38:432
151. Kadaner LI, Fedchenko VM, Ermolov IB (1981) Periodic phenomena in the electrochemical dissolution of niobium under alternating current conditions. *Elektrokhimiya* 17:138
152. Engelgardt GR, Dikuser AI (1986) Thermokinetic instability of electrode processes: part I. Theoretical analysis. *J Electroanal Chem* 207:1–9
153. Schuster R, Kirchner V, Allongue P, Ertl G (2000) Electrochemical micromachining. *Science* 289:98–101. doi:10.1126/science.289.5476.98
154. Schöll E (2005) Nonlinear spatio-temporal dynamics and chaos in semiconductors. Cambridge University Press, Cambridge
155. Josseaux P, Micheau JC, Kirsch de Mesmaecker A (1985) Photocurrent oscillations at photoanodes of CdS films. *Electrochim Acta* 30:1093–1094
156. Marcu V, Tenne R (1988) Photocurrent oscillations in the CdTe electrolyte systems. *J Phys Chem* 92:7089–7092
157. Marcu V, Strehblow HH (1991) Current oscillations of Cd_{0.2}Hg_{0.8}Te in a Na₂S–CsOH solution. *Electrochim Acta* 36:869–875
158. Turner DR (1958) Electropolishing silicon in hydrofluoric acid solutions. *J Electrochem Soc* 105:402–408
159. Gerischer H, Lübke M (1988) Electrolytic growth and dissolution of oxide layers on silicon in aqueous solutions of fluorides. *Ber Bunsenges phys Chem* 92:573–577
160. Chazalviel JN, Etman E, Ozanam F (1991) A voltammetric study of the anodic dissolution of p-Si in fluoride electrolytes. *J Electroanal Chem* 297:533–540
161. Ozanam F, Chazalviel JN, Radi A, Etman M (1991) Current oscillations in the anodic dissolution of silicon in fluoride electrolytes. *Ber Bunsenges Phys Chem* 95:98–101
162. Ozanam F, Chazalviel JN, Radi A, Etman M (1992) Resonant and nonresonant behavior of the anodic dissolution of silicon in fluoride media. An impedance study. *J Electrochem Soc* 139:2491–2501
163. Chazalviel JN, Ozanam F (1992) A theory for the resonant response of an electrochemical system: self-oscillating domains, hidden oscillation, and synchronization impedance. *J Electrochem Soc* 139:2501–2508
164. Stumper J, Greef R, Peter LM (1991) Current oscillations during anodic dissolution of p-Si in ammonium fluoride: an investigation using ring-disc voltammetry and ellipsometry. *J Electroanal Chem* 310:445–452
165. Blackwood DJ, Borazio A, Greef R, Peter LM, Stumper J (1992) Electrochemical and optical studies of silicon dissolution in ammonium fluoride solutions. *Electrochim Acta* 37:889–896
166. Lewerenz HJ, Schlichthörl G (1992) Light-induced oscillating reactions of silicon in ammonium fluoride solutions: part I. Simultaneous photocurrent and excess microwave reflectivity measurements. *J Electroanal Chem* 327:85–92
167. Lewerenz HJ (1992) Anodic oxides on silicon. *Electrochim Acta* 37:847–864
168. Lewerenz HJ, Aggour M (1993) On the origin of photocurrent oscillation at Si electrodes. *J Electroanal Chem* 351:159–168
169. Ozanam F, Chazalviel JN (1993) In-situ infrared characterization of the electrochemical dissolution of silicon in a fluoride electrolyte. *J Electron Spectrosc Relat Phenom* 64 (65):395–402
170. Hassan HH, Sculfort JL, Etman M, Ozanam F, Chazalviel JN (1995) Kinetic and diffusional limitations to the anodic dissolution of p-Si in fluoride media. *J Electroanal Chem* 380:55–61

171. Nast O, Rauscher S, Jungblut H, Lewerenz HJ (1998) Micromorphology changes of silicon oxide on Si(111) during current oscillations: a comparative in situ AFM and FTIR study. *J Electroanal Chem* 422:169–174
172. Ozanam F, Blanchard N, Chazalviel JN (1993) Microscopic, self-oscillating domains at the silicon surface during its anodic dissolution in a fluoride electrolyte. *Electrochim Acta* 38:1627–1630
173. Chazalviel JN, Ozanam F (2010) Current oscillations in the anodic dissolution of silicon: on the origin of a sustained oscillation on the macroscopic scale. *Electrochim Acta* 55:656–665
174. Safi M, Chazalviel JN, Cherkaoui M, Belaïdi A, Gorochov O (2002) Etching of n-type silicon in (HF+oxidant) solutions: in situ characterization of surface chemistry. *Electrochim Acta* 47:2573–2581
175. Amin MA, Frey S, Ozanam F, Chazalviel JN (2008) Macromorphologies in electrochemically formed porous silica. *Electrochim Acta* 53:4485–4494
176. Slimani A, Iratni A, Chazalviel JN, Gabouze N, Ozanam F (2009) Experimental study of macropore formation in p-type silicon in a fluoride solution and the transition between macropore formation and electropolishing. *Electrochim Acta* 54:3139–3144
177. Föll H, Carstensen J, Christophersen M, Hasse G (2000) A new view of silicon electrochemistry. *Phys Stat Sol A* 182:7–16
178. Hasse G, Christophersen M, Carstensen J, Föll H (2000) New insights into Si electrochemistry and pore growth by transient measurements and impedance spectroscopy. *Phys Stat Sol A* 182:23–29
179. Lölkes S, Christophersen M, Langa S, Carstensen J, Föll H (2003) Selforganized formation of crystallographically oriented octahedral cavities during electrochemical pore etching. *Mater Sci Eng B* 101:159–163
180. Christophersen M, Langa S, Carstensen J, Tiginyanu IM, Föll H (2003) A comparison of pores in silicon and pores in III-V compounds materials. *Phys Stat Sol A* 197:197–203
181. Chazalviel JN, Wehrspohn RB, Ozanam F (2000) Electrochemical preparation of porous semiconductors: from phenomenology to understanding. *Mater Sci Eng B* 69–B70:1–10
182. Parkhutik VP, Sasano J, Ogata Y, Matveeva E (2003) Oscillatory electrochemical reaction at corroding silicon surface. *Proc SPIE* 5114:396–405
183. Parkhutik VP (2006) Oscillations of open-circuit potential during immersion plating of silicon in CuSO₄/HF solutions. *Russ J Electrochem* 42:512–522
184. Lehmann V (2002) *Electrochemistry of silicon. Instrumentation, science, materials and applications*. Wiley-VCH, Weinheim

About the Author



Marek Orlik studied at the Faculty of Chemistry of the University of Warsaw, where he in 1990 received his Ph.D. for the studies of electrode mechanisms of cyanide complexes of transition metals, under the supervision of Zbigniew Galus. At the same University in 2000, he completed habilitation for the studies of self-organization phenomena in electrochemical systems. In 2004, he became an Associate Professor at the home Faculty, and in 2010, he was nominated a Titular (full) Professor of Chemistry. In the years 1996–1998, as a scholarship holder of the *Alexander von Humboldt Foundation*, he worked with Karl Doblhofer and Gerhard Ertl in the Fritz Haber Institute of the Max Planck Society in Berlin, studying self-organizing electro-convective phenomena. At the University of Linz (Austria), he cooperated with Gerhard Gritzner in the area of electrode kinetics in nonaqueous solvents and computer modeling of electrode processes. His current research activities, including both experimental and theoretical studies, focus on self-organization phenomena in electroreduction processes of complex compounds, in electrooxidation of metal electrodes, and in homogeneous redox processes involving hydrogen peroxide. He has published several dozen papers in the area

of both classical electrode kinetics and dynamic instabilities in electrochemical and chemical processes. He is also an author of a book "Oscillating reactions. Order and Chaos," published in Poland in 1996 and a coauthor (with Zbigniew Galus) of three chapters, devoted to electrochemistry of gold, silver, and mercury in a recent edition of "Encyclopedia of Electrochemistry" (Wiley, 2006). Besides scientific and educational activity at the University of Warsaw, he also significantly contributes to the chemistry education at the secondary school level, through the long-year involvement in the Polish and International Chemistry Olympiads, as well as is the editor of the Polish journal for school teachers.

About the Editor



Fritz Scholz is Professor at the University of Greifswald, Germany. Following studies of chemistry at Humboldt University, Berlin, he obtained a Dr. rer. nat. and a Dr. sc. nat. (habilitation) from that University. In 1987 and 1989, he worked with Alan Bond in Australia. His main interest is in electrochemistry and electroanalysis. He has published more than 280 scientific papers, and he is editor and coauthor of the book “Electroanalytical Methods” (Springer, 2002, 2005, 2010 and Russian Edition: BINOM, 2006), coauthor of the book “Electrochemistry of Immobilized Particles and Droplets” (Springer, 2005), coeditor of the “Electrochemical Dictionary” (Springer, 2008), and coeditor of volumes 7a and 7b of the “Encyclopedia of Electrochemistry” (Wiley-VCH, 2006). In 1997, he has founded the *Journal of Solid State Electrochemistry* (Springer) and serves as Editor-in-Chief since that time. He is the editor of the series “Monographs in Electrochemistry” (Springer) in which modern topics of electrochemistry are presented. Scholz introduced the technique “Voltammetry of Immobilized Microparticles” for studying the electrochemistry of solid compounds and materials, he introduced three-phase electrodes to determine the Gibbs energies of ion transfer between immiscible liquids, and currently he is studying the interaction of free oxygen radicals with metal surfaces, as well as the interaction of liposomes with the surface of mercury electrodes in order to assess membrane properties.

Index

A

Activator–inhibitor system, 52
Alcohols, anodic oxidation, instabilities, 392
multistability/excitability, 399
Aluminum, oscillatory dissolution, 496
Amplification, 2
Anodic oxidation, 158, 327
temporal instabilities, 327
Anodic polarization, 185, 345
Anodic pre-polarization, 176,
Anodic process, 81, 96, 137, 139, 228, 284
Attractor, 5, 6, 17, 28, 128, 145, 331
Au(111)/Au(110) electrodes, 209
Au(poly) electrodes, 212

B

Basin of attraction, 4
Belousov–Zhabotinsky (BZ) reaction, 36, 470
Bifurcation diagram, cross-shaped, 33
saddle–node, 12
Bifurcations, 2
homoclinic, 37
Birhythmicity, 3
Bismuth, electrode potential oscillations, 500
Bistability, 3, 9, 31
Blue sky bifurcation, 12
Bursting oscillations, 434
1-Butanol, anodic oxidation, instabilities, 399

C

Cadmium, potential oscillations, 500
Canard explosion, 50, 203, 242
Carbon monoxide, anodic oxidation,
oscillations, 345
electrooxidation, 187
slow mass transport, 347

Cathodic processes, temporal instabilities, 197
Chaos, 64
control, 68
Feigenbaum scenario, 64
Pomeau and Manneville, 66
Ruelle, Takens, and Newhouse, 64

Chaotic oscillations, 13
Characteristic (eigenvalue) equation, 15, 16
Closed orbit, 55
Cobalt electrodes, oscillatory oxidation, 485
Co/HCl + CrO₃ system, 485
Co/H₂SO₄ + NO₃⁻, Cl⁻ system, 486
Control parameters, 2
Coordinated azide ligands, 279
Copper, oscillatory electrodisolution, 454
Corrosion processes, temporal instabilities, 425
Crises, 66, 331
Cross-activator–inhibitor, 53
Cu/Cl⁻ system, 455
Cu/H₃PO₄ system, 458
Cu/SO₄²⁻ system, 454
Cu²⁺–tribenzylamine oscillator, 289
Cycles, saddle–node bifurcation, 35

D

Degenerate nodes, 24
Delay-differential equations, 13
Deterministic chaos, 63
Differential equations, autonomous, 4
ODEs, 2
PDEs, 2
Diffusion–convection, 225
Dissipative structures, 1
Dynamical systems, nullcline
representation, 38
Dynamical variables, fast/slow, 42

Dynamic electrochemical impedance spectroscopy (DEIS), 183
Dynamic self-organization, 1

E

Eigenvalues, 16, 23
 complex conjugated pair (principal pair), 57
Eigenvector, 23
Electrocatalytic Koper–Sluyters model, 168
Electrochemical graphite oxide (EGO), 416
Electrochemical impedance spectroscopy (EIS), 111, 183
Electrochemical instabilities, essential/non-essential variables, 102
Electrochemical oscillators, classification based on impedance, 148
Electrochemical systems, stability, 75
Electrochromic oscillator, 358
Electrode potential, 149
Electrosorption, 157, 329
Equilibrium point, 3
Ethanol, anodic oxidation, instabilities, 397
Ethylene, anodic oxidation, oscillations, 415
Excitability, ethanol oxidation, 400
Existence and uniqueness theorem, 55
Explosion (interior crisis), 66, 331

F

False bifurcation, 51
Faradaic process, 80
Farey tree, 469
Feedback loops, 1, 52, 371, 407
Fe/H₂SO₄ oscillatory system, 434
Film breakdown potential, 432
Flade potential, 425
Focus, stable, 5
Fold bifurcation, 12
Formaldehyde, oscillatory oxidation, 382
Formate ions, anodic oxidation, instabilities, 357
Formic acid, oxidation, 370
Franck–FitzHugh model, 441
Frumkin correction, 81, 200
Frumkin effect, 81, 197
Frumkin isotherm, 156

G

Galvanostatic control, 79, 86, 91
Galvanostatic oscillations, 335

Global bifurcations, oscillations, 34
Gold, oscillatory dissolution, 495
Gouy–Chapman–Stern model, 198
Graphite, anodic oxidation, oscillations, 416

H

Hard transition, 28
Hidden negative resistance (HN–NDR), 409
Highly oriented pyrographite (HOPG), 416
Homoclinic orbits, 37, 63
Hopf bifurcation, 2, 17, 18, 25, 57
 subcritical, 28
 supercritical, 26
Hydrazine, anodic oxidation, oscillations, 414
Hydrogen, oscillations in anodic oxidation, 327
 CO, anodic oxidation, bistability/oscillations, 354
Hydrogen peroxide, oscillatory reduction, 294
Hysteresis, 29

I

Ignition potential, 350
Impedance spectroscopy, electrochemical
 pattern formation, 187
 spectra, bifurcations, 128
Indira and Ross model, 477
Indium–thiocyanate polarographic oscillator, 229
Inhibitor, 52
 oscillator, 292
Instabilities, adsorption on electrodes, 156
Intermittencies, 66
Iodate(V) ions, electroreduction, 217
Iodide ions, anodic oxidation, oscillations, 415

J

Jacobian matrix, nullclines, 54

K

Keddham et al. model, Ni/H₂SO₄ system, 479
Koper–Sluyters model, 168
Kramers–Kronig transforms, 116

L

Langmuir–Hinshelwood (LH) mechanism, 347, 352
Lead, oscillatory electrodedissolution, 497

- Limit cycles, 5, 26
Load, 75
 line, 75, 76
Loss of stability, 2
Lyapunov (Liapunov) theorem/stability,
 4, 6, 7
- M**
Manifold, 21
Metal electrodes, anodic dissolution,
 oscillations, 425
 porous salt layer, 429
Methanol, oxidation, 376, 392
Micromachining, metal electrodisolution
 processes, 501
Mixed-mode oscillations (MMO), 13, 210, 330
Multistability, 3
- N**
N-dimensional dynamical system, linear
 stability analysis, 57
Negative differential resistance (NDR),
 75, 77, 427
Neural excitation, 434
Neuronal cells, stimulus–response, 379
Nickel/H₂SO₄, oscillatory dissolution, 473
Nickel(II)–thiocyanate electroreduction, 249
Ni(II)–N₃[−], tristability, 276
Niobium, electrochemical dissolution, 500
Nodes, 18
Nonlinear, 2
Nullclines, 38
 Jacobian matrix, 54
- O**
ODEs, 2
OREGONATOR, 47
- P**
Passivation/dissolution, 425
Passive film, 430
PDEs, 2, 89, 239, 366
Period-doubling bifurcations, 464
Peroxisulfate ions, electroreduction, 197
Phase space, 4
Phase trajectories, 21
Phasors, 112
Pitting corrosion, 432, 434
- Poincaré–Bendixson theorem, 55
Poincaré sections, 68
Point attractor/repeller, 4
Polarographic processes, oscillations, 289
Potentiostatic conditions, 76
Potentiostatic oscillations, 340
Power source, 75
2-Propanol, anodic oxidation,
 instabilities, 397
Pyrite, anodic oxidation, 409
- R**
Relaxation, oscillations, 42
Repeller, 5–7
Resonance, 130, 175, 472, 506
Ruelle–Takens–Newhouse (RTN) chaos, 412
- S**
Saddle–loop (homoclinic) bifurcation, 37
Saddle–node bifurcations, 11, 18, 25, 31, 57
 cycles, 204
 galvanostatic, 88
Saddle–node infinite period (SNIPER)
 bifurcation, 36
Saddle point, 18, 57, 92, 137
Self-activator, 98
Semiconductor electrodes, anodic oscillatory
 dissolution, 504
Semiconductors, cadmium-based, 504
Silicon, electrodisolution, fluoride media, 506
Silver, oscillatory dissolution, 492
Stability, 3
 asymptotic, 3, 7
 impedance, 125
 local, 4, 18
 types, 5
Stability analysis, linear, 7
 zero–pole representation, 174
Stable limit cycle, 17
Stable oscillatory regime, 2
Star nodes, 24
Steady state, half-stable, 11
Stoichiometric network analysis (SNA), 370
Strange attractor, 5, 63
Streaming mercury electrode, impedance, 117
 Ni(II)–thiocyanate electroreduction, 255
Sulfur compounds, oscillatory oxidation, 408
Supercycles, 66
Supporting electrolyte, 198
Synaptic transmission, unidirectional, 435

T

Tangent bifurcations, 164, 465
Temperature overcompensation, formic acid oxidation, 377
Time-resolved surface-enhanced infrared spectroscopy (SEIRAS), 389
Tin, anodic oscillations, 499
Titanium, oscillatory electrooxidation, 500
Trajectories, 4
Transfer function, 112
Transpassive region, 432
Transport overvoltage, 416
Trapping region, 56
Tristability, 278
Tungsten, galvanostatic electrodisolution, 500
Turning point bifurcation, 12

V

Vanadium electrodes, oscillatory oxidation, 489
V/H₃PO₄ system, 490
Volmer–Heyrovsky mechanism, evolution of hydrogen/chlorine, 166

W

Warburg impedance, 114
Wigner–Ville distribution (WVD), 184

Z

Zinc, anodic dissolution, 498